Reconstructing high resolution environmental change from carbonate-rich lakes in Turkey and Mexico using varve microfacies analysis

Nick Primmer

Thesis submitted to The University of Nottingham

For the degree of Doctor of Philosophy

May 2019

Approximate word count (excluding references): 83,000 words

Abstract

Analysis of lacustrine sediment records provide insight into terrestrial environmental change throughout the Holocene; however, poor chronological control often limits a record's ability to identify the precise dynamics and drivers of these changes. Exploring these important aspects of environmental change can develop our understanding of the mechanisms driving long-term climatology and its influence on regional hydrological systems. To fully investigate these past environmental systems, high resolution, climatically-sensitive proxies are required.

Here, microfacies analysis of varved sediment records from Nar Gölü, Turkey and Yaal Chac, Mexico provide long annually-resolved records of environmental, limnological and climatic change, from two regions lacking in continuous, high resolution archives. From Nar Gölü, varves were analysed from discrete sequences deposited during the early-mid and late Holocene (9,064 – 7,630 cal yrs BP and 2,540 – -51 cal yrs BP respectively), and from Yaal Chac, the early-mid Holocene (8,812 – 7,245 cal yrs BP and 5,346 – 4,295 cal yrs BP). These long, continuous depositional archives have permitted the reconstruction of both low- and high-frequency limnological change, where the sequences' incremental chronologies have further enabled the pace and timing of change to be identified and robustly dated.

In both lakes, organic-calcareous varve deposition is driven by the regions' wet-dry seasonality. At Nar Gölü, sedimentological calibration using meteorological data identified the March-May evaporation/precipitation ratio as the primary control on the deposition of endogenic carbonates. Comparing specific carbonate sublayers' mineralogy and thickness with their $\delta^{18}O_{carbonate}$ value further indicates that regional water balance over the last 2,600 years primarily drives carbonate deposition. Considering the sites' similar seasonality and sedimentary microfacies, changes to the endogenic carbonate deposition and mineralogy are used to indicate high resolution changes to lake hydrology and the timing/intensity of dry-season E/P conditions in both lakes.

Spectral analysis of these varved records, which provide incremental timeseries, is used to identify the multi-decadal drivers to depositional variability. The Atlantic Multi-decadal Oscillation (AMO) is likely detected within both lake records at various stages through the Holocene, where changes to sea surface temperatures are known to influence moisture supply and rainfall during each region's respective wet-seasons. From Nar Gölü, changes to cyclicity are also proposed to reflect shifts in the

relative influence of Atlantic-and tropical-derived climates, as the multi-decadal variability of Indian monsoon intensity is also known to drive dry-season aridity.

Sedimentological-inferred changes to past conditions, specifically changes to the regional evaporation/precipitation (E/P) ratio, are finally used to provide the environmental context to societal change. Each region's wet-dry seasonality increases societal vulnerability to drought, where periods of elevated evaporation/precipitation conditions may have influenced food and/or water security, and hence socio-economic stability. Temporal correlation between microfacies and societal changes provide circumstantial evidence that climatic change may have contributed to major societal shifts through the Holocene in both Turkey and Mexico.

Acknowledgements

This PhD was funded, and hence made possible, by NERC via the Doctoral Training Partnership (DTP) Envision, and there are many people I would like to thank for their invaluable contribution of time, resources and support towards the completion of this work.

Firstly, I would like to thank my supervisors Matthew Jones and Sarah Metcalfe, who have endlessly offered their expert advice and support, helping me to focus ideas and vastly improve my research skills. My supervisor Achim Brauer, and his colleagues at the GFZ Potsdam, also deserve thanks for crucial training in microfacies analysis, academic support, and preparation of Yaal Chac's thin sections. I truly appreciate all the time and effort my supervisors have invested into this work.

Much of the data collection from Nar Gölü and Yaal Chac, and its analysis, has been possible through collaboration with engaged international teams. From Nar Gölü's working group, I would like to thank Warren Eastwood, Hakan Yiğitbaşıoğlu, Çetin Şenkul, Neil Roberts, Samantha Allcock, Mustafa Doğan, Aziz Ören, and Jonathan Dean; and from Yaal Chac's team, Roger Medina-Gonzalez, and Gerardo Diaz Duarte (in addition to my supervisors, Matthew Jones and Sarah Metcalfe, within both teams). These people have all offered instrumental academic and logistical support. I would also like to express my gratitude to Teresa Needham, whose lab support has been invaluable.

On a more personal note, my friends and family have all supported me greatly over the last four years. In particular, I would like to thank Ellie, for her constant help and encouragement which has always keep me going; Rowan, for his generous hospitality and boundless positivity; and Rachel, James, and Joe, with whom I could always share a good laugh. Finally, thank you to my family, whose selfless support has got me where I am today.









Table of Contents

Abstract ... 3
Acknowledgements ... 5
Table of Contents ... 6
List of Figures ... 9
List of Tables ... 15
1. Introduction ... 17
1.1 High resolution archives of environmental change ... 17
1.2 Environment-society relationship ... 19
1.3 Study sites ... 21
1.4 Varve sedimentology in lacustrine environments ... 23
1.4.1 Varve formation and preservation ... 23
1.4.2 Varve chronologies ... 29
1.4.3 The use of varves in palaeoclimatology ... 32
1.4.4 The use of varve sedimentology as a palaeoclimatic proxy ... 32
1.4.5 Lacustrine carbonate deposition ... 36
1.5 Aims and objectives ... 42
1.6 Thesis outline ... 45
2. Methodology ... 46
2.1 Core extraction ... 46
2.2 Core preparation ... 49
2.3 Varve sedimentology ... 50
2.3.1 Sediment microstratigraphic analysis ... 51
2.3.1.1 Thin section preparation ... 51
2.3.1.2 Microscopy ... 54
2.3.2 Imagery ... 56
2.3.3 Geochemical analysis (μXRF) ... 57
2.3.3.1 Lacustrine sediment core geochemistry ... 57
2.3.3.2 Catchment bulk sediment geochemistry ... 61
2.3.4 Total carbon content ... 62
2.4 Contemporary environmental monitoring ... 64
2.4.1 Sediment Traps ... 64
2.4.2 Water sampling ... 65
2.4.3 Modern calibration ... 67
2.5 Additional unpublished data ... 68

3. Nar Gölü 71
3.1 Study site and regional climatology 71
3.1.1 Study site 71
3.1.2 Regional climatology 77
3.1.2.1 Contemporary climatology of Turkey 77
3.1.2.2 Holocene climate change 82
3.2 Lithology and chronology 98
3.2.1 Lithology 98
3.2.2 Chronology 103
3.3 Sedimentology: results and interpretation 107
3.3.1 Early-mid Holocene: Units 4-5 107
3.3.1.1 Varve microfacies 108
3.3.1.2 Sediment geochemistry 119
3.3.2 Late Holocene: Unit 1 130
3.3.2.1 Varve microfacies 130
3.3.2.2 Sediment geochemistry 150
3.3.3 Sedimentology: Summary 160
3.4 Discussion 162
3.4.1 Early-mid Holocene: Units 4-5 162
3.4.1.1 Early-mid Holocene spectral analysis 168
3.4.1.2 Environmental context for societal change 170
3.4.2 Late Holocene: Unit 1 171
3.4.2.1 Late Holocene spectral analysis 176
3.4.2.2 Environmental context for societal change 182
3.5 Chapter summary 186
4. Yaal Chac 188
4.1 Study site and regional climatology 188
4.1.1 Study site 188
4.1.2 Regional climatology 194
4.1.2.1 Contemporary climatology 194
4.1.2.2 Holocene climate change 200
4.2 Lithology and chronology 218
4.2.1 Lithology 218
4.2.2 Chronology 221
4.2.2.1 Independent radiometric dating 221
4.2.2.2 Anchoring the laminated Unit 2 225
4.3 Sedimentology: results and interpretation 229

4.3.1 Early-mid Holocene: Unit 2 229
4.3.1.1 Varve microfacies 229
4.3.1.2 Sediment geochemistry 245
4.3.2 Mid-late Holocene: Unit 1 257
4.3.2.1 Sediment geochemistry 259
4.3.4 Additional data 270
4.3.5 Sedimentology: Summary 273
4.4 Discussion 274
4.4.1 Early Holocene (>8,013 cal yrs BP; M2 varve deposition) 274
4.4.2 Mid-Holocene / Northgrippian (8,013 - 4,295 cal yrs BP; M1 varve deposition) 275
4.4.2.1 Early-mid Holocene spectral analysis 284
4.4.3 Late Holocene / Meghalayan (4,295 cal yrs BP - present day) 288
4.4.3.1 Environmental context for societal change 293
4.5 Chapter summary 297
5. Joint conclusions 300
5.1 Linking sediment deposition to environmental processes 300
5.2 High resolution environmental reconstruction 301
5.3 Comparison between Nar Gölü and Yaal Chac 304
5.4 Environmental context for societal change 307
6. References 309
7. Appendix and supplementary material 351

List of Figures

Figure 1.1 *– Global land surface temperature (top) and total rainfall (bottom) in January (left) and July (right); study sites Yaal Chac, Mexico and Nar Gölü, Turkey are marked by yellow circles. The average position of the ITCZ (red dashed line) displays its summer and winter extents, and drives the increased precipitation observed, the belt of low rainfall north of the ITCZ reflects the subtropical high pressure belt's position. Data were collected by NASA's Terra and Tropical Rainfall Measuring Mission (TRMM) satellites, and taken from NASA Earth Observatory (2016).* 22

Figure 1.2 *– Global distribution of lacustrine varves included within the Varves Database (VBD) (after Zolitschka et al. 2015)* 25

Figure 1.3 *– Conceptual diagram displaying the key controls driving carbonate precipitation in lake systems.* 39

Figure 1.4 *– The influence of pH on carbonate species (after Lindsay, 1979)* 40

Figure 2.1 – *Nar Gölü catchment area (grey area) and lake bathymetry (coloured contours). The NAR10 coring site (yellow dot), NAR01/02 coring sites (white dots), and freshwater springs (blue dots) are marked within the lake and catchment. [*Figure *adapted from Jones, 2004; bathymetry data from Smith, 2010]* 48

Figure 2.2 – *A bathymetric map of Yaal Chac. Coring sites YC14 (yellow dot) and YC16 (white dot) are marked in the lake.* 49

Figure 2.3 – *Examples of tie points, marked by white pins, between core drives using the sediment stratigraphy in discontinuously (a) and continuously (b) laminated sediment; images of Yaal Chac's master sequence.* 50

Figure 2.4 *– Method used for preparing a thin section from unconsolidated sediment* 53

Figure 2.5 – *Cross sectional, schematic diagram outlining where sediment was cut in order to obtain a 2cm overlap between thin sections. Due to the narrow diameter of the core, sections were cut over-and-under.* 53

Figure 2.6 – *Itrax µXRF scanner at the University of Aberystwyth. Prepared cores are placed inside its left arm, and cores are moved under the scanner in the middle.* 58

Figure 2.7 – *Distribution of bulk sediment samples (red dots) for geochemical analysis using conventional XRF from Nar Gölü (a) and Yaal Chac (b). The white line on image (b) denotes Yaal Chac's lake edge. Nar Gölü's* Figure *(a) taken from Allcock (2013).* 62

Figure 2.8 – *Schematic diagram and photograph of a sediment trap created and deployed at Nar Gölü during fieldwork in May 2015.* 65

Figure 3.1 – *(a) Nar Gölü's situation within Turkey and the Anatolian Plateau (top), and a topographic map displaying Nar Gölü and its surrounding crater (bottom). (b) Photograph of Nar Gölü (area of ~0.7km^2) taken from the top of the crater's rim, northeast of the lake. The Emergent macrophytes, including Phragmites and Juncus, surround the water, and the alluvial fan with the Pinus plantation can be seen (top left of image). The exposed ignimbrite along the southern edge of the crater, containing the two springs, can also be seen (top left of image).* 72

Figure 3.2 *- δD-δ^{18}O isotope plot comparing the Global Meteoric Water Line, Ankara precipitation, and water samples taken from three catchment springs and from Nar Gölü's surface (Dean et al. 2015b). Those samples furthest from the Meteoric Water Line suggests evaporative enrichment.* 73

Figure 3.3 *– (a) Nar Gölü's thermal stratification and mixing between June 2015 and April 2016, the convergence of temperature through the water column denotes lake mixing (between the dotted line); and (b) the limnological changes through Nar Gölü's vertical profile, as measured in July 2009; photic zone as measured via Secchi-disc measurement (red zone), and the thermo- and chemoclines (grey dotted line) are also displayed.* 74

Figure 3.4 – *Distribution of total annual precipitation in Turkey over 1970-2000 (a) (Fick and Hijmans, 2017), and modern climatology over 1980-2010 of Niğde (b) (data provided by the Turkish Meteorological Service, 2011)* 76

Figure 3.5 – *Average climate over the whole of Turkey between 1970-2000 (Sensoy et al. 2008)*

Figure 3.6 – *Mean temperature (top) and annual precipitation (bottom) over Turkey; data interpolated from monthly data recorded from weather stations between 1960-90 (Fick and Hijhams, 2017)* 78

Figure 3.7 *– The five predominant depression trajectories over Turkey (taken from Karaca et al. 2000)* 79

Figure 3.8 *- Maps displaying the location of study site, Nar Gölü (1), and a selection of other palaeoclimatic records discussed here: Eski Acıgöl (2), Lake Akgöl (3), Lake Pinarbasi (4), Catalhoyük-East (5), Lake Tecer (6), Tell Arslantepe (7), Lake Iznik (8), Lake Sünnet (9), Sofular Cave (10), Lake Gölhisar (11), Lake Van (12), Lake Zeribar (13), Soreq Cave (14), and Dead Sea (15).* 82

Figure 3.9 *– Comparison of a selection of eastern Mediterranean palaeoclimatic record. The order of the records follows a north-south distribution. Wet conditions inferred from each record are shaded in grey, with the 8.2 ka events conditions from Sofular cave shaded in dark grey (Göktürk et al. 2011). 'Rapid Climate Change' events are displayed by dashed boxes (Mayewski et al. 2004). (a) Sofular cave $\delta^{13}C$ (top), initial 234U/238U (middle) and the growth rate (bottom) records (Göktürk et al. 2011); (b) Microcharcoal concentrations from lake Eski Acigöl, Central Anatolia (Turner et al. 2008); (c) Pistachio pollen percentage from Lake Van (Wick et al. 2003); (d) Decidious pollen (%) from the northern Aegean Sea core, GeoTu-SL152 (Kotthoff et al. 2008); (e) $\delta^{18}O$ record from the southern Aegean Sea core LC21 (Rohling et al. 2002); (f) $\delta^{18}O$ record from the Jeita cave, Lebanon (Verheyden et al. 2008); (g) $\delta^{18}O$ and $\delta^{13}C$ records from the Soreq cave, Israel (Bar-Matthews et al. 2003); (h) Sea surface salinity estimates from the northern Red Sea core GeoB5844-2 (Arz et al. 2003). i) $\delta^{18}O$ record from the Qunf Cave, Oman (Fleitmann et al. 2007). [Taken from Göktürk et al. 2011]* 85

Figure 3.10 - *A summary of the timings of wet/arid phases proposed in the literature based from the eastern Mediterranean [taken from Bakker et al. 2013]* 95

Figure 3.11 *- NAR10's composite master sequence (far left column), comprised of various sections from the NAR10 cores' drives (black columns), alongside the NAR01/02 core sequence (red columns); tie points used to correlate core sections are labelled 'Tp'. Sedimentary units (1-7) depict major changes to the sequence's lithostratigraphy. [*Figure *adapted from Allcock, 2013]* 99

Figure 3.12 *– Conceptual model of varve formation at Nar Gölü* 102

Figure 3.13 – *Age-depth model for NAR01/02 (grey line) and NAR10 (black line) master sequences. Repeated varve counts developed the chronologies (solid line), with linear interpolation used to connect floating sequences (dashed line) [from Dean et al. 2015a]* 106

Figure 3.14a *– Identification of aragonite from Nar Gölü via SEM, EDX and thin section microscopy. For each mineralogy, the elemental composition (top left) of the crystals pictured within the SEM image (top right) (Dean, 2014), and plane- and cross-polarised images taken under 200x magnification using a petrographic microscope at the University of Nottingham.* 110

Figure 3.14b *– Identification of calcite from Nar Gölü via SEM, EDX and thin section microscopy. For each mineralogy, the elemental composition (top left) of the crystals pictured within the SEM image (top right) (Dean, 2014), and plane- and cross-polarised images taken under 200x magnification using a petrographic microscope at the University of Nottingham.* 111

Figure 3.15 *– Thickness measurements of the varves' key sedimentological variables from Unit 4-5, subdivided by microfacies classification (grey line). Oxygen isotope data from carbonate material is also shown ($\delta^{18}O$ ‰ VPDB) (from Dean et al. 2015a). Gaps in stratigraphic data reflect sections of poor quality laminations.* 118

Figure 3.16 *- Principle components analysis' primary and secondary axes from Units 4-5, and its identification of Ca and Fe as key elements explaining geochemical variance.* 120

Figure 3.17 *– Comparison between the changes to key elements identified in the PCA (black lines) and the first two significant axes (grey lines) within Units 4-5; subdivided by microfacies classification (dotted lines).* 121

Figure 3.18 *– Changes to sediment microfacies and geochemical composition, relating specifically to calcium carbonate deposition over time, within Units 4-5 and subdivided by microfacies classification (grey lines).*

Figure 3.19 *– Changes to sediment microfacies and geochemical composition, relating specifically to organic deposition over time, within Units 4-5 and subdivided by microfacies classification (grey lines).* 125

Figure 3.20 *– Changes to sediment microfacies and geochemical composition, relating specifically to turbidite deposition over time, from Units 4-5 and subdivided by microfacies classification (grey lines). Correlation between geochemical and microfacies data are displayed (solid orange lines), and the dotted line highlights the detection peak which coincides with the gap in microstratigraphic data. Slight discrepancies between the alignment of turbidites and the detection of allogenic elements may be expected, as Itrax's incremental depth measurements are converted to age through the use of tie-points with the varve chronology.* 127

Figure 3.21 *– Changes to sediment microfacies and geochemical composition of Units 4-5, relating specifically to carbonate deposition, organic content and redox conditions in the hypolimnion over time, and subdivided by microfacies classification (grey lines).* 129

Figure 3.22 *– Identification of dolomite via SEM, EDX and thin section microscopy. For each mineralogy, the elemental composition (top left) of the crystals pictured within the SEM image (top right) (Dean, 2014), and plane- and cross-polarised images taken under 200x magnification using a petrographic microscope.* 132

Figure 3.23 *– Magnified (x10) images of typical varves from each of Nar Gölü's microfacies subclasses, as seen in plane-polarised (left) and cross-polarised (right) light. Coloured boxes display the extent of one varve, its distinct sublayers and the approximate boundaries measured; the colour and label of these boxes correspond with the conceptual diagram of microfacies (Table 7.2). All images are positioned such that the carbonate sublayers are deposited after the organic sublayers.* 139

Figure 3.24 *– Thickness measurements of the varves' key sedimentological variables from Unit 1, subdivided by microfacies classification (grey line). Oxygen isotope data from carbonate material is also shown ($\delta^{18}O$ ‰ VPDB) (from Dean et al. 2015a).* 144

Figure 3.25 *– Average thickness (mm) of calcite (left) and aragonite (right) sublayers according to their oxygen isotope composition. Isotopic values displayed are not corrected for mineral-dependent fractionation (+0.7‰ to the aragonite $\delta^{18}O$, as compared to calcite); applying a correction would effective move aragonite's thickness distribution down one row, thus still maintaining a distinct difference between isotopic-inferred water balance and carbonate sedimentology. Oxygen isotope data are analysed from the carbonate material (data from Jones et al. 2005; Dean et al. 2015a) .* 145

Figure 3.26 *– March-May evaporation/precipitation ratio (red line) alongside aragonite thickness (blue line) between 1935-1988.* 146

Figure 3.27 *– December-February precipitation (red line) alongside calcite thickness (blue line) between 1988-2000.* 147

Figure 3.28 *– Total annual precipitation (red line) alongside total organic thickness (blue line) and organic sublayers with high concentrations of carbonate minerals (green line) between 1935-2000.* 148

Figure 3.29 *– Example section of the Itrax µXRF core scan; variation to Ca (blue line) and Fe (red line) detection through the sediment is displayed.* 150

Fig***ure 3.30*** *- Principle components analysis' primary and secondary axes from Unit 1, and its identification of Ca and Fe as key elements explaining geochemical variance.* 152

Fig***ure 3.31*** *– Comparison between the changes to key elements identified in the PCA (black lines) and the first two significant axes (grey lines) within Unit 1; subdivided by microfacies classification (dotted lines).* 153

Figure 3.32 *– Changes to sediment microfacies and geochemical composition, relating specifically to calcium carbonate deposition over time, within Unit 1 and subdivided by microfacies classification (grey dashed lines).* 155

Figure 3.33 *– Changes to sediment microfacies and geochemical composition, relating specifically to organic deposition over time, within Unit 1 and subdivided by microfacies classification (grey dashed lines).* 157

Figure 3.34 *– Changes to sediment microfacies and geochemical composition, relating specifically to turbidite deposition over time, from Unit 1 and subdivided by microfacies classification (grey dashed lines). Slight disparity between thee geochemical and microfacies dataset is derived from the inclusion of turbidites into the age-depth model.* 160

Figure 3.35 *– Comparison of regional palaeorecords through the early-mid Holocene. (a) Nar Gölü's oxygen isotope record (black) (Dean et al. 2015a) alongside aragonite (blue) and calcite (red) sublayer thicknesses; (b) carbon isotope record from Sofular Cave (Göktürk et al. 2011); (c) oxygen isotope record from Soreq Cave, Israel (Bar-Matthews et al. 2003); (d) oxygen isotope record from Qunf Cave, Oman (Fleitmann et al. 2007).* 164

Figure 3.36 *– Comparison of regional palaeoclimatic archives. Summer temperature reconstructed from alpine tree ring thickness (Büntgen et al. 2016) (a), carbon isotopes from Sofular Cave (Göktürk et al. 2011) (b), Nar Gölü's aragonite (c) and calcite (d) sublayer thicknesses and (i) microfacies classification, Ti-detection from the Cariaco Basin indicative of mean ITCZ latitude (Haug et al. 2001) (e), and wavelet power over the 2-15 year band (f) and 50-130 year band (g), displaying NAO and AMO strength respectively (Ólafsdóttir et al. 2013). The Late Antiquity Little Ice Age (LALIA) (light grey; Büntgen et al. 2016) and the Dark Ages Cold Period (DACP) (dark grey; Helama et al. 2017) are depicted by the grey shading. Defined by Nar Gölü's M2a varve deposition between 1530-1797 AD, Little Ice Age (LIA) conditions are displayed (grey grading).* 175

Figure 3.37 – *Spectral signatures of M2's aragonite sublayer thicknesses during 589 BC – 535 AD (top left) and 1406 – 1988 AD (bottom left), and M1's calcite sublayer thicknesses during 535 – 1406 AD (top right)* 178

Figure 3.38 *– (a) Morlet wavelet analysis of total carbonate thickness across the 2561 contiguous varves; significant cyclicity ($p<0.05$) lies within the black line (yellow-red colour). Significant cyclicity can be seen to change through time; the dotted grey lines represent key cycles. (b) Change in the relative power of cyclicity over time; lines above the dotted line are significant ($p=0.05$ level) at that specific time. Results are displayed alongside the microfacies classification.* 180

Figure 4.1 – *(a) Yaal Chac's situation within Mexico and the Yucatán Peninsula (top), and a topographic map displaying cenote, Yaal Chac and the surrounding low-lying topography (bottom). (b) Photograph displaying Yaal Chac and the surrounding subtropical dry forest biome vegetation. Yaal Chac is much smaller than Nar Gölü, as its maximum diameter measures 125m, as compared to Nar Gölü's 990m. (Image courtesy of Prof Sarah Metcalfe)* 189

Figure 4.2 *- δD-$\delta^{18}O$ isotope plot comparing Meteoric Water Line with water samples taken from lakes across the Yucatán; unpublished data provided by Prof Sarah Metcalfe and undergraduate work, Clapich (2016). Those samples furthest from the Meteoric Water Line suggests evaporative enrichment.* 190

Figure 4.3 *– Yaal Chac's thermal stratification and mixing between December 2016 and November 2017 (a), the convergence of temperature through the water column denotes lake mixing; and the limnological changes through Yaal Chac's vertical profile, as measured in January 2009 (b); photic zone as measured via Secchi-disc measurement (red zone), and the thermo- and chemoclines (grey dotted line) are also displayed.* 192

Figure 4.4 *– Distribution of average annual precipitation over the Yucatán Peninsula over 1970-2000 (a) (Fick and Hijmans, 2017), and the modern climatology of Abala over 1980-2010 (b) (Conagua, 2017)* 193

Figure 4.5 – *Mean temperature (top), annual precipitation (middle) and topography (bottom) of Mexico; climatic data interpolated from monthly data recorded from weather stations* 195

between 1960-90 (Fick and Hijmans, 2017), and topographic map of Mexico, in feet above sea level [adapted from University of Texas State, 1975]

Figure 4.6 – *Map displaying the average summer (black, dashed line) and winter (blue, solid line) ITCZ position (adapted from Taylor et al.2012)* 196

Figure 4.7 *– Maps displaying the location of study site, Yaal Chac (1), and a selection of other palaeoclimatic records discussed here: X'Caamal (2), Tecoh Cave (3), Cenote San José Chulchaca (4), Ria Lagartos Biosphere Reserve (5), Punta Laguna (6), Coba (7), Chichancanab (8), Tzib (9), El Palmar (10), Puerto Arturo (11), Petén Itzá (12), Quexil (13), Macal Chasm (14), Yok Balum (15), Lago Verde (16), Cueva del Diablo (17), Venado Cave (18), Chilibrillo Cave (19), Miragoane (20), Laguna de Salvador (21), Laguna Castilla (22), and Cariaco Basin (23)* 200

Figure 4.8 *- The general timing and dynamics of climatic change as inferred from lacustrine systems within the Yucatán Peninsula. Climatic periods inferred from Lago Puerto Arturo (Wahl et al. 2014), Lake Petén Itzá, North Basin (Hillesheim et al. 2005; Mueller et al. 2009), Lake Petén Itzá, South Basin (Curtis et al. 1998), and Lake Chichancanab (Hodell et al. 1995). [Taken from Wahl et al. 2016]* 203

Figure 4.9 *– Pyrgophorus coronatus $\delta^{18}O$ records from Lake Punta Laguna and Lake Chichancanab, indicating a longer period of aridity throughout the entire Classic Period. (Taken from Curtis et al. 1996)* 209

Figure 4.10 *– (top) $\delta^{18}O$ record from Tecoh Cave speleothem, northwest Yucatán. (bottom) Isotope-inferred precipitation during the TCP (coloured in grey). Numbers refer to each of the short drought phases during a period of increased aridity as inferred by Medina-Elizalde et al. (2010). (Taken from Medina-Elizalde et al. 2010)* 211

Figure 4.11 *– $\delta^{18}O$ record of Aguada X'Caamal (a) (Hodell et al. 2005a), Lake Chichancanab (b) (Hodell et al. 2001), Punta Laguna (c) (Curtis et al. 1996), and Lake Salpetén (d) (Rosenmeier et al. 2002); grey shading denotes the 15^{th} Century, marking a general shift to drier conditions over the last 500 years. Isotopic records displaying the general lack of coherence between sites across the Yucatán (Taken from Hodell et al. 2005a)* 216

Figure 4.12 *– Yaal Chac's (YC14) composite master sequence presenting the MSCL-CIS imagery alongside a schematic diagram of lamination quality. The cumulative depths (cm) of tie points mark the correlation between core sections, and the 1cm sequence gap between drives 02-I and 04-I (grey dotted line) is displayed. The division between stratigraphic Units 1 and 2 (thick blue dotted line) signifies the switch from discontinuously laminated to continuously laminated sediment, and subdivisions of Unit 2 represent distinct changes to the microstratigraphy (thin blue dotted line).* 219

Figure 4.13 – *Bayesian age-depth model for the Yaal Chac's master sequence (a); calibrated radiocarbon dates (darker blue) and ^{210}Pb dates (lighter blue) are displayed with model output (grey dotted line signifies the 95% confidence limits, and shading within these limits indicates the more likely calendar dates; the red line depicts the optimal age-depth model based on the weighted mean age for each depth). Markov Chain Monte Carlo iterations (b) display a desired, stationary distribution; this indicates that the probability distribution is composed of independent model runs. Bacon's intrinsic, gamma distribution of sedimentation rate (green line – based on data from Goring et al. 2012) constrains the model's resultant sedimentation rate (grey histogram) (c); accumulation rate is asymmetrically distributed to account for downcore sediment compaction, and always remains positive. Bacon's intrinsic, beta distribution of model memory (green line) defines the dependence of earlier accumulation rates at any given point; the memory output (grey histogram) denotes low autocorrelation, indicative of a variable accumulation rate.* 225

Figure 4.14 – *Floating varve chronologies of Units 2i and 2iii (green line) anchored using the Bacon age-depth model, displayed alongside a composite image of the full Yaal Chac sequence. Comparable accumulation rates between the radiometric- and varved-based models (green shading) supports annually-resolved varved deposition. Disparity between subunit 2ii's couplet counts and ^{14}C dates (252-320cm; red shading) prevents varve classification within this section.* 227

Figure 4.15a *– Identification of aragonite, calcite and detrital/peloidal carbonates from Yaal Chac's Unit 2 via thin section microscopy (additional images of each type of carbonate* 231

in Supplementary material). The euhedral morphology of aragonite and calcite crystals enabled their mineralogy to be clearly differentiated within their homogenous sublayers. Plane- and cross-polarised images taken under 200x magnification using a petrographic microscope at the University of Nottingham.

Figure 4.15b *– Additional images display the strong similarities in crystal morphology and birefringence between Nar Gölü's and Yaal Chac's aragonite (top) and calcite (bottom) minerals. Each minerals' distinctive shape enabled the identification of Yaal Chac's carbonate sublayers. plane- and cross-polarised images taken under 200x magnification using a petrographic microscope at the University of Nottingham.* 232

Figure 4.16 *– Magnified (x10) images of typical varves from each of Yaal Chac's microfacies subclasses, as seen in plane-polarised (left) and cross-polarised light (right). Coloured boxes display the extent of one varve, its distinct sublayers and the approximate boundaries measured; the colour and label of these boxes correspond with the conceptual diagram of microfacies (Table 7.2). All images are positioned such that the carbonate sublayers are deposited after the organic sublayers.* 240

Figure 4.17 *– Thickness measurements of the varves' key sedimentological variables, subdivided by microfacies classification (grey line). L1 laminations (yellow box) highlights the central couplets not verified to represent annually-resolved varves.* 244

Figure 4.18 *– Example section of the Itrax µXRF core scan; variation to normalised Ca (red line), Sr:Ca (blue line) and total scatter (green line) detection through the sediment is displayed.* 246

Figure 4.19 *– PCA bi-plot of the primary and secondary axes of Yaal Chac's Unit 2 normalised geochemical data; sample scores (black dots) and principle vectors (green lines) display components driving geochemical variability.* 247

Figure 4.20 *– Comparison between the changes to key elements identified in the PCA (black lines) and the first three significant axes (grey lines); subdivided by microfacies classification (dotted lines).* 248

Figure 4.21 *– Changes to sediment microfacies and geochemical composition, relating specifically to calcium carbonate deposition over time, and subdivided by microfacies classification (grey dotted lines). L1 classification (yellow) highlights the central couplets not verified to represent annually-resolved varves.* 250

Figure 4.22 *– Changes to sediment microfacies and geochemical composition, relating specifically to organic deposition over time, and subdivided by microfacies classification (grey lines). L1 classification (yellow) highlights the central couplets not verified to represent annually-resolved varves.* 252

Figure 2.23 *– Changes to sediment microfacies and geochemical composition, relating specifically to turbidite deposition over time, and subdivided by microfacies classification (grey lines). L1 classification (yellow) highlights the central couplets not verified to represent annually-resolved varves.* 254

Figure 2.24 *– Changes to sediment microfacies and geochemical composition, relating specifically to carbonate deposition and redox conditions in the hypolimnion over time, and subdivided by microfacies classification (grey lines). L1 classification (yellow) highlights the central couplets not verified to represent annually-resolved varves.* 256

Figure 4.25 – *Sedimentological and geochemical data from Yaal Chac's Unit 1 (YC14). Plotted against modelled age are sediment depths (a), carbonate lamination thickness (b), normalised element counts of Ca (c), Br (g), Ti (h) and total scatter (f), and bulk carbonate (d) and organic (e) content. Red box denotes the distinct band of detrital carbonates and shells, likely formed during a single, localised event.* 257

Figure 4.26 *- Principle components analysis' primary and secondary axes, and its identification of Ca, Sr and Fe as key elements explaining geochemical variance.* 260

Figure 4.27 *– Comparison between the detection profiles of key elements identified in the PCA (black lines) and the first two significant axes (grey lines). Red box denotes the distinct band of detrital carbonates and shells, likely formed during a single, localised event.* 261

Figure 4.28 *– Example images of calcite crystals deposited within Yaal Chac's Unit 2. Plane- and cross-polarised images taken under 200x magnification using a petrographic microscope at the University of Nottingham.* 263

Figure 4.29 *– Comparison between the Ca and Fe/Mn ratio profiles through Unit 1. Red box denotes the rapid carbonate deposition event layer* 268

Figure 4.30 *– Oxygen $\delta^{18}O$ isotope (‰) (Hooper, 2011), total charcoal (number of particles within 10cm subsamples) (Harwood, 2011), and Okenone and β-carotene pigment concentrations (nm/g) (Stevenson, 2011) from core YC11 (a) are correlated to normalised Ca and Sr/Ca detection profiles from the full YC14 sequence (b); core scan imagery is displayed alongside the respective profiles.* 272

Figure 4.31 *–Thickness of aragonite (blue) and calcite (red) sublayers in Yaal Chac, and $\delta^{18}O$ variability from Lake Chichancanab (purple) (Hodell et al. 1995), Petén Itzá (green) (Curtis et al. 1998), Lake Miragoane (orange) (Hodell et al. 1991), and Ti content from the Cariaco Basin (cyan) (Haug et al. 2001) through the early-mid Holocene; data shown alongside modelled insolation seasonality at 20°N (W/m^2) (dashed black line) (Berger, 1978).* 277

Figure 4.32 *– Conceptual reconstruction of Yaal Chac's mineralogical- and isotopic-inferred freshness (a and b), alongside changes to Caribbean sea level (c), tropical forest cover (d) and insolation seasonality at 20°N (e). The dotted grey line marks the cessation of varve deposition around 4,295 cal yrs BP; this abrupt reduction to carbonate deposition and preservation may reflect long-term lake water dilution, driven by sea level or vegetational-derived changes to groundwater dynamics, and/or changes to carbonate dilution, associated with seasonal organic productivity rates.* 281

Figure 4.33 – *Mid-late Holocene palaeorecords; (a) oxygen isotope record from Aguada X'Caamal (Hodell et al. 2005b); thickness of carbonate sublayers and Ca detection from Yaal Chac's Unit 1 (b); oxygen isotope and sediment density record from Lake Chichancanab (Hodell et al. 2005a) (c); and Ti detection from the Cariaco Basin (Haug et al. 2001). The multi-decadal drought associated with the Terminal Classic Period (TCP) is constrained by the grey box.* 292

Figure 5.1 – *Temporal correlation of Nar Gölü's and Yaal Chac's carbonate microfacies; aragonite (blue line) and calcite (red line) thicknesses increase from their central axis, and Nar Gölü's $\delta^{18}O_{Carbonate}$ (solid black line) is also displayed (Dean et al. 2015a). The dotted black line denotes cessation of well-preserved varves at Nar Gölü at 7,630 ±520 cal yrs BP. Smoothed Ti concentration within Cariaco Basin (purple line) reflects mean ITCZ latitude through the Holocene (Haug et al. 2001).* 306

List of Tables

Table 1.1 *– List of the key datasets discussed is this thesis and their sources, for Nar Gölü (a) and Yaal Chac (b).* 43

Table 3.1 *– Major ion concentrations from Nar Gölü's surface water samples [taken from Dean et al. 2015b]* 75

Table 3.2 *– Descriptions of sedimentary units from Nar Gölü's master sequence, alongside a 5cm-long image representative of the unit. All measurements stated here reflect average thicknesses of individual laminae. Table is adapted from Allcock, 2013 (for more detail see Allcock, 2013)* 100

Table 3.3 *– AMS Radiocarbon dates from NAR01; these dates are over 14,000 years greater than the corresponding varve counts would suggest (Jones, 2004)* 103

Table 3.4 *– Classification of varve microfacies according to thin section microscopy (Unit 4-5)* 113

Table 3.5 *– A conceptual diagram of the microfacies sub-classes from Nar Gölü's Units 4-5* 114

Table 3.6 *– Classification of varve microfacies according to thin section microscopy (Unit 1)* 135

Table 3.7 *– A conceptual diagram of the microfacies sub-classes from Nar Gölü's Unit 1* 137

Table 3.8 *– Effect of sedimentological smoothing on the correlation between MAM E/P ratio and aragonite thickness; red intensity denotes stronger correlations.* 149
Table 3.9 *– Effect of meteorological smoothing on the correlation between MAM E/P ratio and aragonite thickness; red intensity denotes stronger correlations.* 149
Table 3.10 *– Periodicities of varve thicknesses of key sedimentological variables within M4 (a) and, M2a* and M5 (b), significant to p<0.01. Periodicities have been aligned to show synchronicity between variables.* 169
Table 3.11 *– Periodicities of varve thicknesses of key sedimentological variables within Unit 1, significant to p<0.01 (black) and p<0.05 (grey). Periodicities have been aligned to show synchronicity between variables.* 177
Table 3.12 *– Periodicities of carbonate sublayer thicknesses according to their mineralogy, significant to p<0.01 (black) and p<0.05 (grey). Periodicities have been aligned to show synchronicity between variables.* 177
Table 4.1 *– Yaal Chac limnological monitoring data (a) and major ion concentration data (b); data are recorded in January (dry-season) of each year.* 191
Table 4.2 *– Descriptions of sedimentary Units from Yaal Chac's master sequence, alongside a 5cm-long image representative of unit. All measurements stated here reflect average thicknesses of individual laminae.* 220
Table 4.3 *– Uncalibrated radiocarbon dates from samples taken from YC11 and YC14. Surface sediment (depth 0cm) was sampled using an Ekman grab in January 2016. The dotted line denotes samples taken from unit 1 (top) and 2 (bottom). Paired bulk and organic samples used to estimate hardwater error are shaded in green.* 222
Table 4.4 *– Radionuclide ^{210}Pb dates from samples taken from the uppermost sediments of YC11.* 224
Table 4.5 *– Classification of varve microfacies according to thin section microscopy.* 236
Table 4.6 *– A conceptual diagram of the microfacies sub-classes; L1 laminations (yellow shading) are non-varved.* 237
Table 4.7 *– Summary of carbonate mineralogy and their average thickness by microfacies classification; for L1's non-varved laminations, data pertains to the occurrence and thickness of the carbonate sublayers within its couplets.* 242
Table 4.8 *– Clusters of carbonate laminations within Unit 1* 265
Table 4.9 *– Periodicities of key sublayer thicknesses, significant to p<0.01 (black) and p<0.05 (grey). Periodicities have been aligned to show synchronicity between variables. Spectral analysis performed on data from the floating varve chronologies of Subunit 2i (a) and 2iii (b), subdivided by varve microfacies classification (c).* 287

1. Introduction

1.1 High resolution archives of environmental change

Understanding of fine-scale, i.e. sub-decadal, climate variability beyond the instrumental record is limited by the potential resolution of proxy records from natural archives. Both natural and anthropogenic systems operate on annual timescales, responding to changes in intra-, as well as inter-annual variability of environmental processes, such as rapid change and extreme climate events (Zhang *et al.* 2007). Only high resolution records (annual/sub-annual) are capable of identifying these important environmental fluctuations over time. The laminated structure of suitable archives (e.g. tree rings, sedimentary varves, ice cores) delineates incremental time-steps, enabling sub-annual to millennial scale climatic variability to be disentangled; individual climatic events can be distinguished from sub-decadal deviations (Mangili *et al.* 2005), and climatic stability/instability can be identified (Stone and Fritz, 2006). The rate of inferred environmental change can also be determined (Brauer *et al.* 2009), aiding the exploration into threshold system responses including antecedent and resultant environmental conditions. By combining these archives' ability to detect a seasonal climatic signal with an absolute chronology, comprehensive palaeoclimatic reconstructions can be made, able to explore climatological dynamics and contextualising environmental and societal change.

Terrestrial climate variability has been reconstructed throughout the Holocene at varying spatio-temporal resolutions and from a range of natural archives (Smol *et al.* 2001). High resolution interpretations of past climate were first gained from tree ring records (Douglass, 1941); while tree-ring records covering the last century are relatively common, the limited lifespan of trees, organic decay and the necessity to correlate sequences between multiple trees hinder their ability to reconstruct millennial-scale palaeoclimatology (Cook *et al.* 1995). Therefore, the last few decades have seen a growing interest in other annually-resolved archives, including lacustrine and marine varves, ice cores and speleothems, which can provide continuous archives of environmental change spanning multiple millennia (Zolitschka *et al.* 2015), and the analysis of their biotic and abiotic constituents have revealed a wide-range of environmental signals (Fritz *et al.* 2008). However, the spatial paucity and temporal length of these long records has limited our understanding of high resolution palaeoclimate dynamics.

Varved sediment archives can be used to investigate palaeoseasonality with a robust, annually-resolved chronology. They form in lakes with high intra-annual limnological variability, where each lamination reflects season-specific deposition (Zolitschka *et al.* 2015). As their laminated stratigraphy is driven by a seasonal succession to the depositional processes (Kemp, 1996), the chronological control is intrinsic to their formation and each sublayer's sediment is temporally constrained to a specific season (Ojala *et al.* 2012). After their discovery by De Geer (1912), varves were typically used solely as a chronological tool (e.g. Lotter *et al.* 1995). The rich climatic and/or limnological information held within the sediment's composition and structure was overlooked until pioneering work by Lotter (1989) and later by Sturm and Lotter (1995) and Brauer *et al.* (1999), and this use of varve microstratigraphy (microfacies analysis) as an environmental proxy has particularly grown over the last decade.

Microfacies analysis yields the highest resolution environmental information from varved sediment, where the term 'microfacies' refers to the fine-scale description of the sediments' lithology, stratigraphy and palaeontology (Brauer, 2004; Lücke and Brauer, 2004). By examining the microfacies within each year's deposition, the climatic and limnological conditions required to deposit each layer can be inferred at a sub-annual resolution (Brauer, 2004). A comprehensive understanding of lakes intra-annual limnology permits the inference of the most likely environmental conditions acting to drive the observed sediment deposition and preservation (Brauer *et al.* 2009). Consequently, this analysis is capable of reconstructing a wide-range of environmental variables, including hydroclimatic variability (Brauer *et al.* 1999, 2008; Prasad *et al.* 2006; Corella *et al.* 2012; Kaufman *et al.* 2011; Lauterbach *et al.* 2011; Martin-Puertas *et al.* 2012; Francus *et al.* 2013), anthropogenic activity (Kienel *et al.* 2005; Dreibrodt and Wiethold, 2014) and stratification dynamics (Hethke *et al.* 2013). Moreover, the identification of event layers, representing non-seasonal depositional processes, have been used to characterise extreme weather episodes (Mangili *et al.* 2005; van Geel *et al.* 2013), flood occurrence (Swierczynski *et al.* 2013; Czymzik *et al.* 2013; Schlolaut *et al.* 2014) and earthquakes (Brocard *et al.* 2014). Microfacies analysis can therefore develop a rich, holistic reconstruction of intra- and inter-annual environmental variability.

Varve analysis can further permit the investigation into mechanisms driving climatological change (Koutsodendris *et al.* 2011). Atmospheric oscillations, such as the El Niño Southern Oscillation (ENSO) and the North Atlantic Oscillation (NAO), are known to drive aspects of climatological variability across different spatio-temporal scales (e.g. Zanchettin *et al.* 2008). As each oscillation has

a known periodicity, spectral analysis of an annually-resolved timeseries can reveal these oscillations' expression in the depositional record (e.g. Dean *et al.* 2002; Fagel *et al.* 2008). Therefore, the dynamics of these large-scale climatic systems, and hence the mechanisms of palaeoclimatic change and their implications can be explored.

1.2 Environment-society relationship

Societal systems rise and fall over time, and much research has attempted to identify the dominant processes which initiate and drive change. Increasingly, it is suggested that these societal changes are often underpinned by environmental forcing (Coombes and Barber, 2005) – specifically, the direct impact climate has upon food and water security, which is vital for socio-economic stability. Inferred climatic conditions, proposed to help or hinder cultural development, coincide with numerous periods of societal change, both today and throughout the Holocene. The recent outbreak of civil war in Syria (Kelley *et al.* 2015) and the 'collapse' of past civilisations, such as the Akkadian Empire ~4,200 cal yrs BP (Cullen *et al.* 2000), Indus ~3,800 cal yrs BP (Schug *et al.* 2013), Maya ~1,200 cal yrs BP (Hodell *et al.* 1995, 2001; Haug *et al.* 2003; Douglas *et al.* 2015), and Tiwanaku societies ~1,000 cal yrs BP (Binford *et al.* 1997), have all been linked to periods of sustained drought. Similarly, inferred warmer/wetter conditions have been linked to socio-economic growth, improving agricultural food security, e.g. during periods 2,100–1,800 cal yrs BP (100 BC–200 AD) and 1,400–1,200 cal yrs BP (600–750 AD) in Europe (McCormick *et al.* 2012). More recently, widespread cooling from 536 AD in the northern hemisphere, thought to be driven by a series of volcanic eruptions, has been linked to major social reorganisation and intensification of the Justinian plague outbreak (Büntgen *et al.* 2011, 2015; Haldon *et al.* 2014).

While climate's influence on the land's carrying capacity, facilitating societal growth/decline, presents an intuitive and commonly reported climate-society relationship (Coombes and Barber, 2005), it has been criticised for oversimplifying the matter (Redman, 2005; Nelson *et al.* 2007). A robust understanding of both the cause and effect must be considered; in this case, climate's rate of change, timing and magnitude, and society's sensitivity, complexity and resilience (Janssen *et al.* 2006), comparable to an ecological system (Zhang *et al.* 2007).

A society's sensitivity to environmental forcing is chiefly dependent on three factors: social complexity, environmental marginality and resource surplus (Coombes and Barber, 2005). While technological advancements have possibly led to increased resilience to climatic change, any given

society will ultimately be limited by its ability to supply food and water, whether that's from local productivity or through trade. Those operating beyond the land's carry capacity will ultimately be dependent on the importation of these resources, and therefore be vulnerable to other socio-political forces which drive population change (Zhang *et al.* 2007).

Precipitation, and hence water availability, arguably presents the climatic variable most determining societal development; while technological advancements can maximise its retention (e.g. reservoirs and cisterns) and distribution (e.g. canals), a population will depend on a consistent, reliable supply of water (Wilhite, 2000; Scarborough *et al.* 2012). A society nearing the minimum subsistence requirements will be more vulnerable to climatologically driven changes in water availability. As water availability will likely be a first order constraint on population growth, the relationship between water supply and societal success is most prevalent in arid environments or those which depend on seasonal rainfall (Cohen, 1995).

High resolution archives of palaeoclimatology can provide the environmental context to societal change; to investigate the human-environment relationship, climatic variability must be analysed at a temporal resolution sufficiently high to identify conditions able to influence food/water security (Rosen, 2007; Haldon *et al.* 2014). Decadal-centennial reconstructions of climate are unable to identify any nuanced variation with the potential to influence societies (Caseldine and Turney, 2010); apparent long-term 'adverse' climatic trends may even enhance resilience if changes are gradual (Brooks, 2006).

The environmental insight, permitted by varve analysis, can reveal the intra-annual climate variability over successive years (Brauer, 2004), including seasonal changes to the lake's hydroclimate (e.g. Kelts and Hsü, 1978; Haug *et al.* 2001; Tomkins *et al.* 2010; Cuven *et al.* 2011; Dean *et al.* 2013; Amann *et al.* 2015; Roop *et al.* 2016). Therefore, these annually-resolved reconstructions provide the ideal environmental context to explore the human-climate relationship (Berglund, 2003). Firstly, the sediments' sub-annual stratigraphy enables specific environmental conditions or events to be attributed to a specific season or year. Therefore, continuous records of hydroclimate are able to benchmark natural variability, and identify extreme events/years (e.g. Joetzjer *et al.* 2013). This provides the environmental setting, and suggests a society's environmental context and might give insight into their susceptibility to change; for example, the likelihood of short, extreme episodes of drought to undermine societal structures and cause major socio-economic disruption (e.g. Medina-Elizalde *et al.* 2010). Secondly, the robust, incremental chronology

permits environmental change to be well dated. By definition, causality is reactionary, and so dating climatic variation must be reliably dated to occur prior to societal change if climatic forcing is to be inferred. Poor chronologies have often inhibited the ability to assess the complex human-climate relationship (Berger and Guilaine, 2009; Aimers and Hodell, 2011), yet varved records can provide a reliable chronological framework (Schulting, 2010; Feeser *et al.* 2016). Finally, annually-resolved data further provides an indication of the rate of change. They are able to identify abrupt vs gradual climatic change (Brauer *et al.* 2009); important when considering a society's potential to adapt and mitigate adverse conditions.

1.3 Study sites

Central Anatolia, Turkey and the Yucatán Peninsula, Mexico are two regions with rich and complex societal histories throughout the Holocene. These regions have experienced long term climatic change throughout the Holocene (e.g. Wahl *et al.* 2014; Dean *et al.* 2015; Jones *et al.* in review), and supported the development of numerous cultures including the Roman, Seljuk and Ottoman civilisations in Central Anatolia (Hirschfeld, 2004; Haldon *et al.* 2014), and the Mayan and Spanish civilisations in the Yucatán (Demarest and Prudence, 2004; Douglas *et al.* 2015). While the regions' societal succession is relatively well documented, the spatial paucity of suitably high resolution records of climatic change has inhibited our ability to provide a robust environmental perspective (Aimers and Hodell, 2011). Laminated sediment records from Nar Gölü (Turkey) and Yaal Chac (Mexico) have the potential to provide long, continuous records of high resolution environmental change through the Holocene.

Both of these region's societies are highly susceptible to changes in annual rainfall. Each region experiences a strong wet-dry seasonality, which mean societies were heavily dependent on the wet-seasons' rainfall; this increases their vulnerability to the length and intensity of each season (Sönmez *et al.* 2005). Central Anatolia's semi-arid climatology exacerbates the issue by increasing the dependence on sufficient wet season precipitation. Similarly, the Yucatán's flat, karstic geomorphology, and the absence of river systems on the northern peninsula, meant societies' water supply relied on seasonal rainfall to refill artificial reservoirs, and elevate groundwater to infill sinkholes (Scarborough *et al.* 2012).

Nar Gölü and Yaal Chac are located on either side of the sub-tropical high pressure belt, and their regional climate is governed, in part, by its seasonal migration (Metcalfe *et al.* 2000; Wick *et al.*

2003). This high pressure belt is derived from Hadley cell descent, and its location is a function of the inter-tropical convergence zone (ITZC) position (Fig. 1.1). Its migration drives the sites' wet-dry seasonality, which occur in anti-phase from each other: dry conditions in the winter at Yaal Chac and summer at Nar Gölü. Therefore, variation in inferred palaeohydrological seasonality may reflect changes to the annual migration of the ITCZ; this would have profound implications for palaeoclimatic reconstructions due to the ITCZ's dominant control on equatorial and sub-tropical climatology.

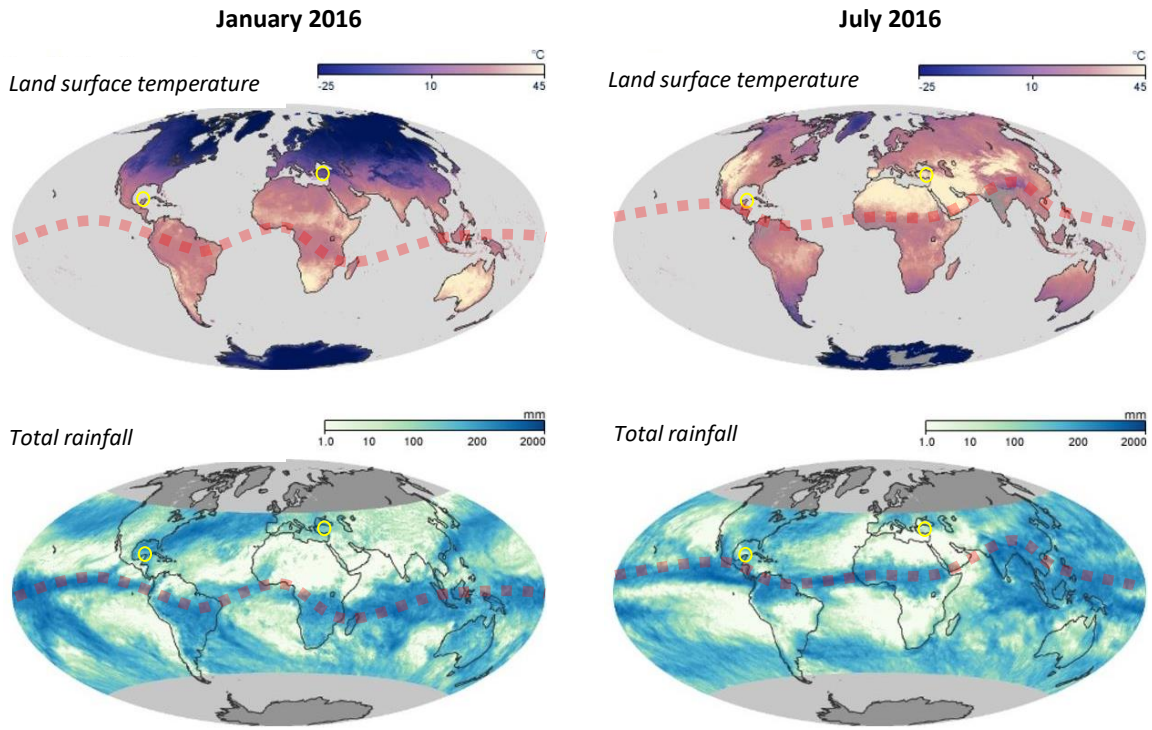


Figure 1.1 *– Global land surface temperature (top) and total rainfall (bottom) in January (left) and July (right); study sites Yaal Chac, Mexico and Nar Gölü, Turkey are marked by yellow circles. The average position of the ITCZ (red dashed line) displays its summer and winter extents, and drives the increased precipitation observed, the belt of low rainfall north of the ITCZ reflects the subtropical high pressure belt's position. Data were collected by NASA's Terra and Tropical Rainfall Measuring Mission (TRMM) satellites, and taken from NASA Earth Observatory (2016).*

Various climatic oscillations are known to drive sub-decadal to centennial scale climatic variability in both regions, the specifics of which are discussed in Sections 3.1 and 4.1, for Nar Gölü and Yaal Chac respectively. As mentioned above, identifying periodicities within the annual records may indicate the effect of specific climatic oscillations driving climatic variability, and their potential to influence societal change can subsequently be inferred.

The dry season is represented in the sediment sequence of Nar Gölü as a distinct sublayer of endogenic carbonate minerals (Jones *et al.* 2005), and a similar dry season sedimentology is also hypothesised in Yaal Chac's record. Endogenic carbonate deposition within lacustrine systems is often climatically sensitive, particularly in tropical regions, where catchment hydrology, sediment input and temperature can drive significant changes to carbonate saturation within lake water (Tucker and Wright, 1990; Gierlowski-Kordesch, 2010). Consequently, the analysis of carbonate sedimentology enables the reconstruction of seasonal hydrological variability, required to assess its potential to influence past societies in these water sensitive regions.

1.4 Varve sedimentology in lacustrine environments

Nar Gölü and Yaal Chac's lacustrine records both display long units of finely-laminated sediment. In Nar Gölü, these laminae have been shown to reflect annually deposited varves (Jones *et al.* 2006; Dean *et al.* 2015b). Owing to the sediments' visual resemblance and the regions' similar wet-dry seasonality, the laminations of Yaal Chac are hypothesised to also represent varves. This section outlines the various environmental conditions required for varve formation and preservation within lacustrine systems, and summarises their use in palaeoenvironmental research.

Throughout this thesis, the origin of carbonate deposition will be clarified through use of descriptive terminology: *endogenic* carbonates relate to in-lake chemical precipitation; *authigenic* carbonates to post-depositional remineralisation; and *detrital* carbonates to inwashed/reworked sediment respectively. Similarly, the source of organic material is differentiated using terms *autochthonous* and *terrestrial*, referring to in-lake productivity and in-washed catchment material respectively.

1.4.1 Varve formation and preservation

Originating from the Swedish word 'varv', meaning revolution or circle, the term 'varve' alludes to the annual cycle of sediment deposition within a water body (Lotter and Sturm, 1994). It was first used to describe laminated sediment from proglacial lakes in Sweden (de Geer, 1912), where the seasonal cycle of glacial meltwater discharge drives an intra-annual change to lacustrine sediments deposited. Each year, or 'varve', is recorded as a couplet of sedimentologically distinct sublayers; the seasonal succession of strong-summer and weak-winter stream discharge leads to the deposition of larger- and finer-grained sediment respectively. Since de Geer's (1912) initial work, an extensive effort to develop the inter-basin Swedish varve chronology (Boygle, 1993) has meant that the term 'varve' is often associated with these proglacial, clastic sediments. However, following the early

discovery of laminated sediment where deposition is driven by biological and chemical intra-annual variability in Switzerland (Nipkow, 1920) and North America (Whittaker, 1922), the definition of 'varves' was expanded to include all annually laminated sediment – so long as an intra-annual succession of depositional processes result in sedimentological distinct sublayers (Zolitschka *et al.* 2015). While most commonly analysed in modern lacustrine systems, varves have also been found in palaeolakes (e.g. Ramrath *et al.* 1999; Munoz *et al.* 2002; Mangili *et al.* 2005; Neugebauer *et al.* 2012) and marine basins (e.g. Bradley, 1931; Hughen *et al.* 1998; Schimmelmann *et al.* 2016) worldwide.

The discovery and study of varved sedimentary records has grown substantially over the last century. In a review of varve-based chronologies worldwide, Ojala *et al.* (2012) constructed the Varves Database (VBD), initially listing 99 published varved sediment records from lacustrine systems. The VDB was last updated following a review by Zolitschka *et al.* (2015), bringing the total number of varved lake chronologies in the database up to 143 (Fig. 1.2), yet further sites have been reported in the subsequent years (e.g. Bonk *et al.* 2016; Saarni *et al.* 2016; Amann *et al.* 2017; Bendle *et al.* 2017; Miller *et al.* 2017). While these lacustrine varve chronologies are located worldwide, mid- to high-latitude sites in the northern hemisphere (>30°N) dominate the VDB, accounting for 94% of all listed sites. Tropical and southern hemisphere sites are greatly underrepresented within varve-based research; here, geographically remote lakes reduce the availability of data pertaining to a site's morphology and seasonal limnology, required to predict whether its sedimentary record is varved (discussed below), and accessibility for coring. While the limnological conditions required for varve deposition are well understood (Zolitschka *et al.* 2015), the identification of varved material within any given lake can only be confirmed following sediment retrieval; therefore, the poor global distribution of varve chronologies is likely to reflect the broader underrepresentation of tropical and southern palaeolimnological and climatological research.

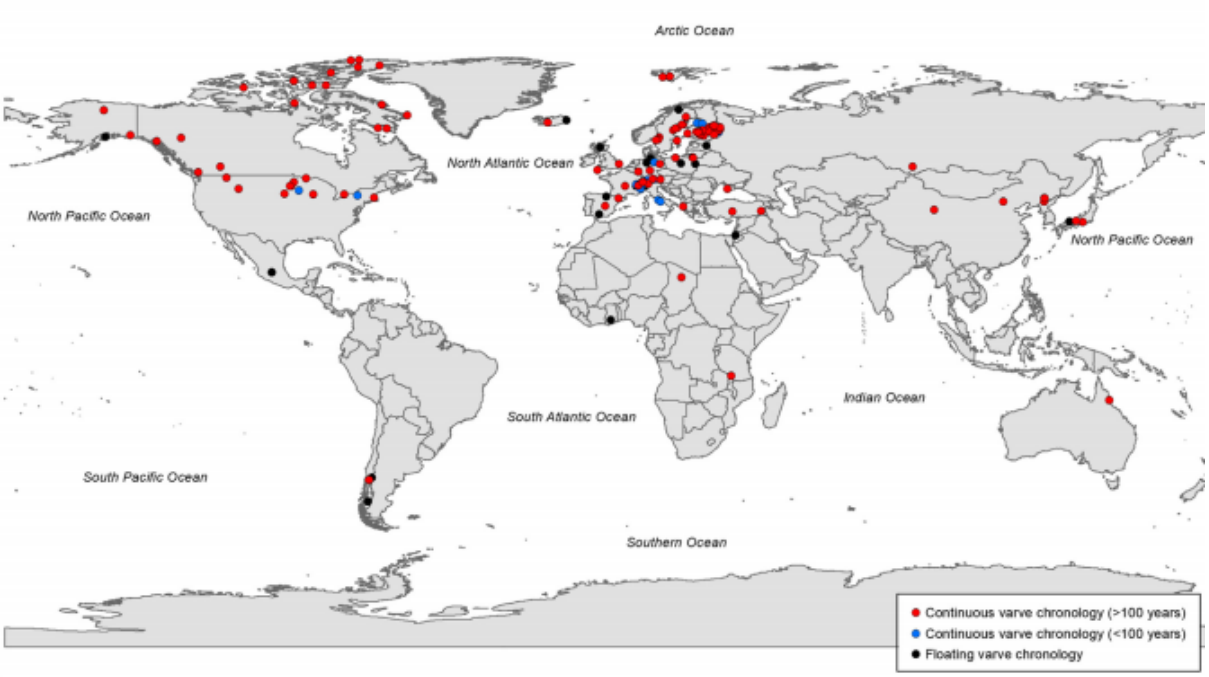


Figure 1.2 *– Global distribution of lacustrine varves included within the 2015 Varve Database (VBD) from Zolitschka et al. (2015); additional sites have since been discovered.*

For varves to be deposited and preserved, various environmental conditions must be met. Fundamentally, the limnological processes driving sediment deposition must vary intra-annually; every varve reflects one year's sediment deposition, delineated by distinct changes to the seasonal sediments' composition and/or structure (Brauer, 2004). Varve chronologies develop when this annual cycle of deposition occurs over multiple, consecutive years. Such consistent, intra-annual fluctuations in limnological processes are predominately regulated by climatic seasonality, albeit via climate's direct or indirect influence on autochthonous and allochthonous sediment deposition (Zolitschka *et al.* 2015). Varves' stratigraphy must be composed of at least two distinct laminae, where each sublayer relates to a specific change in limnic deposition and can be identified via changes to the sediments composition, structure, and/or thickness; so long as the net accumulation reflects a single year of deposition, governed by this seasonal limnological cycle. Note, the climatic-derived control of annual laminations means that that a 'year' does not typically correspond to January-December, and instead relates to an annual biological or hydrological cycle.

There are many different types of varves, each characterised by its principal sublayers' composition and structure. Generally, a sublayer's composition is categorised as clastic, biogenic or endogenic; the following summarises the archetypal origin and processes driving the deposition of each sublayer type:

Clastic

Sediment accumulation is driven by the inwash of allogenic minerals and siliciclastic grains (Brauer and Casanova, 2001). Clastic sublayers are most commonly identified within cold, oligotrophic lakes located within high-altitude (Leonard, 1997; Hughen *et al.* 2000; Anselmetti *et al.* 2007) or -latitude (e.g**.** Lamoureux and Gilbert, 2004; Sun *et al.* 2006; Bird *et al.* 2009) regions. Here, the typically reduced vegetation cover increases the catchment's susceptibility to erosion, thus promoting the influx of minerogenic grains. When also combined with lower limnic productivity, the deposition of organic matter is minimised, thus permitting clastic sublayers composed of homogeneous allogenic material to be formed (Zolitschka *et al.* 2015). While a catchment's geology and geomorphology may govern the long-term viability of clastic deposition, the annual influx is generally considered a function of hydroclimate and land-use, which determine the rates of catchment erosion and sediment transportation (Lamoureux and Gilbert, 2004).

Biogenic

Sediment is composed of organic-derived material, typically originating from autochthonous productivity. Organic productivity can greatly vary intra-annually, primarily driven by seasonal changes to nutrient influx and limnological conditions (Lotter and Birks, 1997; Kato *et al.* 2003; Corella *et al.* 2011; Martin-Puertas *et al.* 2012). Climate-driven weathering of a catchment's geology (e.g. via seasonal rainfall) may directly supply the nutrients which enhance in-lake productivity; alternatively, nutrients may be sourced via the inwash of detrital vegetation, and leaching of organic acids/nutrients from the surrounding soils (Lotter and Birks, 1997). Seasonally variable nutrient influx rates can cause rapid changes to bio-productivity rates, often in the form of algal blooms (Kato *et al.* 2003). The seasonal cycle of limnological conditions (temperature, pH, salinity etc.) may further promote/hinder bio-productivity rates, and drive a succession of algal communities observed within a varve's composition (Bradbury, 1988; Vos *et al.* 1997). In addition, limnological mixing can replenish nutrient concentrations to the hypolimnion, thus leading to multiple algal blooms within each year (Bradbury, 1988).

Endogenic

Sediment accumulation is derived from the endogenic precipitation of minerals following supersaturation, most commonly in the form of calcium carbonate within lacustrine systems (Kelts and Hsü, 1978; Zolitschka *et al.* 2015). Mineralogical supersaturation can be physically and/or biologically induced. First, seasonal bio-productivity, namely algal blooms, can drive

changes to lakewater chemistry, thus influencing mineral solubility; photosynthetic activity increases pH in the epilimnion via its consumption of dissolved CO_2. This biological-driven supersaturation and endogenic mineral precipitation is generally associated with the carbonate mineralisation, predominately in the form of calcite and aragonite (Kelts and Hsü, 1978, Livingstone and Hajdas, 2001; Martin-Puertas *et al.* 2009; Giguet-Covex *et al.* 2010; Kienel *et al.* 2013; Wulf *et al.* 2013). Second, seasonal changes to evaporation and precipitation can physically concentrate a mineral's component ions within the lakewater such that mineralisation occurs (Warren, 1996). This process is further enhanced when a lake is thermo-chemically stratified thus minimising dilution of epilimnetic water. The relative concentration of lakewater ions at the time of supersaturation also dictates the specific mineralogy preferentially precipitated (Kelts and Hsü, 1978). As a result, a sublayer's endogenic component may be composed of multiple minerals as the limnology changes intra-annually. Overall, the combined physical and chemical carbonate supersaturation partially drives endogenic precipitation within study site, Nar Gölü (Jones *et al.* 2006; Dean *et al.* 2015b).

While not exhaustive, these descriptions aim to highlight some of the key processes driving sediment composition and accumulation within varves' sublayers. Anthropogenic activity can also influence all three compositional types via its effect on land use, nutrient flux and pollution. Any combination of these sublayer types may be combined to form a varved sequence, and similarly, each sublayer may be composed of multiple components if deposited coevally; for example, rainfall may drive clastic inwash, nutrient influx and hence biogenic sediment deposition, thus resulting in a clastic-biogenic sublayer. Moreover, the complete composition of varves may change due to substantial changes to the dominant depositional processes (e.g. Brauer and Casanova, 2001).

Following sediment deposition, various physical, chemical and biological factors influence the varves' susceptibility to post-depositional alteration (see Ojala *et al.* 2000). Physical disruption of varves is most commonly associated with bioturbation (Zolitschka *et al.* 2015); the reworking of sediments due to the movement and burrowing of organisms. Therefore, varve-depositing lakes typically contain sub-oxic conditions within the hypolimnion which inhibit the establishment of benthic communities (Lami *et al.* 1994; Jenny *et al.* 2013; Butz *et al.* 2016). Such conditions are typically induced by meromixic or monomixic regimes, thus preventing or limiting the movement of dissolved oxygen, required for aerobic respiration, to the hypolimnion (Hakala, 2004). In addition, benthic anoxia inhibits the aerobic decomposition of biogenic sediments (Sobek *et al.* 2009), where

autochthonous biogenic material, commonly linked to a varved sequences' microstratigraphy, is more susceptible to microbial decomposition than allogenic detrital material (Burdige, 2007). Moreover, anoxic conditions prevent the breakdown of phenolic compounds via enzyme phenol oxidase, thus inhibiting the activity of biodegradative hydrolase enzymes (Freeman *et al.* 2001; Sobek *et al.* 2009). Minimising the decomposition of biogenic sediments ensures that the intra-annual depositional variability is represented within the varved sequence, thus emphasising the role of hypolimnetic anoxia in biogenic preservation.

Hypolimnetic anoxia can be sustained via limnic stratification (Tracey *et al.* 1996), driven by water density gradients down the water column, where the concentration of dissolved solids and water temperature determine specific lakewater density (Boehrer and Schultze, 2008). When epilimnetic and hypolimnetic water densities differ, stratification occurs; this forms two (or more) thermo-chemically distinct water masses which do not mix. Conversely, mixing occurs when density does not vary through the water column, thus acting to homogenise water chemistry and properties. Downcore density variability is primarily governed by lake level and bed morphology, climatology and geochemical cycles; while Boehrer and Schultze (2008) provide a comprehensive review lake stratification, the key limnological drivers are outlined here.

Primarily, a lake's size, depth and shape dictate the viability of sustained stratification. This morphology determines the ability of wind to physically mix water, such that distinct density gradients may not be consistently established; the catchment size and shape similarly effects wind fetch and lake exposure, and hence potential for wind-derived mixing (Boehrer and Schultze, 2008). Secondly, climate's influence on surface water drives density variability down the water column. Air temperature and evaporation rates drive lakewater density via their effect on temperature and dissolved substance concentrations respectively; similarly, ice cover, meltwater and precipitation inflow drive temperature- and salinity-derived water densities predominately in the epilimnion. Thirdly, geochemical cycles affect density via the movement of dissolved solids through the water column, namely through the precipitation/solution of carbonates, and iron and manganese oxides. Moreover, epilimnetic bioproductivity and subsequent hypolimnetic decomposition can maintain a geochemical, and hence density, gradient. The intra-annual dynamics of these factors govern every lake's annual mixing regime, where monomictic and meromictic regimes are most conducive to hypolimnetic anoxia and hence varve preservation (Tracey *et al.* 1996; Ojala *et al.* 2000).

Eutrophication can also drive hypolimnetic anoxia. Rapid rates of bioproductivity in the epilimnion can lead to the rapid deposition of biogenic matter, where aerobic decomposition results in the depletion of dissolved oxygen in the hypolimnion (Smith and Schindler, 2009). Eutrophication is primarily driven by processes effecting nutrient concentrations and limnological properties, where lacustrine shifts to higher trophic states are often associated with anthropogenic nutrient inwash (Smith and Schindler, 2009). The onset of varve deposition/preservation in many lakes has been causally linked to anthropogenic eutrophication, and the resultant anoxic conditions in the hypolimnion (Lami *et al.* 1994; Lotter *et al.* 1997; Kienel *et al.* 2013; Jenny *et al.* 2016).

Varved sequences can be physically reworked directly via gravity-induced slumping of lake bed material, or indirectly via the overflow of these slumping events which can disrupt the structure of the underlying laminations (Mangili *et al.* 2005). Lake bed morphology primarily determines a record's susceptibility to slumping (Zolitschka *et al.* 2015), yet rapid sediment accumulation (Sauerbrey *et al.* 2013) and seismic activity (Inouchi *et al.* 1993; Guyard *et al.* 2007) can also promote bed slope failures. Furthermore, sediment deposited in shallow lakes or littoral zones are sensitive to wind-derived reworking and resuspension; therefore, lakes with small surface area to depth ratios and sheltered by vegetation/catchment geomorphology are less affected by wind-induced turbulence and sediment reworking (Ojala *et al.* 2000). Coring varved sequences from the deepest, and hence flattest, lake region also minimises these incidences of slope failures and impact of wind on varve preservation.

1.4.2 Varve chronologies

Varve deposition delineates times within its annually-resolved stratigraphy, capturing the intra-annual changes to depositional processes. Sustained deposition of varves results in the formation of long, continuous sedimentary records, where varve counts provide an incremental chronology (Zolitschka *et al.* 2015). So long as the prerequisite conditions for varve deposition and preservation are maintained, varve deposition can continue over multiple millennia; for example, Lake Suigetsu in Japan contains around 29,100 contiguous varves (Kitagawa and Van Der Plicht, 1997; Marshall *et al.* 2012) and the mean lacustrine record within the VDB covers ~3300 varve years (median of 1,500 varve years). Chronological error within varved sequences is typically inferred to be very low, ±1-4% (Ojala *et al.* 2012); however, only 43% of chronologies in the VDB quantify error, probably due to an assumed robust chronology.

There are three different types of varve chronology, each with various implications for their chronological precision: (i) *absolute*, varve deposition extends to present-day with each varve corresponding to a calendar-year; (ii) *floating*, sequence requires an independent dating method to anchor the chronology in time; or (iii) *discontinuous*, a sedimentary record contains an absolute and at least one floating chronology. Within the VDB, 82% of chronologies are absolute, 13% are floating and 5% discontinuous.

As alluded to above, varve-based chronological error is often not discussed and accounted for. While varved records offer high resolution chronologies and error is typically very low (<4%) (Ojala *et al.* 2012), an understanding of the sources of chronological error and its quantification provides insight into the degree to which sedimentary change can be precisely dated (Zolitschka, 2007). In addition, many timeseries analytical techniques, such as spectral wavelet and periodogram analysis, assume an error-free chronology with precise and even time-steps, where any chronological error can reduce the strength of resultant signals (Comboul *et al.* 2014). The following highlights some of the key sources of error specific to laminated sediment sequences.

First, temporal inconsistency of varve deposition and preservation may decouple the sediment stratigraphy from varve counts (Comboul *et al.* 2014). Individual years' sediment accumulation may substantially decrease such that distinct laminations are difficult to distinguish, particularly in oligotrophic lakes with low bio-productivity (Brauer, 2004). At a sub-decadal scale, an individual year of extremely low accumulation, where discrete laminations cannot be identified, may contribute to chronological error from 'missing varves' (Tian *et al.* 2005). However, as accumulation rates significantly decrease, negligible sediment deposition/preservation is unlikely to be limited to a single climatic cycle or year; therefore, any stratigraphic uncertainty may be identified and incorporated into varve counts via the assignment of a qualitative indicator of varve quality (Lamoureux, 2002). Varve counts via thin section microscopy enhances the ability to differentiate each years' microstratigraphy (Lotter and Lemcke, 1999), thus increasing the likelihood that each year's sediment accumulation is accounted for (Boës and Fagel, 2005). In the cases where varves are locally disrupted or eroded post-deposition, via the deposition of turbidites or large macrofossils and drop stones, intra-basin correlation of core sequences can form a composite chronology composed of the best-preserved sections of varved material. Here, error can be quantified through repeated varve counts across these intra-basin sequences (Zolitschka, 2007).

On longer temporal scales, the cessation of varve deposition and preservation may be recognised by distinct compositional and/or structural changes to the sedimentology. Independent dating similarly highlights disparities between 'varve' counts and age estimates, identifying periods of laminated but non-varved material (Zolitschka, 2007). In these cases, each varve chronology may be separated and treated as individual floating varve chronologies, which require anchoring via independent dating methods (e.g. Dean *et al.* 2015a).

Second, error can be derived from the independent dating methods used to anchor these floating varve chronologies (e.g. Hajdas *et al.* 1993; Prasad *et al.* 2004). While continuous varves may reflect consecutive years' deposition, thus providing the length of time over which deposition occurred, precisely dating this floating varve chronology is limited by the independent dating method's accuracy. The quantification of these errors is typically unique to each dating technique (e.g. Hajdas *et al.* 1995; Dean *et al.* 2015a).

Third, varve counts may be user dependent, differing according to each person's identification of a varve (Lotter and Lemcke, 1999). Particularly in sequences composed of thin laminations and/or subjected to some post-depositional disturbance, each year's stratigraphic boundaries may be ambiguous. If so, varve counts may not precisely reflect time. Again, counting within thin section microscopy minimises the likelihood of miscounts, as the annual depositional cycle can most easily be identified and counted (Lotter and Lemcke, 1999). This source of error can be quantified through repeated counts, preferably by multiple people (Lotter and Lemcke, 1999).

Chronological uncertainty within varve chronologies is relative to any given point (Comboul *et al.* 2014). Uncertainty may be relatively low when determining the time between two specific varves, yet relatively high when dating them in time. Error derived from counting and 'missing varves' should accumulate over time, from the point anchoring the varved sequence point (Comboul *et al.* 2014); absolute chronologies are anchored using the assumption that the sediment-water interface reflects the year of coring, and floating chronologies are anchored using an independent age-depth model. This variable uncertainty is rarely discussed, and error is typically reported as a simple percentage or deviation (if included at all) (Ojala *et al.* 2012).

1.4.3 The use of varves in palaeoclimatology

Lacustrine sediment records have been extensively used to reconstruct palaeoenvironmental change (Smol *et al.* 2001). Over time, sediment accumulation and its composition changes in response to various physical, chemical and biological drivers. As each unique component responds to specific environmental changes, their compositional variability captures a palaeoenvironmental signal. By understanding the primary processes driving these changes to composition, past conditions can be inferred. Numerous of these so-called proxy records have been used to reconstruct palaeoenvironmental change, including stable isotopes (Leng and Marshall, 2004; Roberts *et al.* 2008), diatom assemblages (Fritz *et al.* 1999; Battarbee *et al.* 2001; Smol and Stoermer, 2010), pollen (Sugita, 1994; Bennett and Willis, 2001), charcoal concentrations (Patterson *et al.* 1987; Whitlock and Larsen, 2001), and more. Analysis of these proxies within varved records enables high resolution reconstructions to be inferred and well-dated within a robust chronology. Proxies may be sampled and assessed within each varve to assess seasonal variability (e.g. Kanamaru *et al.* 2013; Dean *et al.* 2013), or across multiple varves to gain a fixed temporal resolution and smoothing of environmental signal (e.g. Bird *et al.* 2011; Anhäuser *et al.* 2014). As such, varved records are most commonly used as a chronological tool, exploiting the records' intrinsically high resolution and robust chronology (Brauer *et al.* 2008).

Varves' value as a geochronological tool has significantly grown since their first discovery (Francus *et al.* 2013). Varves have been used to extend the radiocarbon calibration curve beyond 10.0 ka BP (Hajdas *et al.* 2000, 2010) and up to 52.8 ka BP (Bronk Ramsey *et al.* 2012), date palaeoclimate proxy data (e.g. Swain, 1978; Lücke *et al.* 2003; Wick *et al.* 2003; Woodbridge and Roberts, 2010), calibrate transfer functions with instrumental data (e.g. Larocque *et al.* 2009) and correlate lacustrine/marine records with ice core data (e.g. Andrén *et al.* 1999; Ringberg *et al.* 2003; Ridge *et al.* 2012).

1.4.4 The use of varve sedimentology as a palaeoclimatic proxy

Similar to other proxies, many limnological conditions and processes control the composition and structure of varves, or 'microfacies' (see section 3.1). Analysis of these microfacies' sedimentology gains the highest resolution of palaeoenvironmental information available from varved records (Zolitschka, 2007). By comprehensively understanding a lake's seasonal limnological cycle, including the intra-annual climatic conditions driving environmental processes, a conceptual model of varve formation can be developed (Zolitschka, 2007; Brauer *et al.* 2009). This model can subsequently be

used to infer the most likely conditions and processes required to produce the observed sedimentology (Mangili *et al.* 2005), where the sub-annual stratigraphy temporally constrains each lamina to a particular season or intra-annual process. Microfacies data are typically collected via thin section microscopy; here, the microstratigraphic composition, structure and fabric can be recorded and the sublayers' thicknesses measured (Brauer, 2004), thus producing a sub-annually resolved record of sedimentological change within a robust chronology.

Microfacies analysis on lacustrine varves has been widely-used to assess changes in the palaeoenvironment, including: reconstructions of high resolution palaeoclimatic change (Brauer *et al.* 1999, 2008; Prasad *et al.* 2006; Martin-Puertas *et al.* 2012; Hethke *et al.* 2013; Neugebauer *et al.* 2015; Czymzik *et al.* 2016); characterisation of abrupt depositional events (Mangili *et al.* 2005; Swierczynski *et al.* 2012; Schlolaut *et al.* 2014; van Daele *et al.* 2014); identification of land use change (Corella *et al.* 2011), and detection of anthropogenic activity and pollution (Kienel *et al.* 2005; Dreibrodt and Wiethold, 2015). Subsequent spectral analysis on these high resolution datasets have further enabled the inference of palaeoclimatological mechanisms and dynamics through the Quaternary period (Prasad *et al.* 2009; Koutsodendris *et al.* 2011; Czymzik *et al.* 2013; Zahrer *et al.* 2013; Schlolaut *et al.* 2014).

Increasingly, this sedimentological analysis is combined with high resolution geochemical analysis, collected via micro X-ray fluorescence (μXRF) scanning (Brauer *et al.* 2009). These complementary datasets provide quantitative profiles of the varve microfacies' composition (e.g. Martin-Puertas *et al.* 2012; Lamoureux and Francus, 2014; Neugebauer *et al.* 2015). The deposition and detection of specific elements are associated with various sedimentary processes (Davies *et al.* 2015). By assessing the geochemical variability within a varve's microfacies, elemental peaks can be linked to the observed, intra-annual sedimentology (Brauer *et al.* 2009). This combined approach permits the sediments' composition to be identified, and subsequently each of these components' geochemical variability to be determined through the chronological record.

Owing to the numerous preconditions required for varve formation and preservation, the presence of varves within a sedimentary sequence has been used as a palaeoenvironmental indicator (Jenny *et al.* 2013, 2016). The onset of varve deposition is typically driven by the establishment of meromixis and hypolimnetic anoxia (Tracey *et al.* 1996; McAndrews and Turton, 2007). Post-industrially, this is typically driven by cultural eutrophication (Giguet-Covex *et al.* 2010; Jenny *et al.* 2016). In addition, anthropogenically-driven climatic warming has been proposed to promote varve

formation in sites predicted to experience warmer annual conditions; here, thermos-chemical stratification is enhanced and oxygen solubility is decreased, thus increasing the prevalence of hypolimnetic anoxia and promoting the onset of varve deposition (Giguet-Covex *et al.* 2010; Deutsch *et al.* 2011; Jenny *et al.* 2016).

As alluded to above, microfacies analysis encompasses all of the varves' compositional and structural components; therefore, specific limnological conditions and processes can be inferred from each sedimentary aspect (Brauer, 2004). The following outlines some of the archetypical relationships identified between microfacies and palaeoenvironment.

The thickness of clastic varves in proglacial lakes has been commonly linked with average air temperature during the melting season (Leonard, 1997; Hughen *et al.* 2000; Cuven *et al.* 2011; Ridge *et al.* 2012). As previously discussed, the seasonal change in meltwater discharge drives intra-annual variation to runoff, sediment transportation, and consequently sediment accumulation rates. Secondary peaks in clastic deposition rates may also relate to summer rainfall, further increasing clastic inwash and sedimentation (Lapointe *et al.* 2012). Within all types of varves, the clastic component is typically interpreted to reflect allogenic inwash. Geochemical analysis is commonly used to detect lithogenic elements associated with catchment erosion and inwash via precipitation (Metcalfe *et al.* 2010; Neugebauer *et al.* 2012), specific elements typically include Fe, Ti, Zr, Rb, K, Si, and Al dependent on local geology (Davies *et al.* 2015). Sedimentological analysis of clastic components in non-proglacial lakes are often limited to the sporadic, rapid inwash events.

Slope bed failures and mass movement events of catchment sediment lead to the rapid deposition of event-layers, or 'turbidites'; within varve-depositing lakes, these events can be well-dated and analysis of their sedimentology can provide insight into the processes and drivers to deposition (Mangili *et al.* 2005). A turbidite's sediment may be derived from either catchment and/or lake bed material, and the rapid movement of this sediment may be induced by a specific environmental forcing, namely flood occurrence, tectonic activity and extremes in precipitation. By understanding the environmental context of each lake, turbidite analysis has been used to reconstruct rainfall-driven inwash (Lamoureux, 2000; Mangili *et al.* 2005), and occurrence of floods (Czymzik *et al.* 2010; Wirth *et al.* 2013; Schlolaut *et al.* 2014) and earthquakes (Inouchi *et al.* 1996; Williams *et al.* 2012; Simonneau *et al.* 2013). Detailed microstratigraphic and geochemical analysis can further enable each turbidite's source and mass movement's mechanism to be distinguished (Schlolaut *et al.* 2014).

While the thickness of biogenic sublayers has been used to infer seasonal bio-productivity (Negendank *et al.* 1999), palaeoenvironmental reconstructions utilising varves' biogenic component is most commonly achieved via the assessment of diatom (Kirilova *et al.* 2011; Koutsodendris *et al.* 2012) and/or chironomid (Simola *et al.* 1996; Eggermont *et al.* 2008) assemblages. Since every species thrives within a specific ecological niche, assemblages can highlight the most likely limnological conditions which would result in the growth and success of observed species.

Since every mineral similarly requires specific conditions to precipitate within the sedimentary record, endogenic components' mineralogy, morphology and stratigraphy have been widely-used to infer palaeoenvironmental change (see section 3.1). Local water chemistry dictates the crystalline mineralogy preferentially precipitated (Kelts and Hsü, 1978); E/P driven changes to lake level and ion concentrations in lake water (Gell *et al.* 1994; Roberts *et al.* 2016), and hypolimnetic re-oxygenation derived from lake circulation (Bradbury, 1988) have been linked to the endogenic precipitation of specific minerals. Subsequent preservation of these minerals similarly require specific conditions at the sediment-water interface; again, past conditions may be inferred by a specific minerals' presence within the sedimentary record.

Mineralogy morphology can provide an indication of its formation process. Endogenic carbonates can be identified via their euhedral crystalline structure (Kelts and Hsü, 1978), where structural rounding indicates subsequent diagenetic dissolution (Brauer *et al.* 2008). The detection of euhedral minerals within varves reveals the occurrence of seasonal limnological supersaturation, and the endogenic crystals' size and concentration reflects the length and intensity of supersaturation within a year (Kelts and Hsü, 1978). The precipitation of micritic carbonates has been associated with pH-driven supersaturation within the micro-environmental around a photosynthetic organism, and the fining of carbonate minerals within a varve has been related to the intensification of supersaturation through the year/season (Brauer *et al.* 2008). Commonly, homogeneous carbonate sublayers within varves are deposited during a rapid precipitation event, or 'whiting', resulting when the carbonate solubility threshold is exceeded across the lake (Kelts and Hsü, 1978). The resultant thickness of these whiting events within a varve has been related to seasonal water balance (Romero-Viana *et al.* 2008; Ariztegui *et al.* 2010) and bio-productivity (Livingstone and Hajdas, 2001). Abrupt, stratigraphic boundaries signify a rapid change to the primary depositional process (Mangili *et al.* 2005), and are characteristic of these rapid precipitation events.

1.4.5 Lacustrine carbonate deposition

Discrete carbonate sublayers delineate the finely-laminated stratigraphy of Nar Gölü's and Yaal Chac's sedimentary records. In Nar Gölü, this carbonate material is primarily deposited via endogenic precipitation (Roberts *et al.* 2016). Within its varved units, carbonate minerals predominately accumulate during annual calcium carbonate ($CaCO_3$) precipitation events, or 'whiting events'. These occur during the summer dry-seasons, when both physical and biochemical processes result in carbonate supersaturation (Dean *et al.* 2015b). Assuming that Yaal Chac's carbonate-rich laminations also reflect annually-resolved varves, the wet-dry seasonality is hypothesised to similarly drive annual whiting events consistently through time. This section first outlines the processes driving lacustrine carbonate deposition, and subsequently focuses on the endogenic carbonate precipitation specifically, due its likely governance on the sequences' stratigraphy.

Depositional processes

Carbonates can form a main component of lake sediments. Their deposition is a product of a numerous environmental variables and processes, which are subject to change greatly both spatially and temporally (Kelts and Hsü, 1978). Four main processes govern the presence and composition of the carbonates within lacustrine sediments:

i. Endogenic, chemical precipitation of inorganic carbonates
ii. Biogenic production of carbonates within living organisms (e.g. calcareous shells)
iii. Influx of allochthonous carbonates
iv. Diagenetic activity

The process leading to the deposition of an individual carbonate grain can be determined through a combined mineralogical and limnological assessment (Mangili *et al.* 2005); for example, the identification of euhedral calcite crystals would indicate endogenic, chemical precipitation. By subsequently understanding the drivers to these depositional processes, the necessary environmental setting required can be inferred (Brauer, 2004). Fundamentally, carbonate deposition is a function of lake water balance, sediment influx and temperature (Gierlowski-Kordesch, 2009), where each factor differentially influences each depositional process listed above. Before focusing

on endogenic precipitation (i), the following briefly outlines the various drivers to lacustrine carbonate deposition (ii-iv).

The deposition of carbonates derived from calcareous shells (ii) is typically regulated by the processes controlling the success/growth of in-lake shelly fauna, such as bivalves, ostracods and gastropods (Gierlowski-Kordesch, 2009). Each species ecological niche is determined by various biotic and abiotic factors. Specifically, a basin's geology, geomorphology and climatology may drive intra-annual changes to lakewater chemistry (temperature, dissolved oxygen, salinity, pH etc.) and availability of nutrients, and in-lake ecology may influence the availability of suitable habitats, food supply, competition and predation (Brönmark and Hansson, 2017). Provided a suitable niche, shelly fauna assimilate carbonate ions from the water into their shell. Following their death, these calcareous shell may be deposited to the lake bed, and hence incorporated into the sedimentary sequence. Subsequent analysis of a shell can identify the organism's taxonomy, thus providing an indication of the necessary environmental conditions for it to grow, around the time of its deposition (e.g. Mezquita *et al.* 1999; Cohen *et al.* 2007; Keatings *et al.* 2010).

The local/regional geology predominately dictates the viability of allochthonous carbonate deposition (iii) within a lake (Matter, 2009). The abundance and exposure of sedimentary carbonate rocks, most commonly limestone and dolostone, and the climatology primarily control weathering rates, and hence supply of transportable grains of detrital carbonate. The movement of these clastic grains to a lake is subsequently determined by water flow, and the catchment's land-use and geomorphology (Matter, 2009); while wind action may also contribute to allogenic carbonate deposition, distinguishing the aeolian carbonate grains from other fine-grained particles (<20μm) is difficult and often ignored (Gierlowski-Kordesch, 2009). The allogenic origin of these carbonate grains may be verified by matching their geochemical composition to the source rock's (Jiang *et al.* 2007). Again, past environmental conditions can be inferred by assessing changes to the concentration and composition of allogenic carbonates through a sedimentary record (e.g. Alonso-Zarza and Calvo, 2000; Koinig *et al.* 2003; Polyak *et al.* 2009).

Diagenetic activity (iv) pertains to the processes which change the composition and/or structure of sediment post-deposition. Specific limnological and sedimentological conditions drive different diagenetic processes, where burial rates and pore water space can regulate the sediments' susceptibility to diagenesis (Finkelstein *et al.* 1999). Diagenetic processes may influence the presence and mineralogy of carbonates within a lacustrine sediment core. Differing carbonate

solubility levels through a lake's water column can result in the dissolution of carbonates, during the time from their formation to burial (Wittkop *et al.* 2009). Carbonate mineralogical changes may result from specific hypolimnetic water chemistry and biogenic processes (Gierlowski-Kordesch, 2009); while Gierlowski-Kordesch (2009) provides a comprehensive list of diagenetic carbonates, the most common minerals are outlined here. Diagenetic dolomite may replace primary endogenic carbonate minerals, specifically high-Mg calcite (discussed below), during periods of elevated Mg:Ca ratios within pore water; this secondary dolomite may further transform into huntite and magnesite with continued increases to Mg:Ca ratios (Müller *et al.* 1972). Similarly, endogenic gypsum may be replaced by secondary carbonates, typically aragonite, via bacterial sulphate reduction within an anoxic hypolimnion (Anadón *et al.* 1992, Finkelstein *et al.* 1999); this diagenetic process reflects a reversible reaction, where oxidising conditions may revert secondary carbonates back into gypsum minerals. Organic sediment may also undergo diagenetic micritisation (Furukawa *et al.* 1997), converting carbon-rich organic matter into carbonate minerals and incorporating cellular proteins in and around its crystalline structure (Ingalls *et al.* 2004). This calcification of organic matter follows the same principles as endogenic carbonate precipitation (discussed in detail below), where biogenic decomposition may alter the lake's pH and geochemistry, consequently driving carbonate mineralisation (Bathurst, 1972).

Endogenic carbonate precipitation

Numerous carbonate minerals can precipitate across a wide range of hydrological conditions; however, calcium carbonate ($CaCO_3$) minerals, namely calcite and aragonite, represent the most common precipitates within freshwater systems worldwide (Gierlowski-Kordesch, 2009). Endogenic precipitation occurs when the water's carbonate solubility level is exceeded, and the resultant mineralogy is governed by the relative ion concentrations in the water (Declet *et al.* 2016). When this supersaturation occurs on a regular seasonal basis, varves can be deposited. This mechanism drives calcareous varve formation in many lacustrine systems (e.g. Kelts and Hsü, 1978; Livingstone and Hajdas, 2001; Lüder *et al.* 2006; Bluszcz *et al.* 2008; Brauer *et al.* 2008; Romero-Viana *et al.* 2008; Kalugin *et al.* 2013), including study sites Nar Gölü (Jones *et al.* 2006). Figure 1.3 displays the key controls determining the endogenic precipitation of calcium carbonate.

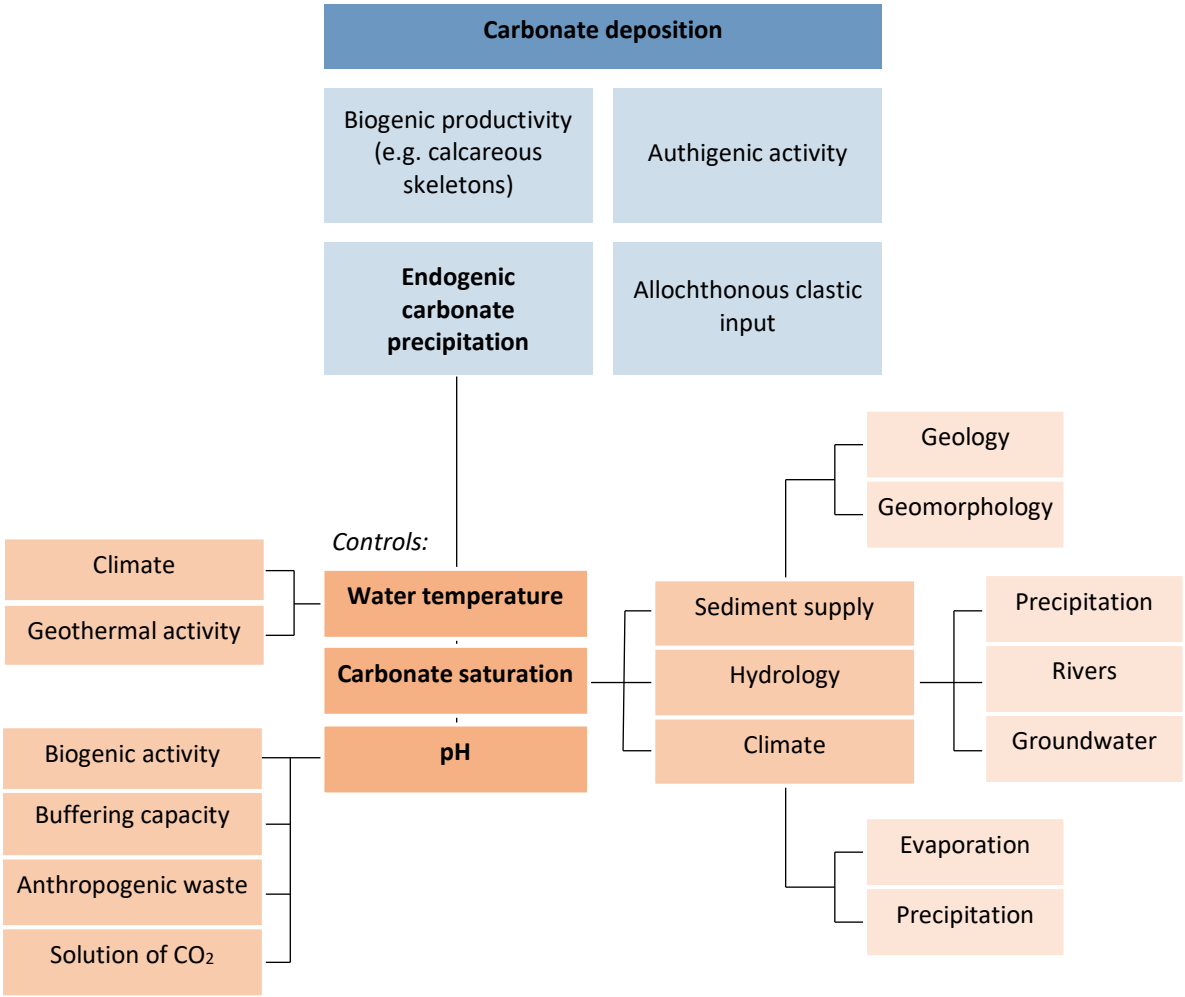


Figure 1.3 *– Conceptual diagram displaying the key controls driving carbonate precipitation in lake systems.*

Fundamentally, endogenic precipitation of calcium carbonate is controlled in equilibrium by the following reversible reaction:

$$CaCO_3 + H_2CO_3 \leftrightharpoons Ca^{+2} + 2HCO^-_3 \quad [1]$$

Where ($CaCO_3$) is solid calcium carbonate, (H_2CO_3) is carbonic acid, (Ca^{+2}) is a positive calcium ion, and (HCO^-_3) is a negative bicarbonate ion. Carbonic acid concentration is controlled in equilibrium by the following reversible reaction:

$$H_2O + CO_2 \leftrightharpoons H_2CO_3 \quad [2]$$

These two equilibria are dynamic, and so any changes to their component concentrations can affect the acting direction of these equations. The concentration of CO_2 in water governs the formation of

carbonic acid, and is in a dynamic equilibrium with atmospheric concentration. Any internal forcing acting to change the water's CO_2 concentration, such as water temperature variation and photosynthetic activity, will lead to water-atmosphere interchange of CO_2 to redress the equilibrium.

In the forward direction of equation [1], the reaction between the aqueous carbonic acid and solid calcium carbonate leads to the neutralisation of the acid and break down of the mineral into its component ions; this feedback causes the high buffering capacity observed in hardwater lakes. Figure 1.4 displays this influence of carbonic acid, and hence pH, on bicarbonate and carbonate concentrations. As pH increases, the dominate carbonate species changes from the carbonic acid to bicarbonate ions, and subsequently to carbonate minerals. Theoretically, carbonic acid and carbonate minerals cannot coexist as their reaction forms the bicarbonate ions; their respective minimum concentrations, and consequently maximum carbonate ion concentrations, occur when pH is 8.34 (Lindsay, 1979).

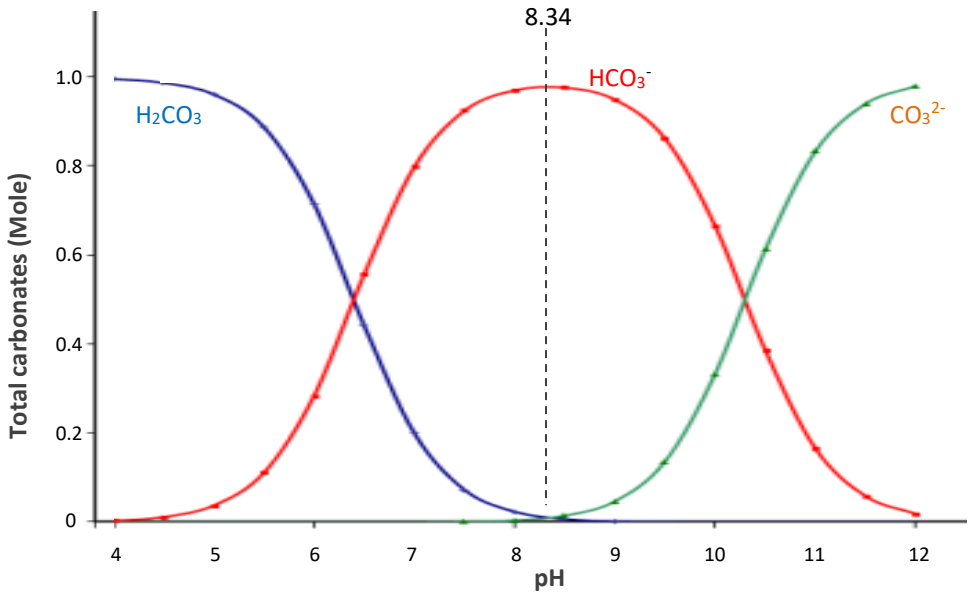


Figure 1.4 – *The influence of pH on carbonate species (after Lindsay, 1979)*

As shown in Figure 1.3, the solubility of carbonates, and hence endogenic precipitation, is primarily a function of water temperature, carbonate saturation and pH. As alluded to above, changes to any one of these may shift the acting direction of equations [1] and [2]; the following outlines the relationship between these environmental parameters and carbonate precipitation:

- *Temperature.* The solubility of CO_2 in water negatively correlates with temperature; therefore, warmer water reduces the formation of carbonic acid (see equation 2). Consequently, the water's pH increases, thus favouring the backwards direction of equation [1] and the precipitation of calcium carbonate.
- *Carbonate saturation.* Increasing the concentration of Ca^{2+} and bicarbonate ions also favours the precipitation of calcium carbonate (the backwards direction of equation 1). Ion concentrations may be enhanced via limnological stratification, sediment influx and evaporation.
- *pH*. Increasing the pH of water, favours the precipitation of calcium carbonate (the backwards direction of equation 1). Both natural and anthropogenic processes may drive pH variability; however, the season blooms of photosynthetic organisms most commonly drives the annual deposition of endogenic carbonates (e.g. Wulf *et al.* 2013). Conversely, aerobic organic deposition releases CO_2, thus enhancing the formation of carbonic acids (see equation 2) and favouring the dissolution of calcium carbonates (forwards direction of equation 1).

The mineralogy of endogenic calcium carbonate is primarily a function of the water's geochemical composition and, to a lesser extent, temperature (Ries, 2005). Most significantly, the water's Mg:Ca ratio determines the precipitation of calcite versus aragonite minerals. Calcite (aragonite) is preferentially precipitated within water with a Mg:Ca ratio below (above) two (Müller *et al.* 1972; Ries, 2006); calcite may be further divided into low- and high-Mg calcite, according to the concentration of Mg within its crystalline structure. While warmer water temperatures increase the inclusion of Mg within calcite, the water's Mg:Ca ratio primarily determines the calcite's Mg content (Morse *et al.* 2007).

The water's Mg:Ca ratio may be controlled by various biotic and abiotic processes. In lacustrine systems, Mg concentrations typically co-vary with salinity, whereas Ca concentrations may be buffered by endogenic carbonate precipitation (McGee *et al.* 2012), the controls of which are discussed above (Fig. 1.4). Consequently, water's Mg:Ca ratios typically reflect changes to a lake's water balance; where Mg:Ca ratios increase in more evaporative systems (e.g. Kelts and Hsü, 1978; Zhang *et al.* 2009; McGee *et al.* 2012). Increased Mg:Ca concentrations result in the greater assimilation of Mg within calcite's crystalline structure (Xia *et al.* 1997).

However, far less Mg is incorporated into aragonite, compared to calcite (Xia *et al.* 1997). Consequently, mineralogical shifts are not necessarily reflected within the sediment's Mg:Ca ratio. Instead, aragonite partitions greater Sr concentrations from the lake water into the crystalline lattice (Valero-Garcés *et al.* 1997). Sr in lake water displays similar dynamics to Mg, where Sr:Ca ratios also increase with salinity and carbonate precipitation (Chivas *et al.* 1986**;** Zhang *et al.* 2009). Within lacustrine records, the sediments' Sr:Ca ratio is often used as a proxy to water balance, where higher values are typically interpreted to reflect increased ionic concentrations, irrespective of specific carbonate mineralogy (e.g. Chivas *et al.* 1986; Xia *et al.* 1997; Last and Vance, 2002; Ito, 2002; Zhang *et al.* 2009; McGee *et al.* 2012); whereas, both water balance and mineralogy can drive changes to the sediments' Mg:Ca ratio.

1.5 Aims and objectives

Through a detailed investigation of varve microfacies and their geochemical composition, this research aims to develop two long, annually-resolved records of sediment deposition from lakes Nar Gölü and Yaal Chac. Subsequent analysis of these study sites' seasonal limnology intends to reveal the environmental drivers of the observed sediment deposition; therefore, specific microstratigraphic variables can be used to infer changes to these depositional drivers through the records. These reconstructions aim to develop understanding of high resolution limnological and climatic change in two regions that have relatively few annually-resolved environmental records. All dates within this thesis are given in *cal yrs BP*, where 'present day' is defined as 1950 AD.

Associations between environmental forcings and microstratigraphy will be corroborated using other proxies. Extensive research over the past 16 years at Nar Gölü has developed palaeoenvironmental reconstructions through the Holocene using numerous proxies deposited within the sediment record; Table 1.1a outlines the key datasets available. Substantial lake monitoring efforts over this period, required to interpret these proxies reliably, have also advanced understanding of the limnological system and how environmental forcing is recorded in the lacustrine sediment (Dean *et al.* 2015b). In this thesis, varve sedimentological data aim to build upon these reconstructions, while increasing their temporal resolution, and provide new reconstructions inferred from Yaal Chac's sediment record, a lake with no previous published research (Table 1.1b).

Table 1.1 *– List of the key datasets discussed is this thesis and their sources, for Nar Gölü (a) and Yaal Chac (b).*

a) **Nar Gölü:**

Data available	Description	Temporal resolution	Reference
Varve microfacies	Record of the composition, structure and thickness of varve sublayers	Seasonal-annual	**This study**
Sediment geochemistry	Itrax µXRF core scan, gaining a profile of element detection	Sub-annual (every 200 µm)	Allcock, 2013; Roberts *et al.* 2016
Stable isotopes	Oxygen and carbon isotope record from:		
	- Carbonates	1-25 years	Jones *et al.* 2005, 2006; Dean *et al.* 2015a, 2017
	- Diatoms	1-25 years	Dean *et al.* 2013
Diatoms	Record of diatoms assemblages	~10 years	Woodbridge and Roberts, 2010, 2011
Pollen	Record of pollen assemblages	~20 years	England *et al.* 2008
Contemporary lake monitoring	Limnology (including water chemistry and mixing regime)	Daily-annual	**This study**; Jones *et al.* 2005; Dean *et al.* 2015b
	Stable isotopes of water	Seasonal-annual	
	Seston sediment traps	Annual	

Table 1.1 (cont.) *– List of the key datasets discussed is this thesis and their sources, for Nar Gölü (a) and Yaal Chac (b).*

b) **Yaal Chac:**

Data available	Description	Temporal resolution	Reference
Varve microfacies	Record of the composition, structure and thickness of varve sublayers	Seasonal-annual	**This study**
Sediment geochemistry	Itrax µXRF core scan, gaining a profile of element detection	Sub-annual (every 200 µm)	**This study**
Sediment X-ray diffraction (XRD)	Carbonate mineralogical change through discontinuous core sequence	~200-250 years (every 10cm)	Undergraduate work (Lem, 2011)
Stable isotopes	Oxygen and carbon isotope record from carbonates	1-25 years	Undergraduate work (Hooper, 2011)
Charcoal	Particulate charcoal from discontinuous core sequence	~200-250 years (every 10cm)	Undergraduate work (Harwood, 2011)
Organic pigments	Chlorophyll and carotenoid pigments from discontinuous core sequence	~100-150 years (every 5 cm)	Undergraduate work (Stevenson, 2011)
Contemporary lake monitoring	Limnology (including water chemistry and mixing regime)	Daily-annual	**This study**; Undergraduate work (Clapich, 2016)
	Stable isotopes of water	Seasonal-annual	
	Seston sediment traps	Annual	

Once established, the high resolution nature of these sedimentary records will facilitate the exploration into subtropical climate dynamics, namely variability to the annual migration of the ITCZ and subtropical high pressure belt, and the sub-decadal/centennial oscillations influencing regional climatology. A combined interpretation of the varved environmental record and influence of regional climate dynamics will aim to provide the environmental context to societal change. By precisely dating and characterising regional hydrological changes, the potential for climate to influence societies may be assessed in these two areas whose complex societal histories were probably vulnerable to changes in seasonal water supply.

1.6 Thesis outline

This thesis first describes the methodology used to collect and analyse data for this research (Chapter 2). The subsequent two chapters are divided accorded to study site: Nar Gölü, Turkey (Chapter 3) and Yaal Chac, Mexico (Chapter 4). Both of these chapters follow a similar structure, containing the following four sections:

1. *Study site and climate* – describes the contemporary environmental setting of each lake, and outlines the current understanding of the region's environmental change through the Holocene.
2. *Lithology and chronology* – discusses the development of sequences' lithologies and chronologies.
3. *Sedimentology* – presents the records' sedimentological results, primarily datasets pertaining to varve microfacies and their geochemical composition.
4. *Discussion and interpretation* – discusses the results' interpretation regarding both environmental and societal change.

Finally, Chapter 5 draws comparisons between the two sites and their records, and concludes the work of this thesis.

2. Methodology

This chapter outlines all the methods used to reconstruct climate using varve analysis from lacustrine records in Turkey and Mexico.

2.1 Core extraction

Numerous cores have been retrieved from the two lakes in order to build a continuous record of lacustrine deposition, and hence environmental change. To reconstruct high resolution climate change, a continuous sequence of undisturbed sediment is required; these recovered sequences should include as many varves, or laminations, as possible. Overlapping parallel cores helps ensure a continuous record is recovered and also permits multi-core comparisons to help identify coring artefacts and imperfections (Petterson *et al.* 1993). Maintaining this sediment integrity is crucial for varve micro-stratigraphy analysis (Bendle *et al.* 2015) and so coring-derived sediment disturbance, which commonly occurs at the top and bottom of drives, was minimised via overlapping cores and, at Nar Gölü, increasing the length of core drives. With the exception of the YC16 core (discussed below), all sediment cores analysed within this thesis was retrieved prior to the start of this research.

At Nar Gölü, an initial coring programme in 2001-02, led by Prof Neil Roberts, extracted a 376cm composite sequence (NAR01/02) using a variety of coring methods (Jones, 2004). A Glew corer (Glew, 1991) was used to retrieve the topmost 65cm sediment, including the sediment-water interface. To retrieve deeper material, Livingstone (Livingstone, 1955) and Mackereth (Mackereth, 1958) corers were used and gained 1m and 3m drives respectively. However, the weight and intrinsic strength of coring equipment through 25m of water inhibited the further retrieval of deeper sediment (Jones, 2004).

To extract deeper material, a second coring operation was carried out in July 2010 using a UWITEC hammer-piston corer (Schultze and Niederreiter, 1990) on a more substantial aluminium platform (Dean, 2014). Operated by representatives from CNRS EDYTEM, the corer was able to take long drives of 2-3m thus minimising sediment disturbance. Overall, 55m of core were extracted and have been correlated to form a 21.5m composite sequence (NAR10) (Roberts *et al.* 2016).

At Yaal Chac, various coring campaigns have established Yaal Chac's sediment record. In January 2011, exploratory coring, by a team led by Prof Sarah Metcalfe, retrieved six 1m-long drives using a Livingstone corer (Livingstone, 1955) (Core YC11 1-6). While these cores reached a maximum sediment depth 275cm, subsequent sedimentological analysis revealed a lack of overlap between core sections, thus failing to obtain a continuous depositional record. In April 2014, the team returned and successfully cored a deeper, near-continuous record from Yaal Chac (YC14). In total, twelve drives were taken from four different cores using a modified, square-rod piston corer (Wright *et al.* 1984) (Core Ø1 Ia-b, Core Ø3 and Core Ø4) and a Livingstone corer (Core Ø1 II-IV, and Core Ø2). A 409cm master sequence was then selected from eight overlapping core drives – details on its composition are discussed in Section 4.2.1. However, two core sections from YC14 did not overlap and so, in January 2016, two additional metres (YC16) were taken using a Livingstone corer to ensure a complete depositional sequence could be produced.

All sediment cores used in this research were extracted from Nar Gölü's and Yaal Chac's deepest regions, thus optimising varve preservation (Fig. 2.1 and 2.2). Here, sub-oxic conditions, which prevent sediment mixing via bioturbation, will be maintained for the longest period within the water body, and the comparatively flat surface reduces the likelihood of gravity-induced slumping which mixes and re-deposits sediment (Zolitschka *et al.* 2015). In order to locate the deepest point, bathymetry was recorded using a Garmin Fish Finder prior to the NAR01/02, YC14 and YC16 coring, and an additional seismic survey produced more detailed bathymetric information prior to the NAR10 cores (Smith, 2010). The cores from Nar Gölü were also extracted away from the alluvial fan to avoid additional slumping associated with active fan formation. Accordingly, the Nar Gölü's sediment records were cored at the lake's deepest point (25m – at time of coring), and Yaal Chac's from a water depth of 12.1m (maximum depth measured of 15.1m); the presence of undisturbed laminations throughout Yaal Chac's master sequences suggests that coring location did not significantly affect varve preservation.

Within the core tubing, excess water was removed and cores were left upright to settle under gravity; this minimised disturbance caused during the transportation, thus preserving the record's integrity. In the wetter Glew cores, Oasis® was pushed into the core-ends to further absorb excess water and hold the sediment in place securely for air transport back to the UK. As soon as possible, cores were refrigerated at 4°C to minimise drying and organic decomposition. The preservation of abrupt boundaries between laminae indicates that the sediments remained undisturbed through the coring and transportation process; stratigraphic information was not lost.

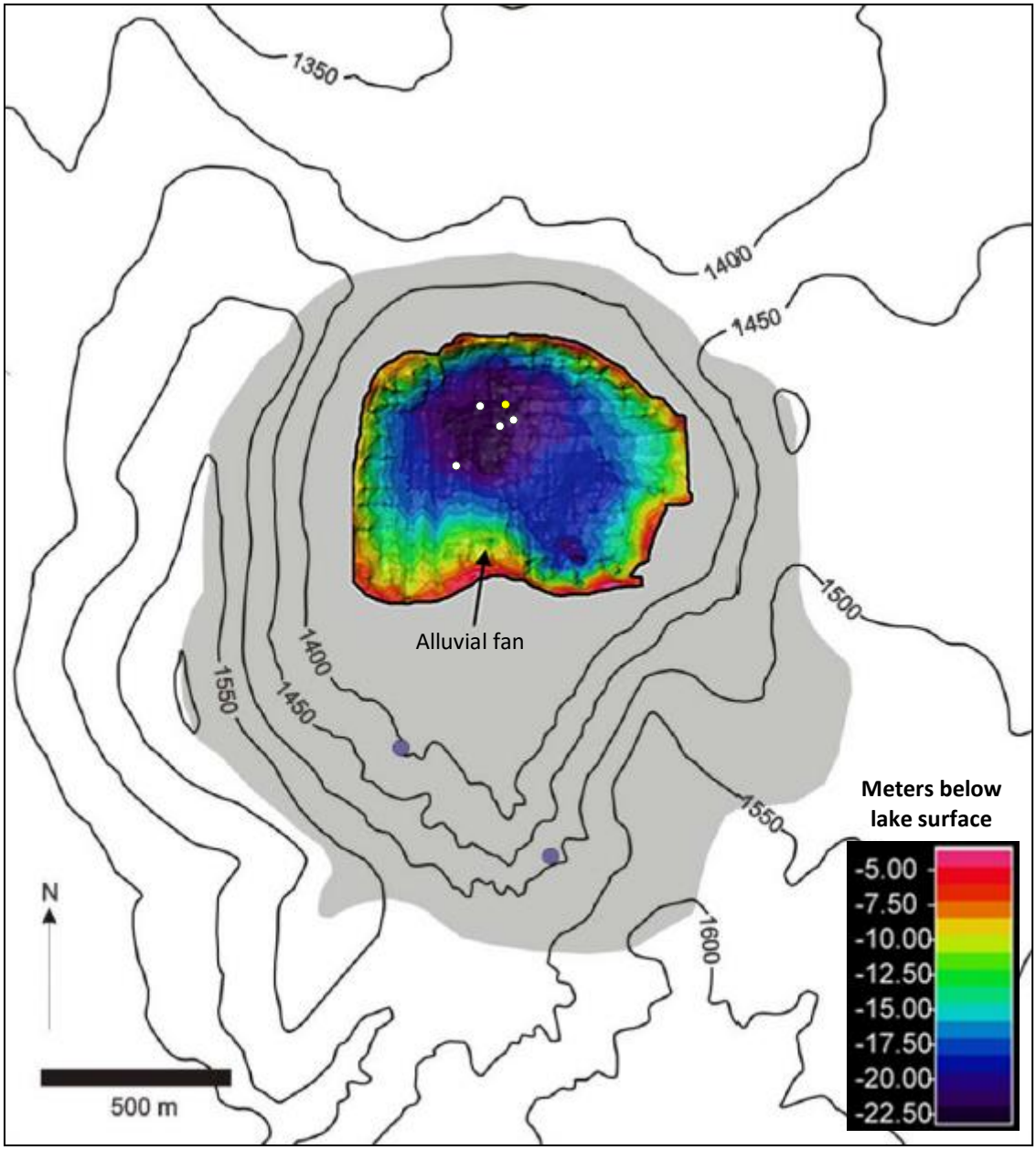


Figure 2.1 – *Nar Gölü catchment area (grey area) and lake bathymetry (coloured contours). The NAR10 coring site (yellow dot), NAR01/02 coring sites (white dots), and freshwater springs (blue dots) are marked within the lake and catchment. [*Figure *adapted from Jones, 2004; bathymetry data from Smith, 2010]*

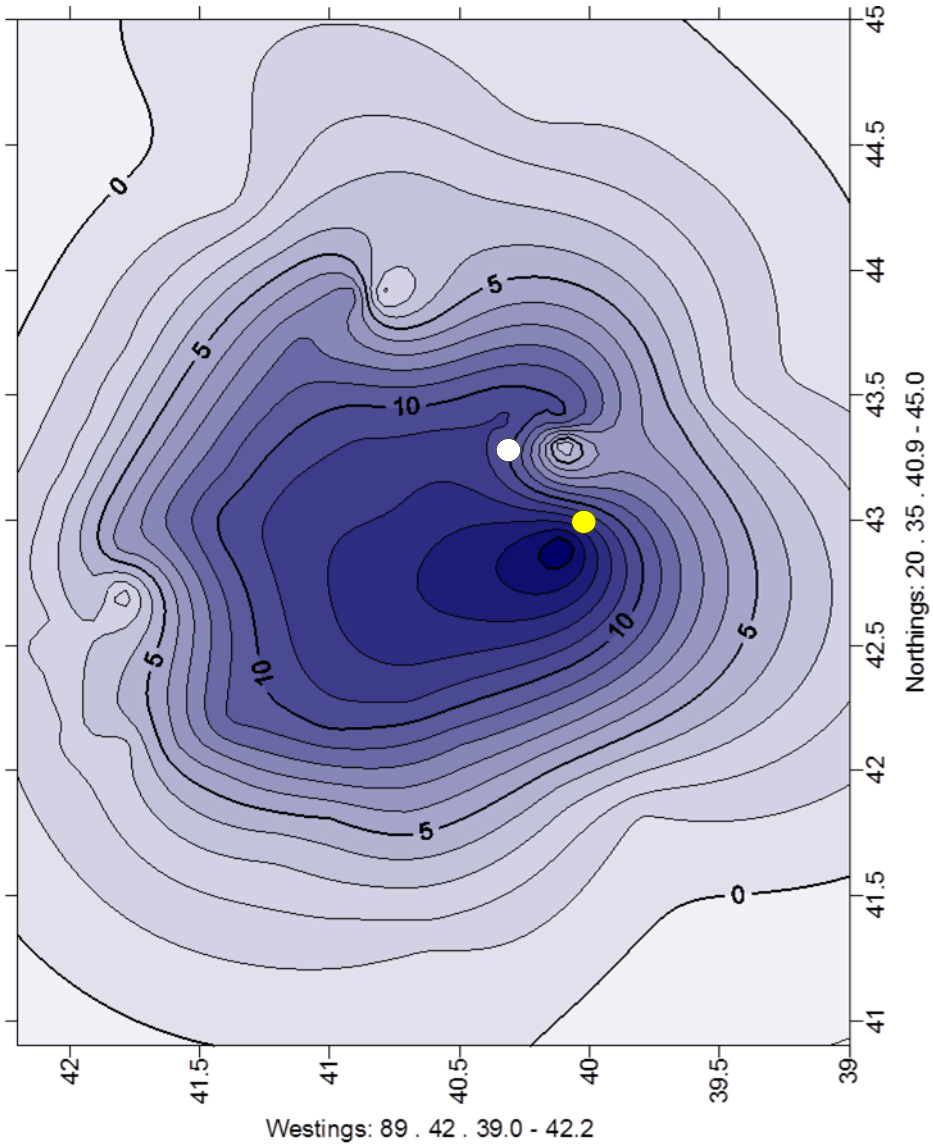


Figure 2.2 – *A bathymetric map of Yaal Chac. Coring sites YC14 (yellow dot) and YC16 (white dot) are marked in the lake.*

2.2 Core preparation

All core sections extracted were opened and prepared within the UK; from Nar Gölü, the NAR01/02 sequence was prepared and subsampled by Jones (2004), and the NAR10 sequence by Allcock (2013) and Dean (2014), and from Yaal Chac, all core sequences (both YC14 and YC16) by the author. This involved cutting the plastic core tubes in half lengthways, and pulling cheese-wire through the sediment to split it into the two half-tubes. One half's sediment was cleaned by scraping off the top ~1-2mm; this removes smearing caused by opening process, and reveals the stratigraphy. These clean sections are used in the core descriptions and are photographed in controlled conditions (Section 2.3.2). Core sections are stored wrapped in non-PVC cling film and layflat tubing, and

refrigerated at 4°C. Using the sediment stratigraphy, core sections were aligned visually to form a composite master sequence (for example, see Fig. 2.3); geochemical analysis via µXRF was later used to support these proposed tie points (see Section 2.3.3). These master sequences aim to build the continuous sequence of deposition with minimal sediment disturbance – full details of their composition and structure are described in Sections 3.2 and 4.2, for Nar Gölü and Yaal Chac respectively.

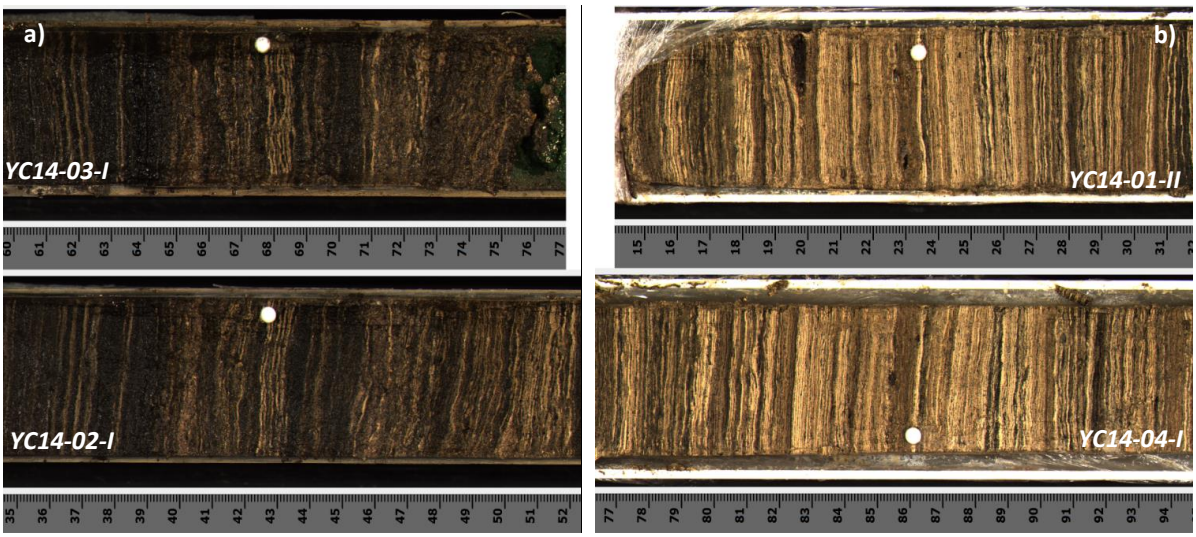


Figure 2.3 – *Examples of tie points, marked by white pins, between core drives using the sediment stratigraphy in discontinuously (a) and continuously (b) laminated sediment; images of Yaal Chac's master sequence.*

2.3 Varve sedimentology

To analyse the varve sedimentology several methods were used to build a picture of their composition and structure. The varves' microstratigraphy was analysed via thin section microscopy (Section 2.3.1) and micro X-ray fluorescence scanning (µXRF) (Section 2.3.3), and broader lithological changes were analysed via photographic imagery (Section 2.3.2) and bulk geochemistry (Section 2.3.4). Used in combination, these methodologies provide comprehensive data on inter- and intra-annual sediment deposition, which is constrained to an annual incremental chronology. The following section describes each of these methods in detail.

2.3.1 Sediment microstratigraphic analysis

Thin section microscopy permits this high resolution analysis of the sediment's microstratigraphy (Brauer, 2004). The following outlines the methods used to create thin sections from the cores' unconsolidated sediment, and analyse them via microscopy.

2.3.1.1 Thin section preparation

To analyse the varve microstratigraphy, sediment thin sections were made from the master sequences of Nar Gölü (Section 3.2) and Yaal Chac (Section 4.2). Thin sections present the best representation of sediment structure and composition (Kemp, 1996) and permit the analysis of sediments *in situ* (Bendle *et al.* 2015); consequently, environmental conditions required to deposit the observed sediments can be inferred (Martin-Puertas *et al.* 2009). Nar Gölü's thin sections were prepared externally by Samantha Allcock and technical staff from the University of Birmingham. Yaal Chac's were made through collaboration between the author and Potsdam's Helmholtz Centre, under the supervision of Prof Achim Brauer. The following methodology is specific to Yaal Chac's thin section preparation and, for the most part, the same methods were used on Nar Gölü's material; footnotes will explain any alterations.

Following training at the Helmholtz Centre in Potsdam, a methodology for creating sediment thin sections was decided. The methodology aimed to maintain the sediment's structural composition necessary for reliable analysis of varve microfacies (Zolitschka *et al.* 2015), and is well established in the literature (e.g. Zolitschka, 1996; Brauer *et al.* 1999, 2000, 2008; Wulf *et al.* 2004; Martin-Puertas *et al.* 2009). The following methodology originates from its first use by Merkt (1971), and closely matches the recommended approach by Boës and Fagel (2005) in their review of possible preparation techniques.

Subsampling 100mm-long by 15mm-wide blocks of sediment along the undisturbed core is achieved by pushing two L-shaped cutters into the sediment before using cheese-wire to cut underneath (Nakagawa *et al.* 2014) (Fig. 2.4a). Due to the relatively low clay content of the Yaal Chac sediments, electro-osmosis cutting, as recommended by Francus and Cosby (2001), is deemed superfluous to requirements. Subsample core-depths should overlap by 2cm to ensure correlation between thin sections is possible. By subsequently matching distinct sublayers within these overlapping thin sections, a continuous sedimentary sequence was analysed (Brauer *et al.* 2008) (Fig. 2.5).

Subsamples from Yaal Chac were placed in aluminium foil boxes, and shock frozen using liquid nitrogen (-196°C), poured around the boxes to avoid direct contact with the sediment, a method first used by Merkt (1971) (Fig. 2.4b). Rapidly freezing sediment minimises volumetric changes by reducing the interstitial ice crystal size thus maintaining structural integrity required for accurate microstratigraphy analysis (Francus, 1998). Nar Gölü's subsamples were instead placed in solvent-resistant moulds, and frozen using a conventional freezer at -20°C; fortunately, subsequent thin section microscopy suggests that this freezing method did not affect the varves' microstratigraphy.

Frozen subsamples are then freeze-dried for 48 hours, to ensure total dehydration; freeze-drying is preferentially used over acetone exchange or oven-drying techniques due to its ease, safety, minimal effect on the physical structure of the sediment associated with water removal via sublimation (Mudroch and MacKnight, 1994), and the preservation of organics that would not be possible using acetone exchange (Boës and Fagel, 2005). Re-pressurisation of the evacuated freeze-drier, following drying, is kept as slow as possible to avoid air turbulence damaging the fragile, dry sections, and minimise the (low) risk of self-combustion of organics (Dräger *et al.* 2016).

Once dry, the subsamples were impregnated with epoxy resin (Araldite 2-component resin) (Fig. 2.4c). Subsample resin-saturation was achieved over 3-4 cycles of resin addition and uptake via capillary action in a gentle vacuum. Boës and Fagel (2005) recommend that the vacuum pressure should not be high enough to boil the resin, as bubbles and rapid uptake can damage the sediment matrix, especially with smaller grain sizes. Resin was left for at least 48 hours within a fume cupboard to set fully. This sediment impregnation also prevents geochemical changes over time, thus enabling reproducible data collection (Brauer *et al.* 2009).

Once set, these resin embedded sections were cut perpendicular to the varves' bedding plane so that they can be stuck to a glass microscope slide, using the same resin to maintain a constant refractive index (Fig. 2.4d); this Araldite 2020 resin also has a similar refractive index to glass. All thin sections were then lapped (i.e. ground) down to the desired thickness of 20µm (Lotter and Lemcke, 1999). Thin section slides were then finished with a cover slip.

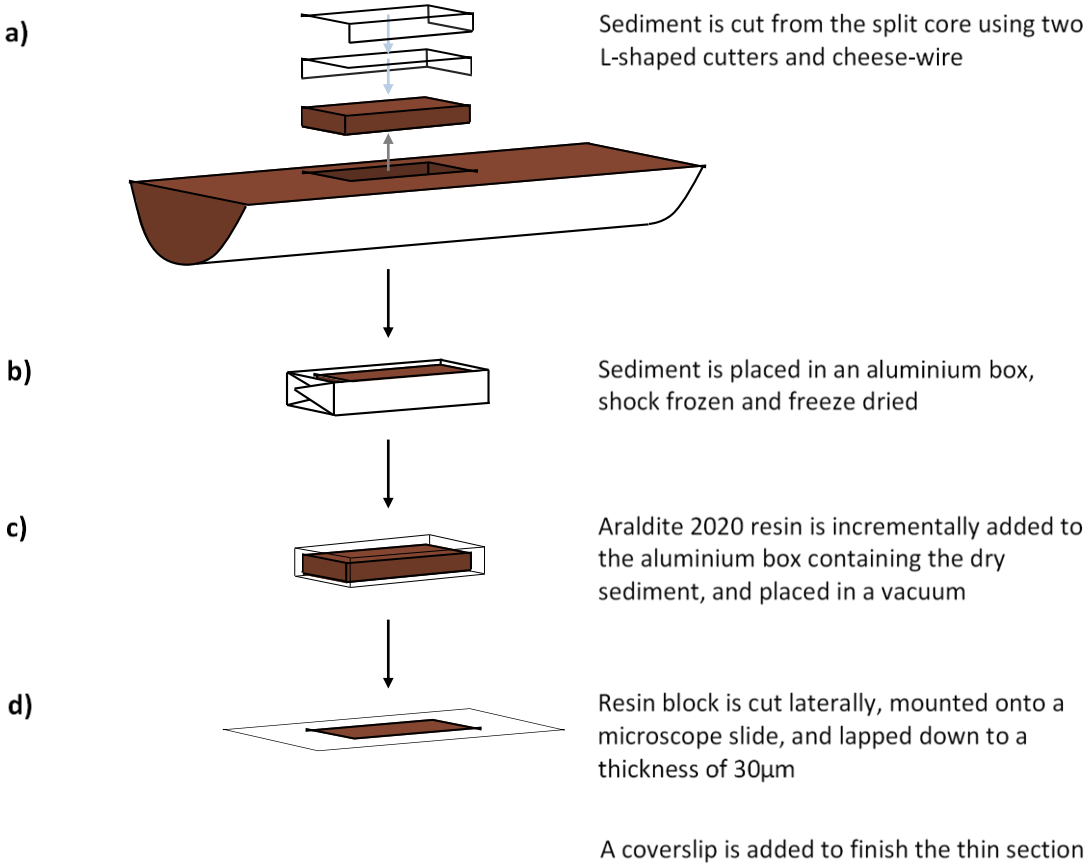


Figure 2.4 – *Method used for preparing a thin section from unconsolidated sediment*

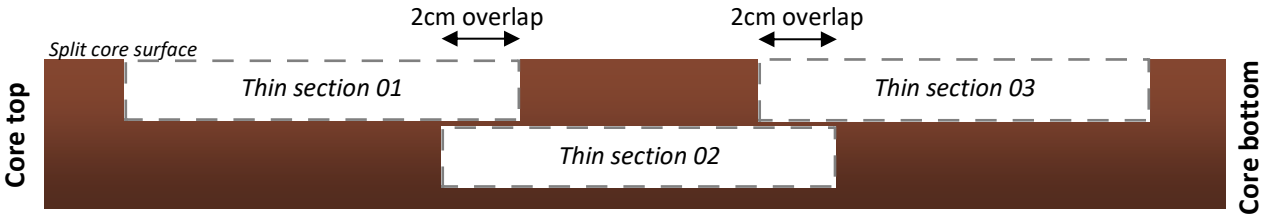


Figure 2.5 – *Cross sectional, schematic diagram outlining where sediment was cut in order to obtain a 2cm overlap between thin sections. Due to the narrow diameter of the core, sections were cut over-and-under.*

2.3.1.2 Microscopy

Varve counting

Varves were initially counted using the high resolution imagery from an SLR camera (see Section 2.3.2) within the software ImageJ, and on freshly split core sections (for Nar Gölü's counting details see Jones, 2004; Allcock, 2013). Counts were then repeated via thin section microscopy from both Nar Gölü's and Yaal Chac's records, which facilitated a more reliable identification of the annual cycle (Brauer, 2004); thin section microscopy is essential for varve counting as the annual cycle can be identified most easily (Boës and Fagel, 2005). When counting, each varve was checked against the conceptual model of varve formation to ensure that a set of laminae reflect a single year (Lotter and Lemcke, 1999). Non-seasonal layers, such as turbidity slumps and catchment mass wasting events, can also be better distinguished in thin section and thus can be excluded from the chronological counts. For these reasons, counts using thin sections are generally considered the most reliable method of constructing a varve chronology (Zolitschka, 1991).

As previously discussed (see Section 1.4.2), error within varve chronologies is typically very low, ±1-3% Ojala *et al.* (2012). Counting varves via thin section microscopy minimised this error (Card, 1997; Ojala *et al.* 2012), and the high resolution imagery was further cross-referenced with the thin sections to check for discrepancies. Any differences between thin section and imagery results are re-assessed to increase the likelihood that results are representative of lake deposition and hence time. Nevertheless, error is quantified by repeating counts, at least three times and preferably independently by more than one person, between discrete core sections (e.g. Brauer *et al.* 2000; Boës and Fagel, 2008).

To correlate varves from one thin section to the next, and hence ensure a continuous sequence, conspicuous laminations or sets of varves were matched together. While this is acknowledged as the most reliable method, as it disregards effects of sediment expansion/shrinkage (Lotter and Lemcke, 1999), distinct layers are not always present within the 2cm overlap. In these cases, sediment depth measurements and core imagery is used to correlate thin sections.

Sedimentation rates (mm/yr) were calculated by counting the number of varves within subsequent 10mm segments (Lotter and Lemcke, 1999) [1]:

$$\text{Sedimentation rate (mm/yr)} = 10 / \text{number of varves counted within 10mm} \quad [1]$$

Due to the average varve thickness (>1mm) from both Nar Gölü and Yaal Chac, segment lengths of 10mm were decided on to gain a more representative sedimentation rate.

Varve thickness

The thickness of each lamina, and hence complete varves, were measured via thin section microscopy. Thickness measurements were made using a microscope reticle on thin sections (e.g. Midowski *et al.* 2004; Swierczynski *et al.* 2013). While numerous automated methods have been developed to run varve counts (Francus *et al.* 2002) and laminae measurements (Varem-Sanders and Campbell, 1996; He *et al.* 2008; Schlolaut *et al.* 2012), comprehensive research on the implementation of such programs by Marshall *et al.* (2012) states that thin section microscopy often remains the most reliable and repeatable methodology. Counts and measurements using thin section microscopy crucially allow the user to interpret the sediment more holistically and use their experience to contextualise observations.

Each lamina of the sequences was measured along a linear transect that bisects the core's width (Lamoureux, 2000, 2002). Measurements only deviated from the transect when the sediments' structure was significantly disrupted or damaged (Francus *et al.* 2002), yet distances were always measured perpendicular to the laminae's bedding plane. The start/end of each measurement was determined subjectively, where the sublayers' sedimentology changed the most abruptly. Total varve thickness was subsequently gained through adding up lamina measurements which form each varve.

Varve microfacies

Data were collected using a petrographic microscope to record details of the varves' micromorphology (Brauer, 2004). Working along a linear transect, the number of laminations within each varve are first recorded. As each of their thicknesses was measured, the sublayers' composition and structure were also identified and categorised accordingly (e.g. 'Fine-grained aragonite crystals'). Sedimentological characteristics were subsequently described, including the presence of grain size sorting and diffuse/abrupt sublayer boundaries. Finally, visual indications of diagenesis (e.g. carbonate dissolution, pyrite formation) are recorded, as sedimentological changes post-deposition will not reflect the corresponding environment at its time of deposition. Each varve is also given a subjective rating on a scale of 0-3 in regards to their quality. Quality primarily pertains to the distinction of varve boundaries, and provides an indication of mixing/disturbance and

chronological integrity (0 = well-mixed, unvarved sediment; 3 = clear varves with distinct laminae boundaries) (Lamoureux, 2002).

Varves which share similar microfacies can then be categorised together; each category reflects a specific succession of annual sediment deposition through the year, and hence a change to the microfacies denotes a change to the limnological/climatic system. This provides larger scale indications of environmental change (Zolitschka *et al.* 2015). The seasonal scale reconstructions are gained through the interpretation of the sub-layers within each microfacies, including the condition required for its deposition and using their thickness to denote magnitude of depositional driver (Brauer, 2004). It is this sublayer interpretation which permits the detection of low-magnitude, rapid climate change (Brauer *et al.* 2008).

To interpret microfacies reliably, a comprehensive understanding of annual limnology and climatology is required (Brauer *et al.* 2009); this is gained through contemporary monitoring efforts (see Section 2.4). Extensive palaeoclimatic research from Nar Gölü using numerous environmental proxies, such as oxygen isotopes (Jones *et al.* 2005, 2006; Dean *et al.* 2013, 2015a, 2015b), pollen (England *et al.* 2008), diatoms (Woodbridge and Roberts, 2010, 2011) and geochemistry (Allcock, 2013, 2017), has already be achieved. As a result, correlations between these environmental reconstructions and varve microfacies parameters can be made. These relationships can potentially aid the interpretation of Yaal Chac's microfacies.

Microfacies data are semi-quantitative in nature; however, the data are used in direct conjunction with quantitative geochemical data gained through micro-X-ray fluorescence (μXRF) (Brauer *et al.* 2009) (see Section 2.3.3).

2.3.2 Imagery

Using a digital SLR camera images were taken along the freshly-split and cleaned core sections from Yaal Chac and Nar Gölü; each photograph captured ~11cm of sequence. A large overlap between pictures (2-3cm) ensured a continuous record and minimised the effect of perspective-induced distortion around the image edges. Light was controlled as far as possible to maintain constant conditions and minimise shadow: windows were blacked out, ceiling lights remained on, and, for the Yaal Chac cores, each picture was taken twice with and without the aid of a close-up spot lamp. Images of the Nar Gölü core were taken previously by Dr Matthew Jones and colleagues, while Yaal

Chac's were taken by the author and Dr Matthew Jones at the University of Nottingham. The images' pixel size, and hence spatial resolution, is small, measuring 0.05mm and 0.03mm for Nar Gölü's and Yaal Chac's photographs respectively.

All of Yaal Chac's core drives were also imaged using BOSCORF's Geotek® Multi-Sensor Core Logging Core Imaging System (MSCL-CIS). This scanner produces a single, continuous image under very well controlled light conditions; therefore, light reflectance and shadows across the sediment topography are minimised, and brightness levels are the same for all images. Colour was calibrated prior to scanning using a printed white standard.

The high resolution images of the Nar Gölü and Yaal Chac cores were taken immediately after the cores had been split and the facies cleaned; this minimises colour changes associated with sediment drying and oxidation (Schnurrenberger *et al.* 2003). However, the MSCL-CIS was used on the Yaal Chac core 12 months after being split open. To minimise the effect of drying and oxidation on colour, the sediment was scraped again prior to scanning, thus revealing fresher, underlying material. No significant change or decay was identified from when the cores were first opened.

2.3.3 Geochemical analysis (µXRF)

2.3.3.1 Lacustrine sediment core geochemistry

Micro X-ray fluorescence (µXRF) using an Itrax core scanner (Cox Analytical Systems) non-destructively measures counts of elements heavier than aluminium along a core (for a technical overview, see Croudace *et al.* 2006). This technique quickly acquires an exceptionally high resolution (up to 60µm), continuous dataset of geochemical composition, which could not be achieved using conventional XRF techniques (Croudace *et al.* 2006); as a result, the use of µXRF scanning on sedimentary sequences has increased rapidly over the last decade (e.g. Moreno *et al.* 2008; Weltje and Tjallingii, 2008; Metcalfe *et al.* 2010; Giralt *et al.* 2011; Kylander *et al.* 2011a; Davies *et al.* 2015). For varved sequences, high resolution scanning is required to detect the fine geochemical changes between sub-annual laminations, and hence identify the constituents of each season's primary sediment deposition (Brauer *et al.* 2008, 2009). Element concentrations can be used as environmental proxies (e.g. Haug *et al.* 2003; Metcalfe *et al.* 2010), and crucially be integrated with thin section analysis to help to quantify palaeoenvironmental change (Brauer *et al.* 2009).

The Itrax scanner uses a molybdenum (Mo) tube to generate high powered X-rays, which are appropriate for transition and heavy elements with detection limits as low as 20ppm for some elements (Cuven *et al.* 2010). These X-rays are focused onto the split core through a slit aperture, parallel to the varves' bedding plane. The high powered beam of X-ray radiation excites the atomic electrons into a higher energy shell, and the subsequent relaxation of electrons re-emits X-ray radiation specific to the element ('fluorescence'). Measuring the re-emitted X-ray power can provide information of the elemental composition of the sediment in question (Croudace *et al.* 2006). Raw data were displayed as counts per second (cps); this equals the spectral peak area divided by count time in seconds.

Both lake records were scanned using an Itrax µXRF core scanner at the Aberystwyth University (Fig. 2.6). Dr Samantha Allcock, with the aid of Prof Henry Lamb and Dr Michael Marshall, scanned Nar Gölü's sequence (NAR10) to a 200µm resolution (Allcock, 2013). The author, along with Dr Sarah Davies, completed Yaal Chac's sequence (YC14) also to a 200µm resolution, and short sections to 60µm resolution. Split cores were cleaned to ensure a fresh, flat surface; increased surface roughness is known reduce elemental counts (Jarvis, 2012). The cores were covered with a thin sheet of pure polypropylene film (4µm thick) to minimise sediment drying and decay, and prevent instrument damage from any contact with sediment (Anderson *et al.* 2012).



Figure 2.6 – *Itrax µXRF scanner at the University of Aberystwyth. Prepared cores are placed inside its left arm, and cores are moved under the scanner in the middle.*

A 4mm wide by 200µm long aperture was selected to focus X-rays onto the sediment. While the aperture can be reduced to 60µm (Croudace *et al.* 2006), the 200µm the resolution was deemed suitable as it is able to gain multiple elements counts within each lamina and not exceed time constraints. The 4mm wide aperture has been shown to minimise signal loss associated with tilted laminae, where the X-ray beam crosses inclined boundaries (Marshall *et al.* 2012).

The same Itrax settings were used on both lake records: 10s count time, 200ms exposure time, 30kV X-ray voltage and 50mA X-ray current. These settings optimise element detection within the constraints of time and resources (Sarah Davies, pers comm, Nov 2015). Up to 36 different elements were detected from the scans, yet those with very low counts per second (<100cps) should be used with caution due to increased error associated with the instrument's sensitivity (Cuven *et al.* 2015). The most abundant elements, and hence those which are most likely to have reliable signals include: potassium (K), calcium (Ca), titanium (Ti), manganese (Mn), iron (Fe), zinc (Zn), bromine (Br), and strontium (Sr).

High-resolution (60µm) radiographic images are produced after the geochemical scan. These images depict density change along the core; light regions indicate less dense organic-rich sediment, and dark regions indicate more dense carbonate-rich sediment. For these radiographs, the scanner's X-ray power was increased to 60 kV voltage and 50 mA current, so that the beam can fully penetrate the entire split core.

Itrax is able to detect elements between Al and U on the periodic table only. As lake sediments contain significant concentrations of elements beyond the detection limits of the scanner (e.g. nitrogen, oxygen, carbon), these light elements act to dilute the detection of elements within the scanner's limits (Elbert *et al.* 2011; Löwemark *et al.* 2011). This effect is most commonly derived from changes in water and organic content; for example, increased organic concentrations will lead to an apparent reduction in elemental counts, particularly lighter elements, within the limits (Elbert *et al.* 2011). Therefore, variation in counts may not necessarily reflect changes to sediment geochemistry, and concentrations of water and organics must be considered. This is an example of the closed sum effect that influences the interpretation of Itrax count data. The closed sum effect means that counts per second do not equate to concentration, and hence are semi-quantitative in nature. When an element's count increases, the proportion of counts from other elements decreases, and hence these counts do not necessarily reflect changes to geochemical composition (Davies *et al.* 2015). To attain concentrations, counts must be calibrated using conventional

geochemical analysis (Boyle, 2001). However, it is recognised that precise concentrations are not required when using Itrax data of 'well detected' elements to analyse relative geochemical change (rates and magnitude) and characterising microfacies (Boyle *et al.* 2015).

The uses of element ratios and data normalisation are useful means of overcoming the closed sum effects. Normalisation also crucially negates the influence of sediment morphology on element counts, so that any variation to counts reflects the geochemical signal only (Kylander *et al.* 2011b; Davies *et al.* 2015). There are numerous ways of normalising raw data, counts per second (e.g. Elbert *et al.* 2011; Löwemark *et al.* 2011; Kylander *et al.* 2011a; Davies *et al.* 2015). However, raw data from Nar Gölü and Yaal Chac was primarily normalised by total scatter, which is gained though Itrax's detection and addition of coherent and incoherent scatter (inc + coh) (Kylander *et al.* 2011b; Berntsson *et al.* 2014; Shala *et al.* 2014). Incoherent and coherent scatter are related to the Compton and Rayleigh scattering of X-ray radiation respectively and their intensity reflects the organic and water content within the sediment (Davies *et al.* 2015). Therefore, normalising data using total scatter acts to minimise the effect of organic/water content and sediment morphology on geochemical signals.

Alternatively, Löwemark *et al.* (2011) propose normalising elements which relate to lithogenic sedimentation by Al to minimise the effect of organic content; however, raw Al counts from both Nar Gölü and Yaal Chac are too low for this technique to be used reliably. Other lithogenic elements, such as Rb, Zr and Ti, can also be used to normalise data (Guyard *et al.* 2007; Shala *et al.* 2014; Davies *et al.* 2015), and these more abundant elements are used in element ratios within this research.

Data were processed to remove unreliable results. Itrax's internal software provides a binary indication of data validity, where surface irregularities (e.g. cracks within the split core) can lead to significant drops to X-ray detection rates (kcps) and increased mean standard error (MSE). Consequently, invalid data reflects a significant reduction to the strength, and thus reliability, of the geochemical signal. At each 200µm increment through the sequence, invalid data is generally indicated when the total counts per second drops below 10,000 and/or when the MSE exceeds 4 (Sarah Davies, pers comm, Nov 2015). All invalid data ('validity' = 0) were deleted prior to analysis in this thesis. Elemental data were similarly checked for anomalous results, and deleted as appropriate. Figures comparing the raw and processed normalised datasets are provided within the supplementary material A.

2.3.3.2 Catchment bulk sediment geochemistry

Bulk sediment was sampled from the catchments' soil and rock of Nar Gölü and Yaal Chac for XRF analysis. This aimed to provide a geochemical signature of potential sediment sources which can be transported and incorporated into the lacustrine record (Jin *et al.* 2006); similarly, it can help identify human disturbance indicators, which can be used to discern geochemical changes derived from human activity and climate in the lake records (Giguet-Covex *et al.* 2011). Comparisons between the core and catchment geochemical signatures provide an insight into catchment processes, and hence environmental conditions, which may lead to specific in-lake deposition (Giguet-Covex *et al.* 2011).

Due to Nar Gölü's small, vegetatively-open catchment, Dr Samantha Allcock was able to take 46 samples (~40g) all round the lake, with a particularly concentration within the alluvial fan and gullies in the southern region, in 2010 (Allcock, 2013; Fig. 2.7a). These samples aimed to gain a representative geochemical signature of all potential sediment sources. At Plymouth University, Allcock first homogenised the samples into powder pills using a Fritsch P5 Planetary Mill (PULVERISETTE 5 classic line with 4 bowl fasteners), and then scanned these pills using Niton XL3t GOLDD series XRF portable scanner, held within a desktop mount (Allcock, 2013).

From Yaal Chac, the author and two undergraduates (Alice Ferns and Georgina Iliff) collected 13 samples within the catchment in 2016, restricted by dense vegetation and time availability (Fig. 2.7b). Nevertheless, samples aimed to reach as far round the lake as possible and include samples at various distances from lake, in order to gain representative catchment samples. All material was retrieved using a trowel to collect topsoil and sub-soil into large plastic sample bags; these were then shipped back to the UK and refrigerated until XRF analysis. Ferns (2016) ground the samples by hand to homogenise material, and scanned them using the bulk sediment XRF instrument, Coulter LS200 with fluid module at the University of Nottingham.

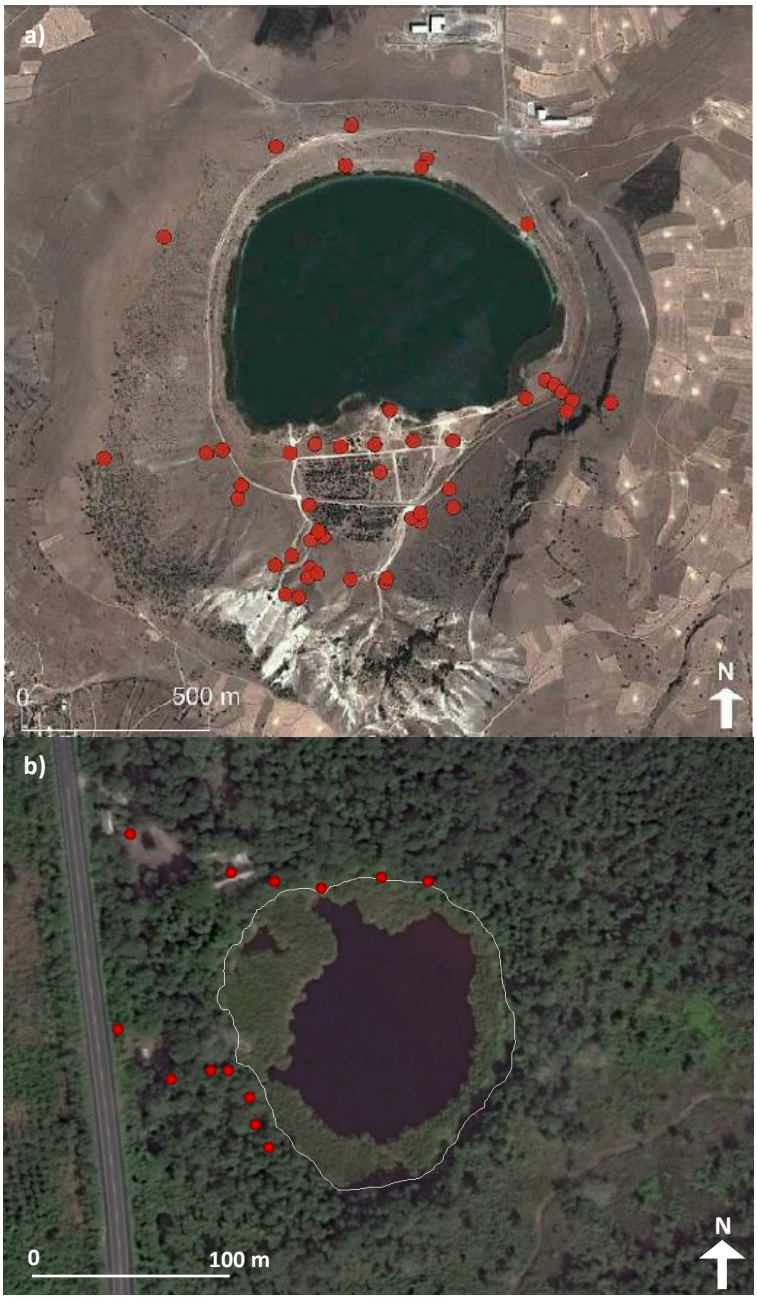


Figure 2.7 – *Distribution of bulk sediment samples (red dots) for geochemical analysis using conventional XRF from Nar Gölü (a) and Yaal Chac (b). The white line on image (b) denotes Yaal Chac's lake edge. Nar Gölü's* Figure *(a) taken from Allcock (2013).*

2.3.4 Total carbon content

Organic and inorganic carbon can be deposited and preserved in sediment records, and their concentrations can be used as indicators of environmental conditions (e.g. Xiao *et al.* 2006). Organic

carbon concentrations are also useful for identifying samples for radiocarbon analysis and their required sample size.

Using a Skalar Primacs Series Total Carbon Analyser at Plymouth University, Dr Samantha Allcock measured total organic carbon (TOC), total inorganic carbon (TIC) and total carbon (TC) content of 512 samples from Nar Gölü's NAR10 sediment record (Allcock, 2013). Catalytic oxidation at 1000°C of sediment samples converts all carbon into gaseous CO_2, which is subsequently measured to record TC. Similarly, acidification of coeval samples converts inorganic carbon into CO_2, which is measured to gain TIC. As a result, TOC is calculated by Equation 2:

$$TOC = TC - TIC \quad [2]$$

TIC and TOC of Yaal Chac's sediment was measured using the more rudimentary method of loss on ignition (LOI). Using a methodology adapted from Dean (1974), LOI is a quick, cheap method to gain estimates of TIC, TOC and TC.

From the Yaal Chac master sequence, subsamples (~1cm^3) were taken every 4cm. First, dry crucibles were weighed to ±0.1mg (Weight A) and subsamples were added to each crucible and reweighed (Weight B). Sediment filled crucibles were dried overnight in an oven at 105°C; dry sediment was reweighed (Weight C). Next, subsamples were placed into a furnace at 550°C for 4 hours burn off the organic content; organic-free sediment was reweighed (Weight D). Finally, subsamples were placed back in a furnace at 950°C for 2 hours to ignite the carbonates; carbonate and organic-free sediment was reweighed (Weight E).

Organic and carbonate content were then calculated using the following Equations [3 & 4]:

$$\text{Organic content (\%):} \quad \frac{C - D}{C - A} * 100 \quad [3]$$

$$\text{Carbonate content (\%):} \quad \frac{D - E}{C - A} * 100 \quad [4]$$

Santisteban *et al.* (2004) recommend that LOI data should be used qualitatively, due to the effect of sediment composition (predominantly clay mineral concentration) on results. Data gained from LOI

were used to identify the optimal samples for Yaal Chac's radiocarbon dating allocation, check the tie points between core sections within the lake's master sequence, and characterise major sedimentological changes.

2.4 Contemporary environmental monitoring

As alluded to above, a comprehensive understanding of the lake system is required to interpret an environmental signal within the varve sedimentology (Brauer *et al.* 2009; Ojala *et al.* 2014). Various efforts have been made when possible to build this understanding of inter- and intra-annual limnology and climatology at both lakes.

2.4.1 Sediment Traps

Suspended within a water body, traps collect sediment falling through the water body that would otherwise be deposited on the lake floor. Sediment traps can be used to estimate annual sedimentation rate, and the timing of depositional events within the year, hence provide insight into the mechanisms of varve formation (Thunell *et al.* 1993). Sediment trap data can aid thin section analysis through gaining understanding of the annual succession of deposition, and thus verify whether sediment laminations are varves (Ojala *et al.* 2014).

Seston sediment traps (adapted from Pennington, 1974) have been deployed within Nar Gölü during various field campaigns between 2001-2007 (Jones, 2004; England, 2006; Woodbridge, 2009) and again 2015-2017. These traps consist of a Perspex tube suspended vertically in the water body, with a bung at the bottom and an open funnel at the top to collect the sediment; floats and weights were used to keep the trap upright at all times (Fig. 2.8). Typically, two traps have been set at different depths within the deepest region of the lake, and collected the following year; the 2014-2015 traps were deployed at 5m and 15m water depth over the lake's deepest region.

In December 2016, ten Seston sediment traps were placed in across Yaal Chac at depths of 1, 3 and 6m. These traps were retrieved in April 2017, thus primarily representing the dry season's sediment deposition, and redeployed to accumulate sediment deposition over the succeeding wet season. In November 2017, these traps were collected, subsampled and sent to Nottingham for sedimentological analysis. Namely, this involved identifying the sediments' composition by creating a smear slide for microscopic examination (e.g. Schnurrenberger *et al.* 2003).

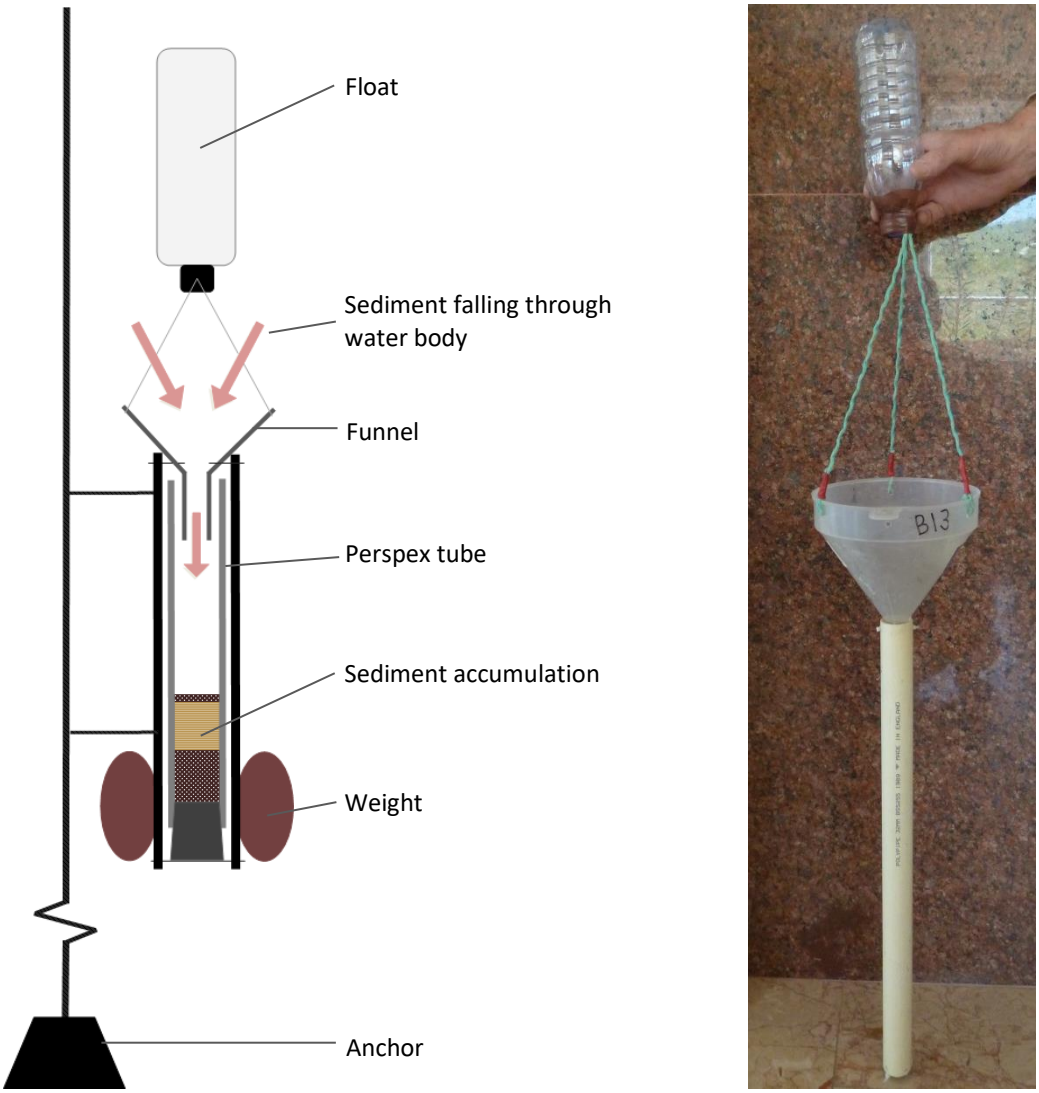


Figure 2.8 – *Schematic diagram and photograph of a sediment trap created and deployed at Nar Gölü during fieldwork in May 2015.*

2.4.2 Water sampling

Understanding the inter- and intra-annual variability of water chemistry can help comprehend the seasonal in-lake processes. These inform interpretations made from the sedimentological record, including the mechanisms and the timings of laminae deposition. Limnological monitoring can identify how and when the lake responds to annual/monthly climate variability; such insight can further help construct a precise model for varve deposition (Zolitschka *et al.* 2015). Lake stratification, required for varve preservation, can also be investigated during this contemporary monitoring (Zolitschka *et al.* 2015). Monthly measurements of all limnological parameters would be ideal, yet time and resources limit this resolution of data collection. Nevertheless, the multi-year records of various parameters provide a good insight into the limnological variability.

Water temperature, pH and conductivity have been measured at both lakes, at various points within the lake and catchment. At Nar Gölü, limnological variables have been recorded annually during 1999-2008, 2011-2012, and 2014-2016 at different depths over the deepest lake region. Between 1999 and 2012, these measurements were typically taken during the summer months, during various field campaigns run by members of the Nar Gölü research group (Jones, 2004; England, 2006; Woodbridge, 2009; Allcock, 2013; Dean, 2014). A handheld YSI multi-parameter (ProPlus) instrument, with a probe at the end of a 15m-long cable, was used to measure these limnological variables every 5m through the water column. For water depths below 15m, a Glew core was used to capture water at depths of 20m and 25m and subsequently pulled up for analysis with the YSI multiparameter probe at the surface. The author participated in these annual field campaign between 2014 and 2016, to help collect this limnological data, and additionally deployedautomatic Tinytag™ data loggers every 5m through the water column to measure temperature every 4 minutes; one Tinytag™ probe was also placed in a nearby tree to record local air temperature.

At Yaal Chac, limnology has also been recorded at various depths using an YSI multi-parameter probe (various models). These limnological measurements were primarily taken during the undergraduate fieldtrip (University of Nottingham) in January, which has visited Yaal Chac annually between 2009 and 2016 (e.g. Clapich, 2016); the author personally collected this data during an undergraduate fieldtrip in January 2016, and independently (with the help of Roger Medina Gonzalez) in November 2017. By using a 20m-long cable, the aforementioned limnological variables were measured *in situ* every 1m through the entire water column, at the lake's deepest point. In December 2016, Sarah Metcalfe and Roger Medina Gonzalez deployed automatic Tinytag™ data loggers, set to record temperature every 30 minutes, at 0.5m, 3.0m and 9.5m water depths. The author subsequently collected these data loggers in November 2017, downloaded the data and redeployed them to their same locations. This high resolution data provides insight into the annual dynamics of lake stratification at both sites.

Water samples from both lakes have also been collected for stable isotope analysis. While driven by numerous environmental variables, the oxygen isotope ratio ($\delta^{18}O$) of closed lake waters is most commonly a function of precipitation and evaporation (Leng and Marshall, 2004). Therefore, by analysing samples which aim to represent each water source and limnological layer, the relative influence of precipitation and evaporation on water can be determined both spatially and temporally. Intra-annual monitoring of stable isotopes helps link the seasonal wet-dry climatology

observed at Nar Gölü and Yaal Chac to their seasonal limnology, including lake stratification and water chemistry (Leng and Marshall, 2004).

At Nar Gölü, water samples have been collected using either a Van Dorn bottle or a Glew corer during the aforementioned years to analyse their stable isotope composition. During this time, samples from the two freshwater springs which feed into Nar Gölü have also been sampled periodically. When sampling, bottles were filled completely and sealed to minimise any isotopic exchange with surrounding air (Dean, 2014). While most of the samples were gained during the summer months, water was taken in September 2011, and February and March 2012 by Jonathan Dean and local residents, thus gaining measures of isotopic composition during both the wet and dry seasons; note that the water sample from February 2012 was taken at the lake edge due to ice cover (Dean *et al.* 2015). The NERC Isotope Geosciences Laboratory (NIGL) analysed these water samples' stable isotopes.

At Yaal Chac, water samples were taken from different depths using a Van Dorn bottle, and bottled as described above. During the various fieldtrips, samples from Yaal Chac and various surrounding sites were taken by the undergraduates. Since 2013, Roger Medina González (Universidad Autónoma de Yucatán) has also sampled Yaal Chac's surface, middle and bottom water on a monthly basis. These samples' oxygen and hydrogen isotopes were tested using a VG Isoprime mass spectrometer and a EuroPyrOH analyser (Jamin *et al.* 2005) at NERC Isotope Geosciences Laboratories, Keyworth (Clapich, 2016).

2.4.3 Modern calibration

Meteorological data from Niğde's weather station, 45km southwest of Nar Gölü (37°58'N; 35°41'E; 1211m asl), was used to assess correlation between varve microstratigraphy and monthly weather and the former dataset included measurements of each month's minimum, average, and maximum temperature (°C), total precipitation (mm) and relative humidity (%). Monthly evaporation was subsequently estimated using the temperature-based formula devised by Romanenko (1961) [5]:

$$ET = 0.0018\,(25 + T_a)^2\,(100 - Rh) \qquad [5]$$

Where ET is the potential evapotranspiration, Ta is the mean air temperature (°C), and Rh is the relative humidity. Limited by the meteorological variables provided, Romanenko's formula provided

the most accurate estimates of evaporation, as compared to six other temperature-based methods reviewed by Xu and Singh (2001). For each month over the 65-year period from Nar Gölü, the evaporation/precipitation ratio was included, and annual and seasonal (e.g. Dec-Feb, Mar-Apr, Jun-Aug, Sep-Nov) time-steps were also calculated using the monthly dataset.

By smoothing each dataset to varying degrees, two key considerations for a reliable calibration were explored. Firstly, smoothing sedimentological data aimed to account for slight discrepancies in the varve chronology, which would act to decouple the dataset from the definite chronology presented in the meteorological dataset. Using a running mean of varying lengths, the influence of chronological errors on correlation can be reduced. Secondly, smoothing meteorological data aimed to compensate for the lake's 8-11 year residence time (Jones *et al.* 2005), which may act to smooth responses to external forcing (Tranvik *et al.* 2009). For this consideration, data was smoothed using a running mean of varying lengths, each calculated from the years prior to a given varve; this attempted to model limnological conditions as a cumulative product of prior climatology.

Datasets were analysed using a Pearson's linear correlation matrix within the PAST statistical software (Hammer *et al.* 2001). Significant results were used to link specific intra-annual conditions to varve sublayer thickness, thus indicating the timing and forcing of specific sediment deposition (Leemann and Niessen, 1994). The lack of varves in the uppermost sediment at Yaal Chac prevents a similar calibration; as such, relationships between wet-dry seasonality and sedimentology made from Nar Gölü's calibration will tentatively be applied to Yaal Chac and its palaeoclimatic reconstructions.

2.5 Additional unpublished data

As part of various undergraduate research projects at the University of Nottingham, additional palaeoenvironmental proxies preserved within Yaal Chac's sediment have been obtained – these include $\delta^{18}O$ isotopes from bulk carbonates (Hooper, 2011), charcoal deposition (Harwood, 2011), organic pigment concentration (Stevenson, 2011), and X-Ray diffraction (XRD) (Lem, 2011). All proxies were subsampled from the earlier and shorter YC11 core sequence; by using the sediments' distinct stratigraphy, this core and its data were subsequently correlated to the YC14 master sequence (see Fig. 4.12). The following briefly outlines the methods used to analyse each of these palaeoenvironmental proxy records:

$\delta^{18}O_{carbonate}$ record principally produced and analysed by undergraduate Sophie Hooper (see Hooper, 2011). Through the YC11 core sequence, $1cm^3$ of material was subsampled every 10cm. Their organic proportion was removed by washing samples in hydrogen peroxide. Samples were then passed through an 80µm Nitex mesh, to separate the bulk carbonate material from any larger ostracod and gastropod shells. The remaining bulk material was dried and ground using a pestle and mortar to homogenise each sample. Samples were then reacted with anhydrous phosphoric acid and left in a 25°C water bath overnight. This reaction produced gaseous CO_2, and its stable isotope content was subsequently measured using a VG Optima mass spectrometer at the NERC Isotope Geosciences Laboratories (NIGL) in the British Geological Survey (BGS). The resultant isotopic ratios ($\delta^{18}O$ ‰) are all compared to the VPDB, based on calibration of the laboratory standards against NSB-19. This methodology follows common practices used for analysing stable isotopes within bulk carbonate material (e.g. Henderson *et al.* 2003; Rosqvist *et al.* 2007).

Charcoal deposition was primarily investigated by undergraduate Gemma Harwood (see Harwood, 2011). Again, $1cm^3$ of sediment was subsampled every 10cm through the YC11 sequence; all depths of these samples correspond to those taken for stable isotope analysis, as discussed above. Samples were pre-treated with hydrogen peroxide, to remove organic material, and hydrochloric acid, to disaggregate material. A *lycopodium* spore tablet was then added to each sample. To increase charcoal recovery (see Turner *et al.* 2008), samples were first sieved through a 212µm mesh, and the finer material separated by density in a centrifuge; here, Sodium Polytungstate (SPT) with a specific gravity of greater than 2.2 was added to each tube, to separate charcoal particles <212µm from the sample's sediment matrix. Finally, the material sorted by sieving and density separation was mounted onto a microscope with a coverslip. Charcoal particles were counted and their longest axis measured, using a light microscope with a reticle in the eyepiece at 100x magnification. For each sample, counts were made until 50 *Lycopodium* spores were also counted. This methodology follows common practices used for charcoal counts within lacustrine sediment records (e.g. Turner *et al.* 2008, 2010).

Organic pigments were analysed by undergraduate Mark Stevenson (see Stevenson, 2011). Around 1-2g of sediment was subsampled every 5cm through the YC11 core sequence, and freeze-dried to remove all moisture. To extract the pigments from samples, a solution of

acetone and methanol was added to the dry sediment. This extraction solution was filtered off, and dried in the dark via evaporation within a nitrogen atmosphere. Immediately prior to High Performance Liquid Chromatography (HPLC), these dried pigments were dissolved in a solution of acetone, ion-pairing regent (IPR) and methanol. These samples were then injected and run through an HPLC system which consists of a Waters 2690 separation module, a Hypersil ODS column, a Waters 996 photodiode array detector and Waters Millenium Chromatography Manager software (see McGowan *et al.* 2008), at the School of Geography, University of Nottingham. The identification and concentration of different pigments within each sample was achieved through analysis of the pigments' chromatic absorbance spectra and retention times. This methodology follows standard practices used to investigate organic pigments within lacustrine sediments (e.g. Buchaca *et al.* 2005; McGovan *et al.* 2008, 2012).

XRD analysis of carbonate minerals was primarily investigated by Rachel Lem (see Lem, 2011). Sediment was subsampled every 10cm through the YC11 core sequence. Each sample was finely ground in a pestle and mortar, mixed with acetone and packed into a 2mm-wide aluminium holder. Samples were run individually within a Bruker-D8-Advance XRD instrument, where the specific pattern of X-Ray diffraction enables the identification of the samples' mineralogy (see Flemming, 2007). This methodology follows the standard practice when using this specific XRD instrument with unconsolidated sediment (e.g. Avramidis *et al.* 2013).

3. Nar Gölü

This chapter covers the contemporary environmental setting of Nar Gölü, Turkey, before discussing the current understanding of the past climatology through Holocene inferred within the region. Subsequently, the lithology and chronology of sediment records NAR01 and NAR10, cored prior to this PhD research, are detailed. Sedimentological results, primarily relating to the sediments' varve microfacies and geochemical composition, are then presented and interpreted to provide further insight into past environmental change, and its potential influence on societal change.

3.1 Study site and regional climatology

This section outlines the physical setting of Nar Gölü, and discusses the intra-annual climatic and limnological variability which would influence sediment deposition.

3.1.1 Study site

Nar Gölü (38°20'25.32"N, 34°27'21.98"E; 1363m asl) is a relatively deep (~21m), closed lake in the Cappadocian region of central Turkey (Fig. 3.1). Formed by a phreatomagmatic eruption, this maar lake infilled the resultant volcanic crater (Gevrek and Kazanci, 2000), with the crater's ridge roughly marking the boundary of the lake's relatively small catchment of ~4.0km^2 (England *et al.* 2008). The crater is composed predominantly of ignimbrite with exposed basalt forming the crater's rim along the western, northern, and eastern edges; these edges have steep scree slopes running down from the basalt (Gevrek and Kazanci, 2000). A normal fault bisects the basin in a NE-SW direction, causing the northern and eastern edges of this basaltic rim to slip at least 3m down (Gevrek and Kazanci, 2000). The southern slope is much shallower and contains two springs, which lead down to an alluvial fan protruding into the lake.

The basin is presently both geothermally and tectonically active. Hot springs flow from the alluvial fan at the lake's edge, and geothermal water has been artificially pumped within the catchment since the early 1990s. While Central Anatolia is not/has not been susceptible to major earthquakes for at least 2000 years (Erdik *et al.* 1985), anecdotal evidence of local minor earthquakes suggests modern tectonic activity.

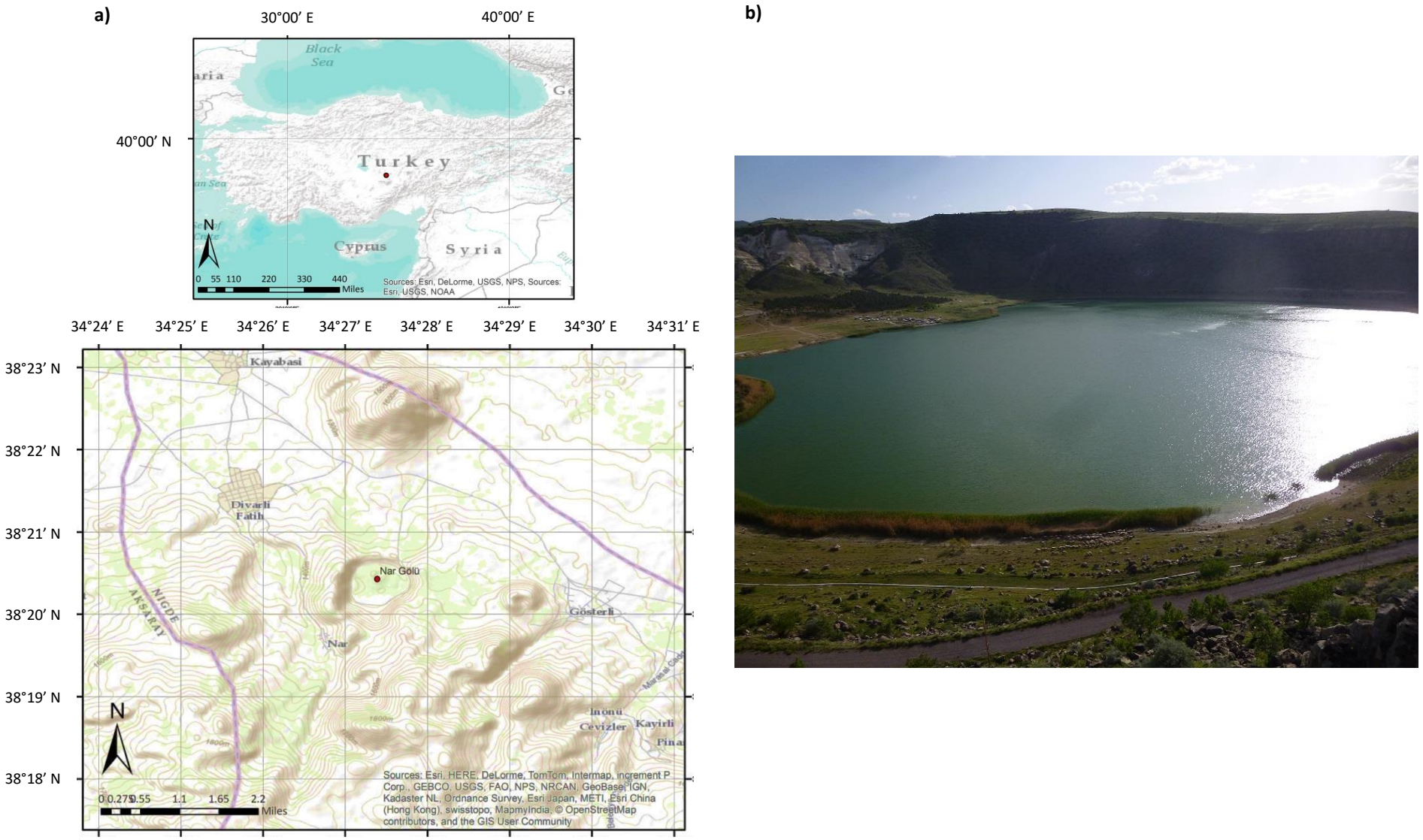


Figure 3.1 – *(a) Nar Gölü's situation within Turkey and the Anatolian Plateau (top), and a topographic map displaying Nar Gölü and its surrounding crater (bottom). (b) Photograph of Nar Gölü (area of ~0.7km^2) taken from the top of the crater's rim, northeast of the lake. The Emergent macrophytes, including Phragmites and Juncus, surround the water, and the alluvial fan with the Pinus plantation can be seen (top left of image). The exposed ignimbrite along the southern edge of the crater, containing the two springs, can also be seen (top left of image).*

The catchment springs supply fresh groundwater to the lake; isotopic analysis of water samples reveal similar δD/δ^{18}O ratios to the global meteoric water line, and precipitation samples from Ankara (2001-2007) (Fig. 3.2). Evaporation enriches the δ^{18}O composition of lakewater samples; this is typical of an endorheic basin, and highlights the control of evaporation and precipitation on isotopic composition (Leng *et al.* 2006). Due to its closed nature, residence time of water is reported to be 8-11 years (Jones *et al.* 2005).

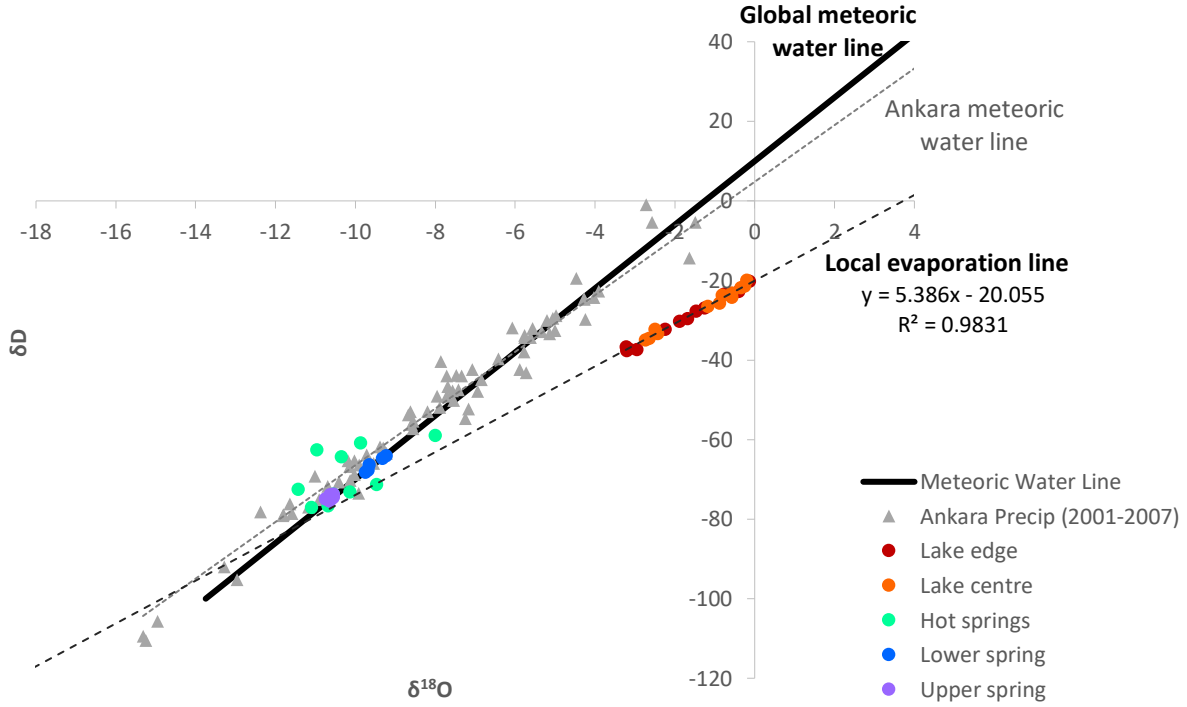


Figure 3.2 *- δD-δ^{18}O isotope plot comparing the Global Meteoric Water Line, Ankara precipitation, and water samples taken from three catchment springs and from Nar Gölü's surface (Dean et al. 2015b). Those samples furthest from the Meteoric Water Line suggests evaporative enrichment.*

Nar Gölü is an oligosaline, alkaline lake (pH 8.0 at the surface) with a maximum depth of 21m, as recorded in April 2017; this represents a substantial recent decline in maximum depth, which measured 26m in July 2001 (Jones *et al.* 2005). Its depth permits thermal and chemical stratification for the majority of the year (March to November), yet water mixes briefly during the winter (Dean *et al.* 2015b) (Fig. 3.3). This lake mixing does not appear to bring sufficient levels of dissolved oxygen to the hypolimnion to support benthic life (Jones *et al.* 2005), thus minimising the impact of bioturbation on the sediment's geochronological integrity (Anderson and Dean, 1988).

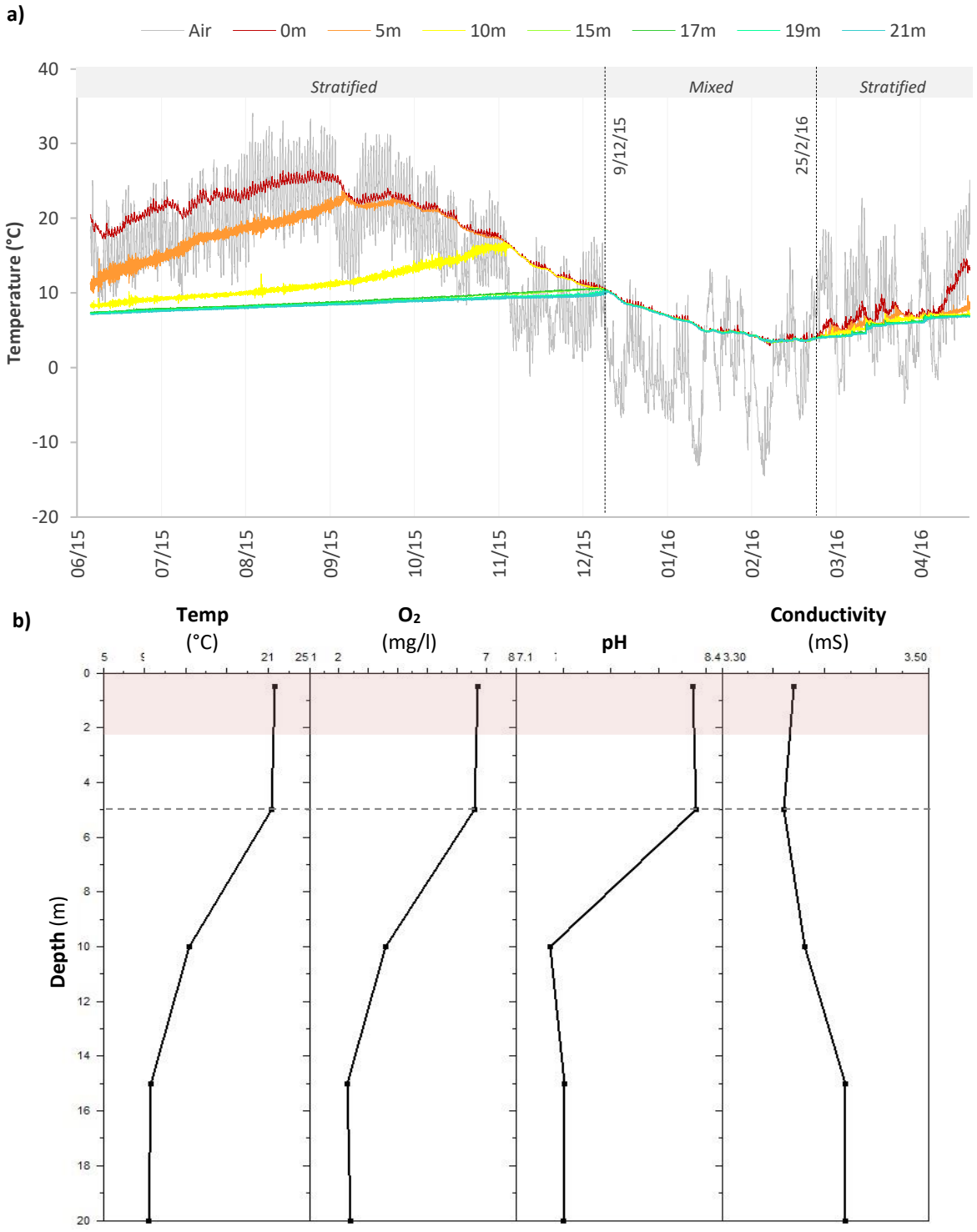


Figure 3.3 *– (a) Nar Gölü's thermal stratification and mixing between June 2015 and April 2016, the convergence of temperature through the water column denotes lake mixing (between the dotted line); and (b) the limnological changes through Nar Gölü's vertical profile, as measured in July 2009; photic zone as measured via Secchi-disc measurement (red zone), and the thermo- and chemoclines (grey dotted line) are also displayed.*

Evaporation also drives the geochemical properties of Nar Gölü's water; concentrations of chloride, sulphate, and sodium ions are notably higher during the summer months (Dean *et al.* 2015b) (Table 3.1). In contrast, a summer decline of Ca^{2+} concentration is driven by endogenic precipitation of calcium carbonate ($CaCO_3$) during abrupt 'whiting' events; one such event was witnessed in July 2012 (Dean *et al.* 2013). The aforementioned concentration of ions by summers' increased evaporation/precipitation ratio, combines with an increased pH, driven by the photosynthetic consumption of CO_2 during algal blooms in spring, to supersaturate lakewater carbonates (Jones *et al.* 2005; Dean *et al.* 2013). The calcium and bicarbonate ions are likely sourced from the underlying Niğde/Kirsehir Massif which includes a cover unit of Eocene limestone, occurrences of travertine, and veins of calcite-aragonite deposition (Toprak and Göncüoğlu, 1993); from these carbonate-rich sources, ions are subsequently transported to Nar Gölü via the deep, geothermally-heated spring water.

Table 3.1 *– Major ion concentrations from Nar Gölü's surface water samples [taken from Dean et al. 2015b]*

	Concentration meq L^{-1}						
	SO_4^{-2}	**Cl-**	**Na^***	**K^***	**Mg^{2+}**	**Ca^{2+}**	**Mg/Ca**
August 1999	3.2	27.4	16.5	3.7	8.5	3.0	2.8
July 2009	3.6	20.1	14.6	3.8	10.1	2.1	4.8
July 2010	3.8	22.7	16.2	3.6	15.4	1.0	15.4
June 2011	2.9	20.2	13.7	4.0	8.8	2.2	4.0
September 2011	4.4	22.4	19.0	3.8	9.4	3.2	2.9
February 2012	3.0	20.2	4.1	0.0	3.2	4.0	0.8
July 2012	4.1	23.9	16.9	3.8	16.5	1.2	13.8
April 2013	3.6	20.2	19.8	3.6	7.1	3.6	2.0

Within the catchment, vegetation is sparse; only small numbers of deciduous oak (*Quercus cerris* type) can be found on the north, west and east slopes (England *et al.* 2008). Agriculture is limited to a few small fields around lake's edge which grow a range of pulses, and a pine tree plantation located on the alluvial fan (Jones *et al.* 2005). Emergent macrophytes, including *Phragmites* and *Juncus,* dominate the majority of the water's boundary (England *et al.* 2008). The present vegetation composition of the surrounding Cappadocian region is classified as dry steppe-forest (England *et al.* 2008).

As recorded by the nearest weather station in Niğde (37°58'53.28"N; 35°41'13.39"E; 1211m asl), 45km southeast of Nar Gölü, annual precipitation is ~372mm with a distinct hot, dry season during the summer months (Fig. 3.4) (Turkish Meteorological Service, 2011). July and August are the warmest months averaging 22°C, with maximum temperatures averaging up to 28°C; while the

coldest months, January and February, average 0.2°C (Dean *et al.* 2013) and display higher levels of temperature variability than summer months (Jones *et al.* 2005).

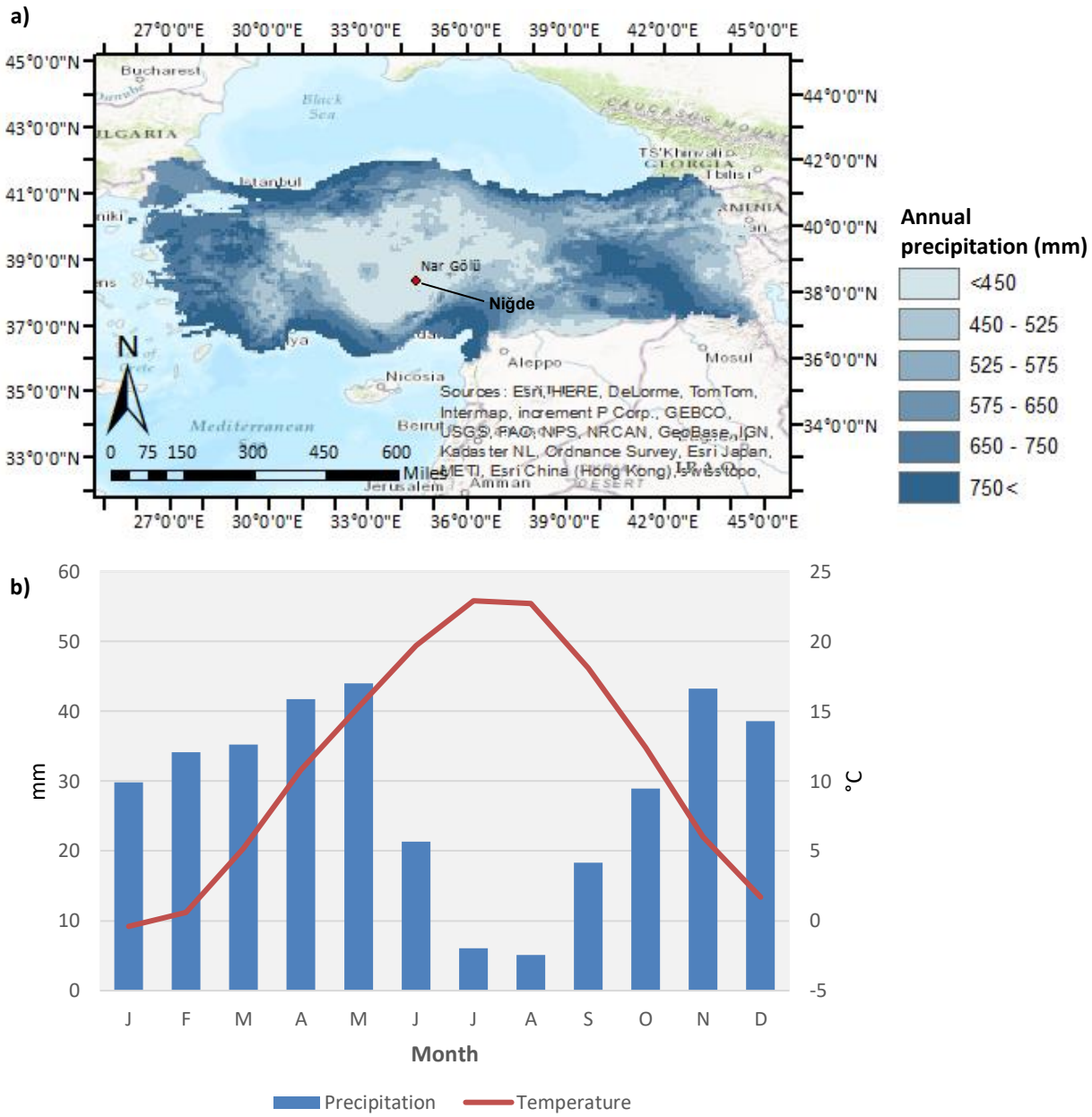


Figure 3.4 – *Distribution of total annual precipitation in Turkey over 1970-2000 (a) (Fick and Hijmans, 2017), and modern climatology over 1980-2010 of Niğde (b) (data provided by the Turkish Meteorological Service, 2011)*

3.1.2 Regional climatology

A lake's sedimentary record is a product of numerous environmental processes. Climatology often determines the relative influence of each process on sediment deposition and preservation, and when these environmental processes vary seasonally, varves may be deposited. In order to understand the limnological processes driving sediment deposition in Nar Gölü, the contemporary climatology, and its drivers, at both sites must be considered. Understanding how each region's climatology changed through the Holocene will further provide the environmental context to sedimentological change. This section outlines the eastern Mediterranean's contemporary climatology (Section 3.1.2.1) and its Holocene variability (Section 3.1.2.2).

3.1.2.1 Contemporary climatology of Turkey

Present day climate in Turkey is characteristically seasonal with warm, dry summers and wetter, cooler winters (see Fig. 3.5). Spatially, the mountain ranges running parallel to the Black Sea, the Northern Anatolian Mountains, and the southern coast of the Mediterranean, the Taurus Mountains, help govern regional climatic regimes in Turkey (Sensoy *et al.* 2008). The southerly Taurus Mountains receive relatively higher rates of precipitation per year and cause a rain shadow effect to inland Turkey, leading to the current semi-arid environment which prevails over much of Anatolia's inland (Akkemik and Aras, 2005). Figure 3.6 displays the spatial variability of temperature and precipitation over Turkey (Hijmans *et al.* 2005). These parameters primarily define the general classification of Turkish climate types: Continental, Mediterranean, and Oceanic (Akman and Ketenoğlu, 1986).

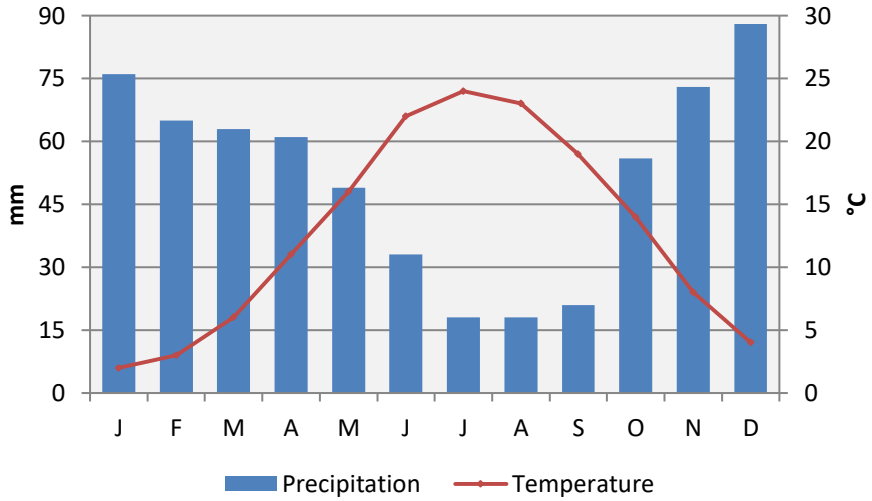


Figure 3.5 – *Average climate over the whole of Turkey between 1970-2000 (Sensoy et al. 2008)*

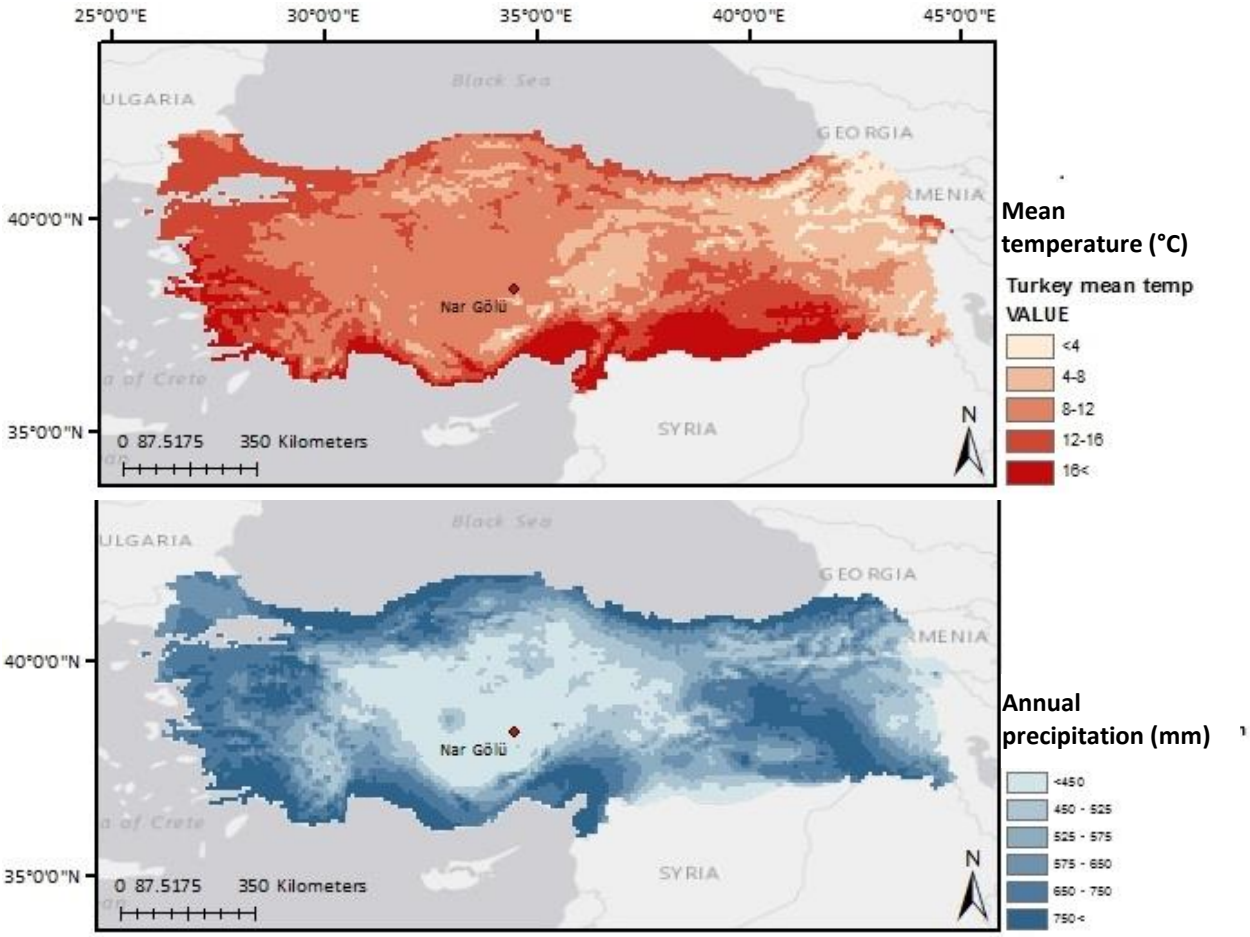


Figure 3.6 – *Mean temperature (top) and annual precipitation (bottom) over Turkey; data interpolated from monthly data recorded from weather stations between 1960-90 (Fick and Hijhams, 2017)*

Turkey lies at the convergence of numerous climatic systems contributing to the high spatial-temporal variability (Digerfeldt *et al.* 2007). The wet-winter and dry-summer regime is predominately controlled by the position of the subtropical anticyclone belt and the dynamics of cyclogenesis (Wick *et al.* 2003; Tzedakis, 2007); depressions bring precipitation to Turkey and tend to follow one of five different paths as shown in Figure 3.7. While paths 1 and 2 are associated with bringing sporadic rainfall to northern Turkey during the summer, paths 3 and 4 tend to dominate the winter months (Karaca *et al.* 2000). During the winter's wet-season, depression frequency and intensity is greatest across Turkey; owing to the complexity of systems determining moisture supply and pathway to Anatolia, winter rainfall displays significantly greater interannual variation, compared to summers' dry-season (Karaca *et al.* 2000).

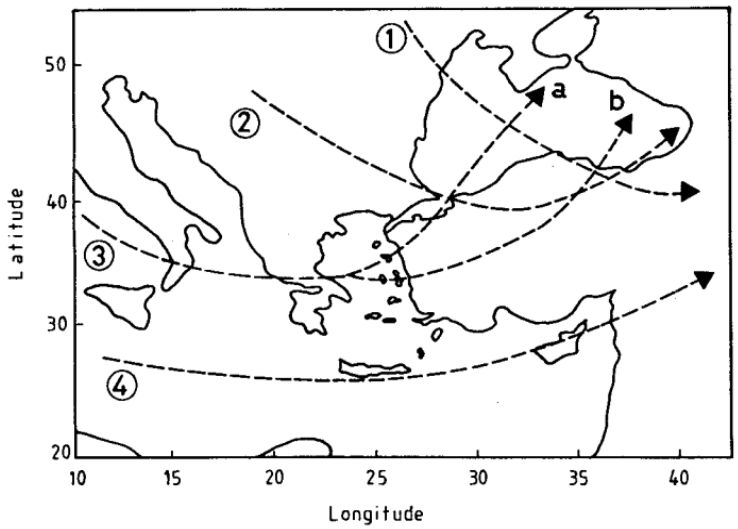


Figure 3.7 *– The five predominant depression trajectories over Turkey (taken from Karaca et al. 2000)*

Turkey's winter wet-season climatology is primarily governed by mid-latitude Westerlies (Rowe *et al.* 2012) and southward excursions of the polar jet stream (Kacara *et al.* 2000). These Westerlies drive low pressure systems from the Atlantic and Mediterranean to Turkey driving wet-season rainfall, where sea surface temperatures from these water bodies additionally influence evaporation rates, and consequently moisture supply (Xoplaki *et al.* 2004; Enzel *et al.* 2008). Meridional sea-land temperature gradients may also help steer these winter depressions laterally across the Mediterranean's relatively warm water (Karaca *et al.* 2000).

At a decadal-centennial-scale, multiple climatic oscillations drive precipitation variability, namely the North Atlantic Oscillation (NAO), the Arctic Oscillation (AO), and the North-Sea Caspian Pattern (NCP) (Cullen and deMenocal, 2000; Unal *et al.* 2012; Dean *et al.* 2013). Heinrich *et al.* (2013) note that

decadal-scale climatic cycles of Turkey, during the last millennium at least, correlate well with these atmospheric indices, and significant peaks of periodicity occur at 26, 32, 40, 55 and 87 years.

The NAO is a decadal scale climate oscillation caused by fluctuations in sea-level pressure between the Arctic and subtropical Atlantic, and consequently effects the transfer of energy and moisture transfer across the Mediterranean (Hurrell *et al.* 2003). In Turkey, the relative influence of the NOA on precipitation varies spatially (Enzel *et al.* 2003), with models suggesting that its phase can explain up to 27% of winter precipitation variability in the southeast, as seen by fluctuations in the Tigris-Euphrates' river streamflow (Cullen and de Menocal, 2000). Negative (positive) NAO phases drive moisture across the Mediterranean (central Europe), thus increasing (decreasing) wet-season conditions in Anatolia (Akkemik and Aras, 2005; Türkeş and Erlat, 2003; Heinrich *et al.* 2013). This influence of the NOA on Turkish precipitation is typically during the winter months only; a weak correlation between spring-summer precipitation from southwest Turkey and the NOA led to the proposal that precipitation during this time, recorded over the last ~660 years, came instead via storm tracks initiating from the Balkans and passing over the Black Sea (Touchan *et al.* 2003, 2007) – a climate mechanism recognised by Karaca *et al.* (2000).

The AO influences Turkey's winter climate in similar ways to the NAO. The AO teleconnection is a measure of geopotential height differences between the Arctic and northern mid-latitudes (Türkeş and Erlat, 2008). While Ambaum *et al.* (2001) postulates that the AO is a less dominant driver of Mediterranean climatic variability, compared to NAO, Türkeş and Erlat (2008) suggest that the AO phase specifically influences multi-decadal variability to winter temperatures. They found a strong, negative correlation between the AO index and air temperature, where AO negative phases are associated with a weakening of the circumpolar vortex allowing warmer westerlies from North Africa to flow over Turkey; conversely, a AO positive phase brings cold, polar southerly air masses over Turkey, due to anomalously high pressure systems in the northeast Atlantic and Europe. Consequently, negative (positive) phases of both AO and NAO are conducive to warmer and wetter (cooler and drier) conditions during Turkey's wet-seasons.

The NCP refers to an upper level (500 hPa) teleconnection between the North Sea and the Caspian Sea, measured using the difference in their geopotential height (Kutiel and Benaroch, 2002). The NCP brings increased southwesterly circulations during its negative phase and northeasterly circulations during its positive phase (Kutiel and Benaroch, 2002; Kutiel *et al.* 2002; Türkeş and Erlat, 2003). NCP phase has been linked to temperature variability throughout the year, with negative

(positive) phases bringing warmer (cooler) conditions to the eastern Mediterranean. Furthermore, precipitation anomalies can be seen to increase regionally according to the NCP and proximity to specific water bodies; for example, northern (southern) sites along the Black Sea (Mediterranean Sea) display increased rainfall during the NCP's positive (negative) phase due to the increased onshore circulations (Kutiel *et al.* 2002). The NCP's influence on precipitation significantly decreases inland, with central regions, such as Cappadocia, displaying no significant control (Kutiel and Türkeş, 2005). Overall, the NCP's relative impact on climate is recognised to be spatially variable, yet it has been identified as the leading cause of temperature variability, particularly during winter, over the Anatolian Plateau (Kutiel *et al.* 2002; Kutiel and Türkeş, 2005; Brunetti and Kutiel, 2011).

Summer's dry-seasonal climatology is driven by the northward migration of the subtropical high pressure belt, associated with descending Hadley Cell convection, and the intensity of the Asian monsoon (Rodwell and Hoskins, 1996; Raicich *et al.* 2003). A strong monsoon causes increased convection over the Indian subcontinent, which subsequently strengthens northeasterly winds originating in the dry, continental Asia and flow over the Eastern Mediterranean thus driving increased summer drought (Raicich *et al.* 2003; Ziv *et al.* 2004; Jones *et al.* 2006; Djamali *et al.* 2010). Moreover, the Asian monsoon's intensity significantly correlates to atmospheric subsidence over the eastern Mediterranean, associated with Hadley Cell descent (Ziv *et al.* 2004). This monsoon-controlled intensity of Hadley cell circulation is conducive to warm, dry conditions experienced during Turkey's summer months (Ziv *et al.* 2004).

3.1.2.2 Holocene climate change

The climatology of the eastern Mediterranean during the Holocene is outlined, with a particular focus on Turkey. Early, middle, and late Holocene periods are delineated roughly according to general climatic conditions and dynamics inferred from regional palaeoclimatic records; these chronological boundaries broadly correspond to the formal subdivision of the Holocene (Walker *et al.* 2018). Figure 3.8 displays the location of Nar Gölü (1) and other key palaeoclimatic records discussion within Section 3.1.2.2.

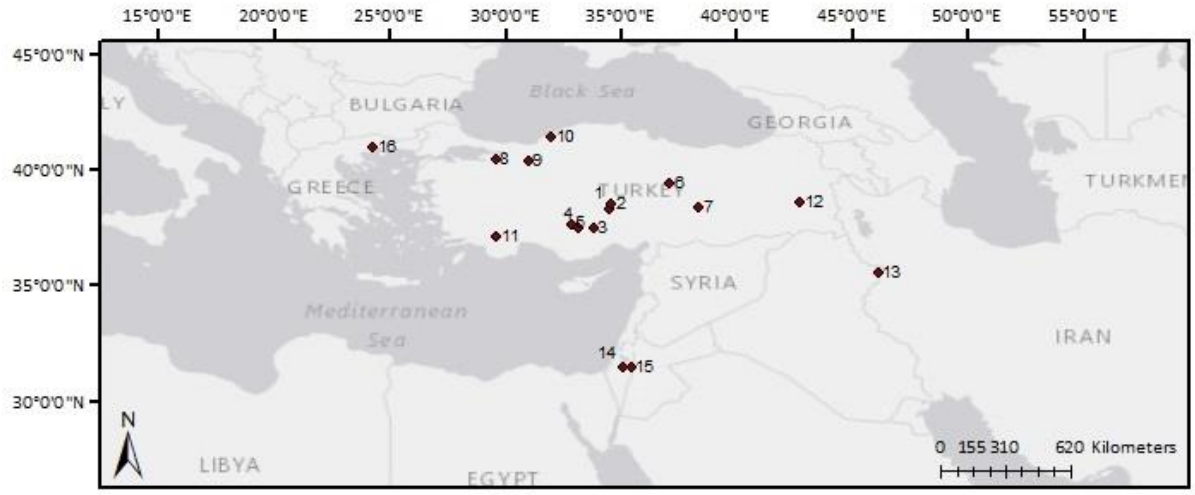


Figure 3.8 *- Maps displaying the location of study site, Nar Gölü (1), and a selection of other palaeoclimatic records discussed here: Eski Acıgöl (2), Lake Akgöl (3), Lake Pinarbasi (4), Catalhoyük-East (5), Lake Tecer (6), Tell Arslantepe (7), Lake Iznik (8), Lake Sünnet (9), Sofular Cave (10), Lake Gölhisar (11), Lake Van (12), Lake Zeribar (13), Soreq Cave (14), and Dead Sea (15).*

i) Early Holocene / Greenlandian Stage (11,700 – 8,200 cal yrs BP)

The onset of Holocene conditions around 11,700 cal yrs BP is a topic of much debate with two opposing discourses depending on the environmental proxies used (Roberts *et al.* 2001; Stevens *et al.* 2001; Roberts *et al.* 2008), namely pollen or stable isotopes. Pollen assemblages commonly show low levels of arboreal pollen during the Greenlandian, until its first maxima in ca. 8,500 cal yrs BP (Roberts, 2002; Wick *et al.* 2003; Turner *et al.* 2010), thus inferring a drier climate with low moisture availability limiting tree advancement (van Zeist and Woldring, 1978; van Zeist and Bottema, 1991; Roberts and Wright, 1993; Stevens *et al.* 2001; Eastwood *et al.* 2007). While deciduous woodland spread across the Mediterranean from southerly refugia at the Holocene's onset (Panagiotopoulos *et al.* 2013), its slow re-advancement and the general prevalence of steppe vegetation is arguably driven by relatively dry climatic conditions (van Zeist and Bottema, 1991); eastern Mediterranean

palynological records typically display low counts of humid-indicator species: oak (*Quercus*), terebinth (*Pistacia*) and juniper (*Juniperus*) (Roberts and Wright, 1993).

However, under-representation of certain arboreal taxa may be partial associated with their lower production of pollen (Shuraki and Sedgley, 1994; Munoz-Reinoso, 2003). Consequently, pollen records may overestimate climatic aridity and fail to depict the vegetational trends, where Roberts (2002) proposes that central Anatolian vegetation cover consisted of 'oak-terebinth-almond parkland' during the early Holocene. Asouti and Hather (2001) also found juniper (*Juniperus*) in Neolithic wood charcoals up to 10,000 cal yrs BP from central Anatolia, and hence deduce that tree abundance could be greater than palynological studies suggest. This ambiguity around the vegetational composition across the eastern Mediterranean may be exacerbated by non-climatic factors, such as the distribution of insect communities. Orchard species, such as pears and hawthorns, are insect pollinated, where the vegetational shift from glacial to interglacial conditions may be limited by the ecosystem response (Woldring and Cappers, 2001). Consequently, regional climatology may not be the principle process driving palynological changes within records, thus reducing pollen's reliability as a palaeoclimatic proxy.

Instead, stable isotope records from lacustrine and speleothem records indicate an abrupt shift to wet climatic conditions with the onset of Holocene conditions (Fig. 3.9); a palaeoclimatic review by Robinson *et al.* (2006) suggests that the early Holocene had the highest levels of precipitation over the last 25,000 years in the eastern Mediterranean. In Eski Acıgöl, central Turkey, oxygen isotopes ($\delta^{18}O$) from carbonate material, and calibrated using contemporary meteorological data, suggest up to ~20% more precipitation during the early Holocene than present day's conditions (Jones *et al.* 2005, 2007). This isotope-inferred wet climatology is consistently identified across the eastern Mediterranean, including Nar Gölü (Dean *et al.* 2015a), Gölhisar Gölü (Eastwood *et al.* 2007), Lake Van (Wick *et al.* 2003), Sofular Cave (Göktürk *et al.* 2011), Soreq Cave (Bar-Matthews *et al.* 1999) and Qunf Cave (Fleitmann *et al.* 2007), where the Holocene's wettest conditions are generally interpreted to prevail between ca. 10,500 and 8,800 cal yrs BP. Oxygen isotope records present a key proxy to inferring palaeohydrological change, with Jones and Roberts (2006) showing that regional E/P conditions primarily drives $\delta^{18}O_{carbonate}$ variability within Nar Gölü, Lake Van and Eski Acıgöl.

Charcoal deposition within Eski Acıgöl also rapidly increases at the onset of wet early Holocene conditions (Turner *et al.* 2008). Here, a palynological shift to increased grassy taxa coincides with increased microcharcoal concentrations, where isotope-inferred shifts to greater moisture

availability drives biomass growth, and thus enhancing fuel availability for wildfires. Studies have shown comparable links between biomass availability and fire occurrence in dry-land biomes, suggesting that fire is most commonly fuel-limited (Camill *et al.* 2003; Brown *et al.* 2005; Pausas and Fernández-Muñoz, 2012). Willcox *et al.* (2009) similarly identify warmer, wetter conditions with high prevalence of steppe-like vegetation at high altitudes during the early Holocene period in northern Syria. Additionally, regional changes to geomorphology also provides physical evidence of wet early Holocene conditions in the Near East: Goodfriend (1999) suggests that the northern boundary of the Negev Desert, Israel, migrated south during this period; and McLaren *et al.* (2004) found the presence of continuous river flow in Jordan over a now dried-out floodplain.

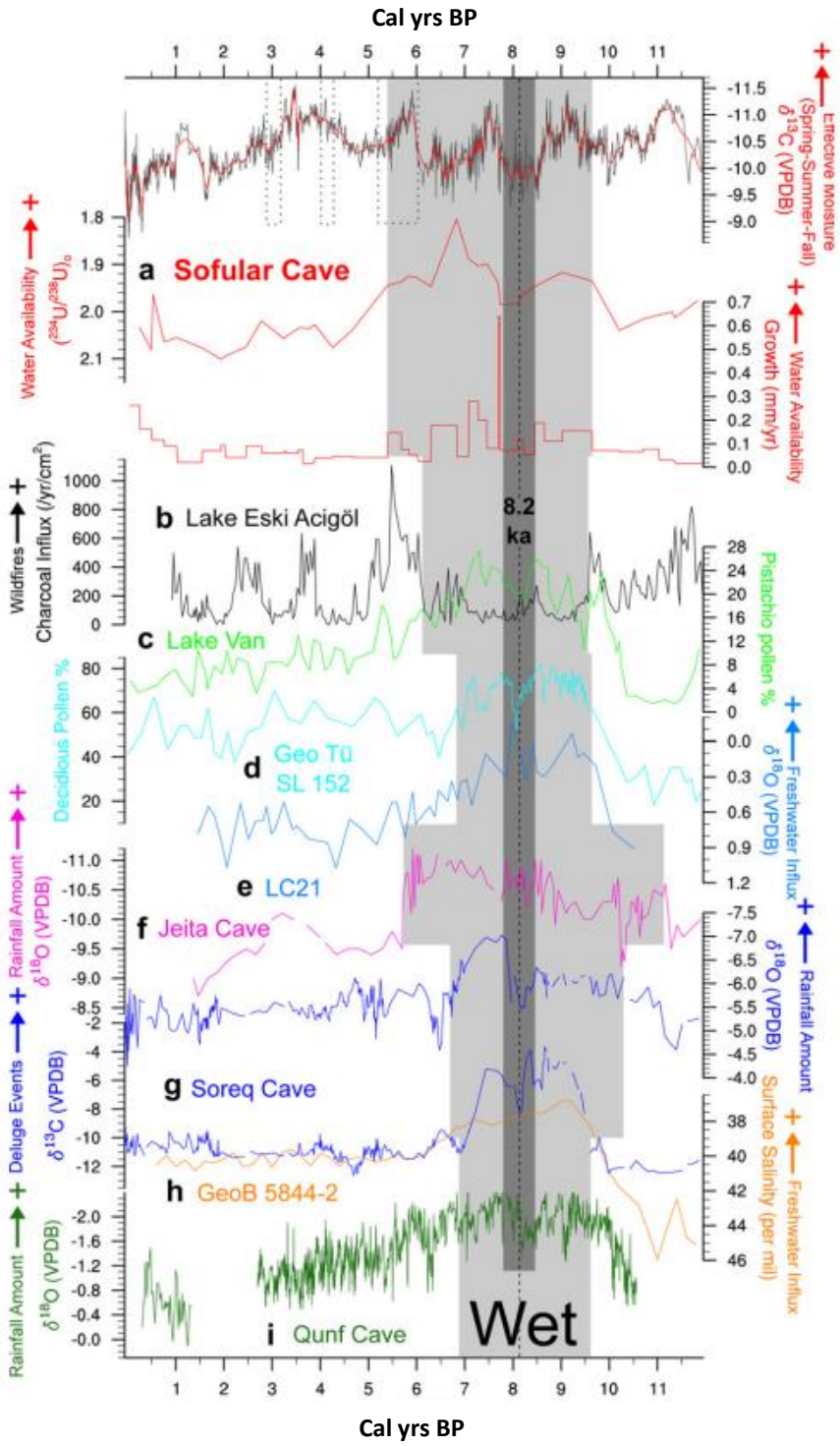


Figure 3.9 *– Comparison of a selection of eastern Mediterranean palaeoclimatic record. The order of the records follows a north-south distribution. Wet conditions inferred from each record are shaded in grey, with the 8.2 ka events conditions from Sofular cave shaded in dark grey (Göktürk et al. 2011). 'Rapid Climate Change' events are displayed by dashed boxes (Mayewski et al. 2004). (a) Sofular cave $\delta^{13}C$ (top), initial 234U/238U (middle) and the growth rate (bottom) records (Göktürk et al. 2011); (b) Microcharcoal concentrations from lake Eski Acigöl, Central Anatolia (Turner et al. 2008); (c) Pistachio pollen percentage from Lake Van (Wick et al. 2003); (d) Decidious pollen (%) from the northern Aegean Sea core, GeoTu-SL152 (Kotthoff et al. 2008); (e) $\delta^{18}O$ record from the southern Aegean Sea core LC21 (Rohling et al. 2002); (f) $\delta^{18}O$ record from the Jeita cave, Lebanon (Verheyden et al. 2008); (g) $\delta^{18}O$ and $\delta^{13}C$ records from the Soreq cave, Israel (Bar-Matthews et al. 2003); (h) Sea surface salinity estimates from the northern Red Sea core GeoB5844-2 (Arz et al. 2003). i) $\delta^{18}O$ record from the Qunf Cave, Oman (Fleitmann et al. 2007). [Taken from Göktürk et al. 2011]*

Since the initial pollen records, multiple different proxies suggest that the first 4,500 years of the Holocene in the eastern Mediterranean were dominated by a relatively wet climatology (Turner *et al.* 2008; Bar-Matthews *et al.* 1997, 2003; Stevens *et al.* 2001; Arz *et al.* 2003; Wick *et al.* 2003; Jones *et al.* 2005, 2007; Migowski *et al.* 2006; Eastwood *et al.* 2007; Verheyden *et al.* 2008; Göktürk *et al.* 2011; Jones and Roberts, 2008; Rowe *et al.* 2012; Dreibrodt *et al.* 2014, Dean *et al.* 2015a, 2017) (Fig. 3.9).

Various environmental processes may drive this apparent disparity between pollen- and isotope-inferred climate (Roberts *et al.* 2001). First, most forest refugia during the Last Glacial Maximum existed on the coasts adjacent to the Mediterranean and Black Seas, thus meaning distances from these refugia to the continental lacustrine systems could be very high; consequently, the delayed response to deciduous vegetation may reflect the long time it takes for these slow-growing taxa to spread inland (Roberts, 2002; Eastwood *et al.* 2007). However, Wick *et al.* (2003) propose that the lack of arboreal pollen cannot be due to migrational lag alone due to the presence of sparse, local deciduous oak pollen across Turkey. Instead, the intensification wet-dry seasonality during the early Holocene may have been detrimental to the growth of deciduous trees, where enhanced flow of a warm, dry Siberian air mass specifically during the growing season likely inhibited growth (Wick *et al.* 2003). These conditions favoured the growth of the drier, steppe vegetation as seen in many studies (Roberts *et al.* 2001; Wick *et al.* 2003; Turner *et al.* 2010), particularly at higher attitudes (Willcox *et al.* 2009). Djamali *et al.* (2010) also justify the slow migration of deciduous oak in the Zagros Mountains, Iran and Iraq, to drought specifically in the spring season, where *Quercus* taxa are particularly vulnerable to long dry seasons. Wright (1993) further supports this idea by proposing that climate adjusted to a dry-summer regime at the onset of the Holocene, where early Holocene $\delta^{18}O_{carbonate}$ (Roberts *et al.* 2011) and micro-charcoal (Turner *et al.* 2010) records indicate the prevalence of wet winter seasonality to match the increased moisture availability following the end of the Last Glacial Maximum (LGM).

This intensification of climatic seasonality may be associated with orbitally-driven increases to insolation seasonality (Berger, 1978). Where the aforementioned wet conditions of the early Holocene were principally driven by enhanced winter precipitation and the enhanced influence of humid Atlantic and Mediterranean systems (Wick *et al.* 2003); this idea of a general increase in east Mediterranean annual precipitation while maintaining a dry growing season, the significance of understanding seasonality arises.

Orland *et al.* (2012) propose that the wet-winter/dry-summer precipitation regime persisted throughout the Holocene. The early-mid Holocene NAO was predominately in its negative phase between 9,000-7,400 cal yrs BP (Wassenburg *et al.* 2016), which is associated with bringing increased winter precipitation to Turkey (Türkeş and Erlat, 2003), while Tzedakis (2007) postulates that enhanced Indian monsoons during the early Holocene could have led to increased aridity over eastern Mediterranean during the dry-summers. The Indian monsoon rainfall has been linked with Mediterranean tropospheric temperatures (Reddaway and Bigg, 1996; Liu and Yanai, 2001), and long term Mediterranean climate can be seen to fluctuate with changing intensities of monsoonal rainfall. By comparing Nar Gölü's $\delta^{18}O_{carbonate}$ record with instrumental records in the late Holocene, Jones *et al.* (2006) show those periods of enhanced monsoonal rainfall correspond with increased isotopic values, and thus infer increased summer evaporation and negative water balance.

During the early Holocene, Fleitmann *et al.* (2003, 2007) show that the Indian monsoon was more intense than present day using $\delta^{18}O$ from carbonate material from Oman and Yemen. As previously discussed (Section 2.1.1), this likely enhanced the strength warm, dry air flow from continental Asia to Turkey (Raicich *et al.* 2003) and the Levant (Ziv *et al.* 2004), thus leading to increased summer aridity; a northward movement of the Inter-Tropical Convergence Zone (ITCZ) would further displace the tropics anticyclonic belt northward and hence suppress the formation of depressions which would bring rain to the eastern Mediterranean (Djamali *et al.* 2010). Tzedakis (2007) further suggests that the enhanced Asian monsoons coincide with periods of insolation maxima which additionally intensified summer drought. This intense summer drought would further support the idea that aridity specific to the growing season inhibited the spread of trees during the early Holocene. Seasonal banding and isotope variability within Soreq Cave's speleothems during the early Holocene (Orland *et al.* 2012) matches stratigraphy of its late Holocene record (Orland *et al.* 2009), thus indicating that high levels of seasonality persisted throughout the entire interglacial. Furthermore, climate modelling (using The Hadley Centre HADSM3 model) also suggests that the strongest seasonality of precipitation within the entire Mediterranean prevailed over Turkey during the early Holocene (Brayshaw *et al.* 2011).

Others argue that the predicted increase in early Holocene precipitation cannot be explained by winter increases alone, thus implicating summers to be wetter as well (Rohling, 1994; Rossignol-Strick, 1999; Bar-Matthews *et al.* 2000). In mid- to high-latitude environments, the Hypsithermal (or 'Holocene Climatic Optimum'), associated with enhanced solar insolation and a northerly migration of ITCZ position (Haug *et al.* 2001), commonly prevailed between ca. 9,000 and 6,000-5,000 cal yrs

BP (Wanner *et al.* 2008), with the eastern Mediterranean basin experiencing a notable increase in sapropel formation between 9,400 and 5,400 cal yrs BP (Rossignol-Strick 1999; Göktürk *et al.* 2011); Bar-Matthews *et al.* (2000) discern peak formation rates at 8,500 and 7,000 cal yrs BP. Eastern Mediterranean sapropels form under periods of enhanced rainfall, where increased freshwater and nutrient input into a marine basin enhances organic productivity, the stratification of the water column, and anoxic benthic conditions (Passier *et al.* 1999). In order to maintain these conditions, Bar-Matthews *et al.* (2000) propose that summers were drought free and hence the wet/wet seasonality did not exist during these formation periods.

However, the River Nile's discharge and, to a lesser extent, direct precipitation into the Mediterranean have been proposed to be the predominate driver of freshwater input and hence sapropel deposition and preservation (Kallel *et al.* 1997; Kotthoff *et al.* 2008). As a result, sapropel formation may provide supplementary evidence of the eastern Mediterranean's wet early Holocene conditions, yet should not be used as a direct proxy for terrestrial seasonality.

The precise mechanism and drivers of climate and seasonality in the eastern Mediterranean, including Turkey, may have varied over the Holocene (Jones and Roberts, 2008; Rohling *et al.* 2009; Göktürk *et al.* 2011). Arz *et al.* (2003) suggest that a 'regional monsoon-type circulation pattern' formed over the southeast Mediterranean during the early Holocene as a result of lower sea surface temperatures and higher land temperatures from the increased insolation (Berger, 1978). This intense heating of land could provide enough convectional strength to overcome the Hadley cell descent; summer depressions over Syria and Iraq still form presently, yet the high pressure induced by the Hadley cell currently suppresses their strength and hence maintain aridity (Trigo et al, 1999). Göktürk *et al.* (2011) support this theory with evidence to suggest that, unlike like present day climate, the Mediterranean and Black Sea climates were coupled; this is inferred from Sofular speleothems, which currently portray Black Sea climate, displaying the marked precipitation increase over the Mediterranean sapropel formation period. While the HADSM3 accurately reconstructs modern climate, Brayshaw *et al.* (2010) recognise that the model fails to account for the possibility of changing climatic drivers, and hence cannot rule out the possibility of wet summers if climatic mechanisms were to alter in time (Black *et al.* 2010).

ii) Mid-Holocene / Northgrippian Stage (8,200 – 4,200 cal yrs BP)

Marking the transition between early-mid Holocene periods, the 8.2 ka BP climate event saw a ~200 year-long, abrupt cooling phase over the Atlantic ocean (Johnsen *et al.* 2001; Rasmussen *et al.* 2006)

caused by the influx of an estimated 1.6 x 10^{14} m^3 of freshwater (Clarke *et al.* 2004) from Lake Agassiz into the Atlantic after the collapse of a Laurentide Ice Sheet ice dam (see Daley *et al.* 2011). Cooler Atlantic SSTs restricted heat (and moisture) transfer to the higher latitudes, thus driving cooler and dry climatic conditions across the northern hemisphere (Hurrell, 1995). While climatic anomalies caused can be seen to prevail for ~100 years over Greenland (Rasmussen *et al.* 2006) and ~100-200 years over Western Europe (Tinner and Lotter, 2001; Prasad *et al.* 2009), the 8.2 ka BP event have been proposed to influence climatology for much longer in the eastern Mediterranean (Marino *et al.* 2009; Ocakoğlu *et al.* 2013) (Fig. 3.9). The intensification of positive NAO phases and weakened Mediterranean circulation have been proposed to extent the duration of the 8.2 ka event's duration over the eastern Mediterranean (Tsimplis and Josey, 2001; Abrantes *et al.* 2012).

The abandonment of Neolithic sites in central Anatolia, such a Catalhöyük-East, and the dispersal of early farmers has been preliminarily associated with this prolonged period of cool, dry conditions (Weninger *et al.* 2006; Mercuri *et al.* 2011). Annual precipitation is modelled to decrease from 800mm to 600mm (Pross *et al.* 2009), or alternatively a reduction of 100-150mm annual precipitation as calculated by Peyron *et al.* (2011), yet precise quantification of temperature change in the eastern Mediterranean has not been fully accomplished; Pross *et al.* (2009) report, using a pollen-inferred climate reconstruction from the Aegean Sea, a 4°C fall in average temperature yet this is believed to be a substantial over-estimation due to their model's limited altitudinal resolution where real climatic temperatures are significantly cooled by katabatic air flow. Kotthoff *et al.* (2008) suggests that the Aegean Sea cooled by roughly -1°C using pollen-infer temperature model, with Renssen *et al.* (2002) also modelling -1.5°C cooling during the 8.2 ka BP event across the Mediterranean using atmosphere–sea ice–ocean model, ECBilt-CLIO. From the eastern Mediterranean's marine records, broad-leaved tree pollen decreased to 53% from 87% (Dormoy *et al.* 2009; Pross *et al.* 2009), and sapropel deposition temporarily ceased (Kotthoff *et al.* 2008).

Much like the early Holocene, the eastern Mediterranean's mid-Holocene climate dynamics remain widely debated, with the key debates again surrounding the timing and amount of precipitation. Much of the literature discusses a mid-Holocene climatic transition (see Ocakoğlu *et al.* 2013), yet high climatic variability prevails for the majority of the Holocene (e.g. Roberts *et al.* 2011); as such, the proposed transition will be first discussed, followed by the occurrence of specific wet/dry phases.

Following the relative wet early Holocene, the eastern Mediterranean generally displays a multi-millennial drying trend until present day (Fig. 3.9); the timing of the onset of this trend, and its dynamics, are unclear. While some palaeoclimatic records indicate long term arid periods (Roberts *et al.* 2001; Migowski *et al.* 2006; Ocakoğlu et al 2013), others highlight the dominance of shorter, phases of aridity maxima lasting up to several hundred years (Migowski *et al.* 2006; Bar-Matthews and Ayalon, 2011; Mecuri *et al.* 2011; Masi *et al.* 2013). However, climate variability can typically be seen to be stabilised through the Holocene to present-day (Mecuri *et al.* 2011; Ocakoğlu *et al.* 2013). Roberts *et al.* (2001, 2011) propose that eastern Mediterranean aridification started at 6,000 cal yrs BP with an oscillatory decline in precipitation, where wet-dry oscillations occur at a 1,500-year periodicity in accordance with Bond events (Bond *et al.* 1997; Bar-Matthews and Ayalon, 2011).

As stated above, at the onset of the Hypsithermal ~9,000 cal yrs BP, precipitation is believed to have increased further to levels greater than present day (Roberts *et al.* 2008; Göktürk *et al.* 2011; Dreibrodt *et al.* 2014). By 8,000 cal yrs BP, vegetation across Anatolia had developed into a "mosaic of woodland with mesic trees and shrubs" (Roberts *et al.* 2001) and *Quercus* pollen had already increased to display the first arboreal pollen maxima around 6,200 cal yrs BP (Eastwood *et al.* 1999; Rossignol-Strick, 1999; Wick *et al.* 2003); the maximum extent of tree cover was then reached at 5,500 cal yrs BP in the eastern Mediterranean, before rapidly declining back to the steppe-grass vegetation (Vannière *et al.* 2011). Peaks in charcoal can also be seen at this time of peak tree cover, thus supporting the wet-winter/dry-summer seasonality regime which led to increased biomass in a fuel-limited environment (Vannière *et al.* 2011). This growth on deciduous woodland in the eastern Mediterranean was likely facilitated by the combination of wet early Holocene conditions and reduced climatic seasonality. Northern Hemisphere (NH) insolation seasonality peaked around 9,000-8,000 cal yrs BP, subsequently decreasing to present day (Berger, 1978). Consequently, this reduction to seasonality may have provided more mesic conditions suitable for arboreal taxa (Roberts *et al.* 2008).

Regional climate modelling suggests that Turkey's precipitation began to decrease relatively slowly and steadily from 8,000 cal yrs BP (Brayshaw *et al.* 2011). This modelled trend is primarily driven by the declining NH insolation, and may be identified across the Mediterranean, such as the Dead Sea, Israel (8,200-5,600 cal yrs BP) (Migowski *et al.* 2006), and both Lake Accesa, Italy, and Tenaghi Philippon, Greece, from 7,800 cal yrs BP (Peyron *et al.* 2011); the high resolution palynological study by Peyron *et al.* (2011) reconstructs a gradual decrease in annual precipitation yet maintaining a seasonal signal stronger than that of present.

Palaeoclimatic proxies from eastern Mediterranean suggest that onset of climatic drying typically occurs between 7,000-6,000 cal yrs BP (Roberts *et al.* 2001; Vannière *et al.* 2011; Mercuri *et al.* 2011). From Turkey, a sustained period of drier climatic conditions can be deduced from diatom-inferred salinity records from Eski Acıgöl between ~7,000-4,000 cal yrs BP (Roberts *et al.* 2001; Jones and Roberts, 2008). Akgöl's sedimentary record similarly displays greater isotopic depletion than present day until 6,000 cal yrs BP (Roberts *et al.* 2008). Ocakoğlu *et al.* (2013) identifies from Lake Sünnet a long term period of gradual aridification and warming starting ~7,300 cal yrs BP. From Israel, Soreq Cave's $\delta^{18}O$ record displays a positive increase in values from 7,000 cal yrs BP, reflecting drier climatic conditions, trending towards present-day conditions (Bar-Matthews *et al.* 1997, 1999); moreover, Bar-Matthews, *et al.* (2003) suggest the that climate was consistently drier than present between 7,000 cal yrs BP and present-day according to the simultaneous oxygen isotopic depletion of foraminifera *Globigerinoides ruber* and speleothems (Emeis *et al.* 2000), with rainfall predicted to reach as low as 220mm per annum at 5,200 cal yrs BP (Emeis *et al.* 2000). From the Aegean Sea, pollen-based climate transfer functions indicate significant drying following 7,200 cal yrs BP (Dormoy *et al.* 2009). Lake Van levels and palaeosalinity records suggest that humid conditions prevailed later, until ~4,000 cal yrs BP (Wick *et al.* 2003). Overall, the mid-Holocene aridification brought conditions closer towards modern Turkish climate (Turner *et al.* 2008).

From 6,000 cal yrs BP, the established vegetation composition of mesic deciduous taxa began to significantly decline and the Eski Acıgöl's lake levels fell, thus depicting the prevalence of conditions much drier than the early Holocene (Roberts *et al.* 2001). Mercuri *et al.* (2011) attribute this drying trend to the decline in NH solar insolation through the Holocene (Berger, 1978; Steig, 1999), and propose that the period between 6,000-5,000 cal yrs BP marked a significant time of climate-driven vegetation change across the eastern Mediterranean, where present-day vegetation communities began to establish (also see Eastwood *et al.* 2007; Kuzucuoğlu *et al.* 2011; Roberts *et al.* 2011).

The vast majority of literature suggest that Turkey, and the eastern Mediterranean, underwent aridification at some point between 8,000-5,000 cal yrs BP (Brayshaw *et al.* 2011). Only Lake Van's record suggests that the onset of this trend occurred later (Wick *et al.* 2003). However, as alluded to above, the oscillatory nature of this regional drying trend may hinder the ability to detect the onset of long-term climatic transitions. For example, short humid periods inferred from Lake Tecer (5,850 and 5,250 cal yrs BP) (Kuzucuoğlu *et al.* 2011), archaeological site Arslantepe (5,400 and 4,300 cal yrs BP) (Masi *et al.* (2013) may interrupt low frequency climatic change. Overall, while it can be

proposed that mid-Holocene aridification varied spatially, it is most likely to have initiated prior to 5,000 cal yrs BP in the eastern Mediterranean.

As alluded to above, notably wet phases have also been identified during the mid-Holocene. Göktürk *et al.* (2011) suggest that rain events were particularly more intense between ~7,500 and 6,100 cal yrs BP over the Eastern Mediterranean. Later in the Holocene, carbon isotopes from central Turkey suggest that the period between ~5,400 and 4,300 cal yrs BP was wetter than present day climate due to increased winter precipitation yet exhibited similar seasonality patterns to present day (Masi *et al.* 2013); a similar wet phase can be identified at the Dead Sea using water level as the primary climatic proxy (Migowski *et al.* 2006), where Dead Sea water level is quantitatively linked to regional climate variation (Enzel *et al.* 2003). Eastwood *et al.* (2007) also detect a wet phase from 6,800 to 5,200 cal yrs BP where precipitation is inferred to be higher than present day from the Gölhisar Gölü $\delta^{18}O$ record, central Turkey. *Quercus* again can be seen to expand around Lake Van, Turkey between 6,200 and 4,000 cal yrs BP in which the maximum extent of forest-steppe vegetation composition can be inferred from pollen (Wick *et al.* 2003).

Conversely, centennial periods of enhanced drought conditions have also been identified throughout the Holocene, typically prevailing between ~5,300-5,000, ~4,200-3,900 and ~3,100-2,900 cal yrs BP (Migowski *et al.* 2006; Masi *et al.* 2013; Ocakoğlu *et al.* 2013; Bar-Matthews and Ayalon, 2011; Roberts *et al.* 2011). These shorter phases of particularly dry conditions are general proposed to prevail within the aforementioned long-term drying trend expressed through the mid-Holocene (Kuzucuoğlu *et al.* 2011). However, the detection of these excursions varies spatio-temporally, where records' poor chronological control/resolution may inhibit the precise timing and dynamics of these periods to be robustly concluded.

Aridity around ~5,200 cal yrs BP may be associated with the occurrence of a Bond event (Bond *et al.* 1997), where peak ice rafted debris generally coincides with changes to various palaeoclimatic records (Kuzucuoğlu *et al.* 2011). Lake Tecer has been proposed to dry up for up to 300 years, and carbon isotopes from Arslanteperom, eastern Anatolia, indicate the intensification of droughts between 5,350 and 5,100 cal yrs BP (Masi *et al.* 2013). Göktürk *et al.*'s (2011) proposition of regional aridification in northern Anatolia initiating from 5,400 cal yrs BP may also be associated with the onset of this dry phase. Similarly, Bar-Matthews and Ayalon's (2011) speleothem record also indicates a major phase of aridity starting from 5,200 cal yrs BP, during a time of generally high climatic instability, lasting around 80 years. This arid phase around 5,200 cal yrs BP is also detected

from other surrounding palaeorecords: climatic reconstructions derived from speleothems from the Soreq Cave (Bar-Matthews *et al.* 2003), $\delta^{18}O$ from Gulf of Oman marine sediment (Cullen *et al.* 2000), geochemical and pollen records from UAE (Parker *et al.* 2006), and pollen records from southeast Italy (Di Rita and Magri, 2009). This aridity phase has also been associated with the demise of the Late Uruk societies in the Levant, which depended on Tigris and Euphrates river discharge (Cullen and DeMenocal, 2000; Staubwasser and Weiss, 2006; Weiss and Bradley, 2013). However, as alluded to above, the detection of this arid phase is not ubiquitous in Turkey, with Lake Van's high resolution record suggests consistent humid conditions until ~4,000 cal yrs BP (Wick *et al.* 2003).

iii) Late Holocene / Meghalayan Stage (4,200 cal yrs BP – Present day)

Around 4,200 cal yrs BP, a multi-centennial dry phase can be detected from central Anatolia (Kuzucuoğlu *et al.* 2011); with Staubwasser and Weiss (2006) suggesting this severe climatic drying can be seen across the eastern Mediterranean and Western Asia. The decreased Dead Sea water level (Migowski *et al.* 2006) and isotope-inferred increases E/P conditions within the Red Sea (Arz *et al.* 2006) prevail for up to 300 years. Around 4,000 cal yrs BP, arboreal pollen, including the humid-indicative *Quercus*, decreased synchronously with increases in charcoal and $\delta^{18}O$ values thus inferring aridification (Wick *et al.* 2003); this decline is inferred to be climatically driven by the increased summer droughts, due to the distinct lack of indications of grazing/agriculture until just 600 years ago (Wick *et al.* 2003). Masi *et al.* (2013) propose that the conditions experienced during this short aridity phase were similar to present day climate. Notable phases of aridity have also been detected around 4,200 cal yrs BP from North Africa (Mercuri *et al.* 2011; Cremaschi and Zerboni, 2009), Italy, (Peyron *et al.* 2011), and Israel (Bar-Matthews and Ayalon, 2011).

This centennial-scale cooling and drying is again associated with the occurrence of Bond events, as palaeoclimatic change coincides with synchronous peaks in ice rafted debris (Kuzucuoğlu *et al.* 2011). This excursion has also been linked with the decline of the Akkadian empire in Mesopotamia (Cullen *et al.* 2000) and also corresponded to the notable collapse of Jericho, Kerak, and Bet Shean (Migowski *et al.* 2006).

The final dry phase of the mid-Holocene around 3,100 cal yrs BP coincides with the collapse of the Canaanite Kingdom located throughout the Levant, where the Dead Sea's record displays notable reductions to lake level, driven by significant reduction to annual rainfall (Migowski *et al.* 2006). This drying trend, prior to the final phase of aridification towards present day conditions, was modelled

by the HADSM3 climate model run by Brayshaw *et al.* (2011). *Quercus* pollen concentrations can be seen to decrease synchronously with reductions in water lever from Lake Van at this time induced by reduced precipitation (Landmann *et al.* 1996); where Landmann *et al.* (1996) hypothesise that this change was driven by a reduction in westerlies' strength, consequently bringing conditions towards present day climate. While this climatic deterioration is inferred to last for around 200 years at Lake Tecer (Kuzucuoğlu *et al.* 2011), the Dead Sea's record indicates that these dry conditions generally persisted until present-day (Migowski *et al.* 2006).

High climatic variability persisted into the late Holocene, with wet-dry oscillations occurring consistently up to the present day in the Eastern Mediterranean (Schilman *et al.* 2001). Following the centennial-scale dry phase around ~3,100-2,900 cal yrs BP, pollen records identify a period of moderately warmer and wetter conditions in Turkey, defined by unambiguous evidence of human impact, named the Beyşehir Occupation (BO) phase (~3,000-1,500 cal yrs BP) (Eastwood *et al.* 1998). A vegetational switch from steppic environments to deciduous woodland in northern Turkey has been climatic-driven, indicative of more mesic conditions (Bottema *et al.* 1995). From Sagalassos, southwest Turkey Archaeological and palynological records provide evidence of the growth of olive (*Olea*) cultivation (Vermoere *et al.* 2003). This agricultural practice would require a 2-3°C rise in winter and spring temperatures (Roberts, 1990), where nearby vegetational shifts also indicate warmer and wetter conditions until 1,400 cal yrs BP (Bakker *et al.* 2013).

The end of the BO phase (around 1,500 cal yrs BP) is marked within Turkey's pollen records by a decline in taxa associated with anthropogenic activity, and the regrowth of arboreal taxa from Gölhisar, southwest Turkey (Eastwood *et al.* 1998). A more recent palynological study by Bakker *et al.* (2012) further suggests that vegetation towards the end of the BO phase was predominately driven by climate change, shifting initially to dry conditions with colder winters. Archaeological findings additionally identify significant settlement abandonment across Turkey around the time of this shift to drier climatic conditions (Vanhaverbeke *et al.* 2009).

Climatology over the last 2,000 years continues to display high spatio-temporal variability, where wet/dry oscillations may be broadly divided into four main periods: the Roman Warm Period, Dark Ages Cold Period, the Medieval Climate Anomaly (MCA), and the Little Ice Age (LIA) (Fig. 3.10). Relative to the entire Holocene, conditions typically reflect the era's driest conditions, yet this comparatively short periods represent variation around the mean climatic conditions.

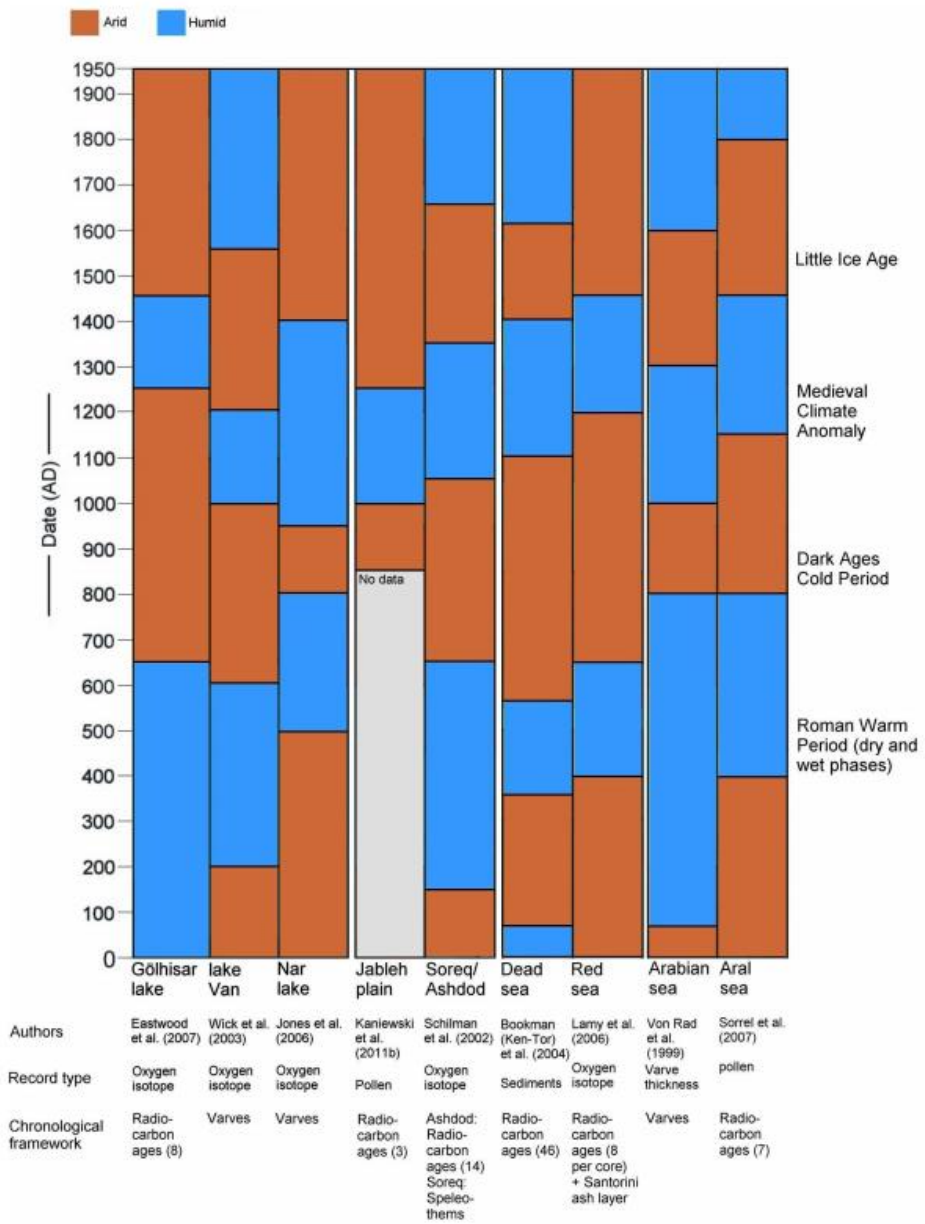


Figure 3.10 *- A summary of the timings of wet/arid phases proposed in the literature based from the eastern Mediterranean [taken from Bakker et al. 2013]*

Nar Gölü's $\delta^{18}O$ record indicates the prevalence of relatively dry conditions from at least 3,500 cal yrs BP until 1,450 cal yrs BP (Jones *et al.* 2006; Dean *et al.* 2015a). Here, climatology shifts rapidly to wetter conditions subsequently persisted from 1,450 to 550 cal yrs BP, interrupted briefly by a period of dry conditions around 1,300-1,150 cal yrs BP (Jones *et al.* 2006). Between 1,650 and 1,150 cal yrs BP, enhanced seasonality is inferred to increase winter precipitation, in the form of snowfall (Dean *et al.* 2013). From Lake Tecer, central Anatolia, severe evaporation and climatic aridity similarly led to the formation of brine in the lake during 1,700-1,550 cal yrs BP, with strong summer droughts prevailing until 1,450 cal yrs BP (Kuzucuoğlu *et al.* 2011). Elsewhere in the eastern

Mediterranean, speleothems' $\delta^{18}O$ record from the Soruq Cave displays drying conditions between 1850 and 1250 cal yrs BP, with evidence of Roman and Byzantine collapse in the Levant, from 1,750 cal yrs BP, associated with this overall cooling and drying (Orland *et al.* 2009).

Driven by changes to solar insolation and/or natural variation from the ocean-atmosphere system (Diaz *et al.* 2011), the MCA typically represents a relatively wet period across the eastern Mediterranean. Wetting of the climate can be seen across Turkey throughout the year, with enhanced winter precipitation detected from Lake Tecer (Kuzucuoğlu *et al.* 2011) and a distinct increased summer (May-June) precipitation between AD 1908-1167 from southwest Turkey (Touchan *et al.* 2007). From Nar Gölü, low $\delta^{18}O_{carbonate}$ values around 900-550 cal yrs BP (Jones *et al.* 2006) also correlate well with warm, wet conditions identified across Europe (Diaz *et al.* 2011). Human activity began to grow slowly, with evidence of increased agricultural activity on previously marginal land (Bakker *et al.* 2013). Inferred wet conditions can also be identified regionally from: marine cores off the coast of Israel (Schilman *et al.* 2001), Soreq cave speleothems (Schilman *et al.* 2002), and pollen assemblages from Syria (Kaniewski *et al.* 2011).

Conversely, the subsequent LIA is associated with generally drier conditions around 500-200 cal yrs BP (Roberts *et al.* 2012; Dean *et al.* 2013; Flohr *et al.* 2017). Nar Gölü's $\delta^{18}O$ (Jones *et al.* 2006) and Lake Tecer's geochemical records (Kuzucuoğlu *et al.* 2011) display synchronous shifts towards drier conditions ~550 cal yrs BP. In southwest Turkey, the onset of dry LIA conditions may have been earlier, with tree ring records suggesting that the driest conditions within the last 900 years prevailed between 755-686 cal yrs BP (Touchan *et al.* 2007). Again, the LIA arid oscillation can also be detected in other eastern Mediterranean sites such as the Dead Sea (Neumann *et al.* 2007), and western Syria (Kaniewski *et al.* 2011). Kaniewski *et al.* (2011) implicates the Syrian climate to be consistently colder and drier than present day up AD 1870.

The wet-MCA/dry-LIA oscillation can also be detected by the palynological study from Sagalassos, southwest Turkey, with sedimentary rates also co-varying with human activity where population growth, associated with favourable conditions during the MCA, synchronously occurred with increased sedimentation rates (Bakker *et al.* 2012).

During the past millennium, periods of prolonged drought very rarely last longer than 2-3 years according to high resolution dendrochronology from the arid northwest Turkey over the last ~300 hundred years (Akkemik and Aras, 2005; Akkemik *et al.* 2008) and southwest Turkey over the last ~660 years (Touchan *et al.* 2003); the singular dry years has a mean periodicity of around 5 years

(Akkemik *et al.* 2008), thus corresponding to the spring drought cyclicity of 4.8 years found by Touchan *et al.* (2003) in southwest Turkey. However, it is important to note that Akkemik *et al.* (2008) define a drought year as one that receives less than -15% rainfall during the year, while Touchan *et al.* (2003) incurs a stricter drought definition with a reduction in spring precipitation of less than -20% from the climatic mean. Short periods of wetter years occur at a slight lower frequency than dry years, yet display similar durations, with very few lasting more than 2 years (Touchan *et al.* 2003; Akkemik *et al.* 2008). Overall, eastern Mediterranean climate began to warm gradually over the last 80 years with slight increases in relative humidity (Kaniewski *et al.* 2011).

3.2 Lithology and chronology

Stratigraphic descriptions through the record's master sequences can provide preliminary compositional and structural information. Core drives were correlated using distinct laminae, both in terms of visual appearance and geochemical composition (from µXRF) to ensure a continuous sequence from present day was retrieved from both lakes. This section presents the core lithology and chronology from Nar Gölü.

3.2.1 Lithology

Correlation of core sections from NAR10 by Samantha Allcock resulted in the composition of a 21.69m sedimentary master sequence (Roberts *et al.* 2016) (Fig. 3.11); only a short gap in the sediment recovery (11.36 – 11.61m) prevented the formation of a continuous record of sediment deposition. Core depth measurements suggest that this gap is around 24.5cm thick. The sediment record from NAR01/02 has also been visually linked to the uppermost 3.60m of the NAR10 master sequence via a series of tie points. These form the references points used to match datasets taken from each sequence. Prior research using the NAR01/02 and NAR10 sequences have provided detailed sediment descriptions (Jones *et al.* 2006; Roberts *et al.* 2016). In summary, the full 21.69m record can be split into seven distinct stratigraphic units (Table 3.2). While Units 1, 3-5, and 7 all display alternating pale-carbonate and dark-organic laminations, they are each defined by the laminae's thickness, colour and relative disturbance level. Non-laminated Units 2 and 6 are predominately composed of homogenous grey marl sediment, with sporadic, pale laminae.

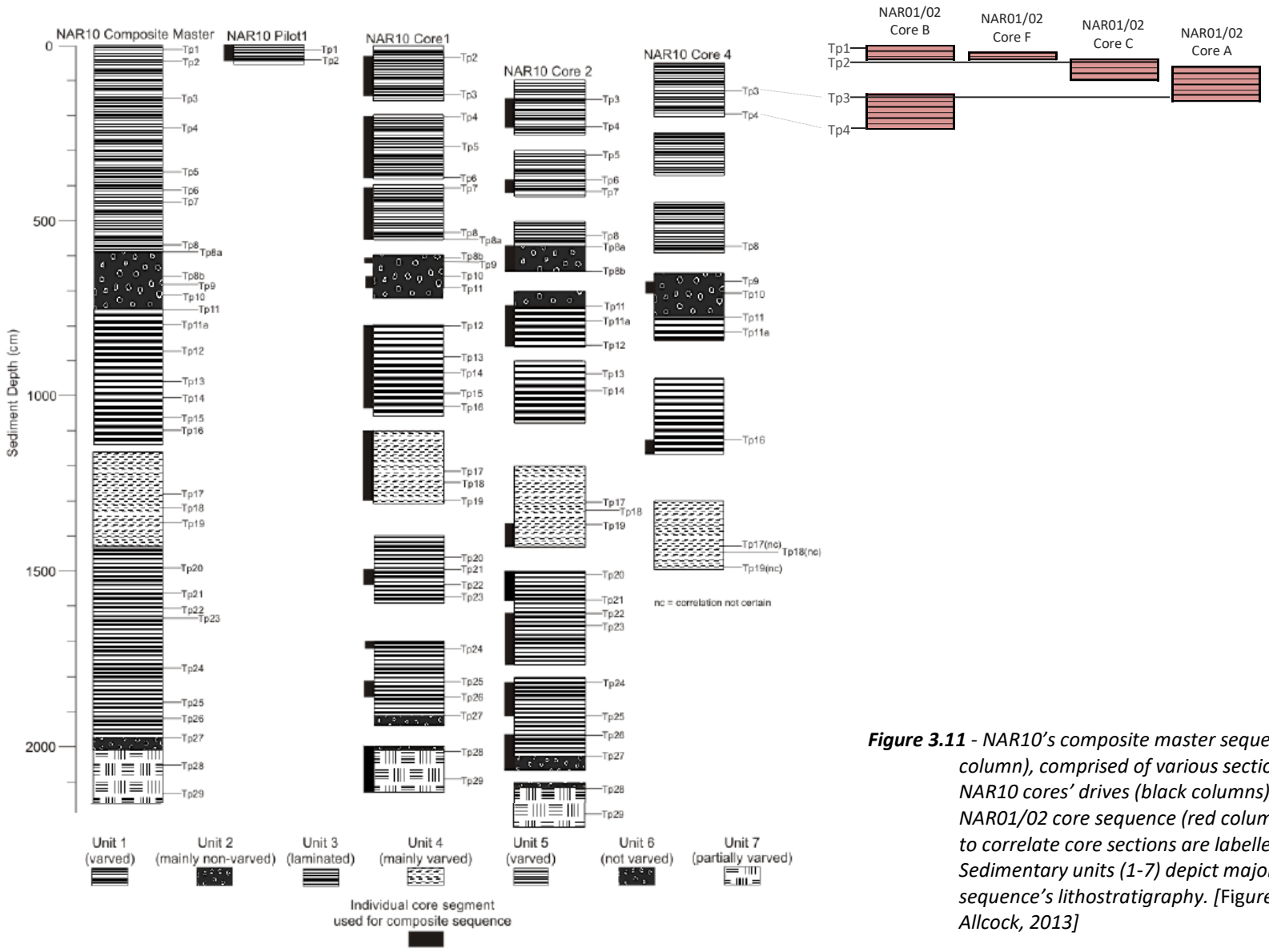


Figure 3.11 *- NAR10's composite master sequence (far left column), comprised of various sections from the NAR10 cores' drives (black columns), alongside the NAR01/02 core sequence (red columns); tie points used to correlate core sections are labelled 'Tp'. Sedimentary units (1-7) depict major changes to the sequence's lithostratigraphy. [*Figure *adapted from Allcock, 2013]*

Table 3.2 *– Descriptions of sedimentary units from Nar Gölü's master sequence, alongside a 5cm-long image representative of the unit. All measurements stated here reflect average thicknesses of individual laminae. Table is adapted from Allcock, 2013 (for more detail see Allcock, 2013)*

Master sequence depth (cm)	Unit	Sediment description	Example image
0.0 - 592.7	1	Alternating black/brown/olive organic-rich and beige calcareous laminations each around 0.5-1.0mm thick; graded, grey event layers are sporadically distributed through the unit with an average thickness of 8mm (maximum 104mm)	
592.7 - 753.7	2	Predominately non-laminated, homogeneous grey-brown sediment; thin, pale laminations are distributed throughout unit	
753.7 - 1138.7	3	Brown/grey/olive (1-4mm) and beige/white/grey laminations (1-4mm); small sections of non-laminated brown/grey sections interspersed through unit	
1136.7 - 1161.2		*Break in sediment sequence due to lack of sediment recovery*	
1161.2 - 1428.2	4	Calcareous-rich sediment; alternating thin black/brown/olive organic-rich (<0.5mm) and thick beige calcareous (0.5-1.0mm) laminations; intermittent sand bands and plant stem additions. Laminations are not well preserved.	
1428.2 - 1974.0	5	Alternating olive organic-rich (<1mm) and beige calcareous (<1mm) laminations; occasional black, red and cream laminae present	

1974.0 - 2013.0	6	Predominately non-laminated, homogeneous grey-brown marl; infrequent brown laminations between the thick, concreted sections	
2013.0 - 2169.0	7	Disturbed but alternating olive organic-rich (<1mm) and beige calcareous (<1mm) laminations; thick, olive-coloured non-laminated sections disrupt laminations.	

Laminated units are confirmed to have been annually deposited, i.e. varved, through the development of a process-related depositional model (Jones *et al.* 2005; Woodbridge and Roberts, 2010) (also see Section 3.2.2). The repeated pattern of deposition observed in the sediment record is consistently replicated within the annual sediment traps placed within Nar Gölü (2001-2017). Sediment traps have subsequently informed the development of the conceptual model of varve deposition, acting to tie seasonal climatological/limnological change to depositional processes (Zolitschka *et al.* 2015) (Fig. 3.12). Accordingly, dark laminae are composed of autochthonous organic detritus which culminates with the deposition of an algal bloom. These are observed to be deposited during autumn/winter, where organic productivity is enhanced by the wet-seasons' inwash of minerogenic nutrients, and in-lake nutrient cycling associated with winter's lake full mixing (Dean *et al.* 2015b). This organic deposition is interrupted by spring/summer endogenic calcium carbonate precipitation, typically in the form of calcite or aragonite. This carbonate supersaturation and precipitation is driven by the combined effect of (i) increased hypolimnion pH, due to the preceding algal bloom's photosynthetic consumption of CO_2, and (ii) increased concentration of ions, driven by the dry-seasons increased evaporation/precipitation (E/P) ratio. Every sediment couplet identified within Nar Gölü's laminated sections corresponds to this conceptual model of varve deposition.

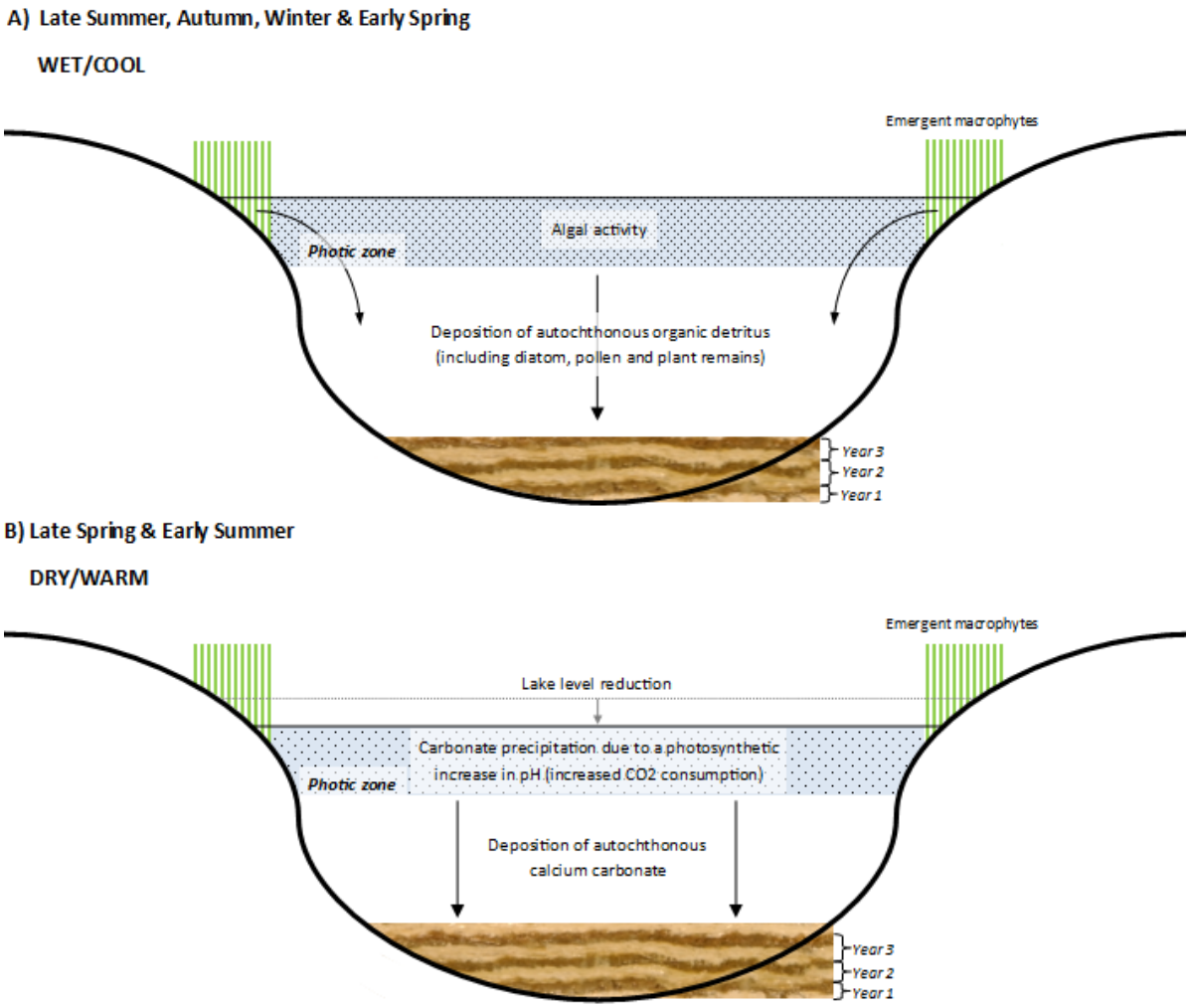


Figure 3.12 *– Conceptual model of varve formation at Nar Gölü*

This conceptual model forms the foundation of all palaeoenvironmental reconstructions based on Nar Gölü's varve sedimentology; by analysing the sediments, the necessary environmental conditions required to lead to this specific deposition can be inferred (Brauer, 2004). Additionally, the model helps identify and isolate non-seasonal layers – sediment deposition which is not consistently regulated by the intra-annual variability (Zolitschka *et al.* 2015). Non-seasonal sublayers, or 'turbidites', are typically a result of rapid deposition of clastic sediment, specifically mass wasting events typically initiated by earthquakes (e.g. Brocard *et al.* 2014) and extreme weather events (e.g. Mangili *et al.* 2005). Turbidites identified in Nar Gölü's record are distinctive grey laminae, which are often graded from coarser to finer grains, as a result of sorting related to a particle's size-dependent settling velocity. Earthquakes and extreme weather events are both possible drivers of turbidite deposition in the tectonically active region of Nar Gölü (Gevrek and Kazanci, 2000).

3.2.2 Chronology

Nar Gölü's sediment chronology has been developed through the combination of varve counts and radiometric dating techniques, namely ^{137}Cs and U-Th dating, on cores NAR01/02 by Matthew Jones (Jones, 2004; Jones *et al.* 2005) and NAR10 by Jonathan Dean (Dean, 2014; Dean *et al.* 2015). The established master chronology combines both core sequences: NAR01/02 forms the uppermost section, covering the last 900 years (0-235cm), and NAR10 extends the record to 12,840 cal yrs BP (235-2133cm) (Dean *et al.* 2015).

The contribution of NAR01/02 to the master sequence is entirely varved (Jones *et al.* 2005). Couplet counts between two ^{137}Cs peaks (6.0cm and 30.5cm composite depth), which probably correspond to its increased atmospheric concentration associated with the 26th April 1986 Chernobyl disaster and 1963 fallout maximum from nuclear weapons testing (Klaminder *et al.* 2012), helped to validate laminae couplets as varves (Jones *et al.* 2005).

Two bulk sediment samples, consisting of organic and carbonate matter, from 162-164cm depth within the NAR01/02 sequence were analysed using AMS radiocarbon dating (Table 3.2). However, these dates were over 14,000 years older than the varve counts would suggest (Jones, 2004). This sizable difference likely reflects the influence of hard water error, where old ^{14}C-depleted material is being deposited/incorporated into the sedimentary record (Deevey and Stuiver, 1964). Jones (2004) proposes that the diffusion of ^{14}C-free volcanic gas into Nar Gölü's geothermal water supply (Olsson, 1986), and subsequent carbon assimilation into the organic and carbonate sediments is the most likely cause for the overestimation of radiocarbon ages. Due to the impact of hard water error, these radiocarbon dates were excluded from the NAR01/02 chronology, and other methods were used when developing the subsequent NAR10 chronology.

Table 3.3 *– AMS Radiocarbon dates from NAR01; these dates are over 14,000 years greater than the corresponding varve counts would suggest (Jones, 2004)*

Publication code	Core sequence	Depth (cm)	Sample material	C14 Age yrs BP	1-sigma error
Beta-168920	NAR01/02	162-164	Bulk organic	14320	50
Beta-169096	NAR01/02	162-164	Bulk carbonate	23450	120

The NAR10 sequence was first correlated to the NAR01/02 record visually, and subsequent varve counts between the two cores matched the established age-depth model (<2% difference) (Allcock, 2013). As a result, thin section microscopy has been used to repeat varve counts from NAR10's unit 1, and thus extend the incremental chronology from 2001 AD to 589 BC.

Using the assumption that the master sequence's topmost sediment were deposited during the year prior to coring (NAR01/02), unit 1's varve counts were anchored to 2001 AD. From this point, error associated with 'missing varves' and counting error accumulates backward through time (Zolitschka, 2007). Repeated counts using thin section microscopy corroborate previous counts of the topmost 900 couplets, thus covering the period 1101-2001 AD, and indicates a counting error of ±1%. While difficult to quantify, the well-preserved and continuous laminations of unit 1 minimises the influence of error derived from 'missing varves'. Considering these two sources of cumulative error, >1% error is added to the number of varve years away from 2001 AD within unit 1's absolute chronology; where '>' is used to highlight that error is likely underrepresented, as 'missing varves' may not be accounted for.

Dean *et al.* (2015a) explain in detail the development of Nar Gölü's chronology prior to the start of unit 1's varves, namely the use of U-Th dating to anchor the floating varve-based chronologies of units 3-5. Dating errors were high due to the low concentrations of uranium; only two samples' dates had an acceptable error: 4,350 ±160-170 cal yrs BP at 1021cm depth, and 11,760 ±520 cal yrs BP at 1949cm depth. The upper date (1021cm) acts to anchor the floating varve chronology located between unit's non-laminated sediment, and sequence gap at 1141cm depth; while the varves are remarkably thick (1-5mm), the sediment accumulation rate, determined through couplet counts and anchored by the radiometric date, supports the inference of annual varve deposition. At the depth of the other date (1949cm), Nar Gölü's oxygen isotope record, known to relate to catchment evaporation and precipitation (Jones *et al.* 2005; Dean *et al.* 2013), suggests a rapid shift from drier to wetter conditions. Such a significant transition in the Eastern Mediterranean around 11,100-12,300 cal yrs BP is likely to represent the onset of the Holocene (Roberts *et al.* 2008). Nearby varved lake Eski Acıgöl's oxygen isotope record corresponds well with Nar Gölü's through much of Holocene and includes this notable Younger Dryas-Holocene transition (Roberts *et al.* 2001). Therefore, the U-Th date was deemed reliable and hence used to also anchor the floating varve sequence found between depths of 1161-1965cm.

From this lower U-Th date (1949cm), uncertainty derived from 'missing varves' and counting error again accumulates through time. Similarly observed within the upper sediment, repeated varve counts on the split core and thin sections indicate a low counting error of ±1% (1161-1965cm). Unit 5's continuous varves are also well-preserved (1428-1974cm), thus diminishing the likelihood of 'missing varves' introducing significant error. However, the varve stratigraphy deteriorates during the subsequent Unit 4; here, varves are discontinuous and poorly preserved, and so the influence of 'missing varves' is likely greater than Units 1 and 5. Nevertheless, within the context of lacustrine sediment records, the chronological error based from varve counts probably remains comparatively low; worldwide error of varve chronologies predominately remains below ±4% (Ojala *et al.* 2012). An additional >1% error accumulates with counts away from the U-Th date at 1949cm (11,760 ±520 cal yrs BP) anchoring the floating varve chronology, and combines with the error associated with the independent dating method.

Overall, Unit 1's continuous varve counts form a chronology from -51 ± >0 to 2,539 ± >26 cal yrs BP (2001 ± >0 AD – 589 ± >26 BC) (0-598cm). Similarly, Units 4-5's varve counts above and below the U-Th date form a 5319 ± >54 year-long, annual chronology between 6,488 and 11,807 ± 574 cal yrs BP (1161-1965cm). Sediment accumulation rates, calculated from varve counts between sediment depths, fit well with the radiometric dates, and hence establishes NAR10's age-depth model (Fig. 3.13).

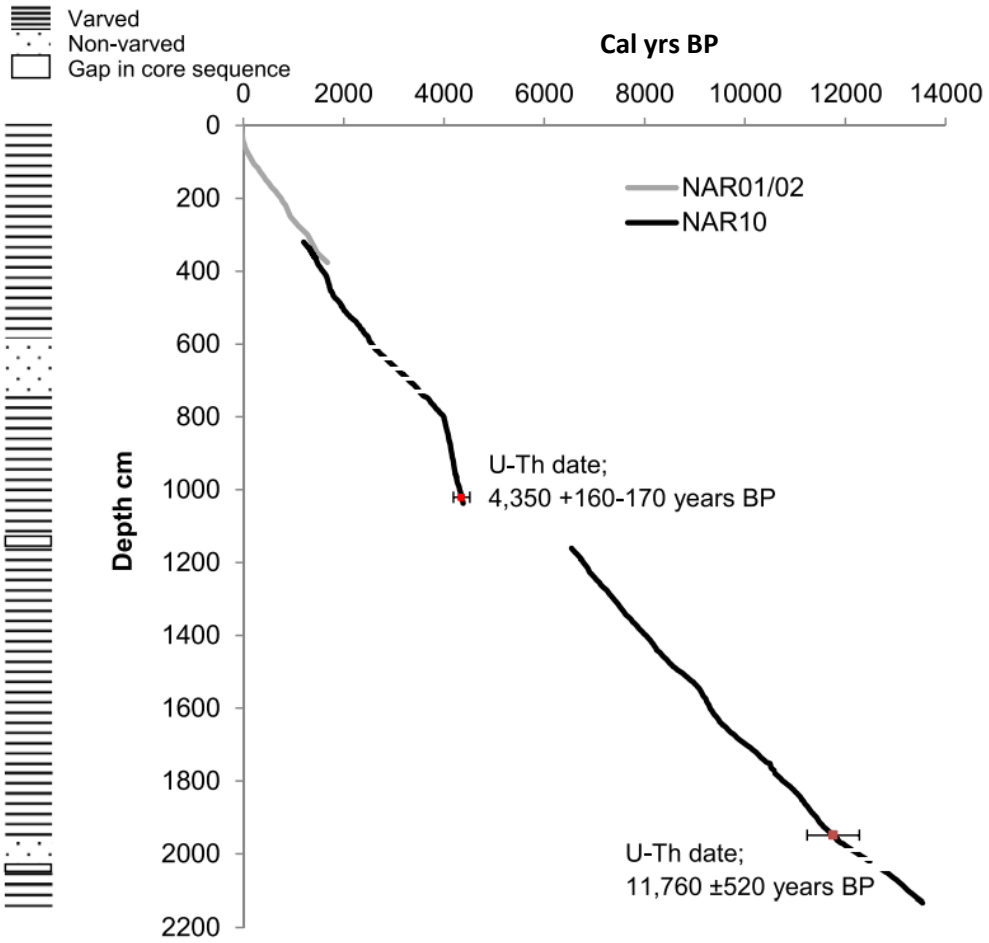


Figure 3.13 – *Age-depth model for NAR01/02 (grey line) and NAR10 (black line) master sequences. Repeated varve counts developed the chronologies (solid line), with linear interpolation used to connect floating sequences (dashed line) [from Dean et al. 2015a]*

3.3 Sedimentology: results and interpretation

This section presents the sedimentological data collected from Nar Gölü's master sequence, and discusses the likely environmental conditions required for each components' deposition and preservation.

Results and interpretations from Unit 4-5's varves deposited during the early-mid Holocene, from ~9064 to ~7630 cal yrs BP are first discussed (see Section 3.3.1). Within a floating varve chronology with comparatively poor stratigraphic boundaries, data was collected from as many varves within these Units as possible. Second, Unit 1's varves, deposited during the late Holocene, from 2539 to -60 cal yrs BP are discussed (Section 3.3.2). Here, the composition and structure of every lamina from the end of the non-laminated Unit 2 to the core's top is presented, and key sedimentological changes are precisely dated.

3.3.1 Early-mid Holocene: Units 4-5

Preliminary microfacies data were collected from the laminated Units 4 and 5 (see Table 3.2 in Section 3.2.1) in an attempt to develop temporal overlap between Nar Gölü's and Yaal Chac's sedimentary records. As previously discussed, varved couplet counts within these units are used to construct an annually-resolved chronology between 1161-1974cm sediment depth (Dean *et al.* 2015a). Anchored by a U-Th date at 1949cm (11,760 ±520 cal yrs BP), these laminations are dated 12,016 – 6,541 ±520 cal yrs BP (Dean *et al.* 2015a). Therefore, the early-mid Holocene cessation of varve deposition in Nar Gölü occurred during the deposition of Yaal Chac's varved unit (Section 4.2.2). However, laminations at the end of Unit 4 are discontinuous and poorly preserved, and so the most recent sedimentological data recorded from Unit 4 is dated at 7,630 ±520 cal yrs BP. Similarly, two short sections of very poorly preserved varves prevent reliable data being collected from 1390-1404cm and 1416-1439cm, dated at 7,948-8,046 and 8,113-8,223 cal yrs BP respectively. In total, 1,229 varves were analysed within a period spanning from 7,630 to 9,064 cal yrs BP. While this represents the latest obtainable microfacies data from Unit 4, earlier varves are well-defined and suitable for further data collection; unfortunately, this was not achievable within this research project's time constraints.

The lithological switch from Unit 5's continuously-laminated sediment to Unit 4's discontinuously-laminated sediment is located within the earlier gap in microfacies data, dated 8,113-8,223 cal yrs BP (1416-1439cm); this sedimentological change is reflected in the collection of data from discrete

periods of varved sediment. Varves recorded within Unit 4 represent shorter periods of well-defined laminations. While varve counts on the split cores provide an annual chronology, poor stratigraphic preservation prevents the collection of reliable sedimentological data through thin section microscopy. However, this sediment disturbance reduces the confidence of the varve-count chronology within Unit 4; while repeated counts identify the user-based error, the influence of missing varves is difficult to quantify (Zolitschka *et al.* 2007). In addition to the U-Th dating error (±520 yrs), the accumulation of ±1% error from varve counts results in an uncertainty of around ±27 yrs at the start of varved data described here (9,064 ±27 cal yrs BP), and at least ±41 at the end (7,630 ±41 cal yrs BP).

3.3.1.1 Varve microfacies

i) Classification

Unit 4-5's varves were categorised into 3 distinct subclasses (M4, M2a* and M5) according to their sedimentological composition and structure. These varves' composition and structure closely resemble those identified in Unit 1 (M1-3). Subclass M2a* reflect varves from Unit 5 which display a strong resemblance Unit 1's M2a varves (see Section 3.2.2.1). The other two subclasses (M4 and M5) represent further variations to Nar Gölü's typical varves, as described by Woodbridge and Roberts (2010), where the carbonate-organic stratigraphy similarly conforms to the conceptual model of varve formation (see Fig. 3.12). As such, Tables 3.4 and 3.5 portrays microfacies defining each subclass, and the following describes their composition and structure.

Generally, Unit 4-5's varves are thinner than those measured from Unit 1's varves (M1-3); situated over 14m below the sediment-water interface, downcore sediment compaction is likely to account for some of this these reduced thickness. This diminishes the ability to make absolute comparisons between Unit 1 and Units 4-5 thickness data. Nevertheless, due to the inability to detrend data (see Section 3.3.2), thicknesses are used to define microfacies subclasses, thus distinguishing varves from M1-3 and M4-5 (and M2a*), and are hence discussed here.

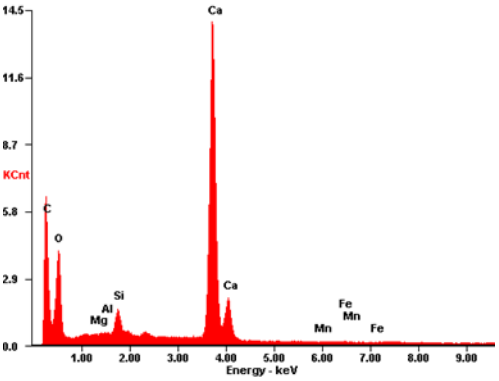
The same sedimentology of carbonate sublayers is observed in both M1-3 and M4 varves, specifically: all carbonate sublayers are composed of homogeneous, fine-grained, euhedral calcite or aragonite crystals, indicative of endogenic precipitation (Kelts and Hsü, 1978); abrupt sublayer boundaries denote a rapid change to the depositional process (Mangili *et al.* 2005), thus suggesting

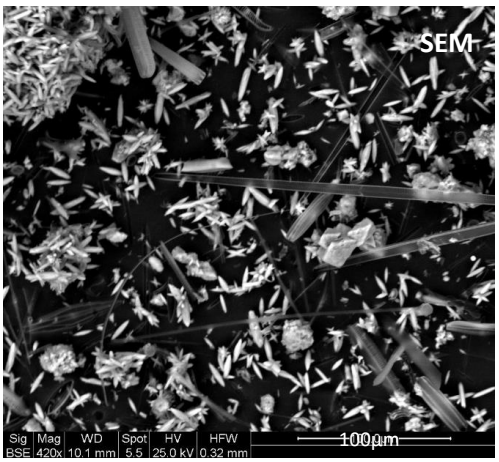
mineralisation is likely to occur during an abrupt 'whiting' event; and very weak, up-core fining may also indicate that carbonate supersaturation intensifies through the precipitation event (Brauer *et al.* 2008).

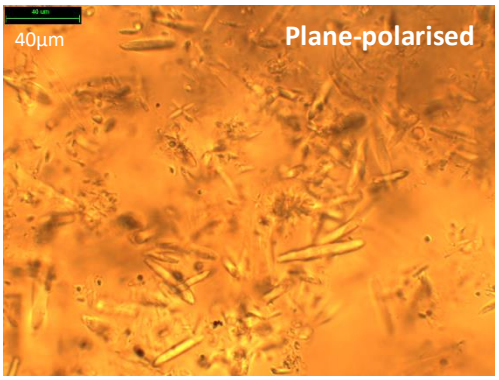
Scanning electron microscopy (SEM) with an energy dispersive X-ray spectroscopy (EDX) probe, run by Jonathan Dean (2014), identified the dominance of calcite and aragonite minerals within Nar Gölü's sedimentary Units 4 and 5 (Dean *et al.* 2015a) (see Fig. 3.14a and b). XRD analysis, also run by Jonathan Dean (2014), further confirmed the presence of these minerals through the Units, and semi-quantitatively determined the proportion of each through the NAR10 sequence. Due to the birefringent optical properties of these minerals, carbonate material could be clearly distinguished from the autochthonous organic deposition and in-washed obsidian in the thin sections under cross-polarised illumination. The crystals' euhedral morphology, rhombic-shaped calcite and needle-shaped aragonite minerals enabled the carbonate mineralogy to be clearly differentiated. The mineralogical shifts between calcite- and aragonite-dominant sediment identified through the record via thin section microscopy also correspond well with XRD and EDX results (Dean, 2014) and μXRF geochemistry of element composition at multiple sediment depths (see section 3.3.1.2).

(i) Aragonite

- Needle-shape characteristic of aragonite
- Euhedral crystalline structure indicative of endogenic precipitation
- No Mg present within crystal







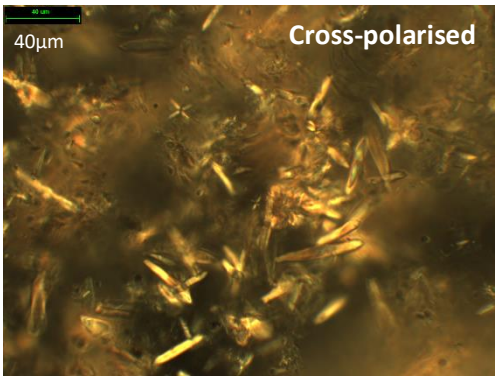


Figure 3.14a *– Identification of aragonite from Nar Gölü via SEM, EDX and thin section microscopy. For each mineralogy, the elemental composition (top left) of the crystals pictured within the SEM image (top right) (Dean, 2014), and plane- and cross-polarised images taken under 200x magnification using a petrographic microscope at the University of Nottingham.*

(ii) Calcite

- Rhombic-shape characteristic of calcite
- Euhedral crystalline structure indicative of endogenic precipitation
- Low concentration of Mg within crystal

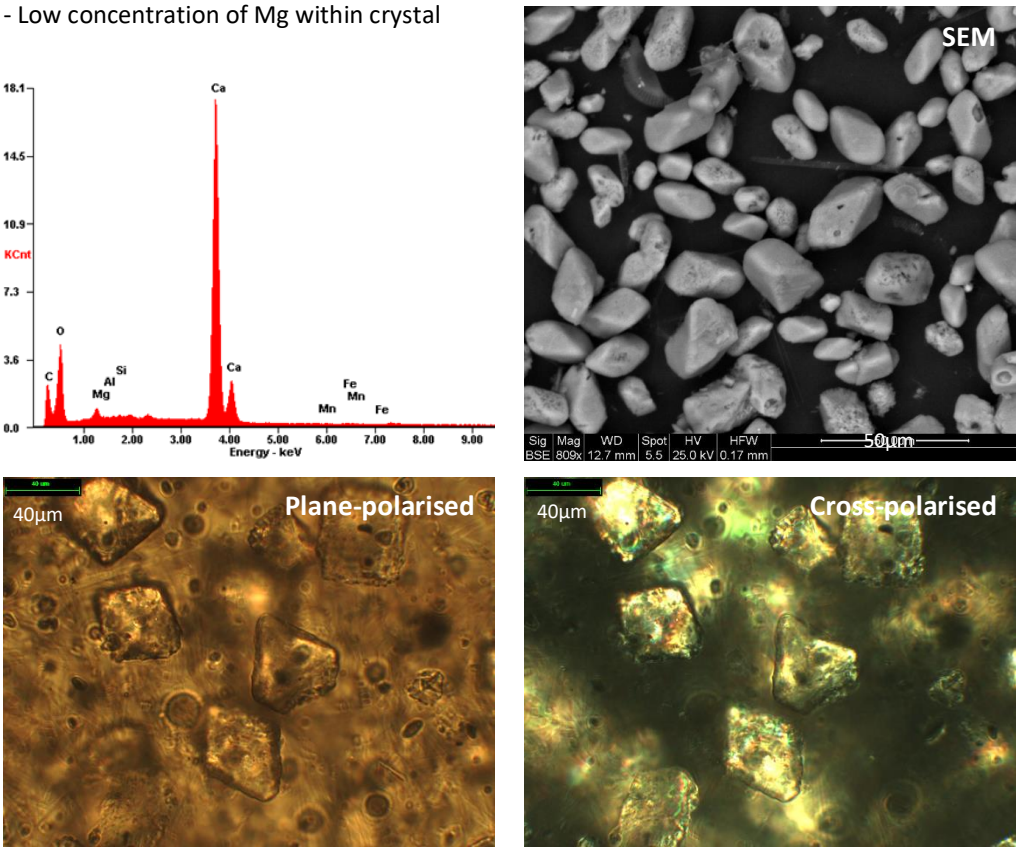


Figure 3.14b *– Identification of calcite from Nar Gölü via SEM, EDX and thin section microscopy. For each mineralogy, the elemental composition (top left) of the crystals pictured within the SEM image (top right) (Dean, 2014), and plane- and cross-polarised images taken under 200x magnification using a petrographic microscope at the University of Nottingham.*

The thickness and presence of calcite/aragonite mineralogies, and their accompanying organic sublayers, define M4 varves' subclasses and distinguish them from M1-3 varves (see Section 3.3.2).

- **M4** carbonate sublayers are dominated by calcite deposition. While 51% of varves also contain an overlying aragonite sublayer, these sublayers are typically much thinner (average 0.20mm) than their accompanying calcite lamina (average 0.78mm). The dominance of calcite is indicative of comparatively fresh limnological conditions (Kelts and Hsü, 1978), which are similarly reflected in the organic sublayers which most often contain very low concentrations of background, micritic carbonate; fresher conditions may prevent the

supersaturation of carbonates within the micro-environmental around a photosynthetic organism and hence minimise the production of micritic carbonate through the year (Kelts and Hsü, 1978). M4's organic sublayers are typically very thin (average 0.15mm), composed of amorphic organic material with varying (low) concentrations of diatoms and unidentifiable, organic detritus.

- **M2a*** varves' composition and structure display a strong resemblance to Unit 1's M2a varves (see Section 3.3.2.1); only the varves' average thickness differentiates these subclasses, as denoted by the classification's asterisk (*). Varves observed in Units 4-5 are generally thinner, averaging 0.64mm (M2a*) as compared to 0.81mm (M2a). While both subclasses' organic sublayers predominately consist of amorphic organic matter with high concentrations of micritic carbonate, the thickness and structure of these sublayers separate these two subclasses. Again, M2a* organic sublayers are thinner, averaging 0.44mm (M2a*) as compared to 0.66-1.20mm (M2a), and typically display fewer distinct sublayers; around 77% of M2a's varves contain an additional amorphic organic sublayer containing low concentrations of micritic carbonate. These low-carbonate organics are not identified within M2a* varves. While downcore sediment compaction may drive this observed disparity between M2a and M2a* thicknesses, the strong sedimentological similarities between the two subclasses indicates that sediment accumulation likely resulted from similar limnological conditions and intra-annual climatology. As previously discussed, the aragonite-rich carbonate mineralogy and the high concentrations of micritic carbonates throughout each year's deposition probably reflects more evaporative limnological conditions, where carbonate supersaturation may occur within a photosynthetic organism's micro-environment.

- **M5** varves' carbonate sublayers typically contain both aragonite and calcite. Averaging 0.78mm, these varves represent the thinnest recorded within Unit 4-5's varves (and NAR10). While compression may partially account for this, these varves' carbonate sublayers are notably thin (averaging 0.43mm) in relation to their corresponding organic sublayers (averaging 0.35mm). Calcite and aragonite sublayers are present in 76% and 96% of M5 varves respectively, and the latter are twice as thick on average (Table 3.5). In the rest of the record, aragonite-rich carbonate sublayers display higher concentrations of micritic carbonates in their organic sublayers, probably owing to the generally evaporative limnology; however, the aragonite-rich M5 varves display amorphic organic sublayers

typically with very low concentrations of background carbonate deposition. This evaporative-indicative carbonate mineralogy and fresh-indicative organic composition may suggest enhanced seasonality, resulting in increased intra-annual variability of limnological conditions.

Table 3.4 *– Classification of varve microfacies according to thin section microscopy.*

	Microfacies classification	Yrs BP	Number of sublayers	Average varve thickness (mm)	
M4	Calcite-rich/ Organic	7630-7948 8046-8113	3	1.01	
M2a*	Aragonite-rich/ Thicker organic	8223-8517	2/3	1.07	
M5	Mixed carbonate/ Thicker organic	8518-9064	3	0.78	

Table 3.5 *– A conceptual diagram of the microfacies sub-classes*

Microfacies	Colour	Sub-layer	Average thickness (mm)	Description
4		**Calcite-rich/ Organic**		
		(i) Aragonite [present in 51% of varves]	0.20	- Euhedral, fine-grained aragonite crystals (<5µm) - Dense and well-defined with abrupt boundaries
		(ii) Calcite [present in 99% of varves]	0.77	- Euhedral calcite crystals (12-16µm) - Dense and well-defined with abrupt boundaries
		(iii) Low-carbonate clastic mix/ Organic	0.15	- Composition dominated by amorphic organic matter - Low concentrations of carbonate minerals
2a*		**Aragonite-rich/ Thicker organic**		
		(i) Aragonite	0.64	- Euhedral, fine-grained aragonite crystals (<5µm) - Dense and well-defined with abrupt boundaries
		(ii) High-carbonate clastic mix	0.42	- Mix layer of amorphic organic matter and carbonate minerals (high concentration)
5		**Mixed carbonate/ Thicker organic**		
		(i) Aragonite [present in 96% of varves]	0.32	- Euhedral, fine-grained aragonite crystals (<5µm) - Dense and well-defined with abrupt boundaries
		(ii) Calcite [present in 76% of varves]	0.17	- Euhedral calcite crystals (12-16µm) - Dense and well-defined with abrupt boundaries
		(iii) Amorphous organic	0.35	- Composition dominated by amorphic organic matter - Very low concentrations of carbonate minerals

ii) Thickness measurements

While thickness data were used to define the microfacies subclasses, this section discusses how sublayer thickness varies over time. As mentioned above, poor stratigraphic preservation prevented the reliable collection of continuous microfacies data within Unit 4. As a result, two data gaps at 1390-1404cm and 1416-1439cm interrupt the sedimentological record; the upper gap splits two sections of contiguous M4 varve deposition in Unit 4, and the lower gap covers the lithological transition from Unit 5 (M2a* and M5 varves) to Unit 4 (M4 varves) (Fig. 3.15). While these stratigraphic boundaries are too disturbed to accurately sublayer thicknesses, laminae counts provide an approximate indication of the period these data gaps cover, dated at 7,948-8,046 and 8,113-8,223 cal yrs BP respectively. Again, turbidites have been removed from the data unless specified, since their deposition is not governed by the seasonal limnological cycle. Figure 3.15 displays the thicknesses of key sedimentological sublayers alongside the $\delta^{18}O_{Carbonate}$ profile provided by Dean *et al.* (2015a), and the location of these data gaps.

Just as in Unit 1 (see Section 3.3.2), carbonate deposition drives the majority of sediment accumulation within Unit 4-5's varves, accounting for ~67% of the total varves thickness; this proportion significantly increases through the record and subclasses, from 55% in M5, to 61% in M2a*, and 77% in M4. This long-term trend is caused by consistently increasing-carbonate and decreasing-organic deposition, and may suggest a gradual change to relative seasonality over the period.

No significant correlation between each year's carbonate and organic thicknesses is identified. Therefore, the seasonal drivers of these respective sublayers may be considered independent from each other through this sequence. It appears that the annual accumulation of organic material does not significantly influence the length/intensity of carbonate precipitation events, despite biogenic productivity's established contribution to driving the supersaturation and precipitation of carbonate minerals (Müller *et al.* 1972).

Within the ~1434-year period covered by sedimentological data, the oxygen isotope ratios of 52 carbonate laminations were analysed (Dean *et al.* 2015a). Again, the thickness of aragonite and calcite sublayers appear to co-vary with their oxygen isotopic composition. With an average of –1.0‰, the aragonite-rich M2a* varves display significant $\delta^{18}O_{Carbonate}$ enrichment, as compared to calcite-rich varves of M4 and M5, which average –2.5‰ and –2.8‰ respectively. These isotopic

shifts exceed the magnitude of mineralogical-dependent fractionation, where aragonite typically displays values +0.7‰ higher than calcite formed within the same hydrology (Grossman and Ku, 1986), thus supporting the use of isotopic variability as a proxy for palaeohydrology (Dean *et al.* 2015a). While the low sampling resolution prevents the inter-varve correlation of isotopic ratio and the corresponding thickness of carbonate mineralogy (as seen in Fig. 3.25), carbonate sedimentology appears to follow the same dynamics as isotope-inferred water balance (Jones *et al.* 2006). Aragonite (calcite) preferentially precipitates during periods of increased (decreased) E/P – again conforming to the established model of mineral precipitation linked to epilimnetic ion concentrations (Kelts and Hsü, 1978).

From 9,064 to 8,518 cal yrs BP (M5), gradually increasing aragonite and decreasing calcite thickness correspond with long-term isotopic enrichment, indicative of increasing E/P conditions. Assuming the relationship between March-May E/P conditions and carbonate thickness, gained from the sedimentological calibration with the meteorological record (Section 3.3.2.1iii), is maintained throughout the Holocene, this observed aragonite/calcite trend may be partially driven by a lengthening of the dry season conditions. Within M5 varve deposition, a multi-decadal period of increased calcite and organic deposition (average thickness of 0.24mm and 0.45mm respectively) coincides with substantial isotopic depletion (–4.7‰) between 8,806-8,886 cal yrs BP. Increased precipitation may drive this mineralogical- and isotopic-inferred freshening of limnological conditions, and enhance the inwash of terrestrial organic detritus and nutrients for autochthonous productivity which contributes to organic sublayer accumulation.

The switch from M5 to M2a* varve deposition at 8,518 cal yrs BP occurs following the eventual cessation of calcite deposition and coeval increase of aragonite precipitation. Averaging 0.64mm, these aragonite sublayers are twice as thick that those from M5 (0.32mm). As previously mentioned, M2a* varves' aragonite-rich sedimentology coincides with isotopic enrichment, averaging –1.0‰ and peaking at 0.0‰ (8,312 cal yrs BP). Organic sublayer thicknesses also significantly increase to an average of 0.42mm, perhaps driven by an intensification of background micritic carbonate precipitation through the year.

The transition from M2a* to M4 varves (around 8,200 cal yrs BP) corresponds well with the onset of the Holocene's Northgrippian Stage (mid-Holocene). The discrete periods of M4 varve deposition display significantly thicker calcite deposition (average 0.77mm) and thinner organic deposition (0.15mm). Again, this calcite-rich mineralogy corresponds with isotopic depletion (average –2.5‰),

indicative of fresher limnological conditions (Dean *et al.* 2015b). Short periods of increased aragonite presence and sublayer thickness between 7,859-7,781 cal yrs BP and 8,113-8,046 cal yrs BP coincide with relative isotopic enrichment peaking at –1.4‰ (~7,827 cal yrs BP) and -1.5‰ (~8,067 cal yrs BP) respectively. Throughout M4 varves, organic sublayer thicknesses are very low (averaging 0.15mm), and display little compositional variance, predominantly consisting of amorphic organic material with very low concentrations of background micritic carbonates.

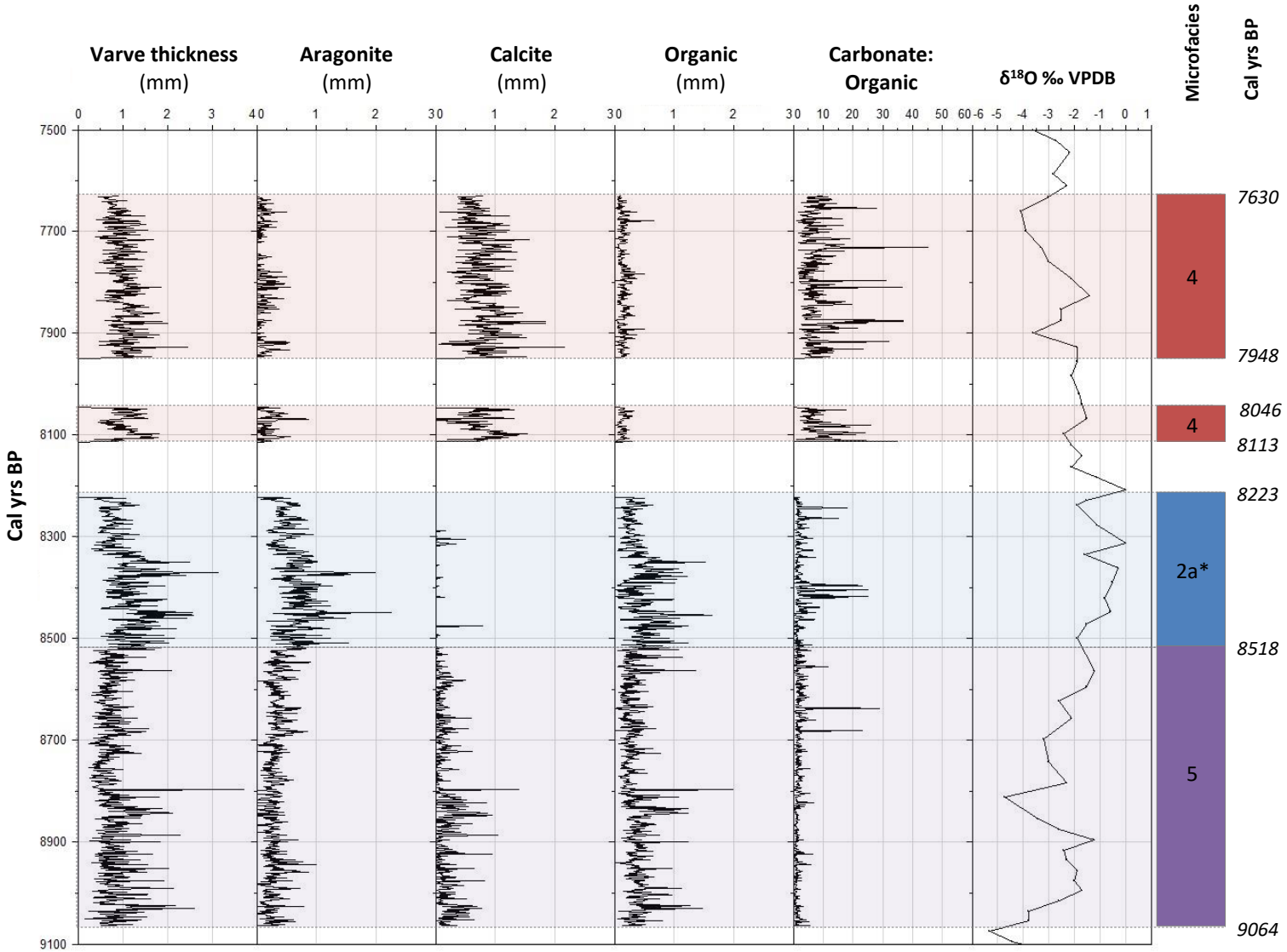


Figure 3.15 *– Thickness measurements of the varves' key sedimentological variables from Unit 4-5, subdivided by microfacies classification (grey line). Oxygen isotope data from carbonate material is also shown ($\delta^{18}O$ ‰ VPDB) (from Dean et al. 2015a). Gaps in stratigraphic data reflect sections of poor quality laminations.*

3.3.1.2 Sediment geochemistry

High resolution geochemical data from the entirety of Units 4 and 5 were gained using the Itrax µXRF core scanner, at the same scanning resolution as Unit 1, 200µm (Allcock, 2013). With an average varve thickness of 1.01mm, multiple data points were obtained within each varve.

The geochemical composition of Unit 4 and 5's varves strongly resembles varves from Unit 1, with a strong dominance of Calcium (Ca), Strontium (Sr) and Iron (Fe) detection. Again, Rubidium (Rb), Potassium (K), Manganese (Mn) and Titanium (Ti) also represent the next most abundant elements. As previously stated, analysis of stratigraphic profiles of elements detected in lower concentrations must be treated with caution, as patterns may not reflect a true geochemical signal (Croudace *et al.* 2006).

By pairing specific varves to their cumulative sediment depth, a floating age-depth model was formed. Therefore, each 200µm-step of the µXRF scan could be converted to a regular time-step consistent with the average accumulation rate between fixed varve count-depth pairs. The following sections plot microfacies and geochemical data alongside each other against the varve-based chronology.

i) Principle Component Analysis

PCA was performed on the normalised µXRF data from the start of microstratigraphic data in Unit 5 at 9,064 cal yrs BP (1544cm), and covers the entirety of Unit 4 until its end at 6,541 cal yrs BP (1162cm). To assess the full geochemical variability within the sequence, data points from turbidites were included.

As identified from Unit 1's PCA, much of the elemental variance can be explained through changes to Ca and Fe, associated with endogenic carbonate precipitation and allogenic inwash respectively (Fig. 3.16). Only the first two axes are significant, acting to explain 99.7% of the total geochemical variability. The primary eigenvector explains 95.6% of this total variance, and strongly correlates with Ca detection (r^2=0.99; P<0.001); whereas, the secondary eigenvector explains just 4.2% of variance, correlating with Fe (r^2=0.62; P<0.001) (Fig. 3.17). The geochemical variance explained by these components is likely driven by independent depositional processes within the seasonal sublayers. The primary eigenvector, and Ca detection, highlights the dominant role of processes controlling endogenic carbonate precipitation; while the secondary eigenvector, and Fe detection,

incorporates environmental factors determining catchment erosion rates and transportation of allogenic material to the lake.

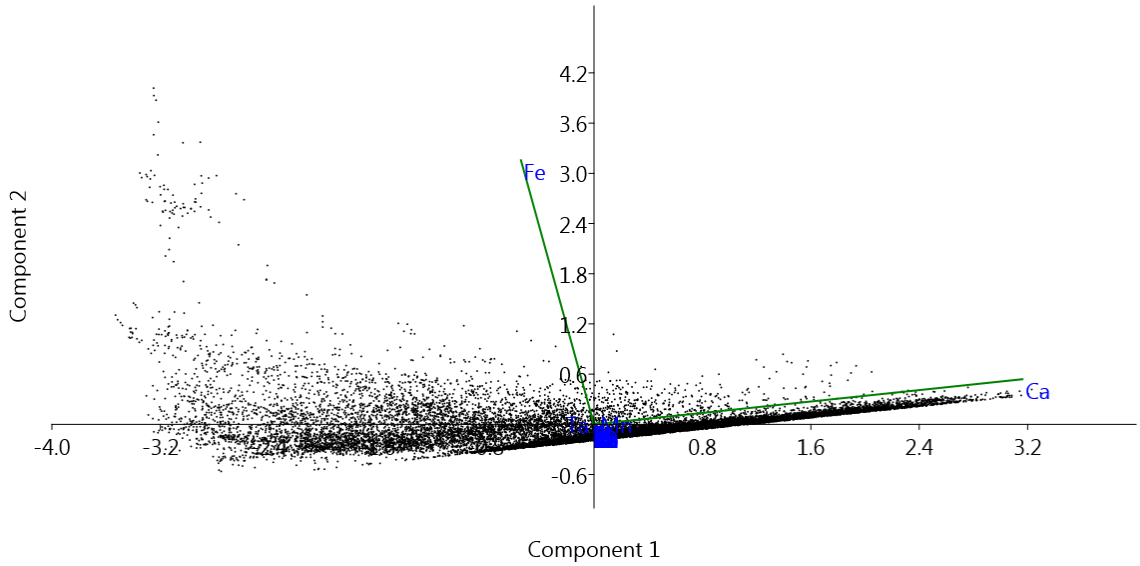


Figure 3.16 *- Principle components analysis' primary and secondary axes from Units 4-5, and its identification of Ca and Fe as key elements explaining geochemical variance.*

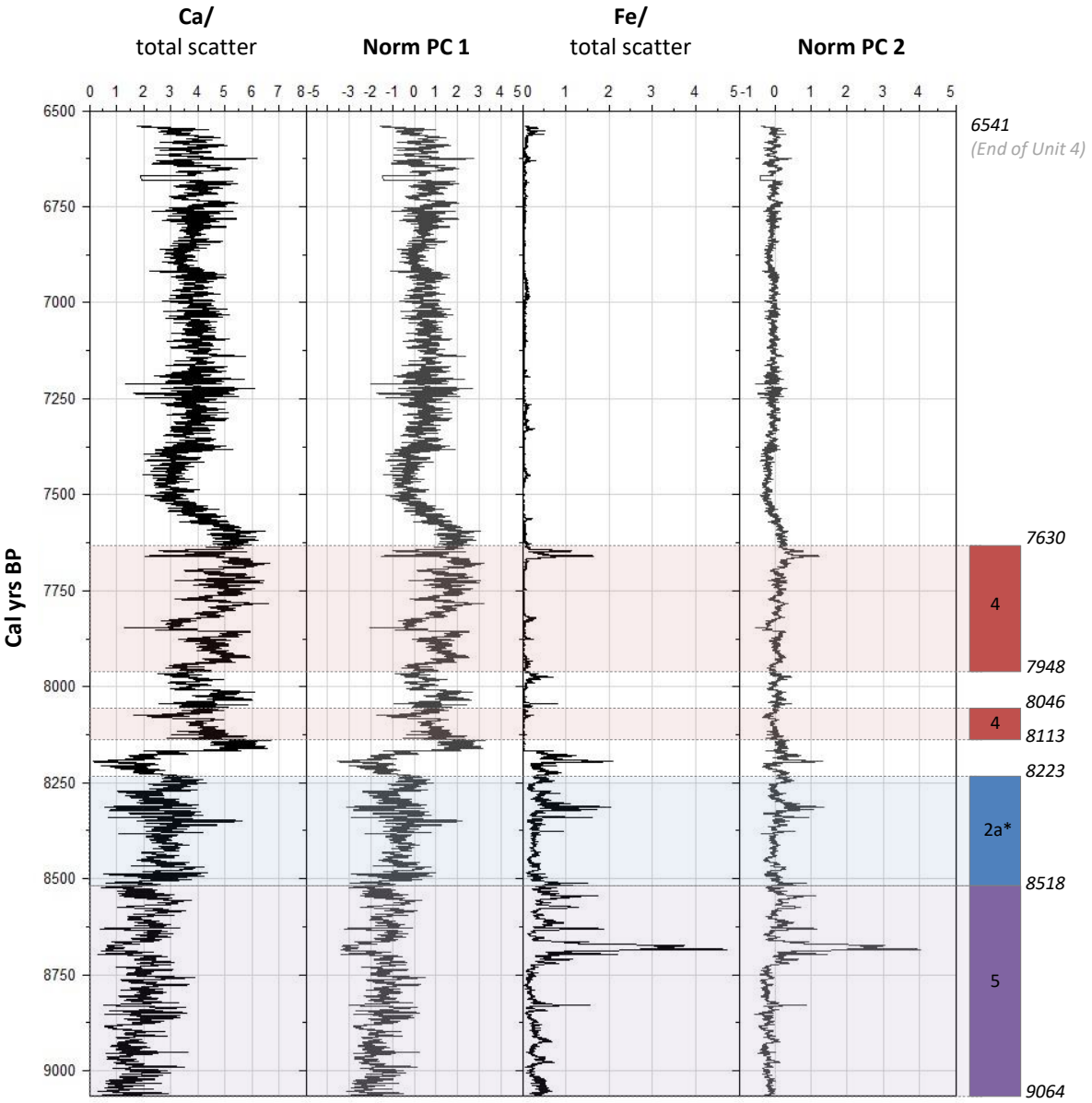


Figure 3.17 *– Comparison between the changes to key elements identified in the PCA (black lines) and the first two significant axes (grey lines) within Units 4-5; subdivided by microfacies classification (dotted lines).*

ii) Carbonates

Endogenic calcium carbonate precipitation drives sediment accumulation in Units 4-5; Figure 3.18 displays the key sedimentological profiles pertaining to its accumulation and geochemical composition through the record. Within the continuously-laminated Unit 5 (M2a* and M5), Ca and Sr strongly co-vary (r^2=0.72; P<0.001). These elements' deposition generally correlates with aragonite thicknesses and $\delta^{18}O_{carbonate}$; where increased E/P conditions, as inferred by isotopic enrichment, enhances calcium carbonate deposition and hence Ca detection. As such, M2a* aragonite-only varves, indicative of increased E/P conditions, display significantly higher values of normalised Ca and Sr (2.53 and 0.29 respectively) than M5 varves (1.83 and 0.20 respectively); where M5 varves contain proportionally less aragonite within their varve microstratigraphy, suggesting comparatively fresher conditions.

Following the switch to sedimentary Unit 4, and hence to M4 varve deposition, Ca and Sr cease to co-vary significantly (r^2=0.01; P>0.05). This geochemical shift corresponds to a mineralogical change from aragonite- to calcite-dominant carbonate deposition; the reduced precipitation of aragonite minerals, which incorporate proportionally more Sr than calcite into the crystal lattice (Kelts and Hsü, 1978), is likely to drive the decreased deposition of Sr within the sedimentary record. This calcite-dominant mineralogy, abrupt shift to lower Sr:Ca ratios and isotopic minimum during M4 varve deposition is indicative of the freshest limnological conditions of Unit 4. However, consistent $\delta^{18}O_{carbonate}$ enrichment following the end of microstratigraphic data at 7,630 cal yrs BP until the end of Unit 4 at 6,541 cal yrs BP suggests increasing E/P conditions. Calcite deposition, and hence low Sr:Ca ratios, persist until around 6,700 cal yrs BP; after which, this isotopic enrichment reaches its peak values of Unit 4, ranging from -0.1‰ to +1.3‰, thus driving the re-emergence of aragonite precipitation (Dean *et al.* 2015a) and consequently increased Sr:Ca ratios.

Throughout NAR10, varve microstratigraphic data displays a strong relationship between the thickness of aragonite/calcite sublayers and oxygen isotope ratio (Fig. 3.25). However, during the period of Unit 4 without microstratigraphic data from 7,630 to 6,541 cal yrs BP, calcite precipitation dominates despite comparatively enriched $\delta^{18}O_{carbonate}$ values. From ~7,300 to 6,700 cal yrs BP, the isotopic ratio averages -0.9‰; at these levels, carbonate sublayers are typically dominated by aragonite precipitation, as observed within M1-3 and M2a*. This disparity between mineralogy and water balance may be associated with the poor laminae preservation. Enhanced overturning of lake water, may partially oxygenate the hypolimnion such that sporadic bioturbation disrupts the varves' preservation (Zolitschka *et al.* 2015), and circulates ions such that epilimnetic ionic concentrations

do not exceed the mineralogical threshold which would result in aragonite precipitation (Kelts and Hsü, 1978). This increased lake circulation may also drive long-term $\delta^{18}O$ enrichment of the lake's water, where the $\delta^{18}O_{lakewater}$ influences the $\delta^{18}O_{carbonate}$ precipitated; the amount and timing of seasonal rainfall and the lake's mixing regime can subsequently drive $\delta^{18}O_{lakewater}$ variability (Leng and Marshall, 2004).

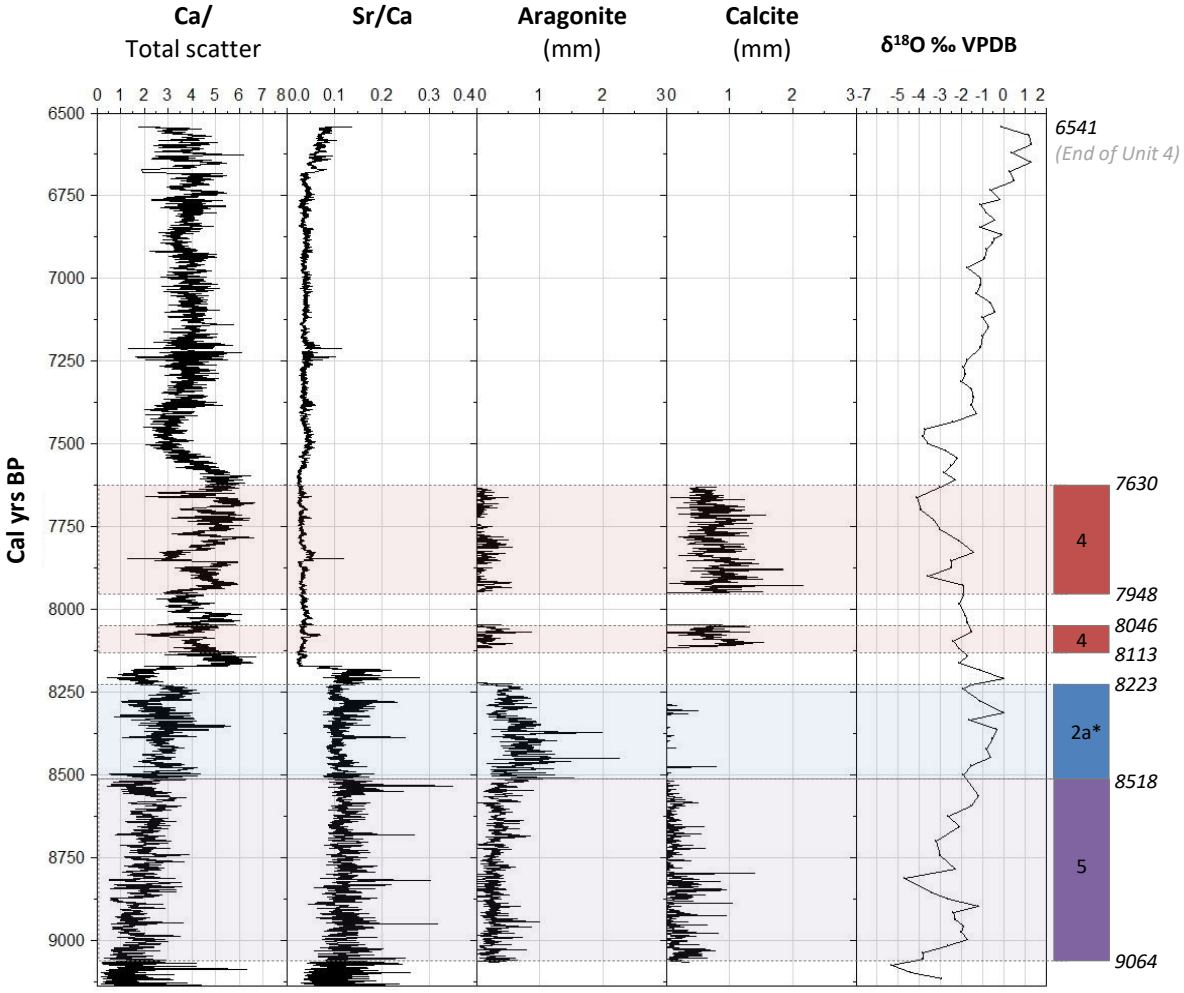


Figure 3.18 *– Changes to sediment microfacies and geochemical composition, relating specifically to calcium carbonate deposition over time, within Units 4-5 and subdivided by microfacies classification (grey lines).*

iii) Organics

Organic sublayers displayed little sedimentological variation, predominately composed of diatoms and organic detritus held within a matrix of amorphic organic material. Only the concentration of background micritic carbonates within these organic sublayers varied notably through the sequence. Therefore, the relative concentration of these carbonates were used to classify organic sublayers, similarly identified within the varves of Unit 1. These organic classifications were grouped to display 'negligible', 'low' and 'high' levels of micritic carbonates, and are plotted alongside µXRF total scatter, commonly used to infer organic content (Davies *et al.* 2015) (Fig. 3.19).

As identified within Unit 1's varves, the concentration of micritic carbonate within organic sublayers typically corresponds with the dominant mineralogy of the carbonate sublayer; higher concentrations are associated with aragonite-rich sublayers, and lower concentrations with calcite-rich sublayers. This trend is observed within M4 and M2a* varves from Units 4-5; however, as mentioned above, M5 varves do not clearly display this pattern. M5's low concentrations of micritic carbonates are associated with an aragonite-rich mineralogy. These opposing E/P signals of carbonate solubility within each year, may highlight the role of climatic seasonality and lake mixing. Intensified dry-season conditions may maintain relatively high ionic concentrations in the epilimnion, required for aragonite precipitation, during the spring/summer whiting event(s), and increased wet-season precipitation may dilute lake water during periods of autochthonous organic deposition.

Total scatter remains steady through Units 4-5, likely reflecting the lack the organic variability generally observed within the varves' stratigraphy. Increased counts at the base of the record (M5 varves) are probably derived from the increased carbonate/organic ratio, primarily driven by decreased carbonate sublayer thicknesses; as such, the stratigraphy during M5 contains proportionally more organic material than the rest of the analysed record. The lowest counts of total scatter coincide with M4 varve deposition, thus corresponding with the thinnest organic sublayers.

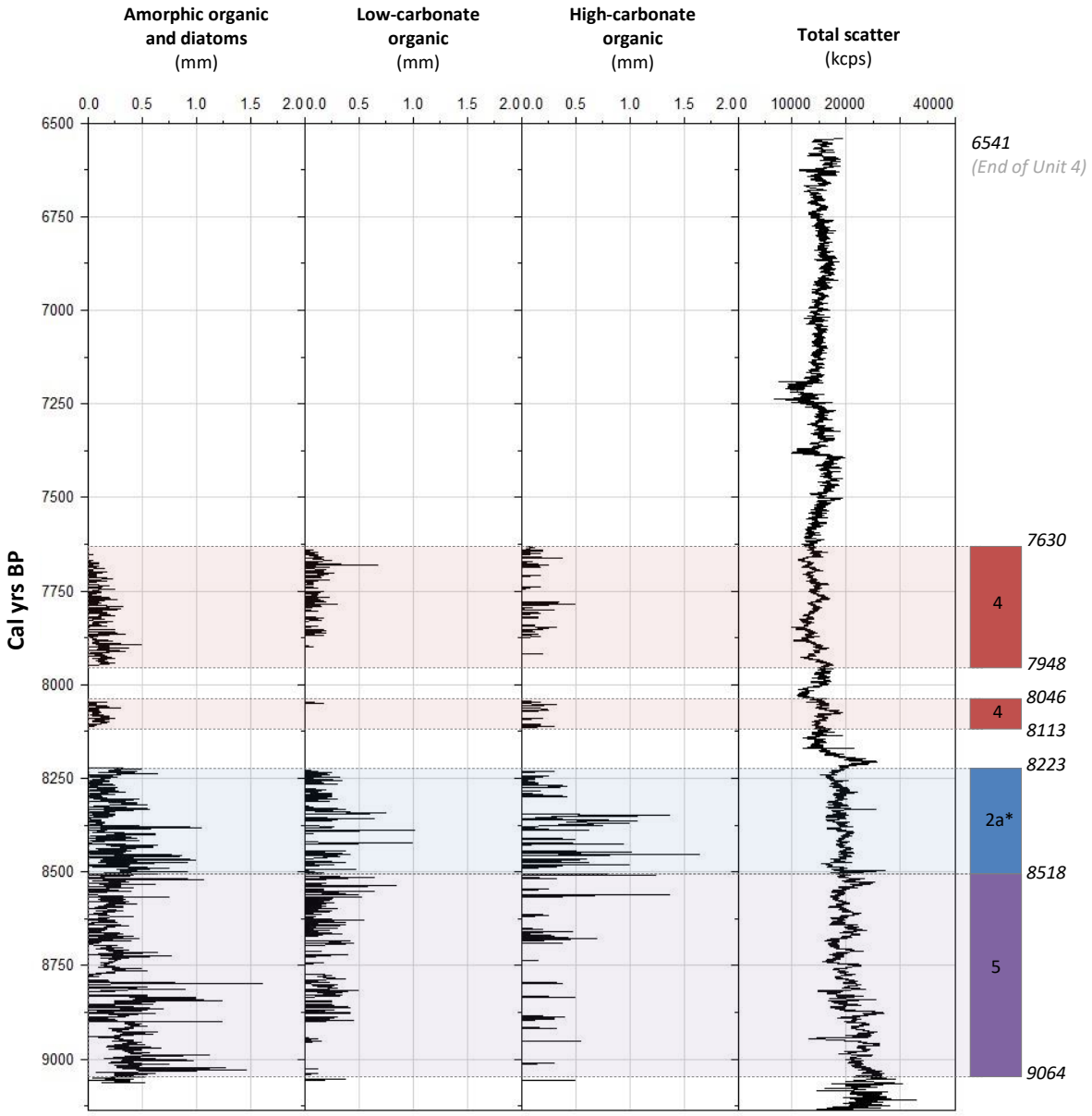


Figure 3.19 *– Changes to sediment microfacies and geochemical composition, relating specifically to organic deposition over time, within Units 4-5 and subdivided by microfacies classification (grey lines).*

iv) Turbidites

Non-seasonal, disturbance sublayers are sporadically identified and measured through Unit 4-5's varves. Their homogeneous composition of clay-rich, clastic matrix containing in-washed obsidian, organic detritus and carbonate material enables turbidites to be easily distinguished within the thin sections from the seasonal varve stratigraphy. Just like those identified within Unit 1, the larger turbidites typically display up-core fining, driven by the increased settling velocities of larger grains (Mangili *et al.* 2005). The presence and thickness of these turbidite sublayers within the varved stratigraphy are displayed in Figure 3.20.

Within the 1,229 varves analysed here, 54 individual turbidites were identified, and display an average thickness of 1.73mm. These turbidites are predominately grouped at the end of M5, and start of M2a* varve deposition, between 8350-8600 cal yrs BP, thus corresponding with Unit 4-5's thickest organic sublayers. Here, the inwash of allogenic material may have increased nutrient supply to the lake, thus enhancing autochthonous productivity and organic sediment accumulation (Lotter and Birks, 1997).

The presence of turbidites generally corresponds with detection peaks of elements associated with catchment erosion and inwash, namely Ti, Fe, and Rb (Davies *et al.* 2015) (Fig. 3.20). A strong, significant correlation of Fe with Ti (r^2=0.78; P<0.001) and Rb (r^2=0.69; P<0.001) supports the interpretation of Fe as a reliable indicator of catchment erosion and inwash, and indicates that the comparatively low count rates of Ti and Rb reflect a true geochemical signal (Davies *et al.* 2015). The period of increased turbidites mentioned above (8,350-8,600 cal yrs BP), displays significantly high detection rates of these allogenic elements. However, one of the most prominent peaks of these elements' detection (1433cm) is located within the non-varved sequence, at the transition between Units 4 (M4 varves) and 5 (M2a* and M5 varves). Here, environmental processes which may initiate turbidite formation can also disturb the sediments' stratigraphy. For example, earthquakes (Inouchi *et al.* 1996) and extreme precipitation events (Mangili *et al.* 2005) can drive slope bed failures and mass wasting events, and further disturb the underlying sediment via liquefaction and bioturbation respectively; where the latter may be initiated via increased lake circulation resulting from the rapid influx of freshwater (Jennings *et al.* 2012).

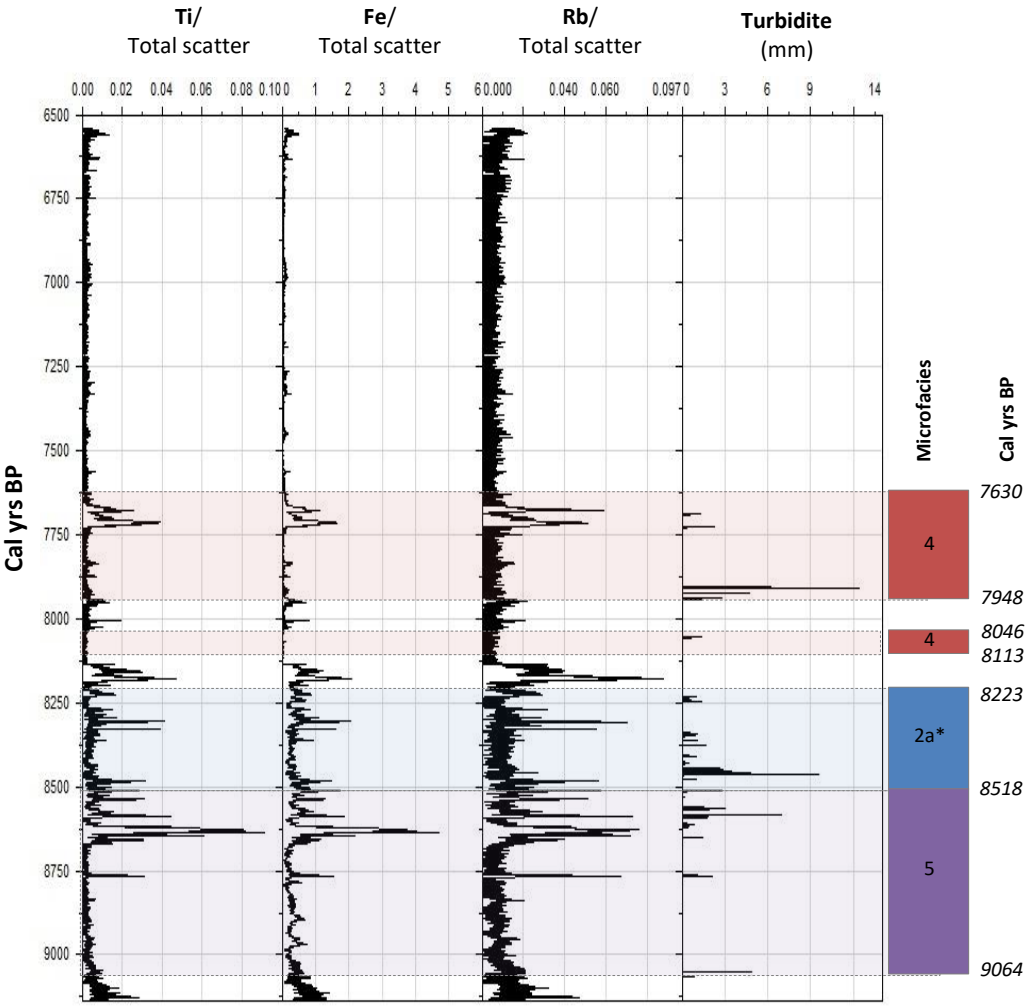


Figure 3.20 *– Changes to sediment microfacies and geochemical composition, relating specifically to turbidite deposition over time, from Units 4-5 and subdivided by microfacies classification (grey lines). Correlation between geochemical and microfacies data are displayed (solid orange lines), and the dotted line highlights the detection peak which coincides with the gap in microstratigraphic data. Slight discrepancies between the alignment of turbidites and the detection of allogenic elements may be expected, as Itrax's incremental depth measurements are converted to age through the use of tie-points with the varve chronology.*

v) Diagenesis

Diagenetic changes to carbonate and organic stratigraphy may have led to the loss of any identifiable relationship between sublayers. While the homogenous composition of euhedral aragonite and calcite crystals indicates primary chemical precipitation (Kelts and Hsü, 1978) with minimal exposure to dissolution (Brauer *et al.* 2008), the geochemical profile of Fe/Mn may reflect changes to hypolimnetic oxygenation, which may enable post-depositional processes to alter the sedimentary signal (Meyers and Ishiwatari, 1993) (Fig. 3.21). This ratio has been used to detect changes to redox conditions, owing to the increased solubility of Mn as compared to Fe in reducing

conditions (Boyle, 2001); as such, increased Fe/Mn ratios have been interpreted to reflect increasing anoxic conditions within the hypolimnion (Haberzettl *et al.* 2007; Davies *et al.* 2015).

Average Fe/Mn detection abruptly decreases from 62.3 kcps in Unit 5 to 2.2 in Unit 4, indicative of a rapid shift to increased oxic conditions in the hypolimnion. Re-oxygenation may be driven by a weakening of annual stratification, which can subsequently lead to bioturbation and sediment disturbance, as identified within Unit 4's discontinuous M4 varves. Through Units 4-5, Fe/Mn negatively correlates with Ca detection (r^2=0.54; P<0.01) and positively correlates with Sr/Ca detection (r^2=0.67; P<0.01) and total scatter (r^2=0.58; P<0.01). Here, increased lake mixing (lower Fe/Mn) may circulate ions such that ionic concentrations in the epilimnion do not exceed the mineralogical threshold, thus resulting in the preferential precipitation of calcite minerals. Enhanced mixing was similarly inferred by the apparent disparity between the calcite-rich mineralogy and long-term $\delta^{18}O_{carbonate}$ enrichment throughout Unit 4 (Section 3.3.1.2ii). Moreover, the increased hypolimnetic DO may promote aerobic decomposition of organic material (Meyers and Ishiwatari, 1993), thus driving the significantly low levels of total scatter and thinnest organic sublayers of the sequence analysed. Conversely, the intensification of lake stratification (higher Fe/Mn) may drive increased ion concentrations in the epilimnion, such that Sr-rich aragonite is preferentially precipitated, and restrict the replenishment of hypolimnetic DO, thus minimising aerobic decomposition of organics. The relatively strong correlation between geochemically-inferred mixing, and organic content and carbonate mineralogy suggests a dominant control the lake's mixing regime on the sedimentology of Units 4-5. Therefore, those environmental factors dictating a lakes mixing regime, primarily lake level and climatic seasonality, are likely to have significantly changed between Units 4 and 5.

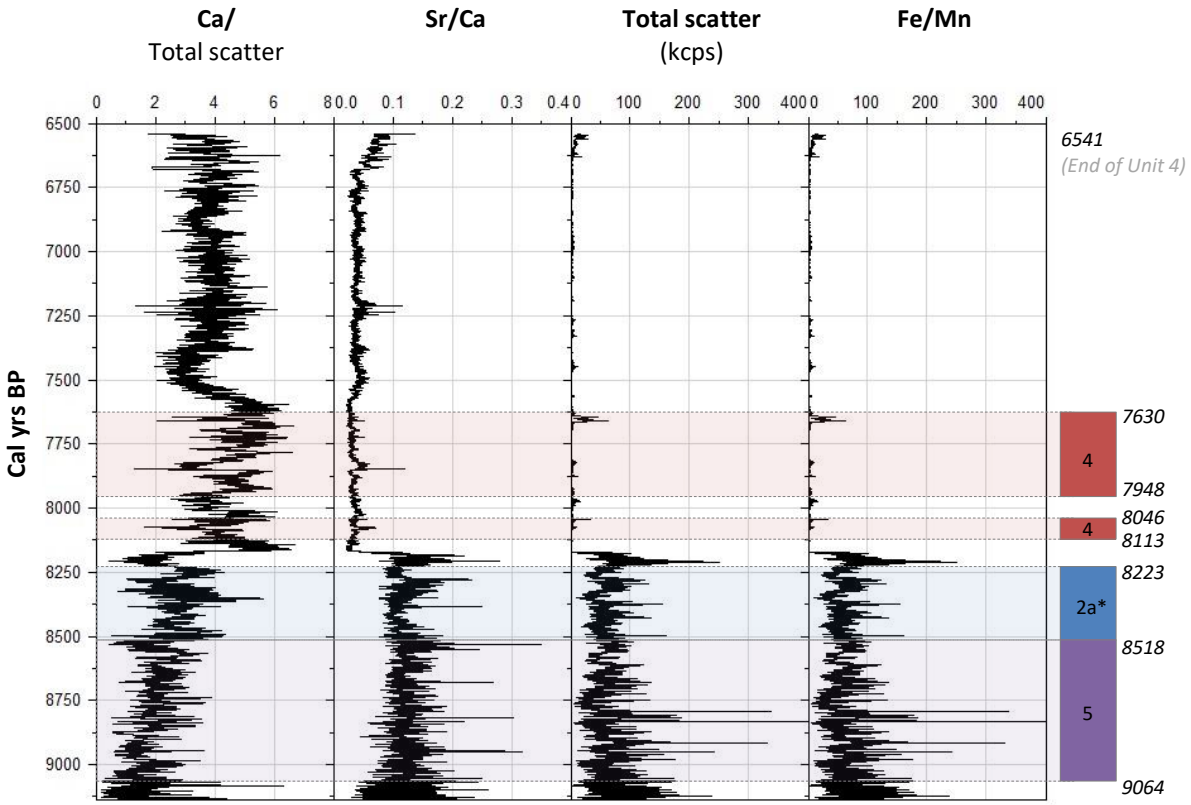


Figure 3.21 *– Changes to sediment microfacies and geochemical composition of Units 4-5, relating specifically to carbonate deposition, organic content and redox conditions in the hypolimnion over time, and subdivided by microfacies classification (grey lines).*

3.3.2 Late Holocene: Unit 1

Data described in this section cover Unit 1's deposition, thus spanning the period from 589 ±26 BC to 2010 ±0 AD (2,539 – -60 cal yrs BP). Geochemical data cover this entire period at a 200µm resolution using the NAR10 cores; whereas, varve microfacies data end in 2001 AD, as the uppermost thin sections were prepared from the NAR01 core. Through thin section microscopy, 2590 contiguous varves have been identified from Unit 1: starting from a transition from non-varved to varved material at 591cm depth and ending at the sediment-water interface from 2001 AD. This corroborates the previous varve chronology (Dean *et al.* 2015a), based on repeated couplet counts using the cores' high resolution imagery, within <1% error. Therefore, ±1% error conservatively accumulates with varve counts from 2001 AD (see Section 1.4.2). Results displayed in this Section will use the chronology developed from thin section microscopy.

3.3.2.1 Varve microfacies

i) Classification

Unit 1's varves were categorized into three main classes (1-3) according to their microfacies composition and structure; two of these classes have further been divided into subclasses (1a-b and 2a-c) (see Table 3.6). Microfacies classifications are only assigned when varves display similar sedimentology for at least 10 consecutive varves. The classes of microfacies described here will be abbreviated to 'M' (e.g. M1a).

These classes represent variations of the 'typical' varve for Nar Gölü described by Woodbridge and Roberts (2010). This initial conceptual model of varve formation, based on steady accumulation of autochthonous organic deposition punctuated by a spring carbonate-precipitation event, is refined here and categorised throughout the record. Variation is specifically derived from changes to distinct sublayer thicknesses, carbonate mineralogy, and composition of the organic sublayers.

As previously discussed, the mineralogy of carbonate sublayers was determined through the use of SEM, EDX, XRD and thin section microscopy (Section 3.3.1.1; Fig 3.14a and b) (also see Dean *et al.* 2015a). In addition to calcite and aragonite, SEM, EDX and XRF confirm the presence of dolomite within the late Holocene sediments, specifically the non-laminated Unit 2 and, at a far lower concentration, the bottom-most 90cm of the varved Unit 1 (Dean *et al.* 2013, 2015a). Here, the dolomite is irregularly-shaped and typically displays many microstructures and pores (Fig. 3.22). This

crystalline morphology suggests that dolomite was not chemically precipitated – crystals of primary endogenic dolomite display a rhombic structure (Sabins, 1962), and its deposition is rare in lacustrine systems. Similarly, the geological composition of Nar Gölü's catchment (basalt and ignimbrite) precludes the possibility of old dolomite being eroded and washed into the lake. Therefore, the dolomite is likely authigenic, formed through the replacement of calcite or aragonite post-deposition; here, anaerobic microbial action typically provides both the alkaline, hypersaline conditions required for its formation, and the nucleus of dolomite growth (Meister *et al.* 2011). Mediated by bacterial activity, dolomite formed in via this process characteristically display high Ca concentrations (Vasconcelos and McKenzie, 1997). The Ca-rich composition of Nar Gölü's dolomite grains, as identified by Dean (2014), supports the inference that minerals are authigenic. In addition, the observed anhedral morphology and presence of microstructures is visually consistent with authigenic dolomite found in other lacustrine systems (Rosen *et al.* 1988; Bontognali *et al.* 2010; Deng *et al.* 2010).

Dolomite

- Microstructure and anhedral crystalline structure indicative of diagenetic source
- High concentration of Mg within material

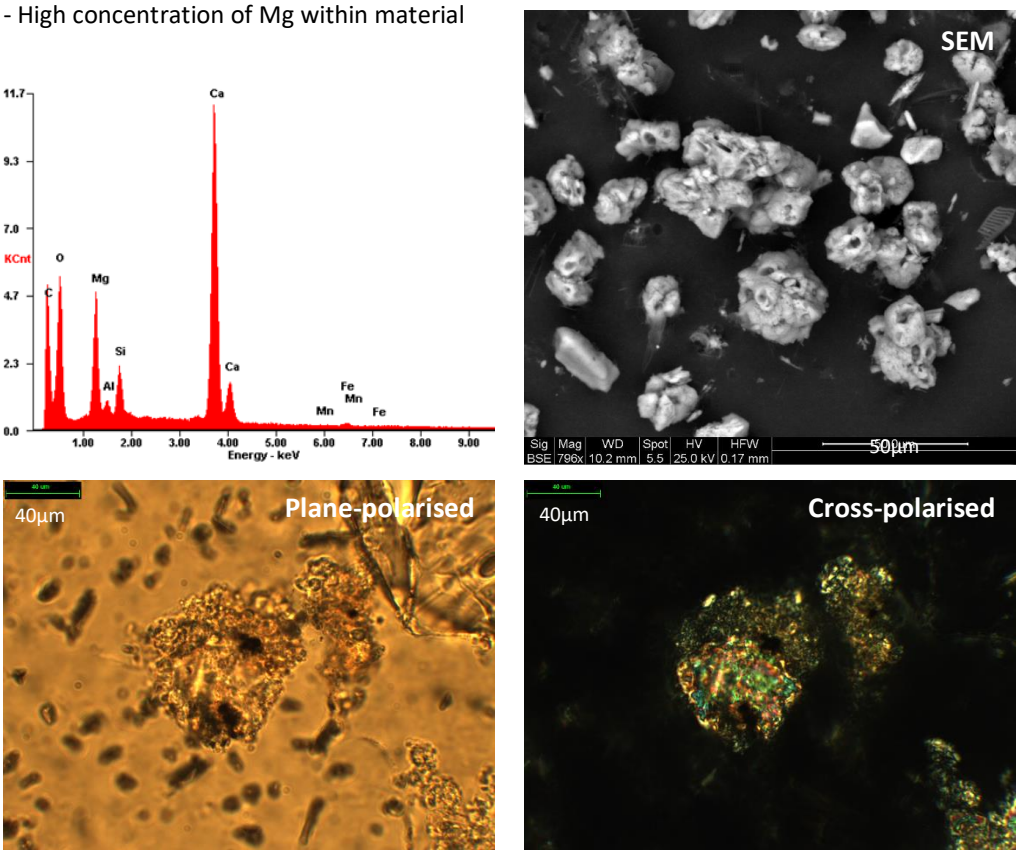


Figure 3.22 *– Identification of dolomite via SEM, EDX and thin section microscopy. For each mineralogy, the elemental composition (top left) of the crystals pictured within the SEM image (top right) (Dean, 2014), and plane- and cross-polarised images taken under 200x magnification using a petrographic microscope.*

Tables 3.6 and 3.7 and Figure 3.23 display these nuanced changes to the archetypal 'carbonate-organic varve' (e.g. Jones *et al.* 2005), and the following describes each classifications' composition and structure:

M1. The deposition of calcite, and absence of aragonite, defines M1. The carbonate sublayer is composed solely of fine-grained (~10-16µm), euhedral calcite crystals (trigonal calcium carbonate – $CaCO_3$), indicative of endogenic precipitation (Kelts and Hsü, 1978), and sharp sublayer boundaries suggest a rapid change to the primary depositional process (Mangili *et al.* 2005). Euhedral crystals do not display dissolution rounding post-mineralisation (e.g. Brauer *et al.* 2008). Calcite sublayers display slight up-core fining of crystals from 14-16µm to 10-15µm. While variation to settling velocity associated with grain size could explain this fining, Brauer *et al.* (2008) suggest that gradation can be driven by intra-annual changes to

carbonate precipitation rates. As supersaturation intensifies through the dry-season, due to increased temperature and evaporitic concentration of ions, crystal nucleation occurs more rapidly leading to the production of smaller, imperfect crystals (Kelts and Hsü, 1978). The organic sublayers of M1 are well mixed, consisting of decayed, amorphic organic matter, diatoms, and micritic and detrital carbonate minerals (<4µm and 5-15µm respectively) (see Woodbridge and Roberts, 2011). The concentration of micritic calcite grains increases moving up through the organic sublayers, but never reaches particularly high concentrations compared to the other microfacies. The succession of sublayers, from well-mixed organic material into carbonate deposition, is well recognised in other lacustrine records (e.g. Kelts and Hsü, 1978; Brauer, 2004; Martín-Puertas *et al.* 2009; Neugebauer *et al.* 2012). This structure supports the inference of Jones *et al.* (2005) that endogenic calcite precipitation is induced by increased biogenic productivity acting to increase in pH via the photosynthetic consumption of CO_2, thus lowering the solubility of $CaCO_3$ (Koschel, 1990; Czymzik *et al.* 2010; Dräger *et al.* 2016); a pattern also observed in M2 and M3.

The subdivision of M1a and M1b reflects variation in the organic sublayers. In M1a, these are typically thicker and contain more background carbonate precipitation throughout compared to M1b. Most M1a varves also contain detrital carbonate within the uppermost organic sublayer; this is likely to originate from the reworking of littoral carbonate material, where lake mixing facilitates its in-lake dispersal (Verschuren, 1999). Thin, discrete layers of dense organic material are also observed in ~38% of M1a varves, yet these are not present in any of M1b varves. The calcite sublayers are largely indistinguishable between microfacies M1a and M1b.

M2. M2 varves structurally resemble those of M1, except the carbonate sublayers are primarily composed of fine-grained (<5µm), euhedral aragonite crystals (orthorhombic calcium carbonate – $CaCO_3$). Again, abrupt sublayer boundaries indicate individual precipitation events, while up-core fining may suggest continued reductions in the water's carbonate solubility through the event; similarly, the crystals' morphology do not display rounding typically associated with dissolution (Brauer *et al.* 2008). Just as in M1 varves, organic sublayers are predominately composed of amorphic organic matter and diatoms, and display increasing concentrations of micritic carbonate precipitates (<4µm); however, concentrations of these background carbonates are typically higher in M2 varves compared to M1. M2 organic sublayers' composition and structure are generally more variable moving

downcore; they often contain larger pieces of detrital carbonate and higher concentrations of in-washed obsidian from the catchment.

M2 has been divided into three subclasses (a-c). M2a represents the simple aragonite-rich varves with carbonate-rich organic sublayers as described above - the other two subclasses display variations to this structure. M2b varves contains an additional calcite sublayer below the aragonite; lying between aragonite- and calcite-only varves, M2b acts as a transitional microfacial-type. The abrupt boundaries of these sublayers and the intra-varve change in carbonate mineralogy suggests two defined precipitation events with different limnological conditions. The switch from calcite to aragonite precipitation indicates increased lake water salinity (Kelts and Hsü, 1978), driven by an increased evaporation/precipitation ratio as the dry season progresses. M2c varves contain a sublayer of detrital dolomite ($CaMg(CO_3)_2$) before the precipitated aragonite laminae; this dolomite-rich layer is highly variable in thickness, and displays abrupt boundaries. The episodic presence of M2c varves may relate to increased catchment instability (Mangili *et al.* 2005) and/or reworking of littoral dolomite; as alluded to above, these detrital carbonate pieces are also present within the organic laminae of M2a varves adjacent to M2c periods, except only in lower concentrations and do not form distinct sublayers. While M2a and M2b have similarly composed organic sublayers, M2c contains much less background carbonate material, typically consisting of amorphic organic matter only.

M3. Dual aragonite sublayers characterise M3. While both the upper and lower sublayers are primarily composed of fine-grained (<5µm), euhedral aragonite crystals, the upper sublayer's aragonite appears within a bright orange matrix when viewed in cross-polarised light. These sublayers are not defined by abrupt boundaries, but instead grade from the grey aragonite into the orange. This colouration may be caused by the possible diagenetic formation of Fe(III) oxyhydroxides, around the aragonite grains (Mingram, 2016, pers. comm.). This process requires oxidising conditions at the sediment-water interface, and an increased concentration of particulate iron deposition (Fortin *et al.* 1993). The sublayers' thickness would be controlled by pore space permitting the down sediment seepage of oxic, iron-rich water (Fortin *et al.* 1993). However, the mineral's formation is reversible, where the subsequent burial of sediment post-deposition, may have caused the reduction of Fe(III) oxyhydroxide within the anoxic conditions. Therefore, the presence of Fe(III) oxyhydroxide within the thin sections may instead be caused by the *in situ* oxidation (and colouration) of the iron-rich laminae during the cores' splitting and preparation in 2010. The organic layer of

M3 is highly variable in both composition and thickness. It characteristically contains high concentrations of background micritic carbonate deposition within a matrix of amorphic organic matter, and diatoms. Pyrite is also observed in high abundance, particularly around organic detritus and diatom frustules, indicative of increased Fe concentrations in the hypolimnion. Around half of the M3 varves contain a thin, dense sublayer of organic material just below the carbonate laminae.

Table 3.6 *– Classification of varve microfacies according to thin section microscopy.*

	Microfacies classification	AD/BC	Number of sublayers	Average varve thickness (mm)	
M1	a. Calcite/ organic mix	1988 – 2001 1195 – 1406 871 – 1119 753 – 848	2/3	1.5	
	b. Calcite/ organic mix (less organic)	535 – 753	2	1.2	
M2	a. Aragonite/ organic mix	1797 – 1988 1406 – 1530 38 – 256 -186 – -56 -460 – -299 -589 – -504	3	1.7	
	b. Aragonite/ organic mix (with calcite)	1530 – 1797 1119 – 1195 848 – 871	4	1.7	
	c. Aragonite and dolomite/ organic mix	-56 – 38 -299 – -186 -504 – -460	3	1.0	
M3	Iron-rich aragonite/ organic mix	256 – 535	3/4	1.1	

Table 3.7 *– A conceptual diagram of the microfacies sub-classes*

Microfacies	Colour	Sub-layer	Average thickness (mm)	Description
1a		**Calcite/organic mix**		
		(i) Calcite	0.88	- Euhedral calcite crystals - Slight fining of grain sizes from ~15µm to 10-15µm through sublayer - Dense and well-defined with abrupt boundaries
		(ii) Low-carbonate clastic mix	0.55	- Mixed layer of amorphic organic matter and carbonate minerals (low concentration) - Also contains low concentrations of diatoms and obsidian
		(iii) Amorphous organic/Diatoms	0.25	*- Amorphic organic matter and diatoms only [present in ~38% of varves]*
1b		**Calcite/organic mix (less organic)**		
		(i) Calcite	0.82	- Euhedral calcite crystals - Slight fining of grain sizes from 18-22µm to 12-15µm through sublayer - Dense and well-defined with abrupt boundaries
		(ii) Low-carbonate clastic mix/ Organic	0.35	*- See 2aii; typically thinner*
2a		**Aragonite/organic mix**		
		(i) Aragonite	0.81	- Euhedral, fine-grained aragonite crystals (<5µm) - Dense and well-defined with abrupt boundaries - Density increases through the sublayer
		(ii) High-carbonate clastic mix	0.66	- Mixed layer of amorphic organic matter and carbonate minerals (high concentration) - Also contains low concentrations of diatoms and obsidian
		(iii) Low-carbonate clastic mix	0.60	- Same as *(ii)* except less carbonate *[present in ~77% of varves]*

2b Aragonite/organic mix (with calcite)

	(i) Aragonite	0.67	*-See 1ai*
	(ii) Calcite	0.52	- Euhedral calcite crystals (12-16µm) - Dense and well-defined with abrupt boundaries
	(iii) High-carbonate clastic mix	0.39	- *See 1aii*
	(iv) Low-carbonate clastic mix	0.37	- *See 1aiii*

2c Detrital aragonite/organic mix

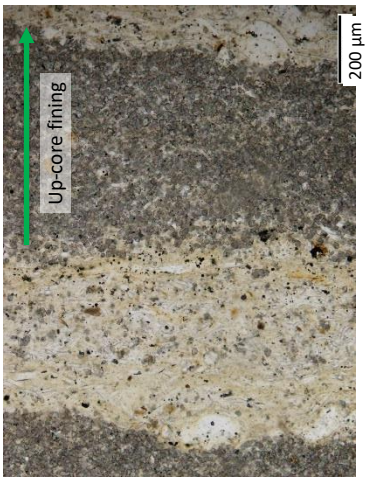
	(i) Aragonite	0.41	- Euhedral, fine-grained aragonite crystals (<5µm) - Dense and well-defined with abrupt boundaries
	(ii) Detrital dolomite	0.45	- Detrital carbonate grains of varying sizes (20-35µm) - Highly variable sublayer thickness
	(iii) Amorphous organic	0.23	- Composition dominated by amorphic organic matter - Very low concentrations of carbonate minerals

3 Orange aragonite/organic mix

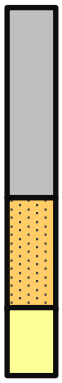
	(i) Aragonite w. diagenetic Fe(III) oxyhydroxides	0.43	- Euhedral, very fine-grained aragonite crystals (<5µm) yet appear orange under Cross-polarised light (<5µm) - Dense and graded into sublayer (ii)
	(ii) Aragonite	0.37	- *Same as (i)* except grey under cross-Polarised light
	(iii) Organic	0.03	*- Very thin, dense, amorphous organic matter [present in ~22% of varves]*
	(iv) High-carbonate clastic mix	0.41	- High variability in composition and thickness - Mixed layer of amorphic organic matter and carbonate minerals (high concentration) - Often contain high concentrations of diatoms and obsidian - Very high concentrations of pyrite, particular around diatom frustules

	Plane polarised	*Cross polarised*	*Composition*

M1a





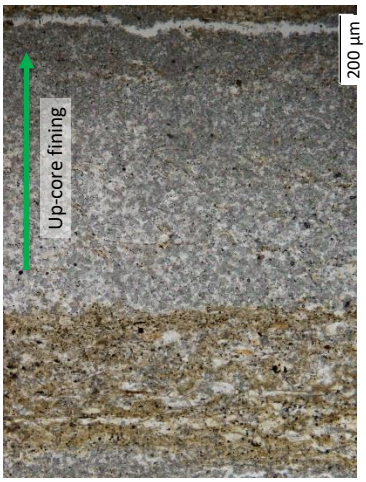


Calcite

Low-carbonate clastic mix

Amorphous organic/diatoms

M1b



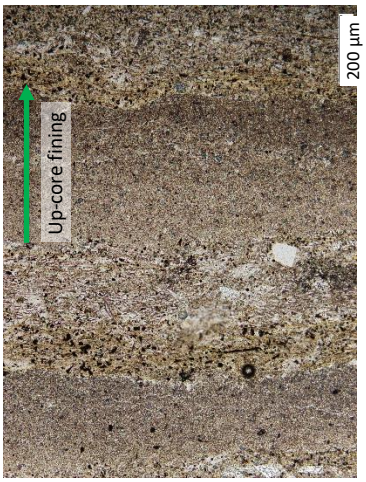




Calcite

Low-carbonate clastic mix

M2a







Aragonite

High-carbonate clastic mix

Low-carbonate clastic mix

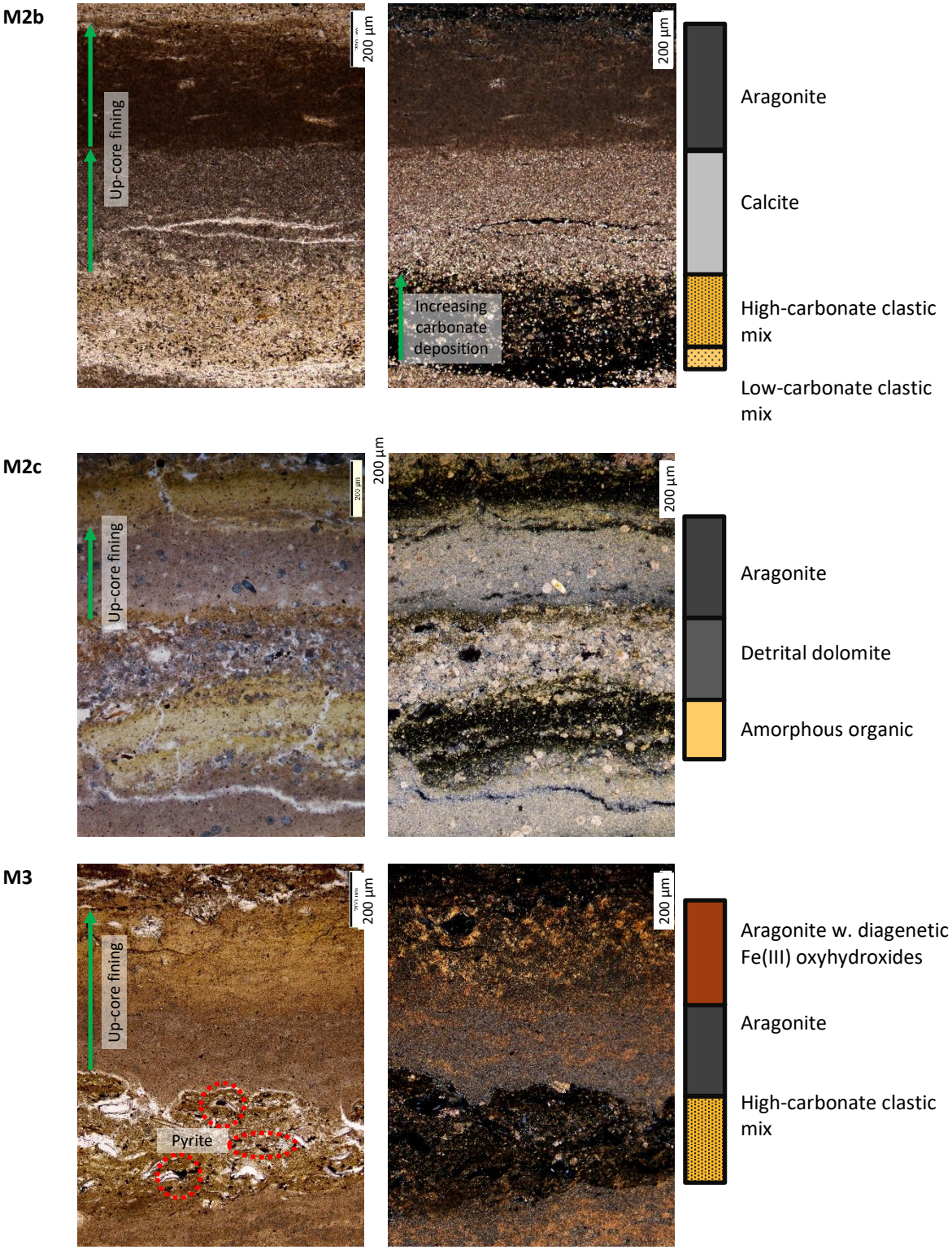


Figure 3.23 *– Magnified (x10) images of typical varves from each of Nar Gölü's microfacies subclasses, as seen in plane-polarised (left) and cross-polarised (right) light. Coloured boxes display the extent of one varve, its distinct sublayers and the approximate boundaries measured; the colour and label of these boxes correspond with the conceptual diagram of microfacies (Table 3.7). All images are positioned such that the carbonate sublayers are deposited after the organic sublayers.*

ii) Thickness measurements

Through thin section microscopy, the thickness of every sublayer, and hence complete varve, was measured to an accuracy of 25μm, thus providing an intra-annual record of deposition over the last 2,590 ±26 years; the key results are displayed in Figure 3.24. Across the entire Unit, the average varve thickness is 1.48 ±0.98 mm. Turbidite layers are omitted from microfacies data unless specified (see Section 3.3.1.1), as they do not reflect the seasonal cycle of sediment deposition directly. Elsewhere, their presence and thickness are associated with extreme weather events, namely extreme precipitation (e.g. Mangili *et al.* 2005; Brocard *et al.* 2014), and earthquake frequency and magnitude (Brocard *et al.* 2014). Therefore, turbidite layers will not be included in microfacies measurements, but instead will be analysed in tandem with the other proxies.

While the total varve thickness appears to increase throughout the record (see Fig. 3.24), interpretations must be made with caution as measurements are not corrected for downcore compaction of sediment. Laminae thickness measurements can be adjusted to negate this influence, but requires data pertaining to downcore porosity (Hughen *et al.* 2000) or bulk density (Maier *et al.* 2013); these datasets are unavailable for the NAR10 core. Nevertheless, Athy's law states that sediment porosity decays exponentially downcore due to compaction (Athy, 1930), and so changes to laminae thicknesses can be interpreted by focusing on trends which would not conform to an exponential curve (Brauer 2017, pers. comm.).

Carbonate precipitation accounts for the majority of sediment accumulation (~60%), most notably around 589 ±26 BC to 753 ±12 AD; here, the average carbonate:organic ratio is significantly greater (63% compared to 57%; $P<0.99$ sig. level) than the succeeding varves (753 ±12 – 2010 ±0 AD). This indicates a notable change to relative seasonality. A reduction to the standard deviation of this ratio over these two periods similarly suggests a switch to increased environmental stability. This greater sedimentological variance in the early record, and the episodes of M2c deposition, which contain detrital dolomite sublayers, support the inference of environmental instability.

While biogenic productivity could act to control the start of the carbonate sublayers' deposition, and hence induce an earlier/later initiation of carbonate deposition, regression analysis does not display a strong relationship between carbonate and organic thicknesses. As the spring/summer carbonate precipitation events are initiated by a biogenic-derived increase to pH (Jones *et al.* 2006), a thicker organic sublayer could indicate increased biological productivity, which could consequentially lead to a longer period of carbonate supersaturation and precipitation. A link between organic and

carbonate thicknesses may act to diminish interpretations of seasonality, as each season's deposition are not independent. However, the lack of correlation suggests that the organic thickness is not a primary control on carbonate thickness. This relationship assumes that organic sublayer thickness represents wet-season productivity consistently through time, and fails to account for diagenetic decay of organic matter. While anoxic conditions inhibit diagenetic decay for much of the year, any changes to the mixing regime could act to increase the role of oxic decomposition (Meyers and Ishiwatari, 1993). Similarly, changes to lake's depth and geochemical profile can change organic decomposition rates as material falls through the water column, thus reducing the strength of organic sublayer thickness as a productivity signal.

The sublayer thickness data were compared to the oxygen isotope ratio ($\delta^{18}O$) record taken from 1,184 carbonate sublayers within the last 2,600 years, where $\delta^{18}O_{carbonate}$ has been shown to reflect Nar Gölü's regional water balance (Jones *et al.* 2005; Dean *et al.* 2015a) (Fig. 7.25). As a result, the lake's hydrology appears to determine both the carbonate sublayers' thickness and mineralogy. Each varve's carbonate sublayer, formed via primary chemical precipitation, is composed of homogenous calcite and/or aragonite, where the ratio of Mg:Ca in the lake determines the specific mineralogy; aragonite precipitates when the ratio is greater than two (Müller *et al.* 1972), and high E/P conditions can act to concentrate these elements past this mineralogical threshold (Kelts and Hsü, 1978). Findings suggest that increasingly depleted $\delta^{18}O$ (and E/P) ratios seem to result in increasingly thicker calcite sublayers, while more enriched $\delta^{18}O$ values (0 to –1‰) are associated with the deposition of the thickest aragonite sublayers.

Mineralogical-dependent fractionation may partially account for this discrepancy between aragonite and calcite isotopic values. However, with a full range of –5.7 to +2.8‰ through the last 2600 years, the $\delta^{18}O_{Carbonate}$ variability exceeds the effect of mineralogical fractionation (Dean *et al.* 2015a), where aragonite minerals typically display ~+0.7‰ higher values as compared to calcite (Grossman and Ku, 1986). Moreover, the concentration of Mg within calcite similarly drives isotopic fractionation, where Tarutani *et al.* (1969) estimate +0.06‰ $\delta^{18}O$ per mole-percent of $MgCO_3$ in calcite precipitated under the same conditions. With an average Ca:Mg ratio of 18.2 mol%, Nar Gölü's endogenic calcite is high-magnesium (Dean, 2014), thus reducing the difference between calcite and aragonite isotopic values derived from fractionation. Therefore, isotopic values are not corrected for mineralogical fractionation. The specific carbonate mineralogy can be used to indicate relative water balance, and their respective thicknesses form a continuous, annual record of regional, March-May E/P conditions.

The deposition of Nar Gölü's most recent varved unit starts at 589 ±26 BC, following a period of non-laminated, dolomite-rich sediment (Roberts *et al.* 2016). This non-laminated section's carbonate mineralogy and enriched $\delta^{18}O$ are indicative of relatively high E/P conditions and the lowest lake levels over the past 3,200 years (Dean *et al.* 2015a; Roberts *et al.* 2016). The onset of varve deposition requires a water column deep enough for stratification, typically over 10m (Ojala *et al.* 2000); therefore, a rise in lake level is inferred at the abrupt switch from non-varved to varved deposition. Initially, aragonite precipitation (M2a varves) may reflect high ion concentrations associated with a relatively shallow, infilling lake, yet the subsequent 1,124 ±12-year long record of enriched $\delta^{18}O$ aragonite suggests a sustained period of elevated E/P ratios during the spring; possibly due to a longer, more severe dry season.

Between 589 ±26 BC and 256 ±17 AD, three short incursions of M2c varves signify additional dolomite deposition within the varve microfacies. This dolomite was likely mineralised prior to 589 ±26 BC and reworked during decadal-centennial periods of decreased lake level. Nar Gölü's bathymetry displays a relatively large shelf around 8-10m above the coring location, associated with the alluvial fan's formation along the lake's southern edge (Fig. 3.1). Authigenic dolomite precipitation may have occurred on this shelf during Unit 2's lower lake levels (<10m). While likely remaining over 10m depth, subsequent reductions to the lake's level are also inferred during M2c varve deposition, where increased aragonite sublayer thicknesses are indicative of elevated E/P conditions (Kelts and Hsü, 1978). Relatively shallower lake levels during Unit 1's deposition may increase the dolomite's susceptibility to resuspension and transportation deeper into the lake, via wind turbulence and/or water flow across the alluvial fan from the southern edge's springs.

Aragonite deposition culminates in the formation of the transitional M3 varves (256 ±17 – 535 ±15 AD). Located prior to the rapid mineralogical switch from aragonite to calcite varves, the proposed Fe(III) oxyhydroxide matrix observed around the fine-grained aragonite suggests distinct limnological conditions, requiring an iron-rich, oxic hypolimnion. Iron enrichment can be driven by two processes: increased influx of terrigenous sediment deposition or up-core diffusion of soluble Fe(II) (Fortin *et al.* 1993). Increased turbidite frequency and detection of Ti and Rb (see Section 3.3.1.1) indicates iron enrichment was driven by changes in catchment supply. Additionally, an early or rapid onset of lake mixing may oxygenate the bottom water sufficiently for this diagenetic process to occur. Over the M3 period, the relative thickness of this Fe-coated aragonite increases, alongside increases in $\delta^{18}O$ values, perhaps reflecting further evaporative-derived concentration of Fe in the lake water. Overall, M3 deposition represents a transitional period reflecting shifting seasonality, evaporitic and precipitation regimes prior to a threshold change in the annual limnology.

Over the course of twelve years prior to 535 ±15 AD, the carbonate mineralogy switches abruptly from aragonite-only (M2) to calcite-only (M1) varve deposition. This short transitional phase suggests a rapid shift in lake water chemistry. The abrupt mineralogical change coincides with a major $\delta^{18}O$ reductions (Fig. 3.24) (Jones *et al.* 2005, Dean *et al.* 2015a); a decreased E/P ratio could dilute the lake water sufficiently for calcite to preferentially precipitate over aragonite, and vice versa.

Calcite mineralogy largely dominates during 535 ±15 – 1406 ±6 AD, deviating into the transitional aragonite-calcite M2b varves during two short episodes, 848 – 871 (±12) AD and 1119-1195 (±9) AD, which correspond to positive excursions in the oxygen isotope record. At 1406 AD, varves switch abruptly back to the aragonite-rich M2 varves (1406 ±6 – 1988 ±0 AD), coinciding with rapid oxygen isotope enrichment. However, this isotope ratio increase does not reach the high levels displayed by the M2 varves pre-256 AD, and the transitional aragonite-calcite M2b varves reappear during 1530 ±5 – 1797 ±2 AD alongside slight isotopic depletion. Just as specific oxygen isotope ratios appears to optimise precipitation rates of different carbonate minerals, ratios between –0.5 to –2.5 $\delta^{18}O$ ‰ facilitate both calcite and aragonite precipitation (Fig. 3.25).

By 1797 ±2 AD, calcite deposition ceased altogether, leaving aragonite-rich M2a varves (Fig. 3.24). A marked increase to aragonite thickness is observed, and while the lack of compaction is likely to drive much of this change, the step-shaped trend suggests aragonite's annual precipitation increases; again peak aragonite deposition occurs alongside isotopic enrichment. Organic thicknesses do not display this step increase, and so its increasing sublayer thicknesses are more likely to be derived from reduced sediment compaction at the top of the core. At 1988 ±0 AD, the microfacies switch rapidly from aragonite-only to calcite-only varves; these represent the uppermost 12 varves prepared in thin section, ending in 2001 ±0 AD. Subsequent sediment trap monitoring revealed that calcite precipitated until 2010 AD, and then aragonite precipitated 2010-2012 AD.

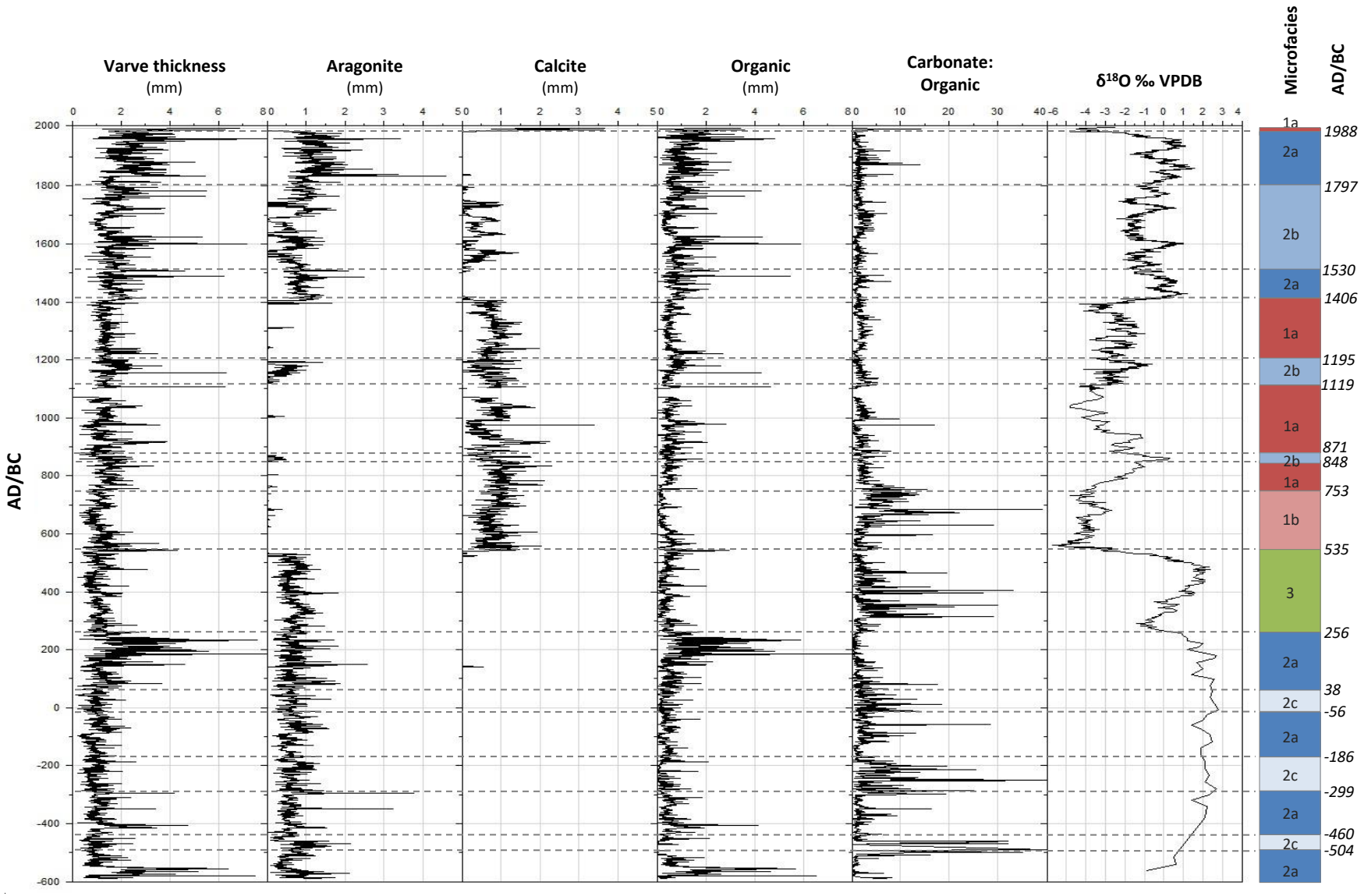
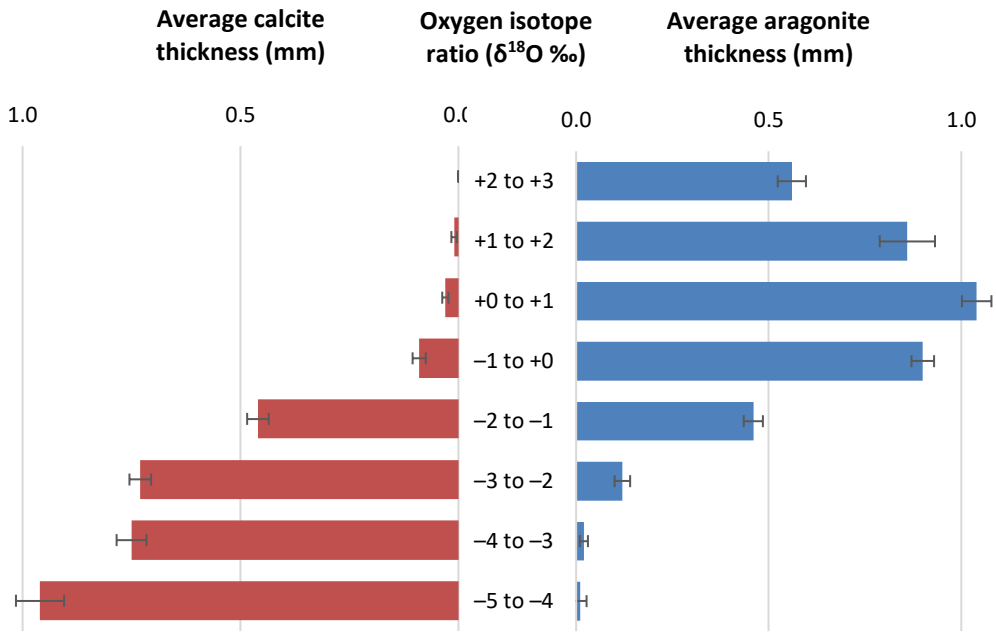


Figure 3.24 *– Thickness measurements of the varves' key sedimentological variables from Unit 1, subdivided by microfacies classification (grey line). Oxygen isotope data from carbonate material is also shown ($\delta^{18}O$ ‰ VPDB) (from Dean et al. 2015a)*

Figure 3.25 *– Average thickness (mm) of calcite (left) and aragonite (right) sublayers according to their oxygen isotope composition. Isotopic values displayed are not corrected for mineral-dependent fractionation (+0.7‰ to the aragonite $\delta^{18}O$, as compared to calcite); applying a correction would effective move aragonite's thickness distribution down one row, thus still maintaining a distinct difference between isotopic-inferred water balance and carbonate sedimentology. Oxygen isotope data are analysed from the carbonate material (data from Jones et al. 2005; Dean et al. 2015a)*



iii) Sedimentological calibration

By temporally tying each years' monthly, seasonal and annual meteorological data to each varves' sedimentological data, the climatic forces driving depositional changes can be identified using correlation matrix analysis (Leemann and Niessen, 1994). The two annually-resolved datasets overlap from 1935 to 2000 AD, thus providing a 65-year long period suitable for this sedimentological calibration.

First, the carbonate sublayers were calibrated. Aragonite-only (M2a) varves are deposited for the majority of the period (1935-1988), while calcite-only (M1a) varves are deposited over the last 12 years of the dataset (1989-2000). As previously discussed, aragonite and calcite precipitate in differing limnological conditions, and their differing crystalline morphology hinders the ability to directly compare sublayer thicknesses across mineralogies. Therefore, carbonate calibration focused on the longer M2a-dominant period, excluding data from the M1a varves.

Correlation analysis revealed a significant positive relationship between the March-May E/P ratio and thickness of aragonite sublayers (r=0.46; P<0.01) (Fig. 3.26), and represents the strongest relationship between the two datasets. These months contribute 35% of the annual precipitation and precede the shift to summer's dry season conditions, thus establishing the limnological conditions prior to carbonate precipitation. Rainfall throughout the year negatively correlates with carbonate thickness, yet the dominate control of spring E/P ratio on carbonate precipitation is likely to reflect the combined influence of wet season conditions and the timing of dry season onset. While this chemical response to seasonal forcing is often proposed at other sites (Livingstone and Hajdas, 2001; Brauer *et al.* 2008; Romero-Viana *et al.* 2008), this long instrumental record provides statistical validation of the conceptual model.

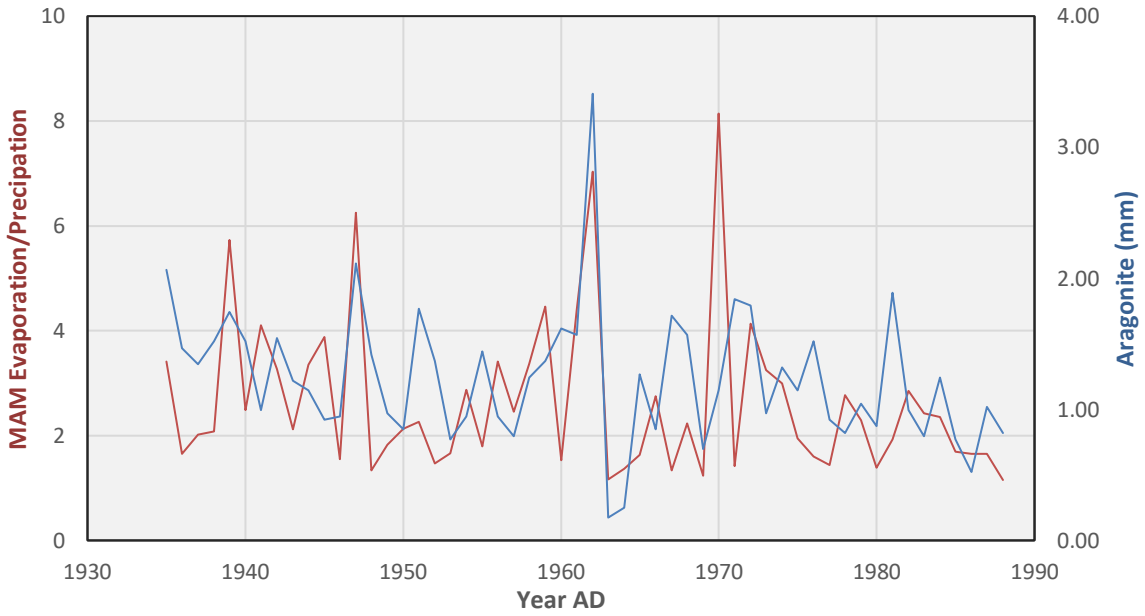


Figure 3.26 *– March-May evaporation/precipitation ratio (red line) alongside aragonite thickness (blue line) between 1935-1988.*

While this calibration displays a linear relationship between aragonite thickness and MAM E/P conditions, aragonite deposition does not linearly co-vary with isotopic composition (Fig. 3.25). The most $\delta^{18}O$ enriched carbonate sublayers (>+1.0‰), interpreted to reflect the dry-seasons' most evaporative limnological conditions (Dean *et al.* 2015b), are associated with reduced aragonite sublayer thicknesses. As such, intermediary aragonite thicknesses may reflect differing lakewater conditions. However, the $\delta^{18}O$ isotopic values range from –4.8‰ to +1.1‰ during the calibration's 65-year long timeseries; only two years (1937 and 1940 AD) display isotope values greater than +1.0‰. Within this $\delta^{18}O$ range, aragonite thickness consistently increases with $\delta^{18}O$ enrichment.

Therefore, aragonite deposition is proposed to primarily respond to MAM E/P conditions, via its effect on lake water balance and carbonate supersaturation.

While the 12-year long calcite record was also analysed for correlation, the small sample size prevented the detection of any results with a significance of $p<0.05$. Nevertheless, a similar relationship between calcite thickness and seasonal meteorology is suggested, particularly favouring higher potential evaporation values through the year. Results also indicate a positive correlation between December-February precipitation and calcite thickness ($r=0.56$; $p=0.06$) (Fig. 3.27). This may indicate that lake dilution prior to the spring-summers' carbonate supersaturation is conducive to calcite precipitation. Fresher water is known to preferentially precipitate calcite over aragonite (Kelts and Hsü, 1978), and so this inferred relationship is plausible. Therefore, it is tentatively suggested that calcite thickness is also driven, in part, by winter precipitation.

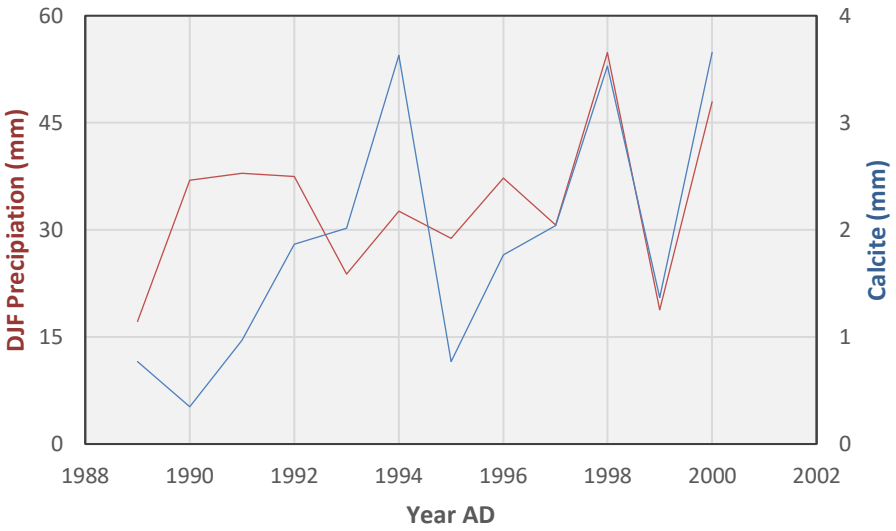


Figure 3.27 *– December-February precipitation (red line) alongside calcite thickness (blue line) between 1988-2000.*

Using the full 1935-2000 timeseries, the organic sublayers were calibrated. While the resultant correlations were generally less strong, a significant negative correlation between total organic thickness and annual rainfall can be identified ($r=0.27$; $p<0.05$) (Fig. 3.28). This appears to conflict with the conceptual model of varve accumulation, where precipitation is hypothesised to promote organic sublayer accumulation via the inwash of catchment material, which can provide nutrients for autochthonous productivity and deposit terrestrial grains (Kelts and Hsü, 1978). However, the strength of correlation increases when examining those organic sublayers containing *high* concentrations of background carbonate material ($r=0.31$; $p=0.01$), and this classification accounts

for 51% of the total organic sublayers thickness over this time period. Similarly, those organic sublayers with *high* concentrations of carbonates also positively correlate with March-May E/P ratio ($r=0.28$; $p<0.05$) and July-August evaporation ($r=0.28$; $p<0.05$) indicating that their accumulation rate is partially driven by carbonate precipitation preceding/following the defined carbonate precipitation events. As previously discussed, these fine carbonate grains deposited within the organic sublayers may relate to the micro-scale supersaturation of carbonates around the immediate vicinity of a photosynthetically-active organism (Kelts and Hsü, 1978). As the epilimnion nears carbonate supersaturation, isolated precipitation of fine-grained carbonate can enhance organic sublayer thickness. Microstratigraphic analysis supports this interpretation as organic sublayers with *high* concentrations of carbonates are typically deposited immediately before the well-defined carbonate sublayer.

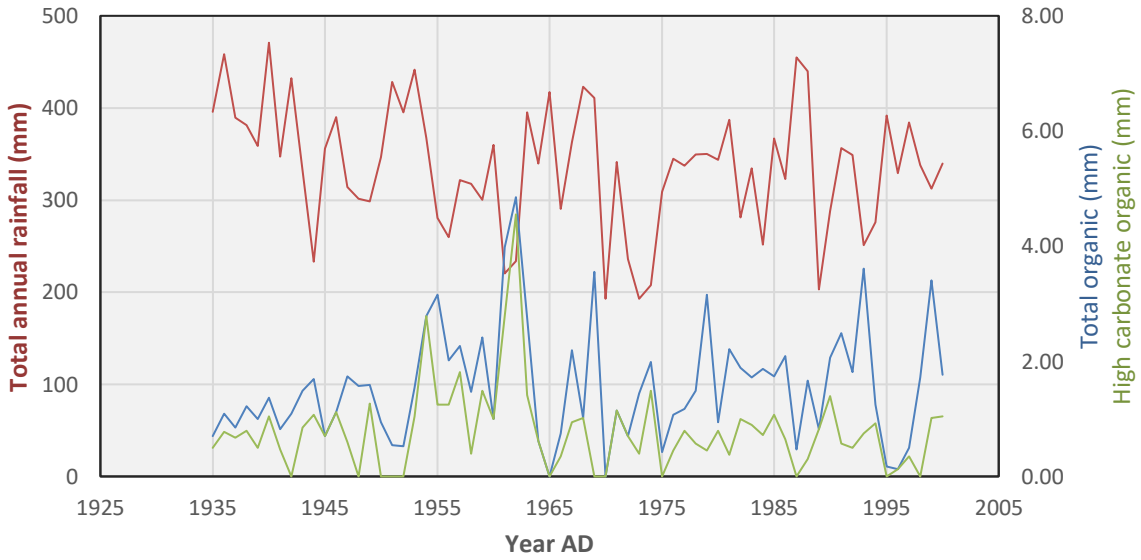


Figure 3.28 *– Total annual precipitation (red line) alongside total organic thickness (blue line) and organic sublayers with high concentrations of carbonate minerals (green line) between 1935-2000.*

The influence of varve chronological error and lake residence time was subsequently examined. First, smoothing was thought to minimise the influence of error within the varve's chronology, acting to decouple the two datasets; however, Table 3.8 displays how the strongest correlation inferred, that between March-May E/P ratio and aragonite thickness, decreases with increased smoothing. This trend suggests there is minimal chronological error, and any effect it has on the correlation is overcome by the climatic signal's strength.

Table 3.8 *– Effect of sedimentological smoothing on the correlation between MAM E/P ratio and aragonite thickness; red intensity denotes stronger correlations.*

Years smoothed	Correlation coefficient	P value
1	0.46	<0.01
3	0.34	0.01
5	0.28	0.05
7	0.33	0.02
9	0.32	0.03
11	0.16	0.29
13	0.17	0.28
15	-0.02	0.88

Second, meteorological data were smoothed to imitate the natural smoothing of limnological conditions derived from the lake's 8-11 year residence time (Dean *et al.* 2015b). Table 3.9 reveals that the same correlation is strongest when the meteorological forcing is either unsmoothed or smoothed using the previous year's conditions (i.e. 1-2 years). Therefore, the influence of antecedent conditions on varve sedimentology appears to be predominantly limited to one year only, thus maintaining a high temporal resolution for annual and sub-annual reconstructions. Each varve's microstratigraphy is a product of the season's environmental conditions, and the sequence's robust chronology permits each varve to be precisely dated. This verifies that varve sedimentology responses to seasonal forcing, and is therefore capable of providing a sub-annual insight into palaeoclimatic change.

Table 3.9 *– Effect of meteorological smoothing on the correlation between MAM E/P ratio and aragonite thickness; red intensity denotes stronger correlations.*

Years smoothed	Correlation coefficient	P value
1	0.46	<0.01
2	0.46	<0.01
3	0.33	0.02
5	0.28	0.03
7	0.32	0.03
9	0.23	0.12
11	0.24	0.11
13	0.31	0.05
15	0.26	0.10

3.3.2.2 Sediment geochemistry

High resolution geochemical data were obtained through Itrax µXRF core scanning along the entirety of the NAR10 sediment sequence (Fig. 3.29). A 200µm scanning resolution meant that interannual geochemical composition was gained, as each varve contained multiple data points through its profile (average varve thickness = 1.48mm). Using the molybdenum (Mo) X-ray tube anode (see Section 2.3.3), elements from aluminium (Al) to thorium (Th) were detected.

Scanning results through Unit 1 show that calcium (Ca), strontium (Sr) and iron (Fe) detection dominate the sediment's geochemical composition. Generally, Ca and Sr co-vary and negatively correlate with Fe; a trend also observed in the full NAR10 record (Allcock, 2013). Rubidium (Rb), potassium (K), manganese (Mn) and titanium (Ti) represent the next most abundant elements, and all together these eight elemental profiles will form the focus of geochemical analysis. Analysis of stratigraphic profiles of elements detected in lower concentrations must be treated with caution, as patterns may not reflect a true geochemical signal (Croudace *et al.* 2006).

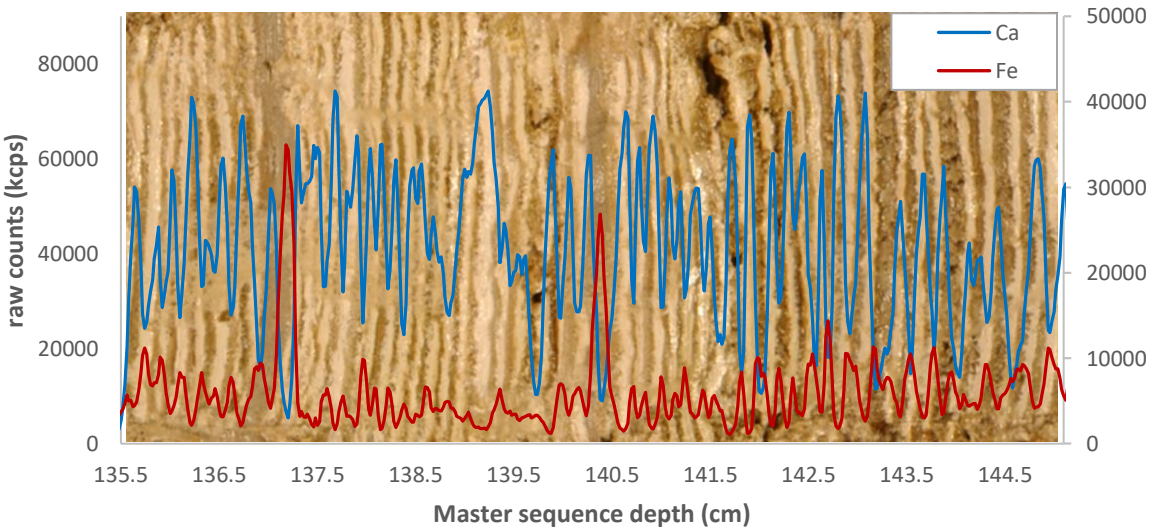


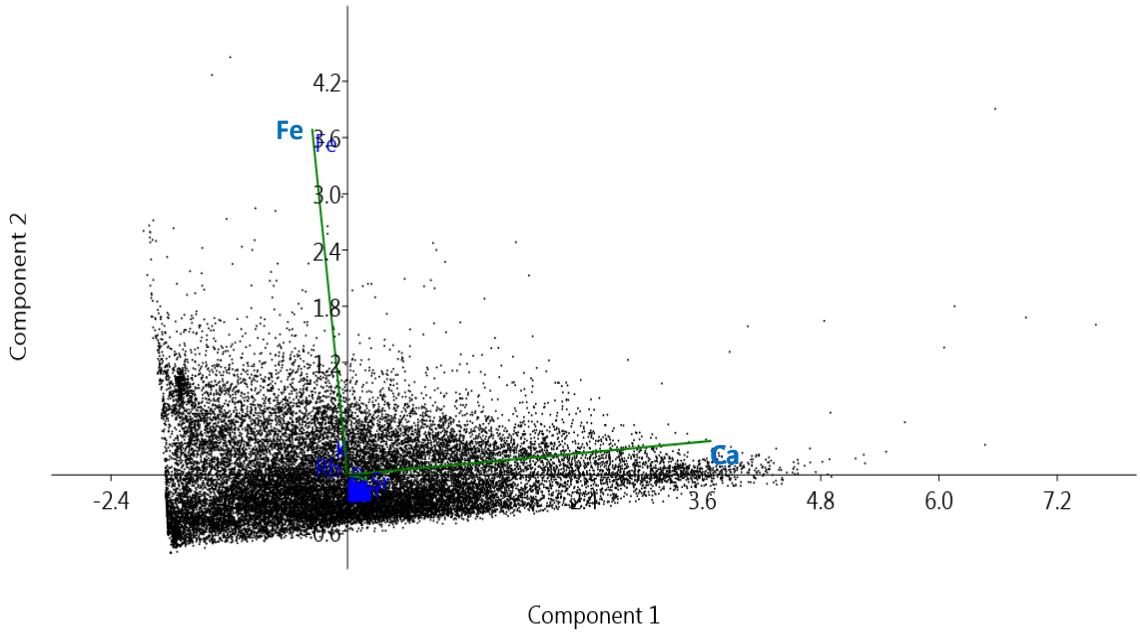
Figure 3.29 *– Example section of the Itrax µXRF core scan; variation to Ca (blue line) and Fe (red line) detection through the sediment is displayed.*

A robust age-depth model was formed by pairing specific varves to their cumulative sediment depth (Section 3.2.2). Therefore, each 200µm-step of the µXRF scan could be converted to a regular time-step consistent with the average accumulation rate between fixed varve count-depth pairs. The following sections plot microfacies and geochemical data alongside each other against the varve-based chronology.

i) Principle Component Analysis

By identifying collinearity within the geochemical, multi-variable dataset, principle component analysis (PCA) acts to reduce the number of dimensions within a dataset and summarise the majority of its variation. The formation of explanatory dimensions, or 'components', helps to identify underlying patterns within multispectral data, and specific processes can be subsequently assigned to each component (e.g. Shanahan *et al.* 2008). Here, PCA of normalised µXRF data (using total scatter; see Section 5.3.3) from Unit 1 was analysed using statistical software *Past 3.14* (Hammer *et al.* 2001).

PCA of Unit 1's geochemical data displays the inverse relationship between the elements associated with endogenic carbonate precipitation (Ca and Sr), and those associated with allogenic, catchment erosion (Fe, Ti, Rb) and autochthonous organic detritus (total scatter, Br) (Davies *et al.* 2015) (Fig. 3.30) – also found within the entire NAR10 sequence (Allcock, 2013). PCA indicates that 88.3% of the elemental variance is derived from the primary eigenvector, which positively correlates with Ca (r^2=0.99; P<0.001) thus demonstrating the dominant role of calcium carbonate precipitation in the sedimentary record (Fig. 3.31). The secondary eigenvector represents 11.0% of geochemical variance, and significantly correlates with Fe (r^2=0.93; P<0.001) (Fig. 3.31), an element which has been linked to sediment influx within the full NAR10 record (Allcock, 2013). These two PCA axes, and thus Ca and Fe profiles, represent two independent depositional processes acting on geochemical composition through the varved sequence; changes in their detection likely represent seasonal changes within the wet and dry-season sublayers.



Fig***ure 3.30*** *- Principle components analysis' primary and secondary axes from Unit 1, and its identification of Ca and Fe as key elements explaining geochemical variance.*

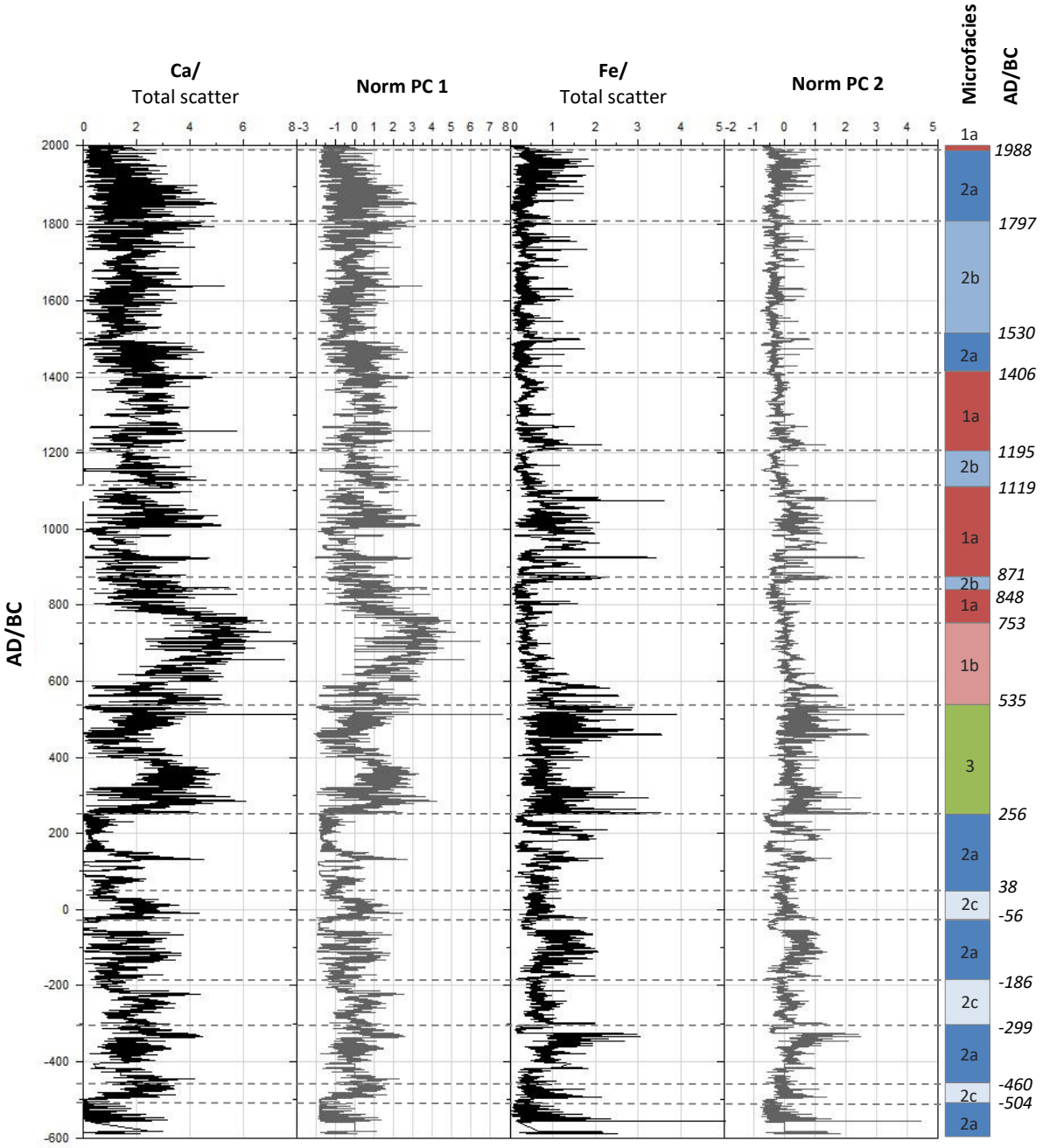


Figure 3.31 *– Comparison between the changes to key elements identified in the PCA (black lines) and the first two significant axes (grey lines) within Unit 1; subdivided by microfacies classification (dotted lines).*

ii) Carbonates

Identified in every varve, endogenic calcium carbonate ($CaCO_3$) drives much of the sediment accumulation. As previously discussed, its precipitation is governed by intra-annual limnological change, predominately driven by biologically-induced pH variability, and water balance (Jones *et al.* 2005; Woodbridge *et al.* 2010). Profiles of Ca and Sr reflect the detection of calcium carbonate minerals (Allcock, 2013), which have been identified throughout the varve microfacies, including the wet seasons' organic sublayers. While Sr is typically incorporated into the crystal lattice of endogenic calcium carbonate, its incorporation is proportionally higher within aragonite compared to calcite (Martín-Puertas *et al.* 2011); as a result, the Ca/Sr ratio has been used to infer mineralogical change of carbonates from Nar Gölü (Allcock, 2013) and other aquatic systems (e.g. Bayon *et al.* 2007; Martín-Puertas *et al.* 2011), with its interpretation relating ion concentration in the epilimnion, and subsequently water balance.

Sedimentological variables pertaining to the deposition of carbonate material within Unit 1 are plotted in FFigure 3.32. Broadly, changes in carbonate-related geochemical composition correspond with microfacies boundaries. Most notably, a step increase to the Ca/Sr ratio coincides with M1b deposition, a classification characterised by intense calcite deposition. Similarly, periods of calcite-dominated M1a varves also display an elevated average Ca/Sr ratio. These coeval geochemical and mineralogical changes are consistent with isotopic depletion (Dean *et al.* 2013) and hence freshening of lake water during the springs' carbonate precipitation events.

Periods of M2c deposition also display small increases in Ca detection, possibly reflecting the increased presence of dolomite, and the start of M3 is marked by a large increase in Ca. However, sublayer thickness measurements do not significantly correlate with elemental counts of Ca or Sr. Disparity between microfacies and geochemical records may reflect different depositional signals. Carbonate sublayer thickness is a function of a season's mass of precipitated carbonate and sediment density (Kelts and Hsü, 1978), which is in turn controlled by seasonal limnology and sediment compression respectively; whereas, stepwise Ca and Sr profiles relate to elemental concentrations within carbonates at specific sediment depths (Liu *et al.* 2013), and these are proposed to represent the minerals' purity, which is controlled by carbonate supersaturation levels in the epilimnion (region of calcium carbonate precipitation). The combined analysis of these datasets permits the investigation into intra-annual climatic characteristics, including dry season length, intensity and antecedent conditions (Dulski *et al.* 2015).

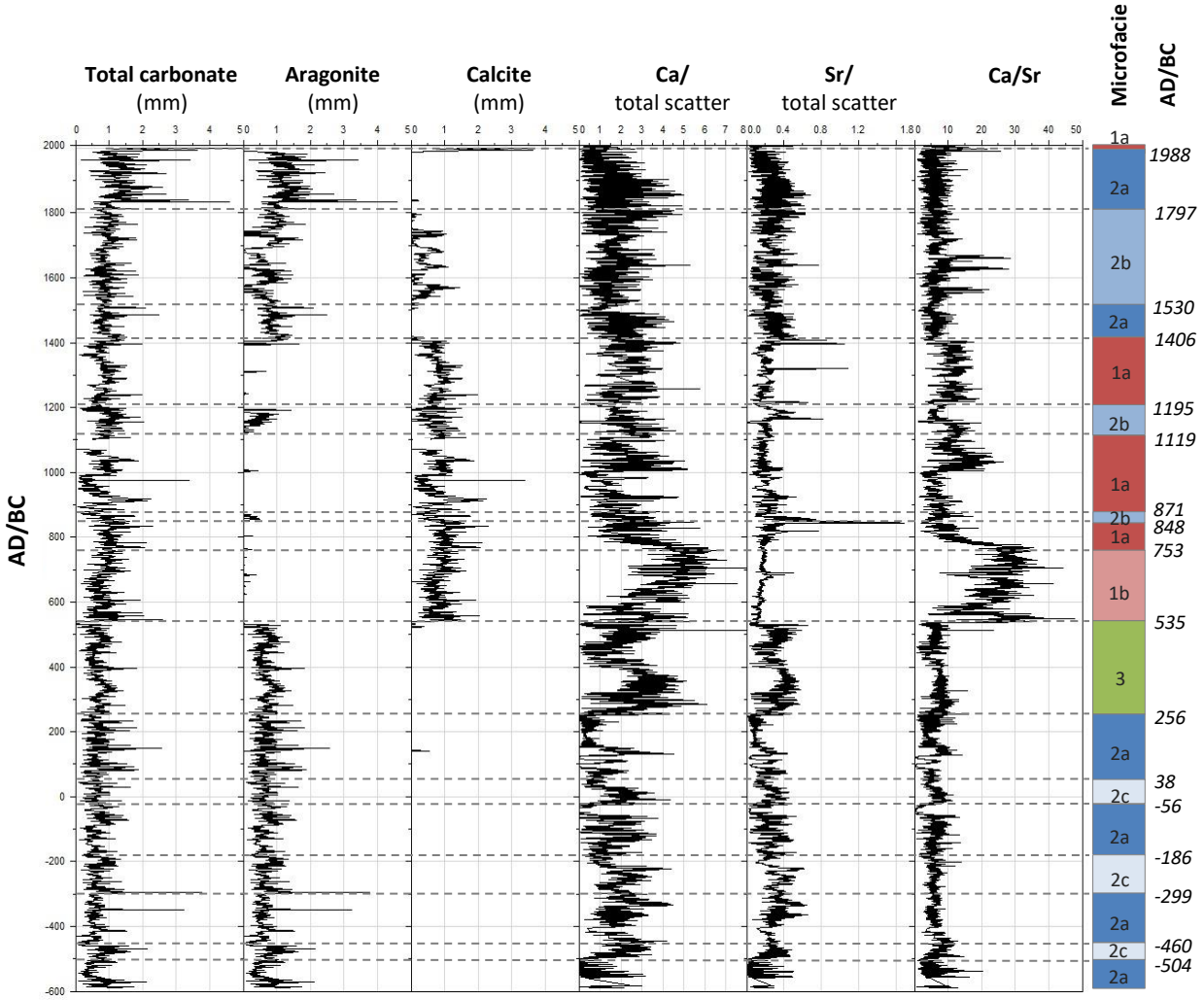


Figure 3.32 *– Changes to sediment microfacies and geochemical composition, relating specifically to calcium carbonate deposition over time, within Unit 1 and subdivided by microfacies classification (grey dashed lines).*

iii) Organics

Organic sublayers were classified according to their composition and concentration of background carbonate minerals (Fig. 3.33). Organic matter typically displayed no identifiable shape or structure, thus appearing as an amorphic, brown matrix containing varying levels of diatoms, micritic carbonates, obsidian, and charcoal. Microfacies reveal that this amorphic organic material is the primary constituent of organic layers, and so total organic thickness is predominately a function of autochthonous productivity and diagenetic decomposition.

Multidecadal peaks in organic sublayer thickness are identified within the carbonate-rich M2a and M2b varves, namely at around 580 BC, 200 AD, 1600 AD, and 1950 AD. Organic sublayer thicknesses most notably increase between 190-256 ±18 AD, immediately before the onset of M3 varve deposition, consistently reaching thickness of 3-8mm. This period likely reflects some of the highest organic productivity and preservation rates of the last 2,600 years. Mean total organic thickness is significantly lower during periods of M1b (0.36mm), M2c (0.23mm) and M3 (0.41mm) deposition, as compared to the other varves (0.79mm). As alluded to above, these specific microfacies do not display the significant correlation between carbonate and organic sublayer thickness, and are associated with notable characteristics of the carbonate sublayer: intense calcite precipitation (M1b), pure aragonite deposition (M3), and dolomite deposition (M2c). Due to the organic matters' composition of light elements (specifically carbon, oxygen and hydrogen) beyond the detection range of Itrax, total scatter from µXRF scanner has been used as a proxy for organic content (Davies *et al.* 2015). A weak positive correlation between total organic thickness and total scatter from the µXRF scan ($P<0.05$) suggests that organic density increases with the sublayers thickness.

The concentration of background carbonate material predominately defines the three major organic subclasses (Fig. 3.33), where 'amorphic organic and diatoms' reflect sublayers containing negligible amounts of carbonate material. These carbonate minerals are suspended within the organic matrix; crystals are micritic (<4µm) and their mineralogy matches that of the varve's dominant carbonate sublayer. The mineralisation of micritic carbonates has been associated with solubility change within the microenvironment, where photosynthetic productivity induces an increased pH in the immediate vicinity around the organism (Kelts and Hsü, 1978). Observed varves display increased micritic carbonate concentrations through the organic sublayers, as the epilimnion's carbonate solubility threshold is neared prior to the spring precipitation events.

The concentration of micritic carbonate within organic sublayers corresponds to microfacies sedimentology. On average, organic sublayers containing 'high' or 'very high' concentrations of micritic carbonate contribute to 50% of the total organic thickness in aragonite-rich varves (M2 and M3), but only 10% in calcite-rich varves (M1). Similarly, organic sublayers with negligible concentrations of micritic carbonate contribute only 26% of the total organic thickness in aragonite-rich varves (M2 and M3), and 51% in calcite-rich varves (M1). It appears the antecedent conditions affect the carbonate sublayers' mineralogy. The balance of ions in the epilimnion, which control the endogenic carbonates' mineralogy (Kelts and Hsü, 1978), must be established prior to the precipitation events to produce the calcite- or aragonite-*only* varves, and consequently influence the formation of micritic carbonate in the preceding organic sublayer.

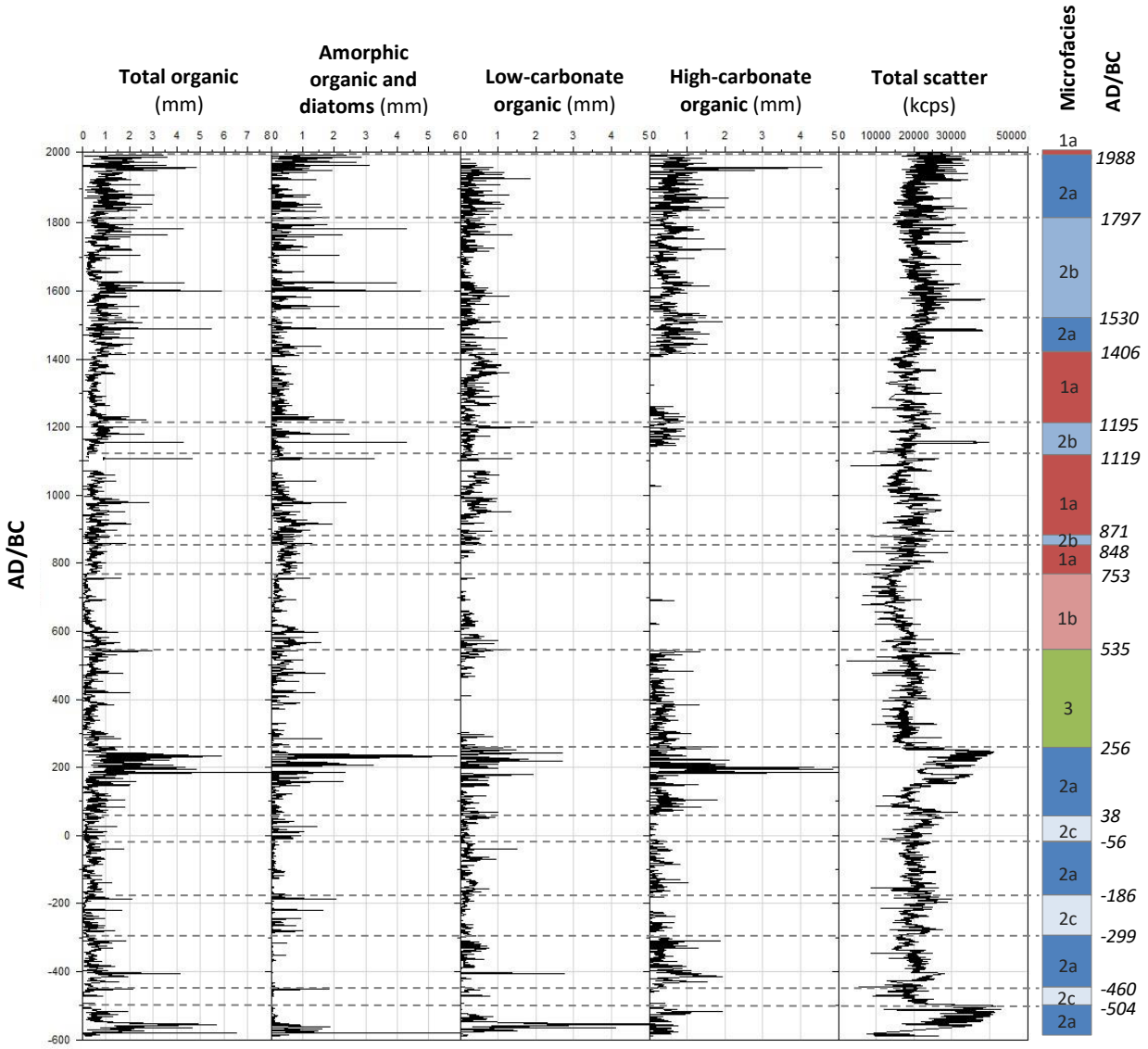


Figure 3.33 *– Changes to sediment microfacies and geochemical composition, relating specifically to organic deposition over time, within Unit 1 and subdivided by microfacies classification (grey dashed lines).*

iv) Turbidites

The term 'turbidite' is used here to describe non-seasonal sublayers, i.e. they are not governed by the seasonal succession of depositional processes. Typically formed by rapid influxes of catchment material or reworking of lake bed sediment due to gravitational failures/turbulence (Corella *et al.* 2012), they can be found at any point within a varve's cycle. Abrupt boundaries indicate that they are deposited within a rapid event (Mangili *et al.* 2005). Characteristically, they appear as homogeneous, grey, clay-rich sediment in the split core, and thin section microscopy similarly shows a well-mixed mass of terrigenous clasts, in-washed obsidian, organic detritus and calcareous material; their allogenic proportion is visually distinct from the autochthonous varved deposition. Larger turbidites typically display up-core fining of grain sizes, indicative of gravitational sorting (Mangili *et al.* 2005).

Turbidite layers are identified throughout Unit 1 (Fig. 3.34). Temporally, these sublayers are grouped together, and these periods correspond with peaks in the Fe, Ti and Rb geochemical profiles. Turbidites are generally more spread through periods of M1 varve deposition, and display the thickest turbidites (up to 10.4cm). Major turbidite layers, those with a thickness greater or equal to 1cm, display a higher recurrence rate and magnitude within calcite varves (M1) in comparison to aragonite varves (M2 and M3). Of the 37 major turbidite layers, 16 occur within the 871-year period of M1 deposition and display an average thickness of 2.9cm; in comparison, 21 major turbidite layers are deposited within the combined 1719-year periods of aragonite-rich varves, with an average thickness of 1.7cm.

Geochemical profiles of Fe, Ti and Rb are also well-established indicators of catchment erosion/sediment influx (Metcalfe *et al.* 2010; Martin-Puertas *et al.* 2011; Davies *et al.* 2015); detection peaks can help identify and characterise turbidites. These elemental profiles can also be used more broadly to indicate sediment influx throughout the varved record. Figure 3.34 displays the occurrence of turbidites and their thickness alongside geochemical composition. These sediment influx proxies are highly variable throughout the record, yet are centred on periods of increased turbidite occurrence, variables significantly correlate ($p<0.05$). Detection is highest for sustained periods between: 190-55 ±22 BC, 400-605 ±16 AD, 900-1140 ±11 AD and 1900-1990 ±1 AD during which, the base-level detection rate of Fe (~0.5 kcps), Ti (~0.01 kcps) and Rb (~0.02 kcps) increases 4-6 times base level measurements.

A number of driving forces can act to increase lacustrine sediment influx. At Nar Gölü, human-derived vegetational change and intense rainfall events have been linked to the geochemical profiles of terrigenous elements (Fe, Ti and Rb) (Allcock, 2013). Similarly, annual rainfall is specifically associated with Ti detection from Laguna de Juanacatlán (Metcalfe *et al.* 2010) and the Cariaco Basin (Haug *et al.* 2001). Strong earthquakes have also been linked to turbidite deposition in Lake Biwa (Inouchi *et al.* 1996). The increased turbidite frequency and magnitude within the calcite varves (M1) of Unit 1 could be driven via increased rainfall, particularly delivered by intense storms; these could cause catchment slope failures (Bookhagen *et al.* 2005), resulting in the observed rapid deposition of allogenic sediment within the varve chronology. This interpretation is supported by the coeval depletion of oxygen isotopes (Dean *et al.* 2013) and mineralogical change from aragonite to calcite precipitation, both indicative of increased freshwater inflow. However, the broader allogenic-geochemical signal does not follow the varve microfacies' classification, thus implying that long-term varve composition and structure is not strongly controlled by catchment inwash.

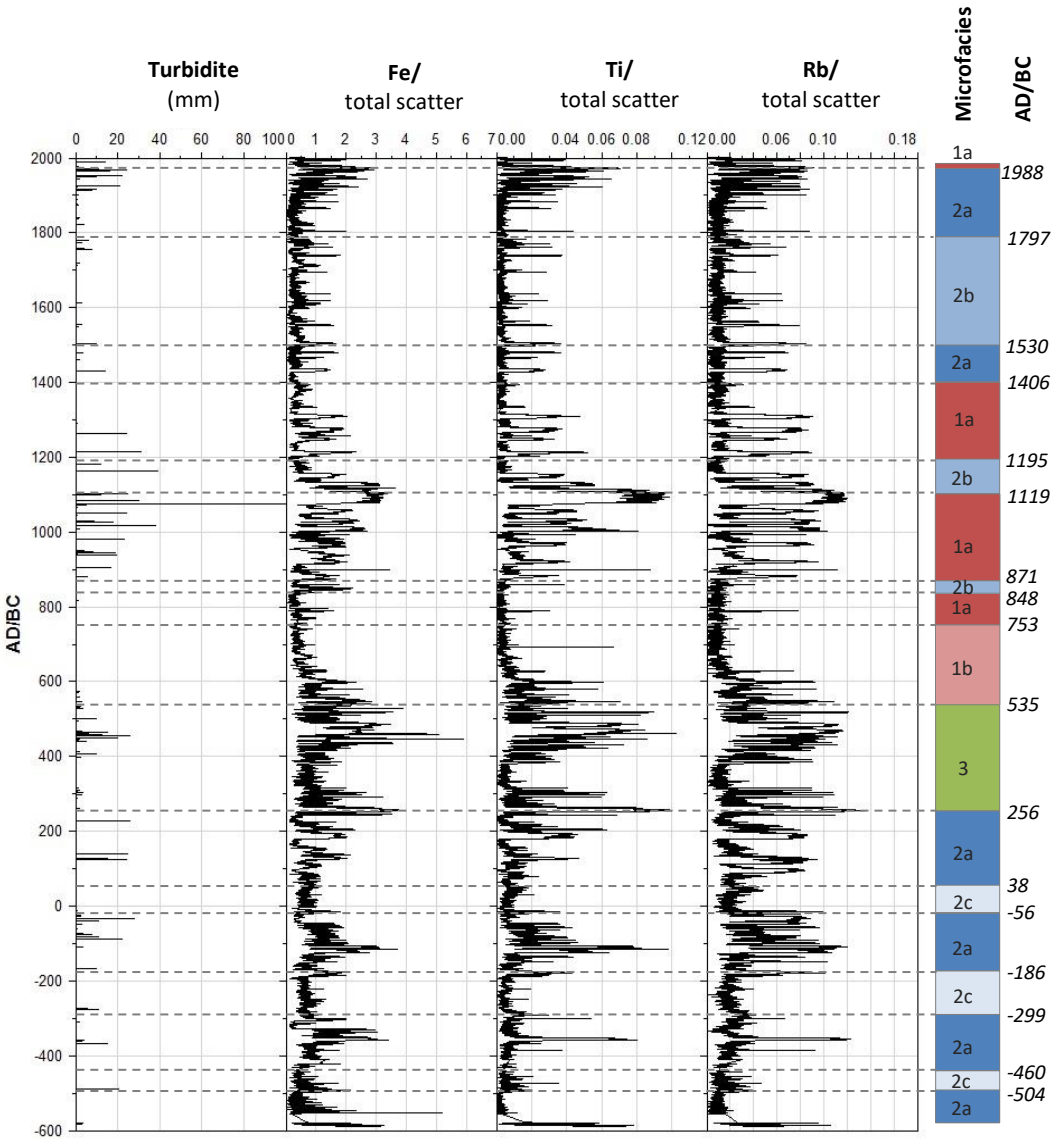


Figure 3.34 *– Changes to sediment microfacies and geochemical composition, relating specifically to turbidite deposition over time, from Unit 1 and subdivided by microfacies classification (grey dashed lines). Slight disparity between thee geochemical and microfacies dataset is derived from the inclusion of turbidites into the age-depth model.*

3.3.3 Sedimentology: Summary

Using thin section microscopy and µXRF scanning, two annually-resolved records of varve sedimentology have been developed from Nar Gölü's master sequence. These two records assessed varves deposited in the late Holocene (589 BC – 2010 AD; 2,539 – -60 cal yrs BP), and the early-mid Holocene (approx. 7,630 to 9,064 cal yrs BP). Microfacies classification identified unique variations in the typical carbonate-organic varve from Nar Gölü. Distinct shifts to varve microfacies were

identified and well-dated, each denoting specific changes to the dominate processes driving sedimentation. Detailed analysis of each varve's components subsequently permitted the necessary environmental conditions required for their deposition and preservation to be inferred.

Throughout both records, endogenic carbonate deposition drives sediment accumulation, where its mineralogy and sublayer thickness are sensitive to climatic and limnological change. Modern calibration identified significant correlation between March-May E/P conditions and aragonite sublayer thickness. The mineralogy and thickness of carbonate sublayers were subsequently linked to $\delta^{18}O_{Carbonate}$ variability, known to respond to regional water balance (Dean *et al.* 2015a). Therefore, the specific carbonate mineralogy may be used as an indicator of relative water balance, and the respective thicknesses of these sublayers form a continuous, annual record of regional, March-May E/P conditions.

The onset of Unit 1's varve deposition corresponds to an inferred rise in lake level. Subsequently, aragonite-rich varves are indicative of long-term high E/P conditions, in comparison to the rest of the late Holocene record. Sporadic periods of dolomite deposition are proposed to correspond with lower levels, exposing dolomite formed during Unit 2's preceding deposition and reworked deeper into the lake. Rapid changes to the varves' dominant carbonate mineralogies and their isotopic composition suggest significant hydroclimatic shifts, most prominently at 535 ±15 AD and 1406 ±7 AD. Prior to this earlier shift, the identification of Fe(III) oxyhydroxides may indicate changes to the lake's mixing regime, increasing DO concentrations in the hypolimnion, and/or the increased inwash of Fe-rich allogenic sediment from the catchment.

In Units 4-5, hydroclimatic shifts are similarly inferred from mineralogical and isotopic changes. However, the sedimentological shift from Unit 5 to Unit 4 is proposed to be driven by increased limnological mixing. Enhanced circulation may increase oxidising conditions in the hypolimnion, thus driving decreased Fn/Mn ratios and promoting organic decomposition, and dilute carbonate ion concentrations, thus resulting in calcite deposition despite increased isotope-inferred E/P conditions.

3.4 Discussion

The analysis of varve microfacies, and their geochemical composition, enable distinct changes to limnological conditions to be identified and dated within Nar Gölü during the early-mid and late Holocene (Sections 3.4.1 and 3.4.2 respectively).

Section 3.4 places Nar Gölü's palaeolimnological record within the context of regional climatic and societal change through the Holocene. Here, changes to varve microfacies are correlated with palaeoclimatic records from other sites, thus providing an insight into the environmental conditions driving depositional change within Nar Gölü. Spectral analysis of the record's incremental timeseries offers a new understanding of high frequency climatic variability and its potential drivers. Sedimentological-inferred environmental changes are subsequently compared to records of societal change, where temporal correlation between sedimentological and anthropogenic records may indicate the influence of climate on socio-economic change.

3.4.1 Early-mid Holocene: Units 4-5

Across Anatolia and the eastern Mediterranean, the early-mid Holocene period (ca. 11,700 – 6,000 cal yrs BP) likely represents the epoch's wettest climatic conditions, with a slight drying trend through the first five millennia (Roberts *et al.* 2001; Stevens *et al.* 2001; Eastwood *et al.* 2007; Kotthoff *et al.*, 2008; Göktürk *et al.* 2011). Within this period, a regional multi-centennial dry period also coincides with the Atlantic-derived 8.2 ka event (Alley *et al.* 1997; Göktürk *et al.* 2011). While Nar Gölü's isotopic record similarly portrays a relatively wet early Holocene with a gradual drying trend through 11,600-6,500 cal yrs BP and a dry oscillation around 8,200 cal yrs BP (Dean *et al.* 2015a) (Fig. 3.35), the microfacies and geochemical record provides a more detailed insight into the limnological response to this changing water balance.

At Nar Gölü, particularly low $\delta^{18}O_{carbonate}$ values (–5.3 to –1.4‰) correspond to the mixed carbonate mineralogy of M5 varves (9,064-8,518 cal yrs BP ±553) and the calcite-dominate sublayers of M4 varves (8,113-7,630 cal yrs BP ±562), thus indicating fresh limnological conditions relative to Nar Gölü's full Holocene record. Following this early-mid Holocene sequence, only M1b varves (1,415-1,197 cal yrs BP; 535-753 AD ±14) display equally low $\delta^{18}O_{carbonate}$ values and calcite-rich mineralogy, suggesting comparably fresh limnological conditions. This wet early Holocene period corresponds well with the 'Holocene climatic hypsithermal' around 9,000-6,000 cal yrs BP (Wanner *et al.* 2008); a

period typically defined by warmer conditions at mid-high latitudes, where orbital precession and obliquity increased NH insolation and its seasonality (Berger, 1978). This early Holocene insolation likely supported a northerly migration to the annual ITCZ position (Haug *et al.* 2001; Schneider *et al.* 2014), consequently enhancing Atlantic and Mediterranean SSTs (Tzedakis, 2007; Marino *et al.* 2009). These warmer SSTs are generally conducive to wetter conditions across the eastern Mediterranean (Dean *et al.* 2015a) (also see Section 3.4.2), via the intensification of cyclogenesis and enhanced propensity of easterly storm tracks (Tzedakis, 2007). Considering these low pressure systems presently dominate the wet-season climatology (Türkeş *et al.* 2009), fresh early Holocene conditions were likely driven by enhanced winter precipitation.

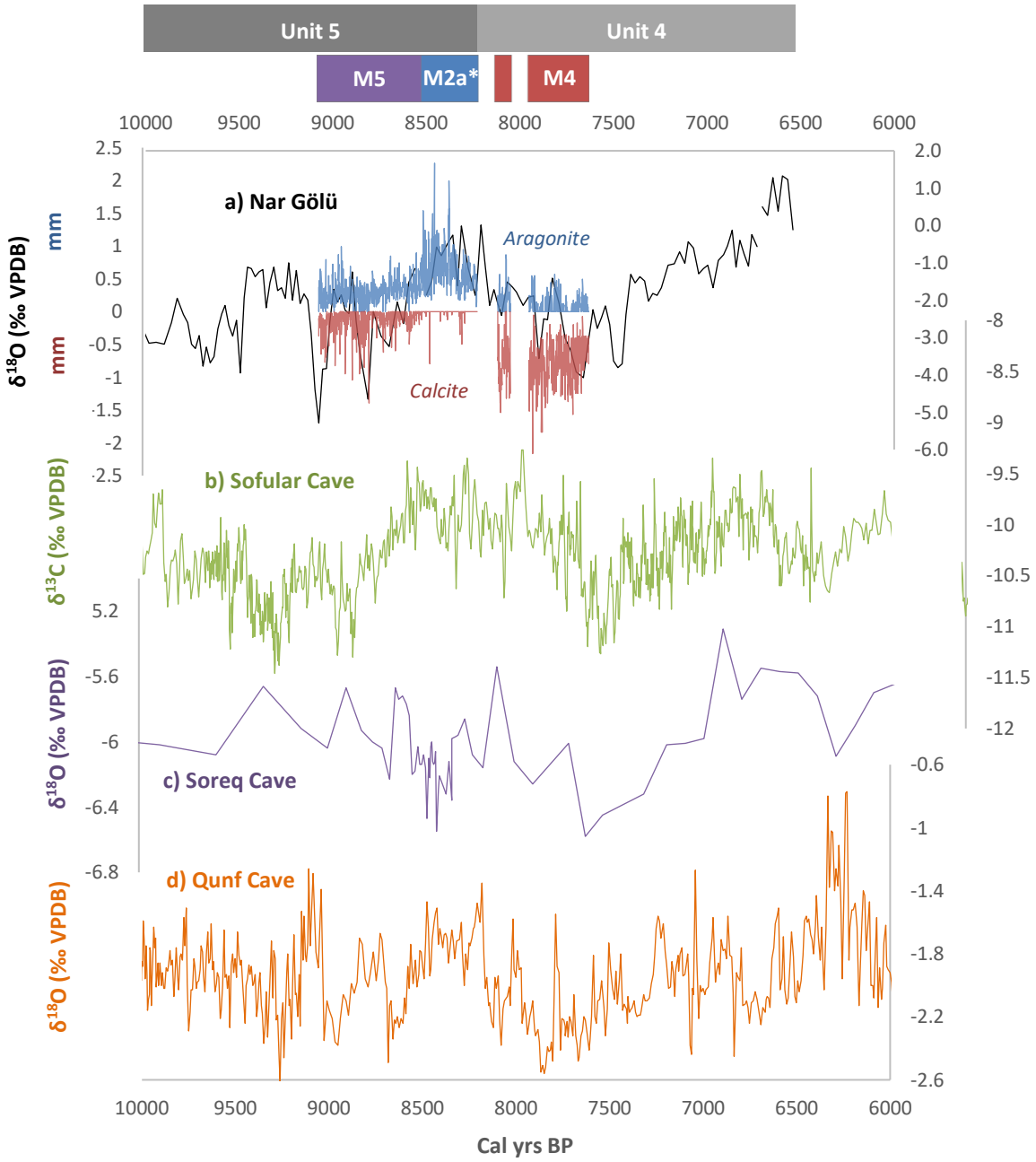


Figure 3.35 *– Comparison of regional palaeorecords through the early-mid Holocene. (a) Nar Gölü's oxygen isotope record (black) (Dean et al. 2015a) alongside aragonite (blue) and calcite (red) sublayer thicknesses; (b) carbon isotope record from Sofular Cave (Göktürk et al. 2011); (c) oxygen isotope record from Soreq Cave, Israel (Bar-Matthews et al. 2003); (d) oxygen isotope record from Qunf Cave, Oman (Fleitmann et al. 2007).*

Varve deposition through Unit 5 (9,064-8,223 cal yrs BP ±556) requires strong climatic seasonality. During this period, the intra-annual variability is capable of driving endogenic carbonate precipitation despite the relatively fresh limnological conditions. Enhanced dry-summer and wet-winter climatic seasonality may drive Nar Gölü's varve deposition, and has been proposed to cause the disparity between Anatolian isotopic and pollen records (Wick *et al.* 2003). While lacustrine isotopes typically identify a major shift to wetter conditions at the Pleistocene-Holocene transition (e.g. Roberts *et al.* 2001; Dean *et al.* 2015a), the expansion of mesic, deciduous oak woodland across Anatolia occurs later, around 8,000 cal yrs BP (Wick *et al.* 2003). This delayed response to climatic amelioration may reflect the intensification of summer drought, within a period of increased annual precipitation. Facilitated by the enhanced insolation seasonality (Schneider *et al.* 2014), this high climatic seasonality is similarly inferred by regional climatic modelling (Brayshaw *et al.* 2011).

Enhanced dry-season conditions may be driven, in part, by Indian monsoon dynamics. During the early Holocene, the northerly ITCZ position (Haug *et al.* 2001) is associated with the intensification of the Indian monsoon (Fleitmann *et al.* 2007). Monsoon strength controls the flow and subsidence of dry continental air across the eastern Mediterranean, thus influencing the region's summer evaporation rates (Raicich *et al.* 2003; Ziv *et al.* 2004) (discussed further in Section 3.4.2). Overall, through Nar Gölü's Unit 5 deposition, increased dry-season E/P conditions likely facilitated annual lake stratification and endogenic carbonate precipitation, within a period of fresher wet-season conditions.

Early Holocene wet conditions across the eastern Mediterranean coincide with sapropel deposition event S1 at 9,000-6,800 cal yrs BP (Ariztegui *et al.* 2000). S1 deposition reflects enhanced marine productivity and benthic anoxia within the Mediterranean's eastern marine basin, resulting in high organic-rich sediment deposition with minimal oxic decomposition (Rohling *et al.* 2015). The region's wet climatic conditions have been proposed to drive S1 deposition, by enhancing the inwash of terrestrial-sourced nutrients and inhibiting marine circulation and ventilation via the surface influx of freshwater (Rossignol-Strick *et al.* 1982; Bar-Matthews *et al.* 2000; Rohling *et al.* 2015). While increased rainfall around the eastern Mediterranean basin likely contributed to S1 formation, enhanced Nile discharge, derived from African Monsoon intensification, is likely the primary driving force (Rossignol-Strick *et al.* 1982). This early Holocene intensification of the African Monsoon was similarly driven by the orbitally-enhanced insolation seasonality, yet its extent is unlikely to have significantly influenced Levantine/Anatolian climatology (Arz *et al.* 2003).

Through Unit 5 (9,064-8,223 cal yrs BP ±556), both microfacies and $\delta^{18}O_{carbonate}$ enrichment indicate long term increases to spring-summer E/P conditions; a trend also identified in palaeorecords across the eastern Mediterranean (Roberts *et al.* 2001; Stevens *et al.* 2001; Eastwood *et al.* 2007). This drying trend culminates in the deposition of aragonite-rich M2a* varves (8,518-8,223 cal yrs BP ±556). With peak aragonite deposition and $\delta^{18}O_{carbonate}$ values of Unit 5, M2a* varve deposition likely reflects the early Holocene's driest limnological conditions. This annual limnology may be comparable to the prevailing conditions over the last two centuries; both M2a* varves and the most recent M2a varves (153 – -29 cal yrs BP ±2) display similar microfacies composition and range of $\delta^{18}O_{carbonate}$ values (–1.9 to +1.2‰).

Within error, M2a* varve deposition coincides with the aforementioned 8.2 ka event (Göktürk *et al.* 2011). This event pertains to widespread cooling across the NH, driven by an outburst of freshwater from the North American proglacial lakes into the Atlantic Sea (Born and Levermann, 2010). This influx of freshwater inhibited the Atlantic's meridional heat transfer, consequently driving cooler temperatures across the NH (Abrantes *et al.* 2012). Consequently, abrupt Atlantic-derived cooling reduced evaporation and moisture supply through the Mediterranean, thus resulting in centennial-scale drying across southern Europe (Magny *et al.* 2003; Gonzalez-Samperiz *et al.* 2009) and the eastern Mediterranean (Bar-Matthews *et al.* 2003; Turner *et al.* 2008; Göktürk *et al.* 2011). Drier conditions are associated with vegetational disturbance across the eastern Mediterranean, typically marked by a short period of reduced deciduous oak pollen in palaeorecords (Wick *et al.* 2003; Kotthoff *et al.* 2008). At Nar Gölü, an abrupt reduction to arboreal pollen (Eastwood *et al.* unpublished) corresponds with M2a* varves' increased turbidite frequency and magnitude, most notable at 8,460 ±549 cal yrs BP; here, catchment disturbance and vegetation cover likely enhanced terrestrial erosion and inwash, despite the reduction to annual rainfall. Additionally, aragonite deposition increases abruptly indicating a rapid onset of drier conditions, where subsequent decreases to its precipitation through M2a* deposition indicates a prolonged weakening of the 8.2 ka event's climatic forcing.

As alluded to by Dean *et al.* (2015a), the duration of the 8.2 ka event's climatic signal varies spatially. From Greenland and western Europe, the climatic excursions range from ~100 years (Rasmussen *et al.* 2006) to ~100-200 years (Tinner and Lotter, 2001; Prasad *et al.* 2009) respectively. However, Nar Gölü's microfacies analysis suggests drier conditions prevailed over central Anatolia for 295 ±3 years. While changes to the $\delta^{18}O_{seawater}$ supplying moisture to the eastern Mediterranean have been

proposed to exaggerate inferred aridity regionally (Marino *et al.* 2009), microfacies analysis at Nar Gölü supports the inference of prolonged dry conditions in Anatolia.

This prolonged aridity excursion may be associated with a change to NAO dynamics. Within this period, strong decadal-scale oscillations, characteristic of NAO cyclicity, are identified from Holzmaar Lake, Germany (Prasad *et al.* 2009), where hydroclimatic reconstructions from Greenland (Thomas *et al.* 2007) and Europe (Magny *et al.* 2003) additionally indicate an increased propensity of positive NAO phases during the 8.2 ka event. Strong, positive NAO phases are associated with drier climatic conditions over Nar Gölü (Cullen and deMenocal, 2000) (discussed further in Section 3.4.2). Furthermore, this intensification of positive NAO phases may increase the strength/frequency of outbreaks of cold, northerly air masses (Tsimplis and Josey, 2001), which may slow the circulation and ventilation of the eastern Mediterranean Sea (Roether *et al.* 1996; Abrantes *et al.* 2012). Consequently, while cooler Atlantic SSTs may drive the 8.2 ka event's initial cooling/drying climatic trends, the intensification of positive NAO phases, and their influence on Mediterranean Sea circulation, likely prolonged the event's climatic signal across the eastern Mediterranean (Abrantes *et al.* 2012).

Throughout the early Holocene, most notably between 9,000 to 8,000 cal yrs BP, continued deglaciation and meltwater flux likely contributed to the occurrence of rapid climate change across the NH and the establishment of post-glacial climatic systems (Mayewski *et al.* 2004; Born and Levermann, 2010; Abrantes *et al.* 2012). This climatological transitions corresponds well with the start of the Northgrippian stage, and Nar Gölü's major lithological transition from Unit 5 to 4 at 8,223 ±556 cal yrs BP.

Following its most northerly extent around 9,000-8,000 cal yrs BP, decreasing NH insolation seasonality likely contributed to these climatic changes (Mayewski *et al.* 2004), and influenced Anatolia's climatic seasonality. The southerly migration of the ITCZ's average latitude (Haug *et al.* 2001) may contribute to a weakening of the Indian monsoons' strength, thus decreasing Anatolian dry-season E/P conditions (Fleitmann *et al.* 2007). Conversely, declining Aegean SSTs, particularly following peak S1 deposition ~7,500 cal yrs BP (Marino *et al.* 2009), likely decreased evaporation and moisture supply to Anatolia, and inhibited the formation of wet-season depressions. Consequently, the eastern Mediterranean's climatic seasonality probably decreased through the early Holocene. Across Anatolia, mesic conditions with less intra-annual variability have been interpreted to enable the growth of oak woodland (Wick *et al.* 2003). At Nar Gölü, the deterioration of varve deposition

and preservation through Unit 4 (8,223-6,541 cal yrs BP ±573) may similarly reflect climate-derived reductions to limnological intra-annual variability. Geochemical analysis highlights increased lake mixing, where decreased evaporation during the dry-seasons may weaken/shorten annual stratification. Through Unit 4 deposition (8,223-6,541 cal yrs BP ±573), reduced wet season rainfall may also drive the long term $\delta^{18}O_{carbonate}$ enrichment and carbonate-rich deposition.

A mineralogical switch from calcite- to aragonite-rich deposition at the end of Unit 4, around 6,800-6,500 cal yrs BP, coincides with geochemical-inferred increases to lake stratification and isotopic-inferred reductions to lake level. Concurrent reductions to inferred lake level and arboreal pollen from the nearby Eski Acıgöl similarly indicate a drying trend from 6,800 to 6,000 cal yrs BP (Roberts *et al.* 2001). Here, the sustained reductions to NH insolation and its seasonality through the early-mid Holocene (Haug *et al.* 2001), and poorly laminated sediment deposition in Nar Gölü reduce the likelihood that this mineralogical change is driven by a re-emergence of strong seasonality. Instead, a millennial-scale drying trend is proposed to reduce the lake level, thus concentrating ions throughout the mixed water body. Consequently, while mixing dilutes eplimnetic water concentrations through much of Unit 4, thus driving calcite precipitation, a sustained aridity trend eventually resulted in the mineralogical switch to aragonite precipitation (Kelts and Hsü, 1978), despite a lack of strong stratification.

3.4.1.1 Early-mid Holocene spectral analysis

Spectral analysis of the varved sequences was again assessed using statistical program *Past 3.14* (Hammer *et al.* 2001). As periodograms require each even time-steps (Comboul *et al.* 2014), cyclicity was assessed within Unit 4's longest varved sequence (M4; 7,948-7,630 cal yrs BP ±562) and Unit 5's contiguous varves (M2a* and M5; 9,064-8,223 cal yrs BP ±556). Significant periodicities of the key sedimentological sublayers over the 318- and 841-year long periods respectively are displayed in Tables 3.10a and b; all cycles displayed are significant to at least $P<0.05$ level, and their lengths are less than a third of the total timeseries' duration. Due to the comparatively short length M4's varved sequence and its comparatively poor preservation, fewer significant cycles were identified within Unit 4 sequence, compared to Unit 1.

***Table 3.10** – Periodicities of varve thicknesses of key sedimentological variables within M4 (a) and, M2a* and M5 (b), significant to p<0.01. Periodicities have been aligned to show synchronicity between variables.*

a)

M4 **7630-7948 cal yrs BP**							
Total varve	*No significant cycles*						
Total carbonate	*No significant cycles*						
Aragonite						134	
Calcite	*No significant cycles*						
Total organic							102

b)

M2a* & M5 **8223-9064 cal yrs BP**						
Total varve						120
Total carbonate			224			
Aragonite	280					
Calcite		249		192		127
Total organic					164	

A significant 127-134-year cycle is detected within the thickness data of each sections' predominant carbonate mineralogy – specifically, aragonite in M4 and calcite in M2a* and M5. Coherent cycles are also present within the carbonate and organic sublayers of Unit 1's varves (M1-3); this expression of corresponding cycles through time indicates the influence of a specific oscillation on regional climatology and depositional drivers. This periodicity is proposed to reflect Indian monsoon intensity, which displays corresponding cycles through the late Holocene (Agnihotri *et al.* 2002; Jones *et al.* 2006). Increased monsoon intensity may drive enhanced climatic seasonality, within a period of relatively fresh limnological conditions, capable of stratifying lake water and supersaturating carbonates within the epilimnion.

The 249-year cycle within M2a* and M5 calcite sublayers (8,223-9,064 cal yrs BP) is also identified within the calcite sublayers of M1a-b (1,415-544 cal yrs BP; 535-1406 AD). However, this 249-year cycle may represent a harmonic of the 127-year cycle within the same sequence. Otherwise, the cycles identified in Units 4-5 (Tables 3.10a-b) are not detected within Unit 1's sedimentary sequence. As previously discussed, lower frequency cycles may reflect harmonics and/or interference from multiple higher frequency cycles, yet the disparity of cycles identified between the Units may suggest differing drivers to climatic variability.

3.4.1.2 Environmental context for societal change

Climatic and environmental change have been proposed to influence societal development throughout the Holocene (Jalut *et al.* 2009). Without the technological advancements and socio-political complexity associated with late Holocene societies, early Holocene development may be more strongly linked to climatology and its direct influence on food and water supply.

Across the eastern Mediterranean, the origins of agriculture have been associated with the prevalence of strong wet-dry seasonality through the late-Pleistocene and early-Holocene, where sedentary societies developed agricultural practises and food storage systems to endure the intense dry-seasons (McCorriston and Hole, 1991). Evidence of agricultural domestication and Neolithic settlement construction may be dated from ~12,900 cal yrs BP in Anatolia and the Levant, and subsequently spreads into Europe through the Holocene (Turney and Brown, 2007). Warmer climatic conditions (+2°C average global temperature), associated with the Holocene climatic optimum (~9,000-6,000 cal yrs BP), and increased annual rainfall in the eastern Mediterranean have been proposed to facilitate this expansion of agriculture and sedentism (Richerson *et al.* 2001; Gupta, 2004).

During the early Holocene, sedentary societies adapted agricultural practices to accommodate environmental variability. Situated on a mound adjacent to the Çarsamba River in central Anatolia, the Neolithic site of Çatalhöyük represents one of world's largest Neolithic settlements (9,400-7,800 cal yrs BP) (Hodder, 2007). However, the strong wet-dry seasonality resulted in the seasonal flooding of surrounding land, rendering it unsuitable for the agriculture of cereals typically consumed; consequently, smaller settlements were established in dryland soils ~13km away to grow cereals for Çatalhöyük (Roberts and Rosen, 2009).

This agricultural system and settlement nucleation was notably modified around 8,300 cal yrs BP, following the cessation of annual flooding around Çatalhöyük (Roberts and Rosen, 2009). These drier climatic conditions are initially associated with the 8.2 ka event's multi-centennial aridity excursion. Without the risk of seasonal flooding, archaeological evidence suggests that the Çatalhöyük relocated across the river, where extensive cereal agriculture was developed on the surrounding alluvial soils (Roberts and Rosen, 2009; Roffet-Salque *et al.* in review). The prevalence of soil formation from 8,200 to 7,800 cal yrs BP further indicates that the cessation flooding exceeded the duration of the 8.2 ka event's aridity (Roffet-Salque *et al.* in review). Nar Gölü sedimentary record not only displays the onset of regional dry conditions associated with 8.2 ka event, but also depicts a climatological shift following this aridity excursion. The transition from Unit 5 to 4 sediment deposition at 8,223 ±556 cal yrs BP coincides well with the fluvial shift identified at Çatalhöyük. At Nar Gölü, inferred weakening of seasonality, via reductions to wet-season precipitation and dry-season evaporation, may explain the change to Çatalhöyük's flooding regime; where annual precipitation is not only decreased, but spread more evenly throughout the year, thus reducing flood occurrence/magnitude.

3.4.2 Late Holocene: Unit 1

The onset of Unit 1's varve deposition at 589 ±26 BC is associated with an increase in lake level, following particularly dry conditions between 1,200 and 600 BC; this dry period resulted in Nar Gölü's lowest lake levels of the last 3,200 years (Roberts *et al.* 2016). However, through Unit 1's first 1,124 ±12 years (589 ±26 BC – 256 ±17 AD), the dominance of aragonite precipitation (M2 varves) and the Unit's high $\delta^{18}O_{Carbonate}$ values indicate a prevalence of continuous relatively high E/P dry-season conditions (see Fig. 3.24). Coeval low spring-summer precipitation periods are similarly identified from Sofular Cave, Turkey (Göktürk *et al.* 2011) and Jeita Cave, Lebanon (Verheyden *et al.* 2008).

Lake level rise, post 589 ±26 BC, is likely driven by a relative increase in wet-season rainfall, leading to strong climatic seasonality which persisted until ~400 AD (Dean *et al.* 2017). While Nar Gölü's lithological shift signifies increased lake levels, the mineralogical and isotopic proxies suggest that Unit 1's lowest lake levels persisted through initial M2 varve deposition (589 ±26 BC – 256 ±17 AD). During this period, increasing Quercus pollen concentrations (England *et al.* 2008) and increased allogenic inwash (Roberts *et al.* 2016) support the inference of wetter annual conditions at Nar Gölü, compared to the prior, dolomite-rich Unit 2 (pre 589 ±26 BC).

Regionally, isotopic and geochemical proxies from Lake Van also indicate the prevalence of three wet oscillations around 900-600 BC, 400-300 BC, and 100 BC–200 AD (Şimşek and Cağatay, 2018). These wetter periods may help maintain a water level sufficiently deep for consistent varve deposition and preservation at Nar Gölü (Ojala *et al.* 2000), despite the period's relatively high E/P dry-season conditions. These centennial-scale climatic oscillations identified at Lake Van (Şimşek and Cağatay, 2018) may additionally contribute to the sporadic deposition of Nar Gölü's M2c varves, containing sublayers of detrital dolomite (Section 3.3.2.1). The first two episodes of M2c deposition, 504-460 ±25 BC and 299-186 ±23 BC, correspond well with relatively dry oscillations inferred at Lake Van. At Nar Gölü, periods of drier conditions may lower the lake level, thus re-exposing the dolomite previously deposited onto the subaqueous alluvial shelf; this would subsequently increase its susceptibly to fluvial/pluvial inwash into deeper lake regions. However, the third period of M2c deposition, 56 BC – 38 AD, instead corresponds with a Lake Van-inferred wet oscillation (100 BC–200 AD) (Şimşek and Cağatay, 2018). Considering both records' chronologies are primarily constructed through varve counts, dating uncertainty is unlikely to account for this apparent discrepancy. While increased annual rainfall may contribute to littoral disturbance and sediment re-suspension, a single $\delta^{18}O$ sample within Nar Gölü's record at 7 ±20 BC (+2.8‰) suggests particularly low lake levels, relative to Unit 1's sequence (Dean *et al.* 2015a). However, due to the section's low sampling resolution for isotopic analysis and non-linear relationship between aragonite thickness and $\delta^{18}O$ value (notably above +1.0‰) (Section 3.25), it is difficult to relate M2c deposition to specific climatic and limnological conditions.

M3 varve deposition (256-535 AD ±18) appears to reflect a transitional limnological phase. Initial $\delta^{18}O_{carbonate}$ depletion likely responds to increasing lake levels, where concurrent increases in turbidite and Ti deposition may indicate the role of enhanced rainfall. Coeval divergence between $\delta^{18}O_{carbonate}$ and $\delta^{18}O_{diatom}$ values has been interpreted to represent an increased influence of snowmelt forming a freshwater lid on Nar Gölü during winters' peak diatom growth (Dean *et al.* 2013). Consequently, this enhanced seasonal influx of freshwater could potentially increase the annual duration of limnic mixing, increasing hypolimnetic oxygen concentrations. The combination of these benthic oxic conditions and the enhanced rainfall-derived inwash of Fe-rich allogenic material may provide the limnological conditions required for the diagenetic precipitation of Fe(III) oxyhydroxides (Fortin *et al.* 1993), characteristic of M3 varves. Nevertheless, the Fe-rich composition of M3's varves and their high concentration of pyrite likely indicates a period of enhanced influx of allogenic material, particularly during the winter' wet seasons.

The aragonite-only mineralogy of M3's varves again indicates the prevalence of evaporative spring-summer conditions, despite the moderate isotopic- and geochemical-inferred increases in annual precipitation (Dean *et al.* 2013). The persistence of high seasonality until ~1400 AD (Dean *et al.* 2017) likely dampens the climate's influence on lake level change. The subsequent switch from aragonite- to calcite-only deposition at 535 ±15 AD mayreflect a threshold response to decreased climatic seasonality, reducing spring-summer E/P conditions and resulting in an overall increase in the lake's level.

The abrupt hydroclimatic shift at 535 ±15 AD coincides with the onset of Late Antiquity Little Ice Age (LALIA) conditions, and the broadly-defined Dark Ages Cold Period (DACP), across the northern hemisphere (Helema *et al.* 2017) (Fig. 3.36). While many northern hemisphere palaeoclimatic records identify significant cooling around 400-765 AD (e.g. McDermott *et al.* 2001; Millet *et al.* 2009; Helema *et al.* 2017; Ladd *et al.* 2017), high resolution records have also precisely dated an abrupt climatic shift at 536 AD using Alpine and Siberian tree rings (Büntgen *et al.* 2011, 2016) and Greenland's GISP2 ice cores (Kobashi *et al.* 2011).

The high degree of synchronicity from spatially diverse sites across the northern hemisphere may indicate the influence of a strong external forcing on these regions' climatology. Recently, LALIA onset has been linked to large volcanic eruptions dated at 536/7 and 540 AD (Sigl *et al.* 2015) leading to aerosol-derived reductions in ground-level receipt of solar insolation (Büntgen *et al.* 2016). While the 536 AD eruption has not been attributed to a specific volcano, tephra geochemistry within Greenland ice cores implicates a North American origin (Sigl *et al.* 2015); whereas, the 540 AD eruption has been attributed to El Chichón, Mexico using distal tephra deposition and beach ridge formation (Nooren *et al.* 2017). Transient climate modelling suggests palaeo-volcanism results in summer cooling across the Northern hemisphere (Miller *et al.* 2012). High resolution modelling, using annually-resolved archives of European and West Asian climate over the last 500 years, identifies summer cooling (-0.5°C) and increased precipitation (+15mm/month) across Turkey, possibly via the intensification of westerlies across the Mediterranean in the years following an eruption (Fischer *et al.* 2007). Within Nar Gölü's closed basin, this season-specific change could reduce the summers' dry-season E/P ratio, consequently diluting lake water and driving the mineralogical switch from aragonite to calcite deposition (Kelts and Hsü, 1978). The temporal synchronicity between inferred palaeoclimatic change and volcanic forcing supports the inference

that the LALIA's rapid climatic shift is distinct from the DACP, generally considered to be a product of a North Atlantic ice-rafted debris event (Bond *et al.* 2001; Helema *et al.* 2016).

Consistent depositional conditions, indicating the freshest period of the last 2,600 years, persist from 535 ±15 to 753 ±13 AD. These inferred conditions are sustained for almost a century longer than the cooling identified in the Alps and Siberia by Büntgen *et al.* (2016), and correspond more closely to the end of the DACP. While volcanic aerosols have been proposed to initiate this cooling, the multi-centennial LALIA may have been extended via sea-ice/ocean feedbacks (Miller *et al.* 2012) and the presence of a significant solar minimum ~668 AD (Steinhilber *et al.* 2009). Reduced solar activity can directly decrease evaporation but also indirectly increase winter precipitation at Nar Gölü; insolation minima can enhance negative NAO phase frequency (Gray *et al.* 2010), acting to drive moisture across the Mediterranean.

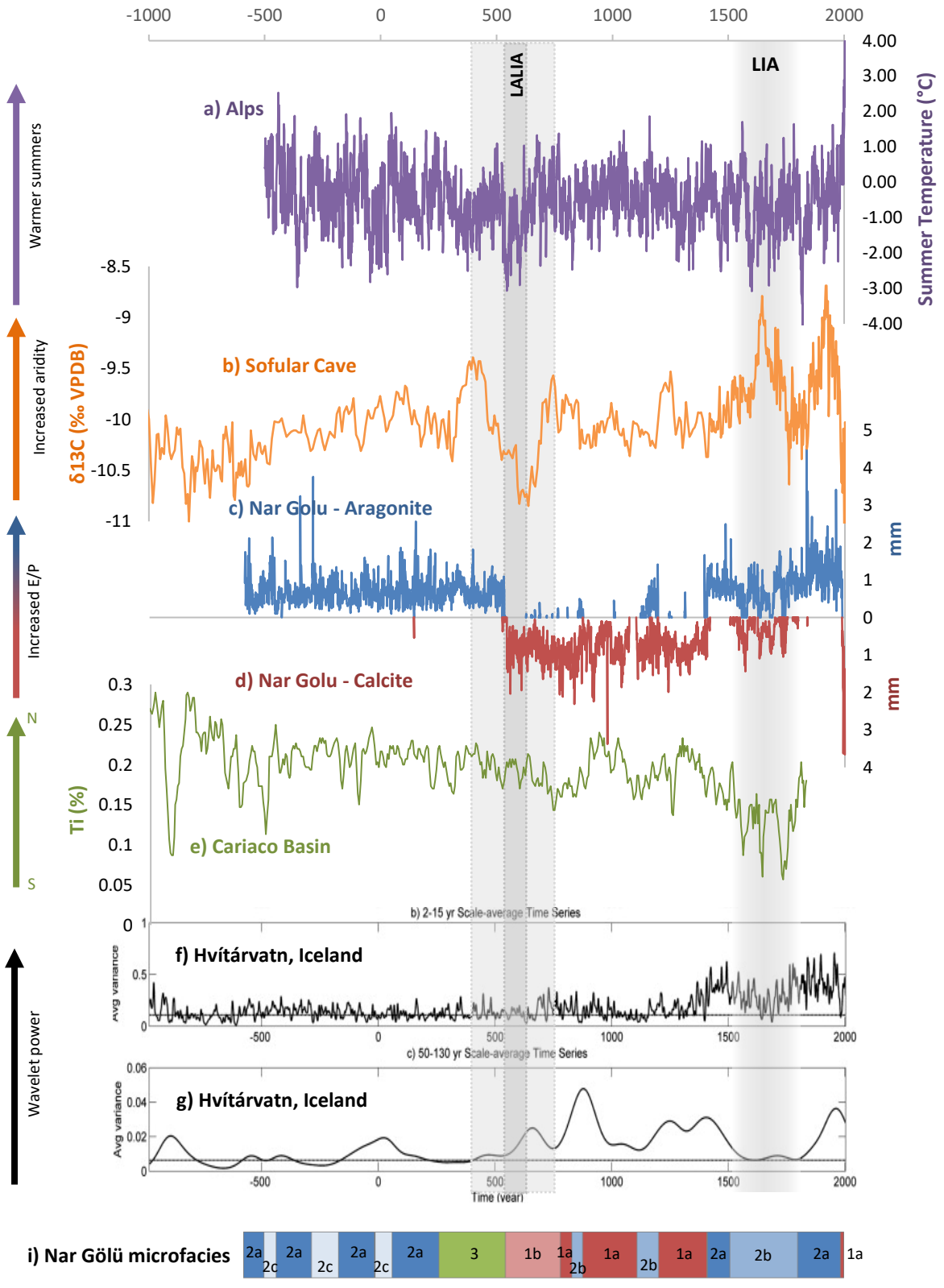


Figure 3.36 *– Comparison of regional palaeoclimatic archives. Summer temperature reconstructed from alpine tree ring thickness (Büntgen et al. 2016) (a), carbon isotopes from Sofular Cave (Göktürk et al. 2011) (b), Nar Gölü's aragonite (c) and calcite (d) sublayer thicknesses and (i) microfacies classification, Ti-detection from the Cariaco Basin indicative of mean ITCZ latitude (Haug et al. 2001) (e), and wavelet power over the 2-15 year band (f) and 50-130 year band (g), displaying NAO and AMO strength respectively (Ólafsdóttir et al. 2013). The Late Antiquity Little Ice Age (LALIA) (light grey; Büntgen et al. 2016) and the Dark Ages Cold Period (DACP) (dark grey; Helama et al. 2017) are depicted by the grey shading. Defined by Nar Gölü's M2a varve deposition between 1530-1797 AD, Little Ice Age (LIA) conditions are displayed (grey grading).*

3.4.2.1 Late Holocene spectral analysis

Throughout the Holocene, ocean-atmosphere oscillations have driven climatic variability across varying timescales, from sub-decadal to multi-millennial (Rossi *et al.* 2011). Each oscillation is associated with a particular climatological mechanism, where specific phases in these cycles are known to influence local-global circulations and their respective climatic systems (e.g. Trigo *et al.* 2002). While oscillations' strength may vary over time, their spectral frequency typically remains constant (Rossi *et al.* 2011). By identifying these spectral signatures within proxy records, the relative contribution of an oscillation to a site's climatological variability can be inferred, and the expression of different oscillations over time provides further insight into changing mechanisms driving regional climate dynamics (Lau and Weng, 1995). Considering these oscillations' broad temporal spectrum, annually-resolved chronologies, such as those provided by varved records, are particularly powerful as they permit the detection of higher frequency decadal-scale oscillations.

Spectral analysis of the annual-resolved thickness data was undertaken using statistical program *Past 3.14* (Hammer *et al.* 2001). Significant periodicities of general sedimentological sublayers over the entire 2,590 year period are displayed in Table 3.11; all cycles displayed are significant to at least $P<0.05$ level, and their lengths are less than a third of the total timeseries' duration. Of note, 135- and 58-year cycles are found within the thickness record relating to the carbonate sublayers. Jones *et al.* (2006) similarly identify these cycles within the calcareous oxygen isotope record through the past 1700 years, thus further affirming the tie between regional water balance and carbonate precipitation; the potential implications of this depositional cyclicity are discussed below. Other periodicities are based around 350-, 250-, 195-, and 110-year cycles, and display significant coherence across different seasonal sublayers (Table 3.11). These longer cycles may reflect harmonics of the higher frequency periodicities and/or interference between multiple cycles (Comboul *et al.* 2014). The low number of significant cycles displayed within organic sublayer thickness measurements may reflect increased variance within the raw data (Table 3.11). Turbidite thickness data contained no significant periodicities.

Table 3.11 *– Periodicities of varve thicknesses of key sedimentological variables within Unit 1, significant to p<0.01 (black) and p<0.05 (grey). Periodicities have been aligned to show synchronicity between variables.*

Aspect of microfacies	Significant periodicities																		
Total varve		341	280	250		193			133	126	114			74					
Total carbonate	398								135		116	100		76	70	58			
Total organic		345	288	256		195	180	157	135	127	110								
Carbonate:Organic					233	195			135										

Cyclicity within periods of aragonite- and calcite-rich varves were also assessed through the record (Table 3.12). The 134- and 57-59–year cycles, identified within the entire total carbonate thickness record, are only significant within the aragonite-dominant M2 varves (589 BC – 535 AD and 1406 – 1988 AD). Whereas, the calcite-dominant M1 varves (535-1406 AD) instead display a distinct 44-year cycle. The 'late calcite' period pertains to calcite thickness within the mixed carbonate M2b varves, and hence represents a shorter section within the 'late aragonite' period. While spectral analysis was performed on the thickness records from each mineralogy, similar 88- and 58-years cycles are identified from both sublayer records. This is somewhat unsurprising considering the calcite and aragonite sublayers of M2b varves are derived from the spring-summer of the same years, and are both primarily controlled by water balance.

Table 3.12 *– Periodicities of carbonate sublayer thicknesses according to their mineralogy, significant to p<0.01 (black) and p<0.05 (grey). Periodicities have been aligned to show synchronicity between variables.*

Aspect of microfacies	Period	Significant periodicities																	
Early aragonite	589BC to 535 AD			134	97			76	70	57									
Late aragonite	1406-1988 AD						88			59									
Mid calcite	535-1406 AD		249		99							44							
Late calcite	1406-1988 AD						85			58			28						

Analysis shows varying cycles within aragonite and calcite deposition, indicative of differing climatological mechanisms (Lau and Weng, 1995). Aragonite-rich varves (589 BC -535 AD ±26 and 1406-1988 AD ±6) display significant 134- and 57- to 59-year cycles (Fig. 3.37). These cycles have also been identified in Nar Gölü's full isotope record and are linked to Indian monsoon intensity (Jones *et al.* 2006) which displays similar periodicities through the late Holocene (von Rad *et al.* 1999; Agnihotri *et al.* 2002). However, Nar Gölü's mineralogical perspective is able to constrain this cyclicity temporally. Indian monsoon strength influences summer evaporation over central Anatolia; intense monsoons enhance dry-continental northeasterly winds, which are conducive to dry conditions regionally (Jones *et al.* 2006). Relative to the entire Holocene, monsoon intensity is inferred to be weakest around 200-1200 AD (Fleitmann *et al.* 2007), thus roughly coinciding with the mineralogical switch observed in Nar Gölü and the apparent signal loss of monsoon-derived cyclicity. Since the monsoon signal is only detected within aragonite-dominant M2 sequences (589 BC -535 AD ±26 and 1406-1988 AD ±6), it is proposed that these periods of more intense monsoon intensity drive the decadal-scale variability of E/P spring-summer conditions at Nar Gölü, and enhance summer evaporative conditions.

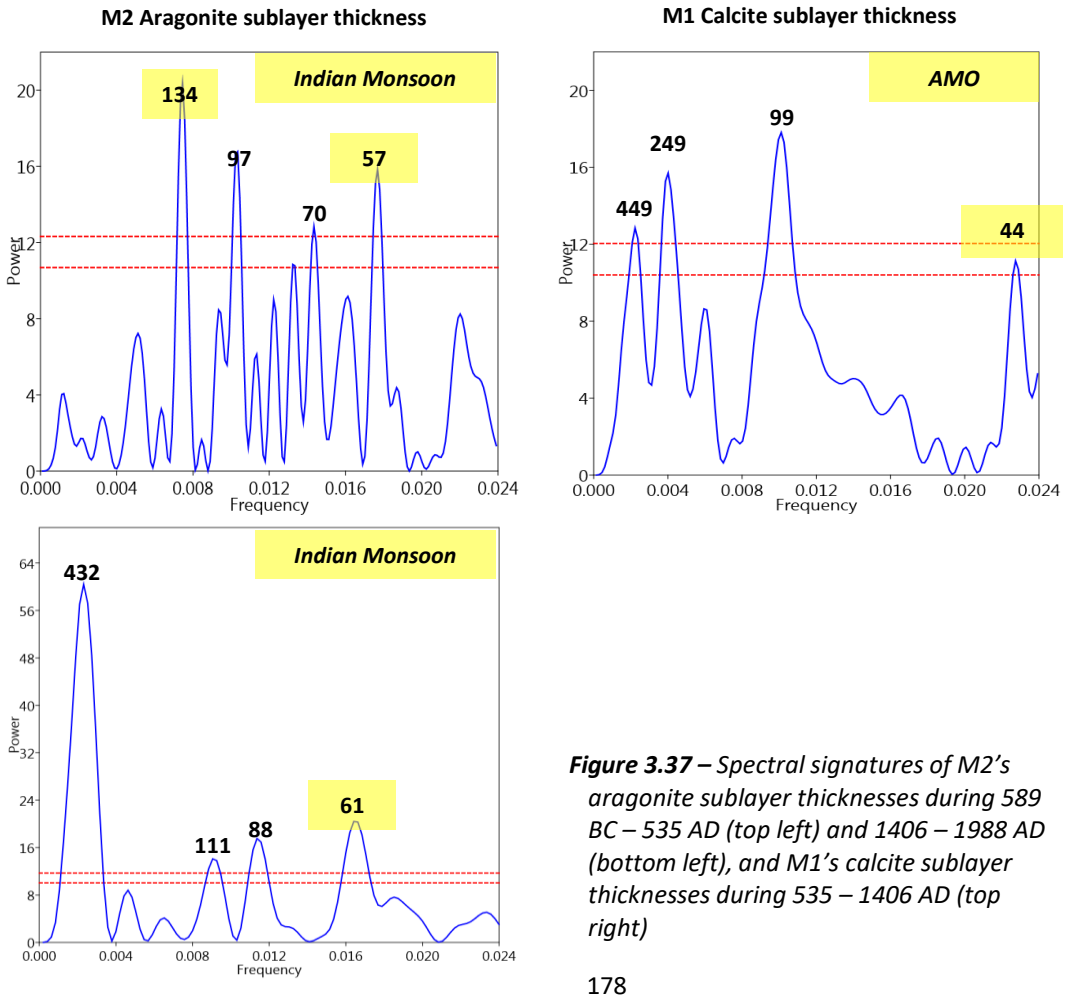


Figure 3.37 *– Spectral signatures of M2's aragonite sublayer thicknesses during 589 BC – 535 AD (top left) and 1406 – 1988 AD (bottom left), and M1's calcite sublayer thicknesses during 535 – 1406 AD (top right)*

During the period of calcite-dominant varves (535-1406 AD ±7) a significant 44-year cycle is detected (Fig. 3.37). This periodicity is equivalent to North Atlantic sea surface temperature (SST) variability, namely that associated with the Atlantic Multidecadal Oscillation (AMO) and North Atlantic Oscillation (NAO) cyclicity. Chylek *et al.* (2012) find a 45- to 65-year cyclicity within $\delta^{18}O$ isotopes from Greenland ice cores proposed to reflect the AMO, and Rossi *et al.* (2011) identify pluri-decadal cycles of 30-50 years acting to explain 10-20% of winter NAO variability over the last 100 years. At Nar Gölü, moisture supply is partially governed by North Atlantic SST; Dean *et al.* (2015a) relate cooler SSTs with drier conditions through the Holocene, where cooler SSTs suppress cyclogenesis and subsequently weaken the storm tracks which bring winter precipitation across the Mediterranean to Turkey. Synchronous increases to North Atlantic average SSTs (up to +0.5°C warmer) (Bond *et al.* 2001; Thornalley *et al.* 2009) and AMO strength (Ólafsdóttir *et al.* 2013) coincide well with Nar Gölü's calcite-dominant varve deposition and AMO signal detection (FFig. 3.36). Here, warmer North Atlantic SSTs are proposed to enhance cyclogenesis, thus increasing precipitation at Nar Gölü, resulting in the sustained period of fresher limnology. Nar Gölü's calcite mineralogy reflects the increased influence of North Atlantic SST on lake water balance between 535-1406 ±15 AD, such that the AMO signal can be detected. While positive (negative) AMO phases have been associated with increased (decreased) Indian monsoon precipitation (Goswami *et al.* 2006), the AMO expression in Nar Gölü's calcite precipitation may reflect the threshold change to the dominant spring/summer climatology, where storm tracks across the Mediterranean are able to override the dry-continental airflow originating from the Indian monsoon.

Wavelet analysis similarly identifies this shift in multi-decadal cyclicity within the carbonate sublayers' thickness record, and indicates how the power of these spectral signals vary through time (Fig. 3.38). Results suggest that the expression of cyclicity is temporally variable over the period; however, it is important to note that each varve's carbonate sublayer may be composed of more than one carbonate mineralogy, thus displaying differing crystalline morphology. These mixed-carbonate microfacies may inhibit the detection of cycles within the adjacent aragonite- and calcite-only sublayers. Nevertheless, wavelet analysis identifies the shift in multi-decadal cyclicity from M2-3 varves' 62-year cycles to M1 varves' 40-year cycles, associated with tropical- and mid-latitude-derived variability respectively. In addition, the 62- and 130-years cycles' power generally decreases from 589 ±26 BC and 535 ±15 AD. This may reflect the concurrent reduction to Indian Monsoon intensity (Fleitmann *et al.* 2007), consequently suppressing its influence on dry-season intensity at Nar Gölü and aragonite deposition.

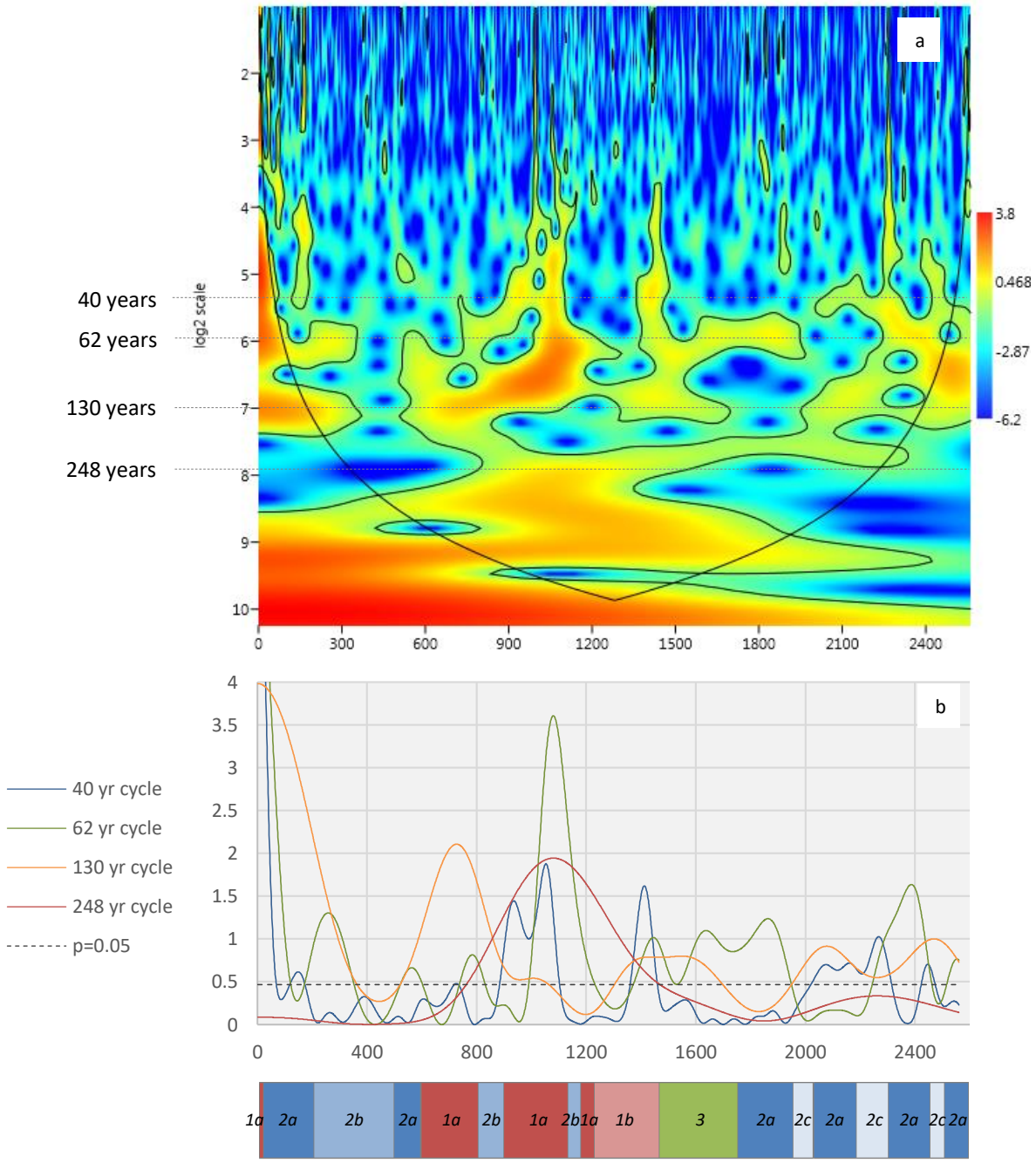


Figure 3.38 *– (a) Morlet wavelet analysis of total carbonate thickness across the 2561 contiguous varves; significant cyclicity (p<0.05) lies within the black line (yellow-red colour). Significant cyclicity can be seen to change through time; the dotted grey lines represent key cycles. (b) Change in the relative power of cyclicity over time; lines above the dotted line are significant (p=0.05 level) at that specific time. Results are displayed alongside the microfacies classification.*

A switch from low latitude- to Atlantic-dominant climatology may also be explained by ITCZ migration (Fig. 3.36). Tropical eruptions, and their general cooling of global temperatures (Schneider *et al.* 2009), have been shown to drive a southward migration of the ITCZ (Ridley *et al.* 2015). Southerly positions diminish Indian monsoon intensity by weakening onshore winds and enhancing cool-water upwelling from the Indian Ocean, thus acting to suppress meridional energy flows northward and dampen the ITCZ's annual migration (Fleitmann *et al.* 2003; Schneider *et al.* 2014). Consequently, periods of weaker monsoons can be prolonged, thus acting to reduce their influence on eastern Mediterranean climatology, and enable Atlantic-derived climatology to drive precipitation variability over the centennial timescale. In addition, the subtropical high pressure belt is known to drive Nar Gölü's dry season climatology (Jones *et al.* 2006). The belt's position is governed by the ITCZ, and a southward migration would subsequently reduce the seasonal propensity of high pressure systems to drive the dry seasons' climatology, over Turkey (see Fig. 3.36).

While NAO's high frequency periodicities (2-15 year) are not identified within Nar Gölü's spectral analysis, its influence on Nar Gölü's contemporary climate, namely winter precipitation, is well established (Touchan *et al.* 2003, 2007). NAO cyclicity is roughly tied to the AMO (Peings and Magnusdottir, 2014), and the increase in AMO strength around 600-1000 AD also occurs in the NAO (Ólafsdóttir *et al.* 2013) (Fig. 3.36). The combined increase in NAO intensity and negative phase frequency, driven by solar activity reductions (Gray *et al.* 2010) during the DACP (ca. 400-700 AD) (Steinhilber *et al.* 2009), are proposed to enhance the influence of Atlantic climatology on Nar Gölü's sediment record, and bring the increased winter precipitation driving calcite deposition.

The later increase to NAO strength inferred during the Little Ice Age (LIA) (1500-1900 AD) (Ólafsdóttir *et al.* 2013) again coincides with a period of calcite precipitation (M2b varves; 1530-1797 AD ±5); however, the presence of aragonite within the M2b varves and moderate isotopic depletion (around -1.4‰ $\delta^{18}O$ VSMOW) suggest limnological freshening is less than that inferred during the LALIA. Global climate models and proxy reconstructions indicate a shift to negative NAO phases during the LIA (Mann *et al.* 2009; Trouet *et al.* 2009), facilitating increasing moisture supply and fresher conditions to Nar Gölü. The presence of various solar minima during this time, such as Maunder (1645-1715 AD), Dalton (1790-1830 AD) and Gleissberg (around 1900) (Steinhilber *et al.* 2009), may also strengthen these negative NAO phases, thus bring fresher lake conditions at Nar Gölü. This inference is supported by the temporal correlation between a peak in calcite thickness and isotopic depletion observed at 1682 ±4 AD with the Maunder minimum. Moreover, the ITCZ's

most southerly extent during the last 2600 years probably occurred through the LIA (Schneider *et al.* 2014). As previously discussed, this could reduce Indian monsoon strength, and its influence on Anatolian dry-season aridity, subsequently permitting Atlantic-derived systems to bring precipitation and fresher conditions to Nar Gölü.

3.4.2.2 Environmental context for societal change

In Cappadocia, climatic instability has been proposed to contribute to long-term societal change through the Holocene (Allcock, 2017). The high resolution timeseries developed here builds on this work, and provides a more nuanced environmental perspective to some key societal turning-points during the Late Holocene.

The establishment and growth of the Byzantine Empire in modern-day Turkey appears to coincide with the abrupt shifts to wetter climatology at 256 ±17 AD (M3 varves) and 535 ±15 AD (M1 varves) (Izdebski *et al.* 2016) (Section 3.3.2.1). While partially offset by the onset and recurrence of plague (discussed below), the wetter climatology brought long-term benefits to agriculture and water supply, and coincided with a widespread expansion of rural settlements (Izdebski *et al.* 2016). This early Byzantine expansion halted during the transitional phase into the mid-Byzantine period around 670-950 AD, associated with the Arab-Byzantine wars and denoted by major socio-political reorganisation (Haldon *et al.* 2014). This period coincides well with net $\delta^{18}O$ enrichment from 660 ±13 AD to 860 ±12 AD (Roberts *et al.* 2016), culminating with the deposition of aragonite-containing M2b varves (848-871 AD ±12) indicative of multi-decadal drought. Since aragonite deposition primarily responds to spring water balance, this particular timing of increased E/P conditions would intensify water availability issues during the extended dry seasons, thus reducing the annual growing seasons' length (Sönmez *et al.* 2005). This probably resulted in severe reductions to the land's carrying capacity, during a period of war and socio-political instability (Izdebski *et al.* 2016). Similar isotope-inferred drying signals have also been interpreted from Lake Tecer (Kuzucuoğlu *et al.* 2011) and Sofular Cave (Göktürk *et al.* 2011) in central and northern Turkey respectively. Such a prolonged aridity excursion could result in effective overpopulation, where a growing society was previously able to depend on the relatively stable, wetter conditions of the previous three centuries (Coombes and Barber, 2005). Coeval reductions to pollen associated with human agriculture, namely cereals, olive, and walnut, have been identified from both Nar Gölü (England *et al.* 2008) and the Dead Sea (Migowski *et al.* 2006; Neumann *et al.* 2007) and indicate land abandonment during this arid period (Izdebski *et al.* 2016). While war and societal re-organisation political primarily define this mid-

Byzantine transition (Izdebski *et al.* 2016), its strong temporal correlation with the climatic record suggests that environmental deterioration may have exacerbated socio-political instability and intensified societal change.

Regional climatology has also been proposed to factor into the sustenance and eventual collapse of the Byzantine Empire. In 1204 AD, the Empire surrendered land and their capital Constantinople fell (Laiou-Thomadakis, 1981). While this has been largely attributed to socio-political instability (e.g. Magdalino, 2008), Nar Gölü's 76-year long period of aragonite deposition (1119-1195 AD ±9) similarly indicates a preceding period of sustained drought; in addition, aragonite deposition consistently increases through the period, exceeding the highest levels since the 6th century AD, thus representing an unprecedented intensification of drought severity over the 76-year long period. The Empire's economy and agricultural extent likely peaked around 1150 AD, responding, in part, to climatic and agriculturally-favourable conditions which prevailed over the preceding ~200 years (Xoplaki *et al.* 2016); increased precipitation inferred from Nar Gölü's calcite-rich mineralogy, and Sofular Cave's isotopic depletion (Göktürk *et al.* 2011), correspond to regional increases in cereal production (Xoplaki *et al.* 2016). Increased resilience to sustained drought episodes, from technological improvements and agricultural surplus from the preceding conditions, may have facilitated this economic growth during the mid-12th century drought (Coombes and Barber, 2005). However, the increasingly unstable socio-political control of the Empire likely exacerbated societal vulnerability to climatic change around ~1150 AD (Xoplaki *et al.* 2016), where the unprecedentedly severe and long period of drought conditions inferred from Nar Gölü may have compounded socio-economy issues. The subsequent fall of Constantinople was likely the culmination of sustained political unrest and climatic-derived reductions to the land's carrying capacity (Xoplaki *et al.* 2016).

Nar Gölü's high resolution hydroclimatic reconstruction also supports White's (2011) hypothesis that central Anatolian drought underpinned the Ottoman Crisis (1580-1610 AD). Following a century-long period of growth and expansion across the eastern Mediterranean, the Ottoman Empire was forced to transport resources from Anatolia to its armies defending the borders. A subsequent series of droughts are proposed to have reduced the land's carrying capacity such that both the general public and military could not be sustained, thus leading to the Celali Rebellions in central Anatolia (White, 2010, 2011). Increases to aragonite thickness and isotopic enrichment centred at 1602 ±4 AD from Nar Gölü's record corroborate this aridity excursion during the intermediate conditions inferred by M2b varve deposition. In particular, varves 1585-6, 1596-7 and 1610 AD (±4) are within the top 5% thickest aragonite sublayers within the M2b period. Major societal reorganisation of the

Ottoman Empire following after this drought-aggravated rebellion and sustained influence of disease. Subsequent drought related to the Maunder Minimum, also identified at Nar Gölü (see above), have been proposed to have delayed/inhibited demographic recovery (White, 2010). Regular and sustained reductions in spring E/P precipitation are likely to increase societal vulnerability to the aforementioned Malthusian checks.

The outbreak of the Mediterranean's two most widespread and deadly plagues (etiological agent *Yersinia pestis*) follow periods of inferred abrupt climatic change to varying extents: the Justinian plague (541-543 AD with repeated outbreaks until ~740 AD) (Haldon *et al.* 2014; Stathakopoulos, 2017) and Black Death (1347-1353 AD with repeated outbreaks until 19th century AD) (Gottfried, 1983; Dean *et al.* 2018). Climate has the ability to increase societal vulnerability to epidemics, primarily through reductions to the land's carrying capacity (Zhang *et al.* 2011b), and promotion of disease vector growth (Stenseth *et al.* 2006; Gage *et al.* 2008).

Generally considered to have evolved in China (Morelli *et al.* 2010), the Justinian plague likely entered into the Mediterranean region via one of the Silk Road trade routes, of which many ran through Turkey (Wagner *et al.* 2014), or via Egyptian grain shipping, with the first recorded outbreak in Constantinople occurring mid-541 AD (Stathakopoulos, 2017). Plague spread velocity has been shown to increase with wetter conditions, associated with the increased rodent and flea prevalence (Parmenter *et al.* 1999; Enscore *et al.* 2002; Xu *et al.* 2011) and flood-induced migration of humans and disease vectors (Xu *et al.* 2014). In arid and semi-arid regions, rodent population growth is also highly sensitive to annual precipitation, where rainfall can explain up to two-thirds of population variability (Previtali *et al.* 2009). Therefore, it is plausible that the preceding, abrupt switch to wetter conditions inferred from Nar Gölü at 535 ±15 AD would favour disease spread, and increase transmission from Anatolia/Levant across the Mediterranean. Moreover, the onset of LALIA's cold conditions has also been linked to decreased agricultural productivity across Europe and the Mediterranean (Büntgen *et al.* 2016) and Anatolia (Haldon *et al.* 2014). Resultant, food shortages would increase human susceptibility to disease (Zhang *et al.* 2011a), where increased dependence on wider land and sea trade networks to provide resources may have further accelerated the spread of the disease (Schmid *et al.* 2015).

The impact and dynamics of the second plague pandemic, or 'Black Death', in the eastern Mediterranean civilisations is less understood (Tsiamis *et al.* 2011). Nevertheless, the Silk Road's role as a pathway of plague into the Mediterranean and Europe means that Turkey's climatology may, in

part, have regulated the successive plague outbreaks. The first, and most significant, outbreak in 1347-1353 AD coincides with a period of relatively fresh conditions at Nar Gölü, as inferred by the calcite-rich M1a varve deposition; moreover, it follows a period of relatively depleted isotopes and thicker calcite sublayers, indicative of notably wet/cold conditions, centred on 1330 ±7 AD. Plague subsequently re-emerges from the Eastern Mediterranean over the next three centuries (Schmid *et al.* 2015), thus coinciding with a cooling/wetting trend inferred from Nar Gölü's mineralogical and isotopic records. Coeval wetter conditions are also inferred from an oxygen isotope record in Gejkar Cave, Iraq (Flohr *et al.* 2017). These cyclical plague outbreaks are sensitive to climatic variability across Central Asia (Stenseth *et al.* 2006) and Europe (Schmid *et al.* 2015). The temporal correlation between plague incidence and eastern Mediterranean climate recorded in the Nar Gölü's varve record again supports a notion of population change facilitated by environmental shifts.

3.5 Chapter summary

Varve sedimentological analysis has provided an annually-resolved archive of hydrological change, capable of identifying key drivers of regional climatology over the last 2,600 years, and from ~9,064 to ~7,630 cal yrs BP ±562. Spectral analysis highlights the influence of Indian monsoon cyclicity on spring E/P variability, and its role in establishing more arid conditions during the early (9064-7630 cal yrs BP ±562) and late Holocene (589 BC -535 AD ±15 and 1406-1988 AD ±6).

During the early Holocene, strong climatic seasonality with relatively fresh limnological conditions are inferred. From 9,064 to ~7,630 ±562 cal yrs BP, a weakening of climatic seasonality and increased E/P conditions may be driven by orbital-derived reductions to NH insolation and its seasonality. During the dry-seasons, the southerly ITCZ migration reduced the Indian monsoon's strength, consequently decreasing dry-season E/P conditions; during the wet-seasons, lower Mediterranean SSTs reduce the strength and frequency low pressure systems moving across Turkey. Within this early Holocene wet period, rapid increases to E/P conditions are associated with the North Atlantic-derived 8.2 ka event. Microfacies analysis suggests these dry conditions prevail for 295 ±3 years at Nar Gölü; much longer than climatic excursions identified from European and western Mediterranean sites (~100-200 years). Here, concurrent increases to the frequency of positive NAO phases and decreases to energy transfer across the Mediterranean basin, via a weakened thermohaline circulation, are proposed to prolong the event's climatic signal in the eastern Mediterranean.

These changes to the annual water balance and climatic seasonality likely influenced the growth and development of agriculture across Anatolia, where Neolithic societies, such as Çatalhöyük display major adaptations to changing environmental conditions.

During the late Holocene, mineralogical switches between aragonite- and calcite-dominant varves, most notably at 535 ±15 AD and 1406 ±7 AD, indicate major shifts to regional hydroclimate. These shifts are proposed to reflect changes to the relative influence of the Indian monsoon- and Atlantic-derived climatology; where stronger monsoons are conducive to enhanced dry-season evaporation at Nar Gölü, and warmer Atlantic SSTs are associated with increased wet-season precipitation. The relative contribution of these systems to Anatolian climatology may be related to ITCZ dynamics, which influences both Indian monsoon strength and the dominance of summer's high pressure

systems over Turkey, and Atlantic SST dynamics, which effects moisture supply to the eastern Mediterranean (notably during the MCA). Increased negative NAO phases may have similarly supported a wetting trend over the LIA, during an otherwise drier period.

These distinct climatological changes drove major changes to the regional water balance. The region's semi-arid, highly seasonal climatology likely exacerbated societal vulnerability to changes in water supply and the land's carry capacity. The high resolution reconstruction of Nar Gölü's palaeohydroclimate is therefore able to portray the environmental context of societal development in Turkey, and identify the conditions which may have intensified socio-political instability.

4. Yaal Chac

This chapter covers the contemporary environmental setting of Nar Gölü, Turkey, before discussing the current understanding of the past climatology through Holocene inferred within the region. Subsequently, the lithology and chronology of sediment records NAR01 and NAR10, cored prior to this PhD research, are detailed. Sedimentological results, primarily relating to the sediments' varve microfacies and geochemical composition, are then presented and interpreted to provide further insight into past environmental change, and its potential influence on societal change.

4.1 Study site and regional climatology

This section outlines the physical setting of Yaal Chac, and discusses the intra-annual climatic and limnological variability which would influence sediment deposition.

4.1.1 Study site

Yaal Chac (20°35'43.33"N, 89°42'40.21"W; 7m asl) is a small cenote (<0.01km^2) in the northwest of the Yucatán peninsula, Mexico (Fig. 4.1). No rivers flow within the Mexican borders of the peninsula owing to the high permeability of the homogenous limestone geology, and the flat topography; the southern Puuc hills represent the only notable change to elevation, reaching ~250m (average elevation of the Yucatán is ~100m). Karstic geomorphology dominates the region, forming cenotes (i.e. sinkholes) and an extensive network of subterranean caves. Formed by this dissolution and breakdown of the calcareous limestone, cenotes are typically hydrologically open lakes, fed by groundwater flowing through this cave network (Pérez *et al.* 2011). Yaal Chac lies within the 'ring of cenotes', an arc of abundant cenotes crossing the northwest Yucatán, marking the impact crater of the Chicxulub meteorite at the Cretaceous-Tertiary boundary (~65.5 million yrs BP) (Perry *et al.* 2009). This catastrophic event is proposed to have increased geological fracturing, thus increasing the limestone permeability leading to intensified dissolution, consequently promoting the formation of these karst lakes (Hildebrand *et al.* 1995).

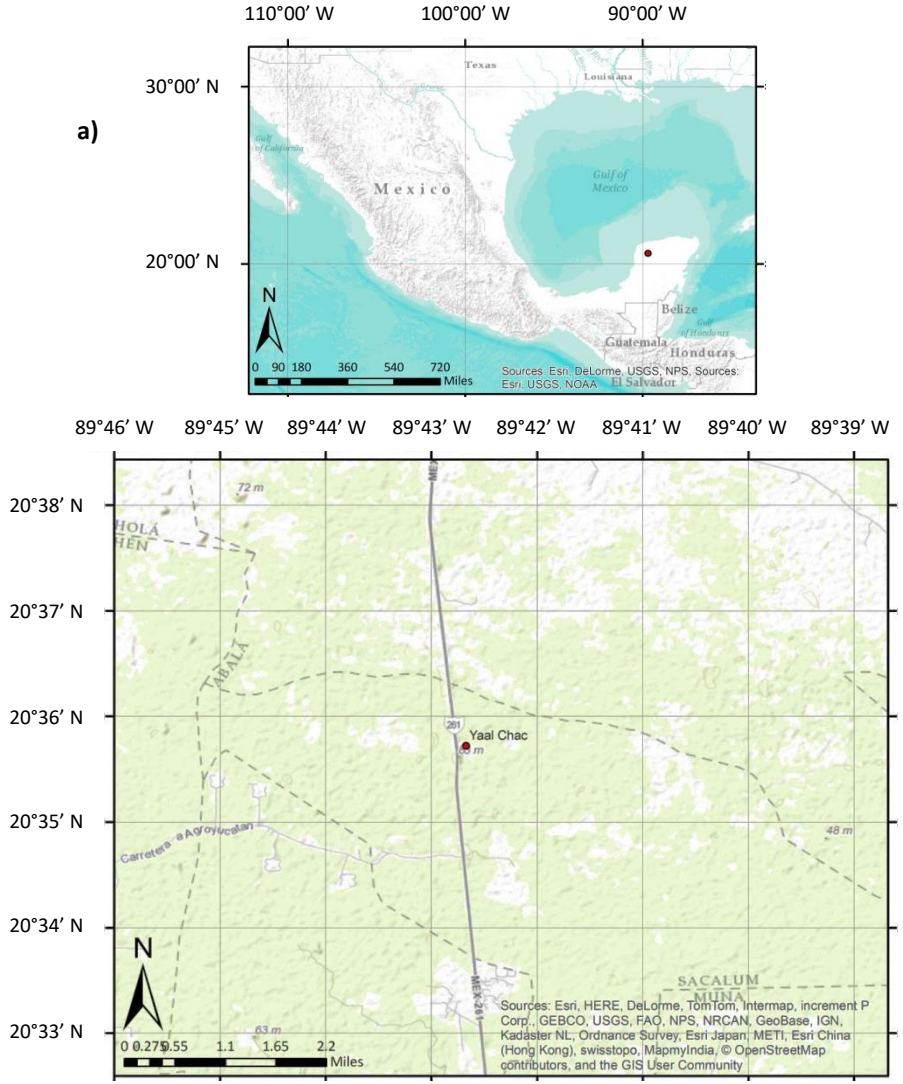




Figure 4.1 – *(a) Yaal Chac's situation within Mexico and the Yucatán Peninsula (top), and a topographic map displaying cenote, Yaal Chac and the surrounding low-lying topography (bottom). (b) Photograph displaying Yaal Chac and the surrounding subtropical dry forest biome vegetation. Yaal Chac is much smaller than Nar Gölü, as its maximum diameter measures 125m, as compared to Nar Gölü's 990m. (Image courtesy of Prof Sarah Metcalfe)*

Contemporary limnological monitoring suggests that Yaal Chac is a closed lake, cut off from the subterranean, interconnected waterways which typically link the other cenotes across the Yucatán. Stable isotope analysis of lake waters shows that Yaal Chac is evaporatively enriched in ^{18}O (annual mean +2.47‰), as compared to Merida's rainfall (-2.24‰) and nearby open systems such as cenotes Chen Ha and Dzibilchaltun (-3.83 and -4.03‰ respectively); in fact, it is more evaporatively enriched than the nearby Aguada X'camaal (+1.11‰), where 'aguada' regionally refers to a hydrologically closed lake (Fig. 4.2).

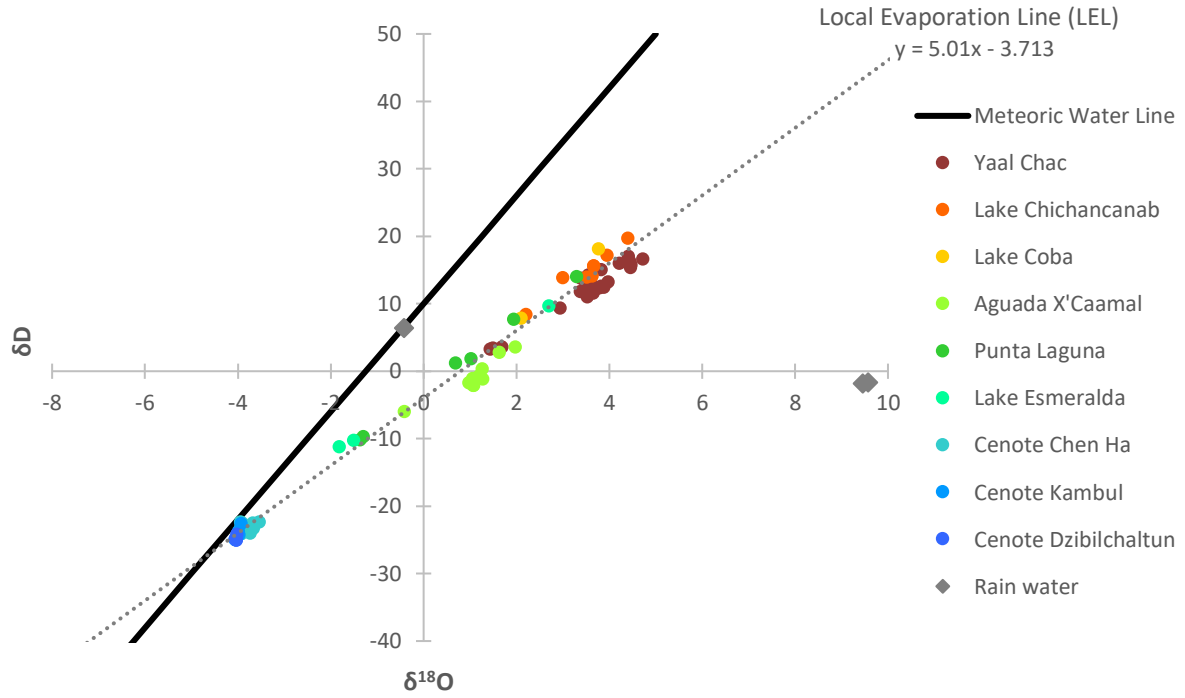


Figure 4.2 *- δD-$δ^{18}O$ isotope plot comparing Meteoric Water Line with water samples taken from lakes across the Yucatán; unpublished data provided by Prof Sarah Metcalfe and undergraduate work, Clapich (2016). Those samples furthest from the Meteoric Water Line suggests evaporative enrichment.*

Limnological monitoring also suggests that Yaal Chac is hypertrophic (Canfield *et al.* 1983); a very high turbidity (~1m transparency) and high total phosphorus concentrations (~44.5 µg L^{-1}) are characteristic of systems with an aguada-like hydrology (Table 4.1) (Schmitter-Soto *et al.* 2002). As measured in January (2009-2015), the lake's surface water displays high concentrations of chloride and sodium ions, likely concentrated by sustained evaporation during winter's dry season. Sediment traps deployed in Yaal Chac identify seasonal calcium carbonate precipitation; similarly identified in Nar Gölü, mineralisation most likely occurs after the dry-seasons' onset, where monitoring in 2016-17 revealed carbonate deposition prior to 10th November in 2017. The homogeneous limestone geology provides an abundant supply of carbonate ions for this endogenic process (Perry *et al.* 2002).

Table 4.1 *– Yaal Chac limnological monitoring data (a) and major ion concentration data (b); data are recorded in January (dry-season) of each year.*

a)

Year	Temp (°C)	O_2 (%)	pH	Alkalinity (mg L)	EC (µS cm^{-1})	Secchi depth (m)	Total P (µg L^{-1})	$\delta^{13}C_{DIC}$ (‰)
2009	27.3	39.9	8.5		5700			
2010	24.5		7.8	398	6374			-10.2
2011	25.2	110.0	8.5	260				
2012								
2013	27.2	26.8	8.0			1.3	54.4	-10.1
2014	22.6		7.9	420		1.3		
2015	27.5		8.2	700	>3999	0.5	34.4	
Average	25.7	58.9	8.1	445	6037	1.0	44.4	-10.2

b)

Year	meq L^{-1}							
	SO_4	Cl	Na	K	Mg	Ca	NO_3	HCO_3
2009	7.9	41.9	38.7	0.9	8.8	1.9		
2010	7.3	73.3	40.7	0.9	9.2	2.0		
2011		36.7						
2012								
2013	10.9	57.3	38.2	1.0	17.8	1.5	0.1	90.0
2014	13.8	35.2	25.5	0.7	23.1	2.1	0.0	14.0
2015	19.0	52.9	35.1	0.9	12.9	5.0	0.0	
Average	11.8	49.5	35.6	0.9	14.4	2.5	0.0	52.0

Monitoring also shows that the lake is thermally and chemically stratified for the majority of the year, where short-term climatic events (e.g. storms) may act to lower the thermocline and increase lake mixing in the upper layers (Fig. 4.3). Lake stratification between December 2016 and November 2017 appears weakest during the winter months, thus corresponding to the site's lowest air temperatures (see below). While lake monitoring most commonly occurs during these winter months, associated with the University of Nottingham's annual undergraduate fieldtrip in January, data suggests that the water column remains thermo-chemically stratified (Fig. 4.3). The lack of evidence displaying benthic activity suggests that sub-oxic conditions likely persist throughout the year, where limnic mixing is likely to be confined to short periods of time.

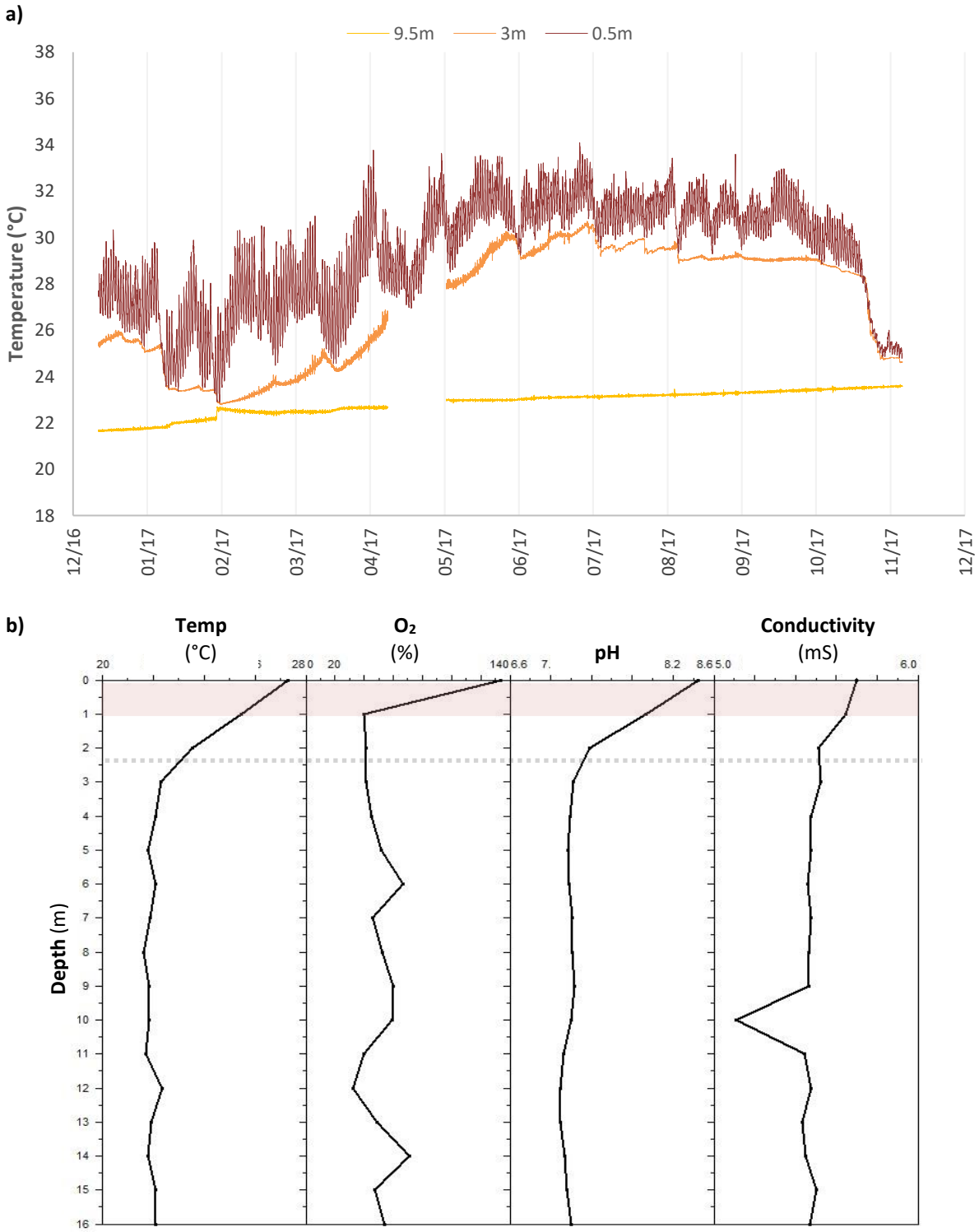


Figure 4.3 *– Yaal Chac's thermal stratification and mixing between December 2016 and November 2017 (a), the convergence of temperature through the water column denotes lake mixing; and the limnological changes through Yaal Chac's vertical profile, as measured in January 2009 (b); photic zone as measured via Secchi-disc measurement (red zone), and the thermo- and chemoclines (grey dotted line) are also displayed.*

Yaal Chac experiences strong climatic seasonality, with a wet-summer and dry-winter climatic regime (Conagua, 2017). Precipitation varies spatially across the Mexican Yucatan; the northwest

coastline is the driest, with annual rainfall increasing along both north-south and west-east gradients (Hodell *et al.* 2005a) (Fig. 4.4a). The nearest weather station, Abala (6.5km northeast of Yaal Chac), receives an average annual precipitation of 1104mm/yr with 81% of this falling between June and October (Fig. 4.4b) (Conagua, 2017). Individual hurricanes can also greatly increase the total precipitation each year in the Yucatán (Hodell *et al.* 2005a). Temperature in the Yucatán remains relatively constant through the year, averaging 26.1°C per year (Pérez *et al.* 2011). It is estimated that 85% of precipitation in the Yucatán is lost via evapotranspiration (Pérez *et al.* 2011). Yaal Chac lies within subtropical dry forest biome vegetation; secondary dry forest and agricultural land surround the lake.

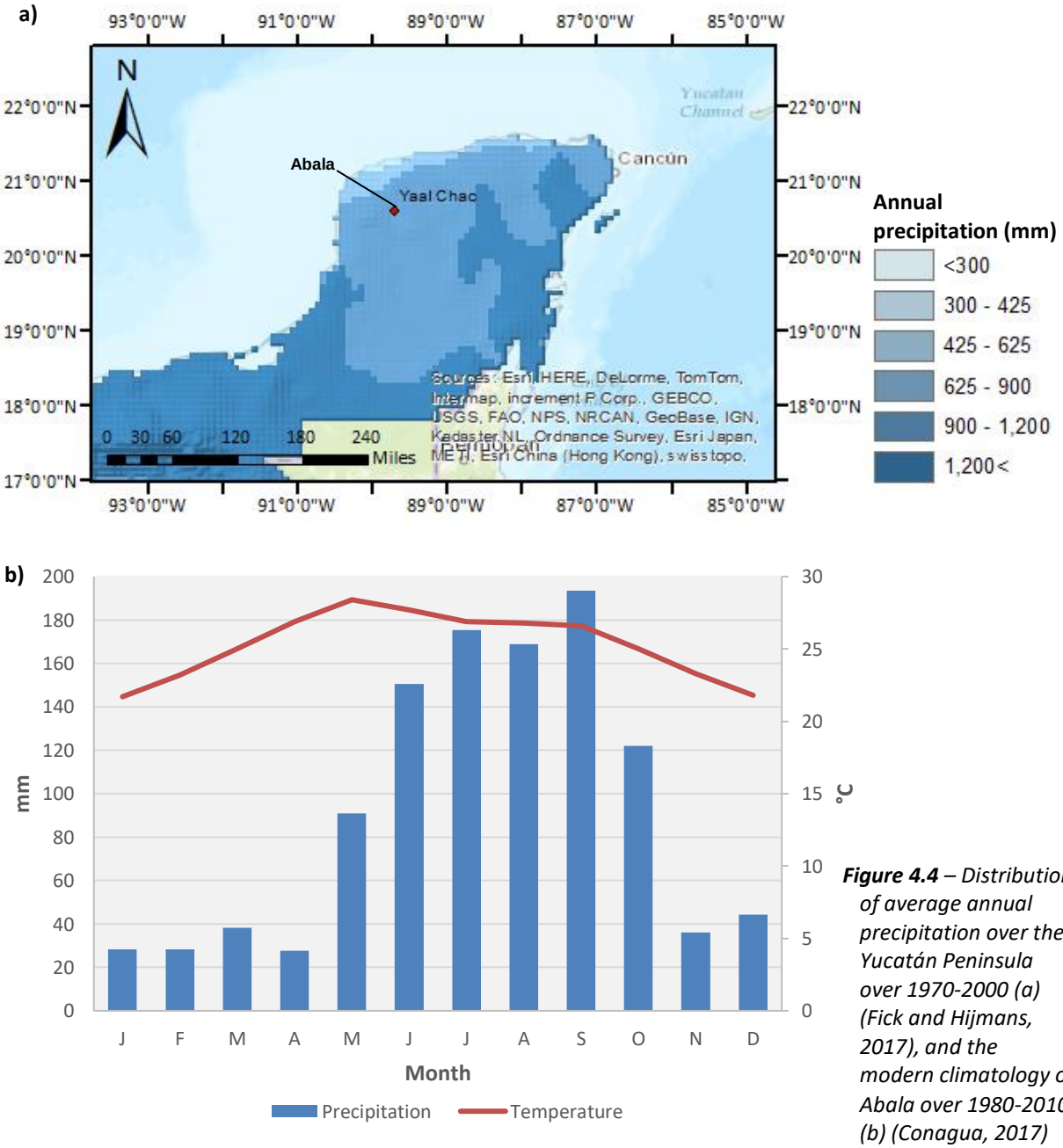


Figure 4.4 *– Distribution of average annual precipitation over the Yucatán Peninsula over 1970-2000 (a) (Fick and Hijmans, 2017), and the modern climatology of Abala over 1980-2010 (b) (Conagua, 2017)*

No prior research has been directly published from Yaal Chac. However, annual undergraduate fieldtrips from the University of Nottingham have facilitated the collection and preliminary interpretation of wide-ranging limnological data: from modern lake water chemistry, to diatom-inferred reconstructions of palaeolimnology.

4.1.2 Regional climatology

A lake's sedimentary record is a product of numerous environmental processes. Climatology often determines the relative influence of each process on sediment deposition and preservation, and when these environmental processes vary seasonally, varves may be deposited. In order to understand the limnological processes driving sediment deposition in Yaal Chac, the contemporary climatology, and its drivers, at both sites must be considered. Understanding how each region's climatology changed through the Holocene will further provide the environmental context to sedimentological change. This section outlines the Yucatán Peninsula's contemporary climatology (Section 4.1.2.1) and its Holocene variability (Section 4.1.2.2).

4.1.2.1 Contemporary climatology

Mexico's climate displays high spatial variability, with conditions between the northwestern and southeastern regions commonly opposing one another (Metcalfe *et al.* 2000). Figure 4.5 depicts this spatial variability of annual temperature and precipitation across Mexico, displaying this general pattern of warmer, wetter conditions over the Yucatán Peninsula, and the relatively cooler, drier conditions in north Mexico; the broad pattern of temperature and rainfall variability correspond well with the country's topography.

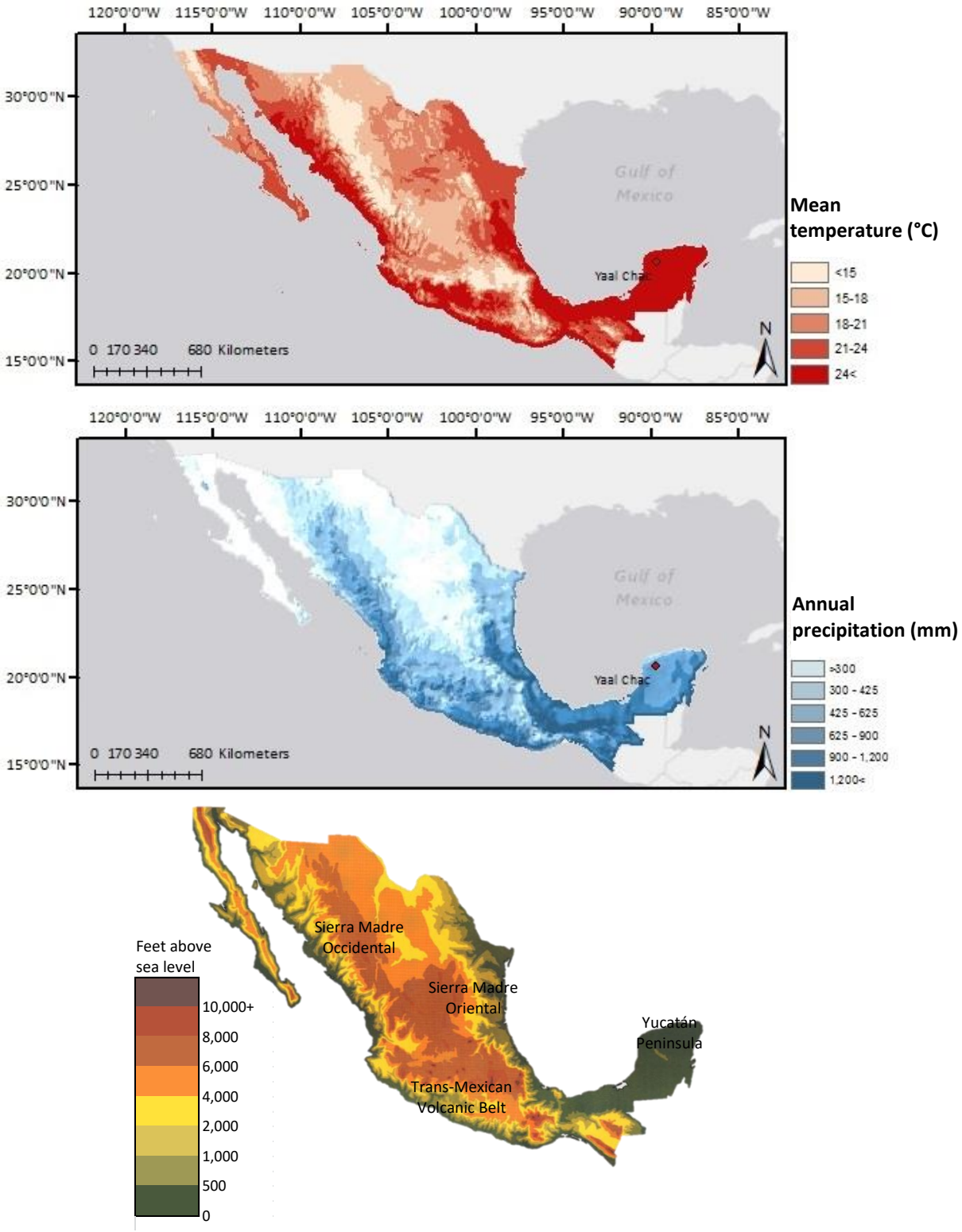


Figure 4.5 – *Mean temperature (top), annual precipitation (middle) and topography (bottom) of Mexico; climatic data interpolated from monthly data recorded from weather stations between 1960-90 (Fick and Hijmans, 2017), and topographic map of Mexico, in feet above sea level [adapted from University of Texas State, 1975]*

The low-lying land of the Yucatán Peninsula displays a highly seasonal climate, with a wet-summer and dry-winter climatic regime. Seasonality is predominately driven by the seasonal migration of the ITCZ (Metcalfe, 1987; Hodell *et al.* 2005a; Lane *et al.* 2009) (Fig. 4.6).

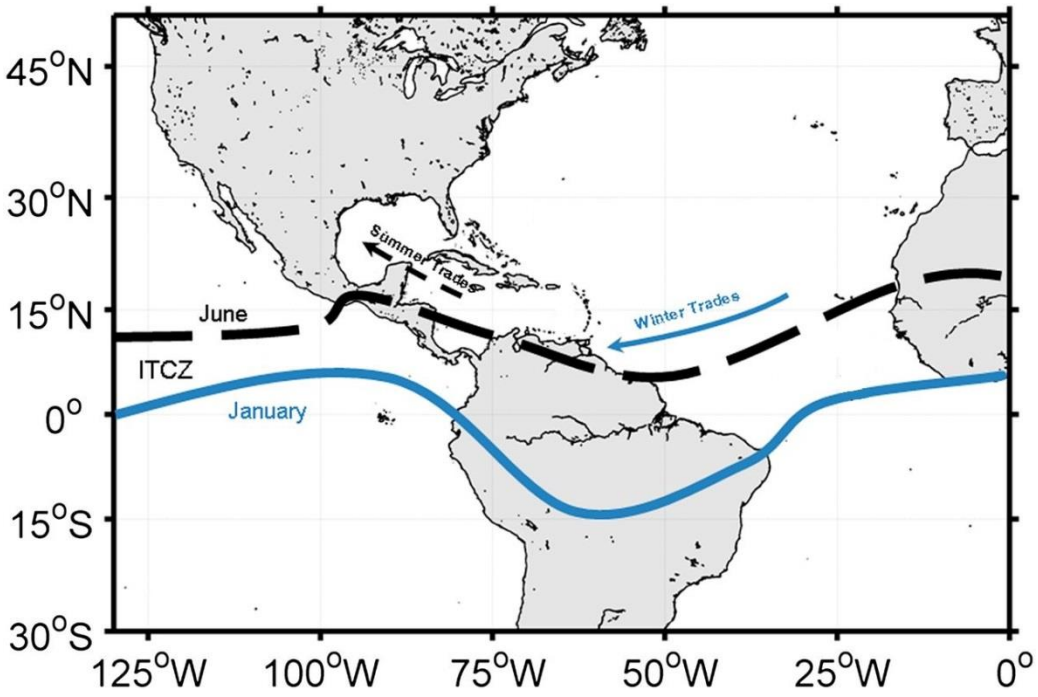


Figure 4.6 – *Map displaying the average summer (black, dashed line) and winter (blue, solid line) ITCZ position (adapted from Taylor et al.2012)*

During the summer months, the ITCZ migrates north. This migration of Hadley Cell circulation displaces the subtropical high pressure belt, enabling easterly trade winds bring warm, moist air in from the Gulf of Mexico, driven along the south side of the Bermuda high pressure system. This summer air flow primarily drives the wet-season climatology (Metcalfe *et al.* 2000, 2015). Seasonal rainfall may be further increased via enhanced atmospheric convection over the Gulf of Mexico and Caribbean Sea, within periods of relative increases to the ITCZ's northern summer extent (Romero-Centeno *et al.* 2007). This northerly extent of ITCZ migration, and hence wet-season climatology, varies inter-annually. The sea surface temperature of the Atlantic and Pacific Oceans influences the intra-annual migration of ITCZ, where warmer temperatures are associated within more northerly summer extents (Hu and Feng, 2002). Over the Yucatán Peninsula, increased wet-season precipitation is associated with increased ITCZ summer latitudes.

The ITCZ-derived intensification of easterly winds and atmospheric convection are conducive to heavy precipitation events over the Yucatán Peninsula leading to around 70-80% of annual precipitation (1100mm) falling within the summer months, from June to September (White and Hood, 2004). During the late-summer/early winter months (August-November), tropical storms and hurricanes may form in the Atlantic and move west across the Peninsula, greatly increasing a specific year's annual rainfall (Boose *et al.* 2003; Hodell *et al.* 2007).

High atmospheric pressure differences between the Gulf of Mexico and the eastern Pacific lead to the formation of the Tehuantepec jet that runs southward across Mexico (Steenburgh *et al.* 1998; Romero-Centeno *et al.* 2007). The Tehuantepec jet weakens during the summer months, due to the reduction of pressure differences between the west Atlantic and east Pacific, yet can be seen to strengthen briefly during July/August facilitated by intensification and westward migration of the Azores-Bermuda high (Romero-Centeno *et al.* 2003). This mid-summer resurgence of Tehuantepec jet strength, and associated increase in northerly trade wind strength, can be seen to temporarily decrease precipitation, commonly known as the 'Mid-Summer Drought' (MSD) or 'canícula', throughout southern and eastern Mexico. This leads to a bimodal distribution of both summer rainfall (Magaña *et al.* 1999; Curtis, 2004) and formation of tropical cyclones over the Caribbean; however, tropical cyclone formation displays a distinct minima during July, when the SSTs rapid cool due to wind-driven upwelling of deeper cold water (Inoue *et al.* 2002; Graves *et al.* 2012). Rauscher *et al.* (2008) recognise that the MSD is a highly regionalised phenomenon with its impacts affecting only: western side of Central America, the Yucatan Peninsula, the Caribbean islands (Cuba), and eastern Mexico. However, Magaña *et al.* (1999) suggest that the relative intensity of the MSD is greatest along the Pacific coast of southern Mexico and diminishes gradually towards the Caribbean coast.

During the winter months, the ITCZ, and consequently the subtropical high pressure belt, migrates southward. Associated with the descending branch of Hadley Cell circulation, this high pressure belt moves over the Yucatán Peninsula, thus favouring atmospheric subsidence, conducive to dry conditions (Shindell *et al.* 2006; Wauchope, 2014); this seasonal dominance of stable high pressure anticyclones also blocks the movement of depressions, and hence moisture, across the Peninsula. Any dry-season rainfall over the Yucatán Peninsula is typically derived from the local effect of 'nortes' – the outbreak of cold polar air from North America, which brings cold fronts over the Gulf of Mexico, picking up moisture, and subsequently driving winter rainfall over the Yucatán (Metcalfe *et al.* 2015). Within the dry-season, enhanced rainfall (20-60mm), cooler temperatures (<22°C) and

strong winds (>80km/h) are associated with nortes; while each outbreak may effect weather conditions for several days, multiple nortes may occur throughout the season, particularly between November and February (Herrera-Silveira, 1996).

Various atmospheric patterns can also be seen to drive climatic variability on different temporal scales; namely the El Nino Southern Oscillation (ENSO), Atlantic Multidecadal Oscillation (AMO) and, to a lesser extent, the North Atlantic Oscillation (NAO).

ENSO pertains to the sub-decadal variability to atmospheric and SSTs differences along the equatorial Pacific Ocean. Contrasting 'El Niño' or 'La Niña' periods prevail when temperature differences across the Pacific are exceeded (see Philander, 1989); for example, Trenberth (1997) proposes that an El Niño (La Niña) phase should be classified when SST anomalies in the eastern Pacific exceed (drops below) 0.4°C for over five months. Using this classification, Trenberth (1997) further suggests that in the last 50 years El Niño conditions prevail for 31% of the time, while La Niña events prevail for 23%. ENSO's variability is orbitally driven via changes to solar insolation (Moy *et al.* 2002) and it proves to be a major driver of Mexican climate at an annual and decadal scale (Kennett *et al.* 2012; Salas *et al.* 2014; Jones *et al.* 2015). While the precise mechanisms in which ENSO influences Yucatán climatology remain contentious, its phase is known to influence position and seasonal migration of the ITCZ; where an El Niño warm oscillation typically moves the ITCZ southward over the tropical Pacific (Haug *et al.* 2001) thus bringing drier conditions to North/Central America (Zebiak *et al.* 2015). Moreover, El Niño oscillations commonly lead to a meridional distribution of summer precipitation anomalies, with decreased rainfall over the Yucatán Peninsula, associated with the weakening of moist easterlies (Magaña *et al.* 2003; Amador *et al.* 2006). These warm oscillations also reduce the frequency of tropical cyclone formation due to the lowering of jet level over the Caribbean thus increasing wind shear (Magaña *et al.* 2003).

Acting on a longer, multidecadal time scale, the AMO pertains to the multi-decadal cycle in Atlantic SSTs with a ~0.4°C range (Rossi *et al.* 2011; Chylek *et al.* 2012). A warm (cold) AMO phase is associated with increasing (decreasing) hurricane intensity and frequency (Elsner, 2006; Trenberth and Shea, 2006; Poore *et al.* 2009) thus bringing heavy rain events to the Yucatán Peninsula. Caron *et al.* (2015) further propose that the AMO phase influences the role of other controls on hurricane activity: during a warm phase, the effect of insolation and atmospheric dust variation on hurricane activity is greater, while during a cold phase, large atmospheric circulations including the NAO exert a greater influence. The AMO phase is also proposed to affect ITCZ position, with Fensterer *et al.*

(2012) inferring drier conditions in Cuba to be driven by cool AMO phases that lead to a southward migration of the ITCZ, consequently enhancing atmospheric subsidence over Cuba. This inference supports Mendoza *et al.* (2007), who suggest that the most severe droughts in the Yucatán during the 500 years coincide with cold AMO phases. The AMO has further been proposed to influence Indian Monsoon rainfall anomalies; during an AMO warm phase, the summer ITCZ positions migrates further north thus strengthening onshore winds and uplifts (Zhang and Delworth, 2006; Luo *et al.* 2011). As alluded to above, this teleconnection could similarly influence Turkish climate (Jones *et al.* 2006).

The NAO (discussed in Section 2.2.1) is also proposed to affect Yucatán climate to a lesser extent, and is probably linked with the AMO (Kerr, 1997, 2000). In the Caribbean, George and Saunders (2001) find that ~46% of tropical north Atlantic wind speed variability can be attributed to fluctuations to the NAO during the winter months. They propose that this can consequently affect precipitation over the following year due to changes to sea surface temperature driven by wind-derived ocean upwelling and enhanced latent heat flux; Yucatán and Central American annual precipitation decreases when the NOA is in its positive phase thus driving stronger trade winds. However, Jury *et al.* (2007) recognise that a positive NAO index is likely to increase atmospheric moisture uptake associated with a warmer tropical ocean, leading them to postulate that a positive NAO generally leads to increased rainfall during the late summer without the lag proposed by George and Saunders (2001); however, they acknowledge that this link is unstable and is not a dominant climatic control over the Yucatán Peninsula and Central America, with a diminishing influence moving west from the Caribbean.

4.1.2.2 Holocene climate change

The apparent Holocene climatology of the Yucatán Peninsula is outlined here. Again, early, mid, and late Holocene periods are primarily delineated according to the region's general climatic conditions and dynamics, as inferred from palaeoclimatic records. These notable climatic changes roughly coincide with the Holocene's formal subdivisions; slight discrepancies between these chronologies are somewhat unsurprising given the large distance between the Yucatán Peninsula and the palaeoclimatic records, from Greenland and India, used to define the Holocene's subdivisions (see Walker *et al.* 2018). Figure 4.7 displays the location of Yaal Chac (1) and other key palaeoclimatic records discussion within Section 4.1.2.2.

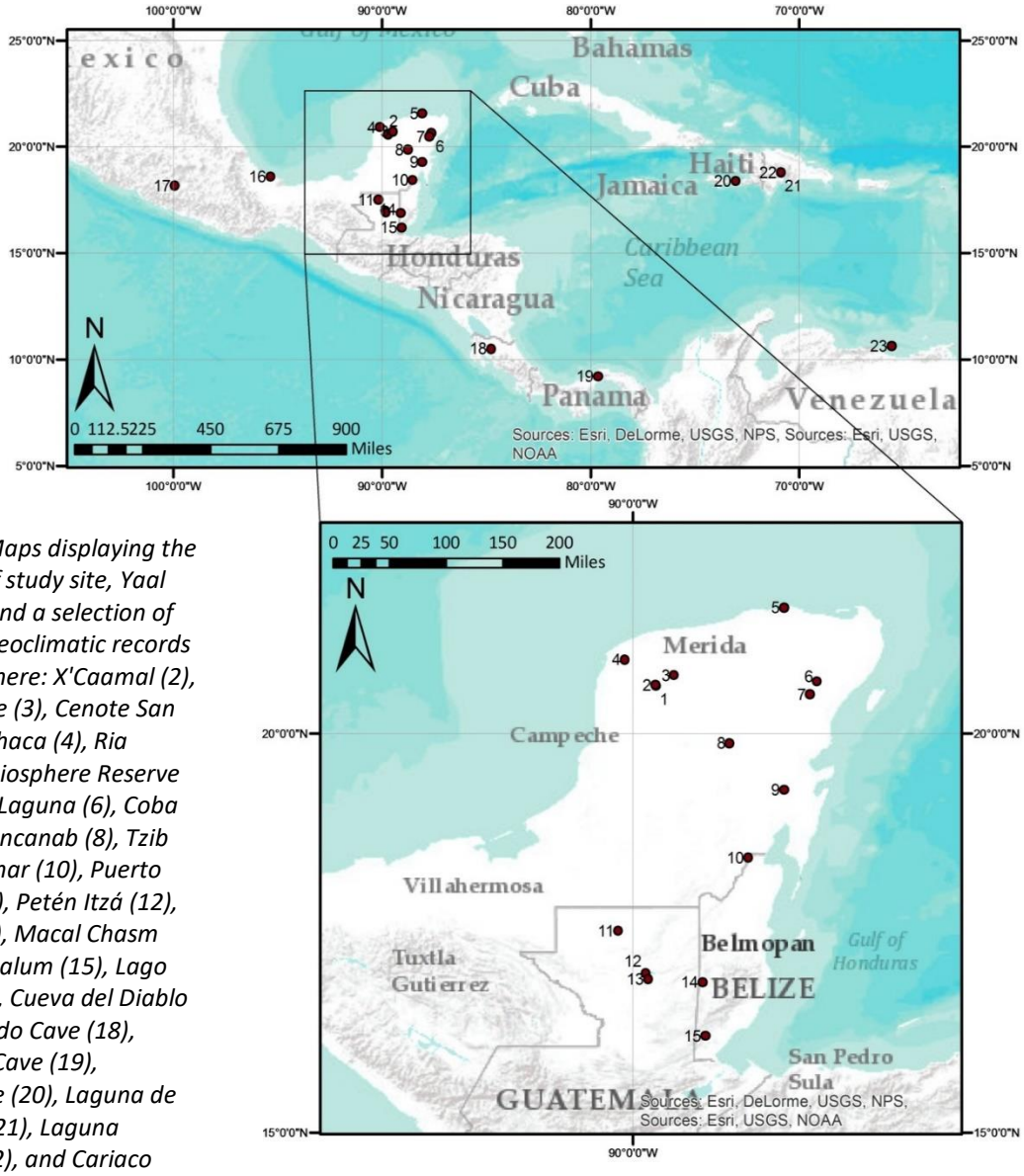


Figure 4.7 *– Maps displaying the location of study site, Yaal Chac (1), and a selection of other palaeoclimatic records discussed here: X'Caamal (2), Tecoh Cave (3), Cenote San José Chulchaca (4), Ria Lagartos Biosphere Reserve (5), Punta Laguna (6), Coba (7), Chichancanab (8), Tzib (9), El Palmar (10), Puerto Arturo (11), Petén Itzá (12), Quexil (13), Macal Chasm (14), Yok Balum (15), Lago Verde (16), Cueva del Diablo (17), Venado Cave (18), Chilibrillo Cave (19), Miragoane (20), Laguna de Salvador (21), Laguna Castilla (22), and Cariaco Basin (23)*

i) Early Holocene / Greenlandian Stage (11,700 – 8,200 cal yrs BP)

At the Pleistocene-Holocene transition (ca. 11,700 cal yrs BP), Yucatán climate is inferred to be significantly colder and drier than present (Curtis *et al.* 1998). Lake Petén Itzá's seismic profile suggests that lake level was around 56m shallower at 11,250 cal yrs BP than present day (Anselmetti *et al.* 2006), with pollen records indicating a vegetational composition of sparse temperate thorn scrub associated with colder environments (Hillesheim *et al.* 2005).

Relatively little is known about the precise environmental response to the onset of Holocene conditions. Sediment deposition within earliest lake records is typically associated with increased sea-levels (Khan *et al.* 2017), which act to elevate groundwater levels across the Yucatán's low-lying, porous limestone (see section 2.4) (Metcalfe *et al.* 2000; Brenner *et al.* 2002); only Petén Itzá's record (Hillesheim *et al.* 2005) extends through the entirety of the early Holocene, where its large, inland basin likely remained comparatively independent of groundwater elevation. While Petén Itzá's record provides a key insight into the climatology of the earliest Holocene, depositional records from other key lacustrine records start from: 10,400 cal yrs BP at Lake Chichancanab, Mexico (Hodell *et al.* 1995); 10,300 cal yrs BP at Lago Paixban, Guatemala (Wahl *et al.* 2016); 8,700 cal yrs BP at Lago Puerto Arturo, Guetemala (Wahl *et al.* 2014); and 8,000 cal yrs BP at Lake Coba, Mexico (Whitmore *et al.* 1996).

In combination with sea-level rise, lake infilling and establishment across the Yucatán Peninsula is attributed to wet early Holocene conditions (Brenner *et al.* 2002). While high $\delta^{18}O$ values with sedimentary records are interpreted to reflect these initially low lake levels (e.g. Hodell *et al.* 1995; Curtis *et al.* 1998), Petén Itzá's palynological record indicates a rapid vegetation response to climatic warming and wetting, where mesic forest became established 11,250 cal yrs BP and remain stable until at least 8,300 cal yrs BP (Hillesheim *et al.* 2005). However, this glacial-interglacial climatic transition was not smooth, with limnological proxies, such as carbonate deposition and oxygen isotope ratios, from Lake Petén Itzá portraying centennial-scale dry events at 11,200, 10,900, 10,700 and 10,400 cal yrs BP (Hillesheim *et al.* 2005). Subsequently, Petén Itzá's mineralogical record displays an abrupt cessation of gypsum precipitation at ~10,300 cal yrs BP, associated with the net increase to lake level driven by wetter climatic conditions (Hillesheim *et al.* 2005; Hodell *et al.* 2008). The charcoal and pollen record of the southern lowland's Lake Quexil, next to Petén Itzá, also indicates the formation of full tropical forest by 10,200 cal yrs BP, associated with the steadily increasing temperature and annual rainfall (Leyden, 2002). From Lake Miragoane, Haiti, a lake

largely independent of sea-level change, isotope-inferred lake level similarly increases from 10,000 cal yrs BP, associated with wetter climatic conditions (Hodell *et al.* 1991).

These early Holocene wet conditions have been linked to a northerly ITCZ position (Haug *et al.* 2011), driven by the early Holocene's high insolation seasonality (Berger, 1978). Regional lacustrine isotope records typically correlate with the Cariaco Basin's Fe and Ti concentrations, where the inwash of these allogenic elements is controlled by the ITCZ's mean latitude (Haug *et al.* 2001). As previously discussed (Section 2.2.1), northerly ITCZ positions displace the subtropical high pressure belt north, thus facilitating the flow of easterly moist, low pressure systems across the Peninsula and intensifying atmospheric convection, both increasing the region's annual precipitation. The ITCZ is inferred to reach its most northerly mean latitude around 9,800-8,000 cal yrs BP (Haug *et al.* 2001); consequently driving the wettest Holocene conditions in the Yucatán Peninsula (Hillesheim *et al.* 2005). This rainfall maxima corresponds to peak abundance of tropical forest taxa in the southern lowlands at 8,600 cal yrs BP (Islebe *et al.* 1996) and the development of an extensive littoral zone around Lake Miragoane, Haiti at 8,200 cal yrs BP (Hodell *et al.* 1991).

ii) Mid-Holocene / Northgrippian Stage (8,200 – 4,200 cal yrs BP)

Around 8,200 cal yrs BP, gypsum precipitation within Petén Itzá's lacustrine record indicates centennial-scale dry period (Hillesheim *et al.* 2005). This climatic anomaly is associated with the 8.2 cal ka BP event (Alley *et al.* 1997).While this climatic oscillation is not generally identified within the available palaeoclimatic records from the Yucatán Peninsula, possibly due to the poor chronological control during the early Holocene, it may be detected from other Central American sites; for example, peak $\delta^{18}O$ values from Venado Cave's speleothems in Costa Rica signify reduced annual rainfall (Lachniet *et al.* 2004a), and a hiatus in speleothem growth from Cueva del Diablo in southwest Mexico also suggests that the 8.2 ka event reflects the driest conditions of the entire Holocene (Bernal *et al.* 2011).

Following the 8.2 ka BP climatic anomaly, a mid-Holocene transition from wetter to drier conditions is widely identified across the Peninsula (Metcalfe *et al.* 2000; Carrillo-Bastos *et al.* 2010; Wahl *et al.* 2014, 2016; Aragón-Moreno *et al.* 2018), marking the start of the Northgrippian Stage (Fig. 4.8); however, the timing and pace of this shift appears highly variable. This high degree of temporal uncertainly is partly associated with many records' poor chronological control, where the limestone

geology of the Peninsula often inhibits the acquisition of precise age-estimates (Brenner *et al.* 2002). Following the wet early Holocene conditions, a drying trend is typically identified from sites between 8,000 and 3,000 cal yrs BP (Curtis *et al.* 1998; Wahl *et al.* 2016; Aragón-Moreno *et al.* 2018). This transition generally coincides with a period of global Rapid Climate Change (RCC) proposed by Mayewski *et al.* (2004), where they suggest that these rapid changes tend be detectable globally and are typically associated with increased aridity in the tropics.

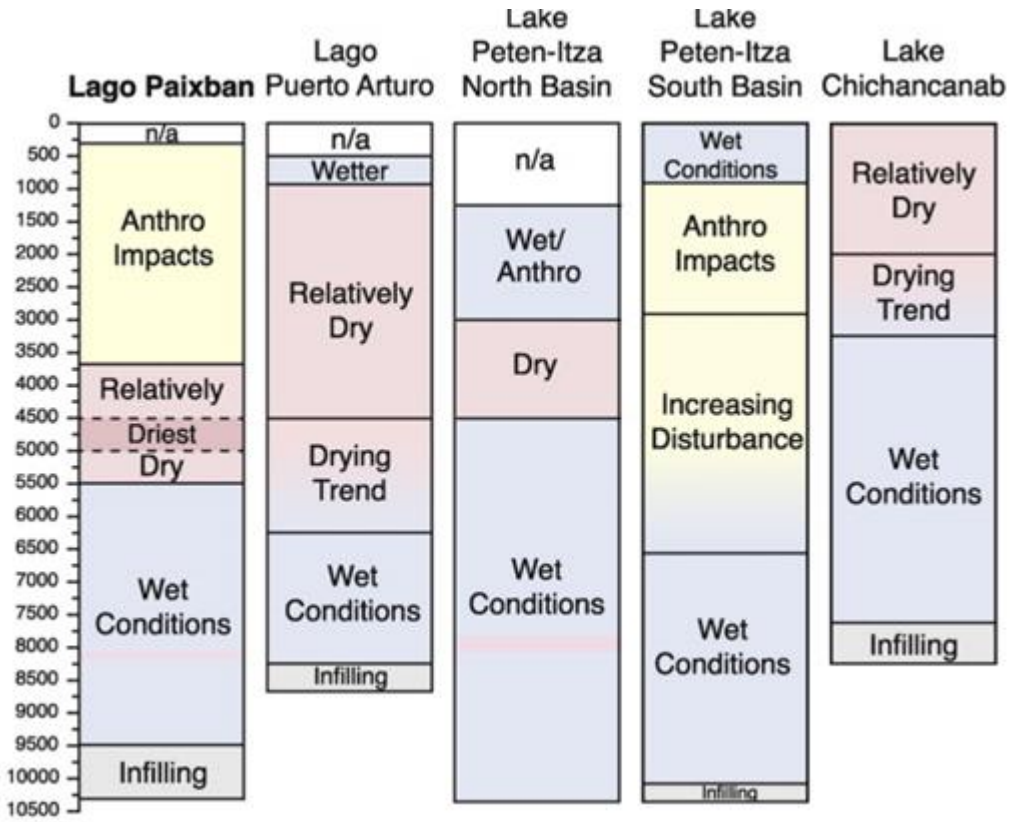


Figure 4.8 *- The general timing and dynamics of climatic change as inferred from lacustrine systems within the Yucatán Peninsula. Climatic periods inferred from Lago Puerto Arturo (Wahl et al. 2014), Lake Petén Itzá, North Basin (Hillesheim et al. 2005; Mueller et al. 2009), Lake Petén Itzá, South Basin (Curtis et al. 1998), and Lake Chichancanab (Hodell et al. 1995). [Taken from Wahl et al. 2016]*

This climatic shift is associated with the orbitally-driven, southerly migration of the ITCZ (Harrison *et al.* 2003; Wahl *et al.* 2016; Aragón-Moreno *et al.* 2018), enhancing the influence of subtropical high pressure belt on regional climatology. McGee *et al.* (2014) suggest that this ITCZ-driven mid-Holocene transition at 6,000 cal yrs BP can be detected worldwide, with southern hemisphere records detecting the complementary increase in precipitation, such as the isotope record from Botuvera Cave, south Brazil (Wang *et al.* 2007). The onset of isotopic depletion from terrestrial

gastropods from Lake Chichancanab, Yucatán (Hodell *et al.* 1995), ostracods from Lake Petén Itzá, Yucatán (Curtis *et al.* 1998), and speleothem calcite from Cueva del Diablo, southwest Mexico (Bernal *et al.* 2011) and Venado Cave, Costa Rica (Lachniet *et al.* 2004b) generally starts from around 8,000-6,000 cal yrs BP. From Lago Puerto Arturo, the $\delta^{18}O$ record suggests that aridification started slowly at first from 6,000 cal yrs BP to 4,500 cal yrs BP, before accelerating from 4,500 cal yrs BP until the Medieval Climatic Anomaly (around 900 cal yrs BP) (Wahl *et al.* 2014). Elsewhere, isotopic records similarly display the onset of aridification from 6,000 cal yrs BP from coral in the southern Caribbean Sea (Giry *et al.* 2013) and from ostracods in Lake Miragoane, Haiti (Hodell *et al.* 1991).

Vegetational composition also displays a strong response to this climatological transition through the mid-Holocene, typically transforming from semi-evergreen forest to the dry tropical forest, as seen during the present-day (Leyden, 2002; Carrillo-Bastos *et al.* 2012; Aragón-Moreno *et al.* 2018). Additionally, from Lake Tzib, low-medium stature, swamp forest taxa, indicative of a humid environment with seasonal flooding, persists until ~6,500 cal yrs BP (Carrillo-Bastos *et al.* 2010).

The millennial scale migration to ITCZ position, the related weakening of insolation seasonality (Berger, 1978), may also reduce the climate's wet-dry seasonality (Wahl *et al.* 2016; Aragón-Moreno *et al.* 2018). Consequently, more mesic conditions between ~5,600-3,650 cal yrs BP have been proposed to initially drive the expansion of tropical forest, where continued reductions to annual rainfall subsequently favoured the growth of dry tropical forest (Aragón-Moreno *et al.* 2018). From Petén Itzá, tropical forest taxa also dominates the vegetational composition until 4,500 cal yrs BP, increasingly switching to dry tropical vegetation thereafter (Curtis *et al.* 1998; Mueller *et al.* 2009), and from El Palmar, a vegetation switch from closed forest to more open mangroves at 4,600 cal yrs BP also indicates more dry, saline conditions (Torrescano and Islebe, 2006). This combined influence of rainfall amount and seasonality on vegetation composition may additionally cause ambiguity into the dynamics of the Holocene's drying trend, and delay the vegetational response to climatic drying.

This mid-Holocene transition may also be associated with the role of ENSO on Yucatán climatic variability. During the early-mid Holocene, Shin *et al.* (2006) discuss the importance of permanent La Niña conditions during the early and middle Holocene in maintaining low sea surface temperatures (SST) of the eastern Pacific, thus enhancing Pacific-Atlantic temperature gradients and leading to the strengthening of easterly trade winds (also see Wahl *et al.* 2014). As alluded to above, these stronger trade wind may enhanced moisture to the Peninsula. As the ITCZ continues to migrate south through the mid-Holocene (Haug *et al.* 2001), the relative influence on centennial-millennial scale climatic

variability decreases; meanwhile, as the strength and intensity of El Niño warm oscillations increases, particularly from 7,000 cal yrs BP (Sandweiss and Richardson, 1996; Barron *et al.* 2005; Tsonis, 2009), its relative influence of Yucatán climatic variability increases (Wahl *et al.* 2016; Aragón-Moreno *et al.* 2018). Moy *et al.* (2002) suggest that El Niño event frequency increased throughout the Holocene until 1,200 cal yrs BP, where it began to decline towards to present-day levels. Bernal *et al.* (2011) propose that the onset of ENSO, and associated reduction in precipitation, caused the "partial decoupling" of southern Mexican climate with the Atlantic Ocean.

iii) Late Holocene / Meghalayan Stage (4,200 cal yrs BP – Present day)

While this drying trend from ~6,000 cal yrs BP is commonly identified in the palaeorecords, climatic inferences from 4,500 cal yrs BP onward appear to diverge. Some propose climate drying to continue (or even accelerate) at this time, while others infer a relative short return to wetter conditions. These inferences tend to be dependent on their spatial location, with northerly Yucatán sites leaning towards the latter. The climate prior to the transition around 4,500 cal yrs BP is proposed to be wetter than present day, according to higher percentages of wet-indicative pollen taxa *Brosimum alicastrum* and *Fabaceae* types (Torrescano and Islebe, 2006).

In the southern lowlands, the long-term drying trend generally persists, where $\delta^{18}O_{carbonate}$ values from Lago Puerto Arturo continue to increase after 4,500 cal yrs BP (Wahl *et al.* 2014). Similarly, increasing *Pyrgophorus sp* and *Assiminea sp* $\delta^{18}O_{carbonate}$ value and decreasing tropical forest pollen taxa from Lake Tzib indicates a sustained drying trend (Carrillo-Bastos *et al.* 2010). Lake Petén Itzá's lake level is inferred to fall by at least 7m due to the increase E/P ratio; this is indicated by the deposition of shallow water sediment facies which only form in water shallower than 23m, where today's water level at the coring site measures 30m deep (Mueller *et al.* 2009). Furthermore, Lake Petén Itzá's (Mueller *et al.* 2009) and Lake Silituc's (Torrescano-Valle and Islebe, 2015) palynological and sedimentological record similarly displays the drying transition with the reduction in forest taxa; here, the deforestation can be attributed to climate change, rather than anthropogenic land clearance, due to the complete lack of *Zea mays* pollen indicative of human activity and agriculture (Leyden, 2002; Mueller *et al.* 2009).

However, dry conditions are not ubiquitously found within the Yucatán's palaeoclimatic records post-4,500 cal yrs BP. As alluded to above, northern Yucatán sites typically display a wetter climatic signal until a much later transition to drier climates around 3,500-2,500 cal yrs BP (Leyden, 2002).

The palynology record from Ria Lagartos Biosphere Reserve (RLBR), northern Yucatán, displays high proportions of taxa characteristic of stable wet, tropical forest environments, such as *Brosimum alicastrum*, *Moraceae* and *Ficus sp,* until 3,500 cal yrs BP (Aragón-Moreno *et al.* 2012), and Lake Chichancanab's record displays notable isotopic depletion within both terrestrial gastropods and ostracods inferring wetter conditions until around 3,000 cal yrs BP (Hodell *et al.* 1995).

Palaeorecords commonly depict varying climatic signals depending on the site and proxy used; while overall the relatively consistent drying trend prevails throughout the Holocene (see Hodell *et al.* 1995), the timings and extent of major climate changes are not well agreed upon, and this issue appears particularly prominent towards and during the late Holocene. One such transition inferred from various studies is at around 3,500 cal yrs BP when climatic drying is commonly inferred to have intensified. Lake Chichancanab's $\delta^{18}O_{carbonate}$ records depicts a notable enrichment (Hodell *et al.* 1995), while concurrent drying is also inferred from a steady decline in the wet indicator species of forest taxa from the RLBR record, as drier taxa *Conocarpus sp*. and *Rhizophora sp*. increase (Aragón-Moreno *et al.* 2012). Palynological records from Lake Miragoane, Haiti, also portray a similar story with the cessation of tropical forest expansion around 3,200 cal yrs BP at the onset of increased aridity (Higuera-Gundy *et al.* 1999). Maximum rates of calcite deposition in Lake Petén Itzá at 3,500 cal yrs BP also suggest that drought was greatest at this time (Mueller *et al.* 2009).

Another centennial-scale period of enhanced aridity is inferred around 2,500 cal yrs BP from Lake Chichancanab (Hodell *et al.* 2001), and 2,200 cal yrs BP from Punta Laguna (Hodell *et al.* 2007). With some of the highest $\delta^{18}O$ values of the last 3,500 years, this ~750-year aridity excursion is may reflect the Holocene's driest conditions (Hodell *et al.* 2007). However, the Punta Laguna $\delta^{18}O$ record alternatively indicates the prevalence of wetter conditions *prior* to this aridity shift at 2,200 cal yrs BP. This period appears to display high climatic variability, yet Punta Laguna's alternative narrative prior to the 2,500 cal yrs BP shift may reflect its northerly location within the Peninsula, where the generally drier climatology would increase its sensitivity to changes in precipitation (Hodell *et al.* 2005b). Nevertheless, records predominately show a drying trend prior to 2,500 cal yrs BP.

While many of the discussed records suggest that the drying trend continued, and even peaked at 1,700 cal yrs BP (e.g. Hodell *et al.* 2001), a short term return to relatively wetter conditions prior this dry phase has been inferred. Carrillo-Bastos *et al.* (2010) detect this phase of wetter conditions around 3,000 cal yrs BP as indicated by changes to pollen assemblage and isotopic ratio from Lake Tzib, northern Yucatán, and Akers *et al.* (2016) equally detects wet conditions from 2,600 to 2,000

cal yrs BP from Macal Chasm's isotopic record. Isotopic depletion from Lake Salpetén, next to Petén Itzá, peaks from 2,400 to 1,900 cal yrs BP further indicates wetter conditions and higher water level in the lowlands (Rosenmeier *et al.* 2002), thus corresponding to the concept that Pre-Classic (pre- AD 200; 1,750 cal yrs BP) wet conditions formed the perennially wet marsh environment which saw the rise of the first Mayan settlements in the Petén region (Hansen *et al.* 2002). Kennett *et al.* (2012) further supports this idea of wet conditions (as inferred from the isotopic record of Yok Balum speleothem) being favourable to cultural expansion and permitted the Mayans to fully establish prior to the Pre-Classic Abandonment phase.

The aforementioned Pre-Classic Abandonment pertains to climatic deterioration around 1,750-1,650 cal yrs BP (AD 150-250) which is believed to have contributed to the Mayan abandonment of major settlements within the Yucatán Peninsula (Gill, 2001; Webster, 2002; Haug *et al.* 2003; Carrillo-Bastos *et al.* 2010; Wahl *et al.* 2014). The $\delta^{18}O$ records display a short period of increased drought frequency and duration from Lake Chichancanab dated AD 90-230 (Hodell *et al.* 2001), and from Lago Puerto Arturo dated AD 150-250 (Wahl *et al.* 2014). Changes to pollen and $\delta^{18}O$ records from the nearby northern Yucatán site, Lake Tzib, from AD 100 are similarly interpreted to suggest dry conditions lasting up to 100 years (Carrillo-Bastos *et al.* 2010). Webster *et al.* (2007) find increased isotopic values from Macal Chasm's speleothems, Belize, at AD 140, and propose this dry phase represents the first major Mayan depopulation event caused by climate. Haug *et al.* (2003) theorise that the Pre-Classic abandonment was derived from a more southerly mean position of the summer ITCZ thus reducing the wet season's precipitation, while Pacific SST reconstructions suggest the presence of a strong El Niño state persistence during this time (Moy *et al.* 2002), thus causing drying conditions in the Yucatán.

Starting at 1,700 cal yrs BP (~250 AD), the Classic Period refers to the peak period of Mayan civilisation, and is characterised by their highest population levels, greatest extent of power, and development of a complex social-economic system (Chase and Chase, 1985). The period itself is well researched due to the complex relationship between the natural environment and human civilisation, with records displaying numerous climatic changes within the Mayan's predominant extent of the Yucatán Peninsula, Belize and Northern Guatemala. However, owing to the issues with radiocarbon dating (due to the hard water effect) and lack of high-resolution climatic records, the precise climatic history, and also its possible effect on Maya society, remains widely debated (Aimers and Hodell, 2011).

Following the Mayan Pre-Classic abandonment (1,750-1,650 cal yrs BP; AD 150-250), conditions are inferred to return to wet conditions (Haug *et al.* 2003; Carrillo-Bastos *et al.* 2010). A high resolution $\delta^{18}O$ record from Yok Balum's speleothems, Belize, depicts a return to wetter conditions for much of the Classic Period; this increased precipitation would have refilled water storage systems thus facilitating a widespread expansion of Mayan civilisations (Kennett *et al.* 2012). Innovation of canal systems and man-made reservoirs around Tikal, Guatemala, further promoted population growth, with the infilling of these water systems also indicating increased precipitation during the Classic Period (Scarborough *et al.* 2012). From Macal Chasm, in the southern Mayan lowlands, a multi-proxy speleothem study also displays a return to wetter conditions for much of the Classic Period until around AD 750 (Akers *et al.* 2016), with the Cariaco Basin's Ti record further indicating wet conditions favourable to the Mayans from 1,400-1,200 cal yrs BP (550-750 AD) (Haug *et al.* 2003). Within this wetter period**,** Akers *et al.* (2016) also identify a short aridity phase dated between 1416-1357 cal yrs BP (534-593 AD), known as the "Mayan Hiatus", according to the temporary cessation of monuments and population throughout the Mayan civilisation and luminescence minima from Macal Chasm's speleothems (also see Medina-Elizalde *et al.* 2010; Kennett *et al.* 2012). From Punta Laguna, Curtis *et al.* (1996) and Hodell *et al.* (2007) also detect this Hiatus during 1,450-1,350 cal yrs BP (500-600 AD) according to an isotope-inferred increased E/P ratio. The Punta Laguna $\delta^{18}O$ record represents a long climatic history, with isotopic measurements taken from inorganic carbonates, ostracods and gastropods all displaying a complementary trend of drying throughout the Classic Period (Curtis *et al.* 1996; Hodell *et al.* 2007); however, it is important to note that hard-water error again limits the precision of the record's chronology and thus the dates of change the authors infer.

Nevertheless, these records suggest that the aridity inferred around 1,750 cal yrs BP (200 AD) represented a short phase following which the climate returned to wetter conditions for much of the Classic Period, at least until a severe aridity phase at the end of the Classic period starting from around 1,200 cal yrs BP (750 AD) (discussed later). However, this mid-Classic return to wetter conditions is not universally recognised. The Punta Laguna record suggests that the aridity maxima found at the end of the Classic Period lies at the end of a much longer dry period spanning from 1,750-850 cal yrs BP (200-1100 AD) (Curtis *et al.* 1996; Hodell *et al.* 2007). These data correlate well with Hodell *et al.*'s (1995) initial study on Yucatán climate which similarly identify the longer aridity trend; Curtis *et al.* (1996) display that the highest isotopic values from Punta Laguna of the last 3,500 years all lie within the Classic Period (Fig. 4.9) (also see Hodell *et al.* 2007). These inferences further correspond to a decline in tropical forest vegetation from Ría Lagartos Biosphere Reserve, Northern

Yucatán, from 1,550 cal yrs BP (400 AD) thus indicating a drier climate until 720 cal yrs BP (1230 AD); for example, the tropical forest taxa *Ficus sp.* decreased from 62% to 8% within this multi-century aridity phase proposed (Aragón-Moreno *et al.* 2012). Curtis *et al.* (1996) infer that the wettest years were only equal to precipitation conditions before and after this prolonged dry period, with conditions progressively deteriorating over time towards the widely accepted drought maxima during the Terminal Classic Period. However, the high-resolution isotopic record form Yok Balum perhaps displays the best climatic signal with drying initiating during the mid-Classic Period at 1,310 cal yrs BP (640 AD) before reaching the severe aridity period post-1,200 cal yrs BP (post-750 AD) (Kennett *et al.* 2012). Moreover, the intensification of agriculture during the Classic Period (Dunning *et al.* 2002; Luzzadder-Beach *et al.* 2012) has been interpreted to be a response of the desiccation trend pre-AD 750 to maintain food security (Douglas *et al.* 2015).

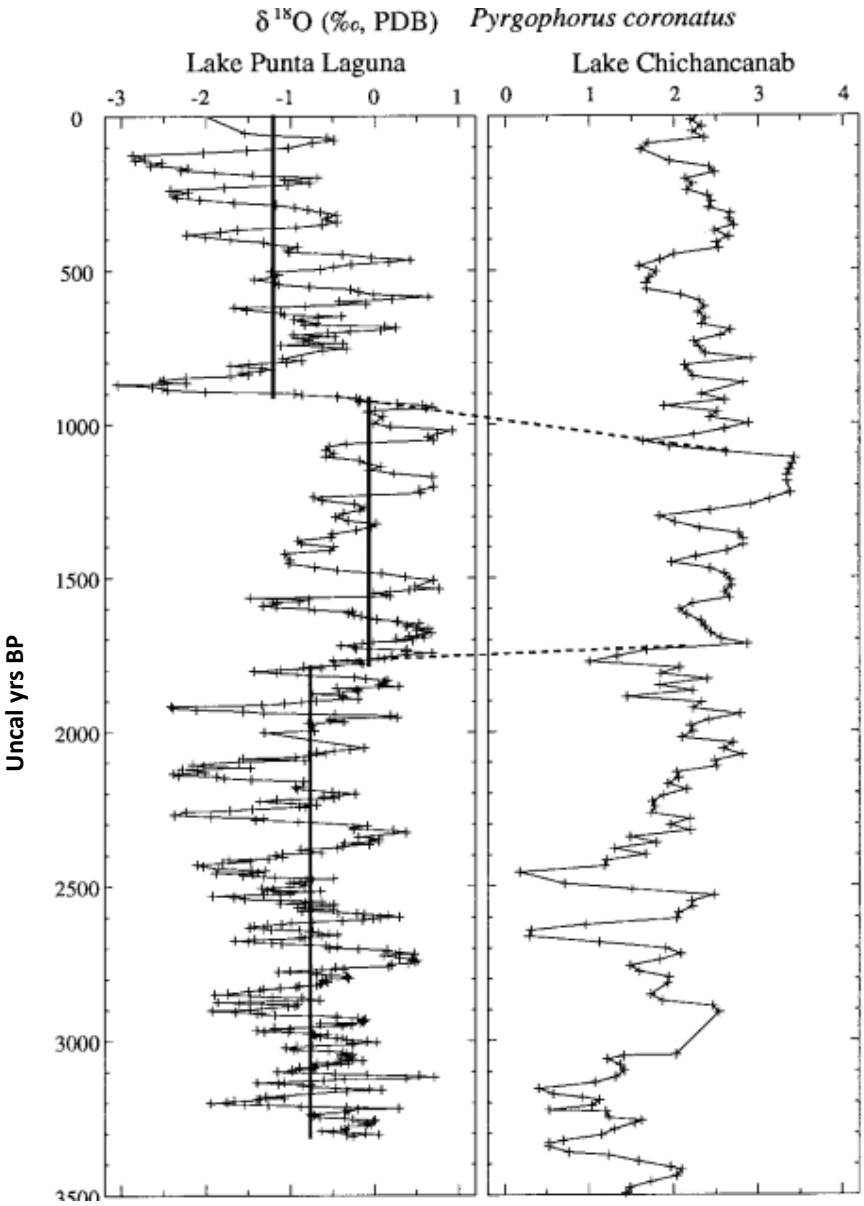


Figure 4.9 *– Pyrgophorus coronatus $\delta^{18}O$ records from Lake Punta Laguna and Lake Chichancanab, indicating a longer period of aridity throughout the entire Classic Period. (Taken from Curtis et al. 1996)*

A significant dry period between 1,200 and 950 cal yrs BP (750 and 1000 AD) has been detected across the Yucatán Peninsula, and has been widely been linked, to varying extents, to the decline of the Mayan civilisation, particularly in the southern lowlands, over the Terminal Classic Period (TCP) between 1,200-1,050 cal yrs BP (750-900 AD) (Hodell *et al.* 1995, 2001, 2005b; Curtis *et al.* 1996; Haug *et al.* 2003; Lane *et al.* 2009; Carrillo-Bastos *et al.* 2010; Medina-Elizalde *et al.* 2010; Aragón-Moreno *et al.* 2012; Kennett *et al.* 2012; Douglas *et al.* 2015; Akers *et al.* 2016); the hypothesis, that climate change contributed to Mayan decline, was first proposed in the early 1980s (Gunn and Adams, 1981) yet the extent to which drought caused the Mayan demise remains subject to debate (Aimers, 2007; Aimers and Hodell. 2011; Kennett *et al.* 2012; Carleton *et al.* 2014).

The theory of a climate-driven Mayan collapse gained significant support when Hodell *et al.* (1995) inferred, utilising oxygen isotopes and sedimentology from Lake Chichancanab, that the most arid phase of the last 7,200 years was between 1,150-950 cal yrs BP (800-1000 AD); Hodell *et al.* (2005b) further used gypsum precipitates to refine this inference by suggesting the presence of two 100-year-long arid phases between 1,180-1,080 cal yrs BP and 1,030-850 cal yrs BP (770-870 AD and 920-1100 AD), with relatively moister conditions prevailing between phases. Complementary findings from other palaeoclimatic studies have since built this concept of a multi-phase period of increased droughts during the TCP. For example, a more recent high resolution speleothem record from Yok Balum cave, Belize, supports the inference of two multidecadal arid phases, with similar dates of 1,130-1,080 cal yrs BP and 930-850 cal yrs BP (820-870 AD and 1020-1100 AD) (Kennett *et al.* 2012).

While defining distinct periods of increase aridity can be open to interpretation (in terms of absolute dating and the magnitude of change required to be defined as a 'dry period'), other studies commonly suggest the presence of sharp drought maxima, usually around three peaks between 1,150-950 cal yrs BP (800- 1000 AD), defining the centre of multidecadal phase of increased drought frequency and severity (Curtis *et al.* 1996; Haug *et al.* 2003; Medina-Elizalde *et al.* 2010). Despite chronological imprecision preventing the reliable dating of the climatic dynamics throughout the Yucatán, Curtis *et al.* (1996) postulate the presence of distinct drought maxima at 1120, 970 and 900 cal yrs BP (830, 980, and 1050 AD) using oxygen isotopes from Punta Laguna. Medina-Elizalde *et al.* (2010), using isotopic records taken from the Tecoh cave's high resolution speleothems, expand on this concept of distinct aridity maxima during the TCP with the detection of 8 peaks, with each drought lasting between 3-18 years long between 1,150 and 1,000 cal yrs BP (800 and 950 AD), thus resulting in the most severe drought of the past 1.5 ka; precipitation, inferred from the $\delta^{18}O$ of

carbonate material, is proposed to be 36-52% lower than present day levels of ~1150mm/yr (Fig. 4.10). Triple oxygen and carbon isotope data from Lake Chichancanab similarly indicate 41-54% reduction to annual rainfall through the TCP (Evans *et al.* 2018). This Figure is in line with the IPCC's projected 30-50% reduction in rainfall by the end of the century (Pachauri *et al.* 2014), and displays the potential severity of future climate change. Kennett *et al.*'s (2012) isotopic record from Yok Balum further supports a 40% reduction in rainfall during the TCP.

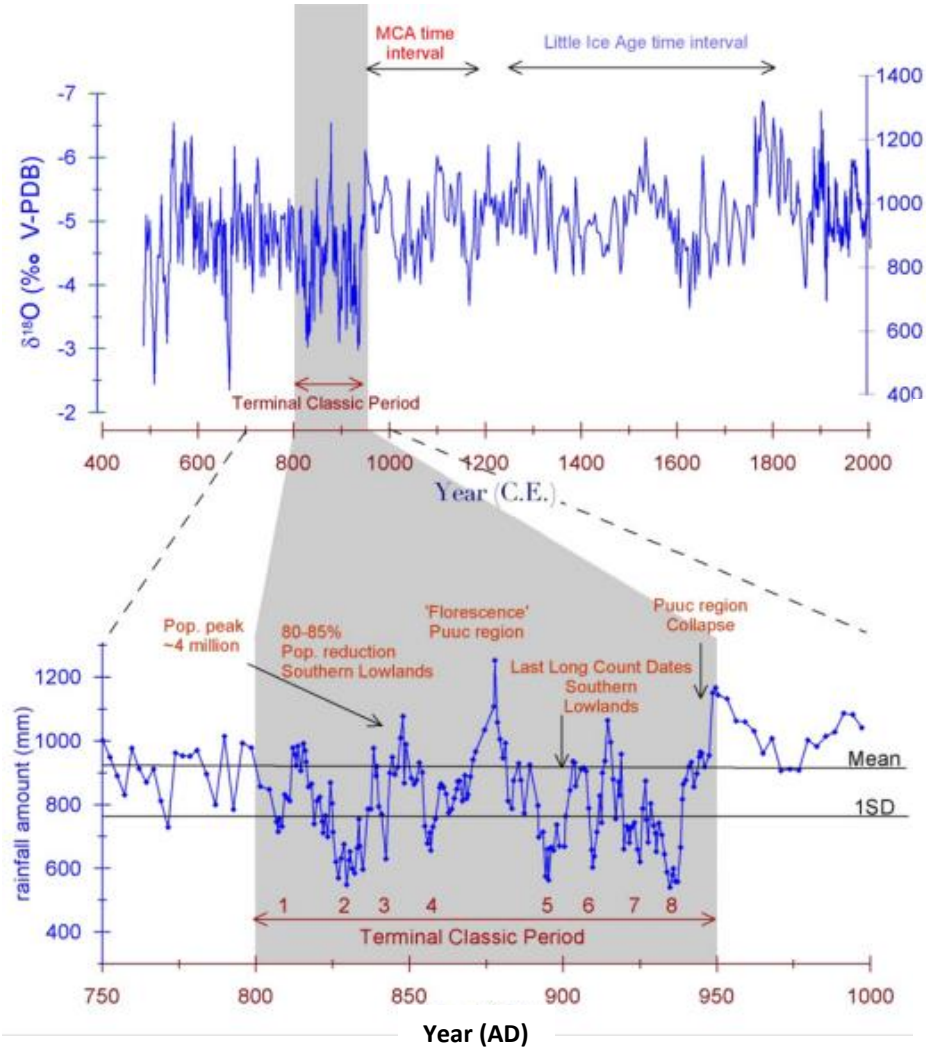


Figure 4.10 *– (top) $\delta^{18}O$ record from Tecoh Cave speleothem, northwest Yucatán. (bottom) Isotope-inferred precipitation during the TCP (coloured in grey). Numbers refer to each of the short drought phases during a period of increased aridity as inferred by Medina-Elizalde et al. (2010). (Taken from Medina-Elizalde et al. 2010)*

Elsewhere, aridity circum-Caribbean around 1,150-950 cal yrs BP (800-1000 AD) is also inferred using stable isotope records from Guadeloupe (Beets *et al.* 2006), and Puerto Rico (Nyberg *et al.* 2001). Similarly, synchronous aridity detected in northern Africa (Street-Perrott *et al.* 2000), further leads Nyberg *et al.* (2001) to postulate that increased aridity was driven by a strong positive state of NOA and/or increased atmospheric high pressure associated with a stronger Hadley circulation. Cold phases of the AMO can lead to a southward migration of it ITCZ thus increasing the prevalence of

the high pressure belt over the Yucatán, with Mendoza *et al.* (2007) finding AMO phase and drought occurrence to be strongly linked. However, solar forcing is proposed to be the overarching driver of climatic change throughout the last 2,000 (Hodell *et al.* 2001; Maasch *et al.* 2005). Mayewski *et al.* (2004) identify this period of time (1,150-950 cal yrs BP; 800-1000) as another period of RCC worldwide. Overall, it appears that the Yucatán climate during the TCP displayed high levels of spatial-temporal variability in precipitation, yet was drier on average with distinct periods of significant drought.

As a result of initial studies, and supported by later findings, Gill (2001) hypothesised that this multi-decadal period of severe aridity lead to the declines in Mayan populations, where reductions to the land's carrying capacity primarily drove socio-political instability. This theory remains the underlying mechanism of climatic-driven Mayan 'collapse'. Archaeological evidence is crucial for linking the Mayan demise with the climatic change inferred above, and can provide important insights into the environmental change. During the TCP, cities were abandoned progressively, typically starting in the southern lowlands and moving north through the Yucatán, with larger cities generally more resilient to political and/or climatic change thus remaining inhabited until later within the period (O'Mansky and Dunning, 2004). Furthermore, short returns to wetter conditions between drought maxima are proposed to prolong the Mayan 'collapse' and led to the spatial variability in city abandonment according to their sensitivity to environmental change and ability to retain water (Hodell *et al.* 2005b). For example, isotope-inferred precipitation increases briefly during 1,090-1,060 cal yrs BP (860-890 AD) within the Puuc region, northern Yucatán Peninsula (Medina-Elizalde *et al.* 2010), thus facilitating population expansion. The subsequent drought maxima, at the time of greatest agricultural demand due to peak population levels, is likely to have contributed to regional abandonment, political disruption and warfare (Carmean *et al.* 2004). This additionally exemplifies the complexities when attributing climate change to societal impact – there is rarely a single driver/control of collapse, with most variables exacerbating others (Aimers, 2007).

Southern lowland Mayan sites in the Petexbatún region, northern Guatemala, saw the first evidence of abandonment, with a near complete collapse by 1,120 cal yrs BP (830 AD) (Dunning and Beach, 2004; Peterson and Haug, 2005). However, isotopic carbon records of deer bones in the region, used as a proxy for diet, suggest that maize cultivation and hence agricultural productivity remained successful during the time of regional abandonment (Emery *et al.* 2000); this implicates the dominance of socio-politically factors leading to cultural collapse in the southern lowlands, and possibly suggests an over-emphasis on either the extent of drought or the extent it affected the

culture. However, Petexbatún's agricultural systems may have been more resilient to climatic changes, as compared to those in the northern Yucatán, due to the greater implementation of land terraces, which manage soil erosion thus maintaining food production to a growing population (Dunning and Beach, 1994; Douglas *et al.* 2015). Douglas *et al.* (2015) infer that desiccation during TCP was most intense in the southern lowlands compared to the northern lowlands, as inferred from Lake Salpeten and Chichancanab respectively. By utilising, hydrogen isotope compositions of n-alkanoic acids, controlled primarily by precipitation and evapotranspiration, they propose a reduction in precipitation of up to 60% of contemporary conditions in the southern lowlands, and a lesser reduction in the north leading to similar, low annual precipitation across the Yucatán.

The northern lowlands maize pollen counts, from Lake Chichancanab, saw a substantial decrease during the TCP, as compared to levels seen earlier in the Classic period, while pollen of native taxa displayed no significant change in abundance before or during the TCP (Leyden, 2002); here, the author suggests that this pattern reflects a natural resilience of native taxa to cyclic drought events, unlike the cultivated maize which could not have succeeded during the TCP due to the crop's narrow ecological niche. Leyden (2002) proposes that, in the northern Yucatán, the TCP's increased aridity would have led to widespread maize crop failures and consequently caused a collapse in the Mayan social framework due the culture's heavy dependence on its harvest. The last archaeological evidence of carved monuments within the central Mayan lowlands is dated around 1,061-1,041 cal yrs BP (889-909 AD) further coinciding with a drought maximum inferred by Medina-Elizalde *et al.* (2010).

Following the end of the TCP, many palaeorecords indicate a significant increase in precipitation, thus coinciding with the start of the Medieval Climate Anomaly (MCA) (Curtis *et al.* 1996; Haug *et al.* 2003; Hodell *et al.* 2005b, 2007; Medina-Elizalde *et al.* 2010; Aragón-Moreno *et al.* 2012; Wahl *et al.* 2014). The period is characterised by La Niña-type conditions (Mann *et al.* 2009; Metcalfe *et al.* 2015), and is driven by increased insolation and northward migration of the Gulf Stream and Kuroshio currents (Goosse *et al.* 2012). While MCA generally lasts between 1,050-650 cal yrs BP (900-1300 AD) in northern hemisphere climatic records (Goosse *et al.* 2012), chronological imprecision typically hinders the precise dating of this climatic phase within the Yucatán Peninsula.

High-resolution studies infer an earlier return to warmer, wetter conditions at 1,020-1,000 cal yrs BP (930-950 AD) (Medina-Elizalde *et al.* 2010). At this earlier time, isotope-inferred precipitation is proposed to increase to near present day levels, around 1150mm, from Tecoh Cave speleothems

(Medina-Elizalde *et al.* 2010). The date of this transition coincides with the Cariaco Basin's titanium record (Haug *et al.* 2003) and the proposed regrowth of Mexican tropical forests initiating ca. AD 900 from Punta Laguna (Curtis *et al.* 1996). However, the MCA is more commonly cited to begin later, from 850 cal yrs BP (1100 AD). Punta Laguna's isotopic record displays notable depletion signifying a return to wetter conditions at this later date (Curtis *et al.* 1996; Hodell *et al.* 2007), with isotopic depletion correlating well with the records from Lake Chichancanab (Hodell *et al.* 2005b) and the poorly-dated Lake Tzib (Carrillo-Bastos *et al.* 2010). Furthermore, speleothem colour, luminescence and isotopic record from Macal Chasm all indicate a return to wet conditions at 800 cal yrs BP (1150 AD) from their well-dated records (Webster *et al.* 2007; Akers *et al.* 2016). Significant tropical forest regrowth at Ría Lagartos Biosphere Reserve, dated at 950 cal yrs BP (1100 AD) (Aragón-Moreno *et al.* 2012), and Lake Coba, dated at 710 cal yrs BP (1240 AD) (Leyden *et al.* 1998; Leyden, 2002), also indicate a return to wetter conditions; this delayed date is attributed to the final stages of Mayan deforestation in the area as the last settlements were abandoned (Leyden, 2002). Reforestation of the southern lowlands is inferred to occur rapidly, with full forest recovery within 80-260 years from Petén Itzá (Mueller *et al.* 2009) and reaching Pre-Classic levels within 150 years (Wahl *et al.* 2013).

The disparity in MCA timings is likely derived from dating error, spatial variation between sites and lack of high-resolution records during this time (Carrillo-Bastos *et al.* 2012). However, the $\delta^{18}O$ and geochemical records from the Gulf of Mexico suggest a short-term cooling of SSTs mid-MCA (Richey *et al.* 2007); this division of SSTs within the MCA might contribute to the inferred early/late discourses discussed above. These Post-Classic conditions are proposed to correspond roughly with those experienced during the Pre-Classic Period (before 1750 cal yrs BP; 200 AD) (Curtis *et al.* 1996). Rapid isotopic depletion from Lago Puerto Arturo indicates that the MCA marked the return of wet conditions comparable to those before 6,200 cal yrs BP (Wahl *et al.* 2014).

Following the MCA, the "Little Ice Age" (LIA) period spanned between 600-100 cal yrs BP (1350-1850 AD), yet dates are again widely debated and spatially variable (Metcalfe and Davies, 2007). The period displays a range of climatic signals across southern North America, with studies inferring both wetting and drying trends; Figure 4.11 exemplifies this apparent spatial climatic variation according to different isotopic records throughout the Yucatán. At the LIA's peak around 350 cal yrs BP (1600 AD), global temperature is proposed to be up to 0.7°C cooler than average of AD 1961–90, according to high resolution tree ring data (Moberg *et al.* 2005).

Evidence of a dry LIA primarily comes from Aguada X'Caamal's $\delta^{18}O$ record, northern Yucatán (Hodell *et al.* 2005a). This displays a distinct drying trend from around 550 cal yrs BP (1400 AD) with up to a 2.2‰ increase in $\delta^{18}O$ over the subsequent two centuries. Concurrent increases in saline, benthic foraminifer *A. beccarii* from X'Caamal (Holdell *et al.* 2005a) (Fig. 4.11), and a succession of mesic *Brosimum* forest taxa to 'drier' herb and grass taxa from nearby Lake San Jose Chulchaca (Whitmore *et al.* 1996) further indicate an increased E/P ratio. However, Medina-Elizalde *et al.* (2010) argue that the increased salinity and isotopic values portrayed from Aguada X'Caamal, indicative of drier conditions, could be a result a changing basin hydrology from an open to a closed system thus reducing the input of fresh groundwater.

Other records inferring consistent dry records are sparse and tend not to span the full LIA. Declining tropical forest taxa from the nearby Ría Lagartos Biosphere Reserve indicate a drying trend over the LIA, yet variability of mangrove and disturbance taxa do not support a solely climatic-driven vegetational change (Aragón-Moreno *et al.* 2012). Similarly, Curtis *et al.* (1996) infer decreased precipitation in the Yucatán around 580-520 cal rs BP (1370-1430 AD), thus corresponding with the abandonment of several major Mayan cities (see Gill, 2001), yet propose a return to wetter conditions for the rest of the LIA period. The Cariaco Basin displays a close resemblance to the X'Caamal record, with titanium levels declining continuously from AD 1350 to AD 1800 with Ti percentages a fifth of those prior to the LIA (Haug *et al.* 2001, 2003). However, the major variation shown in the Cariaco Basin's Ti record during the LIA may suggest a switch to supply-limited deposition thus resulting in the unusual concentration minima.

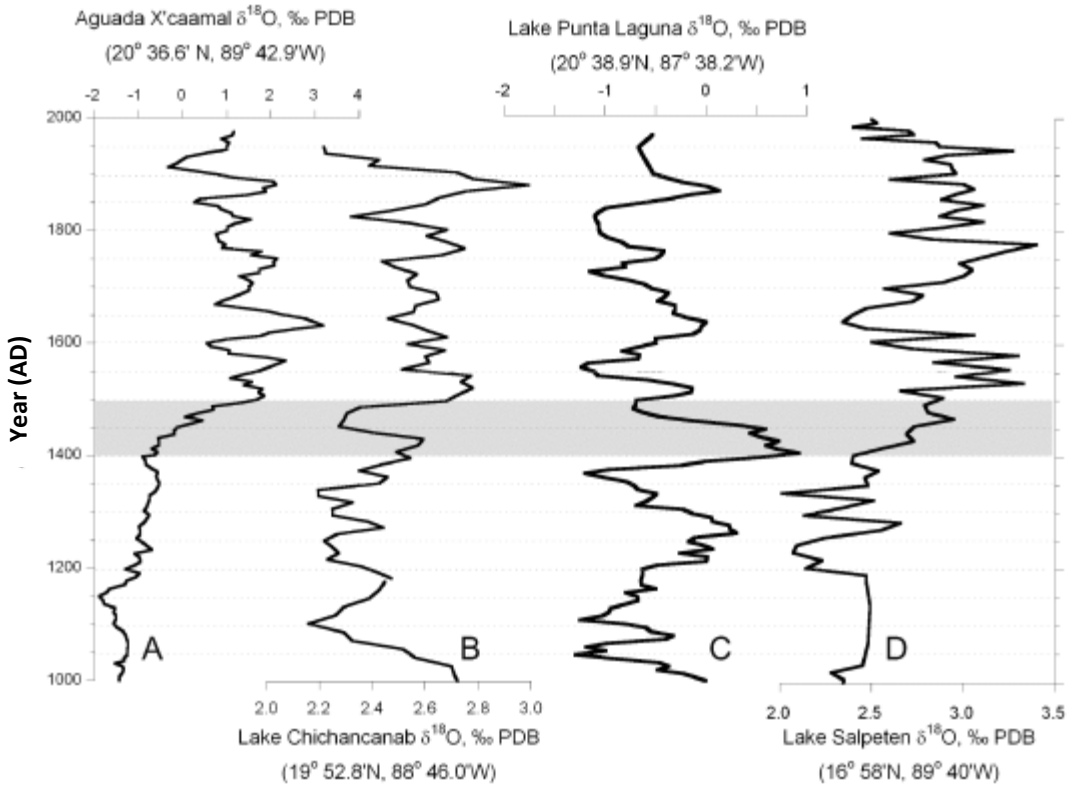


Figure 4.11 *– $\delta^{18}O$ record of Aguada X'Caamal (a) (Hodell et al. 2005a), Lake Chichancanab (b) (Hodell et al. 2001), Punta Laguna (c) (Curtis et al. 1996), and Lake Salpetén (d) (Rosenmeier et al. 2002); grey shading denotes the 15th Century, marking a general shift to drier conditions over the last 500 years. Isotopic records displaying the general lack of coherence between sites across the Yucatán (Taken from Hodell et al. 2005a)*

While the validity of records suggesting that the LIA represent a dry phase in the Yucatán's palaeoclimate is disputed, short fluctuations of dry conditions during the LIA can be identified. For example, Yok Balum's high-resolution speleothem record from Belize indicates a severe period of drought between 415-408 cal yrs BP (1535-1542 AD) corresponds to a period of disease, famine and city abandonment (Kennett *et al.* 2012). In Mexico's central highlands, historical records also infer dry conditions around 400-350 cal yrs BP (1550-1600 AD), where agriculture is believed to have suffered as a result of increased droughts (Endfield and O'Hara, 1997), with Davies *et al.* (2004) finding reforestation attributed to depopulation (associated with the Spanish arrival) initiated at this time.

Lozano-Garcia *et al.* (2007) exemplifies the other side of the debate over LIA conditions with the proposal that tropical forests were densest and lakes were deepest during the LIA over the last 2,000 years (from Lago Verde, Mexico's central highlands); they hypothesise that the inferred -2°C climatic cooling and the associated increased meridional, winter flow increased winter (dry season) precipitation, and demonstrate the importance of seasonality to environmental change. Overall,

precipitation is inferred to increase with reductions in solar activity (also see Hodell *et al.* 2001), namely the two prominent solar minima during the LIA at 450 cal yrs BP (1500 AD) ("Spörer") and 250 cal yrs BP (1700 AD) ("Maunder"), lead to an increase in moisture availability and decreased seasonality (Lozano-Garcia *et al.* 2007). However, the precise mechanisms between Yucatán climate and solar variability are not well understood (Hodell *et al.* 2001). These two peaks in precipitation are also found by Medina-Elizalde *et al.* (2010), where isotope-inferred precipitation is proposed to increase slightly to 1200mm/yr and 1300mm/yr (i.e. wetter than present day's average of ~1150mm/yr) during short periods dated: 460-370 cal yrs BP (1490-1580 AD) and 190-122 cal yrs BP (1760-1828 AD) respectively. Webster *et al.* (2007) also infer wet conditions to prevail throughout the LIA from their luminescence and isotopic records from Macal Chasm, south-central Lowlands near Tikal and Petén Itzá. A similar, but slightly weaker, signal is found in the Punta Laguna record in the eastern Yucatán (Curtis *et al.* 1996).

Lozano-Garcia *et al.* (2007) further suggest an explanation to the apparent discrepancies described here pertaining to the change in precipitation during the LIA. They suggest that the study sites which infer overall wetter conditions during the LIA have an annual net water surplus, with up to 900mm/yr of rainfall in Lago Verde, and so the moderate reduction in summer rainfall is not sufficient to outweigh the decreased summer evaporation and increased winter precipitation. Whereas, those sites from drought sensitive areas, such as X'Caamal on the drier northwest Yucatán Peninsula, are more sensitive to the reduction in summer precipitation, which is significantly outbalanced by summer evaporation thus leading to inferred drier/drought conditions. Overall, LIA's inferred conditions display high spatio-temporal variability. The LIA is not likely to be as wet as the MCA (Kennett *et al.* 2012), and is likely to contain high variability in precipitation (Webster *et al.* 2007; Medina-Elizalde *et al.* 2010; Kennett *et al.* 2012). Records that infer climatic drying tend to be located within drought-sensitive lacustrine systems that are dependent on the summer rainfall. Therefore, a reduction in summer precipitation may be interpreted as a drought in these palaeoclimatic records.

4.2 Lithology and chronology

Stratigraphic descriptions through the record's master sequences can provide preliminary compositional and structural information. Core drives were correlated using distinct laminae, both in terms of visual appearance and geochemical composition (from µXRF) to ensure a continuous sequence from present day was retrieved from both lakes. This section presents the core lithology and chronology from Yaal Chac.

4.2.1 Lithology

Using the stratigraphy to correlate YC14 and YC16 core sections, a 4.09m-long master sequence of sediment deposition was constructed (Fig. 4.12). Sediment from eight YC14 cores forms the vast majority of the record, yet a gap in the sediment recovery prevented correlation between sections 02-I and 04-I. Subsequent YC16 coring succeeded at covering this gap, indicating only that only 1cm is missing from the YC14 sedimentary record.

Yaal Chac's master sequence comprises two main units (Table 4.2). Unit 1 (0-198cm composite depth) is predominately non-laminated, composed of dark, organic material interspersed with discrete clusters of light, carbonate laminae. Unit 2 (197-410cm) is continuously laminated, and visually resembles Nar Gölü's unit 1 varves (only thinner). Units 2's sediment is further divided into 3 distinct subunits (2i-2iii) based on the stratigraphy's composition and structure, primarily gained through microfacies analysis (discussed in Section 4.3.1).

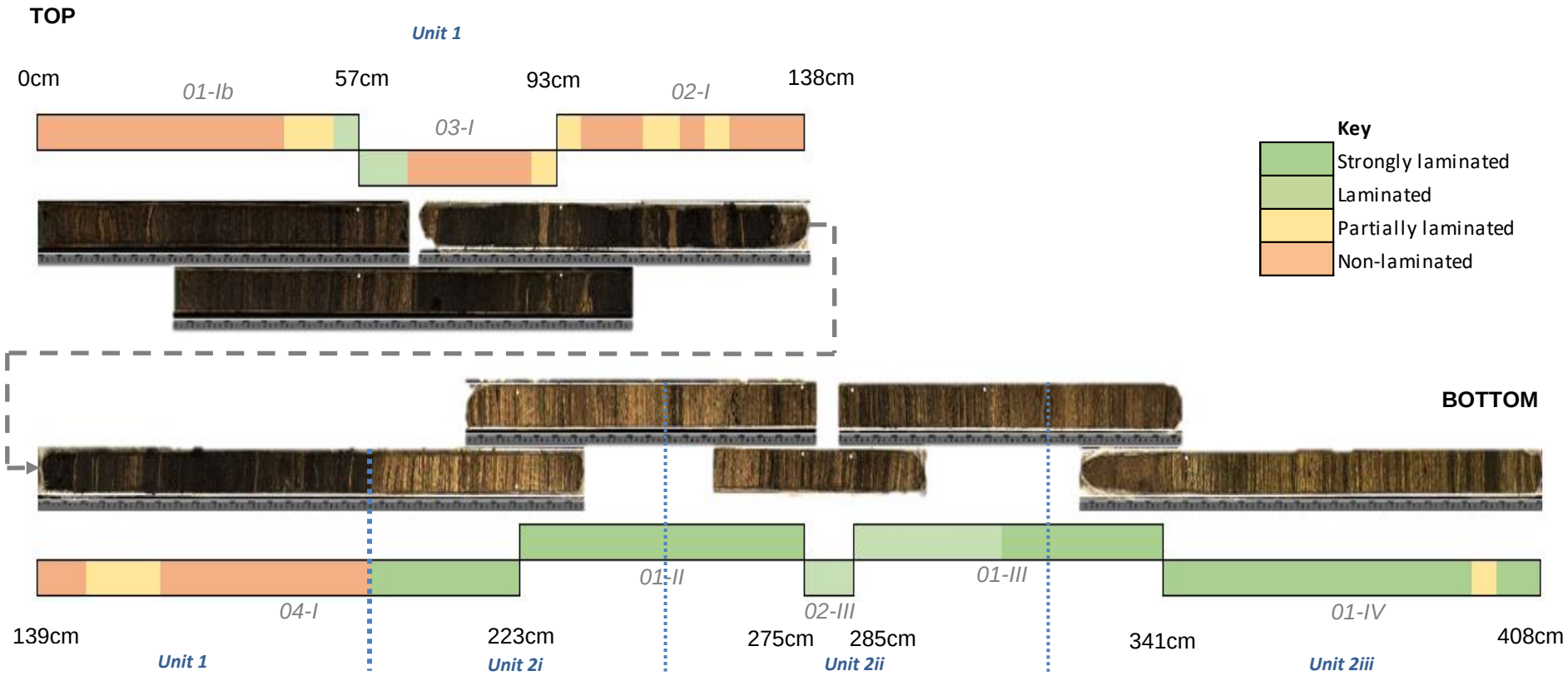


Figure 4.12 *– Yaal Chac's (YC14) composite master sequence presenting the MSCL-CIS imagery alongside a schematic diagram of lamination quality. The cumulative depths (cm) of tie points mark the correlation between core sections, and the 1cm sequence gap between drives 02-I and 04-I (grey dotted line) is displayed. The division between stratigraphic Units 1 and 2 (thick blue dotted line) signifies the switch from discontinuously laminated to continuously laminated sediment, and subdivisions of Unit 2 represent distinct changes to the microstratigraphy (thin blue dotted line).*

Table 4.2 *– Descriptions of sedimentary Units from Yaal Chac's master sequence, alongside a 5cm-long image representative of unit. All measurements stated here reflect average thicknesses of individual laminae.*

Master sequence depth (cm)	Unit	Sediment description	Example image
0.0 – 198.0	1	Homogeneous, black/brown organic-rich sediment with individual and clusters of pale carbonate laminations (0.1-1.0mm); some small sections (up to 5cm) of gritty, grey/brown sediment	
198.0 – 252.1	2i	Continuous, alternating pale cream/beige carbonate (0.2-0.5mm) and dark brown/black organic laminations (<0.2mm); similar to Unit 2iii	
252.1 – 320.0	2ii	Continuous, alternating pale white/cream/beige carbonate (0.2-0.6mm) with thicker dark brown/black organic laminations (0.1-0.7mm)	
320.0 – 409.1	2iii	Continuous, alternating pale white/beige carbonate (0.2-0.6mm) and dark brown/black organic laminations (0.1-0.4mm); similar to Unit 2i	

Yaal Chac's alternating carbonate-organic laminae of Unit 2 visually resemble the varves deposited at Nar Gölü (Section 3.3). Microstratigraphic analysis reveals further similarities. Carbonate sublayers are composed of endogenic calcium carbonate precipitation, also in the form of calcite or aragonite, and the organic sublayers are composed of autochthonous material and amorphic organic detritus. Contemporary monitoring and detailed microstratigraphic analysis highlight the influence of a process-driven model of varve deposition akin to Nar Gölü's (see Fig. 3.12; Section 3.2.1), where the region's wet-dry seasonality drives the intra-annual limnological variability required for varve

deposition (Brauer, 2004). Nar Gölü's conceptual model (Fig. 3.12) could explain the sedimentology observed in Yaal Chac's record, except in anti-phase, where Yaal Chac's wet-dry seasons are instead centred in summer-winter respectively. This process-related model of varve deposition, where annual whiting events similarly delineate the each years' depositional cycle, has also been proposed to drive the deposition of many other calcareous-organic varve sequences (Kelts and Hsü, 1978; Livingstone and Hajdas, 2001; Lüder *et al.* 2006; Bluszcz *et al.* 2008, 2009; Brauer *et al.* 2008; Romero-Viana *et al.* 2008; Kalugin *et al.* 2013; Wulf *et al.* 2013). Linking the detailed microstratigraphic descriptions of repeating couplets (see Section 4.3) to this viable conceptual model of deposition provides strong evidence that these couplets reflect varve deposition (Zolitschka *et al.* 2015). However, couplet counts and radiometric dating methods (specifically ^{14}C and ^{210}Pb) provide further evidence for their annual nature (see Section 4.2.2 below).

This conceptual model of varve deposition can similarly aid non-seasonal turbidite identification. While turbidites also appear as grey, graded clastic sublayers in Yaal Chac's record, there are significantly fewer and are typically thinner, as compared to Nar Gölü. The flat topography of the Yucatán is likely to inhibit the rapid influx of terrigenous material from extreme weather events.

4.2.2 Chronology

4.2.2.1 Independent radiometric dating

A combination of varve counts and radiometric dating techniques established Yaal Chac's sediment chronology. The sedimentary master sequence was formed by correlating overlapping core sections (see Sections 2.1 and 2.2) predominately from the YC14 cores; sediment from YC11 and YC16 cores were subsequently correlated to this 409cm-long YC14 master sequence.

Both bulk sediment and plant samples from YC11 and YC14 cores were analysed using accelerator mass spectrometry (AMS) radiocarbon ^{14}C dating (Bonani *et al.* 1987) at one of three sites: NERC ^{14}C laboratory in East Kilbride, Scotland; Keck Carbon Cycle AMS Facility, University of California, USA; and Beta Analytic in Miami, USA. A total of 21 radiocarbon dates were used to develop an independent age-depth model, check the temporal nature of couplets, and assess hardwater error. Results from these analyses are shown in Table 4.3.

Table 4.3 *– Uncalibrated radiocarbon dates from samples taken from YC11 and YC14. Surface sediment (depth 0cm) was sampled using an Ekman grab in January 2016. The dotted line denotes samples taken from unit 1 (top) and 2 (bottom). Paired bulk and organic samples used to estimate hardwater error are shaded in green.*

Publication Code	Material ID code	Depth (cm)	Sample material	$\delta 13C_{VPDB}$‰ (± error)	C14 Age yrs BP	1-sigma error	Calib 7.1 (IntCal13) (Cal yrs BP)	1-sigma -	1-sigma +
SUERC-67887	YC-16-mid-grab	0	Bulk	-26.5 ±0.5	*modern*		***modern***		
SUERC-72222	YC14 01-Ib (45cm) Bulk	45	Bulk	-25.3 ±0.5	965	37	**860**	825	866
SUERC-70339	YC2 18.5-19.0	68	Bulk	-29.1 ±0.5	831	37	**740**	697	767
SUERC-67888	YC14 03-I (71cm) Organic	71	Plant	-28.2 ±0.5	471	37	**516**	503	530
SUERC-70340	YC2 76.0-76.5	140	Bulk	-29.8 ±0.5	2296	37	**2323**	2308	2352
SUERC-72223	YC14 04-I (159cm) Bulk	159	Bulk	-31.9 ±0.5	3581	35	**3885**	3838	3923
SUERC-70341	YC4 16.5-17.0	159	Bulk	-30.9 ±0.5	3593	37	**3899**	3947	3927
SUERC-72227	YC14 04-I (196cm) Bulk	196	Bulk	-28.9 ±0.5	4468	35	**5157**	5165	5278
SUERC-70342	YC4 84-84.5	196	Bulk	-29.7 ±0.5	3673	36	**4009**	4029	4082
Beta - 292955	YC5/BASE	222	Plant	-28.1 ±0.5	4370	40	**4934**	4868	4969
UCIAMS-186902	YC14 04-I (223cm) Plant	223	Plant	-29.4 ±0.1	4145	20	**4689**	4666	4708
SUERC-67892	YC14 04-I (223cm) Bulk	223	Bulk	-27.6 ±0.5	4763	35	**5518**	5499	5555
SUERC-67890	YC14 01-II (262cm) Plant	262	Plant	-27.3 ±0.5	5349	37	**6132**	6020	6079
SUERC-72228	YC14 02-III (279cm) Plant	279	Plant	-28.5 ±0.5	5197	38	**5954**	5917	5950
SUERC-72229	YC14 02-III (279cm) Bulk	279	Bulk	-28.5 ±0.5	5824	36	**6637**	6600	6674
SUERC-72230	YC14 01-III (313cm) Bulk	313	Bulk	-28.5 ±0.5	7147	37	**7971**	7947	7998
UCIAMS-186903	YC14 01-III (313cm) Plant	313	Plant	-26.3 ±0.1	7110	30	**7946**	7931	7968
SUERC-72231	YC14 01-IV (365cm) Plant	365	Plant	-28.6 ±0.5	7423	38	**8259**	8235	8310
SUERC-72232	YC14 01-IV (365cm) Bulk	365	Bulk	-25.7 ±0.5	7700	38	**8485**	8432	8484
SUERC-67889	YC14 01-IV (389cm) Plant	389	Plant	-27.5 ±0.5	7827	38	**8604**	8560	8636
SUERC-67891	YC14 01-IV (389cm) Bulk	389	Bulk	-24.4 ±0.5	8298	40	**9320**	9265	9406

Owing to the limestone geology, hardwater error (Deevey and Stuiver, 1964) is also known to effect radiocarbon analysis of bulk sediment samples within the Yucatán (Brenner *et al.* 2002). The magnitude of hardwater effect was estimated by obtaining paired radiocarbon dates from bulk carbonate and terrestrial plant macrofossils, and dating sediment deposited at the sediment-water interface (Metcalfe *et al.* 2009). Using a similar methodology, average estimates of hardwater error of 1200-1300 years have been obtained from Yucatán lakes: Punta Laguna (Curtis *et al.* 1996) and Chichancanab (Hodell *et al.* 1995). While limited by the distribution of plant macrofossils through the sequence, five of these pairs were subsampled within YC14's laminated unit. Hardwater error appears to be inconsistent within the Yaal Chac record. The surface sediment date revealed no evidence of hardwater error, yet the differences between the paired dates ranged between 37-627 years uncalibrated (25-829 years calibrated) and do not display any distinct trend with depth. Overall, Yaal Chac's hardwater error appears to be less than these other lakes on the Yucatán Peninsula (Brenner *et al.* 2002). Sedimentological analysis reveals a lack of terrigenous material in much of the record, likely due to its closed hydrology and flat watershed. This may act to diminish the influx and deposition of terrestrial 'old carbon', and hence reduce its influence on radiocarbon analysis. However, despite a similar geomorphology, the influence of hardwater error is comparatively higher within Punta Laguna's chronology (Curtis *et al.* 1996).

To date the uppermost sediment, 14 bulk samples from a surface Glew core were analysed at University College London (UCL) using ^{210}Pb radiometric dating (Oldfield and Appleby, 1984). Radionuclide ^{210}Pb atmospheric fallout occurs naturally and is assumed to remain constant over time at a specific location (Appleby, 2008). With a half-life of 22 years, isotopic decay follows its deposition and subsequent incorporation into the sedimentary sequence. By measuring the changes in its concentration through the record, the age of those sediments can be determined. This technique is ideal for dating sediments deposited up to 180 cal yrs BP (Appleby, 2008), and results of which are displayed in Table 4.4.

Table 4.4 *– Radionuclide ^{210}Pb dates from samples taken from the uppermost sediments of YC11. Sedimentation rate (Sed rate) displays a significant linear relationship with accumulation rate (Acc rate) (r^2=0.88; P<0.01), suggesting a relatively low influence of sediment compaction on the age-depth model within the topmost 28.5cm of the sediment sequence.*

Depth cm	**Drymass** g cm^{-2}	**Date** AD	±	**Acc Rate** g cm^{-2} yr^{-1}	**Sed Rate** cm yr^{-1}	± %
0	0	2013				
0.5	0.0261	2013	2	0.0518	0.904	11.9
3.5	0.2005	2008	2	0.0307	0.481	9.6
6.5	0.4093	2001	2	0.0323	0.452	10.7
9.5	0.6287	1993	2	0.0201	0.291	9.1
12.5	0.8251	1982	2	0.0148	0.217	10.2
13.5	0.9028	1977	2	0.0175	0.166	13.4
15.5	1.1422	1966	3	0.0306	0.265	15.7
18.5	1.4797	1953	4	0.0227	0.187	17.1
21.5	1.8716	1935	6	0.0193	0.166	26
24.5	2.1768	1913	8	0.0094	0.098	42.7
25.5	2.2529	1907	8	0.0195	0.214	86.8
27.5	2.4511	1877	12	0.0024	0.025	41
28.5	2.5418	1823	13	0.0009	0.01	45.1

Bayesian modelling, using R-based software *Bacon* (Blaauw and Christen, 2011), was used to construct Yaal Chac's age-depth model based on the ^{14}C and ^{210}Pb dates. Due to the influence of hardwater error outlined above, dates from bulk sediment samples needed to be corrected. Hardwater error offset was calculated by averaging the four paired dates which display the greatest difference; the paired dates at 313cm are not significantly different, and so the plant macrofossil date is excluded from the modelling as it is deemed to have been contaminated. Within the model, all other plant macrofossil dates are used, and the inferred hardwater error of 498 ±82 years is used to offset dates from all bulk sediment samples. For the four paired dates deemed reliable, only the plant macrofossil analyses are selected due to the negligible effect of hardwater error on them. The resultant Bayesian age-depth model is displayed in Figure 4.13 and, when combined with varve counts from Unit 2, suggests that the record runs from present day to 8812 yrs cal BP (0-409cm).

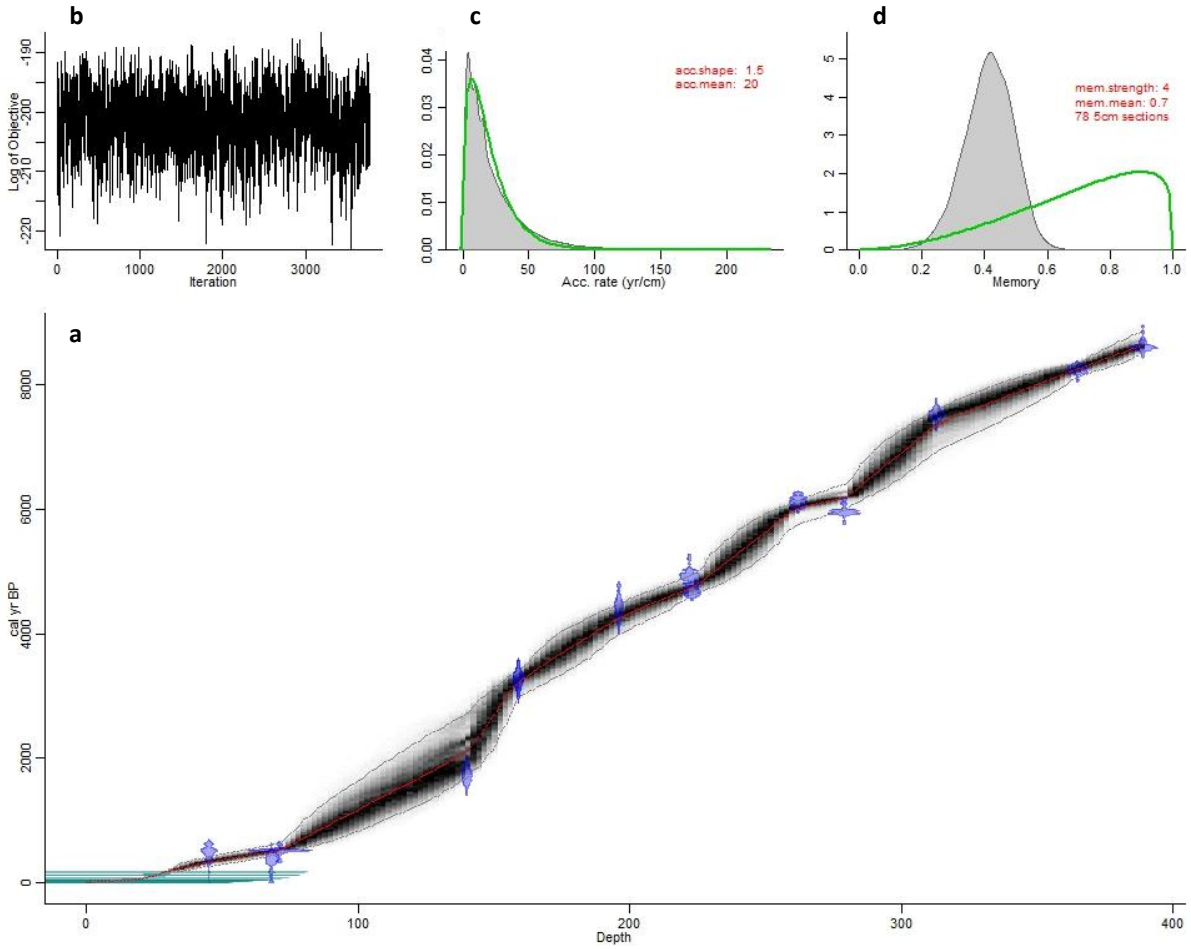


Figure 4.13 – *Bayesian age-depth model for the Yaal Chac's master sequence (a); calibrated radiocarbon dates (darker blue) and ^{210}Pb dates (lighter blue) are displayed with model output (grey dotted line signifies the 95% confidence limits, and shading within these limits indicates the more likely calendar dates; the red line depicts the optimal age-depth model based on the weighted mean age for each depth). Markov Chain Monte Carlo iterations (b) display a desired, stationary distribution; this indicates that the probability distribution is composed of independent model runs. Bacon's intrinsic, gamma distribution of sedimentation rate (green line – based on data from Goring et al. 2012) constrains the model's resultant sedimentation rate (grey histogram) (c); accumulation rate is asymmetrically distributed to account for downcore sediment compaction, and always remains positive. Bacon's intrinsic, beta distribution of model memory (green line) defines the dependence of earlier accumulation rates at any given point; the memory output (grey histogram) denotes low autocorrelation, indicative of a variable accumulation rate.*

4.2.2.2 Anchoring the laminated Unit 2

Using thin section microscopy, 3717 couplets were counted within Yaal Chac's Unit 2 (see Section 2.3.1.2). To assess whether the sediments' stratigraphy reflect varves, the number of couplets was counted between ^{14}C dates within each of the laminated subunits. Within subunits 2i and 2iii, the number of years between the calibrated radiocarbon dates at 196cm and 222cm (subunit 2i), and

365cm and 389cm (subunit 2iii) correspond to the number of couplets within <2% error, thus verifying the annual nature of the sediment deposition. Consequently, varve-based age-depth models were constructed for subunits 2i and 2iii by counting annual couplets between known sediment depths. To anchor these floating varve chronologies, these models were superimposed onto the Bacon-derived age-depth model, and adjusted for optimal overlap between the Bayesian models 95% confidence interval and the varve-based model (Fig. 4.14).

Within subunit 2ii (see Table 4.2), while 1814 years separate calibrated ^{14}C dates at 262cm and 313cm, only 807 couplets were identified. This discrepancy indicates that couplet counts under-represent time during this subunit. It is possible that without a discernible carbonate precipitation sublayer to punctuate the intra-annual deposition, two organic sublayers from different years will lie adjacent to each other. This subunit displays notably thicker organic sublayers (average 0.21mm; as compared to 0.14mm average thickness of all other organic sublayers), which may reflect consecutive organic deposition lacking the consistent carbonate sublayer punctuation. The overall homogeneity of the organic sublayers' sedimentology throughout the entire record reduces the ability to distinguish adjacent organic sublayers deposited in consecutive years. Consequently, subunit 2ii's laminations do not represent annually-resolved varves, and the Bayesian model's output provided the sediments' chronology.

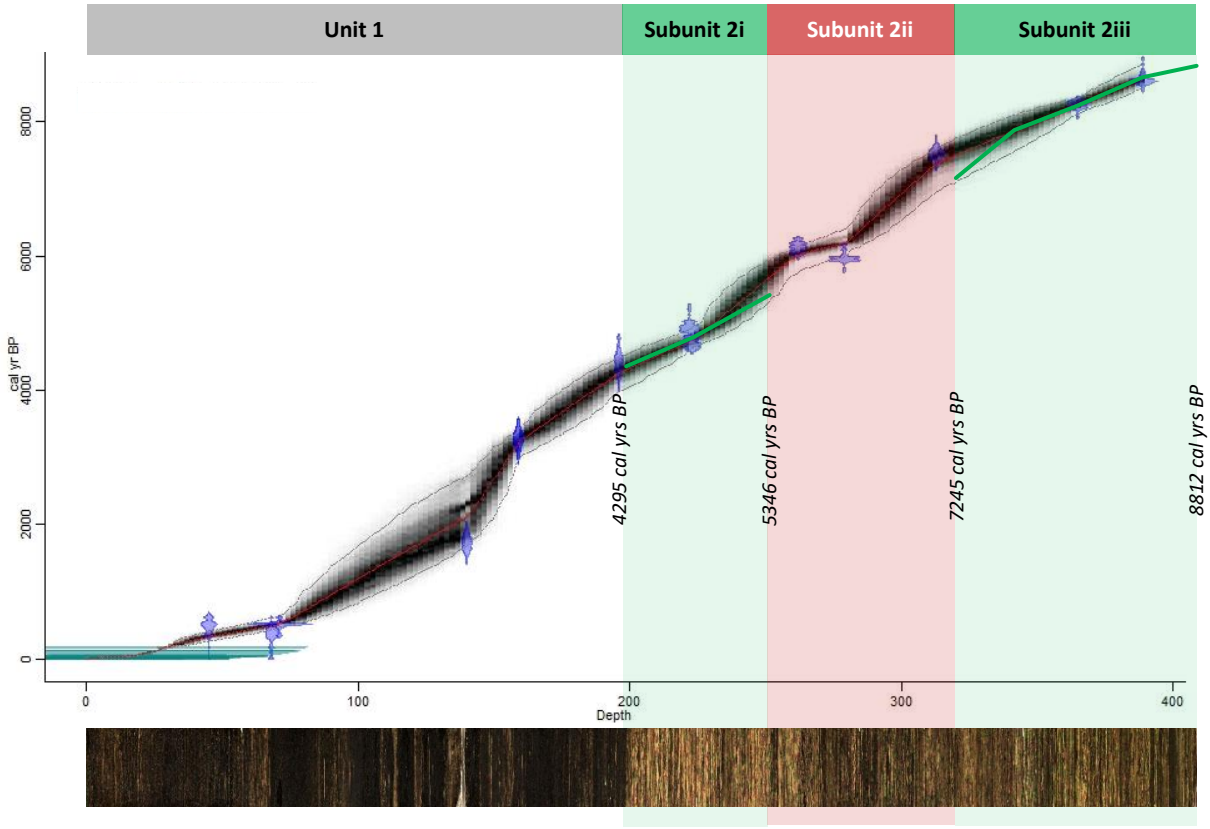


Figure 4.14 – *Floating varve chronologies of Units 2i and 2iii (green line) anchored using the Bacon age-depth model, displayed alongside a composite image of the full Yaal Chac sequence. Comparable accumulation rates between the radiometric- and varved-based models (green shading) supports annually-resolved varved deposition. Disparity between subunit 2ii's couplet counts and ^{14}C dates (252-320cm; red shading) prevents varve classification within this section.*

Within Unit 2, the Bayesian age-depth model runs from the deepest radiocarbon date at 389cm to the start of Unit 1 at 198cm. Model runs suggest that this sediment sequence covers the period from 8,640 ±234 to 4,295 ±260 cal yrs BP. These start and end dates are used to anchor the floating varve chronologies of subunits 2iii and 2i respectively; in this position, the varve-inferred age-depth model remains within the Bayesian models 95% confidence interval and the two models display similar trends to inferred sedimentation rates. Consequently, containing a total of 1668 contiguous varves, subunit 2iii's floating varve chronology is anchored at 8,812 – 7,245 ±234 cal yrs BP; similarly, containing 1051 consecutive varves, subunit 2i's floating varve chronology is anchored at 5,346 – 4,295 ±260 cal yrs BP (Fig. 4.14).

As subunit 2ii's laminae are non-varved, its chronology is primarily determined using the Bayesian age-depth model. Model runs suggest that sediment deposited here (252-320cm) spans from 7,495 ±418 to 5,699 ±339 cal yrs BP. However, these model-inferred dates do not precisely align with the end of subunit 2iii and the start of subunit 2i. For the purposes of displaying sedimentological

changes through the sequence, subunit 2ii was constrained by the start and end dates of the proceeding and preceding varve chronologies. Therefore, subunit 2ii's deposition is proposed to cover the period 7,245 – 5,346 ±418 cal yrs BP; these proposed dates remain within the Bayesian model's 95% confidence interval.

Considering the well-known difficulties of radiocarbon dating bulk sediment samples from lacustrine records in the Yucatán (Brenner *et al.* 2002), subunit 2ii's chronological error is comparatively high. The ^{14}C date from bulk sediment within subunit 2ii (313cm) has been offset by the sequence's average hardwater error (498 ±82 years). As previously discussed, this average is calculated using paired dates elsewhere in the record. Radiocarbon results from Yaal Chac, and other Yucatán lakes (e.g. Curtis *et al.* 1996), show that hardwater error from bulk samples varies downcore; therefore, the Bacon-derived age-depth model may have over- or under-estimated this samples age, thus reducing the Bayesian model's ability to constrain subunit 2ii's start/end dates.

4.3 Sedimentology: results and interpretation

This section presents the sedimentological data collected from Yaal Chac's YC14 master sequence, and assesses the environmental conditions necessary to result in each components' deposition and preservation.

Sediment stratigraphy defines Yaal Chac's lithological units: discontinuous laminations (Unit 1) and continuous laminations (Unit 2) (see Section 4.2.1). The results discussed in this section are divided according to these units. First, the varved unit from the early-mid Holocene (Unit 2; see Section 4.3.1) is discussed, and then sediments deposited during the mid-late Holocene (Unit 1; see Section 4.3.2).

4.3.1 Early-mid Holocene: Unit 2

Bayesian modelling of the ^{14}C age-estimates, combined with varve counts, suggest that Unit 2's sediment was deposited from 9,232 to 4,295 cal yrs BP ±260 (Section 4.2.2). Within this laminated Unit, two floating varve chronologies are anchored at 9,232 – 7,565 cal yrs BP ±234 (subunit 2iii), and 5,346 – 4,295 cal yrs BP ±260 (subunit 2i). Between these varve chronologies, the laminated sediment of subunit 2ii (252-320cm) has been shown to be non-varved. Therefore, the microstratigraphic data presented from this subunit, specifically the sublayer thicknesses, do not correspond to an individual year's sediment deposition. Repeated varve counts suggests an error of <1% within each floating varve chronology; therefore, a conservative ±1% error accumulates with counts from the principle radiocarbon age-estimate anchoring each floating chronology at 8,604 ±234 cal yrs BP (subunit 2iii) to 4,295 ±260 cal yrs BP (subunit 2i). The dating error listed within this chapter will only pertain to the accumulated error derived from varve counts.

4.3.1.1 Varve microfacies

i) Classification

Unit 2i and 2iii's varve microfacies were categorized into two main classes (1-2), which were further divided into four subclasses (1a-b and 2a-b), according to their composition and structure (see Tables 4.5 and 4.6). Each microfacies class described here is abbreviated to 'M' (e.g. M1a). The microfacies of subunit 2ii's non-varved laminations are also discussed alongside the varve microfacies; these laminations are classified and abbreviated to 'L1'. Again, L1 counts underrepresent time. While each distinct carbonate sublayer likely reflects an individual year's

whiting event (see Fig. 3.12), the deposition of L1's intermediary organic sublayers is not constrained to a single year. Consequently, L1's couplet counts underrepresent time by a factor of ~1.7 (1099 couplets; 1,899 ±339 years), where these 'missing varves' effectively prevent the establishment of an incremental chronology.

XRD analysis confirmed the presence of both calcite and aragonite within the varved Unit 2; this analysis was performed on 24 sediment subsamples through the YC11 core, by undergraduate Rachael Lem at the University of Nottingham (Lem, 2011), using a methodology described by Hardy and Tucker (1988). The identification of these minerals within each varve was subsequently achieved through thin section analysis. As previously discussed in Nar Gölü's results (see Section 3.3), carbonate material was clearly differentiated from organic matter when viewed under cross-polarised light, due to the optical birefringence property of carbonate minerals. The morphology of crystals within the homogenous carbonate sublayers enabled the visual identification of aragonite and calcite: needle-shaped aragonite vs rhombic-shaped calcite (Fig. 4.15a). These euhedral crystals identified within Yaal Chac's records strongly resemble the aragonite and calcite minerals found within Nar Gölü's record (Table 4.15b). In addition, changes to the sediments' geochemistry support the visual classification of carbonate mineralogy through the varved Unit 2; specifically, higher (lower) Sr/Ca values correspond to increased aragonite (calcite) sublayer thicknesses (see Section 4.3.1.2), as aragonite incorporates a greater proportion of Sr within its crystalline structure than calcite (Valero-Garcés *et al.* 1997).

Figure 4.15a *– Identification of aragonite, calcite and detrital/peloidal carbonates from Yaal Chac's Unit 2 via thin section microscopy (additional images of each type of carbonate in Supplementary material). The euhedral morphology of aragonite and calcite crystals enabled their mineralogy to be clearly differentiated within their homogenous sublayers. Plane- and cross-polarised images taken under 200x magnification using a petrographic microscope at the University of Nottingham.*

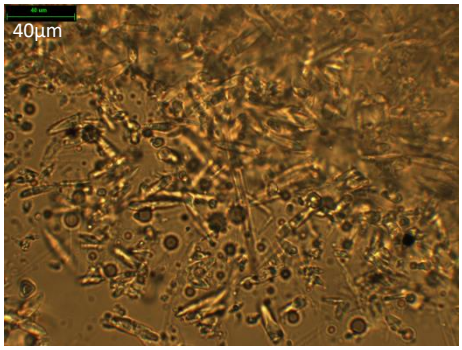
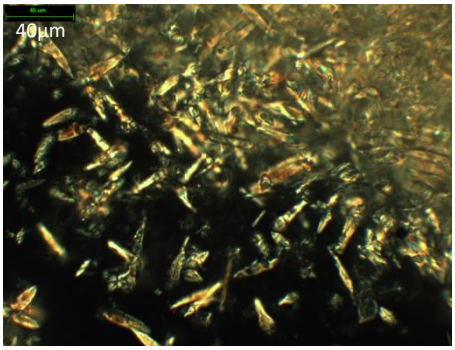
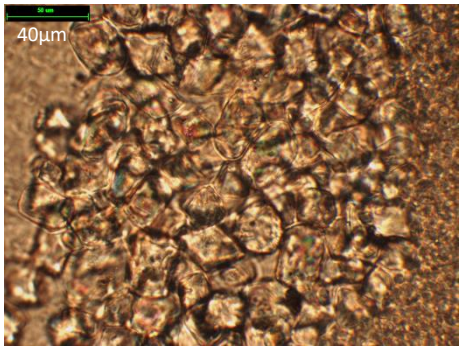
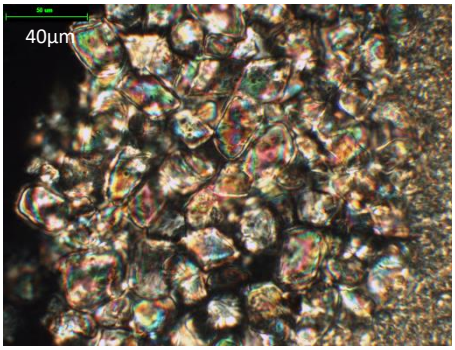
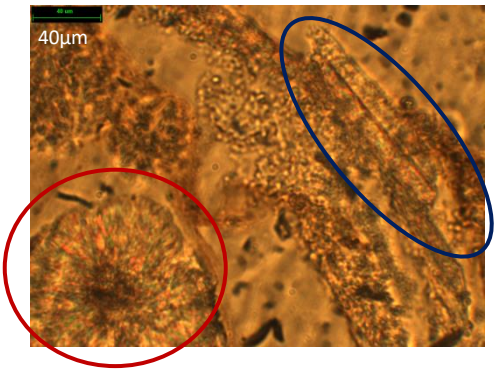
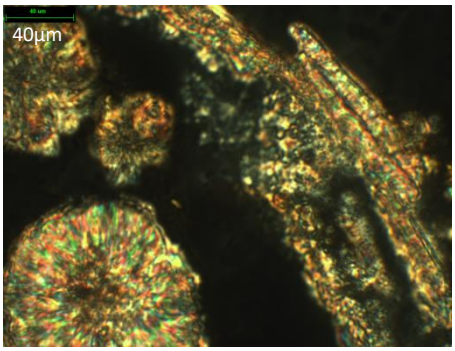
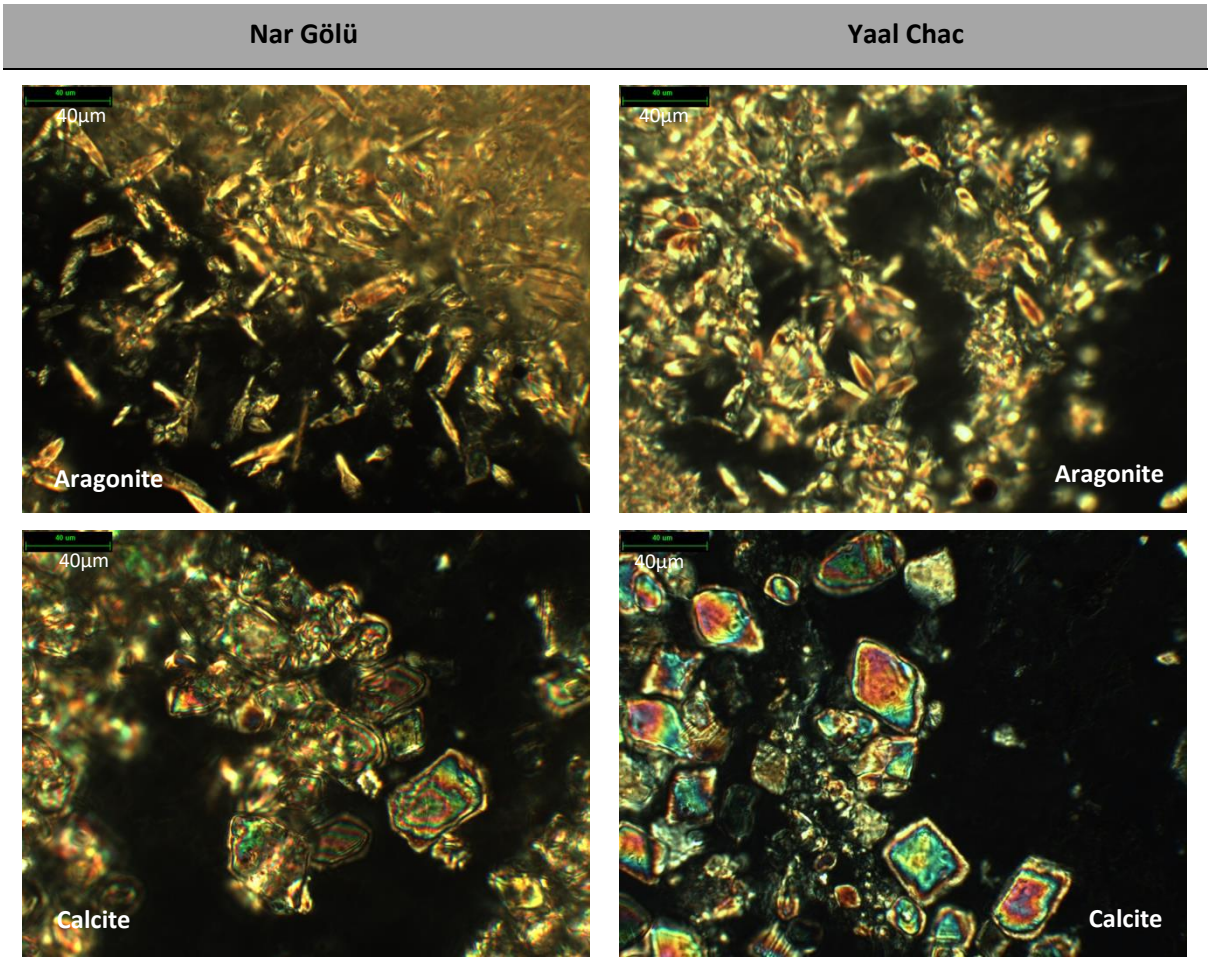
	Plane-polarised	Cross-polarised
Aragonite - Needle-shape characteristic of aragonite - Euhedral crystalline structure		
Calcite - Rhombic-shape characteristic of calcite - Euhedral crystalline structure		
Detrital/ peloidal carbonate - Irregular size and shape of carbonates - *[Bottom left]* peloid grain may represent faecal pellet - *[top right]* linear grain may represent shell fragment		

Figure 4.15b *– Additional images display the strong similarities in crystal morphology and birefringence between Nar Gölü's and Yaal Chac's aragonite (top) and calcite (bottom) minerals. Each minerals' distinctive shape enabled the identification of Yaal Chac's carbonate sublayers. plane- and cross-polarised images taken under 200x magnification using a petrographic microscope at the University of Nottingham.*



Varve deposition in Yaal Chac follows the same conceptual model as Nar Gölü's varves (Section 3.2.1), where the deposition of organic-carbonate varves is driven by the climate's wet-dry seasonality. The carbonate sublayers are comprised solely of homogenous, endogenic calcite and aragonite crystals, similar to those observed in Nar Gölü's record. Endogenic precipitation occurs during a rapid mineralisation event following carbonate supersaturation, driven by biogenic activity and seasonal E/P conditions.

The composition of Yaal Chac's organic sublayers display less interannual variability, compared to Nar Gölü's varves; 99% of organic laminations contain only one distinct sublayer, and 72% of these are identified as thin, bacterial mats and 13% as thicker, amorphic organic material with low

concentrations of diatoms. While some organic sublayers display varying concentrations of endogenic carbonate (14%), they generally consist exclusively of organic matter.

Tables 4.4 and 4.5, Figure 4.16, and the following describes the sedimentological variability used to define each microfacies classification:

M1. The regular presence of calcite deposition defines M1, and its gradually increasing occurrence helps divide the subclasses. All carbonate sublayers are composed of homogeneous, euhedral calcium carbonate crystals ($CaCO_3$), indicative of endogenic precipitation (Kelts and Hsü, 1978). Sharp boundaries define the edges of each carbonate sublayer, suggesting rapid changes in the dominant depositional process (Mangili *et al.* 2005). The composition and structure of these carbonate sublayers can be divided into three distinct types: (i) single calcite-only, (ii) single aragonite-only, or (iii) dual calcite-only followed by aragonite-only. In sublayers with these dual mineralogies, the aragonite always follows calcite, thus reflecting the lake's increased ionic concentration due to the persistence of dry-season's high E/P conditions. M1 varves display a high degree of mineralogical variability; consecutive varves display abrupt switches between these three types of carbonate sublayers. Aragonite and calcite crystals are fine grained, 3-6µm and 10-15µm respectively, and display little or no grading within each sublayer; any grading is expressed as weak up-core fining. Similarly observed and discussed within Nar Gölü's record (Section 3.3), carbonate supersaturation intensifies through the dry season, thus increasing crystal nucleation rate leading to the precipitation of smaller, imperfect grains (Brauer *et al.* 2008).

The frequency of calcite and aragonite deposition helps define M1's subclasses; compared to M1b varves, M1a varves contain proportionally more calcite and fewer aragonite sublayers. Unlike M1a varves, dual calcite-aragonite sublayers in M1b varves typically lack a distinct boundary between the two mineralogies. Due to the short, rapid nature of these precipitation events, the grading between mineralogies may reflect a quick succession of supersaturated periods. Ionic concentration determines the mineralogy precipitated (Kelts and Hsü, 1978), and since aragonite precipitation follows shortly after calcite precipitation, the initial limnology was likely close to the mineralogical threshold.

M2. The absence of any calcite deposition defines M2 varve microfacies. All carbonate sublayers of M2 are composed solely of homogenous, fine grained (6-10µm), euhedral aragonite crystals. Once again, this mineralogical structure is indicative of endogenic precipitation (Kelts and Hsü, 1978), and any (weak) up-core fining is likely to reflect the intensification of carbonate supersaturation through the precipitation event (Brauer *et al.* 2008). M2's organic sublayers are most commonly comprised of bacterial mats, but also contain relatively high concentrations of background carbonate minerals, diatoms and organic detritus.

The presence/absence of sublayers composed of detrital/peloidal carbonate material define M2's subclasses (Figure 4.15a). M2b's varves often contain a sublayer predominantly composed of irregularly sized minerals, often grouped together in oval-shaped peloids. These sublayers can be identified at any point within a varve, indicating that deposition is not linked to the seasonal cycle of sediment deposition (Corella *et al.* 2012), and the sublayers' abrupt boundaries also suggest deposition occurs during a rapid event (Mangili *et al.* 2005). These sublayers often appear as convex lenses within the sediments' stratigraphy, suggesting that their deposition occurs on a local scale (Mangili *et al.* 2005). This sedimentology is characteristic of turbidites (Mangili *et al.* 2005), displaying similar structures to the turbidites described in Nar Gölü's record (see Section 3.3.1 and 3.3.2). Under cross polarised light, minerals visually resemble anhedral carbonates (Fig. 4.15a), where the rapid and non-seasonal deposition of detrital carbonates may reflect the inwash and reworking of eroded limestone from the surrounding catchment; in which case, intense rainfall events (Bookhagen *et al.* 2005) and lake level changes (Dean *et al.* 1999) may drive, in part, the deposition of these sublayers. Alternatively, the local deposition and oval shape of some grains may reflect the deposition of faecal pellets (peloids) from in-lake organisms, where macro-invertebrates feeding within unconsolidated aragonite sediment can cause the pelletisation of carbonates (Tucker and Wright, 2009). For example, brine shrimp *Artemia salina*, present within the northern Yucatán's most saline lacustrine systems (Torrentera and Dodson, 2004), are commonly associated with the formation of carbonate peloids within contemporary sedimentary records (Baltres and Medesan, 1978; Tucker and Wright, 2009). M2a varves do not contain any of these non-seasonal sublayers.

L1. The non-varved laminations of L1 (subunit 2ii; see Section 4.2.1) strongly resemble M1 varves. Carbonate sublayers delineate the sediment's stratigraphy, and are each

indistinguishable from those identified within the varved subunits. Sublayers are composed of euhedral calcite or aragonite crystals, indicative of endogenic precipitation (Kelts and Hsü, 1978), and abrupt boundaries define the sublayer, again signifying rapid changes to the primary depositional processes (Mangili *et al.* 2005). The sedimentological resemblances between the carbonate sublayers of L1 and M1-2 suggest that they form in similar limnological conditions, and hence likely reflect an individual year's whiting event.

The composition of the organic sublayers, however, differentiates L1's laminations from the varves. Organic sublayers from the adjacent M1a and M1b varves typically consist of thin, bacterial mats, which typically contain low concentrations of carbonate minerals and organic detritus. Conversely, L1's organic component displays a greater variability in their composition. While the deposition of bacterial mats is still common, the frequency of thicker amorphic organic deposition increases; these often contain increased concentrations of carbonate minerals, diatoms, shell fragments and larger pieces of organic detritus.

L1's thicker organic sublayers, compared to those measured within M1 and M2 varves, are proposed to reflect multiple years of sediment accumulation, which lack a distinct carbonate sublayer to delineate the annual depositional cycle. During these years, carbonate supersaturation and precipitation may not occur annually, thus resulting in 'missing varves' within the laminated sequence (Zolitschka, 2007). Consequently, L1 couplet counts are proposed to underrepresent time; age-depth modelling suggests L1's 807 couplets were deposited within ~1800 years (see Section 4.2.2).

Table 4.5 *– Classification of varve microfacies according to thin section microscopy.*

	Microfacies classification	Cal yrs BP	Number of sublayers	Average varve thickness (mm)	
M1	a. Calcareous/ Organic	5345-4295	3	0.44	
L1	Calcareous/ Thicker organic	7245-5345	3	0.54	
M1	b. Calcareous/ Organic (declining calcite)	7872-7245	2/3	0.39	
M2	a. Aragonite/ Organic	8013-7872	2	0.50	
	b. Aragonite/ Organic (w. carbonate peloids)	8812-8013	2/3	0.63	

Table 4.6 *– A conceptual diagram of the microfacies sub-classes; L1 laminations (yellow shading) are non-varved.*

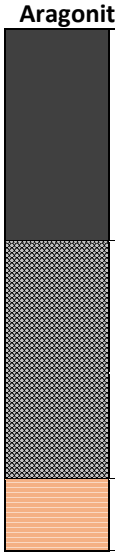
Microfacies	Colour	Sub-layer	Average thickness (mm)	Description
1a		**Calcareous/organic**		
		(i) Aragonite [present in 69% of varves]	0.25	- Very fine grained (3-6µm), euhedral aragonite crystals - Dense and well-defined with abrupt boundaries
		(ii) Calcite [present in 93% of varves]	0.18	- Fine grained (~12µm), euhedral calcite crystals - Dense and well-defined with abrupt boundaries
		(iii) Bacterial mat	0.07	- Amorphic organic matter - Very low concentrations of diatoms/carbonates
L1		**Calcareous/thicker organic (Non-varved)**		
		(i) Aragonite [present in 77% of varves]	0.26	See M1ai
		(ii) Calcite [present in 89% of varves]	0.15	See M1aii
		(iii) Bacterial mat/ amorphic organic	0.17	- Amorphic organic detritus, with higher concentrations of carbonate material, diatoms, and shells
1b		**Calcareous/organic (declining calcite)**		
		(i) Aragonite [present in 90% of varves]	0.26	See M1ai - *Blurred boundary between aragonite and calcite*
		(ii) Calcite [present in 41% of varves]	0.15	See M1aii
		(iii) Bacterial mat	0.08	- Amorphic organic matter - Very low concentrations of diatoms/carbonates

2a Aragonite/organic

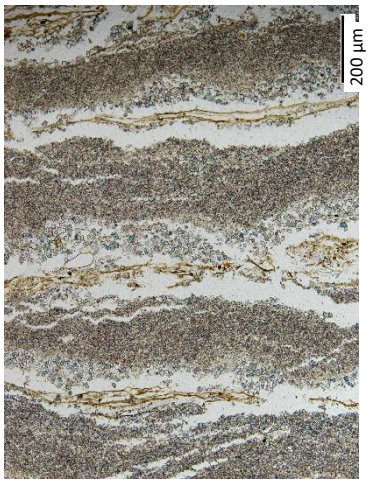
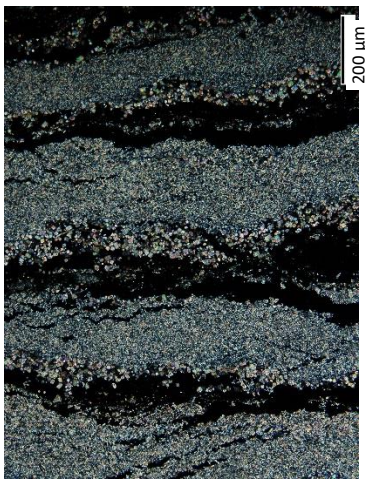
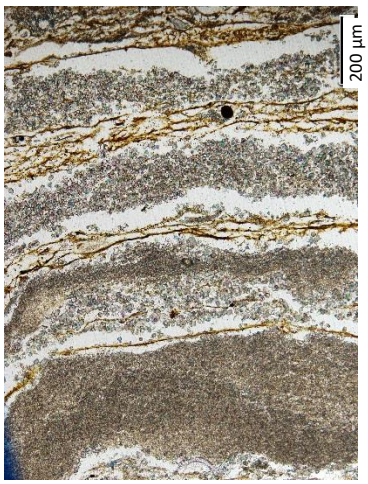
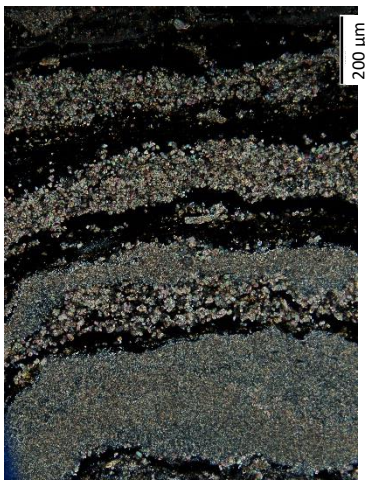
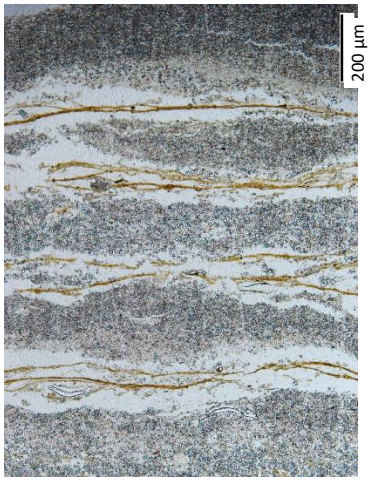
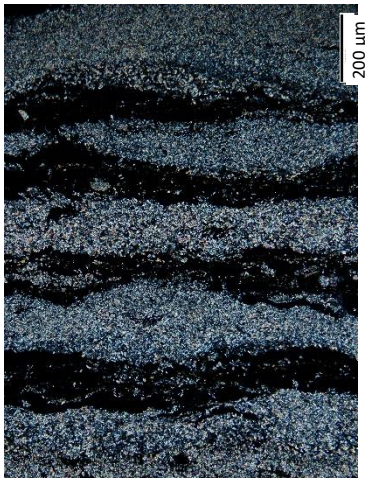


(i) Aragonite	0.30	- Fine grained (~6-10µm), euhedral calcite crystals - Dense and well-defined with abrupt boundaries
(ii) Bacterial mat/ amorphic organic	0.15	- Amorphic organic matter - Higher concentrations of diatoms/carbonates

2b Aragonite/organic (with detrital carbonate)



(i) Aragonite	0.29	- Fine grained (~6-10µm), euhedral calcite crystals - Dense and well-defined with abrupt boundaries
(ii) Detrital/peloidal carbonates [present in 16% of varves]	0.65	- Peloidal clusters of anhedral carbonate material - Typically occur within the aragonite sublayer but can located anywhere within the varve - Low density
(iii) Bacterial mat/ amorphic organic	0.17	- Amorphic organic matter - Higher concentrations of diatoms/carbonates

	Plane polarised	*Cross polarised*	*Composition*
M1a			Aragonite Calcite Bacterial mat
L1 *Non-varved*			Aragonite Calcite Bacterial mat
M1b			Aragonite Bacterial mat

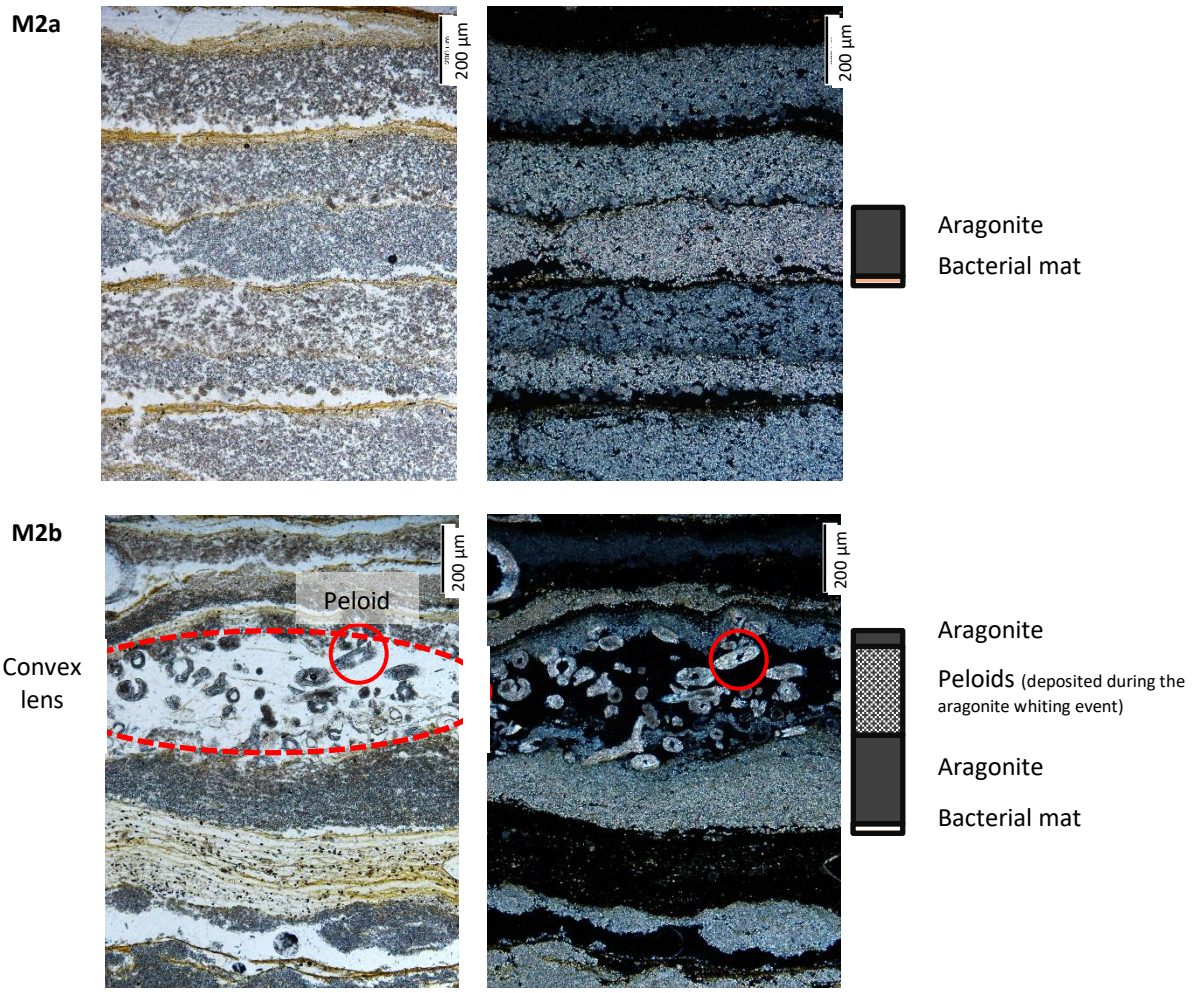


Figure 4.16 *– Magnified (x10) images of typical varves from each of Yaal Chac's microfacies subclasses, as seen in plane-polarised (left) and cross-polarised light (right). Coloured boxes display the extent of one varve, its distinct sublayers and the approximate boundaries measured; the colour and label of these boxes correspond with the conceptual diagram of microfacies (Table 4.6). All images are positioned such that the carbonate sublayers are deposited after the organic sublayers.*

ii) Thickness measurements

Within Unit 2's laminated sediment, all sublayers' composition and structure were identified and their thicknesses measured to an accuracy of 25µm, via thin section microscopy. Changes to key sublayer thickness are displayed in Figure 4.17. The average varve thickness is 0.47 ±0.30mm – significantly thinner than those identified in Nar Gölü's record (average 1.48 ±0.98 mm).

The sporadic deposition of peloidal carbonate sublayers, specifically in M2b varves, has been identified as non-seasonal and turbidite-like. As their deposition is not driven by the seasonal cycle of limnic deposition, thickness measurements will be excluded from microfacies data (unless stated otherwise), consistent with the approach for Nar Gölü. Nevertheless, their occurrence and thickness provide additional palaeoenvironmental insights, and will be analysed together with the other sedimentological proxies.

Sublayer measurements do not display any discernible up-core trend of increasing thicknesses, associated with downcore sediment compression (Biondi *et al.* 1997). At a depth of 198cm, Unit 2's topmost sediment has likely been compacted by the overlying material to its maximum extent; while sedimentation rates and grain size determine the compaction rates between lakes, its influence is generally limited to the top 100cm within Nar Gölü and other varved lacustrine records (e.g. Biondi *et al.* 1997; Hughen *et al.* 2000; Kalugin *et al.* 2013; Maier *et al.* 2013). Therefore, all changes to sublayer thicknesses within Unit 2 are likely to reflect the inter- and intra-annual variability to sediment accumulation.

There is no significant relationship between carbonate and organic sublayer thicknesses, indicating that independent processes drive the respective sublayers' deposition, assuming negligible diagenetic change. Depending on the microfacies, the carbonate sublayer accounts for 71-84% of a total varve's thickness, thus demonstrating the dominance of seasonal carbonate precipitation in sediment accumulation. While average carbonate sublayer thickness increases from 0.28mm (M2b) to 0.34mm (M1a) moving sequentially through time and microfacies classification, variability to the carbonate:organic ratio is primarily driven by changes to organic sublayer thickness (Fig. 4.17).

As previously mentioned, organic thicknesses are greatest within L1's non-varved laminations (252-320cm; subunit 2ii). Without consistent, annual carbonate precipitation to punctuate the accumulation of organic sediment, successive years' organic deposition would appear adjacent to

each other, where the lack of compositional variability also inhibits the ability to distinguish different years' organic sublayers. Particularly fresh conditions, as inferred by the increased thickness (average 0.21mm; 279-313cm) and occurrence (~89%) of calcite within the carbonate sublayers, may prevent carbonate supersaturation on a regular, annual basis. In addition, increased identification of micritic carbonate minerals in L1's organic sublayers (see Section 4.3.1.1) may indicate that mineralisation may instead be limited to the micro-environment around a photosynthetic organism (Kelts and Hsü, 1978).

Since calcite and aragonite crystals preferentially precipitate in differing limnological conditions and display different morphologies (Kelts and Hsü, 1978), the carbonate sublayer thicknesses need to be assessed in relation to mineralogy; Table 4.7 summarises the key dynamics of calcite and aragonite sublayers. During 8,812-7,872 ±10 cal yrs BP (M2 varves) all carbonate sublayers are comprised solely of endogenic aragonite, with an average thickness of 0.29-0.30mm. Following the onset of M1 varves at 7872 ±10 cal yrs BP, the frequency and thickness of aragonite deposition decreases, as the frequency and thickness of calcite deposition increases. Aragonite deposition drives the sediment accumulation of M1b, while calcite deposition drives that of M1a (Table 4.7). This long-term trend of greater calcite and reduced aragonite precipitation is indicative of lakewater freshening; aragonite preferentially precipitates when the lake's Mg/Ca ratio is greater than two (Kelts and Hsü, 1978), and so fresher conditions would decrease the proportion of time this mineralogical threshold is exceeded. Contemporary sediment traps and limnological monitoring reveals that the lakewater's Mg/Ca ratio of ~11 results in the preferential precipitation of aragonite, thus supporting this relationship between lakewater chemistry and carbonate mineralogy.

Table 4.7 *– Summary of carbonate mineralogy and their average thickness by microfacies classification; for L1's non-varved laminations, data pertains to the occurrence and thickness of the carbonate sublayers within its couplets.*

Microfacies	Aragonite		Calcite	
	Presence in varves (%)	Average thickness (mm)	Presence in varves (%)	Average thickness (mm)
1a	69	0.25	93	0.18
L1	77	0.26	89	0.15
1b	90	0.26	41	0.15
2a	100	0.30	0	0
2b	100	0.29	0	0

Unlike the organic sublayers from Nar Gölü, there appears to be no relationship between the presence of micritic carbonates and the mineralogy/thickness of their corresponding carbonate sublayer. This may relate to the differing role of micritic carbonate precipitation within the sediment stratigraphy. In Yaal Chac, organic sublayers containing carbonate minerals are concentrated within L1's non-varved couplets; those inferred to display fresher conditions. As discussed above, if these fresh limnological conditions prevent consistent, annual supersaturation events, the precipitation of micritic carbonates within the micro-environment are proposed to act as a substitute for lake whiting events; whereas, Nar Gölü's micritic carbonates display the intensification of carbonate supersaturation prior to the rapid whiting event.

Organic sublayer thicknesses of Yaal Chac's M2 varves are comparable with those identified within the non-varved subunit 2ii (L1), averaging 1.5-1.7mm. However, unlike L1's chronology, correspondence between couplet counts and Bayesian modelling of the ^{14}C age-estimates within subunit 2iii indicates that M2's thick organic sublayers are not derived from 'missing varves'; similarly, the low concentration of micritic carbonates within these organic sublayers suggests that micro-environmental precipitation does not substitute for the annual whiting event, as proposed for L1's laminations. Alternatively, concurrent high concentrations of non-seasonal, peloidal carbonate in M2b varves may indicate the role of inwashed terrestrial material and reworking of littoral sediments in enhancing organic sublayer thicknesses. In the split core, six well-preserved woody macrofossils were identified within M2b varves (two of which were radiocarbon dated); this reflects the most abundant concentration of terrestrial macrofossils in the entire core, and again indicates an enhanced influence of terrestrial inwash on sediment accumulation. While C:N ratios were not available at this depth, average ratios of 14.7 from the YC11 core's subunit 2i (master sequence depth 198-290cm) indicate the deposition of terrestrially-sourced organic material within Unit 2.

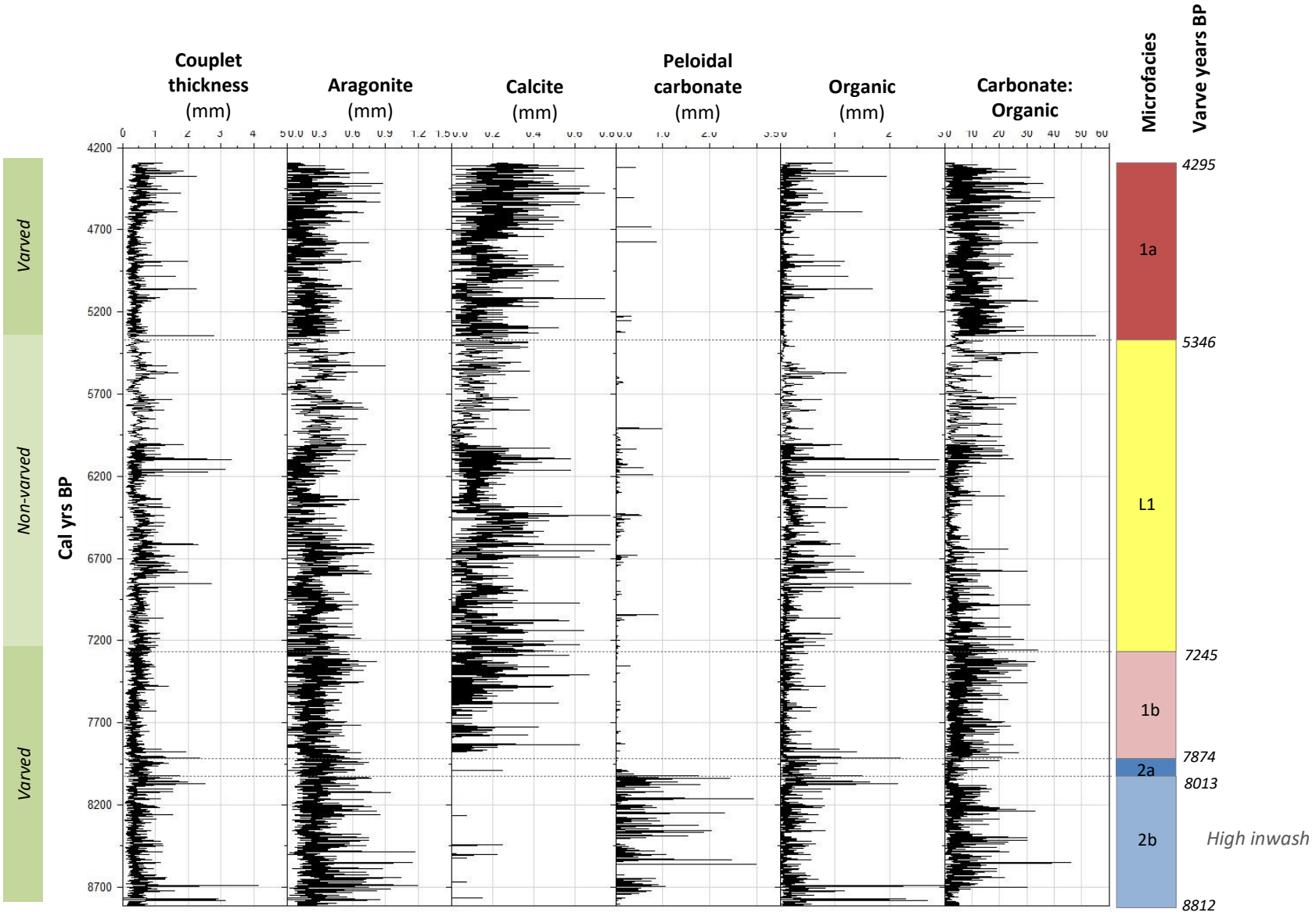


Figure 4.17 *– Thickness measurements of the varves' key sedimentological variables, subdivided by microfacies classification (grey line). L1 laminations (yellow box) highlights the central couplets not verified to represent annually-resolved varves.*

4.3.1.2 Sediment geochemistry

Using Itrax µXRF scanning, geochemical data were retrieved every 200µm through Unit 2's laminated sequence (Fig. 4.18). With an average varve thickness of 0.47 ±0.30mm, scanning is unable to provide elemental counts for every sublayer; the average organic sublayer thickness (0.14mm) is less than the scanning resolution. Therefore, data points will likely suppress each distinct sublayer's geochemical signature by partially detecting elements from the adjacent sublayers. Nevertheless, at least one data point of elemental counts is likely to have been obtained from each varve. Data is able to provide geochemical variability of carbonate minerals, which dominate the Unit's composition, and display the compositional variability undetectable via thin section microscopy.

Calcium (Ca) and strontium (Sr) are the dominate elements detected within Unit 2, averaging 36,100 and 28,900 kcps respectively; while iron (Fe) represents the third most detected element, its average count rate is significantly lower at 1,500 kcps. Total scatter, indicative of non-detectable organic content (Davies *et al.* 2015), also displays high counts (average 23,600 kcps). Ca and Sr negatively correlate with total scatter (r^2=0.65 and 0.22 respectively; P<0.001), reflecting the alternating sublayers of homogeneous calcium carbonate and organic material; correlation coefficients are probably suppressed by the cross-sublayer detection of elements, attributed to the fine laminations, yet relationships still display a high degree of statistical significance. The strong correlation between Fe and Ti detection (r^2=0.71; P<0.001) suggests that Ti's low counts represent a reliable geochemical signal, thus indicating that Fe and Ti deposition is primarily driven by inwash of allogenic material. Any difference between Fe and Ti detection rates may be associated with oxidising and reducing conditions within the hypolimnion (discussed further in Section 4.3.1.2v).

The dominance of Ca, Sr and Fe detection in Yaal Chac's record is very similar to Nar Gölü's geochemical profile. Additionally, the negative correlation between Ca and Sr, and total scatter also portrays the intra-annual variability intrinsic to calcareous-organic varve deposition in both lakes.

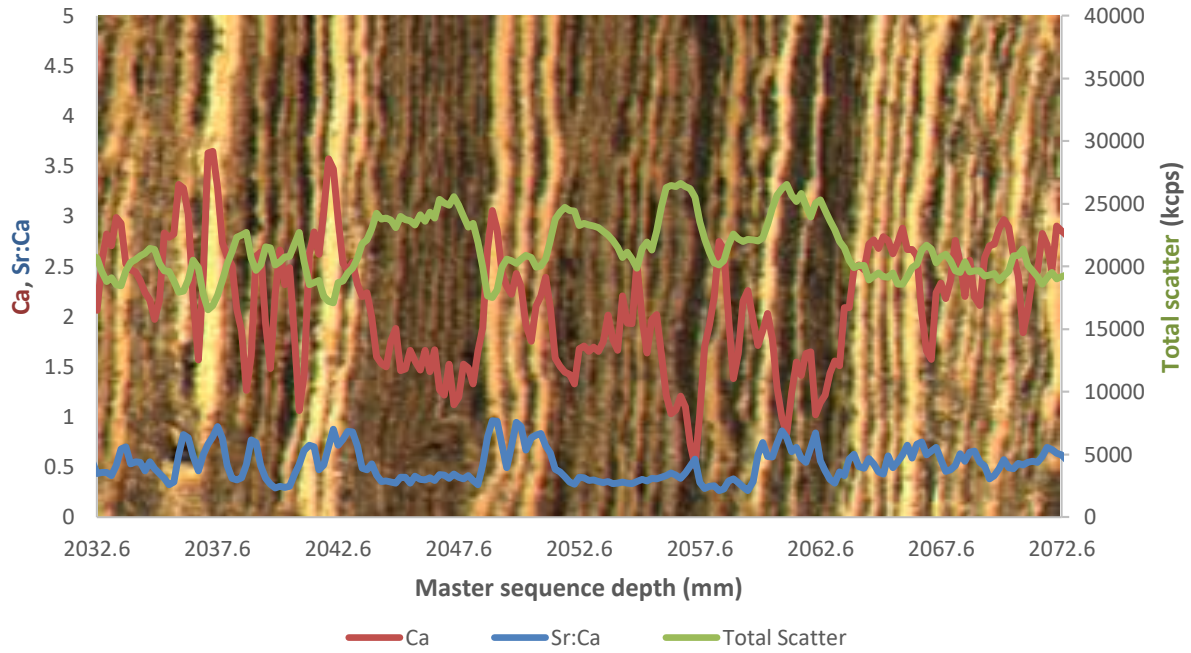


Figure 4.18 *– Example section of the Itrax µXRF core scan; variation to normalised Ca (red line), Sr:Ca (blue line) and total scatter (green line) detection through the sediment is displayed.*

By pairing specific varves to their scanning depth and assuming constant sedimentation rates between these points, the equivalent time-step was calculated for each 200µm-step. The following discusses geochemical variability according to time, alongside the annually-resolved varve sedimentological data. Slight discrepancies observed in the timing of geochemical and sedimentological change may be associated with the uncoupling of datasets between tie points.

i) Principle component analysis

The geochemical variability of Yaal Chac's Unit 2 was assessed and summarised via PCA. Components combine collinear elemental profiles to explain the majority of variability, and reveal underlying trends within the dataset. Specific processes driving elemental deposition and preservation can subsequently be linked to each component (Giralt *et al.* 2011). Figure 4.19 displays the first two axes of the PCA, and Figure 4.20 their correlation with key elemental variability.

Since calcium carbonate deposition drives Unit 2's sediment accumulation, it is unsurprising that Ca and Sr detection high count rates predominately drive geochemical variability. The primary eigenvector explains 85.4% of geochemical variance, and positively correlates with both Ca (r^2=0.92; P<0.001) and Sr (r^2=0.75; P<0.001). The mineralogy of endogenic carbonates also drives much of the sedimentological variability, and hence the secondary eigenvector, explaining 14.4% of geochemical variance, correlates with Sr:Ca (r^2=0.82; P<0.001). The tertiary eigenvector explains just 0.2% of

geochemical variance, and correlates with the sediments' allogenic component Fe (r^2=0.78; P<0.001); as previously discussed, the strong correlation between Fe and Ti indicates that deposition is driven by catchment erosion and inwash processes.

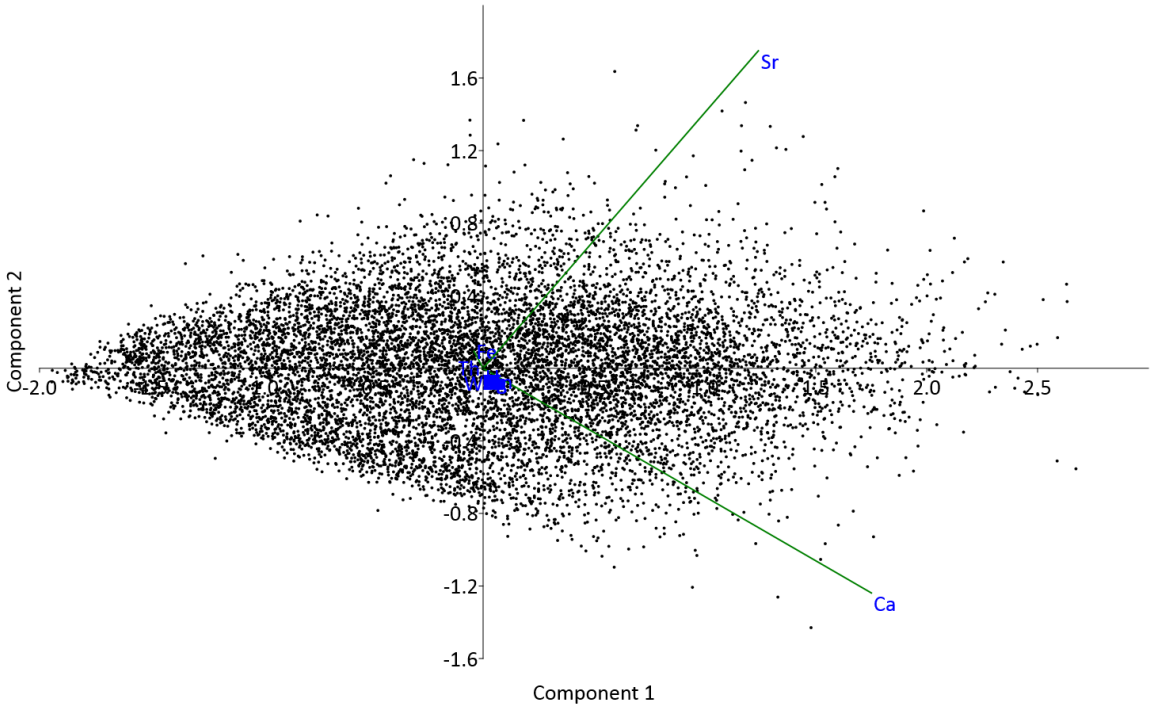


Figure 4.19 *– PCA bi-plot of the primary and secondary axes of Yaal Chac's Unit 2 normalised geochemical data; sample scores (black dots) and principle vectors (green lines) display components driving geochemical variability.*

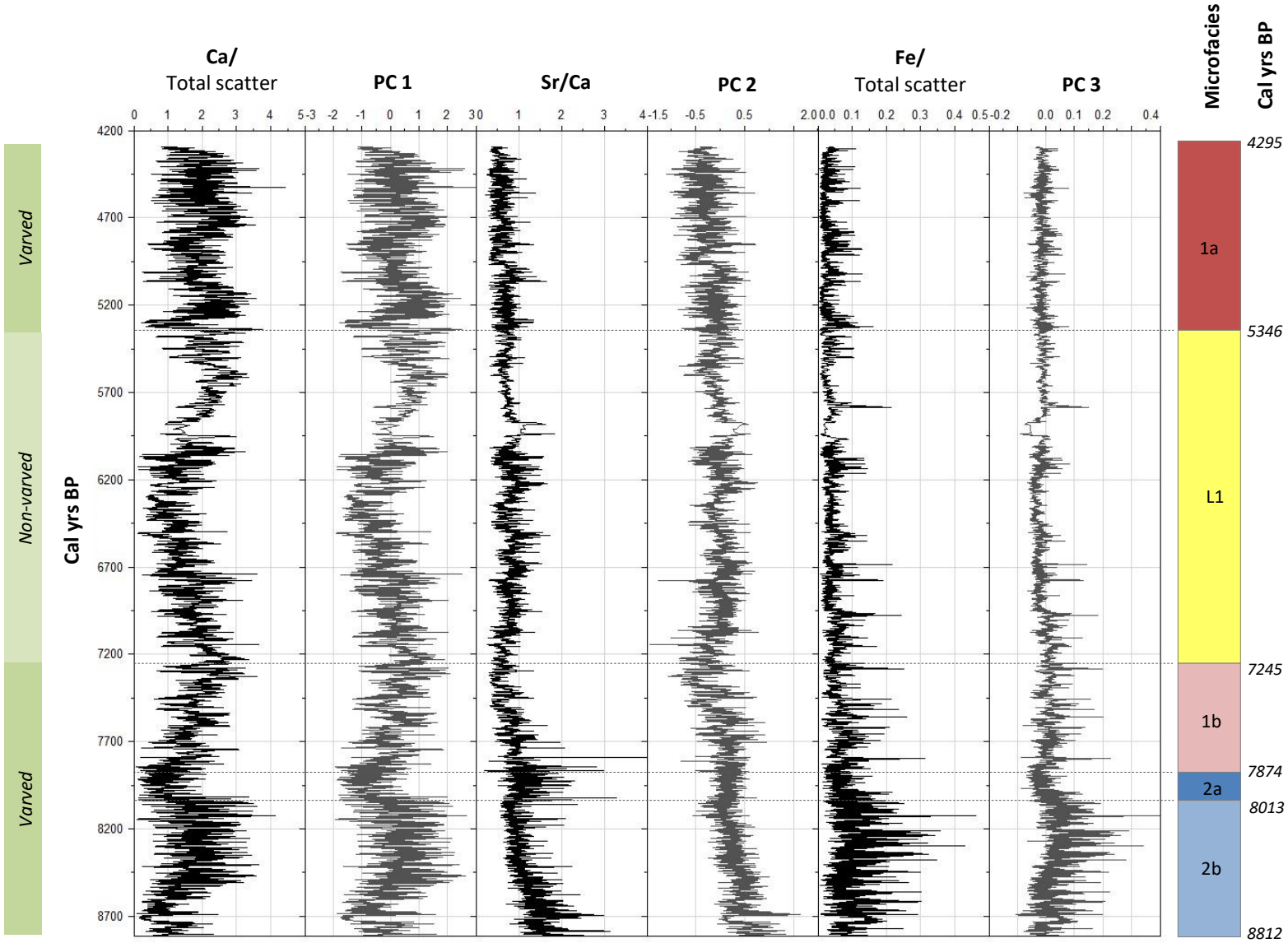


Figure 4.20 *– Comparison between the changes to key elements identified in the PCA (black lines) and the first three significant axes (grey lines); subdivided by microfacies classification (dotted lines).*

ii) Carbonates

As observed in thin section, endogenic calcium carbonate precipitation drives sediment accumulation. Carbonate mineralisation typically occurs during the early dry-season, when water temperature increases in the epilimnion, evaporation concentrations ions and photosynthetic-activity increases pH such that carbonates are supersaturated. However, as previously discussed, the relative ionic concentrations of Mg and Ca determine the specific mineralogies preferentially precipitated (Kelts and Hsü, 1978). When Mg/Ca exceeds (falls below) two, aragonite (calcite) is typically precipitated, and proportionally more (less) Sr is incorporated into the crystalline structure (Müller *et al.* 1972). This dynamic is depicted in Figure 4.21; the Sr/Ca ratio decreases with aragonite sublayer thicknesses, despite consistently high calcium carbonate deposition through the sequence. Since evaporation often drives limnic concentrations across this mineralogical threshold, the Sr/Ca ratio, and hence aragonite detection, are commonly used as a proxy for enhanced E/P climatic conditions (Bayon *et al.* 2007; Zhang *et al.* 2009; Martin-Puertas *et al.* 2011).

In Unit 2, Ca and Sr/Ca geochemical variability generally conform to varve microfacies classifications (Fig. 4.21). The aragonite-rich M2 varves display elevated Sr/Ca ratios, which decrease until the onset of M1's calcite precipitation. Subsequently, Sr/Ca steadily decreases further through M1 and L1 laminae, as aragonite precipitation decreases and calcite increases. However, Ca detection during M2b is highly variable, with peaks coinciding with the identification of non-seasonal, peloidal carbonate sublayers; here, the Ca signal cannot be attributed solely to changes in endogenic carbonate precipitation. If the deposition of these non-seasonal sublayers is associated with the reworking of basin material, their absence alongside the coeval peaks to Sr/Ca during M2a varves, ~8,013-7,874 ±6 cal yrs BP, may indicate sustained drier conditions, where reduced precipitation is not conducive to inwash and reworking of catchment of material into the lake.

Ca detection decreases slightly within the central, non-varved couplets (L1 microfacies), and likely reflects the increased deposition of organic material (Fig. 4.21). During this period, calcite mineralogy dominants the carbonate precipitation events, indicative of fresher limnological conditions. Despite displaying notably thicker calcite sublayers, the non-annual endogenic precipitation likely results in a net reduction to calcium carbonate deposition, and hence the slightly decreased detection of Ca.

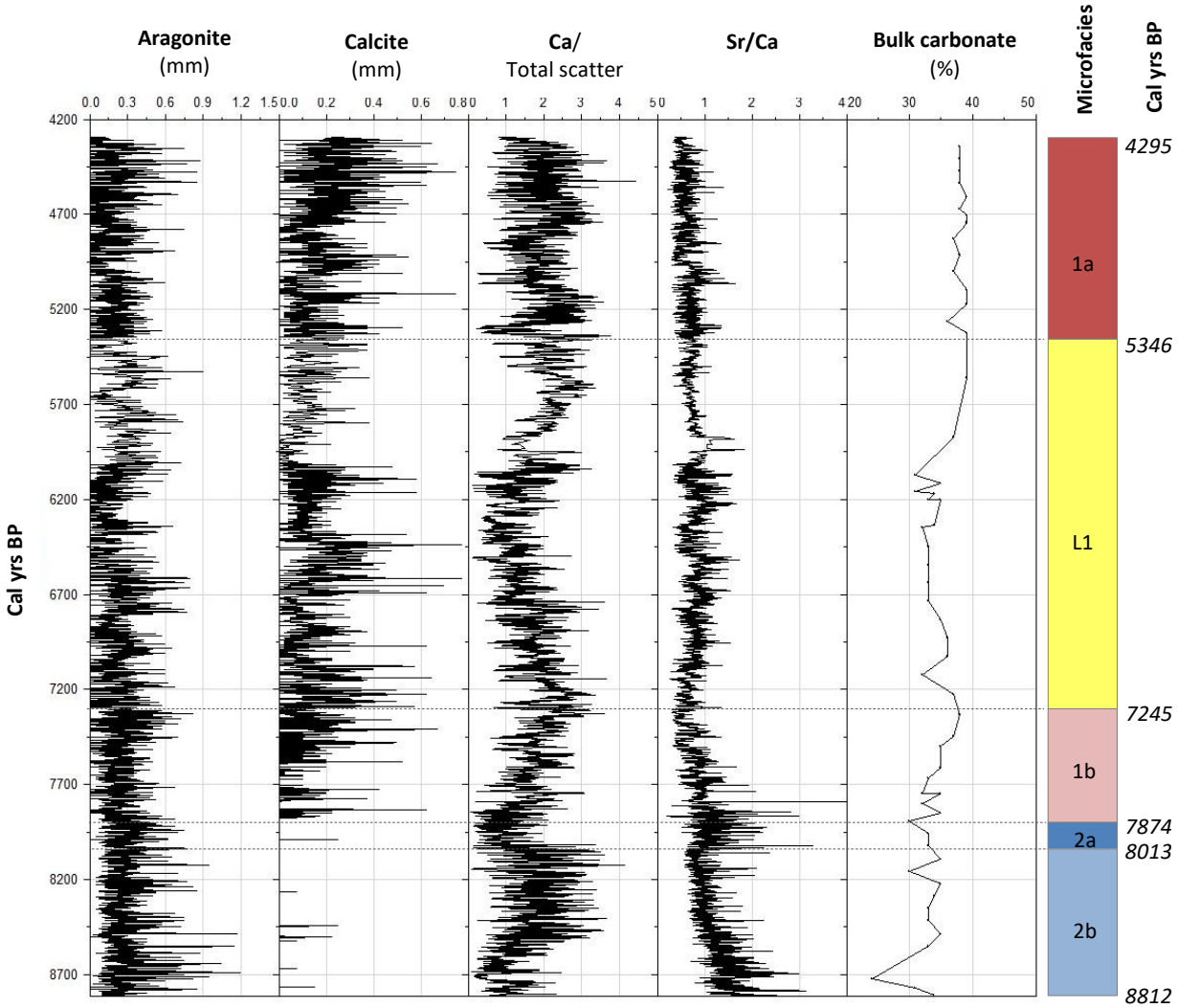


Figure 4.21 *– Changes to sediment microfacies and geochemical composition, relating specifically to calcium carbonate deposition over time, and subdivided by microfacies classification (grey dotted lines). L1 classification (yellow) highlights the central couplets not verified to represent annually-resolved varves.*

iii) Organics

All organic sublayers are primarily composed of amorphic organic matter. Its deposition and preservation within the sediment record is determined by autochthonous productivity rates and diagenetic decomposition. However, organic sublayers are also split into two general classes: 'amorphic organic', composed solely of homogenous organic material, predominately via the deposition of bacterial mats; and 'mixed organic', which also contain varying concentrations of micritic, detrital and/or biogenic carbonate material (Fig. 4.22). While diatoms do not typically preserve well within saline, carbonate-rich lakes (Battarbee *et al.* 2002), the organic sublayers display very few discernible frustules, thus suggesting that diatom blooms may not significantly contribute to carbonate supersaturation events. Again, coherence in trends between the LOI's bulk organic concentration (%) and total scatter (kcps) indicates that the latter provides a reliable, high resolution proxy for organic content.

During M2 deposition, 8,812-7,874 ±9 cal yrs BP, bulk organic concentrations are relatively high (11-28%), corresponding with thicker organic sublayers (average 0.15-0.17mm) and increased total scatter. Two notable peaks in organics are identified at 8,812-8,630 ±2 cal yrs BP (early-M2b deposition), and 8,080-7,910 ±7 cal yrs BP (M2a-b deposition). However, the latter reflects the presence of three thick bands, measuring 29mm, 9mm and 13mm, located at the base of core. These bands were classed as 'mixed organic', and contain very high concentrations of univalve shell fragments held within a matrix of amorphic organic material.

LOI- and µXRF-inferred organic content of M1a and M1b varves is low (~10%), owing to the increased proportion of thin sublayers composed of amorphic organic material. Bulk organic content increases during L1 laminae deposition (~15%), peaking around 6,900-6,000 cal yrs BP. As previously discussed, fresh conditions may prevent the seasonal precipitation of carbonates, which act to punctuate sediment's accumulation. As a result, successive years' organic deposition would increase the subunit 2ii's total organic concentration. During these years without a distinct carbonate precipitation event, the mineralisation of micritic carbonates, observed in a greater abundance within M1b's varves, may effectively replace the rapid whiting events.

The uppermost sediment, 4,610-4,295 ±4 cal yrs BP, displays a final increase in organic sublayer thickness and total scatter prior to the cessation of varve deposition. These sublayers also contain

higher proportions of 'mixed organic' sublayers, reflecting increased concentrations of carbonate material.

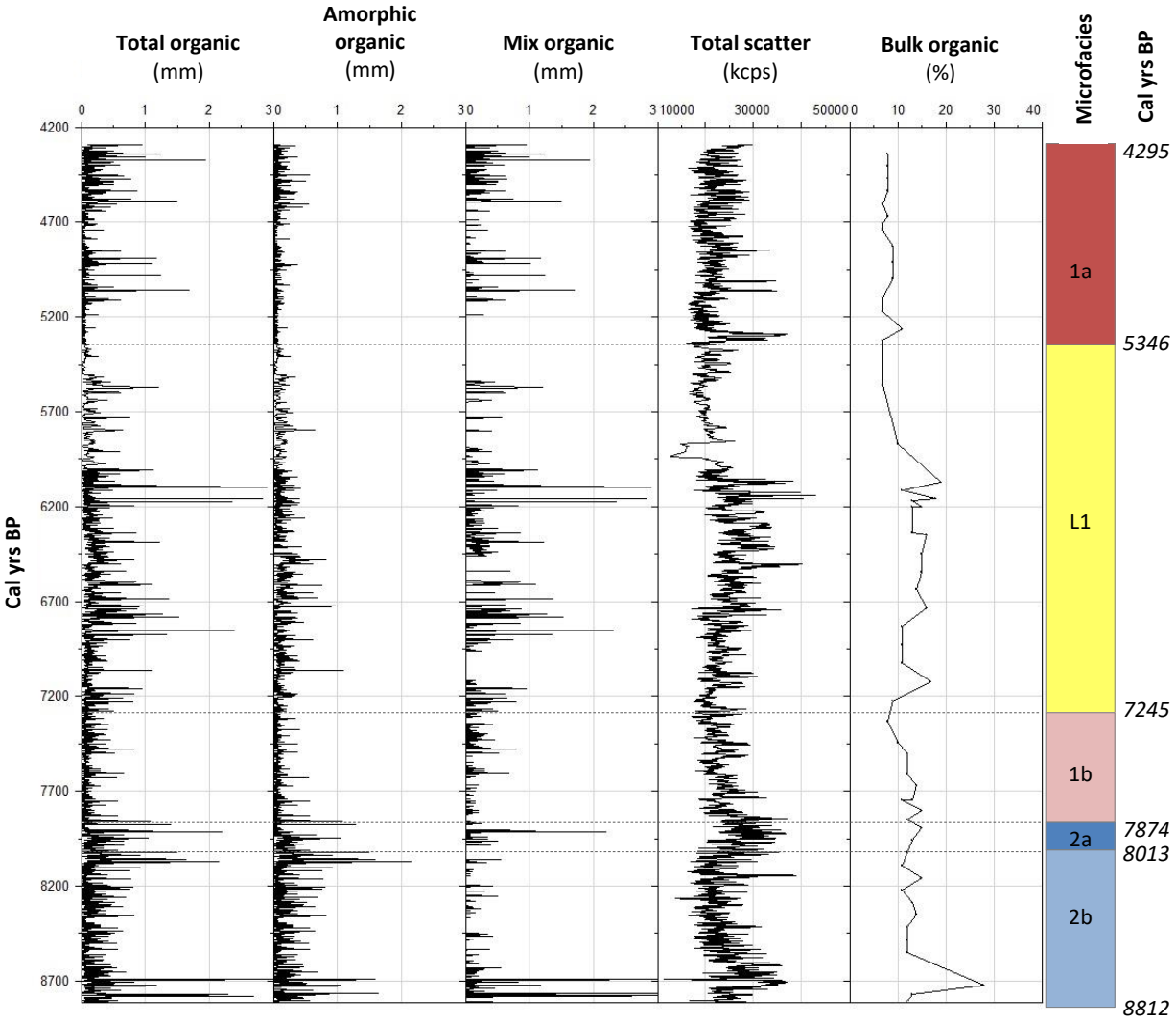


Figure 4.22 *– Changes to sediment microfacies and geochemical composition, relating specifically to organic deposition over time, and subdivided by microfacies classification (grey lines). L1 classification (yellow) highlights the central couplets not verified to represent annually-resolved varves.*

iv) Turbidites

Here, the term turbidite is used to refer to deposition of a non-seasonal sublayer. While the structure and sporadic distribution within the varve stratigraphy strongly resembles those from Nar Gölü's sequence, Yaal Chac's turbidites display a different composition, consisting of peloidal clusters of carbonate material. This compositional dissimilarity is may be derived from the differing geology of their respective catchments; erosion of Yaal Chac's limestone catchment results in the inwash of detrital carbonates, while terrigenous clasts and obsidian are deposited within Nar Gölü's igneous, basaltic-ignimbrite catchment. Turbidites are typically formed via the rapid influx of terrestrial material or the reworking of lake bed sediment due to slope failures, lake level change and turbulence (Dean *et al.* 1999; Corella *et al.* 2012). Extreme precipitation events (Mangili *et al.* 2005), lake level change (Shanahan *et al.* 2006) and earthquakes (Inouchi *et al.* 1996) are known to promote these depositional processes, yet the lack of tectonic activity in the Yucatán can exclude the latter in aiding Yaal Chac's turbidite formation. Alternatively, the non-seasonal deposition of these peloid clasts may reflect the local deposition of faecal pellets from benthic invertabrates, such as brine shrimp, feeding within the carbonate mud (Tucker and Wright, 2009).

As previously discussed, the detection of allogenic elements can also be used to identify the influx of catchment material. Since its deposition is independent of other environmental processes, Ti detection has been established as a reliable proxy for catchment inwash (Haug *et al.* 2001; Metcalfe *et al.* 2010; Davies *et al.* 2015); again, stong correlation between Fe and Ti detection (r^2=0.71; P<0.001) supports the assertion that the low count rates of Ti reflect a true geochemical signal. Figure 4.23 displays these allogenic elements' detection profiles alongside the presence and thickness of turbidites identified from Yaal Chac's Unit 2.

The high concentration and thickness of turbidites define M2b's classification. This turbidite-rich period corresponds to the Unit's highest detection of Ti and Fe, average detection is 2.1 and 2.4 times higher than M1a-M2a sediment respectively. During M2b deposition (8,812-8,013 ±6 cal yrs BP), Ti detection's trend generally follows a normal distribution, peaking ~8,200 cal yrs BP. An abrupt secondary peak, at 8,118 ±5 cal yrs BP, breaks away from the general arching trend and is 13.2 times higher than the Unit's average.

Following M2b deposition, Ti and Fe detection remain relatively low and stable, and do not display any significant variability between microfacies. However, turbidite deposition weakly re-emerges within L1's laminations. These turbidites are present within <1% of L1's couplets and display an

average thickness of 0.15mm. Generally, the geochemical profile does not display a response to the presence of these thin turbidite sublayers; their average thickness is less than Itrax's scanning resolution, thus diluting the detection of allogenic components. Nevertheless, L1's five thickest turbidites, at 7,043 ±410, 6,682 ±353, 6,436 ±256, 6,190 ±209, and 5,909 ±254 cal yrs BP (error derived from Bayesian age-depth model; see Section 4.2.2), correspond to moderate increases in Ti and Fe detection.

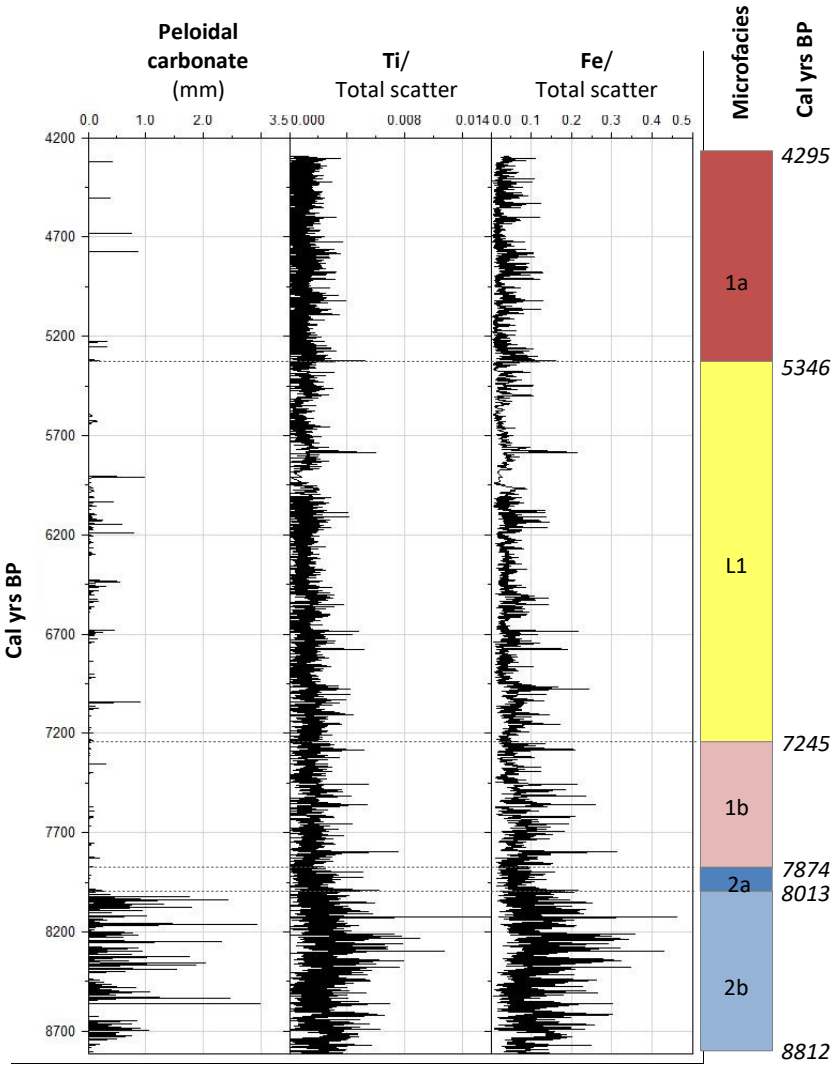


Figure 2.23 *– Changes to sediment microfacies and geochemical composition, relating specifically to turbidite deposition over time, and subdivided by microfacies classification (grey lines). L1 classification (yellow) highlights the central couplets not verified to represent annually-resolved varves.*

v) Diagenesis

Throughout Unit 2, there is very little evidence of diagenetic activity within either of the varve sublayers. The carbonate sublayers' composition of euhedral calcite/aragonite crystals are indicative of primary chemical precipitation (Kelts and Hsü, 1978), and the well-defined crystalline structure suggests dissolution has not affected their morphology post-formation (Brauer *et al.* 2008). Organic decomposition is likely inhibited by sustained suboxic conditions in the hypolimnion. The preservation of varved sediment requires prevailing suboxic conditions for the majority of the year, thus preventing the establishment of benthic organisms which bioturbate the sediment (Zolitschka *et al.* 2015). The lack of intact shells within the stratigraphy further supports proposed suboxic conditions; shelly material is only identified within discrete bands associated within inwash events. Additionally, the Fe/Mn ratio, indicative of redox conditions, remains relatively stable throughout the Unit (Fig. 4.24); values only display a decreasing trend at the onset of M1a deposition. This may reflect a weakening of limnic stratification, following the sustained freshening of lakewater over the entire period of M1-L1 deposition. Increasingly fresh epilimnic conditions may reduce the water column's thermochemical density gradient, thus enhancing lake mixing through the years.

The Fe/Mn ratio correlates negatively with Ca detection (r^2=0.36; P<0.001) and positively with Sr/Ca (r^2=0.16; P<0.001). Contemporary monitoring suggests that Yaal Chac remained thermally stratified for >11 months during 2017 AD (see Section 4.2). If a similar modern mixing regime prevailed during Unit 2's deposition, the limnological conditions required for the seasonal carbonate precipitation and varve preservation would be maintained, namely epilimnic carbonate supersaturation and hypolimnic anoxia respectively. However, the length of time lakewater mixes may vary, which could drive variability in redox conditions and hence Fe/Mn detection; so long as the mixing period remains short enough to inhibit the establishment of benthic organisms. As a result, Fe/Mn is proposed to reflect the duration of mixing, and hence intensity of annual stratification. Weaker stratification (lower Fe/Mn) could replenish the epilimnion with the Ca^{+2} and bicarbonate ions, thus enhancing elemental Ca deposition, while stronger stratification (higher Fe/Mn) could concentrate chemical concentrations such that a great proportion of Sr is incorporated into the carbonate mineralogy. The relatively weak correlations suggest that limnic mixing is not the primary control on carbonate geochemistry. Additionally, covariance between climatology and limnological mixing may drive these observed relationships; for example, reduced (increased) E/P climatic conditions can equally result in reduced (increased) limnic stratification and fresher (less fresh) hydrology.

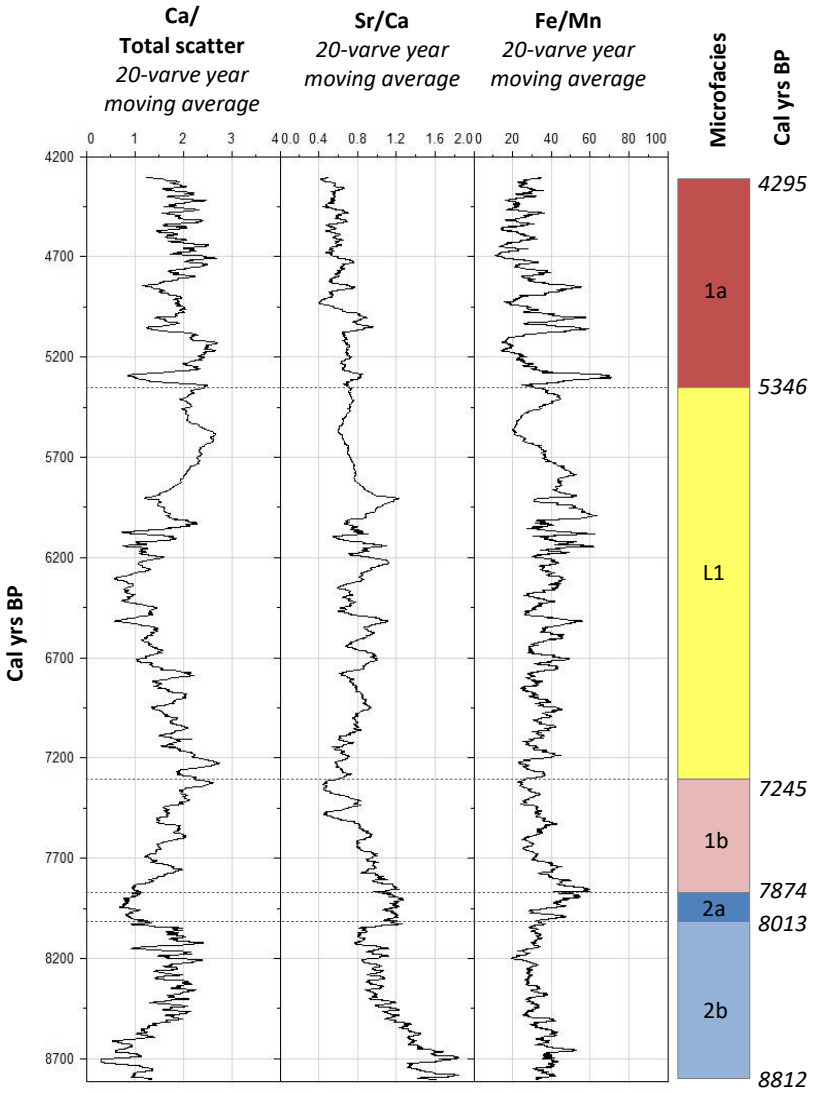


Figure 2.24 *– Changes to sediment microfacies and geochemical composition, relating specifically to carbonate deposition and redox conditions in the hypolimnion over time, and subdivided by microfacies classification (grey lines). L1 classification (yellow) highlights the central couplets not verified to represent annually-resolved varves.*

4.3.2 Mid-late Holocene: Unit 1

Bayesian modelling of the ^{14}C and ^{210}Pb age-estimates suggest that Unit 1's sediment was deposited between 4,295 and -64 cal yrs BP, thus coinciding well with the Holocene's Meghalayan Stage (Walker *et al.* 2018). Sequential radiometric dates from terrestrial plant macrofossils are consistent with continuous sediment deposition, but the sedimentation rate (average ~0.4 mm/yr) varies over time: maximum of 1.36 mm/yr (428 cal yrs BP – present day), and minimum of 0.17 mm/yr (3,059 – 2,064 cal yrs BP) (Fig. 4.25). The inferred increase in sedimentation rate over the last 400 years is probably caused, in part, by a lack of sediment compression. The presence of well-defined laminations distributed throughout the Unit indicates minimal disturbance. Figure 4.25 depicts key sedimentological and geochemical profiles of Unit 1 plotted against the Bacon-derived age estimates, each of these components is discussed below.

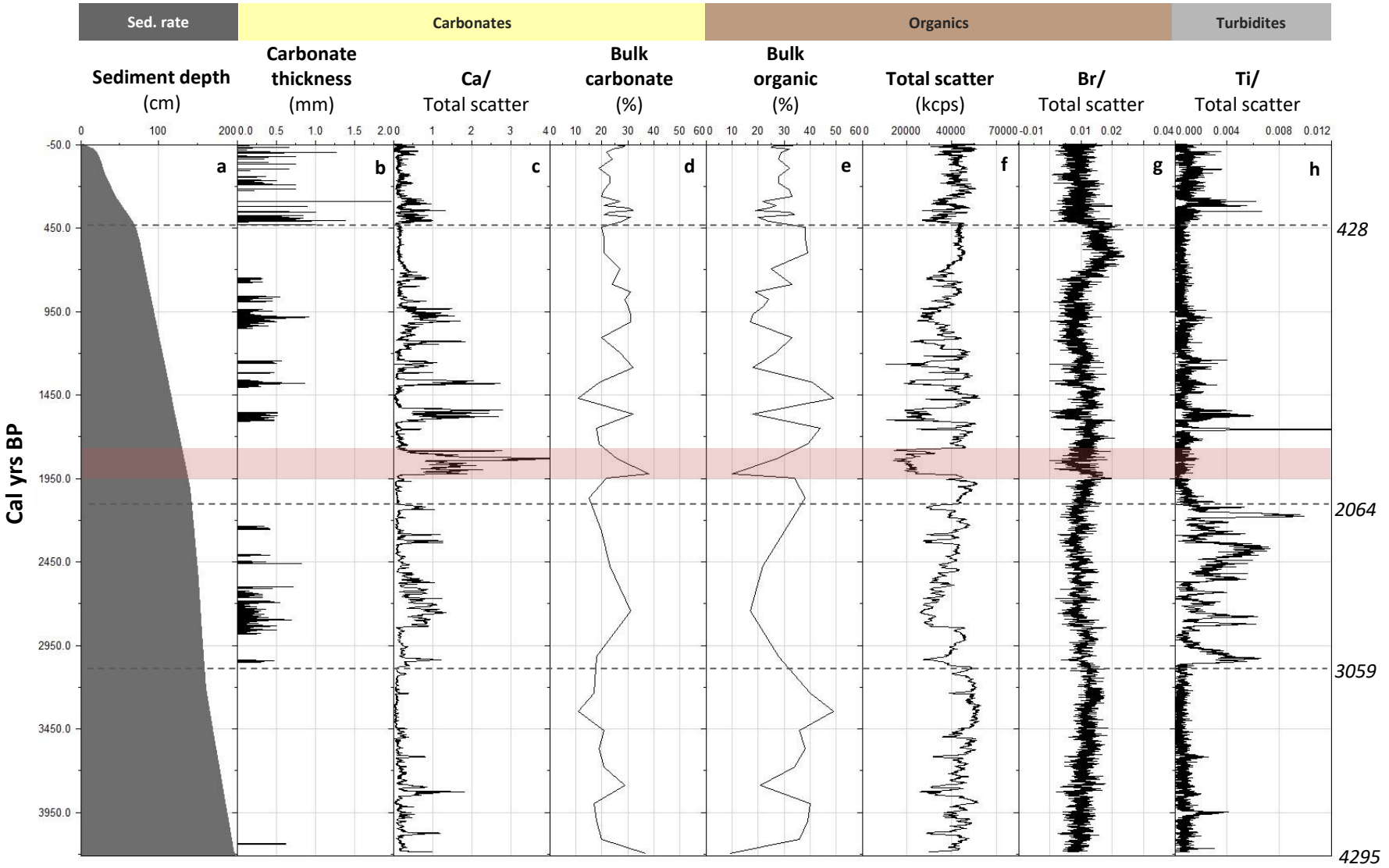


Figure 4.25 – *Sedimentological and geochemical data from Yaal Chac's Unit 1 (YC14). Plotted against modelled age are sediment depths (a), carbonate lamination thickness (b), normalised element counts of Ca (c), Br (g), Ti (h) and total scatter (f), and bulk carbonate (d) and organic (e) content. Red box denotes the distinct band of detrital carbonates and shells, likely formed during a single, localised event.*

4.3.2.1 Sediment geochemistry

i) Principle component analysis

By using PCA of Unit 1's Itrax data, normalised using total scatter (see Section 2.3.3), the elements which explain the majority of the geochemical variability were identified (Fig. 4.26). Analysis indicates that 95.3% of the elemental variance is derived from the primary eigenvector, which positively correlates with Ca (r^2=0.99; P<0.001) thus signifying the leading role of calcium carbonate deposition (Fig. 4.27). While both endogenic precipitation and inwash of detrital limestone contribute to Ca deposition, the dominant presence of euhedral/subhedral crystals within the thin sections indicates that endogenic precipitation primarily drives this geochemical variability. A significant, yet weaker, correlation between the secondary eigenvector and Sr detection (r^2=0.25; P<0.001) is also detected (Fig. 4.27). While this axis only explains 2.6% of geochemical variance, it further highlights the role of endogenic precipitation and the corresponding limnological conditions. As previously discussed, limnic ion concentration determines the minerology of endogenic carbonates, where calcite (aragonite) incorporates a lower (higher) proportion of Sr to Ca into the crystal lattice (Kelts and Hsü, 1978). Finally, the tertiary eigenvector, which explains 2.0% of geochemical variance, strongly correlates with Fe detection (r^2=0.88; P<0.001) (Fig. 4.27). Similar to Unit 2, Fe's strong correlation with Ti (r^2=0.89; P<0.001), and thus association with allogenic, terrestrial inwash (Davies *et al.* 2015), denotes the role of rainfall and/or land use change in driving variability.

Itrax's inability to detect elements lighter than aluminium means that the full geochemical variability of Unit 1's organic component is not represented, while carbonate and terrestrial components may be over represented. Consequently, the processes governing carbonate precipitation and catchment erosion and inwash do not necessarily reflect the main drivers to geochemical variability within the sequence. Nevertheless, average total scatter significantly increases from Unit 2 (23.6 kcps) to Unit 1 (40.1 kcps), thus reflecting the latter Unit's comparatively high organic concentrations.

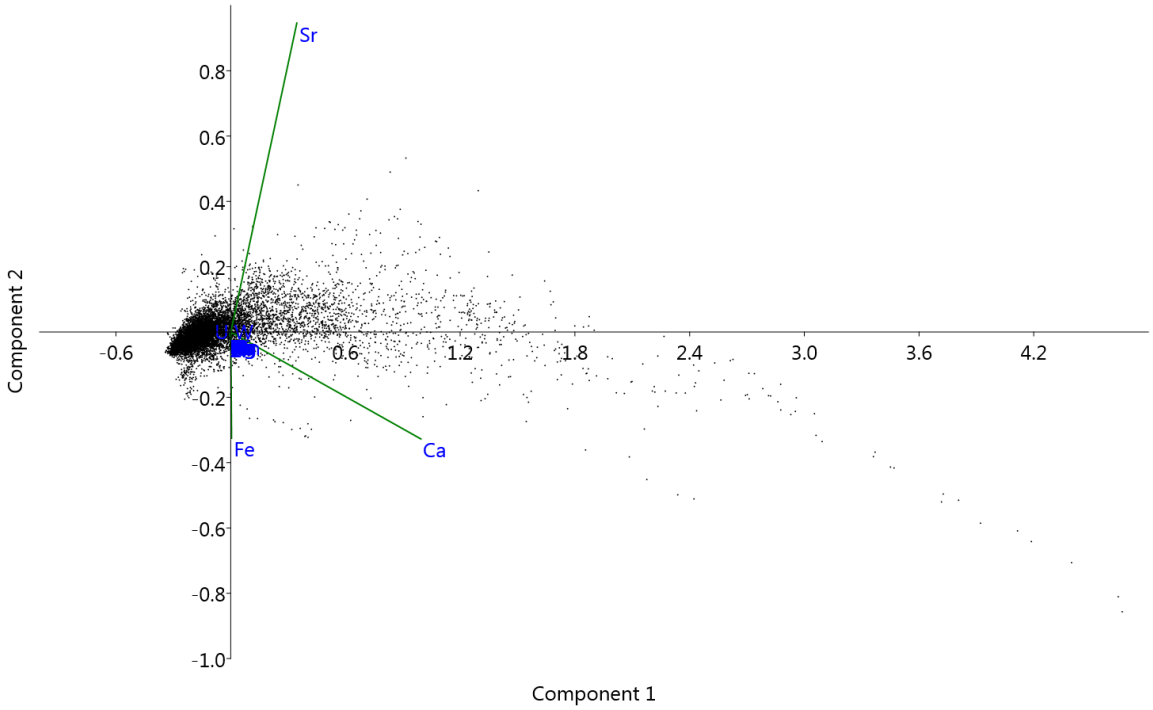


Figure 4.26 *- Principle components analysis' primary and secondary axes, and its identification of Ca, Sr and Fe as key elements explaining geochemical variance.*

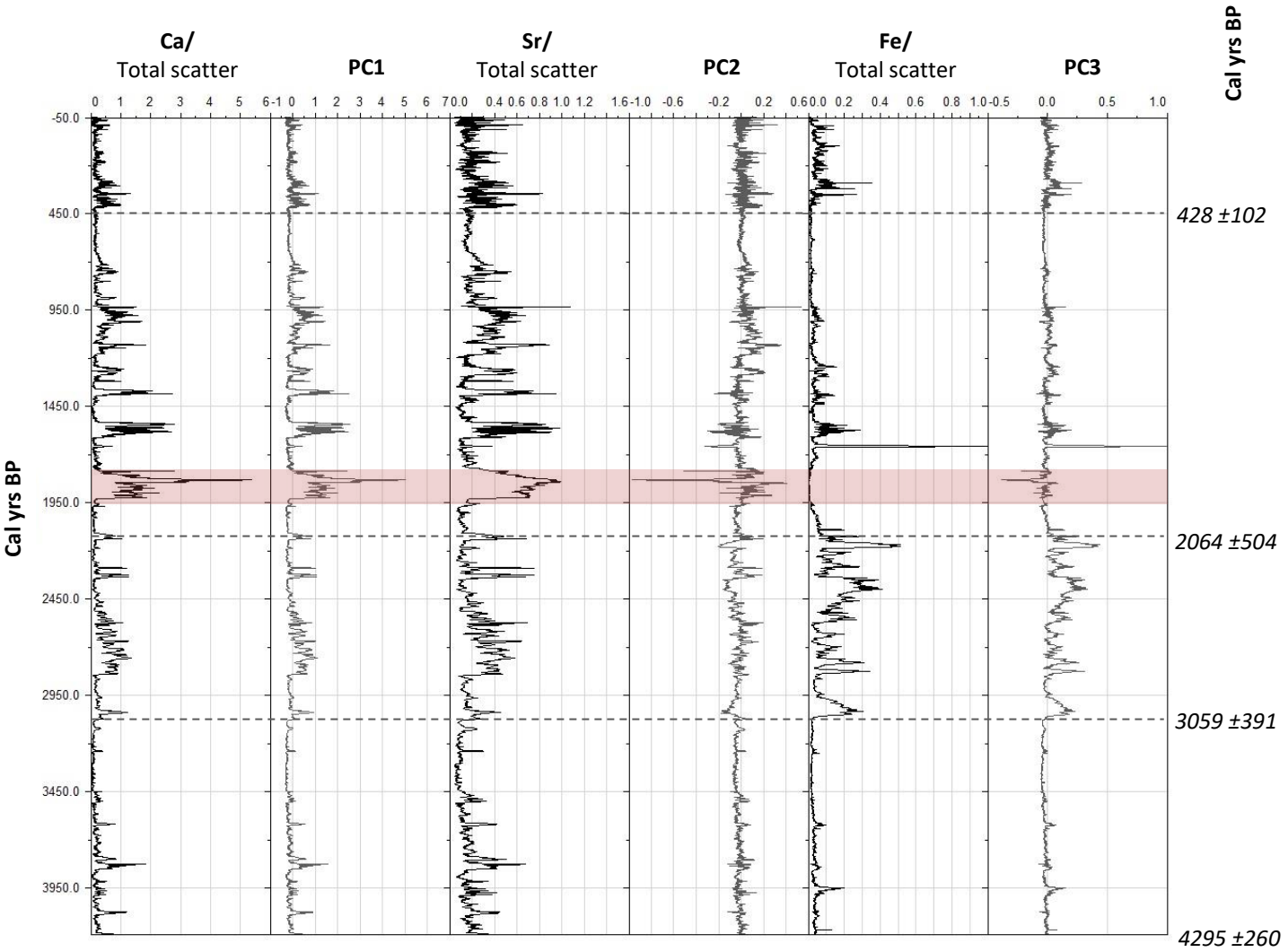


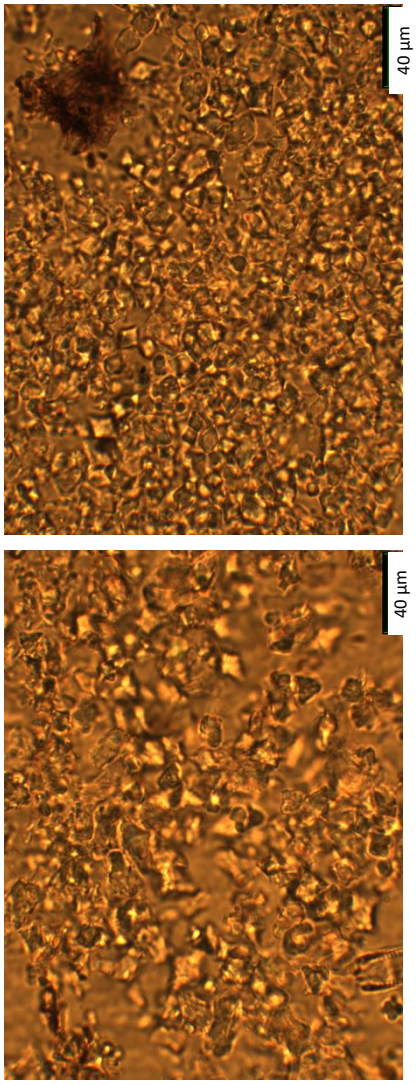
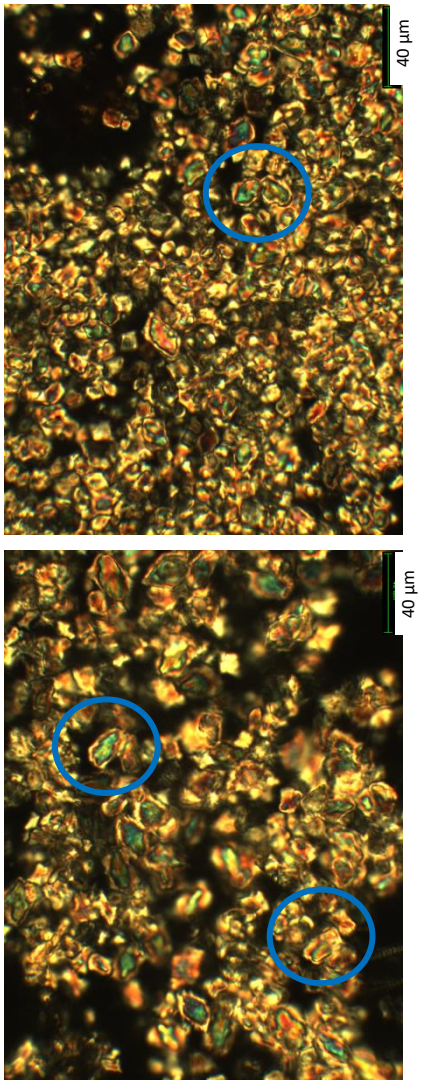
Figure 4.27 *– Comparison between the detection profiles of key elements identified in the PCA (black lines) and the first two significant axes (grey lines). Red box denotes the distinct band of detrital carbonates and shells, likely formed during a single, localised event.*

ii) Carbonates

The carbonate content of Unit 1 is relatively low, averaging ~24% of the total bulk sediments' composition (Fig. 4.25d), as compared to the Unit 2's average ~35%. Similarly, average Ca detection significantly decreases from Unit 2 to Unit 1, averaging 1.64 and 0.31 respectively. However, its concentration is highly variable, ranging from 11-38%; this variability is primarily driven by the deposition of dense, carbonate laminations sporadically distributed through the Unit.

A total of 476 distinct pale laminations were identified and recorded in Unit 1 (Fig. 4.25b). All laminations are composed solely of calcium carbonate crystals ($CaCO_3$) and display relatively little mineralogical variability: 88% are calcite-dominant, 10% are aragonite-dominant, and 2% contain calcite followed by aragonite. As previously discussed, calcite-rich mineralogy is indicative of fresher limnological conditions; low E/P ratios are able to sufficiently reduce ion concentrations, namely the Mg/Ca ratio, to preferentially precipitate calcite during periods of carbonate supersaturation (Müller *et al.* 1972). Carbonate sublayers generally resemble those from Nar Gölü's sediment record. Crystals are typically very fine grained (<8μm) and display a euhedral/subhedral morphology, characteristic of endogenic precipitation (Kelts and Hsü, 1978). However, the proportion of calcite crystals which may be described as subhedral is slightly higher in Unit 1, as compared to the varved Units of Yaal Chac and Nar Gölü. Here, the low concentration of slightly rounded carbonate crystals, with irregular crystal faces, may reflect the dissolution features (Brauer *et al.* 2008). Visually similar crystal morphologies are identified in other hard water lakes and have been associated with the influence of dissolution post-mineralisation, either at the sediment-water interface or as the grain falls through the water column (e.g. Kelts and Hsu, 1978; Brauer *et al.* 2008; Katz and Nishri, 2013) (See Fig**.** 4.28). Further analysis through SEM imaging may provide further evidence of dissolution features, specifically surface etching along crystalline faces (Kelts and Hsu, 1978).

Figure 4.28 *– Example images of calcite crystals deposited within Yaal Chac's Unit 2. Plane- and cross-polarised images taken under 200x magnification using a petrographic microscope at the University of Nottingham.*

	Plane-polarised	Cross-polarised
Unit 1 calcite - Calcite minerals are typically euhedral-subhedral - Some crystals displays slight rounding and irregular faces (for example, those marked with blue circles in the cross-polarised images)		

Carbonate undersaturation in the water column drives dissolution of endogenic carbonate minerals, and may result in the underrepresentation of carbonates in the sediment record (Ohlendrof and Sturm, 2001). Since calcium carbonate is controlled by a dynamic equilibrium, carbonate undersaturation and dissolution can result from decreased temperature and pH down the water column; in Yaal Chac, variability in benthic suboxic conditions may support increased oxidising organic decay, thus releasing CO_2 and consequently decreasing pH. However, the non-laminated sediments' prevailing presence of carbonates yet absence of any discernible structure suggests that distinct laminations have not been lost via dissolution. Sublayers display little or no grading; any

observed up-core fining is again similar to that recorded from Nar Gölü's sequence, and is interpreted to reflect an intensification of carbonate supersaturation through whiting events (Brauer *et al.* 2008). Sublayers also display well-defined abrupt boundaries, indicating a rapid switch to the primary depositional process (Mangili *et al.* 2005).

Over the last 428 ±102 years (0-60 cm), 61 individual carbonate laminations were identified. These are distributed evenly through the sequence, lacking the consistent clustering observed elsewhere within Unit 1. With an average thickness of 0.47mm, laminations generally represent the thickest carbonate sublayers of Unit 1; however, this is probably due to reduced sediment compression. Laminations within the rest of the Unit (4,295 – 428 cal yrs BP; 62-198cm) are typically confined to distinct clusters, where abrupt, alternating carbonate-organic laminations visually resemble varve couplets from Unit 2 (see Section 4.3.1). Unit 1's average carbonate and couplet thickness (0.28mm and 0.54mm respectively) is comparable to Unit 2's varved carbonate and couplet thickness (0.32mm and 0.47mm respectively). As expected, each group of carbonate laminations corresponds to peaks in Ca detection and slight increases to bulk carbonate concentration (Fig. 4.25c and d); LOI's low resolution and use of 1cm subsamples are likely to have smoothed the carbonate content profile, and excluded some of the shorter clusters of laminations. These Ca peaks of 1.5-3.0 are again comparable to the Ca detection levels of Unit 2's varves.

Generally, the deposition of Ca and distinct carbonate sublayers correspond with increased Ti deposition, indicative of catchment erosion and inwash; correlation is most notable during the periods of high Ti deposition between 3059-2064 cal yrs BP, and carbonate clusters within 2064-428 cal yrs BP (Fig. 4.25). Due to the Yucatán's extensive limestone geology, carbonate precipitation is unlikely to be ion limited (Perry *et al.* 2002), where contemporary monitoring highlights the lake's high concentrations of Ca^{2+} and bicarbonate ions. However, the inwash of terrestrially-sourced carbonates may supplement the lake's ion concentrations, thus promoting carbonate supersaturation and endogenic mineralisation.

From 4295 to 428 ±260 cal yrs BP (198-60 cm), there are a total of nine clusters containing at least 10 consecutive, well-defined couplets. However, the short, sporadic nature of these clusters, and the lack of independent dating control within these sequences, inhibit the ability to classify these laminae as varves (Zolitschka *et al.* 2015). The depth, length, and modelled age of these nine clusters of laminations are shown in Table 4.8.

Table 4.8 *– Clusters of carbonate laminations within Unit 1*

Starting depth (cm)	Number of adjacent couplets	Starting age (Cal yrs BP)	AD/BC
66.0	66	**476** ±88	1474
85.4	21	**829** ±299	1121
90.5	39	**964** ±347	986
97.6	82	**1124** ±389	826
107.0	15	**1325** ±443	625
113.1	42	**1463** ±466	487
122.1	54	**1671** ±510	279
151.9	15	**2736** ±415	-786
154.9	60	**2881** ±384	-931

Owing to their strong similarity to the carbonate sublayers of varves from Nar Gölü's Unit 1 and Yaal Chac's Unit 2, it is likely that each carbonate lamination reflects a seasonal carbonate precipitation event. Again, endogenic precipitation results from carbonate supersaturation driven by the combined effect of increased ion concentrations and increased pH, caused by increased E/P ratios and photosynthetically consumption of CO_2 respectively (Zolitschka *et al.* 2015). Therefore, each sublayer is interpreted to represent a single year's dry season, and clusters of these sublayers are tentatively assumed to reflect a series of near-consecutive years.

At 132-137cm sediment depth, a distinct band of bivalve shells and detrital carbonate material is observed (Fig. 4.25 – red box). This well-mixed, gritty layer does not appear in the corresponding YC16 core section (used to bridge the coring gap between YC14 cores 02-I and 04-I), thus indicating that its deposition is not representative of the Yaal Chac's sediment archive. Its homogenous composition of shells and detrital carbonate suggests that material originated from the littoral zone where some terrestrial limestone, and its inhabiting organisms, may have been transported deeper into the lake. It is proposed that this band represents a single, inwash event effecting the immediate vicinity of the core's location. Since YC16 was able to confirm that sediment depths from the sequence before and after, its inclusion within the age-depth model remains valid. However, data from this band must be treated with caution, and it's likely to represent a single depositional event.

iii) Organics

With an average content of 30%, organic matter forms the majority of Unit 1 sediment. The organic matrix appears amorphic, and is likely formed primarily by the deposition of autochthonous biogenic productivity. The deposition of bacterial mats is observed within Unit 2's varves, where larger organic sublayers in the varved Unit are also speculated to be supplemented by diatom blooms and inwash of terrestrial organic material (see Section 3.3.1); these sources of organic deposition are proposed to continue through the lithological units. Thin sections do not display any major changes to the composition or structure of organic components, and appear to remain relatively stable over time.

LOI bulk organic concentration and total scatter profiles from µXRF scanning display strong similarity, supporting the µXRF data's validity as a proxy for organic content (Burnett *et al.* 2011; Davies *et al.* 2015) and consequently increasing the organic signal's resolution. Total scatter displays a strong, negative, logarithmic correlation to Ca detection (r^2=0.81; P<0.001); while this relationship may be partially attributed to uncertainty associated with the closed sum effect (see Section 2.3.3), total scatters link to the LOI profile and the lack of response from the Br and Ti profiles indicate that total scatter provides a reasonable organic content signal. Through the Unit, the sediment abruptly see-saws between organic-dominant and carbonate-dominant composition.

While Br detection has been used as a proxy for biological productivity and deposition (Fedotov *et al.* 2012; Kalugin *et al.* 2013; Davies *et al.* 2015), it displays a relatively weak correlation with total scatter within Unit 1 (r=0.35; P<0.001). The Br profile remains comparatively stable through the sequence, and only notably increases between 428-701 cal yrs BP (67-84cm) alongside coeval increases in bulk organic content and total scatter, highlighting a period of dark, homogeneous, organic-rich sediment (~40%).

The organic-rich Unit also contains shell fragments, and micritic and detrital calcium carbonate throughout. Also observed within Nar Gölü's organic sublayers, micritic carbonate may be formed when photosynthetic activity raises the pH within the immediate vicinity of the organism, across the carbonate saturation threshold (Kelts and Hsü, 1978). The gradual changes to organic composition and structure, as displayed in thin section and the Br detection profile, irrespective of carbonate precipitation events, suggests that the drivers to organic deposition are more sensitive to long-term

changes to productivity instead of seasonal limnological variability. The rapid carbonate precipitation events appear to interrupt the continual deposition of organic material.

The organic components within sedimentary records are controlled by both deposition and preservation processes. Catchment vegetation and its proximity to the lake margin regulate the input of terrestrial organic matter and contribute to nutrient influx (Cole *et al.* 2006). Sediment sampled from the YC11 (master sequence depth 148-198cm) displays an average C:N ratio of 14, indicating the presence of terrestrially-sourced organic material (Kaushal and Binford, 1999). However, the lack of any significant correlation between Ti and total scatter suggests that the inwash of terrestrially-sourced nutrients does not drive major changes to autochthonous productivity. Organic decomposition may affect preservation rates within the record. While contemporary limnological monitoring reveals an anoxic hypolimnion and thermal stratification prevailing for the majority of the year, mixing regimes and hence oxic conditions may vary through Unit 1's deposition. Due to the earlier presence of varves in Unit 2 (which require the prevalence of sub-oxic conditions) and deposition of undisturbed carbonate laminations in Unit 1, anoxic benthic conditions were likely sustained over the past 4,300 years.

Increased average Fe/Mn ratio from Unit 2 (33.90) to Unit 1 (41.94) may indicate enhanced anoxic conditions in the hypolimnion, inhibiting organic decomposition. While both Fe and Mn solubility increase in a reducing environmental, Mn is more sensitive to change (Boyle, 2001), and so the Fe/Mn ratio has been interpreted to reflect changing redox conditions linked to benthic DO and enhanced lake stratification (Haberzettl *et al.* 2007; Davies *et al.* 2015). In Yaal Chac's Unit 1, the peak Fe/Mn values appear to correspond weakly with the deposition of carbonate laminations (Fig. 4.29). Lake stratification may enhance the concentration of carbonate ions within the epilimnion, thus permitting promoting carbonate supersaturation and mineralisation.

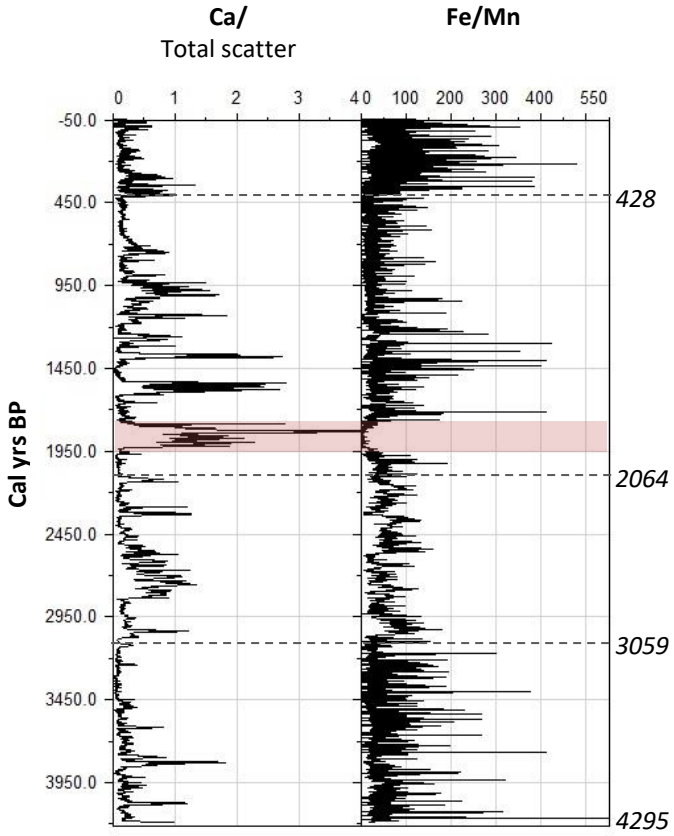


Figure 4.29 *– Comparison between the Ca and Fe/Mn ratio profiles through Unit 1. Red box denotes the rapid carbonate deposition event layer*

iv) Terrigenous input

Owing to the dominant limestone geology of the catchment and peninsula, differentiating between terrestrial and limnological sources of carbonate in thin section is difficult; sediment appears to consist exclusively of carbonate and organic material, albeit from varying sources. As previously discussed, lithogenic elements Fe and Ti are well-used indicators of catchment inwash, primarily driven by precipitation (Haug *et al.* 2001; Metcalfe *et al.* 2010), or land use change (Roberts *et al.* 2016). These elements are sourced from the surrounding catchment; conventional XRF detects Fe (III) oxide (Fe_2O_3) and Ti oxide (TiO_2) within soil sampled around Yaal Chac (~49,100 and 3,305 ppm respectively), where the lower concentration of Ti within the soil likely translates to the lower values within the lacustrine record. While lithogenic weathering initially mobilises Fe within an environment (Cornell and Schwertmann, 2003), biotic processes can govern its concentration in soils (Schwertmann, 1991), deposition in lake sediments (Davison, 1993; Emmenegger *et al.* 2001) and diagenesis (Davison, 1993; Boyle, 2001). In contrast, Ti concentration and mobility are largely independent of biogenic processes (Haug *et al.* 2001), thus providing a reliable indicator of terrestrial inwash (Davies *et al.* 2015). Nevertheless, a strong correlation between Fe and Ti (r^2=0.79;

P<0.001), indicates that variability is primarily a function of catchment inwash, and verifies that Ti's low counts are representative of a reliable geochemical signal. Ti detection is used here as the primary indicator of catchment inwash.

The period 3,059-2,064 cal yrs BP displays a notable, sustained increase to Ti detection (Fig. 4.25h); normalised counts are generally 2-6 times greater than Unit 1's average. Within this comparatively Ti-rich period, detection coevally decreases alongside deposition of the 60-couplet long cluster of carbonate laminations and peak Ca detection starting at 2,881 ±546 cal yrs BP. Despite an apparent increased influx of terrestrial material, this 995-year long period represents the lowest sedimentation rate of Unit 1 (~0.17 mm/yr).

At 127cm depth, a homogeneous clay lamination is identified and dated at 1,783 ±572 cal yrs BP. This grey lamina is composed solely of clastic grains, and the detection of lithogenic elements Ti, Fe, and Rb all display YC14 sequence's maximum detection rates within this 3mm-thick sublayer. Abrupt boundaries and up-core fining suggest this sediment deposition occurred rapidly within a single inwash event.

4.3.4 Additional data

Cross-core correlation between YC11 and YC14 core sequences revealed large gaps within YC11's sediment retrieval. As a result, YC11's sediment and proxy records *fail* to cover: a central ~45cm-long section within YC14 Unit 1, and bottom-most ~130cm (Fig. 4.30). Nevertheless, the following describes the results from additional palaeoenvironmental proxies taken from the YC11 sequence, and analysed by undergraduate students; the methodologies used gain these datasets are outlined in Section 2.5.

Isotope $\delta^{18}O$ enrichment corresponds to calcium carbonate precipitation (Hooper, 2011). Most notably, the abrupt sedimentological transition from Unit 2 to Unit 1 coincides with rapid isotopic depletion from +2.55‰ to -0.16‰ on average. Unit 1's clusters of endogenic carbonate laminations also display sharp isotopic enrichment; increased isotopic ratios of +1.99‰ and +2.35‰ are detected during the deposition of clusters at dated 476 and 829 cal yrs BP respectively. However, due to YC11's coring gap, isotopic data are unavailable for the period in time in which the largest clusters of carbonate laminations were identified in YC14 and dated between 960 and 1,670 cal yrs BP (280-990 AD). Various environmental drivers can act to effect $\delta^{18}O_{lakewater}$ and its subsequent translation into $\delta^{18}O_{carbonate}$. The large range of $\delta^{18}O_{carbonate}$ (-1.94 to +3.66‰) indicates that the isotopic variability cannot be solely explained by water temperature-driven fractionation of $-0.24‰°C^{-1}$ (Leng *et al.* 2006) and calcite-aragonite mineralogical fractionation, where $\delta^{18}O_{aragonite}$ is typically +0.7‰ greater than $\delta^{18}O_{calcite}$ formed at the same temperature (Kim *et al.* 2007). While changes to $\delta^{18}O_{rainfall}$ may act to drive $\delta^{18}O_{carbonate}$ variability, Yaal Chac's hydrologically closed nature increases the relative influence of evaporation on $\delta^{18}O_{carbonate}$ (Leng and Marshall, 2004) In addition, $\delta^{18}O_{carbonate}$ has been commonly interpreted to reflect lake water balance in other closed lakes in the Yucatán through the Holocene, such as Lake Chichancanab (Hodell *et al.* 1995), Punta Laguna (Curtis *et al.* 1996), and Aguada X'Caamal (Hodell *et al.* 2005b).

Using 10cm-long subsamples, particulate charcoal was identified and counted through the three YC11 drives (Harwood, 2011). Charcoal concentration increases to a peak at 32-42cm, roughly dated 450-630 cal yrs BP. Three smaller peaks protrude from this generally increasing trend at 74-84cm, 175-185cm and 216-226cm, approximately dated at 940, 3,400, and 4,700 cal yrs BP. This charcoal trend does not appear to correlate clearly with any sedimentological proxy from YC14. Charcoal variability reflects fire activity within the catchment, and typically originates from human activity or lightning. Vegetation composition and climate can also drive charcoal variability. Dry conditions can

promote organic burning, while wet climates can conversely increase combustible biomass, so long as seasonal dry conditions allow burning (Turner *et al.* 2008, 2010).

Fossil pigments have predominantly been used to infer changes to a lake's trophic state (Leavitt *et al.* 1999) and climatic variability (Battarbee *et al.* 2002), as their assemblage and concentrations are influenced by numerous physical and biochemical parameters (Lami *et al.* 2000). Since pigments are susceptible to oxidising decomposition, their presence can also indicate anoxic conditions in the hypolimnion or rapid burial, typically driven by lake stratification and high sediment accumulation rates respectively (Lami *et al.* 2000). In Figure 4.30, okenone and β-carotene variability have been portrayed (Stevenson, 2011). Okenone is associated with anaerobic sulphur bacteria, and its fossil concentration has been interpreted to reflect anoxic conditions within the hypolimnion (Lami *et al.* 2000). Present within all algae, β-carotene has been identified as the best indicator of photosynthetic biomass and hence bioproductivity (Leavitt, 1993). In Yaal Chac, both pigment concentrations display similar trends throughout the sedimentary records; concurrent increases may relate to increased nutrient availability and lake stratification, where nutrient influx may be concentrated within the epilimnion thus enhancing bioproductivity and subsequent preservation. Unit 2's broad freshening trend, as inferred from YC11's depleting oxygen isotopes and YC14's increasing calcite deposition, may indicate increased rainfall driving this nutrient influx, resulting in increased okenone and β -carotene pigment detection through the Unit; the latter additionally continues to a peak at 164cm (approx. 3,200 cal yrs BP). Later in the sequence, both pigments also peak at 53cm (approx. 470 cal yrs BP) during a period of low carbonate, organic-rich sediment deposition. Again, increased rainfall could drive nutrient inwash and fresher limnology. Excluding these larger peaks, smaller okenone concentration peaks roughly coincide with carbonate deposition, which may indicate enhanced lake stratification and carbonate supersaturation in the epilimnion.

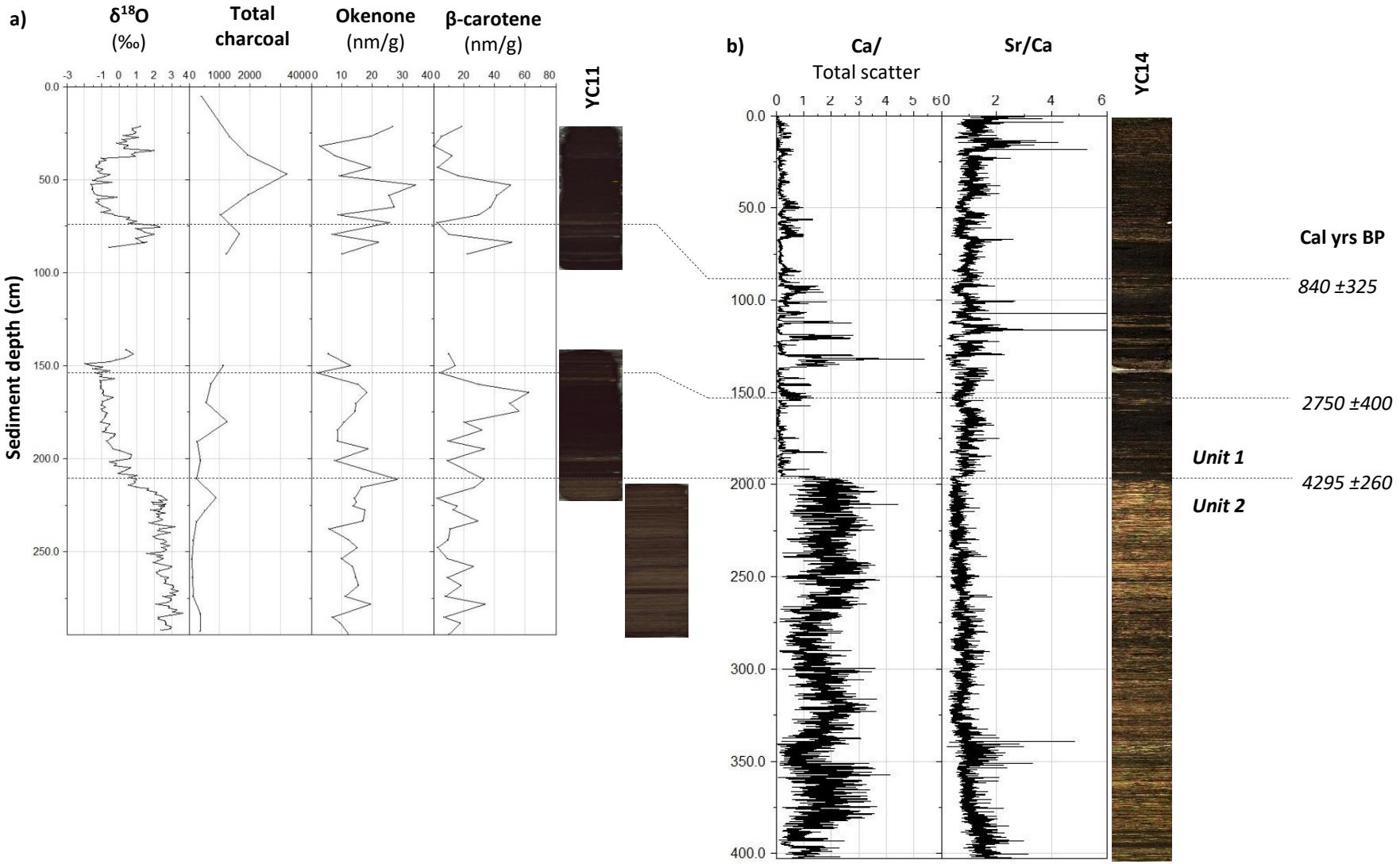


Figure 4.30 *– Oxygen $\delta^{18}O$ isotope (‰) (Hooper, 2011), total charcoal (number of particles within 10cm subsamples) (Harwood, 2011), and Okenone and β-carotene pigment concentrations (nm/g) (Stevenson, 2011) from core YC11 (a) are correlated to normalised Ca and Sr/Ca detection profiles from the full YC14 sequence (b); core scan imagery is displayed alongside the respective profiles.*

4.3.5 Sedimentology: Summary

High resolution sedimentological data has been collected from Yaal Chac's full record. From the early-mid Holocene (8,812-4,295 ±260 cal yrs BP), distinct changes to varve microfacies and their geochemical composition enabled past changes to the climatic and limnological conditions to be inferred. Long-term freshening was identified from the record's long term shift from aragonite- to calcite-dominant precipitation during the seasonal whiting events; a coeval reduction to geochemically-inferred stratification may also dilute epilimnetic ion concentrations, thus contributing to this gradual mineralogical shift. A period of non-varved couplets (7,245-5,346 ±418 cal yrs BP) also likely reflects centennial-scale fresher conditions, where the carbonate solubility level is not exceeded consistently on an annual basis, thus preventing the dry-seasons' whiting events from delineating each year's sedimentation.

Following the transition to discontinuously laminated sediment (Unit 1) at 4,295 ±260 cal yrs BP, the sediments' total carbonate concentration abruptly decreases. However, endogenic carbonate is deposited within discrete sublayers of finely laminated sections, which visually resemble Unit 2's varved sediment. These clusters of increased carbonate deposition correspond with periods of enhanced geochemically-inferred terrestrial inwash and limnological stratification, which is proposed to replenish and concentrate Ca^{2+} and bicarbonate ions in the epilimnion such that calcium carbonate is precipitated.

4.4 Discussion

The analysis of varve microfacies, and their geochemical composition, enabled distinct changes to limnological conditions to be identified and dated within Yaal Chac through the early-mid Holocene (Section 4.3). Section 4.4 places this palaeolimnological record within the context of regional climatic and societal change through the Holocene. Yaal Chac's sedimentary record provides a new high resolution insight into the timing and dynamics of environmental change within the Yucatán Peninsula. These inferred changes are subsequently compared to records of societal change, where temporal correlation between sedimentological and anthropogenic records may indicate the influence of climate on socio-economic change.

Yaal Chac's environmental record is discussed chronologically through the Holocene; periods are defined here according to microfacies classification. When discussing the mid-Holocene (Section 4.4.2), the long-term environmental trends are discussed first, followed by a more focussed assessment of environmental conditions driving lamina deposition within each sedimentary subunit (2i-iii; see Section 4.2.1).

4.4.1 Early Holocene (>8,013 cal yrs BP; M2 varve deposition)

Due to the Yucatán Peninsula's flat topography and highly permeable geology, sea level strongly governs the peninsula's groundwater elevation (Bauer-Gottwein *et al.* 2011). As sea level rose during the Early Holocene, so did the groundwater, such that lacustrine systems within the Yucatán's lowlands were re-established (Brenner *et al.* 2002). Consequently, the formation of sedimentary records corresponds with rising lake levels from ~9,000 cal yrs BP (Metcalfe *et al.* 2000).

The basal sediment of Yaal Chac's YC14 master sequence is dated to 8,812 ±251 cal yrs BP. This basal date is reasonable within the context of regional lake establishment. Sedimentology for the first 931 years is characterised by endogenic aragonite precipitation, increased organic and Ti concentrations, and presence of terrestrial macrofossils and univalve shells. The high concentration of turbidites and allogenic elements identified at the base of the Yaal Chac's sediment record may highlight the role of lake infilling, and the resultant reworking of littoral sediment and shelly fauna. Relatively low lake levels may also enhance ion concentrations within the epilimnion, thus driving the aragonite-dominant mineralogy (Kelts and Hsü, 1978).

During the late glacial, very dry conditions likely prevailed regionally, driving an open-vegetation ecosystem (Leyden *et al.* 1994). Early Holocene isotopic records from Yucatán's lacustrine systems initially display relatively enriched $\delta^{18}O$ values (Hodell *et al.* 1995; Curtis *et al.* 1998). Considering the governance of evaporation on the water balance of closed lake within the Yucatán Peninsula, these high $\delta^{18}O$ values likely reflect low lake levels as the basin infills (Hodell *et al.* 1995). Palynological records display a rapid transition from open to comparatively closed tropical forest vegetation within the Yucatán, representing a shift to increased annual rainfall and humidity (Leyden *et al.* 1994; Carrillo-Bastos *et al.* 2010). This increased precipitation may have contributed to the lake establishment regionally. However, the increasingly dense tropical vegetation has been proposed to limit surface inflow into lake Petén Itza, thus prolonging the lacustrine $\delta^{18}O$ enrichment despite the palynological-inferred wet conditions of the early Holocene (Brenner *et al.* 2002).

Despite increasing sea levels through the early-mid Holocene, minor sea level oscillations inferred around 8,900, 8,600 and 8,400 cal yrs BP, associated with pulses of North American glacial meltwater discharge and isostatic adjustments (Moseley *et al.* 2015), may also have contributed to regional lake level fluctuations. At Yaal Chac, sporadic periods of low lake levels could re-expose the limestone basin and littoral sediment through this period. This may enhance terrestrial erosion rates and sediment resuspension, thus driving the deposition of non-seasonal event layers and increased Ti detection through the M2b varves (8,812-8,013 cal yrs BP). The presence of varved sediment deposition indicates the prevalence of a seasonal climatology during the early Holocene, at least from 8,812 ±251 cal yrs BP; where a northerly ITCZ position, primarily driven by precession-derived increases to the NH insolation seasonality, likely enhanced the climatological seasonality (Hodell *et al.* 1991).

4.4.2 Mid-Holocene / Northgrippian (8,013 - 4,295 cal yrs BP; M1 varve deposition)

Given the strong similarities between Yaal Chac's and Nar Gölü's varve sedimentology and seasonal climatology, the intra-annual processes driving sediment deposition in Nar Gölü may also provide an insight into the mechanisms governing Yaal Chac's early-mid Holocene varve deposition. As previously discussed, contemporary monitoring in Nar Gölü revealed that the annual carbonate precipitation events typically occur during the onset of dry-season conditions, May-July (Dean *et al.* 2015b), where the preceding March-May E/P conditions predominately drive the carbonate deposition (see Section 3.3.2.1iii). Furthermore, calcite and aragonite mineralogies, and their respective sublayers' thickness, correspond with their isotopic composition, a proxy for regional

water balance (Dean *et al.* 2013, 2015a). While Yaal Chac is not presently depositing continuous varves, sediment traps reveal carbonate precipitation to similarly occur during the annual dry-season. Therefore, within Yaal Chac's varved Unit 2, the intra-annual variability of carbonate supersaturation and precipitation may similarly be governed by the onset and intensity of each years' dry-season.

Similar to Nar Gölü's sediment deposition, the precipitation and mineralogy of these carbonate-rich varves is most likely driven by hydrological variability, specifically via E/P conditions and/or changes to groundwater elevation. The extensive carbonate geology of the Yucatán Peninsula and Yaal Chac's high buffering capacity reduces the likelihood that carbonate precipitation may be limited by Ca^{2+} and bicarbonate ions (Perry *et al.* 2002). Yaal Chac's homogeneous, amorphic organic sublayers (see Section 4.3.1.1), may reflect the occurrence of bacterial/algal blooms within the epilimnion, as also witnessed during recent fieldwork (Sarah Metcalfe, pers comm, Apr 2014). While blooms of photosynthetic organisms may contribute to carbonate supersaturation (Kelts and Hsü, 1978), the composition and thickness of Yaal Chac's organic sublayers do not appear to influence the mineralogy or thickness of the carbonate sublayers. Therefore, it is likely that only seasonal climatology is capable of driving annual carbonate supersaturation through the varved sequences. Whereas, over longer (decadal to millennial) timescales, carbonates' mineralogy and microfacies variability may be additionally driven by changes in groundwater dynamics (Whitmore *et al.* 1996); specifically, groundwater's elevation, ion concentrations, water chemistry, and inflow could all contribute to long-term sedimentological changes (e.g. van Hengstum *et al.* 2010).

Owing to the low number of palaeoenvironmental records covering the early-mid Holocene from the Yucatán Peninsula, the region's palaeoclimatology during this time period is not well understood. Yaal Chac's carbonate sedimentology indicates a multi-millennial, freshening trend from 8,812 ±17 to 4,295 ±260 cal yrs BP (see Section 4.3.1); aragonite sublayer thicknesses and their Sr:Ca content consistently decrease through the M2 varves until the onset of M1's varves, which subsequently display steady increases to calcite deposition and thickness (Fig. 4.17). As alluded to above, consistent varve deposition requires a degree of limnological seasonality (Zolitschka *et al.* 2015). Consequently, despite the fresher limnological conditions, an annual dry-season likely persisted throughout the Holocene. Applying the sediment-climatic links inferred at Nar Gölü, the millennial-scale freshening signal observed within Yaal Chac Unit 2 record may reflect an increasingly shorter and/or less intense dry season. Alternatively, this mineralogical-inferred freshening trend

may be driven by increased lake level or enhanced groundwater inflow, acting to dilute ion concentrations such that calcite is preferentially precipitated.

Caribbean sea level is inferred to increase throughout the Holocene; rapidly at first, estimated increases of +3-4m/kyr until 7,000 cal yrs BP, and decelerating to +0-1m/kyr until present-day (Gabriel *et al.* 2009; Milne and Peros, 2013; Khan *et al.* 2017). The Yucatán's groundwater would likely display a corresponding increase to its elevation over time (Covich and Stuiver, 1974). Considering groundwater's influence of lake establishment and infilling across the Yucatán (Brenner *et al.* 2002), Yaal Chac's lake level may increase with groundwater elevation throughout the Holocene. A deeper lake would likely dilute relative ion concentrations, thus drive the millennial-scale freshening trend inferred through Unit 2's laminated sequence, 8,812-4,295 ±260 cal yrs BP.

Circum-Caribbean palaeoclimatic records from Haiti (Hodell *et al.* 1991), Florida (Grimm *et al.* 1993), and Cuba (Fensterer *et al.* 2013) remain largely independent from Caribbean sea-level rise and Yucatán's groundwater dynamics. These records similarly display initial wetting trends, peaking between 8,000 and 6,000 cal yrs BP, prior to long-term drying through the mid-late Holocene. Petén Itzá's sediment density record (Hillesheim *et al.* 2005) also displays a comparable wetting and drying trend, where density minima around 9,000-7,500 cal yrs BP are interpreted to reflect the epoch's wettest conditions. While relatively rapid $\delta^{18}O$ depletion within Petén Itzá's (Curtis *et al.* 1998), Lake Chichancanab's (Hodell *et al.* 1995) and Lago Puerto Arturo's (Wahl *et al.* 2014) isotopic records indicate abrupt limnological freshening within the period 8,000-6,500 cal yrs BP, their isotopic profiles do not correlate strongly with Lake Miragoane's climatically-sensitive record (Hodell *et al.* 1991) (Fig. 4.31).

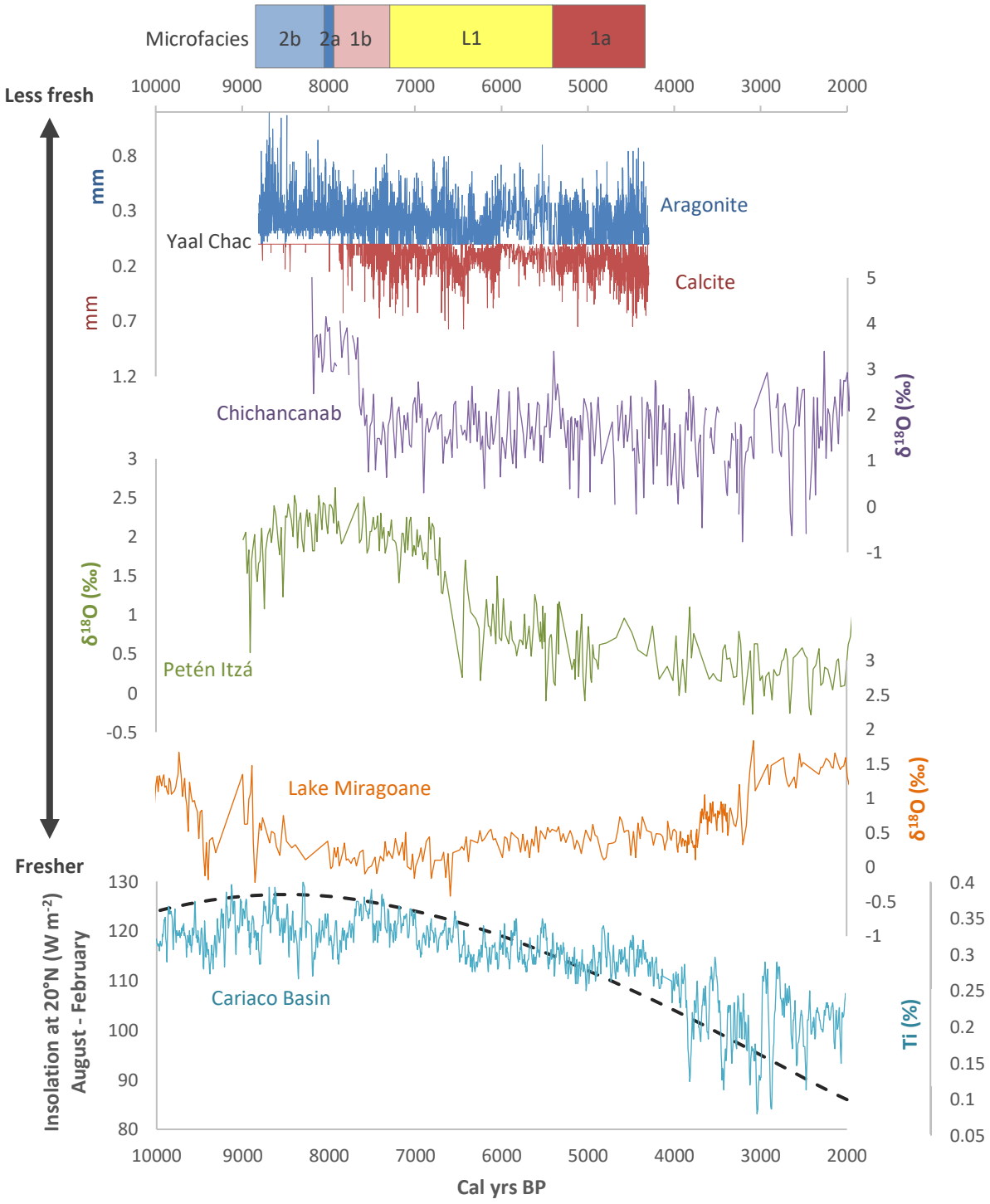


Figure 4.31 *–Thickness of aragonite (blue) and calcite (red) sublayers in Yaal Chac, and $\delta^{18}O$ variability from Lake Chichancanab (purple) (Hodell et al. 1995), Petén Itzá (green) (Curtis et al. 1998), Lake Miragoane (orange) (Hodell et al. 1991), and Ti content from the Cariaco Basin (cyan) (Haug et al. 2001) through the early-mid Holocene; data shown alongside modelled insolation seasonality at 20°N (W/m^2) (dashed black line) (Berger, 1978).*

The mean ITCZ latitude is reconstructed to reach its most northerly extent during the Holocene's thermal maximum, around 9,000-8,000 cal yrs BP, and subsequently migrates southward until the LIA, around 500 cal yrs BP (Haug *et al.* 2001; Schneider *et al.* 2014). Orbital-derived variation to seasonal insolation is known to influence mean ITCZ position, where increased NH seasonality results in a northerly migration to the ITCZ (Haug *et al.* 2001). More northerly ITCZ positions displace the subtropical high pressure systems, enabling easterly winds to bring moisture from the Caribbean across the Yucatán, thus driving wetter climatological conditions during the wet-season (Metcalfe *et al.* 2015; Aragon-Moreno *et al.* 2018). Through the early-mid Holocene, Ti-inferred ITCZ position (Haug *et al.* 2001) corresponds well with modelled insolation seasonality at 20°N. This, in turn, drives millennial-scale hydroclimatic variability, as inferred from palaeoclimatic records from the climatically-sensitive Lake Miragoane, Haiti (Hodell *et al.* 1991) (Fig. 4.31). The Yucatán Peninsula's palynological records similarly suggest that vegetation responded to ITCZ migration, and consequently precipitation variability, through the early-mid Holocene. As a result, the re-establishment of tropical forest and wetlands across the Yucatán lowlands was facilitated by the peak rainfall conditions during the early-mid Holocene (Leyden *et al.* 1993, 1994).

This long-term wetting-then-drying climatic trend is not inferred from the Yaal Chac's microfacies records and other lacustrine isotope records within the Yucatán (Hodell *et al.* 1995, Curtis *et al.* 1998; Hillesheim *et al.* 2005) (Fig. 4.31). Instead, these records generally display sustained freshening trends, most likely indicative of increasing water level. Here, orbitally forced insolation changes cannot explain the long term climatic trends, where the rising groundwater elevation is proposed to dominate the long-term limnological change.

While Unit 2's long term mineralogical switch from aragonite- to calcite-dominate sediment indicates a millennial-scale limnological freshening, the loss of varve deposition within subunit 2ii (L1 laminations; 7,245-5,346 ±339 cal yrs BP) has also been proposed to reflect a period of increased fresh conditions. As previously discussed, L1 contains 1099 distinct couplets deposited within a period of 1,899 ±339 years, as estimated using Bayesian age-depth modelling of radiocarbon dates. Compared to the adjacent varved subunits, fresher limnological conditions have been proposed to prevent carbonate supersaturation on a seasonal basis, thus resulting in the couplet counts' underrepresentation of time (see Section 4.2.2).

The effect of seasonality, water depth and lake stratification across varying timescales are proposed to drive the apparent disparity between inferred fresh limnological conditions driving both M1a's

calcite-rich varves and L1's 'missing varves'. While groundwater-derived increases to lake level could result in the gradual change to dominant mineralogy, changes to the seasonal dynamics of epilimnic water chemistry may drive the incidence of 'missing varves' (Zolitschka, 2007). Figure 10.2 and the following examine the palaeolimnological reconstruction inferred from Yaal Chac, divided according to its lithological subunits:

*Subunit 2iii (*8,812-7,245 cal yrs BP*)*

Due this rapid early Holocene sea-level rise, Yaal Chac's level is proposed to increase most rapidly during subunit 2iii varve deposition (8,812-7,245 cal yrs BP) (Fig 4.32). While this period probably contained its shallowest lake levels of the Holocene, varve deposition indicates that the water must have been deep enough for lake stratification with prevailing anoxic conditions in the hypolimnion, typically >10m deep (Ojala *et al.* 2000). High climatic seasonality (Hodell *et al.* 1991) would drive seasonal carbonate supersaturation, where the comparatively low lake level and high salinity would result in the preferential precipitation of aragonite (Kelts and Hsü, 1978). As Yaal Chac's lake level increases with sea-level change through the 1,567-year long period, lake water salinity would gradually decrease leading to the onset of calcite precipitation (7,874 ±10 cal yrs BP). Increased precipitation, as inferred from the re-establishment of tropical forests (Islebe *et al.* 1996; Islebe and Hooghiemstra, 1997), driven by an orbitally-derived northerly ITCZ position (Hillesheim *et al.* 2005), may similarly contribute to this limnological freshening. Within shorter decadal-centennial scales, intra-annual E/P variability may drive changes to carbonate thickness. Similarly, enhanced lake stratification may drive shorter periods of increased ion concentrations in the epilimnion, thus favouring aragonite precipitation (Kelts and Hsü, 1978); these inferred limnological conditions are most notable during M2a varve deposition (8,013-7,874 ±6 cal yrs BP), which display concurrent increases to its sediments' Fe:Mn and Sr:Ca ratios.

While the 8,200 cal yrs BP climatic anomaly (Alley *et al.* 1997) is inferred to drive a ~200-year long period of increased E/P conditions in Central America (Lachniet *et al.* 2004; Hillesheim *et al.* 2005; Wahl *et al.* 2014), Yaal Chac's carbonate microfacies do not display a significant response. Subunit 2iii's persistent freshening trend is proposed to primarily respond to rising groundwater elevation and lake level, thus suppressing the centennial-scale climatic signal. Nevertheless, allogenic-element Ti detections displays a notable peak around 8,200 cal yrs BP within Yaal Chac's record, indicative of enhanced catchment erosion and inwash. Considering anthropogenic activity is unlikely to significantly influence land use through the early Holocene (Brenner *et al.* 2002), the inferred-dry event may have disturbed local vegetation, thus enhancing terrestrial erosion and inwash of

allogenic material. Unfortunately, a distinct lack of pollen records from the northern Yucatán prevents the establishment of this relationship. However, the dense tropical forests, which require high annual rainfall, identified within the southern Lowlands would probably be sensitive to multi-centennial periods of drier climatic conditions (Leyden *et al.* 1994), yet palynological records have lacked the chronological control to reliably detect vegetation's response to the 8.2 ka event.

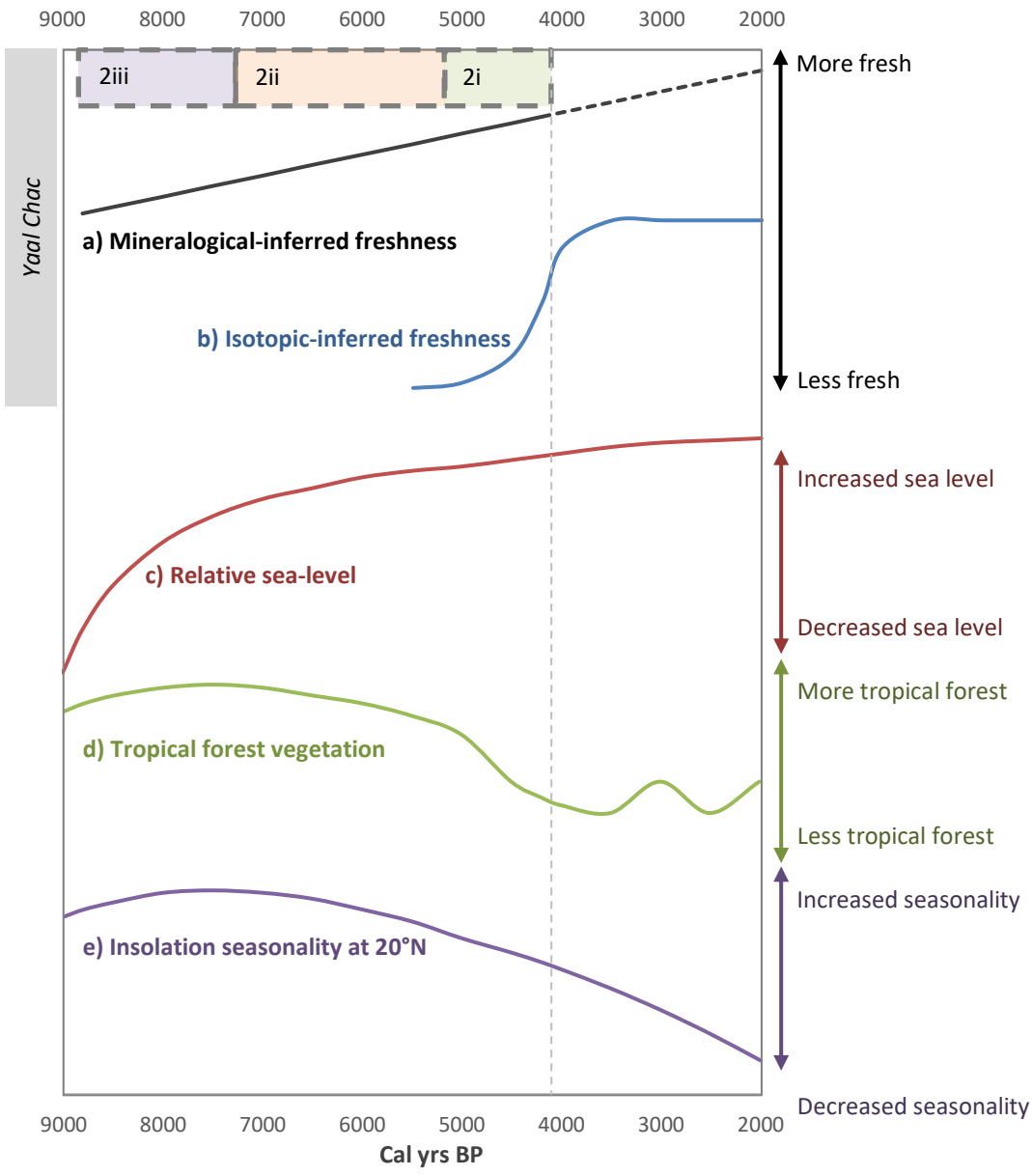


Figure 4.32 *– Conceptual reconstruction of Yaal Chac's mineralogical- and isotopic-inferred freshness (a and b), alongside changes to Caribbean sea level (c), tropical forest cover (d) and insolation seasonality at 20°N (e). The dotted grey line marks the cessation of varve deposition around 4,295 cal yrs BP; this abrupt reduction to carbonate deposition and preservation may reflect long-term lake water dilution, driven by sea level or vegetational-derived changes to groundwater dynamics, and/or changes to carbonate dilution, associated with seasonal organic productivity rates.*

Subunit 2ii (7,245-5,346 cal yrs BP)

Within subunit 2ii (7,245-5,346 cal yrs BP), continued lake level rise may sustain the millennial-scale freshening trend, as inferred from the net switch from aragonite- to calcite-dominated precipitation. The occurrence of 'missing varves' likely reflects years in which the epilimnion's carbonate solubility level is not exceeded across the lake. The basin's limestone geology probably maintained high concentrations of Ca^{2+} and bicarbonate ions, thus retaining a high buffering capacity and reducing the likelihood that the omission of individual years' whiting events were limited by ion availability and/or lake acidification (Perry *et al.* 2002). Similarly, the deposition of well-defined laminae with euhedral carbonate crystals and moderately high Fe/Mn content suggests that the loss of varved deposition is not related to processes effecting varve preservation, namely carbonate dissolution and bioturbation respectively. As previously discussed (Section 4.3.1.1), the deposition of micritic carbonates, formed around a photosynthetic organism's immediate vicinity, is proposed to reflect a restricted extent of carbonate precipitation during the dry-season. Again, decadal periods of aragonite deposition may be associated with enhanced lake stratification, consequently increasing epilimnic ion concentrations.

Reduced limnological seasonality, favouring overall fresher conditions, may also contribute to the loss of varve deposition (Zolitschka *et al.* 2015). Considering Yaal Chac's subtropical climatology, increased rainfall and/or reduced evaporation during the dry-season could inhibit carbonate supersaturation in the epilimnion, thus preventing the occurrence of annual whiting events; changes to humidity/wind would likely drive intra-annual evaporation rates, due to the high air temperature which prevails throughout the year. Increased turbidite frequency within this subunit indicates enhanced catchment erosion and inwash (Mangili *et al.* 2005), thus highlighting the potential role of rainfall in driving fresher limnological conditions and increased allogenic deposition. While annual rainfall may decline as the ITCZ's migrates southward from 8,000 cal yrs BP (Haug *et al.* 2001), its mean latitude remains the highest of the mid-late Holocene, thus sustaining comparatively high annual rainfall (Hillesheim *et al.* 2005). Concurrent orbitally-derived reductions in insolation seasonality at Yaal Chac (Berger, 1978) may result in non-varved sediment deposition, where the declining E/P seasonality cannot sufficiently supersaturate the increasingly deep lake.

Alternatively, the increased occurrence of storm events, and the resultant influx of freshwater, prior to the dry-season could also inhibit carbonate supersaturation during the subsequent months. Considering that present-day hurricanes typically occur between June and October (Boose *et al.* 2003), an increased frequency of these extreme events could reasonably contribute to the incidence

of 'missing varves'. Groundwater elevation has been observed to respond rapidly to contemporary hurricane activity over the northern Yucatan, rising up to 1m following a hurricane Gilbert in 1988 (Marin *et al.* 1990). Prior to 5,000 cal yrs BP, weaker and less frequent El Niño oscillations (Moy *et al.* 2002) and stronger West African monsoons (deMenocal *et al.* 2000; Nguetsop *et al.* 2004) may have led to an intensification of hurricane activity during this mid-Holocene period (Donnelly and Woodruff, 2007). A coastal overwash record from Belize also indicates two periods of enhanced hurricane activity, 6,050-5,750 cal yrs BP and 6,900-6,700 cal yrs BP, within the period of Yaal Chac's L1 deposition (McCloskey and Liu, 2012). However, this increase to hurricane activity is not ubiquitously identified across the Caribbean (McCloskey and Liu, 2012). A Bahaman record does not suggest this increased hurricane activity (Toomey *et al.* 2013), linking suppressed ocean-atmospheric temperature gradients to the precession-derived increases to NH insolation and northerly ITCZ position (Korty *et al.* 2012). This potential disparity between Yaal Chac's subunit 2ii deposition and lack of Bahaman hurricane activity may reflect the sites' differing locations within hurricane pathways (Wallace *et al.* 2014). The period's weak El Niño conditions are conducive to straight-moving Atlantic storms (Colbert and Soden, 2012), thus increasing the propensity for low pressure systems to move west across the Yucatán, instead of east over the Bahamas. Increased turbidite deposition within Yaal Chac through Subunit 2ii and increased inwash of terrigenous elements in Petén Itzá 7,300-4,800 cal yrs BP may similarly indicate enhanced rainfall-derived inwash across the Yucatán (Curtis *et al.* 1998).

Subunit 2i (5,346-4,295 cal *yrs BP)*

The calcite-rich minerology indicates the freshest limnological conditions of Unit 2. While slower, increasing sea-level may still contribute to increasing Yaal Chac's lake level, and hence drive this continued freshening trend; accordingly, this period may reflect highest lake levels of Unit 2. While the insolation's modelled seasonality is the lowest of Unit 2 (8,812-4,295 cal yrs BP) (Berger, 1978), the return of annual carbonate precipitation may be facilitated by the concurrent reductions to ITCZ-derived rainfall (Haug *et al.* 2001) and deceleration of sea- and groundwater-level rise (Gabriel *et al.* 2009). Increased limnological mixing, as inferred from the sediments' Fe/Mn ratio, may additionally promote ion circulation, thus reducing epilimnic ion concentrations and result in the preferential precipitation of calcite. Short periods of enhanced stratification similarly correspond with increased aragonite precipitation.

4.4.2.1 Early-mid Holocene spectral analysis

As previously discussed (see Section 3.4.2.1), ocean-atmosphere oscillations drive climatic variability to varying extents and across various temporal scales (Rossi *et al.* 2011). By matching the frequencies of oscillations identified within a timeseries with known climatic oscillations (e.g. ENSO, NAO etc.), the forcing governing a site's decadal-millennial scale climatic variability may be inferred (Lau and Weng, 1995). Using *Past 3.14* (Hammer *et al.* 2001), spectral analysis identified significant periodicities with the varved subunits over varying time scales (Tables 4.9a-c). Cyclicity was assessed with the two floating varve chronologies (subunits 2i and 2iii) preceding and proceeding non-varved laminae (subunit 2ii) (Table 4.9a-b), and according to microfacies classification (Table 4.9c); all cycles listed are significant to at least $P<0.05$, and their lengths are less than a third of the total timeseries' duration. Due to the uneven time-steps of subunit 2ii (L1 couplets; see Section 4.2.1), data from L1's non-varved couplets could not be reliably assessed for cyclicity (Comboul *et al.* 2014).

Sublayers within the varved subunits 2i and 2iii display different cycles across various temporal scales (Table 4.9a-b). While the multi-millennial scale variability is proposed to be primarily governed by sea-level and groundwater elevation variability, decadal-centennial scale variability to carbonate sublayer thicknesses are likely driven by seasonal E/P conditions. The differing cycles identified between subunits may indicate a climatological shift (Lau and Weng, 1995), whereby different oscillations govern each subunits' sediment deposition across various time scales; alternatively, lower frequency oscillations may be driven by wave-interference from multiple higher frequency periodicities (Gershunov *et al.* 1999), and ultimately driven by similar climatic oscillations.

Within subunit 2iii, only one significant cycle is identified, a 73-year oscillation in the calcite thickness timeseries (Table 4.9b). However, calcite is only present within the period of M2a varves (8,013-7,874 cal yrs BP) (Fig. 4.17). The relatively short duration of this varved calcite deposition (139 years) within subunit 2iii reduces the ability of spectral analysis to reliably detect a 73-year cycle. Overall, the lack of significant cycles within subunit 2iii's microfacies may reflect a comparatively strong influence of non-climatic processes, such as lake infilling and sea level change, on carbonate deposition and preservation within the early record.

Within subunit 2i (5,346-4,295 cal yrs BP), coherent 311- and 135-142-year cycles are identified in both aragonite and calcite timeseries (Table 4.9a). These equivalent cycles indicate that the same forcing drives the thickness variability of both carbonate mineralogies (Lau and Weng, 1995).

Considering the majority subunit 2i's carbonate sublayers (M1a varves) are comprised of both calcite and aragonite components, cycle coherence also suggests that forcing of oscillations acts specifically on the water chemistry which dictates the carbonate mineralogy preferentially precipitated. These centennial oscillations may reflect harmonics of the lower frequency cycle detected within subunit 2iii's aragonite sublayers (~600-year cycles; Table 4.9b). If so, similar climatic oscillations may drive decadal-centennial scale variability of aragonite deposition through both subunits. Additionally, aragonite thicknesses display a 59-year cycle. While this may also reflect a harmonic of lower frequency oscillations, its detection only within the aragonite sublayer record may indicate the influence of climatic forcing conducive to more evaporative limnological conditions.

Spectral analysis was also performed according to microfacies classification (Table 4.9c). Within the calcite sublayers of M1a and M1b, cycles of 142- and 73-years are detected respectively. These periodicities, detected before and after the non-varved subunit 2ii, may reflect harmonics driven by a similar climatic oscillation. While a significant cycle of 597-years is identified within the aragonite timeseries of subunit 2iii, no significant aragonite periodicities are detected within its component microfacies classes, M1b and M2; here, the longer timeseries of subunit 2iii likely resulted in the statistical significance.

The 59-year cycle detected within the aragonite sublayer timeseries is proposed to correspond with the AMO's 45-65 year cycle (Chylek *et al.* 2012). The AMO is known to drive the Yucatán's rainfall variability across decadal timescales (Mendoza *et al.* 2007), and is simulated to be strongest during the early-mid Holocene (Wei and Lohmann, 2012), thus coinciding with the deposition of Yaal Chac's Unit 2. Warmer (cooler) Atlantic SSTs increase (decrease) evaporation and moisture transfer via easterly winds to the Yucatán, thus increasing (decreasing) rainfall and storm frequency during the summer months (Poore *et al.* 2009). Furthermore, AMO cyclicity influences the extent of ITCZ migration, where warm (cold) phases are associated with more northerly (southerly) ITCZ mean latitudes (Green *et al.* 2017). As previously discussed, northward shifts to the ITCZ's mean latitude further increases summer rainfall in the Yucatán, where the Peninsula's wet-seasons would be prolonged by the increased influence of the ITCZ's low pressures system (Aragón-Moreno *et al.* 2018).

Pacific Decadal Oscillation's (PDO) warm (cold) phases also drive northerly (southerly) ITCZ migration (Green *et al.* 2017), and consequently precipitation variability at Yaal Chac (Hillesheim *et al.* 2005). Therefore, Yaal Chac's 59-year cyclicity of aragonite thicknesses may alternatively be driven by the

PDO's 50-60-year cycle. However, contemporary climatology suggests that the PDO primarily influences conditions in the Yucatán via its effect on ENSO. While the precise influence ENSO has on Yucatán climatology is uncertain, Pavia *et al.* (2006) suggest that warm (cold) PDO phases are conducive to wetter (drier) winters during El Niño ENSO phases. Prior to 4,000 cal yrs BP, El Niño oscillations were significantly less frequent and intense (Moy *et al.* 2002), thus minimising the relative influence of ENSO (and PDO) on Yaal Chac's decadal climatic variability.

Within the organic sublayer timeseries, significant cycles of 228- and 48-year cycles are only detected within M2 varve deposition. This overall lack of cyclicity detected within the sequence's organic sublayers suggests that climatic oscillations may not significantly drive variation to organic deposition and/or preservation. Decomposition of organic sediment post-deposition would decrease spectral analysis' ability to identify multi-temporal scale oscillations driving, in part, autochthonous productivity variability. These cycles do not appear to correspond with any known climatic oscillation, and these frequencies may result from the wave interference of multiple oscillations (Gershunov *et al.* 1999).

M2's detrital carbonate sublayers display a significant 163-year cycle. These turbidite-like sublayers have been associated with lake infilling (see Section 4.3.1.1), where each depositional event may relate to: a seasonal lowering of lake level, re-exposing and reworking detrital material in the littoral zone; or increased precipitation, thus enhancing terrestrial inwash. Rainfall variability could drive both of these depositional processes; however, each process would likely be associated to opposing hydrological conditions. Nevertheless, a ~163-year climatic oscillation could reasonable drive, in part, this early Holocene rainfall variability and influence to 'turbidite' deposition. As alluded to above, both the AMO and the PDO could reasonably contribute to this decadal-centennial scale rainfall variability influencing terrestrial inwash. However, considering M2 deposition reflects a period of significant limnological changes proposed to be derived from changes in sea-level, groundwater elevation, and lake level, linking the sporadic deposition of terrestrially-sourced material to climatic oscillations is unfeasible.

Aspect of Microfacies	Significant periodicities				
a) 5346-4295 yrs BP subunit 2i					
Total Carbonate					
Aragonite	311	135	59		
Calcite	311	142			
Total Organic	*No significant cycles*				
b) 8812-8013 yrs BP subunit 2iii					
Total Carbonate	*No significant cycles*				
Aragonite	*No significant cycles*				
Calcite	73				
Total Organic	*No significant cycles*				
c) Microfacies classification					
M1a Aragonite	311	135	59		
M1a Calcite	311	142			
M1a Organic					
M1b Aragonite					
M1b Calcite	73				
M1b Organic					
M2 Aragonite					
M2 Detrital	163				
M2 Organic	228			48	

Table 4.9 *– Periodicities of key sublayer thicknesses, significant to p<0.01 (black) and p<0.05 (grey). Periodicities have been aligned to show synchronicity between variables. Spectral analysis performed on data from the floating varve chronologies of Subunit 2i (a) and 2iii (b), subdivided by varve microfacies classification (c).*

4.4.3 Late Holocene / Meghalayan (4,295 cal yrs BP - present day)

At the Meghalayan Stage's onset, the abrupt switch from Unit 2's carbonate-rich varves to Unit 1's organic-rich sediment at 4,295 ±260 cal yrs BP likely reflects a threshold response to shifting limnological conditions. This sedimentological transition occurs during a millennial-scale drying trend, typically identified across the Yucatán (Hodell *et al.* 1995; Curtis *et al.* 1998; Hillesheim *et al.* 2005; Mueller *et al.* 2009; Wahl *et al.* 2014; Aragón-Moreno *et al.* 2018) and Caribbean (Hodell *et al.* 1991 Grimm *et al.* 1993; Fensterer *et al.* 2013) – associated with the southerly migration of the ITCZ (Haug *et al.* 2001). While this drying trend may be expected to increase endogenic carbonate mineralisation within Yaal Chac, the onset of Unit 1 deposition reflects a rapid reduction to carbonate concentration within the sedimentary record. Instead, the onset of Unit 1 deposition is likely driven by other environmental changes, altering the limnological processes governing Yaal Chac's carbonate deposition and preservation; these include rising (yet decelerating) sea levels, decreasing insolation seasonality, and precipitation-derived reductions to tropical forest (see Fig. 4.32). The following discusses each of these potential environmental drivers to Yaal Chac's sedimentological record.

First, sustained Caribbean Sea level increase (Gabriel *et al.* 2009) would continue to raise the Yucatán's groundwater elevation, and consequently Yaal Chac's lake level; around 4,000 cal yrs BP, Caribbean Sea level is inferred to be around 3m lower than present day (Khan *et al.*, 2017). Accelerated depletion of $\delta^{18}O_{Carbonate}$ precedes Yaal Chac's lithological switch, starting at ~4,700 cal yrs BP and continues until ~3,700 cal yrs BP; here, average isotopic values decrease from +2.6‰ to -1.0‰ respectively. As previously mentioned, isotopic composition from the Yucatán's closed lakes typically reflects lake level variability. Therefore, Yaal Chac's isotopic trend may reflect increasing lake levels, despite net reductions to annual rainfall, where the limnological freshening eventually prevents the carbonate solubility threshold from being exceeding on an annual basis.

Second, decreasing insolation seasonality through the Holocene (Berger, 1978) may reduce the intra-annual variability of regional E/P conditions. Carbonate supersaturation and precipitation may be inhibited by this reduced E/P seasonality, where the weakening of lake stratification and/or enhanced dry-season precipitation may dilute epilimnetic ion concentrations, such that the carbonate solubility level is not often exceeded. A growing influence of nortés on regional climatology, seasonal northerly flows known to bring moisture to the Yucatán (see Section 4.1.2), may drive these wetter dry-season conditions. Additionally, reduced climatic seasonality may increase the length of the annual growing season, thus enhancing autochthonous organic

productivity. While this may initially drive calcite precipitation (Kelts and Hsü, 1978), subsequent decomposition of this enhanced organic deposition has been proposed to decrease hypolimnetic pH and favour carbonate dissolution post-mineralisation within Derby Lake, USA (Wittkop *et al.* 2009). While Yaal Chac's anoxic hypolimnion may limit rates of organic decomposition (Bastviken *et al.* 2004), rounding of calcite crystals within Unit 1 indicates the influence of dissolution post-mineralisation. Additionally, carbonate deposition through a deeper water column may increase the influence of dissolution of calcite grains. Again, reduced climatic seasonality may increase the lake's susceptibility to mixing, where contemporary monitoring highlights the occurrence of short episodes of weaker stratification (~7 days) within a year which may re-oxygenate (in part) the lake's water column. Within a dry-season, these periods of weaker stratification typically occur following incidence of nortés, due the influx of colder, fresh water to the lake's surface. Overall, reduced seasonality through the Holocene may inhibit carbonate precipitation and promote its dissolution through the Holocene.

While changes to seasonality may influence the strength of limnological stratification, anoxic conditions are likely to persist within Yaal Chac's hypolimnion throughout the Holocene. Average Fe/Mn values increase from 33.9 in Unit 2 to 41.9 in Unit 1, indicating enhanced anoxic conditions in the hypolimnion post-4,295 cal yrs BP. The presence of individual undisturbed laminations within Unit 1 further suggests that the loss of varve stratigraphy is not derived from bioturbation, which would require benthic oxic conditions. Here, the intensification of hypolimnetic anoxia, despite weaker climatic seasonality, may relate to the isotopic-inferred deepening of Yaal Chac's lake levels.

As previously discussed, lake stratification may influence carbonate saturation and precipitation in opposing ways between Units 1 and 2. In Unit 2, due to the annual mineralisation of Ca^{2+} and bicarbonate ions in the epilimnion and subsequent transfer to hypolimnion, increased lake mixing may be required to replenish the surface water's ion concentrations. Whereas, in Unit 1, enhanced stratification may be required to promote carbonate saturation in the epilimnion, thus inducing carbonate precipitation despite the fresher limnological conditions. Considering that mineralisation if unlikely to be limited by ion supply (Perry *et al.* 2002), the inwash of terrestrially-sourced carbonate material may additionally contribute to carbonate saturation within Unit 1; correlation between Ca and Ti deposition is identified throughout the Unit, but is most notable between 3,059 and 2,064 ±605 cal yrs BP (see Section 4.25).

Third, vegetation change identified across the Peninsula (Aragón-Moreno *et al.* 2012, 2018; Torrescano-Valle and Islebe, 2015) may effect groundwater dynamics, and hence carbonate solubility levels within Yaal Chac. Driven by ITCZ-derived reductions to annual rainfall and seasonality through the mid-Holocene (Wanner *et al.* 2008; Carrillo-Bastos *et al.* 2013), inferred regional forest cover decreases to transform the Yucatán to a more-open ecosystem, with the transition typically centred on ~5,000 cal yrs BP (Islebe *et al.* 1996; Mueller *et al.* 2009; Rosenmeier *et al.* 2016; Aragón-Moreno *et al.* 2018). From Salpetén in the southern lowlands, this reduction to vegetation density has been proposed to decrease interception and evapotranspiration, and increase infiltration and groundwater flux (Rosenmeier *et al.* 2016). Consequently, this enhanced surface and subsurface flow is inferred to result in higher lake levels, despite overall reductions to annual rainfall (Rosenmeier *et al.* 2002, 2016). However, Rosenmeier *et al.* (2016) note that the Petén basins' steep topography may increase the lakes' sensitivity to vegetation-derived changes to runoff; whereas, within the comparatively flat northern lowlands, the inferred vegetational transitions would instead result in greater downward seepage of water. Nevertheless, a Peninsula-wide change to vegetation composition may elevate groundwater levels and contribute to the fresher limnological conditions inferred at Yaal Chac; a pollen record from or near Yaal Chac would be required to fully examine this relationship.

This mid-Holocene environmental transition across the Yucatán has been linked to a shift in the principle climatic forcing. Prior to ~4,000 cal yrs BP, the climatology of the Yucatán Peninsula and Caribbean is dominated by the ITCZ; its more northerly position, associated with the orbitally-derived increases to insolation seasonality, drives the region's strong wet-dry seasonality and increased annual precipitation (Metcalfe *et al.* 2015). However, as the ITCZ migrates southward through the Holocene (Haug *et al.* 2001), its relative influence on regional climatology decreases (Aragón-Moreno *et al.* 2018) (see Fig. 4.33). This southward shift to the ITCZ's mean latitude is associated with increasing El Niño intensity and frequency (Haug *et al.* 2001). Consequently, as ENSO activity increasingly intensifies over the last ~5,000 years (Moy *et al.* 2002; Conroy *et al.* 2008), its relative influence on the region's climatology increases and ultimately surpasses the ITCZ's annual migration as the dominant forcing through the late Holocene (Bernal *et al.* 2011; Fritz *et al.* 2011; Aragón-Moreno *et al.* 2018). This climatological transition reflects a shift from Atlantic- to Pacific-derived forcing (Jones *et al.* 2015; Muñoz *et al.* 2017), and the resultant climatology is inferred to become comparatively drier and more variable (Metcalfe *et al.* 2009; Fritz *et al.* 2011; Carrillo-Bastos *et al.* 2010, 2013).

Following this mid-Holocene shift to more open vegetation (Curtis *et al.* 1998; Aragón-Moreno *et al.* 2018), the geochemical profile of allogenic elements through Yaal Chac's sediment record may similarly indicate enhanced catchment disturbance (Davies *et al.* 2015); Ti detection increases substantially from 3,059 to 2,064 cal yrs BP and displays a high degree of variability through the period. This sequence corresponds well with the onset of 'Maya clay' deposition identified in a small number of lakes located within the Yucatán's southern lowlands; this allogenic sediment deposition is strongly associated with anthropogenic forest clearance (Binford *et al.* 1987). Alternatively, enhanced El Niño warm oscillations between ~3,500 and 2,400 cal yrs BP (Moy *et al.* 2002) may drive increase E/P conditions and thus vegetational disturbance within the Yucatán (Aragón-Moreno *et al.* 2018) facilitating catchment erosion and inwash in Yaal Chac. Concurrent increases to Ca detection in Yaal Chac may similarly indicate these increased E/P conditions. Both anthropogenic and/or ENSO-related vegetation clearance may reasonably drive coeval $\delta^{18}O$ depletion from Lake Salpetén (Rosenmeier *et al.* 2016).

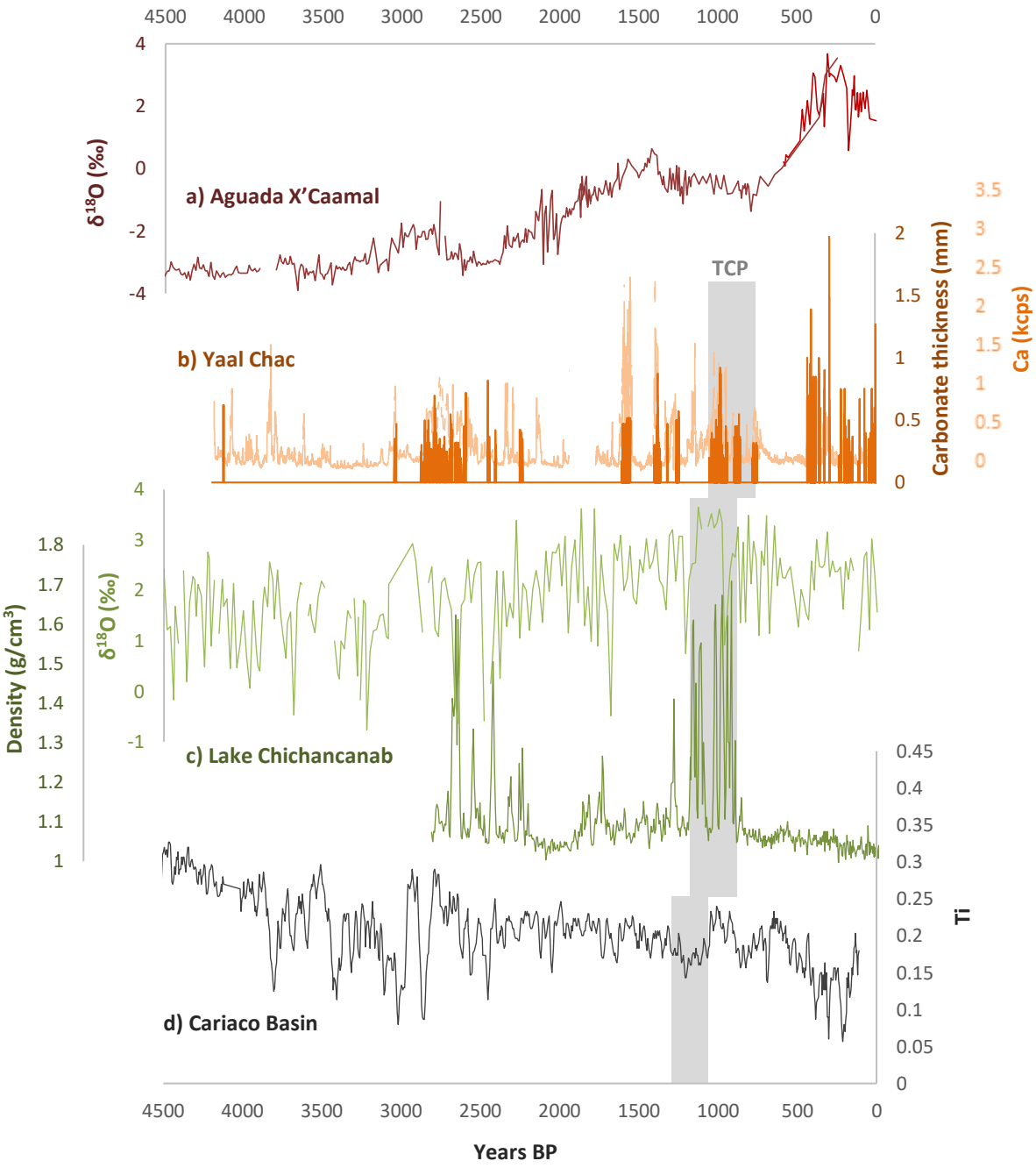


Figure 4.33 – *Mid-late Holocene palaeorecords; (a) oxygen isotope record from Aguada X'Caamal (Hodell et al. 2005b); thickness of carbonate sublayers and Ca detection from Yaal Chac's Unit 1 (b); oxygen isotope and sediment density record from Lake Chichancanab (Hodell et al. 2005a) (c); and Ti detection from the Cariaco Basin (Haug et al. 2001). The multi-decadal drought associated with the Terminal Classic Period (TCP) is constrained by the grey box.*

4.4.3.1 Environmental context for societal change

Over the last four millennia, the Yucatán Peninsula has been home to the Maya civilisation through the numerous rises and falls. Owing to the karstic landscape, these societies often depended on natural cenotes and aguadas, and rain-fed cisterns (regionally known as *chultuns*) for their freshwater supply (Mays *et al.* 2013). Therefore, the Maya are thought to have been highly sensitive to changes in annual rainfall, which drive changes to groundwater elevation and lake levels, and refills man-made water storage systems (Lucero *et al.* 2011). In addition, where there is no viable access to groundwater, the dry-wet seasonality likely increased societal vulnerability to climatic variability, as the seasonal water supply must sustain a population through each dry-season, which can vary in length and intensity (Lucero *et al.* 2011). Consequently, multi-decadal periods of sustained drought have been commonly linked to Maya socio-economic decline across the Yucatán Peninsula (Hodell *et al.* 1995, 2001, 2005b; Curtis *et al.* 1996; Haug *et al.* 2003; Webster *et al.* 2007; Carrillo-Bastos *et al.* 2010; Medina-Elizalde *et al.* 2010; Aragón-Moreno *et al.* 2012; Kennett *et al.* 2012; Douglas *et al.* 2015); however, the precise extent to which drought causally influenced societies remains subject to debate (Aimers, 2007; Aimers and Hodell. 2011; Kennett *et al.* 2012; Carleton *et al.* 2014).

As previously discussed, the microstratigraphy of Unit 1's carbonate clusters closely resemble Unit 2's annual carbonate sublayers; specifically, their homogenous composition of endogenic calcite (or aragonite) and abrupt depositional boundaries are characteristic of seasonal calcium carbonate mineralisation events (see Section 4.3.1). Therefore, each distinct carbonate sublayer within Unit 1 is proposed to reflect the mineralisation from an individual year's dry season, and the number of sublayers in each cluster provides an indication of the cluster's minimum duration. As sea level remains stable through the last 5,000 years (Khan *et al.* 2017), variability to Yaal Chac's freshness are likely primarily driven by climatic-derived changes to inwash, evaporation and groundwater elevation through Unit 1 (4,295 cal yrs BP – present day). Consequently, multi-decadal periods of increased seasonal E/P conditions, capable of supersaturating carbonates in the epilimnion via evaporation, are likely to drive the precipitation and deposition of carbonate clusters.

The earliest two clusters, dated 2,881-2,821 ±452 cal yrs BP (931 – 871 BC) and 2,736-2,721 ±492 cal yrs BP (786 – 771 BC) occur within the Maya Pre-Classic Period, 4,000-1,710 cal yrs BP (2000 BC – 240 AD); during which, the Maya civilisation grew and a developed an increasingly complex socio-economic system (Chase and Chase, 1985). Within chronological error, the deposition of these

carbonate clusters coincides with multi-decadal droughts and vegetational disturbance are inferred during the early Pre-Classic, around 3,175 cal yrs BP (1225 BC) and 2,957 cal yrs BP (1007 BC), where subsequent wet conditions facilitated the Maya Pre-Classic development and population growth (Akers *et al.* 2016). Enhanced Ti between 3,059-2,064 cal yrs BP (1109 – 114 BC) within Yaal Chac's record highlights a distinct period of increased catchment erosion and inwash (Davies *et al.* 2015). The combined influence of synchronous mid Pre-Classic humid conditions ~2,350-2,110 cal yrs BP (~400 – 160 BC) (Medina-Elizalde *et al.* 2016) and anthropogenic deforestation and soil erosion associated with Maya Pre-Classic expansion 2,950-1,710 cal yrs BP (1000 BC – 240 AD) (Anselmetti *et al.* 2007) may drive this multi-millennial trend of increased terrestrial inwash at Yaal Chac; coeval $\delta^{18}O$ minima from the nearby Aguada X'Caamal similarly indicates enhanced inwash during this period (Hodell *et al.* 2005b).

The Pre-Classic Abandonment period (150 – 200 AD) marks the temporary cessation of Maya construction and population decline (Webster *et al.* 2007), and has similarly been linked to sustained dry climatic conditions. A high resolution speleothem isotope record taken from Río Secreto, Natural Reserve indicates two periods of sustained drought conditions 1,772-1,741 cal yrs BP (178 – 209 AD) and 1,721-1,699 cal yrs BP (229 – 251 AD), with -55 ±13% and -49 ±12% reductions to annual precipitation respectively (Medina-Elizalde *et al.* 2016). Within error, concurrent drought is similarly identified from more southerly sites, such as Rio Hondo, Mexico-Belize (Aragón-Moreno *et al.* 2018), Macal Chasm, Belize (Akers *et al.* 2016) and Petén Itzá, Guatemala (Rosenmeier *et al.* 2002). While coeval laminations are not identified within Yaal Chac's record, increased Ca detection around 2,050 ±420 cal yrs BP (100 BC) may reflect the onset of increased drought frequency and intensity prior to the Pre-Classic Abandonment. The Río Secreto's speleothem record indicates coeval drought oscillations at 163-139 BC, 108-98 BC, 73-62 BC, and 13-3 BC (Medina-Elizalde *et al.* 2016). In Yaal Chac, increased terrestrial erosion and inwash, as inferred by synchronous increases to Ti detection, further minimises the likelihood that carbonate mineralisation is ion-limited, and the sediment's rich composition of micritic carbonate grains may indicate endogenic carbonate precipitation drives sediment accumulation. However, the lack of consistent varve stratigraphy may reflect insufficient intra-annual limnological variability (Zolitschka *et al.* 2015), where relatively dry climatic conditions prevail year-round thus driving non-laminated carbonate precipitation. This tentatively inferred period of non-seasonal drought could potentially contribute to the major societal reorganisation of the Abandonment period, and the onset of increasingly dry conditions inferred from Lake Chichancanab (Hodell *et al.* 1995) and Punta Laguna, northern Yucatán (Curtis *et al.* 1996).

During the subsequent Maya Classic Period (1,700-1,050 cal yrs BP; 250-900 AD), the civilisation grew, further developing an increasingly complex socio-economic system with larger settlements and unique architectural style (Price *et al.* 2010). Relatively dry conditions are inferred to persist and possibly intensify through the period (Hodell *et al.* 1995, 2005; Curtis *et al.* 1996; Akers *et al.* 2016); these conditions have been proposed to encourage cultural adaptation and improved societal resilience to drought (Douglas *et al.* 2015). However, the long-term climatic-derived reductions to water supply, and consequently decreased carrying capacity despite a growing population, likely drove increased vulnerability to water security through the Classic Period (Turner and Sabloff, 2012). As previously discussed (see Section 3.4.2), these environmentally-derived reductions to carrying capacity can contribute to socio-economic instability, underpinning societal decline via other societal forcing, such as war and famine (Zhang *et al.* 2011).

Episodes of prolonged, yet moderate, drought are inferred throughout the early-mid Classic Period, particular between 1,750-1,450 cal yrs BP (200 – 500 AD), and are suggested to result in a shift into more intensive maize cultivation, focusing on water conservation (Douglas *et al.* 2015). Within the mid-Classic Period, the Maya Hiatus (1,416-1,357 cal yrs BP; 534-593 AD), a period of reduced construction and temporary reduction in Maya population growth, has similarly been linked to a preceding period of enhanced E/P conditions at 517 AD (Webster *et al.* 2007). Within Yaal Chac's record, three distinct clusters, each containing at least 10 carbonate laminations, correspond with the early-mid Classic Period. Assuming these clusters' are nearly annually-resolved akin to Unit 2's varves, these clusters were deposited 1,671-1,617 cal yrs BP (279 – 333 AD) (±510), 1,463-1,421 cal yrs BP (487 – 529 AD) (±466), and 1,325-1,310 cal yrs BP (625 – 640 AD) (±443). As discussed above, these clusters are proposed to reflect multi-decadal periods of increased dry-season E/P conditions. Lasting at least 15-54 years long, the duration and/or intensity of these drought episodes do not appear to result in major societal reorganisation, yet may encourage societies to improve their water management strategies to provide for the Classic Period's growing population (Dunning *et al.* 1998; Douglas *et al.* 2015). Yaal Chac's second cluster within this early-mid Classic Period coincides particularly well with the Maya hiatus, and being the Period's longest episode of drought may contribute to the aforementioned cessation to societal growth and development (Webster *et al.* 2007).

The Maya 'collapse' has been commonly been linked to severe drought or droughts, during Terminal Classic Period (TCP) (1,200-1,050 cal yrs BP; 750-900 AD) (Haug *et al.* 2003; Hodell *et al.* 2005a) (Fig. 4.33). During this time, palaeorecords across the Yucatán typically indicate the highest E/P

conditions of the Holocene (e.g. Hodell *et al.* 1995; Curtis *et al.* 1996; Medina-Elizalde *et al.* 2010; Akers *et al.* 2016), where previous cultural adaptations to drought conditions were unable to protect societies from the length and intensity of drought conditions (Douglas *et al.* 2015). During the 150-year long TCP, around 8 individual drought maxima are dated between 1,142 and 1,015 cal yrs BP (808 and 935 AD) from the nearby Tecoh Cave (Medina-Elizalde *et al.* 2010) resulting in up to 40% reduction of annual rainfall through this period (Medina-Elizalde *et al.* 2012). With 82 distinct laminations, Unit 2's longest cluster is dated around 1,124-1,042 cal yrs BP (826 – 908 AD) (±389), indicative of the longest continuous period of dry-season increased E/P conditions of the last 4,000 years. These conditions correspond well with the timing and length of inferred-drought within the northwest Yucatán. Such a prolonged period of enhanced E/P conditions could result in severe reductions to the land's carrying capacity (Douglas *et al.* 2015). Consequently, high population could exacerbate the socio-political instability identified through the TCP across the Maya lowlands (Zhang *et al.* 2011). The deposition of two shorter clusters at Yaal Chac at 964-925 cal yrs BP (986 – 1025 AD) (±347) and 829-808 cal yrs BP (1121 – 1142 AD) (±299) further indicate that relatively dry conditions persisted following the TCP's driest conditions. Similar dry conditions are inferred to persist until ~850 cal yrs BP (~1100 AD) from other lowland sites, such as Lake Chichancanab (Hodell *et al.* 2005) and Punta Laguna (Curtis *et al.* 1996). However, sites closer to Yaal Chac, namely Aguada X'Caamal (Hodell *et al.* 2005b) and Tecoh Cave (Medina-Elizalde *et al.* 2010), indicate relatively wet conditions during the two centuries following the TCP.

While the TCP reflects a period of significant population decline and social reorganisation, the Maya civilisation did not truly 'collapse'. Through the Post-Classic Period (900 – 1517 AD), Maya were able to re-establish a complex socio-economic system and construct some of the civilisation's largest settlements, such as Chichén Itzá (Andrews, 1993). This societal re-growth particularly occurred within the Yucatán's northern lowlands (Carmean *et al.* 2004), where the TCP drought is inferred to have been less intense compared to the southern lowlands (Douglas *et al.* 2015), and the low-lying, flat topography likely ensured that the groundwater elevation remained close enough to ground-level for freshwater extraction; Yaal Chac's record does not display any evidence that it dried up, and ceased depositing sediment, through its entire sequence.

The deposition of Yaal Chac's latest carbonate cluster, 476-410 cal yrs BP (1474 – 1540 AD) (±88), probably corresponds to the onset of LIA's relatively dry climatology, as inferred from the nearby Aguada X'Caamal around 500 cal yrs BP (1450 AD) (Hodell *et al.* 2005b). Concurrent reductions to mesic pollen taxa (Leyden *et al.* 1998) and $\delta^{18}O$ enrichment from Lake Chichancanab (Hodell *et al.*

2005a) and Salpetén (Rosenmeier *et al.* 2002) similarly indicate a shift to slightly drier conditions across the Yucatán Peninsula. Cooler SSTs during the LIA (Nyberg *et al.* 2002) are proposed drive the dry climatology by reducing Atlantic evaporation, thus decreasing moisture supply to the Yucatán (Hodell *et al.* 2005b). While the LIA's onset likely reflects the driest conditions of the last six centuries (Hodell *et al.* 2005b), the subsequent deposition of individual carbonate laminations throughout the uppermost 77cm of the sequence indicates that, relative to the rest of the Holocene, high E/P conditions prevail until present-day. Increased Ti detection from around 400 cal yrs BP (1550 AD) may reflect this climatic-driven vegetational disturbance, permitting increased catchment erosion, and/or vegetation change associated with anthropogenic activity.

4.5 Chapter summary

Yaal Chac's sedimentological record reflects distinct limnological changes across all temporal scales. The sediment record's basal age of 8,812 ±251 cal yrs BP likely corresponds with rising groundwater elevation, driven by increasing sea-level, such that Yaal Chac infills. Subsequently, a millennial-scale freshening trend, as inferred by the switch from aragonite- to calcite-rich endogenic precipitation, probably reflects increasing lake depth until ca. 4,200 cal yrs BP, this deepening is primarily driven by continued increases to sea-level and groundwater elevation, most rapidly during the early Holocene.

Through the early-mid Holocene, regional climatology is primarily governed by the ITCZ's mean annual position and seasonal migration. Peak insolation seasonality within the NH, due to orbital precession, resulted in the ITCZ most northerly position during the Holocene's thermal maximum, around 9,000-8,000 cal yrs BP. These northerly ITCZ positions displace subtropical high pressure systems and intensify easterly air flows during the summer wet-seasons. Consequently, the early-mid Holocene likely reflected the region's wettest Holocene conditions, and permitted the growth of tropical forest across the Peninsula. However, as NH insolation's seasonality decreased through the Holocene, the ITCZ migrated south, and consequently decreased annual rainfall and its relative influence of Yucatán climatology. On a decadal-centennial scale, the AMO is proposed to drive variability to carbonate deposition in Yaal Chac. AMO's phases influence both moisture supply to the Yucatán, and ITCZ's mean annual latitude, thus driving rainfall variability and limnological conditions across these shorter timescales.

The loss of regular varve deposition within subunit 2ii (7,245-5,346 cal yrs BP) is proposed to result from a combination of high annual rainfall and high lake level. These fresh limnological conditions

prevented the carbonate solubility level from being exceeded every year. During the deposition of the adjacent varved sequences (subunit 2iii and 2i), annual carbonate precipitation was facilitated by relatively low lake levels, thus increasing ion concentrations, and low annual rainfall, thus decreasing limnological dilution, at 8,812-7,245 cal yrs BP and 5,346-4,295 cal yrs BP respectively. The increased propensity of straight-moving storms across the Peninsula during the non-varved subunit 2ii may also contribute to seasonal ion dilution, thus preventing annual carbonate mineralisation.

At 4,295 ±260 cal yrs BP, the abrupt cessation of varve deposition likely reflects a threshold response to changing limnological conditions. This sedimentological transition coincides well with the onset of the Meghalayan Stage and with it, inferred shifts to drier and more vegetatively-open systems across the Yucatán Peninsula, associated with an orbitally-derived southward migration of the ITCZ. In Yaal Chac, despite this drying trend, carbonate supersaturation and precipitation may have been inhibited by fresher limnological conditions. A freshening trend may be related to elevated groundwater levels, driven by sea level rise and/or vegetation-derived changes to evapotranspiration and infiltration. Alternatively, a weakening of climatic and limnological seasonality may decrease carbonate deposition and preservation rates. Orbitally-derived reductions to insolation seasonality may diminish intra-annual E/P variability. Consequently, weaker stratification and/or wetter dry-season conditions, possibly associated with the increasing occurrence of meridional nortés, may dilute epilimnetic ion concentrations and prevent carbonate supersaturation. Weakened wet-dry seasonality may also increase the duration of the annual growing season, where subsequent decomposition of autochthonous organic material could decrease hypolimnetic pH, thus favouring carbonate dissolution. The sedimentological transition identified within Yaal Chac's record may be driven one (or more) of these environmental changes, yet the relative influence of each may only be identified through the analysis of additional environmental proxies, most significantly pollen.

This mid-Holocene transition may also reflect a shift to the Yucatán's climatological forcing. As the ITCZ migrates southward, its relative influence on Yucatán climatology decreases. This southward migration also drives the increasing intensity and frequency of ENSO's El Niño phases from ~5,000 cal yrs BP; consequently, the relative influence on ENSO cyclicity on regional climatology increases.

Within Yaal Chac's non-varved Unit 1, carbonate precipitation and deposition corresponds well with periods of sustained drought conditions, as identified in other palaeorecords. The deposition of carbonate laminations is probably driven by short periods of enhanced dry-season E/P conditions,

capable of supersaturating carbonates. Clusters of carbonate laminations coincide with notable societal declines to the Maya population, where the Maya were likely highly susceptible to climatic-derived changes to annual rainfall. Most notably, the longest cluster of contiguous carbonate laminations in Unit 1 corresponds to the Maya's largest population decline, during the TCP.

5. Joint conclusions

Using microfacies analysis of varved sediment records from Nar Gölü, Turkey and Yaal Chac, Mexico, this research has developed two unprecedentedly high resolution records of past limnological, environmental and climatic change through the Holocene; from Nar Gölü, these records reflect varve deposition during the early-mid and late Holocene (9,064 – 7,630 cal yrs BP and 2,540 – -51 cal yrs BP respectively), and from Yaal Chac, the early-mid Holocene (8,812 – 7,245 cal yrs BP and 5,346 – 4,295 cal yrs BP). By investigating the complex composition, structure, and succession of varve sedimentology, this research has developed a more nuanced understanding of high-resolution environmental change in central Anatolia and the Yucatán Peninsula. In this concluding chapter, some of the key findings from each lake are first summarised, before comparing the two records during their common time periods.

5.1 Linking sediment deposition to environmental processes

Lake monitoring has developed understanding of the sites' contemporary limnological variability and seasonal depositional processes, giving important insights into interpretations of past sedimentological changes. Governed by the sites' strong wet-dry seasonality, the annual supersaturation and precipitation of calcium carbonate primarily determines the records' varve stratigraphy and drives sediment accumulation (see Fig. 3.12; Section 3.2.1). The dynamics of this annual carbonate deposition were principally investigated at Nar Gölü, due to the lake's contemporary deposition of varves and the availability of coeval monitoring and multi-proxy data. By comparing the microstratigraphic data with the instrumental and isotopic records, relationships between seasonal climate and sediment deposition were established (see Section 3.3.2.1). Sedimentological calibration with Ankara's meteorological archive revealed that thickness of a varve's aragonite sublayer to be most strongly associated with the March-May E/P ratio. Correlation between the oxygen isotope ratio and carbonate sublayers' sedimentology further suggests that regional water balance primarily determines both the mineralogy and thickness of seasonal endogenic carbonate deposition. As a result, microfacies analysis of Nar Gölü's carbonate sublayers indicate high resolution changes to lake hydrology and the timing/intensity of dry-season E/P conditions.

Contemporary monitoring at Yaal Chac identified similar limnological seasonality, which drives an intra-annual succession of sediment depositional processes. While varves may not be presently

deposited in Yaal Chac, analysis of its calcareous-organic stratigraphy revealed the presence of varved sequences through the early-mid Holocene, similar to those identified from Nar Gölü. The sites' comparable wet-dry climatology, closed basin hydrology and microfacies composition meant that relationships identified between environmental and sedimentological changes at Nar Gölü could be tentatively applied at Yaal Chac. However, without the equivalent duration of monitoring and other proxy data, as available from Nar Gölü, the drivers to certain key sedimentology changes within Yaal Chac's record cannot be definitively concluded as yet (see below).

Further high resolution monitoring could establish more robust links between the intra-annual limnology and sediment deposition and preservation in both lakes. While this research has confirmed the role of regional water balance and E/P conditions on carbonate sedimentology, principally during the transition from wet- to dry-seasons, the influence of rainfall timing, intensity and amount on carbonate mineralisation is not well understood. Deploying additional, more advanced sediment traps, which capture specific months' deposition such that its captured material may be compared with coeval data regarding local weather and limnology, including stratification, could help hone our understanding of lacustrine carbonate dynamics in these lakes; consequently, improving interpretations of past climatic and limnological change.

5.2 High resolution environmental reconstruction

By applying the understanding of carbonate deposition outlined above to varve microfacies analysis, palaeohydrological changes were identified from Nar Gölü and Yaal Chac through the Holocene (Sections 3.4 and 4.4 respectively).

Over the last 2,600 years, Nar Gölü's aragonite-rich M2 varves, indicative of more evaporative spring-summer conditions, are primarily deposited between 589 BC–535 AD ±26 (2,539–1,415 cal yrs BP) and 1406–1988 AD ±6 (544– -33 cal yrs BP). During these periods, spectral analysis highlights the influence of Indian monsoon cyclicity on spring E/P variability, where the intensification of Indian monsoons establishes drier, more evaporative conditions at Nar Gölü (Section 3.4.2). Within a period of eight varve years around 535 AD, Nar Gölü's mineralogy switches from aragonite- to calcite-only carbonate sublayers, signifying an abrupt shift to fresher limnological conditions. This transition coincides well with the onset of LALIA, as identified from European and Siberian tree ring records (Büntgen et al 2016). While the inferred rapid hydroclimatic shift may be initially forced by a series of tropical volcanoes (Sigl *et al.* 2015), including El Chichón, Mexico (Nooren *et al.* 2017), Nar Gölü's

fresher conditions are proposed to be perpetuated by the increased influence of Atlantic-derived climatology, as indicated by the detection of a distinct 44-year cyclicity within the calcite sublayer thickness timeseries, which likely reflects the AMO and NAO. A southward migration of the ITCZ may have reduced Indian monsoon strength and the dominance of summer high pressure systems over Turkey, and/or centennial-scale North Atlantic SST warming (notably during the MCA) are proposed to increase Atlantic-derived precipitation at Nar Gölü. These multi-centennial periods of aragonite- and calcite-rich microfacies deposition may reflect shifts to the relative influence of low- and mid-latitude forcing driving Anatolian climatological variability.

During the early Holocene, Nar Gölü's particularly low $\delta^{18}O_{carbonate}$ values indicate some of the Holocene's freshest limnological conditions (Dean *et al.* 2015a), thus resulting in the deposition of calcite-rich M5 varves between >9,064 and 8,518 cal yrs BP. High NH insolation seasonality, due to orbital forcing, likely drove a strong wet-dry climatology, and sufficient limnological intra-annual variability for varve deposition. However, this inferred wet climatology, also identified across the eastern Mediterranean (Göktürk *et al.* 2011), was interrupted by a 295-year long period of relatively drier conditions, as indicated by deposition of aragonite-rich M2a* varves (8,518-8,223 cal yrs BP). Within chronological error, this M2a* deposition is proposed to correspond with the 8.2 ka event, when severe cooling of Atlantic SSTs probably restricted moisture supply to the eastern Mediterranean, thus driving increased E/P conditions and aragonite deposition at Nar Gölü. Microfacies analysis further supports inferences, typically made from isotopic records (Marino *et al.* 2009; Dean *et al.* 2015), that the 8.2 ka event's climatic signal prevailed for longer within the eastern Mediterranean, compared to records from Greenland and Europe (Rasmussen *et al.* 2006). Increased positive NAO phases and weakened Mediterranean circulation may have prolonged Anatolian dry conditions associated with the 8.2 ka event.

Following the onset of Unit 4 sediment deposition around 8,223 ±556 cal yrs BP, orbitally-driven reductions to climatic seasonality is proposed to have inhibited varve deposition and preservation, and enhanced Nar Gölü's seasonal mixing. Wetter dry-seasons and drier wet-seasons may be associated with an ITCZ-driven weakening of the Indian monsoon and insolation-driven cooling of Mediterranean SSTs respectively. Overall reductions in annual rainfall likely drove the isotope-inferred decline in lake level, where the enhanced lake mixing is proposed to have prolonged relatively dilute epilimnetic ion concentrations and the preferential precipitation of calcite.

Yaal Chac's early-mid Holocene record conversely displays a multi-millennial freshening signal (8,812 – 4295 cal yrs BP), despite regional palaeoclimatic records typically displaying drying conditions, associated with the southward migration of the ITCZ. Instead, Yaal Chac's onset of sediment deposition at 8,812 ±251cal yrs BP and subsequent mineralogical-inferred freshening is proposed to be driven by rising sea level, which elevated the Yucatán's groundwater and lake levels. As previously discussed (Section 4.4.2), AMO cyclicity drives the multi-decadal variability of carbonate deposition, via its influence on moisture supply to the Peninsula. At 4,295 ±260 cal yrs BP, the abrupt cessation of varve deposition likely reflects a threshold response to changing limnological conditions, which act to inhibit annual carbonate precipitation and preservation. Multiple environmental changes may drive this sedimentological transition, specifically: sustained increases to sea- and groundwater-level, orbital-derived reductions to climatic seasonality, and/or vegetation-derived changes to groundwater dynamics. However, like many lacustrine records from the Yucatán, further data is required to disentangle the specific drivers of rapid sedimentological change; this is an important area for future work.

Within the subsequent non-varved Unit following 4,295 ±260 cal yrs BP, clusters of carbonate laminae likely reflect multi-decadal periods of increased E/P conditions, capable of supersaturating carbonates on an annual/near-annual basis. These periods of drier conditions typically coincide with droughts inferred from regional palaeoclimatic records. Within this Unit, carbonate deposition often corresponds with the detection of allogenic sediments, thus indicating that increased ion influx may contribute to endogenic carbonate deposition. Despite the Yucatán's limestone geology, this relationship highlights the need to consider calcium and bicarbonate ion dynamics when interpreting lacustrine carbonate deposition regionally.

Environmental reconstructions based on varve microfacies analysis rely on the identification of the most likely limnological conditions which would result in the observed sedimentology. Therefore, additional proxies can refine these sedimentological-based inferences of possible conditions discussed within this thesis. In Yaal Chac, considering that both climatic and non-climatic processes have been interpreted to drive sedimentological change across multiple temporal scales, other proxies may help disentangle the specific processes driving changes to lacustrine deposition and preservation. In particular, a pollen record from Yaal Chac would provide valuable insight into the timing and magnitude of vegetation change and help assess the primary processes driving sedimentological changes, including the abrupt transition at 4,295 ±260 cal yrs BP. Specifically, a palynological record may indicate both anthropogenic activity, known to effect catchment erosion

and groundwater dynamics, and changes to additional climatic parameters, such as hydrological seasonality, moisture supply, and humidity.

Future work on Nar Gölü's sedimentary record could also extend microfacies analysis to the late glacial-early Holocene. This period is not well understood within the eastern Mediterranean, and varve analysis could provide a new high resolution insight into the environmental transition and the dominant climatology driving decadal-centennial variability (Roberts *et al.* 2016) (see Section 3.4.1).

5.3 Comparison between Nar Gölü and Yaal Chac

Throughout Nar Gölü's and Yaal Chac's sedimentary records, varve microfacies display strong similarities. The deposition of their calcareous-organic varves conform to a common conceptual model of varve formation (see Chapter 6), thus reflecting a comparable succession of limnological and depositional processes through each year (Brauer, 2004). Varved sequences from these two lakes only overlap temporally during the early-mid Holocene, from 8,812 ±251 cal yrs BP to 7,630 ±561 cal yrs BP, thus corresponding to the onset of varve deposition at Yaal Chac and the cessation of well-preserved varves at Nar Gölü respectively (Fig. 5.1). While the high uncertainty anchoring each records' floating chronology prevents definitive correlation of the short-lived changes in these limnological environments, the millennial-scale sedimentological (and isotopic) changes indicate opposing trends through the early-mid Holocene: with inferred drying at Nar Gölü, and freshening at Yaal Chac (Fig. 5.1).

In both Anatolia and the Yucatán Peninsula, the southward migration of the ITCZ, and the associated sub-tropical high pressure belt, has been suggested to drive millennial-scale drying trends regionally through the Holocene (Roberts *et al.* 2016; Aragón-Moreno *et al.* 2018). While this hydroclimate trend may be identified within Nar Gölü's record (also see Dean *et al.* 2015), the opposing conditions inferred from Yaal Chac are proposed to reflect limnological freshening derived from rising sea- and groundwater-levels (see Section 4.4). However, orbitally-derived reductions to NH insolation seasonality, driving this southward migration of the ITCZ, are proposed to effect sediment deposition within both lakes. This decreased seasonality is proposed to have weakened the intra-annual succession of depositional processes, thus driving, in part, the cessation of varve deposition and preservation in each lakes' early-mid Holocene sedimentary Unit (see Sections 3.4.1 and 4.4.3).

Spectral analysis of both lakes' varved sequences may also highlight the influence of similar climatic oscillations of sediment deposition. During the period of synchronous varve deposition within the two lakes (approx. 8,800-7,630 cal yrs BP) (Fig. 5.1), spectral analysis does not display any significant cycles within Yaal Chac's timeseries; here, the strong influence of non-climatic processes, such as sea level change, has been interpreted to cause this lack of depositional cyclicity (Section 4.4.3). Nevertheless, the detection of significant ~44- and ~59-year cycles within Nar Gölü's calcite and Yaal Chac's aragonite timeseries at differing periods within the Holocene mostly likely correspond to the AMO's 45-65 year cyclicity (Chylek *et al.* 2012). This multi-decadal cycle, affecting Atlantic SSTs, varies moisture supply to each region, where warmer (cooler) Atlantic SSTs are known to enhance (reduce) rainfall during the respective region's wet-season. This rainfall variability influences the lakes' hydrology, and thus the supersaturation and deposition of carbonates within each lake.

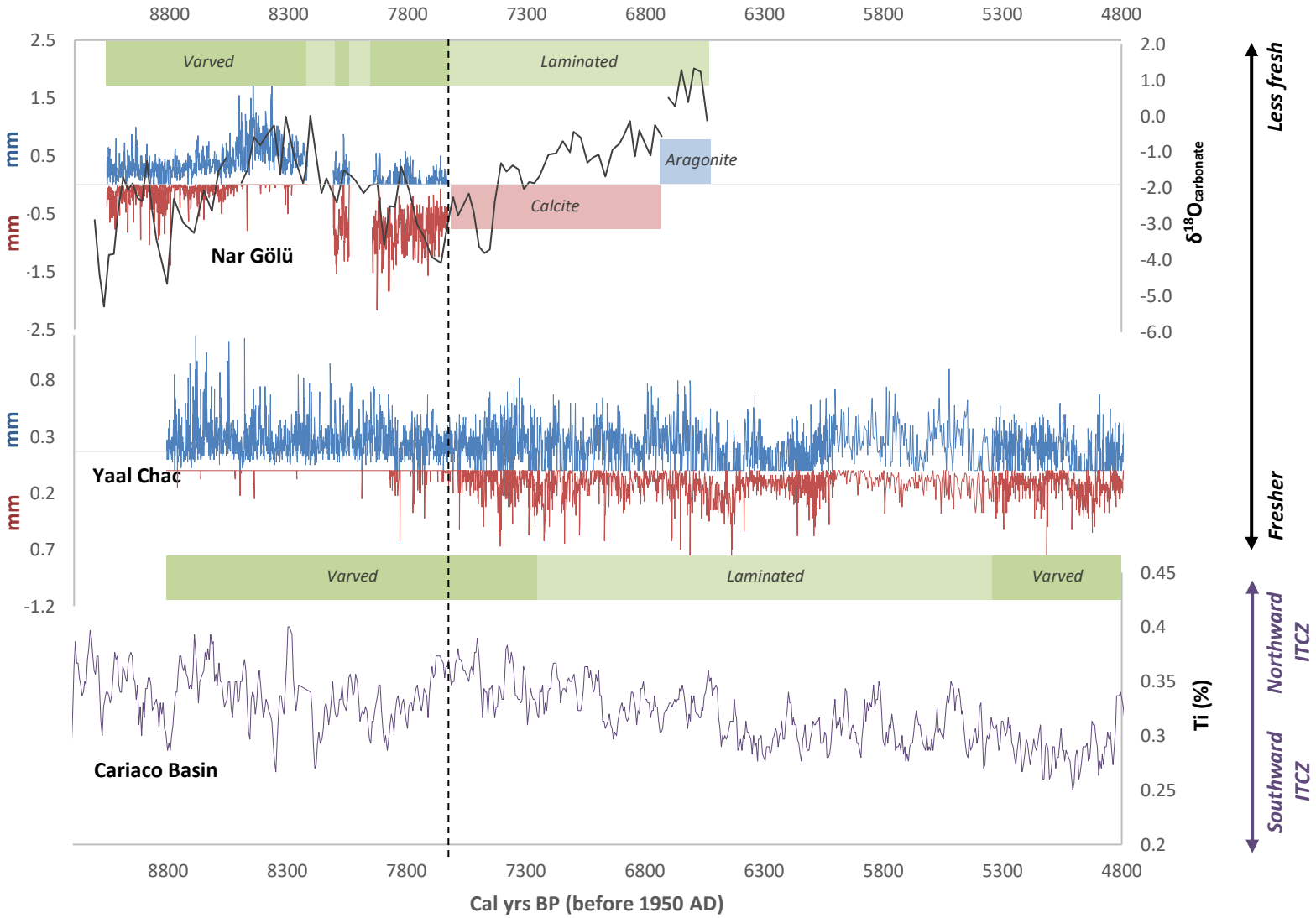


Figure 5.1 – *Temporal correlation of Nar Gölü's and Yaal Chac's carbonate microfacies; aragonite (blue line) and calcite (red line) thicknesses increase from their central axis, and Nar Gölü's $\delta^{18}O_{Carbonate}$ (solid black line) is also displayed (Dean et al. 2015a). The dotted black line denotes cessation of well-preserved varves at Nar Gölü at 7,630 ±520 cal yrs BP. Smoothed Ti concentration within Cariaco Basin (purple line) reflects mean ITCZ latitude through the Holocene (Haug et al. 2001).*

5.4 Environmental context for societal change

Throughout the Holocene, societies from both Anatolia and the Yucatán Peninsula are known to rise and fall. The regions' highly seasonal climatology likely exacerbated societal vulnerability to changes in water supply and the land's carrying capacity. However, the complexity of these human systems inhibits the identification of the primary processes driving reorganisation. The records produced as part of this thesis contribute to the ongoing debate about the relationship between climatic and societal change. Sediment deposition in both lakes has been shown to be sensitive, to varying extents, to changes in regional water balance. Consequently, inferred changes to E/P conditions within the lacustrine records may reasonably impact upon food and water security, which underpins socio-economic security. Correlation between the inferred timing and direction of environmental shifts and societal change provides strong circumstantial evidence that climatology has contributed, in part, to socio-economic change at various times through the Holocene.

During the late Holocene, the inferred shift to wetter climatic conditions in Nar Gölü at 535 ±15 AD coincides well with the growth of the Byzantine Empire in modern-day Turkey. Here, wetter conditions likely benefited agricultural productivity and water supply, thus contributing to the well-documented expansion of rural settlements (Izdebski *et al.* 2016). This cultural development may have initially been offset by the onset and recurrence of the Justinian Plague (541-543 AD), where these wetter conditions may have also accelerated disease spread by increasing rat populations. Subsequent declines to the Byzantine Empire over the following 700 years also correspond with periods of aragonite deposition (848-871 AD ±12 and 1119-1195 AD ±9), indicators of drier climatic conditions regionally.

During the early Holocene, the reorganisation of Çatalhöyük's settlement and agricultural practices similarly coincides with inferred drier conditions associated with the 8.2 ka event. The ~300-years of drier climatology are associated with the relocation of Çatalhöyük and the establishment of wheat agriculture on the surrounding floodplain, where prior wetter conditions rendered the land unsuitable for farming due to regular flooding.

At Yaal Chac, evidence of climate change contributing to societal change comes from Unit 1's discontinuously laminated sequence. As discussed above, clusters of carbonate laminations are proposed to reflect short periods of enhanced E/P conditions. These periods of inferred multi-decadal drought typically coincide with notable periods of Maya decline (Hodell *et al.* 2005a; Evans

et al. 2018). The Peninsula's karstic geomorphology likely increased peoples' vulnerability to changes to water supply (Isendahl, 2011); the Maya would depend on rainfall to refill water storage systems and maintain groundwater elevations sufficient for water extraction. While there is no evidence to suggest that Yaal Chac dried up, the deposition of the record's longest laminated cluster (c. 1,124-1,206 cal yrs BP) coincides with the Maya Terminal Classic Period, marking a period of significant population decline and political reorganisation. However, populations appear least affected by this multi-decadal drought in the northern lowlands around Yaal Chac, where fresh groundwater possibly remained accessible due to the particularly low topography (Isendahl, 2011).

Throughout the sedimentary sequences analysed here, transitions between microfacies commonly coincide well with known periods of societal growth or decline; from Nar Gölü, the varves' high resolution chronologies further permit both the timing and pace of environmental changes to be reliably identified during periods with well-documented human occupation. Moreover, this growth (decline) typically corresponds with inferred environmental conditions that would likely be more (less) favourable to food/water security. Nevertheless, causality between environmental forcing and societal change cannot be reliably concluded; temporal correlation is not sufficient. Instead, this work provides new supporting evidence that climatic change may contribute to social reorganisation at various times through the Holocene. Additional proxies may provide a more holistic picture of environmental conditions, required to identify the precise mechanism driving societal change, and more comparisons with local archaeological data would further increase the reliability of linking limnological changes to anthropogenic activity.

6. References

Abrantes, F., Voelker, A., Sierro, F. J., Naughton, F., Rodrigues, T., Cacho, I., Ariztegui, D., Brayshaw, D., Sicre, M.-A., & Batista, L. (2012). 1 - Paleoclimate Variability in the Mediterranean Region. In P. Lionello (Ed.), The Climate of the Mediterranean Region. Oxford: Elsevier. 1-86

Agnihotri, R., Dutta, K., Bhushan, R., & Somayajulu, B. L. K. (2002). Evidence for solar forcing on the Indian monsoon during the last millennium. Earth and Planetary Science Letters, 198, 521-527

Aimers, J. (2007). What Maya Collapse? Terminal Classic Variation in the Maya Lowlands. Journal of Archaeological Research, 15, 329-377

Aimers, J., & Hodell, D. (2011). Societal collapse: Drought and the Maya. Nature, 479, 44-45

Akers, P. D., Brook, G. A., Railsback, L. B., Liang, F., Iannone, G., Webster, J. W., Reeder, P. P., Cheng, H., & Edwards, R. L. (2016). An extended and higher-resolution record of climate and land use from stalagmite MC01 from Macal Chasm, Belize, revealing connections between major dry events, overall climate variability, and Maya sociopolitical changes. Palaeogeography, Palaeoclimatology, Palaeoecology, 459, 268-288

Akkemik, Ü., & Aras, A. (2005). Reconstruction (1689–1994 AD) of April–August precipitation in the southern part of central Turkey. International Journal of Climatology, 25, 537-548

Akkemik, Ü., D'Arrigo, R., Cherubini, P., Köse, N., & Jacoby, G. C. (2008). Tree-ring reconstructions of precipitation and streamflow for north-western Turkey. International Journal of Climatology, 28, 173-183

Akman, Y., & Ketenoğlu, O. (1986). The climate and vegetation of Turkey. In “Plant Life of SW Asia”. Proceedings of the Royal Society of Edinburgh, 113-122

Allcock, S. L. (2013). Living with a changing climate: Holocene climate variability and socio-evolutionary trajectories, central Turkey. PhD Thesis. Plymouth University.

Allcock, S. L. (2017). Long-term socio-environmental dynamics and adaptive cycles in Cappadocia, Turkey during the Holocene. Quaternary International, 446, 66-82

Alley, R. B., Mayewski, P. A., Sowers, T., Stuiver, M., Taylor, K. C., & Clark, P. U. (1997). Holocene climatic instability: A prominent, widespread event 8200 yr ago. Geology, 25, 483-486

Alonso-Zarza, A. M., & Calvo, J. P. (2000). Palustrine sedimentation in an episodically subsiding basin: the Miocene of the northern Teruel Graben (Spain). Palaeogeography, Palaeoclimatology, Palaeoecology, 160, 1-21

Amador, J. A., Alfaro, E. J., Lizano, O. G., & Magaña, V. O. (2006). Atmospheric forcing of the eastern tropical Pacific: A review. Progress in Oceanography, 69, 101-142

Amann, B., Szidat, S., & Grosjean, M. (2015). A millennial-long record of warm season precipitation and flood frequency for the North-western Alps inferred from varved lake sediments: implications for the future. Quaternary Science Reviews, 115, 89-100

Amann, B., Lamoureux, S. F., & Boreux, M. P. (2017). Winter temperature conditions (1670–2010) reconstructed from varved sediments, western Canadian High Arctic. Quaternary Science Reviews, 172, 1-14

Ambaum, M. H., Hoskins, B. J., & Stephenson, D. B. (2001). Arctic oscillation or North Atlantic oscillation? Journal of Climate, 14, 3495-3507

Anadón, P., Rosell, L., & Talbot, M. R. (1992). Carbonate replacement of lacustrine gypsum deposits in two Neogene continental basins, eastern Spain. Sedimentary Geology, 78, 201-216

Anderson, R. Y., & Dean, W. E. (1988). Lacustrine varve formation through time. Palaeogeography, Palaeoclimatology, Palaeoecology, 62, 215-235

Anderson, N. J., Liversidge, A. C., McGowan, S., & Jones, M. D. (2012). Lake and catchment response to Holocene environmental change: spatial variability along a climate gradient in southwest Greenland. Journal of Paleolimnology, 48, 209-222

Andrén, T., Björck, J., & Johnsen, S. (1999). Correlation of Swedish glacial varves with the Greenland (GRIP) oxygen isotope record. Journal of Quaternary Science, 14(4), 361-371

Anhäuser, T., Sirocko, F., Greule, M., Esper, J., & Keppler, F. (2014). D/H ratios of methoxyl groups of the sedimentary organic matter of Lake Holzmaar (Eifel, Germany): A potential palaeoclimate/-hydrology proxy. Geochimica et Cosmochimica Acta, 142, 39-52

Anselmetti, F. S., Ariztegui, D., Hodell, D. A., Hillesheim, M. B., Brenner, M., Gilli, A., McKenzie, J. A., & Mueller, A. D. (2006). Late Quaternary climate-induced lake level variations in Lake Petén Itzá, Guatemala, inferred from seismic stratigraphic analysis. Palaeogeography, Palaeoclimatology, Palaeoecology, 230(1–2), 52-69

Anselmetti, F. S., Bühler, R., Finger, D., Girardclos, S., Lancini, A., Rellstab, C., & Sturm, M. (2007). Effects of Alpine hydropower dams on particle transport and lacustrine sedimentation. Aquatic Sciences, 69(2), 179-198

Anselmetti, F. S. H., D. A.; Ariztegui, D.; Brenner, M.; Rosenmeier, M. F. (2007). Quantification of soil erosion rates related to ancient Maya deforestation. Geology, 35(10), 915-918

Appleby, P. G. (2008). Three decades of dating recent sediments by fallout radionuclides: a review. The Holocene, 18(1), 83-93

Aragón-Moreno, A. A., Islebe, G. A., & Torrescano-Valle, N. (2012). A 3800-yr, high-resolution record of vegetation and climate change on the north coast of the Yucatan Peninsula. Review of Palaeobotany and Palynology, 178, 35-42

Aragón-Moreno, A. A., Islebe, G. A., Roy, P. D., Torrescano-Valle, N., & Mueller, A. D. (2018). Climate forcings on vegetation of the southeastern Yucatán Peninsula (Mexico) during the middle to late Holocene. Palaeogeography, Palaeoclimatology, Palaeoecology, 495, 214-226

Arbuszewski, J. A., deMenocal, P. B., Cléroux, C., Bradtmiller, L., & Mix, A. (2013). Meridional shifts of the Atlantic intertropical convergence zone since the Last Glacial Maximum. Nature Geoscience, 6, 959-962

Ariztegui, D., Anselmetti, F. S., Robbiani, J. M., Bernasconi, S. M., Brati, E., Gilli, A., & Lehmann, M. F. (2010). Natural and human-induced environmental change in southern Albania for the last 300years — Constraints from the Lake Butrint sedimentary record. Global and Planetary Change, 71, 183-192

Ariztegui, D., Asioli, A., Lowe, J. J., Trincardi, F., Vigliotti, L., Tamburini, F., Chondrogianni, C., Accorsi, C. A., Bandini Mazzanti, M., Mercuri, A. M., Van der Kaars, S., McKenzie, J. A., & Oldfield, F. (2000). Palaeoclimate and the formation of sapropel S1: inferences from Late Quaternary lacustrine and marine sequences in the central Mediterranean region. Palaeogeography, Palaeoclimatology, Palaeoecology, 158, 215-240

Arz, H. W., Lamy, F., Pätzold, J., Müller, P. J., & Prins, M. (2003). Mediterranean Moisture Source for an Early-Holocene Humid Period in the Northern Red Sea. Science, 300, 118-121

Asouti, E., & Hather, J. (2001). Charcoal analysis and the reconstruction of ancient woodland vegetation in the Konya Basin, south-central Anatolia, Turkey: results from the Neolithic site of Catalhoyuk East. Vegetation History and Archaeobotany, 10, 23-32

Athy, L. F. (1930). Density, porosity, and compaction of sedimentary rocks. AAPG Bulletin, 14, 1-24

Avramidis, P., Samiotis, A., Kalimani, E., Papoulis, D., Lampropoulou, P., & Bekiari, V. (2013). Sediment characteristics and water physicochemical parameters of the Lysimachia Lake, Western Greece. Environmental earth sciences, 70, 383-392

Bakker, J., Paulissen, E., Kaniewski, D., De Laet, V., Verstraeten, G., & Waelkens, M. (2012). Man, vegetation and climate during the Holocene in the territory of Sagalassos, Western Taurus Mountains, SW Turkey. Vegetation History and Archaeobotany, 21, 249-266

Bakker, J., Paulissen, E., Kaniewski, D., Poblome, J., De Laet, V., Verstraeten, G., & Waelkens, M. (2013). Climate, people, fire and vegetation: new insights into vegetation dynamics in the Eastern Mediterranean since the 1st century AD. Climate of the Past, 9, 57-87

Baltres, A., & Medeşsan, A. (1978). High-magnesian calcite in fecal pellets of *Artemia salina* from Techirghiol Lake. Sedimentary Geology, 20, 281-290

Bar-Matthews, M., & Ayalon, A. (2011). Mid-Holocene climate variations revealed by high-resolution speleothem records from Soreq Cave, Israel and their correlation with cultural changes. The Holocene, 21, 163-171

Bar-Matthews, M., Ayalon, A., Gilmour, M., Matthews, A., & Hawkesworth, C. J. (2003). Sea–land oxygen isotopic relationships from planktonic foraminifera and speleothems in the Eastern Mediterranean region and their implication for paleorainfall during interglacial intervals. Geochimica et Cosmochimica Acta, 67, 3181-3199

Bar-Matthews, M., Ayalon, A., & Kaufman, A. (1997). Late Quaternary Paleoclimate in the Eastern Mediterranean Region from Stable Isotope Analysis of Speleothems at Soreq Cave, Israel. Quaternary Research, 47, 155-168

Bar-Matthews, M., Ayalon, A., & Kaufman, A. (2000). Timing and hydrological conditions of Sapropel events in the Eastern Mediterranean, as evident from speleothems, Soreq cave, Israel. Chemical Geology, 169, 145-156

Bar-Matthews, M., Ayalon, A., Kaufman, A., & Wasserburg, G. J. (1999). The Eastern Mediterranean paleoclimate as a reflection of regional events: Soreq cave, Israel. Earth and Planetary Science Letters, 166, 85-95

Barron, J. A., Bukry, D., & Dean, W. E. (2005). Paleoceanographic history of the Guaymas Basin, Gulf of California, during the past 15,000 years based on diatoms, silicoflagellates, and biogenic sediments. Marine Micropaleontology, 56, 81-102

Bastviken, D., Persson, L., Odham, G., & Tranvik, L. (2004). Degradation of dissolved organic matter in oxic and anoxic lake water. Limnology and Oceanography, 49, 109-116

Bathurst, R. G. (1972). Carbonate sediments and their diagenesis (Vol. 12): Elsevier.

Battarbee, R. W., Grytnes, J.-A., Thompson, R., Appleby, P. G., Catalan, J., Korhola, A., Birks, H. J. B., Heegaard, E., & Lami, A. (2002). Comparing palaeolimnological and instrumental evidence of climate change for remote mountain lakes over the last 200 years. Journal of Paleolimnology, 28, 161-179

Battarbee, R. W., Jones, V. J., Flower, R. J., Cameron, N. G., Bennion, H., Carvalho, L., & Juggins, S. (2001). Diatoms. In J. P. Smol, H. J. B. Birks, W. M. Last, R. S. Bradley & K. Alverson (Eds.), Tracking Environmental Change Using Lake Sediments: Terrestrial, Algal, and Siliceous Indicators. Dordrecht: Springer Netherlands. 155-202

Bauer-Gottwein, P., Gondwe, B. R. N., Charvet, G., Marín, L. E., Rebolledo-Vieyra, M., & Merediz-Alonso, G. (2011). Review: The Yucatán Peninsula karst aquifer, Mexico. Hydrogeology Journal, 19, 507-524.

Bayon, G., Pierre, C., Etoubleau, J., Voisset, M., Cauquil, E., Marsset, T., Sultan, N., Le Drezen, E., & Fouquet, Y. (2007). Sr/Ca and Mg/Ca ratios in Niger Delta sediments: Implications for authigenic carbonate genesis in cold seep environments. Marine Geology, 241, 93-109

Beets, C. J., Troelstra, S. R., Grootes, P. M., Nadeau, M. J., Borg, K. v. d., Jong, A. F. M. d., Hofman, C. L., & Hoogland, M. L. P. (2006). Climate and pre-Columbian settlement at Anse à la Gourde, Guadeloupe, Northeastern Caribbean. Geoarchaeology, 21, 271-280.

Bendle, J. M., Palmer, A. P., & Carr, S. J. (2015). A comparison of micro-CT and thin section analysis of Lateglacial glaciolacustrine varves from Glen Roy, Scotland. Quaternary Science Reviews, 114, 61-77

Bendle, J. M., Palmer, A. P., Thorndycraft, V. R., & Matthews, I. P. (2017). High-resolution chronology for deglaciation of the Patagonian Ice Sheet at Lago Buenos Aires (46.5°S) revealed through varve chronology and Bayesian age modelling. Quaternary Science Reviews, 177, 314-339

Bennett, K. D., & Willis, K. J. (2001). Pollen. In J. P. Smol, H. J. B. Birks, W. M. Last, R. S. Bradley & K. Alverson (Eds.), Tracking Environmental Change Using Lake Sediments: Terrestrial, Algal, and Siliceous Indicators. Dordrecht: Springer Netherlands. 5-32

Berger, A. (1978). Long-Term Variations of Daily Insolation and Quaternary Climatic Changes. Journal of the Atmospheric Sciences, 35, 2362-2367

Berger, J.-F., & Guilaine, J. (2009). The 8200calBP abrupt environmental change and the Neolithic transition: A Mediterranean perspective. Quaternary International, 200, 31-49

Berglund, B. E. (2003). Human impact and climate changes—synchronous events and a causal link? Quaternary International, 105, 7-12

Bernal, J. P., Lachniet, M., McCulloch, M., Mortimer, G., Morales, P., & Cienfuegos, E. (2011). A speleothem record of Holocene climate variability from southwestern Mexico. Quaternary Research, 75, 104-113

Berntsson, A., Rosqvist, G. C., & Velle, G. (2013). Late-Holocene temperature and precipitation changes in Vindelfjällen, mid-western Swedish Lapland, inferred from chironomid and geochemical data. The Holocene, 24, 78-92

Binford, M. W., Brenner, M., Whitmore, T. J., Higuera-Gundy, A., Deevey, E. S., & Leyden, B. (1987). Ecosystems, paleoecology and human disturbance in subtropical and tropical America. Quaternary Science Reviews, 6, 115-128

Binford, M. W., Kolata, A. L., Brenner, M., Janusek, J. W., Seddon, M. T., Abbott, M., & Curtis, J. H. (1997). Climate Variation and the Rise and Fall of an Andean Civilization. Quaternary Research, 47, 235-248

Biondi, F., Lange, C. B., Hughes, M. K., & Berger, W. H. (1997). Inter-decadal signals during the last millennium (AD 1117–1992) in the Varve record of Santa Barbara Basin, California. Geophysical Research Letters, 24, 193-196

Bird, B. W., Abbott, M. B., Finney, B. P., & Kutchko, B. (2009). A 2000 year varve-based climate record from the central Brooks Range, Alaska. Journal of Paleolimnology, 41, 25-41

Bird, B. W., Abbott, M. B., Vuille, M., Rodbell, D. T., Stansell, N. D., & Rosenmeier, M. F. (2011). A 2,300-year-long annually resolved record of the South American summer monsoon from the Peruvian Andes. Proceedings of the National Academy of Sciences, 108(21), 8583-8587

Blaauw, M., & Christen, J. A. (2011). Flexible paleoclimate age-depth models using an autoregressive gamma process. Bayesian analysis, 6, 457-474

Black, E., Brayshaw, D. J., & Rambeau, C. M. C. (2010). Past, present and future precipitation in the Middle East: insights from models and observations. Philosophical Transactions of the Royal Society A: Mathematical, Physical and Engineering Sciences, 368(1931), 5173-5184

Bluszcz, P., Kirilova, E., Lotter, A. F., Ohlendorf, C., & Zolitschka, B. (2008). Global Radiation and Onset of Stratification as Forcing Factors of Seasonal Carbonate and Organic Matter Flux Dynamics in a Hypertrophic Hardwater Lake (Sacrower See, Northeastern Germany). Aquatic Geochemistry, 14, 73-98

Bluszcz, P., Luecke, A., Ohlendorf, C., & Zolitschka, B. (2009). Seasonal dynamics of stable isotopes and element ratios in authigenic calcites during their precipitation and dissolution, Sacrower See (northeastern Germany). Journal of Limnology, 68, 257-273

Boehrer, B., & Schultze, M. (2008). Stratification of lakes. Reviews of Geophysics, 46, doi: https://doi.org/10.1029/2006RG000210

Boës, X., & Fagel, N. (2005). Impregnation method for detecting annual laminations in sediment cores: an overview. Sedimentary Geology, 179, 185-194

Bonani, G., Beer, J., Hofmann, H., Synal, H.-A., Suter, M., Wölfli, W., Pfleiderer, C., Kromer, B., Junghans, C., & Münnich, K. O. (1987). Fractionation, precision and accuracy in 14C and 13C measurements. Nuclear Instruments and Methods in Physics Research Section B: Beam Interactions with Materials and Atoms, 29, 87-90

Bond, G., Kromer, B., Beer, J., Muscheler, R., Evans, M. N., Showers, W., Hoffmann, S., Lotti-Bond, R., Hajdas, I., & Bonani, G. (2001). Persistent Solar Influence on North Atlantic Climate During the Holocene. Science, 294, 2130-2133

Bond, G., Showers, W., Cheseby, M., Lotti, R., Almasi, P., deMenocal, P., Priore, P., Cullen, H., Hajdas, I., & Bonani, G. (1997). A Pervasive Millennial-Scale Cycle in North Atlantic Holocene and Glacial Climates. Science, 278, 1257-1266

Bonk, A., Kinder, M., Enters, D., Grosjean, M., Meyer-Jacob, C., & Tylmann, W. (2016). Sedimentological and geochemical responses of Lake Żabińskie (north-eastern Poland) to erosion changes during the last millennium. Journal of Paleolimnology, 56, 239-252

Bontognali, T. R. R., Vasconcelos, C., Warthmann, R. J., Bernasconi, S. M., Dupraz, C., Strohmenger, C. J., & Mckenzie, J. A. (2010). Dolomite formation within microbial mats in the coastal Sabkha of Abu Dhabi (United Arab Emirates). Sedimentology, 57, 824-844

Bookhagen, B., Thiede, R. C., & Strecker, M. R. (2005). Late Quaternary intensified monsoon phases control landscape evolution in the northwest Himalaya. Geology, 33, 149-152

Bookhagen, B. T., Rasmus C.; Strecker, Manfred R. (2005). Late Quaternary intensified monsoon phases control landscape evolution in the northwest Himalaya. Geology, 33, 149-152

Boose, E. R., Foster, D. R., Plotkin, A. B., & Hall, B. (2003). Geographical and historical variation in hurricanes across the Yucatan Peninsula. The lowland Maya area. Haworth. New York, NY, 495-516

Born, A., & Levermann, A. (2010). The 8.2 ka event: Abrupt transition of the subpolar gyre toward a modern North Atlantic circulation. Geochemistry, Geophysics, Geosystems, 11, doi: https://doi.org/10.1029/2009GC003024

Boygle, J. (1993). The Swedish varve chronology - a review. Progress in Physical Geography, 17, 1-19

Boyle, J. (2001). Redox remobilization and the heavy metal record in lake sediments: a modelling approach. Journal of Paleolimnology, 26, 423-431

Boyle, J. (2002). Inorganic geochemical methods in palaeolimnology Tracking environmental change using lake sediments. Springer. 83-141

Boyle, J. F., Chiverrell, R. C., & Schillereff, D. (2015). Approaches to water content correction and calibration for µXRF core scanning: comparing X-ray scattering with simple regression of elemental concentrations Micro-XRF Studies of Sediment Cores. Springer. 373-390

Bradley, W. H. (1931). Nonglacial marine varves. American Journal of Science, Series 5 Vol. 22, 318-330

Brauer, A. (2004). Annually Laminated Lake Sediments and Their Palaeoclimatic Relevance. In H. Fischer, T. Kumke, G. Lohmann, G. Flöser, H. Miller, H. von Storch & J. F. W. Negendank (Eds.), The Climate in Historical Times: Towards a Synthesis of Holocene Proxy Data and Climate Models (pp. 109-127). Berlin, Heidelberg: Springer Berlin Heidelberg.

Brauer, A., & Casanova, J. (2001). Chronology and depositional processes of the laminated sediment record from Lac d'Annecy, French Alps. Journal of Paleolimnology, 25, 163-177

Brauer, A., Endres, C., Günter, C., Litt, T., Stebich, M., & Negendank, J. F. W. (1999). High resolution sediment and vegetation responses to Younger Dryas climate change in varved lake sediments from Meerfelder Maar, Germany. Quaternary Science Reviews, 18, 321-329

Brauer, A., Mingram, J., Frank, U., Günter, C., Georg, S., Wulf, S., Zolitschka, B., & Negendank, J. F. W. (2000). Abrupt environmental oscillations during the Early Weichselian recorded at Lago Grande di Monticchio, southern Italy. Quaternary International, 73–74, 79-90

Brauer, A., Haug, G. H., Dulski, P., Sigman, D. M., & Negendank, J. F. W. (2008a). An abrupt wind shift in western Europe at the onset of the Younger Dryas cold period. Nature Geoscience, 1, 520-524

Brauer, A., Mangili, C., Moscariello, A., & Witt, A. (2008b). Palaeoclimatic implications from micro-facies data of a 5900 varve time series from the Piànico interglacial sediment record, southern Alps. Palaeogeography, Palaeoclimatology, Palaeoecology, 259, 121-135

Brauer, A., Dulski, P., Mangili, C., Mingram, J., & Liu, J. (2009). The potential of varves in high-resolution paleolimnological studies. Pages News, 17(3), 96-98

Brayshaw, D. J., Rambeau, C. M. C., & Smith, S. J. (2011). Changes in Mediterranean climate during the Holocene: Insights from global and regional climate modelling. The Holocene, 21, 15-31

Brenner, M., Rosenmeier, M. F., Hodell, D. A., & Curtis, J. H. (2002). Paleolimnology of the Maya lowlands. Ancient Mesoamerica, 13, 141-157

Brocard, G., Adatte, T., Magand, O., Pfeifer, H.-R., Bettini, A., Arnaud, F., Anselmetti, F. S., & Moran-Ical, S. (2014). The recording of floods and earthquakes in Lake Chichój, Guatemala during the twentieth century. Journal of Paleolimnology, 52, 155-169

Bronk Ramsey, C., Staff, R. A., Bryant, C. L., Brock, F., Kitagawa, H., van der Plicht, J., Schlolaut, G., Marshall, M. H., Brauer, A., Lamb, H. F., Payne, R. L., Tarasov, P. E., Haraguchi, T., Gotanda, K., Yonenobu, H., Yokoyama, Y., Tada, R., & Nakagawa, T. (2012). A Complete Terrestrial Radiocarbon Record for 11.2 to 52.8 kyr B.P. Science, 338, 370-374

Brönmark, C., & Hansson, L. A. (2017). The biology of lakes and ponds: Oxford University Press.

Brooks, N. (2006). Cultural responses to aridity in the Middle Holocene and increased social complexity. Quaternary International, 151, 29-49

Brown, K. J., Clark, J. S., Grimm, E. C., Donovan, J. J., Mueller, P. G., Hansen, B. C. S., & Stefanova, I. (2005). Fire cycles in North American interior grasslands and their relation to prairie drought. Proceedings of the National Academy of Sciences of the United States of America, 102, 8865-8870

Brunetti, M., & Kutiel, H. (2011). The relevance of the North-Sea Caspian Pattern (NCP) in explaining temperature variability in Europe and the Mediterranean. Natural Hazards Earth System Science, 11, 2881-2888

Buchaca, T., Felip, M., & Catalan, J. (2005). A comparison of HPLC pigment analyses and biovolume estimates of phytoplankton groups in an oligotrophic lake. Journal of Plankton Research, 27, 91-101

Buntgen, U., Myglan, V. S., Ljungqvist, F. C., McCormick, M., Di Cosmo, N., Sigl, M., Jungclaus, J., Wagner, S., Krusic, P. J., Esper, J., Kaplan, J. O., de Vaan, M. A. C., Luterbacher, J., Wacker, L., Tegel, W., & Kirdyanov, A. V. (2016). Cooling and societal change during the Late Antique Little Ice Age from 536 to around 660 AD. Nature Geosci, 9, 231-236

Büntgen, U., Tegel, W., Nicolussi, K., McCormick, M., Frank, D., Trouet, V., Kaplan, J. O., Herzig, F., Heussner, K.-U., Wanner, H., Luterbacher, J., & Esper, J. (2011). 2500 Years of European Climate Variability and Human Susceptibility. Science, 331, 578-582

Burdige, D. J. (2007). Preservation of organic matter in marine sediments: controls, mechanisms, and an imbalance in sediment organic carbon budgets? Chemical reviews, 107, 467-485

Burnett, A. P., Soreghan, M. J., Scholz, C. A., & Brown, E. T. (2011). Tropical East African climate change and its relation to global climate: A record from Lake Tanganyika, Tropical East Africa, over the past 90+ kyr. Palaeogeography, Palaeoclimatology, Palaeoecology, 303, 155-167

Butz, C., Grosjean, M., Poraj-Górska, A., Enters, D., & Tylmann, W. (2016). Sedimentary Bacteriopheophytin a as an indicator of meromixis in varved lake sediments of Lake Jaczno, north-east Poland, CE 1891–2010. Global and Planetary Change, 144, 109-118

Camill, P., Jr, C. E. U., Teed, R., Geiss, C. E., Aldinger, J., Dvorak, L., Jon, K., Limmer, J., & Walkup, K. (2003). Late-Glacial and Holocene Climatic Effects on Fire and Vegetation Dynamics at the Prairie-Forest Ecotone in South-Central Minnesota. Journal of Ecology, 91, 822-836

Canfield Jr, D. E., & Jones, J. R. (1983). Assessing the trophic status of lakes with aquatic macrophytes. Lake and Reservoir Management, 1, 446-451

Card, V. M. (1997). Varve-counting by the annual pattern of diatoms accumulated in the sediment of Big Watab Lake, Minnesota, AD 1837–1990. Boreas, 26, 103-112

Carleton, W. C., Campbell, D., & Collard, M. (2014). A reassessment of the impact of drought cycles on the Classic Maya. Quaternary Science Reviews, 105, 151-161

Carmean, K., Dunning, N., & Kowalski, J. K. (2004). High times in the hill country: a perspective from the Terminal Classic Puuc region. The Terminal Classic in the Maya Lowlands: Collapse, Transition, and Transformation, University Press of Colorado, Boulder, 424-449

Caron, L.-P., Boudreault, M., & Bruyère, C. (2015). Changes in large-scale controls of Atlantic tropical cyclone activity with the phases of the Atlantic multidecadal oscillation. Climate Dynamics, 44, 1801-1821

Carrillo-Bastos, A., Islebe, G. A., & Torrescano-Valle, N. (2012). Geospatial analysis of pollen records from the Yucatán peninsula, Mexico. Vegetation History and Archaeobotany, 21, 429-437

Carrillo-Bastos, A., Islebe, G. A., & Torrescano-Valle, N. (2013). 3800 Years of Quantitative Precipitation Reconstruction from the Northwest Yucatan Peninsula. PLoS One, 8, e84333

Carrillo-Bastos, A., Islebe, G. A., Torrescano-Valle, N., & González, N. E. (2010). Holocene vegetation and climate history of central Quintana Roo, Yucatán Península, Mexico. Review of Palaeobotany and Palynology, 160, 189-196

Caseldine, C. J., & Turney, C. (2010). The bigger picture: towards integrating palaeoclimate and environmental data with a history of societal change. Journal of Quaternary Science, 25, 88-93

Chase, A. F., & Chase, D. Z. (1985). Postclassic temporal and spatial frames for the Lowland Maya: a background. The Lowland Maya Postclassic. University of Texas Press, Austin, 9-22

Chivas, A. R., De Deckker, P., & Shelley, J. M. G. (1986). Magnesium and strontium in non-marine ostracod shells as indicators of palaeosalinity and palaeotemperature. Paper presented at the Paleolimnology IV, Dordrecht.

Chylek, P., Folland, C., Frankcombe, L., Dijkstra, H., Lesins, G., & Dubey, M. (2012). Greenland ice core evidence for spatial and temporal variability of the Atlantic Multidecadal Oscillation. Geophysical Research Letters, 39. doi: https://doi.org/10.1029/2012GL051241

Clapich, J. L. (2016). An assessment of the differences in hydrology between cenotes and aguadas, Yucatan, Mexico. 3rd year undergraduate project, University of Nottingham.

Clarke, G. K. C., Leverington, D. W., Teller, J. T., & Dyke, A. S. (2004). Paleohydraulics of the last outburst flood from glacial Lake Agassiz and the 8200 BP cold event. Quaternary Science Reviews, 23, 389-407

Cohen, A. S., Stone, J. R., Beuning, K. R. M., Park, L. E., Reinthal, P. N., Dettman, D., Scholz, C. A., Johnson, T. C., King, J. W., Talbot, M. R., Brown, E. T., & Ivory, S. J. (2007). Ecological consequences of early Late Pleistocene megadroughts in tropical Africa. Proceedings of the National Academy of Sciences, 104, 16422-16427

Cohen, J. E. (1995). Population growth and earth's human carrying capacity. Science, 269(5222), 341.

Colbert, A. J., & Soden, B. J. (2012). Climatological Variations in North Atlantic Tropical Cyclone Tracks. Journal of Climate, 25, 657-673

Cole, J. J., Carpenter, S. R., Pace, M. L., Van de Bogert, M. C., Kitchell, J. L., & Hodgson, J. R. (2006). Differential support of lake food webs by three types of terrestrial organic carbon. Ecology Letters, 9, 558-568

Comboul, M., Emile-Geay, J., Evans, M. N., Mirnateghi, N., Cobb, K. M., & Thompson, D. M. (2014). A probabilistic model of chronological errors in layer-counted climate proxies: applications to annually banded coral archives. Clim. Past, 10, 825-841

Conroy, J. L., Overpeck, J. T., Cole, J. E., Shanahan, T. M., & Steinitz-Kannan, M. (2008). Holocene changes in eastern tropical Pacific climate inferred from a Galápagos lake sediment record. Quaternary Science Reviews, 27, 1166-1180

Cook, E. R., Briffa, K. R., Meko, D. M., Graybill, D. A., & Funkhouser, G. (1995). The 'segment length curse' in long tree-ring chronology development for palaeoclimatic studies. The Holocene, 5, 229-237

Coombes, P., & Barber, K. (2005). Environmental determinism in Holocene research: causality or coincidence? Area, 37, 303-311

Corella, J. P., Amrani, A. E., Sigró, J., Morellón, M., Rico, E., & Valero-Garcés, B. L. (2011). Recent evolution of Lake Arreo, northern Spain: influences of land use change and climate. Journal of Paleolimnology, 46, 469-485

Corella, J. P., Brauer, A., Mangili, C., Rull, V., Vegas-Vilarrúbia, T., Morellón, M., & Valero-Garcés, B. L. (2012). The 1.5-ka varved record of Lake Montcortès (southern Pyrenees, NE Spain). Quaternary Research, 78, 323-332

Corella, J. P., Brauer, A., Mangili, C., Rull, V., Vegas-Vilarrúbia, T., Morellón, M., & Valero-Garcés, B. L. (2012). The 1.5-ka varved record of Lake Montcortès (southern Pyrenees, NE Spain). Quaternary Research, 78, 323-332

Cornell, R. M., & Schwertmann, U. (2003). The iron oxides: structure, properties, reactions, occurrences and uses: John Wiley & Sons.

Covich, A., & Stuiver, M. (1974). Changes in oxygen 18 as a measure of long-term fluctuations in tropical lake levels and molluscan populations1. Limnology and Oceanography, 19, 682-691

Cremaschi, M., & Zerboni, A. (2009). Early to Middle Holocene landscape exploitation in a drying environment: Two case studies compared from the central Sahara (SW Fezzan, Libya). Comptes Rendus Geoscience, 341, 689-702

Croudace, I. W., Rindby, A., & Rothwell, R. G. (2006). ITRAX: description and evaluation of a new multi-function X-ray core scanner. Special publication-geological society of London, 267, 51.

Cullen, H. M., & deMenocal, P. B. (2000). North Atlantic influence on Tigris–Euphrates streamflow. International Journal of Climatology, 20, 853-863

Cullen, H. M., deMenocal, P. B., Hemming, S., Hemming, G., Brown, F. H., Guilderson, T., & Sirocko, F. (2000). Climate change and the collapse of the Akkadian empire: Evidence from the deep sea. Geology, 28, 379-382

Curtis, J., Brenner, M., Hodell, D., Balser, R., Islebe, G., & Hooghiemstra, H. (1998). A multi-proxy study of Holocene environmental change in the Maya Lowlands of Peten, Guatemala. Journal of Paleolimnology, 19, 139-159

Curtis, J. H., Hodell, D. A., & Brenner, M. (1996). Climate Variability on the Yucatan Peninsula (Mexico) during the Past 3500 Years, and Implications for Maya Cultural Evolution. Quaternary Research, 46, 37-47

Curtis, S. (2004). Diurnal cycle of rainfall and surface winds and the mid-summer drought of Mexico/Central America. Climate Research, 27, 1-8

Cuven, S., Francus, P., Crémer, J. F., & Bérubé, F. (2015). Optimization of Itrax core scanner protocols for the micro X-ray fluorescence analysis of finely laminated sediment: A case study of lacustrine varved sediment from the high arctic Micro-XRF Studies of Sediment Cores. Springer. 279-303

Cuven, S., Francus, P., & Lamoureux, S. (2010). Estimation of grain size variability with micro X-ray fluorescence in laminated lacustrine sediments, Cape Bounty, Canadian High Arctic. Journal of Paleolimnology, 44, 803-817

Cuven, S., Francus, P., & Lamoureux, S. (2011). Mid to Late Holocene hydroclimatic and geochemical records from the varved sediments of East Lake, Cape Bounty, Canadian High Arctic. Quaternary Science Reviews, 30, 2651-2665

Czymzik, M., Brauer, A., Dulski, P., Plessen, B., Naumann, R., von Grafenstein, U., & Scheffler, R. (2013). Orbital and solar forcing of shifts in Mid- to Late Holocene flood intensity from varved sediments of pre-alpine Lake Ammersee (southern Germany). Quaternary Science Reviews, 61, 96-110

Czymzik, M., Dulski, P., Plessen, B., von Grafenstein, U., Naumann, R., & Brauer, A. (2010). A 450 year record of spring-summer flood layers in annually laminated sediments from Lake Ammersee (southern Germany). Water Resources Research, 46. doi: https://doi.org/10.1029/2009WR008360

Czymzik, M., Muscheler, R., & Brauer, A. (2016). Solar modulation of flood frequency in central Europe during spring and summer on interannual to multi-centennial timescales. Clim. Past, 12, 799-805

Daley, T. J., Thomas, E. R., Holmes, J. A., Street-Perrott, F. A., Chapman, M. R., Tindall, J. C., Valdes, P. J., Loader, N. J., Marshall, J. D., Wolff, E. W., Hopley, P. J., Atkinson, T., Barber, K. E., Fisher, E. H., Robertson, I., Hughes, P. D. M., & Roberts, C. N. (2011). The 8200 yr BP cold event in stable isotope records from the North Atlantic region. Global and Planetary Change, 79, 288-302

Davies, S. J., Lamb, H. F., & Roberts, S. J. (2015). Micro-XRF Core Scanning in Palaeolimnology: Recent Developments. In I. W. Croudace & R. G. Rothwell (Eds.), Micro-XRF Studies of Sediment Cores. Springer Netherlands. Vol. 17, 189-226

Davies, S. J., Metcalfe, S. E., MacKenzie, A. B., Newton, A. J., Endfield, G. H., & Farmer, J. G. (2004). Environmental changes in the Zirahuén Basin, Michoacán, Mexico, during the last 1000 years. Journal of Paleolimnology, 31, 77-98

Davison, W. (1993). Iron and manganese in lakes. Earth-Science Reviews, 34, 119-163

de Geer, G. (1912). Greochronologie der letzten 12000 Jahre. Geologische Rundschau, 3, 457-471

Dean Jr, W. E. (1974). Determination of carbonate and organic matter in calcareous sediments and sedimentary rocks by loss on ignition: comparison with other methods. Journal of Sedimentary Research, 44, 242-248

Dean, J. M., Kemp, A. E. S., Bull, D., Pike, J., Patterson, G., & Zolitschka, B. (1999). Taking varves to bits: Scanning electron microscopy in the study of laminated sediments and varves. Journal of Paleolimnology, 22, 121-136

Dean, J. (2014). Stable isotope analysis and U-Th dating of late glacial and Holocene lacustrine sediments from central Turkey. PhD thesis. University of Nottingham.

Dean, J. R., Jones, M. D., Leng, M. J., Sloane, H. J., Roberts, C. N., Woodbridge, J., Swann, G. E. A., Metcalfe, S. E., Eastwood, W. J., & Yigitbasioglu, H. (2013). Palaeo-seasonality of the last two millennia reconstructed from the oxygen isotope composition of carbonates and diatom silica from Nar Golu, central Turkey. Quaternary Science Reviews, 66, 35-44

Dean, J. R., Jones, M. D., Leng, M. J., Noble, S. R., Metcalfe, S. E., Sloane, H. J., Sahy, D., Eastwood, W. J., & Roberts, C. N. (2015a). Eastern Mediterranean hydroclimate over the late glacial and Holocene, reconstructed from the sediments of Nar lake, central Turkey, using stable isotopes and carbonate mineralogy. Quaternary Science Reviews, 124, 162-174

Dean, J. R., Eastwood, W. J., Roberts, N., Jones, M. D., Yiğitbaşıoğlu, H., Allcock, S. L., Woodbridge, J., Metcalfe, S. E., & Leng, M. J. (2015b). Tracking the hydro-climatic signal from lake to sediment: A field study from central Turkey. Journal of Hydrology, 529, 608-621

Dean, J. R., Jones, M. D., Leng, M. J., Metcalfe, S. E., Sloane, H. J., Eastwood, W. J., & Roberts, C. N. (2017). Seasonality of Holocene hydroclimate in the Eastern Mediterranean reconstructed using the oxygen isotope composition of carbonates and diatoms from Lake Nar, central Turkey. The Holocene. doi: 10.1177/0959683617721326

Dean, K. R., Krauer, F., Walløe, L., Lingjærde, O. C., Bramanti, B., Stenseth, N. C., & Schmid, B. V. (2018). Human ectoparasites and the spread of plague in Europe during the Second Pandemic. Proceedings of the National Academy of Sciences. doi: https://doi.org/10.1073/pnas.1715640115

Dean, W., Anderson, R., Platt Bradbury, J., & Anderson, D. (2002). A 1500-year record of climatic and environmental change in ElkLake, Minnesota I: Varve thickness and gray-scale density. Journal of Paleolimnology, 27, 287-299

Declet, A., Reyes, E., & Suárez, O. (2016). Calcium carbonate precipitation: a review of the carbonate crystallization process and applications in bioinspired composites. Reviews on Advanced Materials Science, 44, 87-107

Deevey, E. S., & Stuiver, M. (1964). Distribution of natural isotopes of carbon in Linsley pond and other New England lakes, Limnology and Oceanography, 9, 1-11

Demarest, A. A., & Prudence, M. (2004). The Terminal Classic in the Maya Lowlands: Assessing Collapses, Terminations, and Transformations. In: Demarest, A., Rice, P. and Rice, D. (eds.) The Terminal Classic in the Maya Lowlands, University Press of Colorado, 545-572

deMenocal, P., Ortiz, J., Guilderson, T., & Sarnthein, M. (2000). Coherent High- and Low-Latitude Climate Variability During the Holocene Warm Period. Science, 288, 2198-2201

deMenocal, P. B. (2001). Cultural responses to climate change during the late Holocene. Science (New York, N.Y.), 292, 667-673

Deng, S., Dong, H., Lv, G., Jiang, H., Yu, B., & Bishop, M. E. (2010). Microbial dolomite precipitation using sulfate reducing and halophilic bacteria: Results from Qinghai Lake, Tibetan Plateau, NW China. Chemical Geology, 278, 151-159

Deutsch, C., Brix, H., Ito, T., Frenzel, H., & Thompson, L. (2011). Climate-Forced Variability of Ocean Hypoxia. Science, 333, 336-339

Di Rita, F., & Magri, D. (2009). Holocene drought, deforestation and evergreen vegetation development in the central Mediterranean: a 5500 year record from Lago Alimini Piccolo, Apulia, southeast Italy. The Holocene, 19, 295-306

Diaz, H. F., Trigo, R., Hughes, M. K., Mann, M. E., Xoplaki, E., & Barriopedro, D. (2011). Spatial and Temporal Characteristics of Climate in Medieval Times Revisited. Bulletin of the American Meteorological Society, 92, 1487-1500

Digerfeldt, G., Sandgren, P., & Olsson, S. (2007). Reconstruction of Holocene lake-level changes in Lake Xinias, central Greece. The Holocene, 17, 361-367

Djamali, M., Akhani, H., Andrieu-Ponel, V., Braconnot, P., Brewer, S., de Beaulieu, J.-L., Fleitmann, D., Fleury, J., Gasse, F., Guibal, F., Jackson, S. T., Lézine, A.-M., Médail, F., Ponel, P., Roberts, N., & Stevens, L. (2010). Indian Summer Monsoon variations could have affected the early-Holocene woodland expansion in the Near East. The Holocene, 20, 813-820

Donnelly, J. P., & Woodruff, J. D. (2007). Intense hurricane activity over the past 5,000 years controlled by El Niño and the West African monsoon. Nature, 447, 465-468

Dörfler, W., Feeser, I., van den Bogaard, C., Dreibrodt, S., Erlenkeuser, H., Kleinmann, A., Merkt, J., & Wiethold, J. (2012). A high-quality annually laminated sequence from Lake Belau, Northern Germany: Revised chronology and its implications for palynological and tephrochronological studies. The Holocene, 22, 1413-1426

Dormoy, I., Peyron, O., Combourieu Nebout, N., Goring, S., Kotthoff, U., Magny, M., & Pross, J. (2009). Terrestrial climate variability and seasonality changes in the Mediterranean region between 15 000 and 4000 years BP deduced from marine pollen records. Climate of the Past, 5, 615-632

Douglas, P. M. J., Pagani, M., Canuto, M. A., Brenner, M., Hodell, D. A., Eglinton, T. I., & Curtis, J. H. (2015). Drought, agricultural adaptation, and sociopolitical collapse in the Maya Lowlands. Proceedings of the National Academy of Sciences, 112, 5607-5612

Douglas, P. M. J., Pagani, M., Eglinton, T. I., Brenner, M., Hodell, D. A., Curtis, J. H., Ma, K. F., & Breckenridge, A. (2014). Pre-aged plant waxes in tropical lake sediments and their influence on the chronology of molecular paleoclimate proxy records. Geochimica et Cosmochimica Acta, 141, 346-364

Douglass, A. E. (1941). Crossdating in dendrochronology. Journal of Forestry, 39, 825-831

Dräger, N., Brauer, A., Brademann, B., Tjallingii, R., Słowiński, M., Błaszkiewicz, M., & Schlaak, N. (2016). Spontaneous self-combustion of organic-rich lateglacial lake sediments after freeze-drying. Journal of Paleolimnology, 55, 185-194

Dräger, N., Theuerkauf, M., Szeroczyńska, K., Wulf, S., Tjallingii, R., Plessen, B., Kienel, U., & Brauer, A. (2016). Varve microfacies and varve preservation record of climate change and human impact for the last 6000 years at Lake Tiefer See (NE Germany). The Holocene, doi:10.1177/0959683616660173

Dreibrodt, S., Lubos, C., Lomax, J., Sipos, G., Schroedter, T., & Nelle, O. (2014). Holocene landscape dynamics at the tell Arslantepe, Malatya, Turkey – Soil erosion, buried soils and settlement layers, slope and river activity in a middle Euphrates catchment. The Holocene, 24, 1351-1368

Dreibrodt, S., & Wiethold, J. (2014). Lake Belau and its catchment (northern Germany): A key archive of environmental history in northern central Europe since the onset of agriculture. The Holocene, 25, 296-322

Dulski, P., Brauer, A., & Mangili, C. (2015). Combined µ-XRF and Microfacies Techniques for Lake Sediment Analyses. In I. W. Croudace & R. G. Rothwell (Eds.), Micro-XRF Studies of Sediment Cores: Applications of a non-destructive tool for the environmental sciences. Dordrecht: Springer Netherlands. 325-349

Dunning, N., Beach, T., Farrell, P., & Luzzadder-Beach, S. (1998). Prehispanic Agrosystems and Adaptive Regions in the Maya Lowlands. Culture & Agriculture, 20, 87-101

Dunning, N. P., & Beach, T. (1994). Soil Erosion, Slope Management, and Ancient Terracing in the Maya Lowlands. Latin American Antiquity, 5, 51-69

Dunning, N. P., & Beach, T. (2004). Ecology and Agriculture of the Petexbatun Region: An Ancient Perspective on Rainforest Adaptation. Vanderbilt University Press, Nashville, TN.

Dunning, N. P., Luzzadder-Beach, S., Beach, T., Jones, J. G., Scarborough, V., & Culbert, T. P. (2002). Arising from the bajos: The evolution of a neotropical landscape and the rise of Maya civilization. Annals of the Association of American Geographers, 92, 267-283

Eastwood, W. J., Leng, M. J., Roberts, N., & Davis, B. (2007). Holocene climate change in the eastern Mediterranean region: a comparison of stable isotope and pollen data from Lake Gölhisar, southwest Turkey. Journal of Quaternary Science, 22, 327-341

Eastwood, W. J., Roberts, N., & Lamb, H. F. (1998). Palaeoecological and Archaeological Evidence for Human Occupance in Southwest Turkey: The Beyşehir Occupation Phase. Anatolian Studies, 48, 69-86

Eastwood, W. J., Roberts, N., Lamb, H. F., & Tibby, J. C. (1999). Holocene environmental change in southwest Turkey: a palaeoecological record of lake and catchment-related changes. Quaternary Science Reviews, 18, 671-695

Eggermont, H., Verschuren, D., Fagot, M., Rumes, B., Van Bocxlaer, B., & Kröpelin, S. (2008). Aquatic community response in a groundwater-fed desert lake to Holocene desiccation of the Sahara. Quaternary Science Reviews, 27, 2411-2425

Elbert, J., Grosjean, M., von Gunten, L., Urrutia, R., Fischer, D., Wartenburger, R., Ariztegui, D., Fujak, M., & Hamann, Y. (2011). Quantitative high-resolution winter (JJA) precipitation reconstruction from varved sediments of Lago Plomo 47°S, Patagonian Andes, AD 1530–2002. The Holocene. doi: 10.1177/0959683611425547

Elsner, J. B. (2006). Evidence in support of the climate change–Atlantic hurricane hypothesis. Geophysical Research Letters, 33, doi: https://doi.org/10.1029/2006GL026869

Emeis, K.-C., Struck, U., Schulz, H.-M., Rosenberg, R., Bernasconi, S., Erlenkeuser, H., Sakamoto, T., & Martinez-Ruiz, F. (2000). Temperature and salinity variations of Mediterranean Sea surface waters over the last 16,000 years from records of planktonic stable oxygen isotopes and alkenone unsaturation ratios. Palaeogeography, Palaeoclimatology, Palaeoecology, 158, 259-280

Emery, K. F., Wright, L. E., & Schwarcz, H. (2000). Isotopic Analysis of Ancient Deer Bone: Biotic Stability in Collapse Period Maya Land-use. Journal of Archaeological Science, 27, 537-550

Emmenegger, L., Schönenberger, R., Sigg, L., & Sulzberger, B. (2001). Light-induced redox cycling of iron in circumneutral lakes. Limnology and Oceanography, 46, 49-61

Endfield, G. H., & O'Hara, S. L. (1997). Conflicts Over Water in 'The Little Drought Age' in Central Mexico. Environment and History, 3, 255-272

England, A. (2007). Late Holocene palaeoecology of Cappadocia (Central Turkey): an investigation of annually laminated sediments from Nar Golu crater lake. PhD Thesis. University of Birmingham.

England, A., Eastwood, W. J., Roberts, C. N., Turner, R., & Haldon, J. F. (2008). Historical landscape change in Cappadocia (central Turkey): a palaeoecological investigation of annually laminated sediments from Nar lake. Holocene, 18, 1229-1245

Enscore, R. E., Biggerstaff, B. J., Brown, T. L., Fulgham, R. E., Reynolds, P. J., Engelthaler, D. M., Levy, C. E., Parmenter, R. R., Montenieri, J. A., Cheek, J. E., Grinnell, R. K., Ettestad, P. J., & Gage, K. L. (2002). Modeling relationships between climate and the frequency of human plague cases in the southwestern United States, 1960-1997. The American Journal of Tropical Medicine and Hygiene, 66, 186-196

Enters, D., Dörfler, W., & Zolitschka, B. (2008). Historical soil erosion and land-use change during the last two millennia recorded in lake sediments of Frickenhauser See, northern Bavaria, central Germany. The Holocene, 18, 243-254

Enzel, Y., Amit, R., Dayan, U., Crouvi, O., Kahana, R., Ziv, B., & Sharon, D. (2008). The climatic and physiographic controls of the eastern Mediterranean over the late Pleistocene climates in the southern Levant and its neighboring deserts. Global and Planetary Change, 60, 165-192

Enzel, Y., Bookman, R., Sharon, D., Gvirtzman, H., Dayan, U., Ziv, B., & Stein, M. (2003). Late Holocene climates of the Near East deduced from Dead Sea level variations and modern regional winter rainfall. Quaternary Research, 60, 263-273

Erdik, M., Doyuran, V., Akkaş, N., & Gülkan, P. (1985). A probabilistic assessment of the seismic hazard in Turkey. Tectonophysics, 117, 295-344

Evans, N. P., Bauska, T. K., Gázquez-Sánchez, F., Brenner, M., Curtis, J. H., & Hodell, D. A. (2018). Quantification of drought during the collapse of the classic Maya civilization. Science, 361, 498-501

Fagel, N., Boës, X., & Loutre, M. F. (2008). Climate oscillations evidenced by spectral analysis of Southern Chilean lacustrine sediments: the assessment of ENSO over the last 600 years. Journal of Paleolimnology, 39, 253-266

Fedotov, A. P., Phedorin, M. A., Enushchenko, I. V., Vershinin, K. E., Melgunov, M. S., & Khodzher, T. V. (2012). A reconstruction of the thawing of the permafrost during the last 170years on the Taimyr Peninsula (East Siberia, Russia). Global and Planetary Change, 98-99, 139-152

Feeser, I., Dörfler, W., Czymzik, M., & Dreibrodt, S. (2016). A mid-Holocene annually laminated sediment sequence from Lake Woserin: The role of climate and environmental change for cultural development during the Neolithic in Northern Germany. The Holocene, 26, 947-963

Fensterer, C., Scholz, D., Hoffmann, D., Spötl, C., Pajón, J. M., & Mangini, A. (2012). Cuban stalagmite suggests relationship between Caribbean precipitation and the Atlantic Multidecadal Oscillation during the past 1.3 ka. The Holocene. doi: 10.1177/0959683612449759

Fensterer, C., Scholz, D., Hoffmann, D. L., Spötl, C., Schröder-Ritzrau, A., Horn, C., Pajón, J. M., & Mangini, A. (2013). Millennial-scale climate variability during the last 12.5ka recorded in a Caribbean speleothem. Earth and Planetary Science Letters, 361, 143-151

Fick, S. E., & Hijmans, R. J. (2017). WorldClim 2: new 1-km spatial resolution climate surfaces for global land areas. International Journal of Climatology, 37, 4302-4315

Finkelstein, D. B. H., R. L.; Altaner, S. P. (1999). Origin and diagenesis of lacustrine sediments, upper Oligocene Creede Formation, southwestern Colorado. GSA Bulletin, 111, 1175-1191

Fischer, E. M., Luterbacher, J., Zorita, E., Tett, S. F. B., Casty, C., & Wanner, H. (2007). European climate response to tropical volcanic eruptions over the last half millennium. Geophysical Research Letters, 34, doi: https://doi.org/10.1029/2006GL027992

Fleitmann, D., Burns, S. J., Mangini, A., Mudelsee, M., Kramers, J., Villa, I., Neff, U., Al-Subbary, A. A., Buettner, A., Hippler, D., & Matter, A. (2007). Holocene ITCZ and Indian monsoon dynamics recorded in stalagmites from Oman and Yemen (Socotra). Quaternary Science Reviews, 26, 170-188

Fleitmann, D., Burns, S. J., Mudelsee, M., Neff, U., Kramers, J., Mangini, A., & Matter, A. (2003). Holocene Forcing of the Indian Monsoon Recorded in a Stalagmite from Southern Oman. Science, 300, 1737-1739

Flemming, R. L. (2007). Micro X-ray diffraction (μXRD): a versatile technique for characterization of Earth and planetary materials. Canadian Journal of Earth Sciences, 44, 1333-1346

Flohr, P., Fleitmann, D., Zorita, E., Sadekov, A., Cheng, H., Bosomworth, M., Edwards, L., Matthews, W., & Matthews, R. (2017). Late Holocene droughts in the Fertile Crescent recorded in a speleothem from northern Iraq. Geophysical Research Letters, 44, 1528-1536

Fortin, D., Leppard, G. G., & Tessier, A. (1993). Characteristics of lacustrine diagenetic iron oxyhydroxides. Geochimica et Cosmochimica Acta, 57, 4391-4404

Francus, P. (1998). An image-analysis technique to measure grain-size variation in thin sections of soft clastic sediments. Sedimentary Geology, 121, 289-298

Francus, P., & Cosby, C. (2001). Sub-sampling unconsolidated sediments: A solution for the preparation of undistrubed thin-sections from clay-rich sediments. Journal of Paleolimnology, 26, 323-326

Francus, P., Keimig, F., & Besonen, M. (2002). An algorithm to aid varve counting and measurement from thin-sections. Journal of Paleolimnology, 28, 283-286

Francus, P., Ridge, J. C., & Johnson, M. D. (2013). The rise of varves. GFF, 135, 229-230

Freeman, C., Ostle, N., & Kang, H. (2001). An enzymic 'latch' on a global carbon store. Nature, 409, 149

Fritz, S. C. (2008). Deciphering climatic history from lake sediments. Journal of Paleolimnology, 39, 5-16

Fritz, S. C., Cumming, B., Gasse, F., Laird, K. R., Stoermer, E., & Smol, J. (1999). Diatoms as indicators of hydrologic and climatic change in saline lakes. The diatoms: applications for the environmental and earth sciences. Cambridge University Press, 41-72

Fritz, S. C. B., S.; Rigsby, C. A.; Baker, P. A.; Calder-Church, A.; Conley D. J. (2011). Caribbean hydrological variability during the Holocene as reconstructed from crater lakes on the island of Grenada. Journal of Quaternary Science, 26, 829-838

Furukawa, Y., Lavoie, D., & Stephens, K. (1997). Effect of biogeochemical diagenesis on sediment fabric in shallow marine carbonate sediments near the Dry Tortugas, Florida. Geo-Marine Letters, 17, 283-290

Gabriel, J. J., Reinhardt, E. G., Peros, M. C., Davidson, D. E., van Hengstum, P. J., & Beddows, P. A. (2009). Palaeoenvironmental evolution of Cenote Aktun Ha (Carwash) on the Yucatan Peninsula, Mexico and its response to Holocene sea-level rise. Journal of Paleolimnology, 42, 199-213

Gage, K. L., Burkot, T. R., Eisen, R. J., & Hayes, E. B. (2008). Climate and Vectorborne Diseases. American Journal of Preventive Medicine, 35, 436-450

Gell, P. A., Barker, P. A., De Deckker, P., Last, W. M., & Jelicic, L. (1994). The Holocene history of West Basin Lake, Victoria, Australia; chemical changes based on fossil biota and sediment mineralogy. Journal of Paleolimnology, 12, 235-258

George, S. E., & Saunders, M. A. (2001). North Atlantic Oscillation impact on tropical North Atlantic winter atmospheric variability. Geophysical Research Letters, 28, 1015-1018

Gershunov, A., Barnett, T. P., & Cayan, D. R. (1999). North Pacific interdecadal oscillation seen as factor in ENSO-related North American climate anomalies. Eos, Transactions American Geophysical Union, 80, 25-30

Gershunov, A., Barnett, T. P., & Cayan, D. R. (1999). North Pacific interdecadal oscillation seen as factor in ENSO-related North American climate anomalies. Eos, Transactions American Geophysical Union, 80, 25-30

Gevrek, A. İ., & Kazanci, N. (2000). A Pleistocene, pyroclastic-poor maar from central Anatolia, Turkey: influence of a local fault on a phreatomagmatic eruption. Journal of Volcanology and Geothermal Research, 95, 309-317

Gierlowski-Kordesch, E. H. (2010). Lacustrine carbonates. Developments in Sedimentology, 61, 1-101.

Giguet-Covex, C., Arnaud, F., Poulenard, J., Disnar, J.-R., Delhon, C., Francus, P., David, F., Enters, D., Rey, P.-J., & Delannoy, J.-J. (2011). Changes in erosion patterns during the Holocene in a currently treeless subalpine catchment inferred from lake sediment geochemistry (Lake Anterne, 2063 m a.s.l., NW French Alps): The role of climate and human activities. The Holocene. doi: 10.1177/0959683610391320

Giguet-Covex, C., Arnaud, F., Poulenard, J., Enters, D., Reyss, J.-L., Millet, L., Lazzaroto, J., & Vidal, O. (2010). Sedimentological and geochemical records of past trophic state and hypolimnetic anoxia in large, hard-water Lake Bourget, French Alps. Journal of Paleolimnology, 43, 171-190

Gill, R. B. (2001). The great Maya droughts: water, life, and death: UNM Press.

Giralt, S., Rico-Herrero, M. T., Vega, J. C., & Valero-Garcés, B. L. (2011). Quantitative climate reconstruction linking meteorological, limnological and XRF core scanner datasets: the Lake Sanabria case study, NW Spain. Journal of Paleolimnology, 46, 487-502

Giry, C., Felis, T., Koelling, M., Wei, W., Lohmann, G., & Scheffers, S. (2013). Controls of Caribbean surface hydrology during the mid-to late Holocene: insights from monthly resolved coral records. Climate of the Past, 9, 841-858

Glew, J. R. (1991). Miniature gravity corer for recovering short sediment cores. Journal of Paleolimnology, 5, 285-287

Göktürk, O. M., Fleitmann, D., Badertscher, S., Cheng, H., Edwards, R. L., Leuenberger, M., Fankhauser, A., Tüysüz, O., & Kramers, J. (2011). Climate on the southern Black Sea coast during the Holocene: implications from the Sofular Cave record. Quaternary Science Reviews, 30, 2433-2445

González-Sampériz, P., Utrilla, P., Mazo, C., Valero-Garcés, B., Sopena, M. C., Morellón, M., Sebastián, M., Moreno, A., & Martínez-Bea, M. (2009). Patterns of human occupation during the early Holocene in the Central Ebro Basin (NE Spain) in response to the 8.2 ka climatic event. Quaternary Research, 71, 121-132

Goodfriend, G. A. (1999). Terrestrial stable isotope records of Late Quaternary paleoclimates in the eastern Mediterranean region. Quaternary Science Reviews, 18, 501-513

Goosse, H., Crespin, E., Dubinkina, S., Loutre, M.-F., Mann, M., Renssen, H., Sallaz-Damaz, Y., & Shindell, D. (2012). The role of forcing and internal dynamics in explaining the "Medieval Climate Anomaly". Climate Dynamics, 39, 2847-2866

Goring, S., Williams, J. W., Blois, J. L., Jackson, S. T., Paciorek, C. J., Booth, R. K., Marlon, J. R., Blaauw, M., & Christen, J. A. (2012). Deposition times in the northeastern United States during the Holocene: establishing valid priors for Bayesian age models. Quaternary Science Reviews, 48, 54-60

Goswami, B. N., Madhusoodanan, M. S., Neema, C. P., & Sengupta, D. (2006). A physical mechanism for North Atlantic SST influence on the Indian summer monsoon. Geophysical Research Letters, 33, L02706

Gottfried, R. S. (2010). Black Death. Simon and Schuster Publishing. 8-31

Graves, S. J., Li, X., Keiser, K., & Smith, D. K. (2012). Building a Climatology of Mountain Gap Wind Jets and Related Coastal Upwelling. Paper presented at the High Performance Computing, Networking, Storage and Analysis (SCC), 2012 SC Companion

Gray, L. J., Beer, J., Geller, M., Haigh, J. D., Lockwood, M., Matthes, K., Cubasch, U., Fleitmann, D., Harrison, G., Hood, L., Luterbacher, J., Meehl, G. A., Shindell, D., van Geel, B., & White, W. (2010). Solar influences on climate. Reviews of Geophysics, 48, doi: 10.1029/2009RG000282

Green, B., Marshall, J., & Donohoe, A. (2017). Twentieth century correlations between extratropical SST variability and ITCZ shifts. Geophysical Research Letters, 44, 9039-9047

Grimm, E. C., Jacobson, G. L., Watts, W. A., Hansen, B. C. S., & Maasch, K. A. (1993). A 50,000-Year Record of Climate Oscillations from Florida and Its Temporal Correlation with the Heinrich Events. Science, 261, 198

Grossman, E. L., & Ku, T.-L. (1986). Oxygen and carbon isotope fractionation in biogenic aragonite: Temperature effects. Chemical Geology: Isotope Geoscience section, 59, 59-74

Grottoli, A. G., & Eakin, C. M. (2007). A review of modern coral δ18O and δ14C proxy records. Earth-Science Reviews, 81, 67-91

Gunn, J., & Adams, R. E. W. (1981). Climatic change, culture, and civilization in North America. World Archaeology, 13, 87-100

Gupta, A. K. (2004). Origin of agriculture and domestication of plants and animals linked to early Holocene climate amelioration. Current Science Bangalore, 87, 54-59

Gupta, P., Noone, D., Galewsky, J., Sweeney, C., & Vaughn, B. H. (2009). Demonstration of high-precision continuous measurements of water vapor isotopologues in laboratory and remote field deployments using wavelength-scanned cavity ring-down spectroscopy (WS-CRDS)

technology. Rapid Communications in Mass Spectrometry: An International Journal Devoted to the Rapid Dissemination of Up-to-the-Minute Research in Mass Spectrometry, 23, 2534-2542

Guyard, H., Chapron, E., St-Onge, G., Anselmetti, F. S., Arnaud, F., Magand, O., Francus, P., & Mélières, M.-A. (2007). High-altitude varve records of abrupt environmental changes and mining activity over the last 4000 years in the Western French Alps (Lake Bramant, Grandes Rousses Massif). Quaternary Science Reviews, 26, 2644-2660

Haberzettl, T., Corbella, H., Fey, M., Janssen, S., Lücke, A., Mayr, C., Ohlendorf, C., Schäbitz, F., Schleser, G. H., Wille, M., Wulf, S., and Zolitschka, B. (2007). Lateglacial and Holocene wet—dry cycles in southern Patagonia: chronology, sedimentology and geochemistry of a lacustrine record from Laguna Potrok Aike, Argentina. The Holocene, 17, 297-310

Hajdas, I., Bonani, G., & Goślar, T. (1995). Radiocarbon Dating the Holocene in the Gościąż Lake Floating Varve Chronology. Radiocarbon, 37, 71-74

Hajdas, I., Bonani, G., & Zolitschka, B. (2000). Radiocarbon dating of varve chronologies; Soppensee and Holzmaar lakes after ten years. Radiocarbon, 42, 349-353

Hajdas, I., Ivy, S. D., Beer, J., Bonani, G., Imboden, D., Lotted, A. F., Sturm, M., & Suter, M. (1993). AMS radiocarbon dating and varve chronology of Lake Soppensee: 6000 to 12000 14C years BP. Climate Dynamics, 9, 107-116

Hajdas, I., & Michczynski, A. (2010). Age-depth model of Lake Soppensee (Switzerland) based on the high-resolution 14C chronology compared with varve chronology. Radiocarbon, 52, 1027-1040

Hakala, A. (2004). Meromixis as a part of lake evolution; observations and a revised classification of true meromictic lakes in Finland. Boreal Environment Research, 9, 37-53

Haldon, J., Roberts, N., Izdebski, A., Fleitmann, D., McCormick, M., Cassis, M., Doonan, O., Eastwood, W., Elton, H., & Ladstätter, S. (2014). The Climate and Environment of Byzantine Anatolia: Integrating Science, History, and Archaeology. Journal of Interdisciplinary History. 45, 113-161

Haltia-Hovi, E., Saarinen, T., & Kukkonen, M. (2007). A 2000-year record of solar forcing on varved lake sediment in eastern Finland. Quaternary Science Reviews, 26, 678-689

Hammer, Ø., Harper, D., & Ryan, P. (2001). PAST-palaeontological statistics, ver. 1.89. Palaeontologia electronica, 4, 1-15

Hansen, R. D., Bozarth, S., Jacob, J., Wahl, D., & Schreiner, T. (2002). Climatic and environmental variability in the rise of maya civilization: A preliminary perspective from northern Peten. Ancient Mesoamerica, 13, 273-295

Harrison, S. P., Kutzbach, J. E., Liu, Z., Bartlein, P. J., Otto-Bliesner, B., Muhs, D., Prentice, I. C., & Thompson, R. S. (2003). Mid-Holocene climates of the Americas: a dynamical response to changed seasonality. Climate Dynamics, 20, 663-688

Harwood, G. R. (2011). A regional fire history of the Yucatan, displayed by charcoal quantities in a core from Yaal Chac, Mexico. 3rd year undergraduate project, University of Nottingham.

Haug, G. H., Hughen, K. A., Sigman, D. M., Peterson, L. C., & Röhl, U. (2001). Southward migration of the intertropical convergence zone through the Holocene. Science, 293, 1304-1308

Haug, G. H., Günther, D., Peterson, L. C., Sigman, D. M., Hughen, K. A., & Aeschlimann, B. (2003). Climate and the collapse of Maya civilization. Science, 299, 1731-1735

He, Z., Munro, M., Gopalan, G., Kulkarni, V., Schowengerdt, R. A., & Hughes, M. K. (2008). System and algorithm design for a new generation tree-ring image analysis system. Optical Engineering, 47, 027003

Heinrich, I., Touchan, R., Dorado Liñán, I., Vos, H., & Helle, G. (2013). Winter-to-spring temperature dynamics in Turkey derived from tree rings since AD 1125. Climate Dynamics, 41, 1685-1701

Helama, S., Jones, P. D., & Briffa, K. R. (2017). Dark Ages Cold Period: A literature review and directions for future research. The Holocene, doi: 10.1177/0959683617693898

Henderson, A. C. G., Holmes, J. A., Zhang, J., Leng, M. J., & Carvalho, L. R. (2003). A carbon-and oxygen-isotope record of recent environmental change from Qinghai Lake, NE Tibetan Plateau. Chinese Science Bulletin, 48, 1463-1468Herrera-Silveira, J. A. (1996). Salinity and nutrients in a tropical coastal lagoon with groundwater discharges to the Gulf of Mexico. Hydrobiologia, 321, 165-176

Hethke, M., Fürsich, F. T., Jiang, B., & Pan, Y. (2013). Seasonal to sub-seasonal palaeoenvironmental changes in Lake Sihetun (Lower Cretaceous Yixian Formation, NE China). International Journal of Earth Sciences, 102, 351-378

Heun, M., Schäfer-Pregl, R., Klawan, D., Castagna, R., Accerbi, M., Borghi, B., & Salamini, F. (1997). Site of Einkorn Wheat Domestication Identified by DNA Fingerprinting. Science, 278, 1312

Higuera-Gundy, A., Brenner, M., Hodell, D. A., Curtis, J. H., Leyden, B. W., & Binford, M. W. (1999). A 10,300 14C yr Record of Climate and Vegetation Change from Haiti. Quaternary Research, 52, 159-170

Hijmans, R. J., Cameron, S. E., Parra, J. L., Jones, P. G., & Jarvis, A. (2005). Very high resolution interpolated climate surfaces for global land areas. International Journal of Climatology, 25, 1965-1978

Hildebrand, A. R., Pilkington, M., Connors, M., Ortiz-Aleman, C., & Chavez, R. E. (1995). Size and structure of the Chicxulub crater revealed by horizontal gravity gradients and cenotes. Nature, 376, 415-417

Hillesheim, M. B., Hodell, D. A., Leyden, B. W., Brenner, M., Curtis, J. H., Anselmetti, F. S., Ariztegui, D., Buck, D. G., Guilderson, T. P., Rosenmeier, M. F., & Schnurrenberger, D. W. (2005). Climate change in lowland Central America during the late deglacial and early Holocene. Journal of Quaternary Science, 20, 363-376

Hirschfeld, Y. (2004). A climatic change in the early Byzantine period? Some archaeological evidence. Palestine exploration quarterly, 136, 133-149

Hodder, I. (2007). Çatalhöyük in the Context of the Middle Eastern Neolithic. Annual Review of Anthropology, 36, 105-120

Hodell, D. A., Anselmetti, F. S., Ariztegui, D., Brenner, M., Curtis, J. H., Gilli, A., Grzesik, D. A., Guilderson, T. J., Müller, A. D., Bush, M. B., Correa-Metrio, A., Escobar, J., & Kutterolf, S. (2008). An 85-ka record of climate change in lowland Central America. Quaternary Science Reviews, 27, 1152-1165

Hodell, D. A., Brenner, M., & Curtis, J. H. (2005). Terminal Classic drought in the northern Maya lowlands inferred from multiple sediment cores in Lake Chichancanab (Mexico). Quaternary Science Reviews, 24, 1413-1427

Hodell, D. A., Brenner, M., & Curtis, J. H. (2007). Climate and cultural history of the Northeastern Yucatan Peninsula, Quintana Roo, Mexico. Climatic Change, 83, 215-240

Hodell, D. A., Brenner, M., Curtis, J. H., & Guilderson, T. (2001). Solar Forcing of Drought Frequency in the Maya Lowlands. Science, 292, 1367-1370

Hodell, D. A., Brenner, M., Curtis, J. H., Medina-González, R., Ildefonso-Chan Can, E., Albornaz-Pat, A., & Guilderson, T. P. (2005). Climate change on the Yucatan Peninsula during the Little Ice Age. Quaternary Research, 63, 109-121

Hodell, D. A., Curtis, J. H., & Brenner, M. (1995). Possible role of climate in the collapse of Classic Maya civilization. Nature, 375, 391-394

Hodell, D. A., Curtis, J. H., Jones, G. A., Higuera-Gundy, A., Brenner, M., Binford, M. W., & Dorsey, K. T. (1991). Reconstruction of Caribbean climate change over the past 10,500 years. Nature, 352, 790-793

Hooper, S. (2011). A study of stable isotopes in authigenic and biogenic carbonates in cenote Yaal Chac. 3rd year undergraduate project, University of Nottingham.

Hu, Q., & Feng, S. (2002). Interannual Rainfall Variations in the North American Summer Monsoon Region: 1900-98*. Journal of Climate, 15, 1189-1202

Hughen, K. A., Overpeck, J. T., & Anderson, C. (2000). Recent warming in a 500-year palaeotemperature record from varved sediments, Upper Soper Lake, Baffin Island, Canada. The Holocene, 10, 9-19

Hughen, K. A., Overpeck, J. T., Lehman, S. J., Kashgarian, M., Southon, J. R., & Peterson, L. C. (1998). A new 14 C calibration data set for the last deglaciation based on marine varves. Radiocarbon, 40, 483-494

Hurrell, J. W. (1995). Decadal trends in the North Atlantic Oscillation: regional temperatures and precipitation. Science, 269, 676-679

Hurrell, J. W., Kushnir, Y., Ottersen, G., & Visbeck, M. (2003). An overview of the North Atlantic oscillation. Geophysical Monograph-American Geophysical Union, 134, 1-36

Ingalls, A. E., Aller, R. C., Lee, C., & Wakeham, S. G. (2004). Organic matter diagenesis in shallow water carbonate sediments. Geochimica et Cosmochimica Acta, 68, 4363-4379

Inouchi, Y., Kinugasa, Y., Kumon, F., Nakano, S., Yasumatsu, S., & Shiki, T. (1996). Turbidites as records of intense palaeoearthquakes in Lake Biwa, Japan. Sedimentary Geology, 104, 117-125

Inoue, M., Handoh, I. C., & Bigg, G. R. (2002). Bimodal distribution of tropical cyclogenesis in the Caribbean: Characteristics and environmental factors. Journal of Climate, 15, 2897-2905

Isendahl, C. (2011). The weight of water: a new look at pre-Hispanic Puuc Maya water reservoirs. Ancient Mesoamerica, 22, 185-197

Islebe, G. A., & Hooghiemstra, H. (1997). Vegetation and climate history of montane Costa Rica since the last glacial. Quaternary Science Reviews, 16, 589-604

Islebe, G. A., Hooghiemstra, H., Brenner, M., Curtis, J. H., & Hodell, D. A. (1996). A Holocene vegetation history from lowland Guatemala. The Holocene, 6, 265-271

Ito, E. (2002). Mg/Ca, Sr/Ca, δ18O and δ13C chemistry of Quaternary lacustrine ostracode shells from the North American continental interior. The Ostracoda: Applications in Quaternary Research, 267-278

Izdebski, A., Pickett, J., Roberts, N., & Waliszewski, T. (2016). The environmental, archaeological and historical evidence for regional climatic changes and their societal impacts in the Eastern Mediterranean in Late Antiquity. Quaternary Science Reviews, 136, 189-208

Jalut, G., Dedoubat, J. J., Fontugne, M., & Otto, T. (2009). Holocene circum-Mediterranean vegetation changes: Climate forcing and human impact. Quaternary International, 200, 4-18

James W. Wood. (1998). A Theory of Preindustrial Population Dynamics Demography, Economy, and Well-Being in Malthusian Systems. Current Anthropology, 39, 99-135

Jamin, E., Martin, F., Santamaria-Fernandez, R., & Lees, M. (2005). Detection of Exogenous Citric Acid in Fruit Juices by Stable Isotope Ratio Analysis. Journal of Agricultural and Food Chemistry, 53, 5130-5133

Jane, B. (1993). The Swedish varve chronology - a review. Progress in Physical Geography: Earth and Environment, 17, 1-19

Janssen, M. A., Schoon, M. L., Ke, W., & Börner, K. (2006). Scholarly networks on resilience, vulnerability and adaptation within the human dimensions of global environmental change. Global Environmental Change, 16, 240-252

Jarvis, S. (2012). Optimising, understanding and quantifying Itrax XRF data. PhD Thesis. University of Southampton.

Jennings, E., Jones, S., Arvola, L., Staehr, P. A., Gaiser, E., Jones, I. D., Weathers, K. C., Weyhenmeyer, G. A., Chiu, C.-Y., & De Eyto, E. (2012). Effects of weather-related episodic events in lakes: an analysis based on high-frequency data. Freshwater Biology, 57, 589-601

Jenny, J.-P., Arnaud, F., Dorioz, J.-M., Covex, C. G., Frossard, V., Sabatier, P., Millet, L., Reyss, J.-L., Tachikawa, K., Bard, E., Pignol, C., Soufi, F., Romeyer, O., & Perga, M.-E. (2013). A spatiotemporal investigation of varved sediments highlights the dynamics of hypolimnetic hypoxia in a large hard-water lake over the last 150 years. Limnology and Oceanography, 58, 1395-1408

Jenny, J.-P., Arnaud, F., Dorioz, J.-M., Covex, C. G., Frossard, V., Sabatier, P., Millet, L., Reyss, J.-L., Tachikawa, K., Bard, E., Pignol, C., Soufi, F., Romeyer, O., & Perga, M.-E. (2013). A spatiotemporal investigation of varved sediments highlights the dynamics of hypolimnetic hypoxia in a large hard-water lake over the last 150 years. Limnology and Oceanography, 58, 1395-1408

Jenny, J.-P., Francus, P., Normandeau, A., Lapointe, F., Perga, M.-E., Ojala, A., Schimmelmann, A., & Zolitschka, B. (2016). Global spread of hypoxia in freshwater ecosystems during the last three centuries is caused by rising local human pressure. Global Change Biology, 22, 1481-1489

Jian, T., Thomas, A. B., & Feng Sheng, H. (2005). Comparison of varve and 14C chronologies from Steel Lake, Minnesota, USA. The Holocene, 15, 510-517

Jin, Z., Li, F., Cao, J., Wang, S., & Yu, J. (2006). Geochemistry of Daihai Lake sediments, Inner Mongolia, north China: Implications for provenance, sedimentary sorting, and catchment weathering. Geomorphology, 80, 147-163

Joetzjer, E., Douville, H., Delire, C., Ciais, P., Decharme, B., & Tyteca, S. (2013). Hydrologic benchmarking of meteorological drought indices at interannual to climate change timescales: a case study over the Amazon and Mississippi river basins. Hydrology and Earth System Sciences, 17, 4885-4888

Johnsen, S. J., Dahl-Jensen, D., Gundestrup, N., Steffensen, J. P., Clausen, H. B., Miller, H., Masson-Delmotte, V., Sveinbjörnsdottir, A. E., & White, J. (2001). Oxygen isotope and palaeotemperature records from six Greenland ice-core stations: Camp Century, Dye-3, GRIP, GISP2, Renland and NorthGRIP. Journal of Quaternary Science, 16, 299-307

Jones, M. D., Leng, M. J., Roberts, C. N., Turkes, M., & Moyeed, R. (2005). A coupled calibration and modelling approach to the understanding of dry-land lake oxygen isotope records. Journal of Paleolimnology, 34, 391-411

Jones, M. D., Metcalfe, S. E., Davies, S. J., & Noren, A. (2015). Late Holocene climate reorganisation and the North American Monsoon. Quaternary Science Reviews, 124, 290-295

Jones, M. D., & Neil Roberts, C. (2008). Interpreting lake isotope records of Holocene environmental change in the Eastern Mediterranean. Quaternary International, 181, 32-38

Jones, M. D., Roberts, C. N., & Leng, M. J. (2007). Quantifying climatic change through the last glacial–interglacial transition based on lake isotope palaeohydrology from central Turkey. Quaternary Research, 67, 463-473

Jones, M. D., Roberts, C. N., Leng, M. J., & Türkeş, M. (2006). A high-resolution late Holocene lake isotope record from Turkey and links to North Atlantic and monsoon climate. Geology, 34, 361-364

Jury, M., Malmgren, B. A., & Winter, A. (2007). Subregional precipitation climate of the Caribbean and relationships with ENSO and NAO. Journal of Geophysical Research: Atmospheres, 112, D16107

Kallel, N., Paterne, M., Duplessy, J. C., VergnaudGrazzini, C., Pujol, C., Labeyrie, L., Arnold, M., Fontugne, M., & Pierre, C. (1997). Enhanced rainfall in the Mediterranean region during the last sapropel event. Oceanologica Acta, 20, 697-712

Kalugin, I., Darin, A., Rogozin, D., & Tretyakov, G. (2013). Seasonal and centennial cycles of carbonate mineralisation during the past 2500 years from varved sediment in Lake Shira, South Siberia. Quaternary International, 290, 245-252

Kanamaru, K., Francus, P., François, R., Besonen, M., & Laj, C. (2013). New insight into Saanich Inlet varved sediments (British Columbia, Canada) from micro-scale analysis of sedimentary facies and micro-XRF core scanning analyses. GFF, 135, 316-339

Kaniewski, D., Van Campo, E., Paulissen, E., Weiss, H., Bakker, J., Rossignol, I., & Van Lerberghe, K. (2011). The medieval climate anomaly and the little Ice Age in coastal Syria inferred from pollen-derived palaeoclimatic patterns. Global and Planetary Change, 78, 178-187

Karaca, M., Deniz, A., & Tayanç, M. (2000). Cyclone track variability over Turkey in association with regional climate. International Journal of Climatology, 20, 1225-1236

Kato, M., Fukusawa, H., & Yasuda, Y. (2003). Varved lacustrine sediments of Lake Tougou-ike, Western Japan, with reference to Holocene sea-level changes in Japan. Quaternary International, 105, 33-37

Katz, A., & Nishri, A. (2013). Calcium, magnesium and strontium cycling in stratified, hardwater lakes: Lake Kinneret (Sea of Galilee), Israel. Geochimica et Cosmochimica Acta, 105, 372-394

Kaufman, C. A., Lamoureux, S. F., & Kaufman, D. S. (2011). Long-term river discharge and multidecadal climate variability inferred from varved sediments, southwest Alaska. Quaternary Research, 76, 1-9

Kaushal, S., & Binford, M. W. (1999). Relationship between C:N ratios of lake sediments, organic matter sources, and historical deforestation in Lake Pleasant, Massachusetts, USA. Journal of Paleolimnology, 22, 439-442

Keatings, K., Holmes, J., Flower, R., Horne, D., Whittaker, J. E., & Abu-Zied, R. H. (2010). Ostracods and the Holocene palaeolimnology of Lake Qarun, with special reference to past human–environment interactions in the Faiyum (Egypt). Hydrobiologia, 654, 155-176

Kelts, K., & Hsü, K. (1978). Freshwater carbonate sedimentation Lakes. Springer. 295-323

Kennett, D. J., Breitenbach, S. F., Aquino, V. V., Asmerom, Y., Awe, J., Baldini, J. U., Bartlein, P., Culleton, B. J., Ebert, C., & Jazwa, C. (2012). Development and disintegration of Maya political systems in response to climate change. Science, 338, 788-791

Kerr, R. A. (1997). A New Driver for the Atlantic's Moods and Europe's Weather? Science, 275, 754-755

Kerr, R. A. (2000). A North Atlantic Climate Pacemaker for the Centuries. Science, 288, 1984-1985

Khan, N. S., Ashe, E., Horton, B. P., Dutton, A., Kopp, R. E., Brocard, G., Engelhart, S. E., Hill, D. F., Peltier, W. R., Vane, C. H., & Scatena, F. N. (2017). Drivers of Holocene sea-level change in the Caribbean. Quaternary Science Reviews, 155, 13-36

Kienel, U., Dulski, P., Ott, F., Lorenz, S., & Brauer, A. (2013). Recently induced anoxia leading to the preservation of seasonal laminae in two NE-German lakes. Journal of Paleolimnology, 50, 535-544

Kienel, U., Schwab, M. J., & Schettler, G. (2005). Distinguishing climatic from direct anthropogenic influences during the past 400 years in varved sediments from Lake Holzmaar (Eifel, Germany). Journal of Paleolimnology, 33, 327-347

Kim, S.-T., O'Neil, J. R., Hillaire-Marcel, C., & Mucci, A. (2007). Oxygen isotope fractionation between synthetic aragonite and water: Influence of temperature and Mg2+ concentration. Geochimica et Cosmochimica Acta, 71, 4704-4715

Kirilova, E. P., Heiri, O., Bluszcz, P., Zolitschka, B., & Lotter, A. F. (2011). Climate-driven shifts in diatom assemblages recorded in annually laminated sediments of Sacrower See (NE Germany). Aquatic Sciences, 73, 201-210

Kitagawa, H., & Van Der Plicht, J. (1997). A 40,000-Year Varve Chronology from Lake Suigetsu, Japan: Extension of the 14C Calibration Curve. Radiocarbon, 40, 505-515

Klaminder, J., Appleby, P., Crook, P., & Renberg, I. (2012). Post-deposition diffusion of 137Cs in lake sediment: Implications for radiocaesium dating. Sedimentology, 59, 2259-2267

Kobashi, T., Kawamura, K., Severinghaus, J. P., Barnola, J.-M., Nakaegawa, T., Vinther, B. M., Johnsen, S. J., & Box, J. E. (2011). High variability of Greenland surface temperature over the past 4000 years estimated from trapped air in an ice core. Geophysical Research Letters, 38, doi: 10.1029/2011GL049444

Koinig, K. A., Shotyk, W., Lotter, A. F., Ohlendorf, C., & Sturm, M. (2003). 9000 years of geochemical evolution of lithogenic major and trace elements in the sediment of an alpine lake – the role of climate, vegetation, and land-use history. Journal of Paleolimnology, 30, 307-320

Korty, R. L., Camargo, S. J., & Galewsky, J. (2012). Variations in Tropical Cyclone Genesis Factors in Simulations of the Holocene Epoch. Journal of Climate, 25, 8196-8211

Koschel, R. (1990). Pelagic calcite precipitation and trophic state of hardwater lakes. Ergebnisse der Limnologie, 33, 713 - 722

Kotthoff, U., Pross, J., Müller, U. C., Peyron, O., Schmiedl, G., Schulz, H., & Bordon, A. (2008). Climate dynamics in the borderlands of the Aegean Sea during formation of sapropel S1 deduced from a marine pollen record. Quaternary Science Reviews, 27, 832-845

Koutsodendris, A., Brauer, A., Pälike, H., Müller, U. C., Dulski, P., Lotter, A. F., & Pross, J. (2011). Sub-decadal- to decadal-scale climate cyclicity during the Holsteinian interglacial (MIS 11) evidenced in annually laminated sediments. Climate of the Past, 7, 987-999

Koutsodendris, A., Müller, U. C., Pross, J., Brauer, A., Kotthoff, U., & Lotter, A. F. (2010). Vegetation dynamics and climate variability during the Holsteinian interglacial based on a pollen record from Dethlingen (northern Germany). Quaternary Science Reviews, 29, 3298-3307

Koutsodendris, A., Pross, J., Müller, U. C., Brauer, A., Fletcher, W. J., Kühl, N., Kirilova, E., Verhagen, F. T. M., Lücke, A., & Lotter, A. F. (2012). A short-term climate oscillation during the Holsteinian interglacial (MIS 11c): An analogy to the 8.2ka climatic event? Global and Planetary Change, 92-93, 224-235

Kutiel, H., & Benaroch, Y. (2002). North Sea-Caspian Pattern (NCP) – an upper level atmospheric teleconnection affecting the Eastern Mediterranean: Identification and definition. Theoretical and Applied Climatology, 71, 17-28

Kutiel, H., Maheras, P., Turkes, M., & Paz, S. (2002). North Sea Caspian Pattern (NCP) - an upper level atmospheric teleconnection affecting the eastern Mediterranean - implications on the regional climate. Theoretical and Applied Climatology, 72, 173-192

Kutiel, H., & Türkeş, M. (2005). New Evidence for The Role of The North Sea — Caspian Pattern on The Temperature and Precipitation Regimes in Continental Central Turkey. Geografiska Annaler: Series A, Physical Geography, 87, 501-513

Kuzucuoğlu, C., Dörfler, W., Kunesch, S., & Goupille, F. (2011). Mid- to late-Holocene climate change in central Turkey: The Tecer Lake record. The Holocene, 21, 173-188

Kylander, M. E., Ampel, L., Wohlfarth, B., & Veres, D. (2011). High-resolution X-ray fluorescence core scanning analysis of Les Echets (France) sedimentary sequence: new insights from chemical proxies. Journal of Quaternary Science, 26, 109-117

Kylander, M. E., Lind, E. M., Wastegård, S., & Löwemark, L. (2011). Recommendations for using XRF core scanning as a tool in tephrochronology. The Holocene, 22, 371-375

Lachniet, M. S., Asmerom, Y., Burns, S. J., Patterson, W. P., Polyak, V. J., & Seltzer, G. O. (2004). Tropical response to the 8200 yr B.P. cold event? Speleothem isotopes indicate a weakened early Holocene monsoon in Costa Rica. Geology, 32, 957-960

Lachniet, M. S., Burns, S. J., Piperno, D. R., Asmerom, Y., Polyak, V. J., Moy, C. M., & Christenson, K. (2004). A 1500-year El Niño/Southern Oscillation and rainfall history for the Isthmus of Panama from speleothem calcite. Journal of Geophysical Research: Atmospheres, 109, doi: 10.1029/2004JD004694

Ladd, M., Viau, A. E., Way, R. G., Gajewski, K., & Sawada, M. C. (2017). Variations in precipitation in North America during the past 2000 years. The Holocene. doi: 10.1177/0959683617735583

Laiou-Thomadakis, A. E. (1980). The Byzantine Economy in the Mediterranean Trade System; Thirteenth-Fifteenth Centuries. Dumbarton Oaks Papers, 34/35, 177-222

Lami, A., Niessen, F., Guilizzoni, P., Masaferro, J., & Belis, C. A. (1994). Palaeolimnological studies of the eutrophication of volcanic Lake Albano (Central Italy). Journal of Paleolimnology, 10, 181-197

Lami, A., Guilizzoni, P., & Marchetto, A. (2000). High resolution analysis of fossil pigments, carbon, nitrogen and sulphur in the sediment of eight European Alpine lakes: the MOLAR project. 2000, 14. doi: 10.4081/jlimnol.2000.s1.15

Lamoureux, S. (2000). Five centuries of interannual sediment yield and rainfall-induced erosion in the Canadian High Arctic recorded in lacustrine varves. Water Resources Research, 36, 309-318

Lamoureux, S. (2002). Varve chronology techniques. Tracking environmental change using lake sediments, 247-260

Lamoureux, S., & Francus, P. (2014). Layers within layers: Quantifying seasonal versus event processes in Arctic clastic varved sediments. PAGES Magazine, 22, 6-7

Lamoureux, S. F., & Gilbert, R. (2004). A 750-yr record of autumn snowfall and temperature variability and winter storminess recorded in the varved sediments of Bear Lake, Devon Island, Arctic Canada. Quaternary Research, 61, 134-147

Landmann, G., Reimer, A., & Kempe, S. (1996). Climatically induced lake level changes at Lake Van, Turkey, during the Pleistocene/Holocene Transition. Global Biogeochemical Cycles, 10, 797-808

Lane, C. S., Horn, S. P., Mora, C. I., & Orvis, K. H. (2009). Late-Holocene paleoenvironmental change at mid-elevation on the Caribbean slope of the Cordillera Central, Dominican Republic: a multi-site, multi-proxy analysis. Quaternary Science Reviews, 28, 2239-2260

Lapointe, F., Francus, P., Lamoureux, S. F., Saïd, M., & Cuven, S. (2012). 1750 years of large rainfall events inferred from particle size at East Lake, Cape Bounty, Melville Island, Canada. Journal of Paleolimnology, 48, 159-173

Larocque, I., Grosjean, M., Heiri, O., Bigler, C., & Blass, A. (2009). Comparison between chironomid-inferred July temperatures and meteorological data AD 1850–2001 from varved Lake Silvaplana, Switzerland. Journal of Paleolimnology, 41, 329-342

Lau, K. M., & Weng, H. (1995). Climate Signal Detection Using Wavelet Transform: How to Make a Time Series Sing. Bulletin of the American Meteorological Society, 76, 2391-2402

Lauterbach, S., Brauer, A., Andersen, N., Danielopol, D. L., Dulski, P., Hüls, M., Milecka, K., Namiotko, T., Obremska, M., Von Grafenstein, U., & Declakes, P. (2011). Environmental responses to Lateglacial climatic fluctuations recorded in the sediments of pre-Alpine Lake Mondsee (northeastern Alps). Journal of Quaternary Science, 26, 253-267

Leavitt, P. R. (1993). A review of factors that regulate carotenoid and chlorophyll deposition and fossil pigment abundance. Journal of Paleolimnology, 9, 109-127

Leemann, A., & Niessen, F. (1994). Varve formation and the climatic record in an Alpine proglacial lake: calibrating annually- laminated sediments against hydrological and meteorological data. The Holocene, 4, 1-8

Lem, R. (2011). Using sediment mineralogy to infer the climatic history of Cenote Yaal Chac, Yucatan Peninsula. 3rd year undergraduate project, University of Nottingham.

Leng, M. J., & Barker, P. A. (2006). A review of the oxygen isotope composition of lacustrine diatom silica for palaeoclimate reconstruction. Earth-Science Reviews, 75, 5-27

Leng, M. J., & Marshall, J. D. (2004). Palaeoclimate interpretation of stable isotope data from lake sediment archives. Quaternary Science Reviews, 23, 811-831

Leng, M. J., Lamb, A. L., Heaton, T., Marshall, J. D., Wolfe, B., Jones, M. D., Holmes, J. A., & Arrowsmith, C. (2006). Isotopes in lake sediments. In M. J. Leng (Ed.), Isotopes in Palaeoenvironmental Research. Dordrecht: Springer Netherlands. 147-184

Leonard, E. M. (1997). The relationship between glacial activity and sediment production: evidence from a 4450-year varve record of neoglacial sedimentation in Hector Lake, Alberta, Canada. Journal of Paleolimnology, 17, 319-330

Leyden, B. W. (2002). Pollen evidence for climatic variability and cultural disturbance in the Maya lowlands. Ancient Mesoamerica, 13, 85-101.

Leyden, B. W., Brenner, M., Hodell, D. A., & Curtis, J. H. (1993). Late Pleistocene climate in the Central American lowlands. Climate change in continental isotopic records, 165-178Leyden, B. W., Brenner, M., & Dahlin, B. H. (1998). Cultural and Climatic History of Cobá, a Lowland Maya City in Quintana Roo, Mexico. Quaternary Research, 49, 111-122

Leyden, B. W., Brenner, M., Hodell, D. A., & Curtis, J. H. (1994). Orbital and internal forcing of climate on the Yucatan Peninsula for the past ca. 36 ka. Palaeogeography, Palaeoclimatology, Palaeoecology, 109, 193-210

Lindsay, W. L. (1979). Chemical equilibria in soils. John Wiley and Sons Ltd.

Liu, X., Colman, S. M., Brown, E. T., Minor, E. C., & Li, H. (2013). Estimation of carbonate, total organic carbon, and biogenic silica content by FTIR and XRF techniques in lacustrine sediments. Journal of Paleolimnology, 50, 387-398

Liu, X., & Yanai, M. (2001). Relationship between the Indian monsoon rainfall and the tropospheric temperature over the Eurasian continent. Quarterly Journal of the Royal Meteorological Society, 127, 909-937

Livingstone, D. A. (1955). A Lightweight Piston Sampler for Lake Deposits. Ecology, 36, 137-139

Livingstone, D. M., & Hajdas, I. (2001). Climatically relevant periodicities in the thickness of biogenic carbonate varves in Spooensee, Switzerland (9740-6870 calendar yr BP). Journal of Paleolimnology, 25, 17-24

Lotter, A., & Sturm, M. (1994). The study of environmental dynamics by means of laminated sediments: results from Switzerland. Paper presented at the PACT.

Lotter, A. F., & Birks, H. J. B. (1997). The separation of the influence of nutrients and climate on the varve time-series of baldeggersee, Switzerland. Aquatic Sciences, 59, 362-375

Lotter, A. F., Birks, H. J. B., & Zolitschka, B. (1995). Late-glacial pollen and diatom changes in response to two different environmental perturbations: volcanic eruption and Younger Dryas cooling. Journal of Paleolimnology, 14, 23-47

Lotter, A. F., & Lemcke, G. (1999). Methods for preparing and counting biochemical varves. Boreas, 28, 243-252

Lotter, A. F., Sturm, M., Teranes, J. L., & Wehrli, B. (1997). Varve formation since 1885 and high-resolution varve analyses in hypertrophic Baldeggersee (Switzerland). Aquatic Sciences, 59, 304-325

Löwemark, L., Chen, H. F., Yang, T. N., Kylander, M., Yu, E. F., Hsu, Y. W., Lee, T. Q., Song, S. R., & Jarvis, S. (2011). Normalizing XRF-scanner data: A cautionary note on the interpretation of high-resolution records from organic-rich lakes. Journal of Asian Earth Sciences, 40, 1250-

1256Lozano-García, M. d. S., Caballero, M., Ortega, B., Rodríguez, A., & Sosa, S. (2007). Tracing the effects of the Little Ice Age in the tropical lowlands of eastern Mesoamerica. Proceedings of the National Academy of Sciences, 104, 16200-16203

Lucero, L. J., Gunn, J. D., & Scarborough, V. L. (2011). Climate change and Classic Maya water management. Water, 3, 479-494

Lücke, A., & Brauer, A. (2004). Biogeochemical and micro-facial fingerprints of ecosystem response to rapid Late Glacial climatic changes in varved sediments of Meerfelder Maar (Germany). Palaeogeography, Palaeoclimatology, Palaeoecology, 211, 139-155

Lücke, A., Schleser, G. H., Zolitschka, B., & Negendank, J. F. W. (2003). A Lateglacial and Holocene organic carbon isotope record of lacustrine palaeoproductivity and climatic change derived from varved lake sediments of Lake Holzmaar, Germany. Quaternary Science Reviews, 22, 569-580

Lüder, B., Kirchner, G., Lücke, A., & Zolitschka, B. (2006). Palaeoenvironmental Reconstructions Based on Geochemical Parameters from Annually Laminated Sediments of Sacrower See (northeastern Germany) Since the 17th Century. Journal of Paleolimnology, 35, 897-912

Luo, F., Li, S., & Furevik, T. (2011). The connection between the Atlantic Multidecadal Oscillation and the Indian Summer Monsoon in Bergen Climate Model Version 2.0. Journal of Geophysical Research: Atmospheres, 116. doi: 10.1029/2011JD015848

Luzzadder-Beach, S., Beach, T. P., & Dunning, N. P. (2012). Wetland fields as mirrors of drought and the Maya abandonment. Proceedings of the National Academy of Sciences, 109, 3646-3651

Maasch, K. A., Mayewski, P. A., Rohling, E. J., Stager, J. C., Karlen, W., Meeker, L. D., & Meyerson, E. A. (2005). A 2000-YEAR CONTEXT FOR MODERN CLIMATE CHANGE. Geografiska Annaler: Series A, Physical Geography, 87, 7-15

Mackereth, F. (1958). A portable core sampler for lake deposits. Limnology and Oceanography, 3, 181-191

Magaña, V., Amador, J. A., & Medina, S. (1999). The midsummer drought over Mexico and Central America. Journal of Climate, 12, 1577-1588

Magaña, V. O., Vázquez, J. L., Pérez, J. L., & Pérez, J. B. (2003). Impact of El Niño on precipitation in Mexico. Geofisica Internacional Mexico, 42, 313-330

Magdalino, P., (2008). The Empire of the Komnenoi (1118-1204). In: Shepard, J. (Ed.), The Cambridge History of the Byzantine Empire Ca. 500-1492. Cambridge University Press, Cambridge, 627-663.

Magny, M., Bégeot, C., Guiot, J., & Peyron, O. (2003). Contrasting patterns of hydrological changes in Europe in response to Holocene climate cooling phases. Quaternary Science Reviews, 22, 1589-1596

Maier, D. B., Rydberg, J., Bigler, C., & Renberg, I. (2013). Compaction of recent varved lake sediments. GFF, 135, 231-236

Mangili, C., Brauer, A., Moscariello, A., & Naumann, R. (2005). Microfacies of detrital event layers deposited in Quaternary varved lake sediments of the Piànico-Sèllere Basin (northern Italy). Sedimentology, 52, 927-943

Mann, M. E., & Jones, P. D. (2003). Global surface temperatures over the past two millennia. Geophysical Research Letters, 30, doi: https://doi.org/10.1029/2003GL017814

Mann, M. E., Zhang, Z., Rutherford, S., Bradley, R. S., Hughes, M. K., Shindell, D., Ammann, C., Faluvegi, G., & Ni, F. (2009). Global signatures and dynamical origins of the Little Ice Age and Medieval Climate Anomaly. Science, 326, 1256-1260

Marin, L., Perry, E., Pope, K., Duller, C., Booth, C., & Villasuso, M. (1990). Hurricane Gilbert: its effects on the aquifer in northern Yucatan, Mexico. Paper presented at the Selected papers on

hydrogeology from the 28th International Geological Congress, Washington, DC. Verlag Heinz Heise, Hannover.

Marino, G., Rohling, E. J., Sangiorgi, F., Hayes, A., Casford, J. L., Lotter, A. F., Kucera, M., & Brinkhuis, H. (2009). Early and middle Holocene in the Aegean Sea: interplay between high and low latitude climate variability. Quaternary Science Reviews, 28, 3246-3262

Marshall, M., Schlolaut, G., Nakagawa, T., Lamb, H., Brauer, A., Staff, R., Ramsey, C. B., Tarasov, P., Gotanda, K., Haraguchi, T., Yokoyama, Y., Yonenobu, H., & Tada, R. (2012). A novel approach to varve counting using μXRF and X-radiography in combination with thin-section microscopy, applied to the Late Glacial chronology from Lake Suigetsu, Japan. Quaternary Geochronology, 13, 70-80

Martin-Puertas, C., Matthes, K., Brauer, A., Muscheler, R., Hansen, F., Petrick, C., Aldahan, A., Possnert, G., & van Geel, B. (2012). Regional atmospheric circulation shifts induced by a grand solar minimum. Nature Geosci, 5, 397-401

Martín-Puertas, C., Valero-Garcés, B. L., Brauer, A., Mata, M. P., Delgado-Huertas, A., & Dulski, P. (2009). The Iberian–Roman Humid Period (2600–1600 cal yr BP) in the Zoñar Lake varve record (Andalucía, southern Spain). Quaternary Research, 71, 108-120

Martín-Puertas, C., Valero-Garcés, B. L., Mata, M. P., Moreno, A., Giralt, S., Martínez-Ruiz, F., & Jiménez-Espejo, F. (2011). Geochemical processes in a Mediterranean Lake: a high-resolution study of the last 4,000 years in Zoñar Lake, southern Spain. Journal of Paleolimnology, 46, 405-421

Masi, A., Sadori, L., Zanchetta, G., Baneschi, I., & Giardini, M. (2013). Climatic interpretation of carbon isotope content of mid-Holocene archaeological charcoals from eastern Anatolia. Quaternary International, 303, 64-72

Mayewski, P. A., Rohling, E. E., Curt Stager, J., Karlén, W., Maasch, K. A., David Meeker, L., Meyerson, E. A., Gasse, F., van Kreveld, S., Holmgren, K., Lee-Thorp, J., Rosqvist, G., Rack, F., Staubwasser, M., Schneider, R. R., & Steig, E. J. (2004). Holocene climate variability. Quaternary Research, 62, 243-255

Mays, L., Antoniou, G. P., & Angelakis, A. N. (2013). History of water cisterns: legacies and lessons. Water, 5, 1916-1940

McAndrews, J. H. & Turton, C. L. (2007). Canada geese dispersed cultigen pollen grains from prehistoric iroquoian fields to Crawford lake, Ontario, Canada. Palynology, 31, 9-18

McCloskey, T. A., & Liu, K.-b. (2012). A 7000 year record of paleohurricane activity from a coastal wetland in Belize. The Holocene, 23, 278-291

McCormick, M., Büntgen, U., Cane, M. A., Cook, E. R., Harper, K., Huybers, P., Litt, T., Manning, S. W., Mayewski, P. A., More, A. F. M., Nicolussi, K., & Tegel, W. (2012). Climate Change during and after the Roman Empire: Reconstructing the Past from Scientific and Historical Evidence. The Journal of Interdisciplinary History, 43, 169-220

McCormick, M., Büntgen, U., Cane, M. A., Cook, E. R., Harper, K., Huybers, P., Litt, T., Manning, S. W., Mayewski, P. A., More, A. F. M., Nicolussi, K., & Tegel, W. (2012). Climate Change during and after the Roman Empire: Reconstructing the Past from Scientific and Historical Evidence. The Journal of Interdisciplinary History, 43, 169-220

McCorriston, J., & Hole, F. (1991). The Ecology of Seasonal Stress and the Origins of Agriculture in the Near East. American Anthropologist, 93, 46-69

McDermott, F., Mattey, D. P., & Hawkesworth, C. (2001). Centennial-Scale Holocene Climate Variability Revealed by a High-Resolution Speleothem δ18O Record from SW Ireland. Science, 294, 1328-1331

McGee, D., Donohoe, A., Marshall, J., & Ferreira, D. (2014). Changes in ITCZ location and cross-equatorial heat transport at the Last Glacial Maximum, Heinrich Stadial 1, and the mid-Holocene. Earth and Planetary Science Letters, 390, 69-79

McGee, D., Quade, J., Edwards, R. L., Broecker, W. S., Cheng, H., Reiners, P. W., & Evenson, N. (2012). Lacustrine cave carbonates: Novel archives of paleohydrologic change in the Bonneville Basin (Utah, USA). Earth and Planetary Science Letters, 351, 182-194

McGowan, S., Juhler, R. K., & Anderson, N. J. (2008). Autotrophic response to lake age, conductivity and temperature in two West Greenland lakes. Journal of Paleolimnology, 39, 301-317

McGowan, S., Barker, P., Haworth, E. Y., Leavitt, P. R., Maberly, S. C. & Pates, J. (2012), Humans and climate as drivers of algal community change in Windermere since 1850. Freshwater Biology, 57, 260-277McLaren, S. J., Gilbertson, D. D., Grattan, J. P., Hunt, C. O., Duller, G. A. T., & Barker, G. A. (2004). Quaternary palaeogeomorphologic evolution of the Wadi Faynan area, southern Jordan. Palaeogeography, Palaeoclimatology, Palaeoecology, 205, 131-154

Medina-Elizalde, M., Burns, S. J., Lea, D. W., Asmerom, Y., von Gunten, L., Polyak, V., Vuille, M., & Karmalkar, A. (2010). High resolution stalagmite climate record from the Yucatán Peninsula spanning the Maya terminal classic period. Earth and Planetary Science Letters, 298, 255-262.

Medina-Elizalde, M., Burns, S. J., Polanco-Martínez, J. M., Beach, T., Lases-Hernández, F., Shen, C.-C., & Wang, H.-C. (2016). High-resolution speleothem record of precipitation from the Yucatan Peninsula spanning the Maya Preclassic Period. Global and Planetary Change, 138, 93-102

Medina-Elizalde, M., & Rohling, E. J. (2012). Collapse of Classic Maya Civilization Related to Modest Reduction in Precipitation. Science, 335, 956-959

Meister, P., Reyes, C., Beaumont, W., Rincon, M., Collins, L., Berelson, W., Stott, L., Corsetti, F., & Nealson, K. H. (2011). Calcium and magnesium-limited dolomite precipitation at Deep Springs Lake, California. Sedimentology, 58, 1810-1830

Mendoza, B., García-Acosta, V., Velasco, V., Jáuregui, E., & Díaz-Sandoval, R. (2007). Frequency and duration of historical droughts from the 16th to the 19th centuries in the Mexican Maya lands, Yucatan Peninsula. Climatic Change, 83, 151-168

Mercuri, A. M., Sadori, L., & Uzquiano Ollero, P. (2011). Mediterranean and north-African cultural adaptations to mid-Holocene environmental and climatic changes. The Holocene, 21, 189-206

Merkt, J. v. (1971). Zuverlässige Auszählungen von Jahresschichten in Seesedimenten mit Hilfe von Gross-Dünnschliffen. Archiv für Hydrobiologie, 69(2), 145-154.

Metcalfe, S., Breen, A., Murray, M., Furley, P., Fallick, A., & McKenzie, A. (2009). Environmental change in northern Belize since the latest Pleistocene. Journal of Quaternary Science, 24, 627-641

Metcalfe, S., & Davies, S. (2007). Deciphering recent climate change in central Mexican lake records. Climatic Change, 83, 169-186

Metcalfe, S. E. (1987). Historical Data and Climatic Change in Mexico: A Review. The Geographical Journal, 153, 211-222

Metcalfe, S. E., Barron, J. A., & Davies, S. J. (2015). The Holocene history of the North American Monsoon: 'known knowns' and 'known unknowns' in understanding its spatial and temporal complexity. Quaternary Science Reviews, 120, 1-27

Metcalfe, S. E., Jones, M. D., Davies, S. J., Noren, A., & MacKenzie, A. (2010). Climate variability over the last two millennia in the North American monsoon region, recorded in laminated lake sediments from Laguna de Juanacatlán, Mexico. The Holocene. doi: 10.1177/0959683610371994

Metcalfe, S. E., O'Hara, S. L., Caballero, M., & Davies, S. J. (2000). Records of Late Pleistocene–Holocene climatic change in Mexico — a review. Quaternary Science Reviews, 19, 699-721

Meyers, P. A., & Ishiwatari, R. (1993). Lacustrine organic geochemistry—an overview of indicators of organic matter sources and diagenesis in lake sediments. Organic geochemistry, 20, 867-900

Mezquita, F., Tapia, G., & Roca, J. R. (1999). Ostracoda from springs on the eastern Iberian Peninsula: ecology, biogeography and palaeolimnological implications. Palaeogeography, Palaeoclimatology, Palaeoecology, 148, 65-85

Migowski, C., Agnon, A., Bookman, R., Negendank, J. F. W., & Stein, M. (2004). Recurrence pattern of Holocene earthquakes along the Dead Sea transform revealed by varve-counting and radiocarbon dating of lacustrine sediments. Earth and Planetary Science Letters, 222, 301-314

Migowski, C., Stein, M., Prasad, S., Negendank, J. F. W., & Agnon, A. (2006). Holocene climate variability and cultural evolution in the Near East from the Dead Sea sedimentary record. Quaternary Research, 66, 421-431

Miller, D. R., Castañeda, I. S., Bradley, R. S., & MacDonald, D. (2017). Local and regional wildfire activity in central Maine (USA) during the past 900 years. Journal of Paleolimnology, 58, 455-466

Miller, G. H., Geirsdóttir, Á., Zhong, Y., Larsen, D. J., Otto-Bliesner, B. L., Holland, M. M., Bailey, D. A., Refsnider, K. A., Lehman, S. J., Southon, J. R., Anderson, C., Björnsson, H., & Thordarson, T. (2012). Abrupt onset of the Little Ice Age triggered by volcanism and sustained by sea-ice/ocean feedbacks. Geophysical Research Letters, 39. doi: 10.1029/2011GL050168

Millet, L., Arnaud, F., Heiri, O., Magny, M., Verneaux, V., & Desmet, M. (2009). Late-Holocene summer temperature reconstruction from chironomid assemblages of Lake Anterne, northern French Alps. The Holocene, 19, 317-328

Milne, G. A., & Peros, M. (2013). Data–model comparison of Holocene sea-level change in the circum-Caribbean region. Global and Planetary Change, 107, 119-131

Moberg, A., Sonechkin, D. M., Holmgren, K., Datsenko, N. M., & Karlen, W. (2005). Highly variable Northern Hemisphere temperatures reconstructed from low- and high-resolution proxy data. Nature, 433, 613-617

Morelli, G., Song, Y., Mazzoni, C. J., Eppinger, M., Roumagnac, P., Wagner, D. M., Feldkamp, M., Kusecek, B., Vogler, A. J., Li, Y., Cui, Y., Thomson, N. R., Jombart, T., Leblois, R., Lichtner, P., Rahalison, L., Petersen, J. M., Balloux, F., Keim, P., Wirth, T., Ravel, J., Yang, R., Carniel, E., & Achtman, M. (2010). Yersinia pestis genome sequencing identifies patterns of global phylogenetic diversity. Nature Genetics, 42, 1140-1142

Moreno, A., Valero-Garcés, B. L., González-Sampériz, P., & Rico, M. (2008). Flood response to rainfall variability during the last 2000 years inferred from the Taravilla Lake record (Central Iberian Range, Spain). Journal of Paleolimnology, 40, 943-961

Morse, J. W., Arvidson, R. S., & Lüttge, A. (2007). Calcium carbonate formation and dissolution. Chemical reviews, 107, 342-381

Moseley, G. E., Richards, D. A., Smart, P. L., Standish, C. D., Hoffmann, D. L., ten Hove, H., & Vinn, O. (2015). Early–middle Holocene relative sea-level oscillation events recorded in a submerged speleothem from the Yucatán Peninsula, Mexico. The Holocene, 25, 1511-1521

Moy, C. M., Seltzer, G. O., Rodbell, D. T., & Anderson, D. M. (2002). Variability of El Niño/Southern Oscillation activity at millennial timescales during the Holocene epoch. Nature, 420, 162-165

Mudroch, A., & MacKnight, S. D. (1994). Handbook of techniques for aquatic sediments sampling. Boca Raton.

Mueller, A. D., Islebe, G. A., Hillesheim, M. B., Grzesik, D. A., Anselmetti, F. S., Ariztegui, D., Brenner, M., Curtis, J. H., Hodell, D. A., & Venz, K. A. (2009). Climate drying and associated forest decline in the lowlands of northern Guatemala during the late Holocene. Quaternary Research, 71, 133-141

Müller, G., Irion, G., & Förstner, U. (1972). Formation and diagenesis of inorganic Ca− Mg carbonates in the lacustrine environment. Naturwissenschaften, 59, 158-164

Muñoz, A., Ojeda, J., & Sánchez-Valverde, B. (2002). Sunspot-like and ENSO/NAO-like periodicities in lacustrinelaminated sediments of the Pliocene Villarroya Basin (La Rioja,Spain). Journal of Paleolimnology, 27, 453-463

Muñoz, P., Gorin, G., Parra, N., Velásquez, C., Lemus, D., Monsalve-M, C., & Jojoa, M. (2017). Holocene climatic variations in the Western Cordillera of Colombia: A multiproxy high-resolution record unravels the dual influence of ENSO and ITCZ. Quaternary Science Reviews, 155, 159-178

Munoz-Reinoso, J. C. (2003). Juniperus oxycedrus ssp macrocarpa in SW Spain: Ecology and conservation problems. Journal of Coastal Conservation, 9, 113-122

N., T. M., & A., J. S. (2001). Forcing of the Mediterranean Sea by atmospheric oscillations over the North Atlantic. Geophysical Research Letters, 28, 803-806

Nancollas, G. H., & Reddy, M. M. (1971). The crystallization of calcium carbonate. II. Calcite growth mechanism. Journal of Colloid and Interface Science, 37, 824-830

Negendank, J. F., Zolitschka, B., Rein, B., Brauer, A., Brüchmann, C., Sanchez, A., & Vos, H. (1999). Varves and solar variability (Lake Holzmaar, Eifel, Germany). Bulletin de la Société belge de Géologie, 106, 53-61

Nelson, D. R., Adger, W. N., & Brown, K. (2007). Adaptation to Environmental Change: Contributions of a Resilience Framework. Annual Review of Environment and Resources, 32, 395-419

Neugebauer, I., Brauer, A., Schwab, M. J., Dulski, P., Frank, U., Hadzhiivanova, E., Kitagawa, H., Litt, T., Schiebel, V., Taha, N., Waldmann, N. D., & Dsddp Scientific Party (2015). Evidences for centennial dry periods at ~3300 and ~2800 cal. yr BP from micro-facies analyses of the Dead Sea sediments. The Holocene, 25, 1358-1371

Neugebauer, I., Brauer, A., Dräger, N., Dulski, P., Wulf, S., Plessen, B., Mingram, J., Herzschuh, U., & Brande, A. (2012). A Younger Dryas varve chronology from the Rehwiese palaeolake record in NE-Germany. Quaternary Science Reviews, 36, 91-102

Neumann, F. H., Kagan, E. J., Schwab, M. J., & Stein, M. (2007). Palynology, sedimentology and palaeoecology of the late Holocene Dead Sea. Quaternary Science Reviews, 26, 1476-1498

Nguetsop, V. F., Servant-Vildary, S., & Servant, M. (2004). Late Holocene climatic changes in west Africa, a high resolution diatom record from equatorial Cameroon. Quaternary Science Reviews, 23, 591-609

Nipkow, F. (1920). VorläuFige Mitteilungen über Untersuchungen des Schlammabsatzes im Zürichsee. Zeitschrift für Hydrologie, 1, 100-122

Nooren, K. H., W. Z.; van der Plicht, H.; Sigl, M.; van Bergen, M. J.; Torrescano-Valle, D. G. N.; Islebe, G.; Huizinga, A.; Winkels, T.; Middelkoop, H. (2017). Explosive eruption of El Chichón volcano (Mexico) disrupted 6th century Maya civilization and contributed to global cooling. Geology, 45, 175-178

Nyberg, J., Kuijpers, A., Malmgren, B. A., & Kunzendorf, H. (2001). Late Holocene Changes in Precipitation and Hydrography Recorded in Marine Sediments from the Northeastern Caribbean Sea. Quaternary Research, 56, 87-102

Nyberg, J., Malmgren, B. A., Kuijpers, A., & Winter, A. (2002). A centennial-scale variability of tropical North Atlantic surface hydrography during the late Holocene. Palaeogeography, Palaeoclimatology, Palaeoecology, 183, 25-41

O'Mansky, M., & Dunning, N. P. (2004). Settlement and Late Classic political disintegration in the Petexbatun region, Guatemala. The Terminal Classic in the Maya lowlands: collapse, transition, and transformation, 83-101.

Ocakoğlu, F., Kır, O., Yılmaz, İ. Ö., Açıkalın, S., Erayık, C., Tunoğlu, C., & Leroy, S. A. G. (2013). Early to Mid-Holocene Lake level and temperature records from the terraces of Lake Sünnet in NW Turkey. Palaeogeography, Palaeoclimatology, Palaeoecology, 369, 175-184

Ohlendorf, C., & Sturm, M. (2001). Precipitation and Dissolution of Calcite in a Swiss High Alpine Lake. Arctic, Antarctic, and Alpine Research, 33, 410-417

Ojala, A. E., Bigler, C., & Weckström, J. (2014). understanding varve formation processes from sediment trapping and limnological monitoring. Past Global Changes, 22, 8-9

Ojala, A. E., Saarinen, T., & Salonen, V.-P. (2000). Preconditions for the formation of annually laminated lake sediments in southern and central Finland. Boreal Environment Research, 5, 243-255

Ojala, A. E. K., Francus, P., Zolitschka, B., Besonen, M., & Lamoureux, S. F. (2012). Characteristics of sedimentary varve chronologies – A review. Quaternary Science Reviews, 43, 45-60

Ólafsdóttir, K. B., Geirsdóttir, Á., Miller, G. H., & Larsen, D. J. (2013). Evolution of NAO and AMO strength and cyclicity derived from a 3-ka varve-thickness record from Iceland. Quaternary Science Reviews, 69, 142-154

Oldfield, F., & Appleby, P. (1984). Empirical testing of 210 Pb-dating models for lake sediments Lake sediments and environmental history. Leicester University Press

Orland, I. J., Bar-Matthews, M., Ayalon, A., Matthews, A., Kozdon, R., Ushikubo, T., & Valley, J. W. (2012). Seasonal resolution of Eastern Mediterranean climate change since 34ka from a Soreq Cave speleothem. Geochimica et Cosmochimica Acta, 89, 240-255

Orland, I. J., Bar-Matthews, M., Kita, N. T., Ayalon, A., Matthews, A., & Valley, J. W. (2009). Climate deterioration in the Eastern Mediterranean as revealed by ion microprobe analysis of a speleothem that grew from 2.2 to 0.9 ka in Soreq Cave, Israel. Quaternary Research, 71, 27-35

Pachauri, R. K., Allen, M., Barros, V., Broome, J., Cramer, W., Christ, R., Church, J., Clarke, L., Dahe, Q., & Dasgupta, P. (2014). Climate Change 2014: Synthesis Report. Contribution of Working Groups I, II and III to the Fifth Assessment Report of the Intergovernmental Panel on Climate Change.

Panagiotopoulos, K., Aufgebauer, A., Schäbitz, F., & Wagner, B. (2013). Vegetation and climate history of the Lake Prespa region since the Lateglacial. Quaternary International, 293, 157-169

Parker, A. G., Goudie, A. S., Stokes, S., White, K., Hodson, M. J., Manning, M., & Kennet, D. (2006). A record of Holocene climate change from lake geochemical analyses in southeastern Arabia. Quaternary Research, 66, 465-476

Parmenter, R. R., Yadav, E. P., Parmenter, C. A., Ettestad, P., & Gage, K. L. (1999). Incidence of plague associated with increased winter-spring precipitation in New Mexico. The American Journal of Tropical Medicine and Hygiene, 61, 814-821

Passier, H. F., Middelburg, J. J., de Lange, G. J., & Böttcher, M. E. (1999). Modes of sapropel formation in the eastern Mediterranean: some constraints based on pyrite properties. Marine Geology, 153, 199-219

Patterson, W. A., Edwards, K. J., & Maguire, D. J. (1987). Microscopic charcoal as a fossil indicator of fire. Quaternary Science Reviews, 6, 3-23

Pausas, J. G., & Fernandez-Munoz, S. (2012). Fire regime changes in the Western Mediterranean Basin: from fuel-limited to drought-driven fire regime. Climatic Change, 110, 215-226

Pavia, E. G., Graef, F., & Reyes, J. (2006). PDO–ENSO Effects in the Climate of Mexico. Journal of Climate, 19, 6433-6438

Peings, Y., & Magnusdottir, G. (2014). Forcing of the wintertime atmospheric circulation by the multidecadal fluctuations of the North Atlantic Ocean. Environmental Research Letters, 9, 034018

Pennington, W. (1974). Seston and Sediment Formation in Five Lake District Lakes. Journal of Ecology, 62, 215-251

Pérez, L., Bugja, R., Lorenschat, J., Brenner, M., Curtis, J., Hoelzmann, P., Islebe, G., Scharf, B., & Schwalb, A. (2011). Aquatic ecosystems of the Yucatán Peninsula (Mexico), Belize, and Guatemala. Hydrobiologia, 661, 407-433

Perry, E., Paytan, A., Pedersen, B., & Velazquez-Oliman, G. (2009). Groundwater geochemistry of the Yucatan Peninsula, Mexico: Constraints on stratigraphy and hydrogeology. Journal of Hydrology, 367, 27-40

Perry, E., Velazquez-Oliman, G., & Marin, L. (2002). The Hydrogeochemistry of the Karst Aquifer System of the Northern Yucatan Peninsula, Mexico. International Geology Review, 44, 191-221

Peterson, L., & Haug, G. (2005). Climate and the Collapse of Maya Civilization A series of multi-year droughts helped to doom an ancient culture. American Scientist, 93, 322-329

Petterson, G., Renberg, I., Geladi, P., Lindberg, A., & Lindgren, F. (1993). Spatial uniformity of sediment accumulation in varved lake sediments in northern Sweden. Journal of Paleolimnology, 9, 195-208

Peyron, O., Goring, S., Dormoy, I., Kotthoff, U., Pross, J., de Beaulieu, J.-L., Drescher-Schneider, R., Vannière, B., & Magny, M. (2011). Holocene seasonality changes in the central Mediterranean region reconstructed from the pollen sequences of Lake Accesa (Italy) and Tenaghi Philippon (Greece). The Holocene, 21, 131-146

Philander, G. (1989). El Nino and La Nina. American Scientist, 77, 451-459

Platt Bradbury, J. (1988). A climatic-limnologic model of diatom succession for paleolimnological interpretation of varved sediments at Elk Lake, Minnesota. Journal of Paleolimnology, 1, 115-131

Polyak, L., Bischof, J., Ortiz, J. D., Darby, D. A., Channell, J. E., Xuan, C., Kaufman, D. S., Løvlie, R., Schneider, D. A., & Eberl, D. D. (2009). Late Quaternary stratigraphy and sedimentation patterns in the western Arctic Ocean. Global and Planetary Change, 68, 5-17

Poore, R., DeLong, K., Richey, J., & Quinn, T. (2009). Evidence of multidecadal climate variability and the Atlantic Multidecadal Oscillation from a Gulf of Mexico sea-surface temperature-proxy record. Geo-Marine Letters, 29, 477-484

Prasad, S., Brauer, A., Rein, B., & Negendank, J. F. W. (2006). Rapid climate change during the early Holocene in western Europe and Greenland. The Holocene, 16, 153-158

Prasad, S., Witt, A., Kienel, U., Dulski, P., Bauer, E., & Yancheva, G. (2009). The 8.2 ka event: Evidence for seasonal differences and the rate of climate change in Western Europe. Global and Planetary Change, 67(3), 218-226. doi: https://doi.org/10.1016/j.gloplacha.2009.03.011

Prasad, S. V., H.; Negendank, J. F. W.; Waldmann, N.; Goldstein, S. L.; Stein, M. (2004). Evidence from Lake Lisan of solar influence on decadal- to centennial-scale climate variability during marine oxygen isotope stage 2. Geology, 32, 581-584

Press, W. H., Teukolsky, S. A., Vetterling, W. T., & Flannery, B. P. (1992). Numerical recipes in C++. The art of scientific computing. Cambridge University Press

Previtali, M. A., Lima, M., Meserve, P. L., Kelt, D. A., & Gutiérrez, J. R. (2009). Population dynamics of two sympatric rodents in a variable environment: rainfall, resource availability, and predation. Ecology, 90, 1996-2006

Price, T. D., Burton, J. H., Sharer, R. J., Buikstra, J. E., Wright, L. E., Traxler, L. P., & Miller, K. A. (2010). Kings and commoners at Copan: Isotopic evidence for origins and movement in the Classic Maya period. Journal of Anthropological Archaeology, 29, 15-32

Pross, J., Kotthoff, U., Müller, U. C., Peyron, O., Dormoy, I., Schmiedl, G., Kalaitzidis, S., & Smith, A. M. (2009). Massive perturbation in terrestrial ecosystems of the Eastern Mediterranean region associated with the 8.2 kyr B.P. climatic event. Geology, 37, 887-890

Raicich, F., Pinardi, N., & Navarra, A. (2003). Teleconnections between Indian monsoon and Sahel rainfall and the Mediterranean. International Journal of Climatology, 23, 173-186

Ramrath, A., Nowaczyk, N. R., & Negendank, J. F. w. (1999). Sedimentological evidence for environmental changes since 34,000 years BP from Lago di Mezzano, central Italy. Journal of Paleolimnology, 21, 423-435

Ranere, A. J., Piperno, D. R., Holst, I., Dickau, R., & Iriarte, J. (2009). The cultural and chronological context of early Holocene maize and squash domestication in the Central Balsas River Valley, Mexico. Proceedings of the National Academy of Sciences, 106, 5014-5018

Rasmussen, S. O., Andersen, K. K., Svensson, A. M., Steffensen, J. P., Vinther, B. M., Clausen, H. B., Siggaard-Andersen, M. L., Johnsen, S. J., Larsen, L. B., Dahl-Jensen, D., Bigler, M., Röthlisberger, R., Fischer, H., Goto-Azuma, K., Hansson, M. E., & Ruth, U. (2006). A new Greenland ice core chronology for the last glacial termination. Journal of Geophysical Research: Atmospheres, 111. doi: 10.1029/2005JD006079

Rauscher, S., Giorgi, F., Diffenbaugh, N., & Seth, A. (2008). Extension and Intensification of the Meso-American mid-summer drought in the twenty-first century. Climate Dynamics, 31, 551-571

Reddaway, J. M., & Bigg, G. R. (1996). Climatic change over the Mediterranean and links to the more general atmospheric circulation. International Journal of Climatology, 16, 651-661

Redman, C. L. (2005). Resilience Theory in Archaeology. American Anthropologist, 107, 70-77

Renssen, H., Goosse, H., & Fichefet, T. (2002). Modeling the effect of freshwater pulses on the early Holocene climate: The influence of high-frequency climate variability. Paleoceanography, 17, 10-16

Richerson, P. J., Boyd, R., & Bettinger, R. L. (2001). Was agriculture impossible during the Pleistocene but mandatory during the Holocene? A climate change hypothesis. American Antiquity, 66, 387-411

Richey, J. N., Poore, R. Z., Flower, B. P., & Quinn, T. M. (2007). 1400 yr multiproxy record of climate variability from the northern Gulf of Mexico. Geology, 35, 423-426

Ridge, J. C., Balco, G., Bayless, R. L., Beck, C. C., Carter, L. B., Dean, J. L., Voytek, E. B., & Wei, J. H. (2012). The new North American Varve Chronology: A precise record of southeastern Laurentide Ice Sheet deglaciation and climate, 18.2-12.5 kyr BP, and correlations with Greenland ice core records. American Journal of Science, 312, 685-722.

Ridley, H. E., Asmerom, Y., Baldini, J. U. L., Breitenbach, S. F. M., Aquino, V. V., Prufer, K. M., Culleton, B. J., Polyak, V., Lechleitner, F. A., Kennett, D. J., Zhang, M., Marwan, N., Macpherson, C. G., Baldini, L. M., Xiao, T., Peterkin, J. L., Awe, J., & Haug, G. H. (2015). Aerosol forcing of the position of the intertropical convergence zone since ad 1550. Nature Geoscience, 8, 195-197

Ries, J. B. (2005). Aragonite production in calcite seas: effect of seawater Mg/Ca ratio on the calcification and growth of the calcareous alga Penicillus capitatus. Paleobiology, 31, 445-458

Ries, J. B. (2006). Mg fractionation in crustose coralline algae: Geochemical, biological, and sedimentological implications of secular variation in the Mg/Ca ratio of seawater. Geochimica et Cosmochimica Acta, 70, 891-900

Ringberg, B., BjÖRck, J., & Hang, T. (2003). Correlation of stadial and interstadial events in the south Swedish glacial varves with the GRIP oxygen isotope record. Boreas, 32, 427-435

Roberts, N. (2002). Did prehistoric landscape management retard the post-glacial spread of woodland in Southwest Asia? Antiquity, 76(294), 1002-1010

Roberts, N. & Rosen. A. (2009). Diversity and Complexity in Early Farming Communities of Southwest Asia: New Insights into the Economic and Environmental Basis of Neolithic Çatalhöyük. Current Anthropology, 50, 393-402

Roberts, N., & Wright, H. E., Jr. (1993). Vegetational, lake-level, and climatic history of the near east and southwest Asia: University of Minnesota Press

Roberts, N., Reed, J. M., Leng, M. J., Kuzucuoğlu, C., Fontugne, M., Bertaux, J., Woldring, H., Bottema, S., Black, S., Hunt, E., & Karabiyikoğlu, M. (2001). The tempo of Holocene climatic change in the eastern Mediterranean region: new high-resolution crater-lake sediment data from central Turkey. The Holocene, 11, 721-736

Roberts, N., Jones, M. D., Benkaddour, A., Eastwood, W. J., Filippi, M. L., Frogley, M. R., Lamb, H. F., Leng, M. J., Reed, J. M., Stein, M., Stevens, L., Valero-Garcés, B., & Zanchetta, G. (2008). Stable isotope records of Late Quaternary climate and hydrology from Mediterranean lakes: the ISOMED synthesis. Quaternary Science Reviews, 27, 2426-2441

Roberts, N., Brayshaw, D., Kuzucuoğlu, C., Perez, R., & Sadori, L. (2011). The mid-Holocene climatic transition in the Mediterranean: Causes and consequences. The Holocene, 21, 3-13

Roberts, N., Allcock, S. L., Arnaud, F., Dean, J. R., Eastwood, W. J., Jones, M. D., Leng, M. J., Metcalfe, S. E., Malet, E., Woodbridge, J., & Yiğitbaşıoğlu, H. (2016). A tale of two lakes: a multi-proxy comparison of Lateglacial and Holocene environmental change in Cappadocia, Turkey. Journal of Quaternary Science, 31, 348-362

Robinson, S. A., Black, S., Sellwood, B. W., & Valdes, P. J. (2006). A review of palaeoclimates and palaeoenvironments in the Levant and Eastern Mediterranean from 25,000 to 5000 years BP: setting the environmental background for the evolution of human civilisation. Quaternary Science Reviews, 25, 1517-1541

Rodwell, M. J., & Hoskins, B. J. (1996). Monsoons and the dynamics of deserts. Quarterly Journal of the Royal Meteorological Society, 122, 1385-1404

Roether, W., Manca, B. B., Klein, B., Bregant, D., Georgopoulos, D., Beitzel, V., Kovačević, V., & Luchetta, A. (1996). Recent Changes in Eastern Mediterranean Deep Waters. Science, 271(5247), 333-335

Rohling, E. J. (1994). Review and new aspects concerning the formation of eastern Mediterranean sapropels. Marine Geology, 122, 1-28

Rohling, E. J., Hayes, A., Mayewski, P. A., & Kucera, M. (2009). Holocene climate variability in the eastern Mediterranean, and the End of the Bronze Age. In: Bachhuber, C. and Roberts, R.G. (eds.) Forces of Transformation: The end of the Bronze Age in the Mediterranean, Banea Publication Series, 1, 2-5

Rohling, E. J., Marino, G., & Grant, K. M. (2015). Mediterranean climate and oceanography, and the periodic development of anoxic events (sapropels). Earth-Science Reviews, 143, 62-97

Romanenko, V. (1961). Computation of the autumn soil moisture using a universal relationship for a large area. Proc. of Ukrainian Hydrometeorological Research Institute, 3, 12-25

Romero-Centeno, R., Zavala-Hidalgo, J., Gallegos, A., & O'Brien, J. J. (2003). Isthmus of Tehuantepec wind climatology and ENSO signal. Journal of Climate, 16, 2628-2639

Romero-Centeno, R., Zavala-Hidalgo, J., & Raga, G. B. (2007). Midsummer Gap Winds and Low-Level Circulation over the Eastern Tropical Pacific. Journal of Climate, 20, 3768-3784

Romero-Viana, L., Julià, R., Camacho, A., Vicente, E., & Miracle, M. R. (2008). Climate signal in varve thickness: Lake La Cruz (Spain), a case study. Journal of Paleolimnology, 40, 703-714

Roop, H. A., Levy, R., Dunbar, G. B., Vandergoes, M. J., Howarth, J., Fitzsimons, S., Moon, H. S., Zammit, C., Ditchburn, R., Baisden, T., & Yoon, H. I. (2016). A hydroclimate-proxy model based on sedimentary facies in an annually laminated sequence from Lake Ohau, South Island, New Zealand. Journal of Paleolimnology, 55, 1-16

Rosen, M. R., Miser, D. E., & Warren, J. K. (1988). Sedimentology, mineralogy and isotopic analysis of Pellet Lake, Coorong region, South Australia. Sedimentology, 35, 105-122

Rosen, A. M. (2007). Civilizing climate: social responses to climate change in the ancient Near East. Altamira Press

Rosenmeier, M. F., Hodell, D. A., Brenner, M., Curtis, J. H., & Guilderson, T. P. (2002). A 4000-Year Lacustrine Record of Environmental Change in the Southern Maya Lowlands, Petén, Guatemala. Quaternary Research, 57, 183-190

Rosqvist, G. C., Leng, M. J., & Jonsson, C. (2007). North Atlantic region atmospheric circulation dynamics inferred from a late-Holocene lacustrine carbonate isotope record, northern Swedish Lapland. The Holocene, 17, 867-873

Rossi, A., Massei, N., & Laignel, B. (2011). A synthesis of the time-scale variability of commonly used climate indices using continuous wavelet transform. Global and Planetary Change, 78, 1-13

Rossignol-Strick, M. (1999). The Holocene climatic optimum and pollen records of sapropel 1 in the eastern Mediterranean, 9000–6000 yrs BP. Quaternary Science Reviews, 18, 515-530

Rossignol-Strick, M., Nesteroff, W., Olive, P., & Vergnaud-Grazzini, C. (1982). After the deluge: Mediterranean stagnation and sapropel formation. Nature, 295, 105-108

Rowe, P. J., Mason, J. E., Andrews, J. E., Marca, A. D., Thomas, L., van Calsteren, P., Jex, C. N., Vonhof, H. B., & Al-Omari, S. (2012). Speleothem isotopic evidence of winter rainfall variability in northeast Turkey between 77 and 6 ka. Quaternary Science Reviews, 45, 60-72

Saarni, S., Muschitiello, F., Weege, S., Brauer, A., & Saarinen, T. (2016). A late Holocene record of solar-forced atmospheric blocking variability over Northern Europe inferred from varved lake sediments of Lake Kuninkaisenlampi. Quaternary Science Reviews, 154, 100-110

Sabins, J. F. F. (1962). Grains of detrital, secondary, and primary dolomite from Cretaceous strata of the Western Interior. Geological Society of America Bulletin, 73, 1183-1196

Salas, M. A., Cerda, M. E. H., Cruz, J. V., Romero, E. A., & Barrié, C. T. L. (2014). The influence of strong El Niño phases on the rainfall over the Yucatan Peninsula, Mexico. Analele stiintifice ale Universitatii" Alexandru Ioan Cuza" din Iasi-seria Geografie, 60, 15-28

Sandweiss, D. H., & Ill, J. B. R. (1996). GeoarchaeologiCal Evidence from Peru for a 5000 Years BP Onset of El Niño. Science, 273, 1531-1533

Sandweiss, D. H., & Quilter, J. (2008). El Niño, catastrophism, and culture change in ancient America: Dumbarton Oaks Pub Service.

Santisteban, J. I., Mediavilla, R., López-Pamo, E., Dabrio, C. J., Zapata, M. B. R., García, M. J. G., Castaño, S., & Martínez-Alfaro, P. E. (2004). Loss on ignition: a qualitative or quantitative method for organic matter and carbonate mineral content in sediments? Journal of Paleolimnology, 32, 287-299

Sauerbrey, M., Juschus, O., Gebhardt, A., Wennrich, V., Nowaczyk, N., & Melles, M. (2013). Mass movement deposits in the 3.6 Ma sediment record of Lake El'gygytgyn, Far East Russian Arctic. Climate of the Past, 9, 1949-1967

Scarborough, V. L., Dunning, N. P., Tankersley, K. B., Carr, C., Weaver, E., Grazioso, L., Lane, B., Jones, J. G., Buttles, P., Valdez, F., & Lentz, D. L. (2012). Water and sustainable land use at the ancient tropical city of Tikal, Guatemala. Proceedings of the National Academy of Sciences, 109, 12408-12413

Scarborough, V. L., Dunning, N. P., Tankersley, K. B., Carr, C., Weaver, E., Grazioso, L., Lane, B., Jones, J. G., Buttles, P., Valdez, F., & Lentz, D. L. (2012). Water and sustainable land use at the ancient tropical city of Tikal, Guatemala. Proceedings of the National Academy of Sciences of the United States of America, 109, 12408-12413

Schilman, B., Ayalon, A., Bar-Matthews, M., Kagan, E. J., & Almogi-Labin, A. (2002). Sea-land paleoclimate correlation in the Eastern Mediterranean region during the late Holocene. Israel Journal of Earth Sciences, 51, 181-190

Schilman, B., Bar-Matthews, M., Almogi-Labin, A., & Luz, B. (2001). Global climate instability reflected by Eastern Mediterranean marine records during the late Holocene. Palaeogeography, Palaeoclimatology, Palaeoecology, 176, 157-176

Schimmelmann, A., Lange, C. B., Schieber, J., Francus, P., Ojala, A. E. K., & Zolitschka, B. (2016). Varves in marine sediments: A review. Earth-Science Reviews, 159, 215-246

Schlolaut, G., Marshall, M. H., Brauer, A., Nakagawa, T., Lamb, H. F., Staff, R. A., Bronk Ramsey, C., Bryant, C. L., Brock, F., Kossler, A., Tarasov, P. E., Yokoyama, Y., Tada, R., & Haraguchi, T. (2012). An automated method for varve interpolation and its application to the Late Glacial chronology from Lake Suigetsu, Japan. Quaternary Geochronology, 13, 52-69

Schlolaut, G., Brauer, A., Marshall, M. H., Nakagawa, T., Staff, R. A., Ramsey, C. B., Lamb, H. F., Bryant, C. L., Naumann, R., & Dulski, P. (2014). Event layers in the Japanese Lake Suigetsu 'SG06'sediment core: description, interpretation and climatic implications. Quaternary Science Reviews, 83, 157-170

Schmid, B. V., Büntgen, U., Easterday, W. R., Ginzler, C., Walløe, L., Bramanti, B., & Stenseth, N. C. (2015). Climate-driven introduction of the Black Death and successive plague reintroductions into Europe. Proceedings of the National Academy of Sciences, 112, 3020-3025

Schmitter-Soto, J., Comín, F., Escobar-Briones, E., Herrera-Silveira, J., Alcocer, J., Suárez-Morales, E., Elías-Gutiérrez, M., Díaz-Arce, V., Marín, L., & Steinich, B. (2002). Hydrogeochemical and biological characteristics of cenotes in the Yucatan Peninsula (SE Mexico). Hydrobiologia, 467, 215-228.

Schneider, D. P., Ammann, C. M., Otto-Bliesner, B. L., & Kaufman, D. S. (2009). Climate response to large, high-latitude and low-latitude volcanic eruptions in the Community Climate System Model. Journal of Geophysical Research: Atmospheres, 114, doi: 10.1029/2008JD011222

Schneider, T., Bischoff, T., & Haug, G. H. (2014). Migrations and dynamics of the intertropical convergence zone. Nature, 513, 45-57

Schnurrenberger, D., Russell, J., & Kelts, K. (2003). Classification of lacustrine sediments based on sedimentary components. Journal of Paleolimnology, 29, 141-154

Schug, G. R., Blevins, K. E., Cox, B., Gray, K., & Mushrif-Tripathy, V. (2013). Infection, disease, and biosocial processes at the end of the Indus Civilization. PLoS One, 8, e84814.

Schulting, R. (2010). Holocene environmental change and the Mesolithic-Neolithic transition in north-west Europe: revisiting two models. Environmental Archaeology, 15, 160-172

Schultze, E., & Niederreiter, R. (1990). Paläolimnologische Untersuchungen an einem Bohrkern aus dem Profundal des Mondsees (Oberösterreich). Linz Biological Contributions, 22: 231-235

Schwertmann, U. (1991). Solubility and dissolution of iron oxides. In Y. Chen & Y. Hadar (Eds.), Iron Nutrition and Interactions in Plants: "Proceedings of the Fifth International Symposium on Iron Nutrition and Interactions in Plants", 11–17 June 1989. Dordrecht: Springer Netherlands. 3-27

Sensoy, S., Demircan, M., Ulupinar, Y., & Balta, İ. (2008). Climate of Turkey. Climate of Turkey. 2007. Devlet Meteoroloji İşleri Genel Müdürlüğü, 13 Feb. 2009. http://www. dmi. gov. tr/index. aspx. [Last accessed: June 18]

Shala, S., Helmens, K. F., Jansson, K. N., Kylander, M. E., Risberg, J., & Löwemark, L. (2014). Palaeoenvironmental record of glacial lake evolution during the early Holocene at Sokli, NE Finland. Boreas, 43, 362-376

Shanahan, T. M., Overpeck, J. T., Hubeny, J. B., King, J., Hu, F. S., Hughen, K., Miller, G., & Black, J. (2008). Scanning micro-X-ray fluorescence elemental mapping: A new tool for the study of laminated sediment records. Geochemistry, Geophysics, Geosystems, 9. doi: 10.1029/2007GC001800

Shanahan, T. M., Overpeck, J. T., Wheeler, C. W., Beck, J. W., Pigati, J. S., Talbot, M. R., Scholz, C. A., Peck, J., & King, J. W. (2006). Paleoclimatic variations in West Africa from a record of late

Pleistocene and Holocene lake level stands of Lake Bosumtwi, Ghana. Palaeogeography, Palaeoclimatology, Palaeoecology, 242, 287-302

Shin, S.-I., Sardeshmukh, P. D., Webb, R. S., Oglesby, R. J., & Barsugli, J. J. (2006). Understanding the mid-Holocene climate. Journal of Climate, 19, 2801-2817

Shindell, D. T., Faluvegi, G., Miller, R. L., Schmidt, G. A., Hansen, J. E., & Sun, S. (2006). Solar and anthropogenic forcing of tropical hydrology. Geophysical Research Letters, 33. doi: 10.1029/2006GL027468

Shuraki, Y. D., & Sedgley, M. (1994). Effect of pistil age and pollen parent on pollen-tube growth and fruit production of pistachio. Journal of Horticultural Science, 69, 1019-1027

Sigl, M., Winstrup, M., McConnell, J. R., Welten, K. C., Plunkett, G., Ludlow, F., Büntgen, U., Caffee, M., Chellman, N., Dahl-Jensen, D., Fischer, H., Kipfstuhl, S., Kostick, C., Maselli, O. J., Mekhaldi, F., Mulvaney, R., Muscheler, R., Pasteris, D. R., Pilcher, J. R., Salzer, M., Schüpbach, S., Steffensen, J. P., Vinther, B. M., & Woodruff, T. E. (2015). Timing and climate forcing of volcanic eruptions for the past 2,500 years. Nature, 523, 543-546

Simola, H., Meriläinen, J. J., Sandman, O., Marttila, V., Karjalainen, H., Kukkonen, M., Julkunen-Tiitto, R., & Hakulinen, J. (1996). Palaeolimnological analyses as information source for large lake biomonitoring. Hydrobiologia, 322, 283-292

Simonneau, A., Chapron, E., Vannière, B., Wirth, S., Gilli, A., Di-Giovanni, C., Anselmetti, F., Desmet, M., & Magny, M. (2013). Mass-movement and flood-induced deposits in Lake Ledro, southern Alps, Italy: implications for Holocene palaeohydrology and natural hazards. Climate of the Past, 9, 825-840

Şimşek, F., & Çağatay, M. N. (2018). Late Holocene high resolution multi-proxy climate and environmental records from Lake Van, eastern Turkey. Quaternary International, 486, 57-72

Smith, V. H., & Schindler, D. W. (2009). Eutrophication science: where do we go from here? Trends in Ecology & Evolution, 24, 201-207

Smol, J. P., Birks, H., & Last, W. M. (2001). Tracking environmental change using lake sediments: Volume 3: Terrestrial, algal, and siliceous indicators (Vol. 3): Springer Science & Business Media.

Smol, J. P., & Stoermer, E. F. (2010). The diatoms: applications for the environmental and earth sciences. Cambridge University Press. 8-45

Sobek, S., Durisch-Kaiser, E., Zurbrügg, R., Wongfun, N., Wessels, M., Pasche, N., & Wehrli, B. (2009). Organic carbon burial efficiency in lake sediments controlled by oxygen exposure time and sediment source. Limnology and Oceanography, 54, 2243-2254

Sönmez, F. K., Komuscu, A. L. I. Ü., Erkan, A., & Turgu, E. (2005). An Analysis of Spatial and Temporal Dimension of Drought Vulnerability in Turkey Using the Standardized Precipitation Index. Natural Hazards, 35, 243-264

Stathakopoulos, D. C. (2017). Famine and pestilence in the late Roman and early Byzantine empire: a systematic survey of subsistence crises and epidemics: Routledge. 2-50

Staubwasser, M., & Weiss, H. (2006). Holocene climate and cultural evolution in late prehistoric–early historic West Asia. Quaternary Research, 66, 372-387

Steenburgh, W. J., Schultz, D. M., & Colle, B. A. (1998). The structure and evolution of gap outflow over the Gulf of Tehuantepec, Mexico. Monthly Weather Review, 126, 2673-2691

Steig, E. J. (1999). Mid-Holocene climate change. Science, 286, 1485-1487

Steinhilber, F., Beer, J., & Fröhlich, C. (2009). Total solar irradiance during the Holocene. Geophysical Research Letters, 36. doi: 10.1029/2009GL040142

Stenseth, N. C., Samia, N. I., Viljugrein, H., Kausrud, K. L., Begon, M., Davis, S., Leirs, H., Dubyanskiy, V. M., Esper, J., Ageyev, V. S., Klassovskiy, N. L., Pole, S. B., & Chan, K.-S. (2006). Plague

dynamics are driven by climate variation. Proceedings of the National Academy of Sciences, 103, 13110-13115

Stevens, L. R., & Dean, W. E. (2008). Geochemical evidence for hydroclimatic variability over the last 2460 years from Crevice Lake in Yellowstone National Park, USA. Quaternary International, 188, 139-148

Stevens, L. R., Wright, H. E., & Ito, E. (2001). Proposed changes in seasonality of climate during the Lateglacial and Holocene at Lake Zeribar, Iran. The Holocene, 11, 747-755

Stevenson, M. (2011). A 6600 year record of chlorophyll and carotenoid pigments from Cenote Yaal Chac, Yucatán Peninsular. 3rd year undergraduate project, University of Nottingham.

Stone, J. R. F., S. C. (2006). Multidecadal drought and Holocene climate instability in the Rocky Mountains. Geology, 34, 409-412

Street-Perrott, F., Holmes, J., Waller, M., Allen, M., Barber, N., Fothergill, P., Harkness, D., Ivanovich, M., Kroon, D., & Perrott, R. (2000). Drought and dust deposition in the West African Sahel: a 5500-year record from Kajemarum Oasis, northeastern Nigeria. The Holocene, 10, 293-302

Sturm, M., & Lotter, A. (1995). Lake sediments as environmental archives. EAWAG News E, 38, 6-9

Sugita, S. (1994). Pollen Representation of Vegetation in Quaternary Sediments: Theory and Method in Patchy Vegetation. Journal of Ecology, 82, 881-897

Sun, Q., Chu, G., Liu, J., & Gao, D. (2006). A 150-year Record of Heavy Metals in the Varved Sediments of Lake Bolterskardet, Svalbard. Arctic, Antarctic, and Alpine Research, 38, 436-445

Swain, A. M. (1978). Environmental changes during the past 2000 years in north-central Wisconsin: Analysis of pollen, charcoal, and seeds from varved lake sediments. Quaternary Research, 10, 55-68

Swierczynski, T., Brauer, A., Lauterbach, S., Martín-Puertas, C., Dulski, P., von Grafenstein, U., & Rohr C. . (2012). A 1600 yr seasonally resolved record of decadal-scale flood variability from the Austrian Pre-Alps. Geology, 40, 1047-1050

Swierczynski, T., Lauterbach, S., Dulski, P., Delgado, J., Merz, B., & Brauer, A. (2013). Mid- to late Holocene flood frequency changes in the northeastern Alps as recorded in varved sediments of Lake Mondsee (Upper Austria). Quaternary Science Reviews, 80, 78-90

Tarutani, T., Clayton, R. N., & Mayeda, T. K. (1969). The effect of polymorphism and magnesium substitution on oxygen isotope fractionation between calcium carbonate and water. Geochimica et Cosmochimica Acta, 33, 987-996

Taylor, G. T., Muller-Karger, F. E., Thunell, R. C., Scranton, M. I., Astor, Y., Varela, R., Ghinaglia, L. T., Lorenzoni, L., Fanning, K. A., Hameed, S., & Doherty, O. (2012). Ecosystem responses in the southern Caribbean Sea to global climate change. Proceedings of the National Academy of Sciences. doi: 10.1073/pnas.1207514109

Thomas, E. R., Wolff, E. W., Mulvaney, R., Steffensen, J. P., Johnsen, S. J., Arrowsmith, C., White, J. W. C., Vaughn, B., & Popp, T. (2007). The 8.2ka event from Greenland ice cores. Quaternary Science Reviews, 26, 70-81

Thornalley, D. J. R., Elderfield, H., & McCave, I. N. (2009). Holocene oscillations in temperature and salinity of the surface subpolar North Atlantic. Nature, 457, 711-714

Thunell, R., Pride, C., Tappa, E., & Muller-Karger, F. (1993). Varve formation in the Gulf of California: Insights from time series sediment trap sampling and remote sensing. Quaternary Science Reviews, 12, 451-464.

Tinner, W. L., A. F. (2001). Central European vegetation response to abrupt climate change at 8.2 ka. Geology, 29, 551-554.

Tomkins, J. D., Lamoureux, S. F., Antoniades, D., & Vincent, W. F. (2010). Autumn snowfall and hydroclimatic variability during the past millennium inferred from the varved sediments of meromictic Lake A, northern Ellesmere Island, Canada. Quaternary Research, 74, 188-198.

Toomey Michael, R., Curry William, B., Donnelly Jeffrey, P., & Hengstum Peter, J. (2013). Reconstructing 7000 years of North Atlantic hurricane variability using deep-sea sediment cores from the western Great Bahama Bank. Paleoceanography, 28, 31-41

Toprak, V., & Göncöoğlu, M. C. (1993). Tectonic control on the development of the Neogene-Quaternary Central Anatolian Volcanic Province, Turkey. Geological Journal, 28, 357-369

Torrence, C., & Compo, G. P. (1998). A Practical Guide to Wavelet Analysis. Bulletin of the American Meteorological Society, 79, 61-78

Torrentera, L., & Dodson, S. I. (2004). Ecology of the brine shrimp Artemia in the Yucatan, Mexico, Salterns. Journal of plankton research, 26, 617-624

Torrescano, N., & Islebe, G. (2006). Tropical forest and mangrove history from southeastern Mexico: a 5000 yr pollen record and implications for sea level rise. Vegetation History and Archaeobotany, 15, 191-195

Torrescano-Valle, N., & Islebe, G. A. (2015). Holocene paleoecology, climate history and human influence in the southwestern Yucatan Peninsula. Review of Palaeobotany and Palynology, 217, 1-8

Torsten, H., Hugo, C., Michael, F., Stephanie, J., Andreas, L., Christoph, M., Christian, O., Frank, S., Gerhard, H. S., Michael, W., Sabine, W., & Bernd, Z. (2007). Lateglacial and Holocene wet—dry cycles in southern Patagonia: chronology, sedimentology and geochemistry of a lacustrine record from Laguna Potrok Aike, Argentina. The Holocene, 17, 297-310

Toscano, M. A., & Macintyre, I. G. (2003). Corrected western Atlantic sea-level curve for the last 11,000 years based on calibrated 14C dates from Acropora palmata framework and intertidal mangrove peat. Coral Reefs, 22, 257-270

Touchan, R., Akkemik, Ü., Hughes, M. K., & Erkan, N. (2007). May–June precipitation reconstruction of southwestern Anatolia, Turkey during the last 900 years from tree rings. Quaternary Research, 68, 196-202

Touchan, R., Garfin, G. M., Meko, D. M., Funkhouser, G., Erkan, N., Hughes, M. K., & Wallin, B. S. (2003). Preliminary reconstructions of spring precipitation in southwestern Turkey from tree-ring width. International Journal of Climatology, 23, 157-171

Tracey, B., Lee, N., & Card, V. (1996). Sediment indicators of meromixis: comparison of laminations, diatoms, and sediment chemistry in Brownie Lake, Minneapolis, USA. Journal of Paleolimnology, 15, 129-132

Tranvik, L. J., Downing, J. A., Cotner, J. B., Loiselle, S. A., Striegl, R. G., Ballatore, T. J., Dillon, P., Finlay, K., Fortino, K., Knoll, L. B., Kortelainen, P. L., Kutser, T., Larsen, S., Laurion, I., Leech, D. M., McCallister, S. L., McKnight, D. M., Melack, J. M., Overholt, E., Porter, J. A., Prairie, Y., Renwick, W. H., Roland, F., Sherman, B. S., Schindler, D. W., Sobek, S., Tremblay, A., Vanni, M. J., Verschoor, A. M., von Wachenfeldt, E., & Weyhenmeyer, G. A. (2009). Lakes and reservoirs as regulators of carbon cycling and climate. Limnology and Oceanography, 54, 2298-2314

Trenberth, K. E. (1997). The definition of El Niño. Bulletin of the American Meteorological Society, 78, 2771-2777

Trenberth, K. E., & Shea, D. J. (2006). Atlantic hurricanes and natural variability in 2005. Geophysical Research Letters, 33. doi: 10.1029/2006GL026894

Trigo, I. F., Davies, T. D., & Bigg, G. R. (1999). Objective Climatology of Cyclones in the Mediterranean Region. Journal of Climate, 12, 1685-1696

Trigo, R. M., Osborn, T. J., Corte-Real, J. M. (2002). The North Atlantic Oscillation influence on Europe climate impacts and associated physical mechanisms. Climate Research, 20, 9-17

Trouet, V., Esper, J., Graham, N. E., Baker, A., Scourse, J. D., & Frank, D. C. (2009). Persistent Positive North Atlantic Oscillation Mode Dominated the Medieval Climate Anomaly. Science, 324, 78-81

Tsiamis, C., Poulakou-Rebelakou, E., Tsakris, A., & Petridou, E. (2011). Epidemic waves of the Black Death in the Byzantine Empire (1347–1453 AD). Infez Med, 19, 194-201

Tsimplis, M. N., & Josey, S. A. (2001). Forcing of the Mediterranean Sea by atmospheric oscillations over the North Atlantic. Geophysical Research Letters, 28, 803-806

Tsonis, A. (2009). Dynamical changes in the ENSO system in the last 11,000 years. Climate Dynamics, 33, 1069-1074

Tucker, M. E., & Wright, V. P. (1990). Carbonate Mineralogy and Chemistry Carbonate Sedimentology. Blackwell Publishing Ltd. 284-313

Türkeş, M., & Erlat, E. (2003). Precipitation changes and variability in Turkey linked to the North Atlantic oscillation during the period 1930–2000. International Journal of Climatology, 23, 1771-1796

Türkeş, M., Koç, T., & Sariş, F. (2009). Spatiotemporal variability of precipitation total series over Turkey. International Journal of Climatology, 29, 1056-1074

Turner, B. L., & Sabloff, J. A. (2012). Classic Period collapse of the Central Maya Lowlands: Insights about human–environment relationships for sustainability. Proceedings of the National Academy of Sciences, 109, 13908-13914

Turner, R., Roberts, N., & Jones, M. D. (2008). Climatic pacing of Mediterranean fire histories from lake sedimentary microcharcoal. Global and Planetary Change, 63, 317-324

Turner, R., Roberts, N., Eastwood, W. J., Jenkins, E., & Rosen, A. (2010). Fire, climate and the origins of agriculture: micro-charcoal records of biomass burning during the last glacial–interglacial transition in Southwest Asia. Journal of Quaternary Science, 25, 371-386

Turney, C. S., & Brown, H. (2007). Catastrophic early Holocene sea level rise, human migration and the Neolithic transition in Europe. Quaternary Science Reviews, 26, 2036-2041

Tzedakis, P. C. (2007). Seven ambiguities in the Mediterranean palaeoenvironmental narrative. Quaternary Science Reviews, 26, 2042-2066

Unal, Y. S., Deniz, A., Toros, H., & Incecik, S. (2012). Temporal and spatial patterns of precipitation variability for annual, wet, and dry seasons in Turkey. International Journal of Climatology, 32, 392-405

Valero-Garcés, B. L., Laird, K. R., Fritz, S. C., Kelts, K., Ito, E., & Grimm, E. C. (1997). Holocene Climate in the Northern Great Plains Inferred from Sediment Stratigraphy, Stable Isotopes, Carbonate Geochemistry, Diatoms, and Pollen at Moon Lake, North Dakota. Quaternary Research, 48, 359-369

Van Daele, M. M., J.; Silversmit, G.; Schmidt, S.; Fontijn, K.; Heirman, K.; Vandoorne, W.; De Clercq, M.; Van Acker, J.; Wolff, C.; Pino, M.; Urrutia, R.; Roberts, S.J.; Vincze, L.; De Batist, M. (2014). The 600 yr eruptive history of Villarrica Volcano (Chile) revealed by annually laminated lake sediments. GSA Bulletin, 126, 481-498

van Geel, B., Engels, S., Martin-Puertas, C., & Brauer, A. (2013). Ascospores of the parasitic fungus Kretzschmaria deusta as rainstorm indicators during a late Holocene beech-forest phase around lake Meerfelder Maar, Germany. Journal of Paleolimnology, 50, 33-40

van Hengstum, P. J., Reinhardt, E. G., Beddows, P. A., & Gabriel, J. J. (2010). Linkages between Holocene paleoclimate and paleohydrogeology preserved in a Yucatan underwater cave. Quaternary Science Reviews, 29, 2788-2798

Van Zeist, W., & Woldring, H. (1978). A postglacial pollen diagram from Lake Van in east Anatolia. Review of Palaeobotany and Palynology, 26, 249-276

van Zeist, W., & Bottema, S. (1991). Late Quaternary vegetation of the Near East. Reichert.

Vanhaverbeke, H., Vionis, N., Poblome, J., & Waelkens, M. (2009). What happened after the 7th century AD? A different Perspective on Post-Roman Rural Anatolia. Nederlands Instituut voor het Nabije Oosten

Vannière, B., Power, M. J., Roberts, N., Tinner, W., Carrión, J., Magny, M., Bartlein, P., Colombaroli, D., Daniau, A. L., Finsinger, W., Gil-Romera, G., Kaltenrieder, P., Pini, R., Sadori, L., Turner, R., Valsecchi, V., & Vescovi, E. (2011). Circum-Mediterranean fire activity and climate changes during the mid-Holocene environmental transition (8500-2500 cal. BP). The Holocene, 21, 53-73

Varem-Sanders, T. M. L., & Campbell, I. D. (1996). DendroScan: a tree-ring width and density measurement system. Northern Forestry Centre

Vasconcelos, C., & McKenzie, J. A. (1997). Microbial mediation of modern dolomite precipitation and diagenesis under anoxic conditions (Lagoa Vermelha, Rio de Janeiro, Brazil). Journal of Sedimentary Research, 67(3), 378-390

Verheyden, S., Nader, F. H., Cheng, H. J., Edwards, L. R., & Swennen, R. (2008). Paleoclimate reconstruction in the Levant region from the geochemistry of a Holocene stalagmite from the Jeita cave, Lebanon. Quaternary Research, 70, 368-381

Vermoere, M., Vanhecke, L., Waelkens, M., & Smets, E. (2003). Modern and ancient olive stands near Sagalassos (south-west Turkey) and reconstruction of the ancient agricultural landscape in two valleys. Global Ecology and Biogeography, 12, 217-235

Verschuren, D. (1999). Influence of depth and mixing regime on sedimentation in a small, fluctuating tropical soda lake. Limnology and Oceanography, 44, 1103-1113

von Rad, U., Schaaf, M., Michels, K. H., Schulz, H., Berger, W. H., & Sirocko, F. (1999). A 5000-yr Record of Climate Change in Varved Sediments from the Oxygen Minimum Zone off Pakistan, Northeastern Arabian Sea. Quaternary Research, 51, 39-53

Vos, H., Sanchez, A., Zolitschka, B., Brauer, A., & Negendank, J. F. W. (1997). Solar activity variations recorded in varved sediments from the crater lake of Holzmaar – a maar lake in the Westeifel volcanic field, Germany. Surveys in Geophysics, 18, 163-182

Wagner, D. M., Klunk, J., Harbeck, M., Devault, A., Waglechner, N., Sahl, J. W., Enk, J., Birdsell, D. N., Kuch, M., Lumibao, C., Poinar, D., Pearson, T., Fourment, M., Golding, B., Riehm, J. M., Earn, D. J. D., DeWitte, S., Rouillard, J.-M., Grupe, G., Wiechmann, I., Bliska, J. B., Keim, P. S., Scholz, H. C., Holmes, E. C., & Poinar, H. (2014). Yersinia pestis and the Plague of Justinian 541–543 AD: a genomic analysis. The Lancet Infectious Diseases, 14, 319-326

Wahl, D., Estrada-Belli, F., & Anderson, L. (2013). A 3400 year paleolimnological record of prehispanic human–environment interactions in the Holmul region of the southern Maya lowlands. Palaeogeography, Palaeoclimatology, Palaeoecology, 379–380, 17-31

Wahl, D., Byrne, R., & Anderson, L. (2014). An 8700 year paleoclimate reconstruction from the southern Maya lowlands. Quaternary Science Reviews, 103, 19-25

Wahl, D., Hansen, R. D., Byrne, R., Anderson, L., & Schreiner, T. (2016). Holocene climate variability and anthropogenic impacts from Lago Paixban, a perennial wetland in Peten, Guatemala. Global and Planetary Change, 138, 70-81

Walker, M., Head, M. H., Berklehammer, M., Bjorck, S., Cheng, H., Cwynar, L., Fisher, D., Gkinis, V., Long, A,. Lowe, J., Newnham, R., Rasmussen, S. O., & Weiss, H. (2018) Formal ratification of the subdivision of the Holocene Series/Epoch (Quaternary System/Period): two new Global Boundary Stratotype Sections and Points (GSSPs) and three new stages/subseries. Episodes, 41, 213-223

Wallace, D. J., Woodruff, J. D., Anderson, J. B., & Donnelly, J. P. (2014). Palaeohurricane reconstructions from sedimentary archives along the Gulf of Mexico, Caribbean Sea and

western North Atlantic Ocean margins. Geological Society, London, Special Publications, 388, 481-501

Wang, X., Auler, A. S., Edwards, R. L., Cheng, H., Ito, E., Wang, Y., Kong, X., & Solheid, M. (2007). Millennial-scale precipitation changes in southern Brazil over the past 90,000 years. Geophysical Research Letters, 34. doi: 10.1029/2007GL031149

Wanner, H., Beer, J., Bütikofer, J., Crowley, T. J., Cubasch, U., Flückiger, J., Goosse, H., Grosjean, M., Joos, F., Kaplan, J. O., Küttel, M., Müller, S. A., Prentice, I. C., Solomina, O., Stocker, T. F., Tarasov, P., Wagner, M., & Widmann, M. (2008). Mid- to Late Holocene climate change: an overview. Quaternary Science Reviews, 27, 1791-1828

Warren, J. K. (1996). Evaporites, brines and base metals: What is an evaporite? Defining the rock matrix. Australian Journal of Earth Sciences, 43, 115-132

Wassenburg, J. A., Dietrich, S., Fietzke, J., Fohlmeister, J., Jochum, K. P., Scholz, D., Richter, D. K., Sabaoui, A., Spötl, C., Lohmann, G., Andreae, Meinrat O., & Immenhauser, A. (2016). Reorganization of the North Atlantic Oscillation during early Holocene deglaciation. Nature Geoscience, 9, 602-606

Wauchope, R. (2014). Handbook of Middle American Indians, Volume 1: Natural Environment and Early Cultures: University of Texas Press

Webster, D. L. (2002). The fall of the ancient Maya: solving the mystery of the Maya collapse. Thames & Hudson New York.

Webster, J. W., Brook, G. A., Railsback, L. B., Cheng, H., Edwards, R. L., Alexander, C., & Reeder, P. P. (2007). Stalagmite evidence from Belize indicating significant droughts at the time of Preclassic Abandonment, the Maya Hiatus, and the Classic Maya collapse. Palaeogeography, Palaeoclimatology, Palaeoecology, 250, 1-17

Wei, W., & Lohmann, G. (2012). Simulated Atlantic Multidecadal Oscillation during the Holocene. Journal of Climate, 25, 6989-7002

Weiss, H., & Bradley, R. (2013). What drives societal collapse? The Anthropology of Climate Change: An Historical Reader, 151-160

Weltje, G. J., & Tjallingii, R. (2008). Calibration of XRF core scanners for quantitative geochemical logging of sediment cores: Theory and application. Earth and Planetary Science Letters, 274, 423-438

Weninger, B., Alram-Stern, E., Bauer, E., Clare, L., Danzeglocke, U., Jöris, O., Kubatzki, C., Rollefson, G., Todorova, H., & van Andel, T. (2006). Climate forcing due to the 8200 cal yr BP event observed at Early Neolithic sites in the eastern Mediterranean. Quaternary Research, 66, 401-420

White, D. A., & Hood, C. S. (2004). Vegetation patterns and environmental gradients in tropical dry forests of the northern Yucatan Peninsula. Journal of Vegetation Science, 15, 151-160

White, S. (2010). Rethinking disease in Ottoman history. International Journal of Middle East Studies, 42, 549-567

White, S. (2011). The climate of rebellion in the early modern Ottoman Empire. Cambridge University Press

Whitlock, C., & Larsen, C. (2001). Charcoal as a Fire Proxy. In J. P. Smol, H. J. B. Birks, W. M. Last, R. S. Bradley & K. Alverson (Eds.), Tracking Environmental Change Using Lake Sediments: Terrestrial, Algal, and Siliceous Indicators. Dordrecht: Springer Netherlands. 75-97

Whitmore, T. J., Brenner, M., Curtis, J. H., Dahlin, B. H., & Leyden, B. W. (1996). Holocene climatic and human influences on lakes of the Yucatan Peninsula, Mexico: an interdisciplinary, palaeolimnological approach. The Holocene, 6, 273-287

Whittaker, E. J. (1922). Bottom deposits of McKay Lake, Ottawa. Proceedings and Transactions of the Royal Society of Canada, 16, 143-159

Wick, L., Lemcke, G., & Sturm, M. (2003). Evidence of Lateglacial and Holocene climatic change and human impact in eastern Anatolia: high-resolution pollen, charcoal, isotopic and geochemical records from the laminated sediments of Lake Van, Turkey. The Holocene, 13, 665-675

Wilhite, D. A. (2000). Drought as a natural hazard: concepts and definitions. University of Nebraska

Willcox, G., Buxo, R., & Herveux, L. (2009). Late Pleistocene and early Holocene climate and the beginnings of cultivation in northern Syria. The Holocene, 19, 151-158

Williams, J. B., Schwab, M. J., & Brauer, A. (2012). An early first-century earthquake in the Dead Sea. International Geology Review, 54, 1219-1228

Wirth, S. B., Gilli, A., Simonneau, A., Ariztegui, D., Vannière, B., Glur, L., Chapron, E., Magny, M., & Anselmetti, F. S. (2013). A 2000 year long seasonal record of floods in the southern European Alps. Geophysical Research Letters, 40, 4025-4029

Wittkop, C. A. T., J. L.; Dean, W. E.; Guilderson, T. P. (2009). A lacustrine carbonate record of Holocene seasonality and climate. Geology, 37, 695-698

Woldring, H., & Cappers, R. (2001). The origin of the 'wild orchards' of Central Anatolia. Turkish Journal of Botany, 25(1), 1-9.

Woodbridge, J. (2009). Late-holocene lake diatom-inferred palaeoclimate from central Turkey. Phd Thesis. Plymouth University.

Woodbridge, J., & Roberts, N. (2010). Linking neo- and palaeolimnology: a case study using crater lake diatoms from central Turkey. Journal of Paleolimnology, 44, 855-871

Woodbridge, J., & Roberts, N. (2011). Late Holocene climate of the Eastern Mediterranean inferred from diatom analysis of annually-laminated lake sediments. Quaternary Science Reviews, 30, 3381-3392

Woodbridge, J., Roberts, N., & Cox, E. J. (2010). Morphology and ecology of a new centric diatom from Cappadocia (central Turkey). Diatom Research, 25, 195-212

Wright, H. E., Jr. (1993). Environmental Determinism in Near Eastern Prehistory. Current Anthropology, 34, 458-469

Wright, H. E., Mann, D. H., & Glaser, P. H. (1984). Piston Corers for Peat and Lake Sediments. Ecology, 65, 657-659

Wulf, S., Kraml, M., Brauer, A., Keller, J., & Negendank, J. F. W. (2004). Tephrochronology of the 100 ka lacustrine sediment record of Lago Grande di Monticchio (southern Italy). Quaternary International, 122, 7-30

Wulf, S., Ott, F., Słowiński, M., Noryśkiewicz, A. M., Dräger, N., Martin-Puertas, C., Czymzik, M., Neugebauer, I., Dulski, P., Bourne, A. J., Błaszkiewicz, M., & Brauer, A. (2013). Tracing the Laacher See Tephra in the varved sediment record of the Trzechowskie palaeolake in central Northern Poland. Quaternary Science Reviews, 76, 129-139

Xia, J., Haskell, B. J., Engstrom, D. R., & Ito, E. (1997). Holocene climate reconstructions from tandem trace-element and stable-isotope composition of ostracodes from Coldwater Lake, North Dakota, U.S.A. Journal of Paleolimnology, 17, 85-100

Xiao, J., Wu, J., Si, B., Liang, W., Nakamura, T., Liu, B., & Inouchi, Y. (2006). Holocene climate changes in the monsoon/arid transition reflected by carbon concentration in Daihai Lake of Inner Mongolia. The Holocene, 16, 551-560

Xoplaki, E., González-Rouco, J. F., Luterbacher, J., & Wanner, H. (2004). Wet season Mediterranean precipitation variability: influence of large-scale dynamics and trends. Climate Dynamics, 23, 63-78

Xoplaki, E., Fleitmann, D., Luterbacher, J., Wagner, S., Haldon, J. F., Zorita, E., Telelis, I., Toreti, A., & Izdebski, A. (2016). The Medieval Climate Anomaly and Byzantium: A review of the evidence

on climatic fluctuations, economic performance and societal change. Quaternary Science Reviews, 136, 229-252

Xu, C. Y., & Singh, V. P. (2001). Evaluation and generalization of temperature-based methods for calculating evaporation. Hydrological Processes, 15, 305-319

Xu, L., Liu, Q., Stige, L. C., Ben Ari, T., Fang, X., Chan, K.-S., Wang, S., Stenseth, N. C., & Zhang, Z. (2011). Nonlinear effect of climate on plague during the third pandemic in China. Proceedings of the National Academy of Sciences, 108, 10214-10219

Xu, L., Stige, L. C., Kausrud, K. L., Ben Ari, T., Wang, S., Fang, X., Schmid, B. V., Liu, Q., Stenseth, N. C., & Zhang, Z. (2014). Wet climate and transportation routes accelerate spread of human plague. Proceedings of the Royal Society B: Biological Sciences, 281, doi: 10.1098/rspb.2013.3159

Zahrer, J., Dreibrodt, S., & Brauer, A. (2013). Evidence of the North Atlantic Oscillation in varve composition and diatom assemblages from recent, annually laminated sediments of Lake Belau, northern Germany. Journal of Paleolimnology, 50, 231-244

Zebiak, S. E., Orlove, B., Muñoz, Á. G., Vaughan, C., Hansen, J., Troy, T., Thomson, M. C., Lustig, A., & Garvin, S. (2015). Investigating El Niño-Southern Oscillation and society relationships. Wiley Interdisciplinary Reviews: Climate Change, 6, 17-34

Zhang, D. D., Brecke, P., Lee, H. F., He, Y.-Q., & Zhang, J. (2007). Global climate change, war, and population decline in recent human history. Proceedings of the National Academy of Sciences, 104, 19214-19219

Zhang, D. D., Lee, H. F., Wang, C., Li, B., Pei, Q., Zhang, J., & An, Y. (2011a). The causality analysis of climate change and large-scale human crisis. Proceedings of the National Academy of Sciences, 108, 17296-17301

Zhang, D. D., Lee, H. F., Wang, C., Li, B., Zhang, J., Pei, Q., & Chen, J. (2011b). Climate change and large-scale human population collapses in the pre-industrial era. Global Ecology and Biogeography, 20, 520-531

Zhang, J., Holmes, J. A., Chen, F., Qiang, M., Zhou, A., & Chen, S. (2009). An 850-year ostracod-shell trace-element record from Sugan Lake, northern Tibetan Plateau, China: Implications for interpreting the shell chemistry in high-Mg/Ca waters. Quaternary International, 194, 119-133

Zhang, R., & Delworth, T. L. (2006). Impact of Atlantic multidecadal oscillations on India/Sahel rainfall and Atlantic hurricanes. Geophysical Research Letters, 33, doi: 10.1029/2006GL026267

Ziv, B., Saaroni, H., & Alpert, P. (2004). The factors governing the summer regime of the eastern Mediterranean. International Journal of Climatology, 24, 1859-1871

Zolitschka, B. (1991). Absolute dating of late Quaternary Lacustrine sediments by high resolution varve chronology. In J. P. Smith, P. G. Appleby, R. W. Battarbee, J. A. Dearing, R. Flower, E. Y. Haworth, F. Oldfield & P. E. O'Sullivan (Eds.), Environmental History and Palaeolimnology: Proceedings of the Vth International Symposium on Palaeolimnology. Dordrecht: Springer Netherlands. 59-61

Zolitschka, B. (1996). Image analysis and microscopic investigation of annually laminated lake sediments from Fayetteville Green Lake (NY, USA) Lake C2 (NWT, Canada) and Holzmaar (Germany): a comparison. Geological Society, London, Special Publications, 116, 49-55

Zolitschka, B. (2007). Varved lake sediments. In: Elias, S. (ed.) A Encyclopedia of Quaternary Science. Oxford: Elsevier. 3105-3114

Zolitschka, B., Francus, P., Ojala, A. E. K., & Schimmelmann, A. (2015). Varves in lake sediments – a review. Quaternary Science Reviews, 117, 1-

7. Appendix and supplementary material

Appendix A

Nar Gölü's varve microfacies dataset – including the composition and thickness of sublayers within the NAR01 and NAR10 master sequence, as collected through thin section microscopy – provided within the Excel Workbook:

Nar Golu - Varve microfacies - Thin section microscop.xlsx

Within this workbook, spreadsheets include data from sedimentary Units 1 and 4-5.

Appendix B

Yaal Chac's varve microfacies dataset – including the composition and thickness of sublayers within the YC14 master sequence, as collected through thin section microscopy – provided within the Excel Workbook:

Yaal Chac - Varve microfacies - Thin section microscop.xlsx

Within this workbook, spreadsheets include data from sedimentary Units 1 and 2.

Appendix C

Yaal Chac's raw Itrax µXRF geochemical data – provided within the Excel Workbook:

Yaal Chac - Itrax uXRF - YC14.xlsx

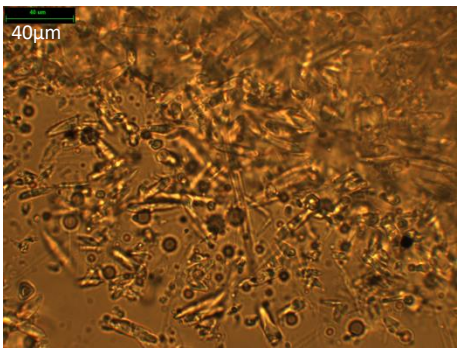
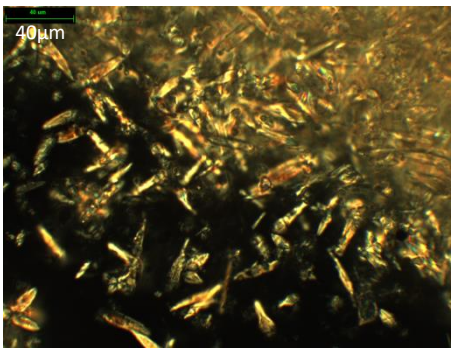
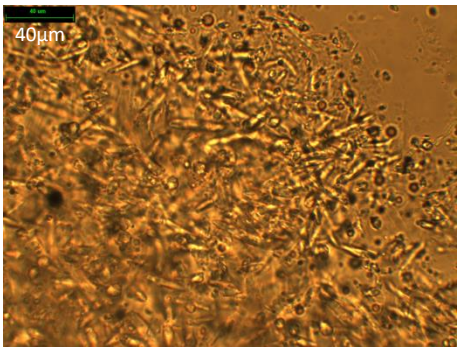
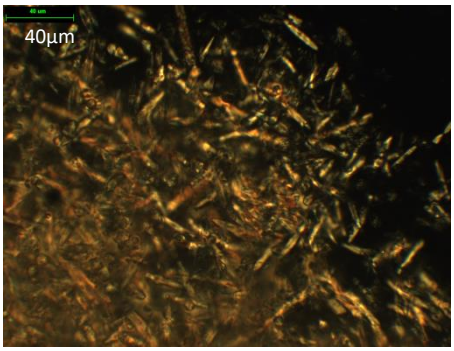
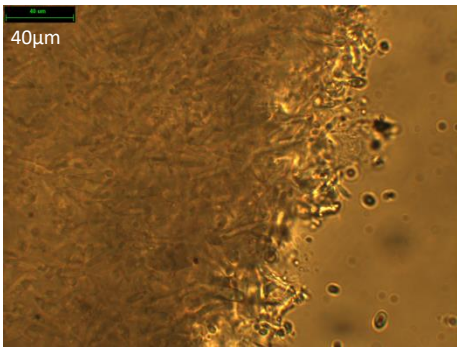
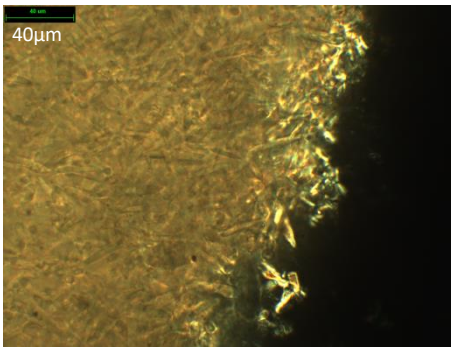
Appendix D

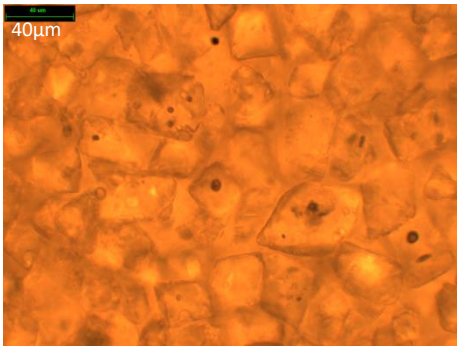
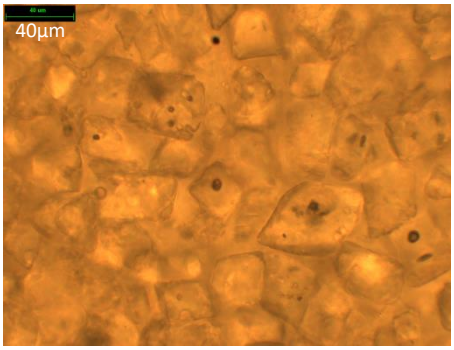
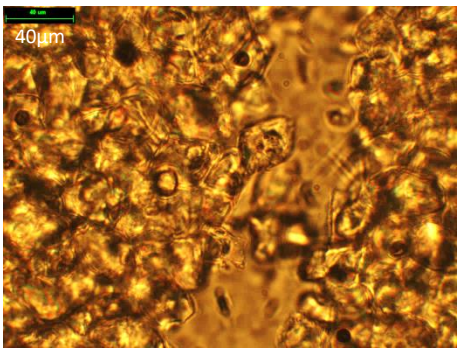
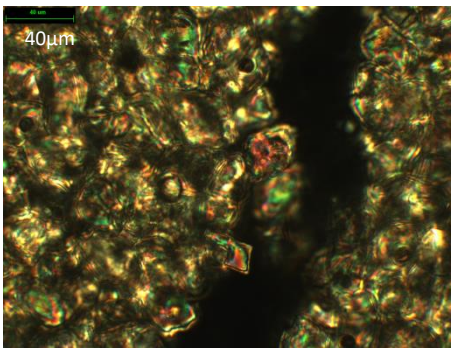
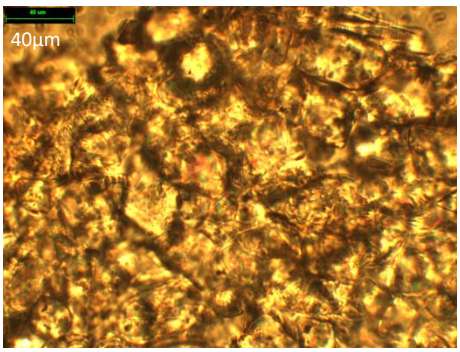
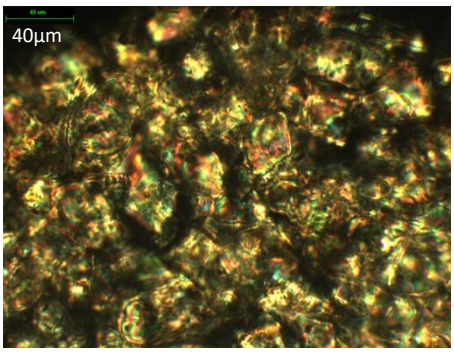
The following list describes the additional, unpublished datasets from Yaal Chac collected and analysed by past undergraduate students from the University of Nottingham, School of Geography:

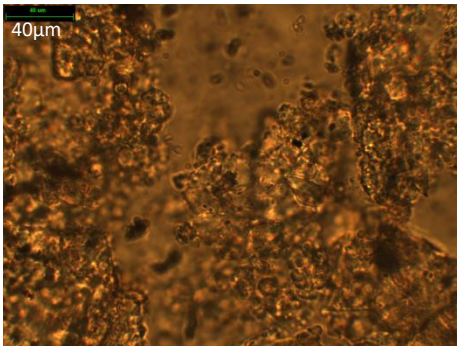
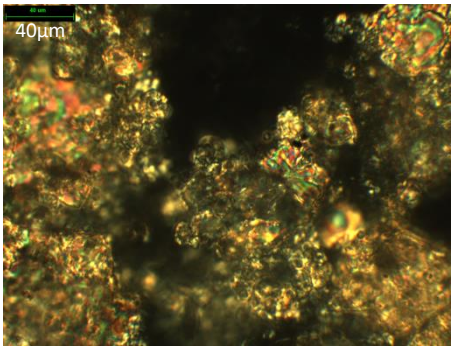
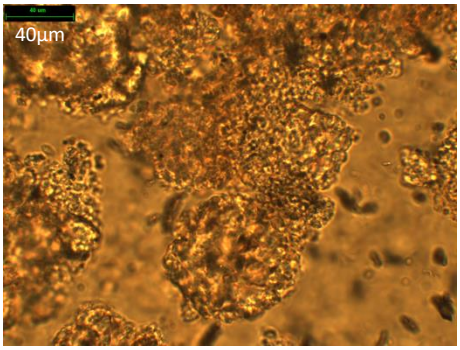
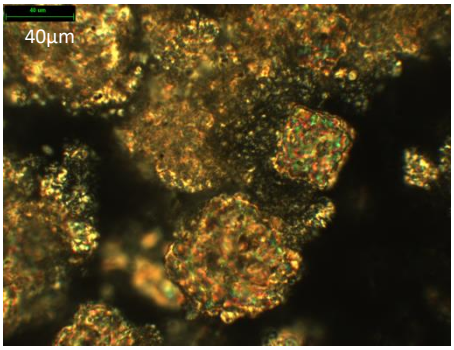
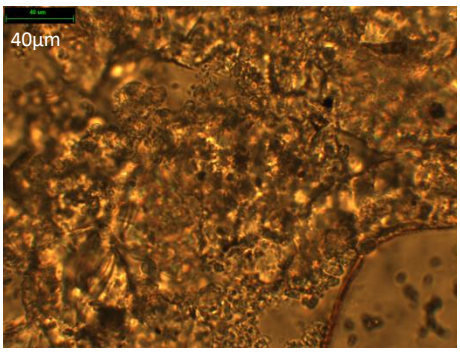
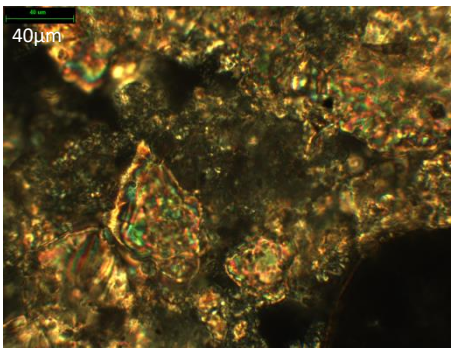
- **Stable isotope record** from carbonate material every 10cm through the YC11 core sequence (Hooper, 2015)
- **Charcoal record** from samples every 10cm through the YC11 core sequence (Harwood, 2015)
- **Organic pigment record** from samples every 5cm through the YC11 core sequence (Stevenson, 2014)
- **XRD mineralogical record** of samples every 10cm through the YC11 core sequence (Lem, 2011)

To request access to these datasets, please contact Prof Sarah Metcalfe (Sarah.Metcalfe@nottingham.ac.uk).

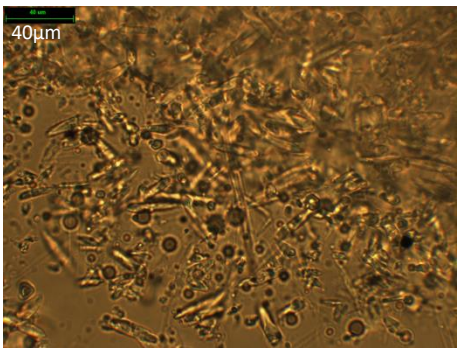
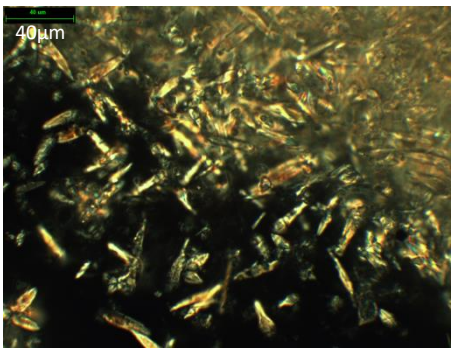
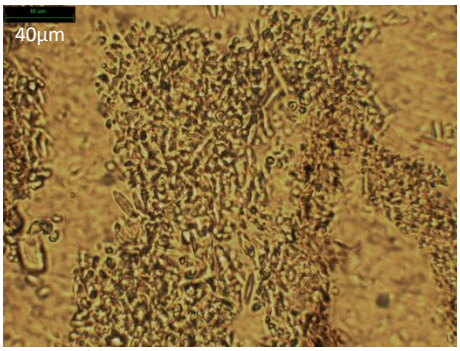
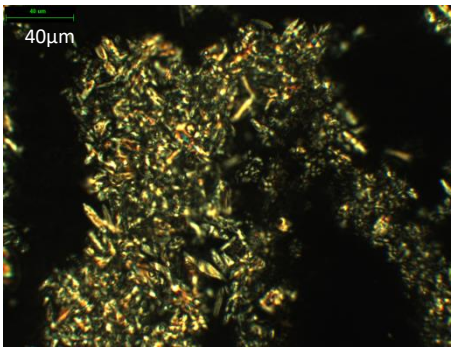
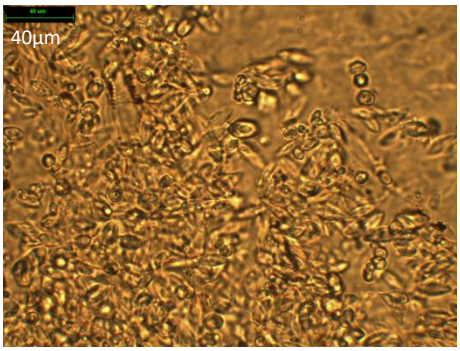
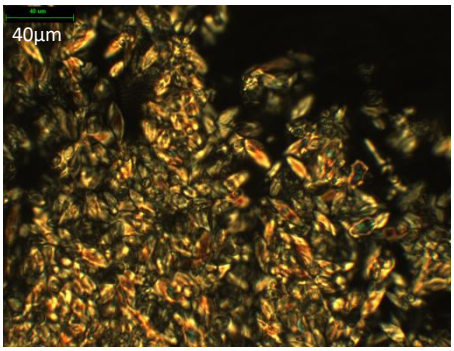
Supplementary material A *– Additional images of aragonite, calcite and dolomite minerals from* ***Nar Gölü****'s Unit 2 via thin section microscopy. The euhedral morphology of aragonite and calcite crystals enabled their mineralogy to be clearly differentiated within their homogenous sublayers. Plane- and cross-polarised images taken under 200x magnification using a petrographic microscope at the University of Nottingham.*

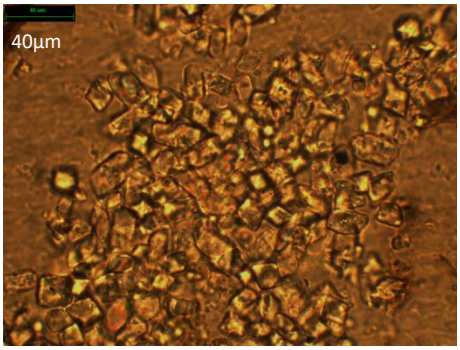
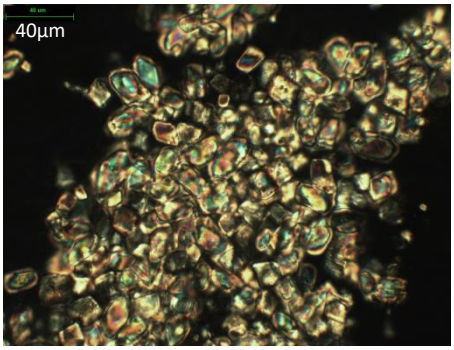
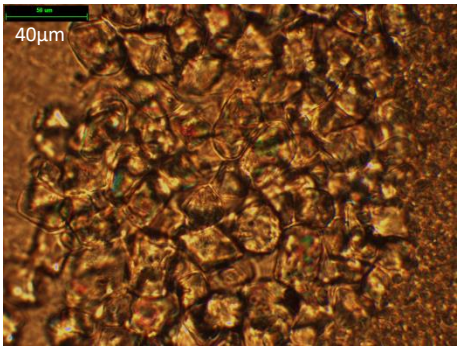
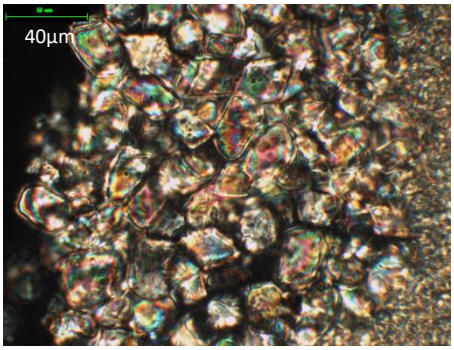
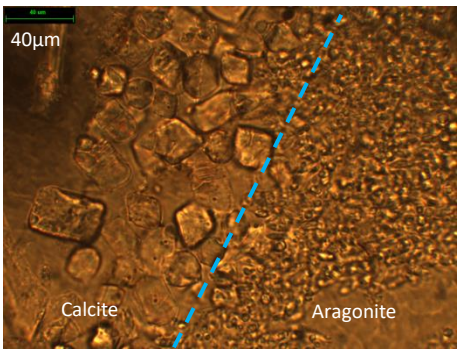
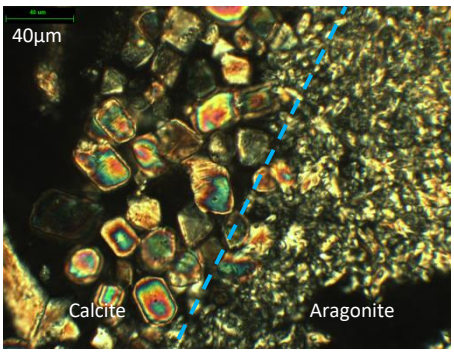
	Plane-polarised	Cross-polarised
Aragonite - Needle-shape characteristic of aragonite - Euhedral crystalline structure		
		
		

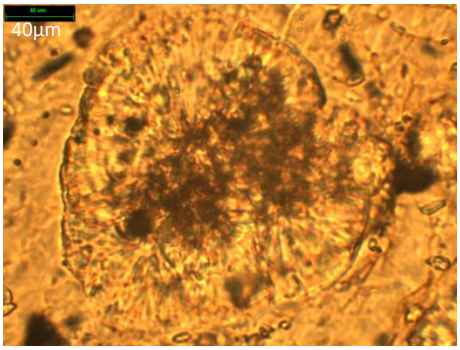
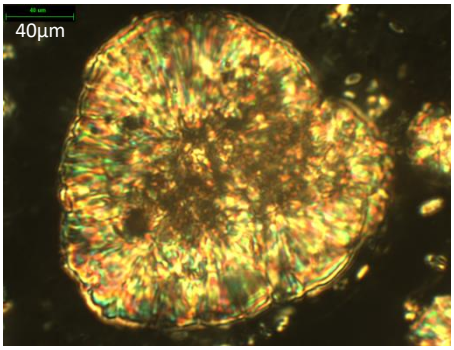
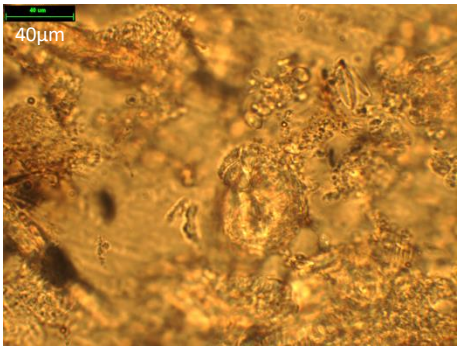
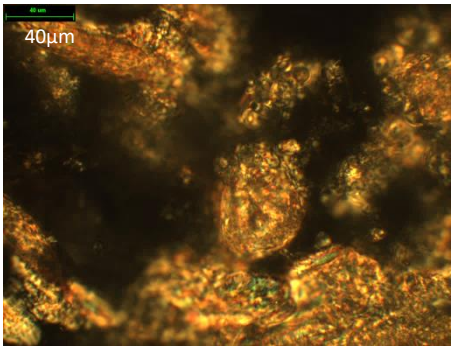
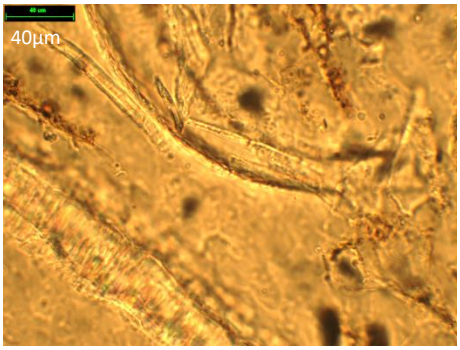
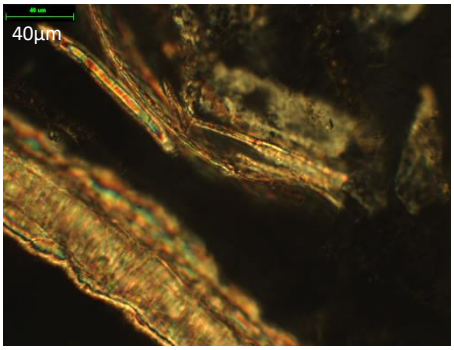
	Plane-polarised	Cross-polarised
Calcite - Rhombic-shape characteristic of calcite - Euhedral crystalline structure		
		
		

	Plane-polarised	Cross-polarised
Dolomite - Microstructures and anhedral crystalline structure indicative of diagenetic source - High concentration of Mg within material		
		
		

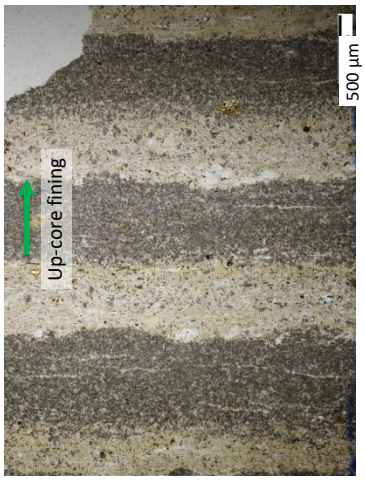
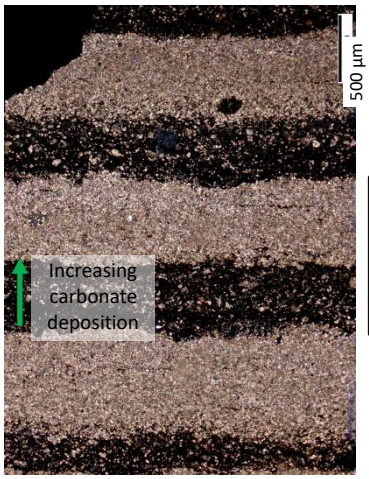
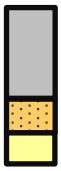
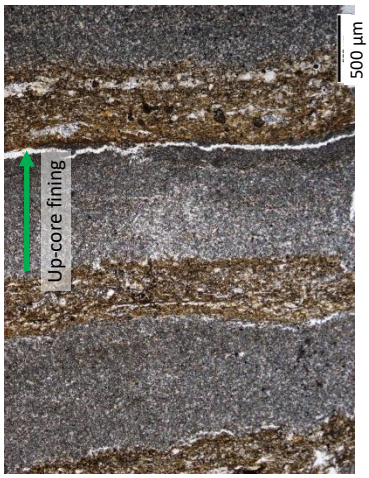
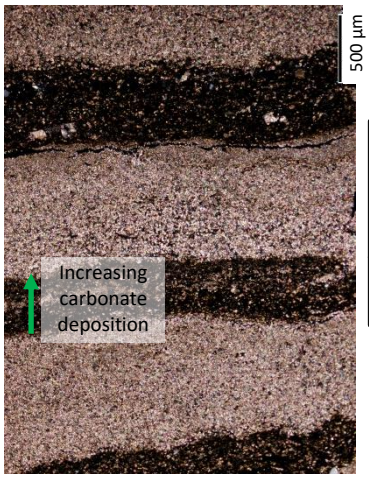
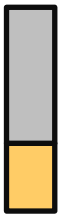
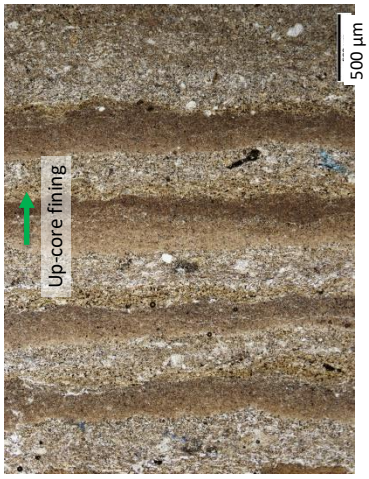
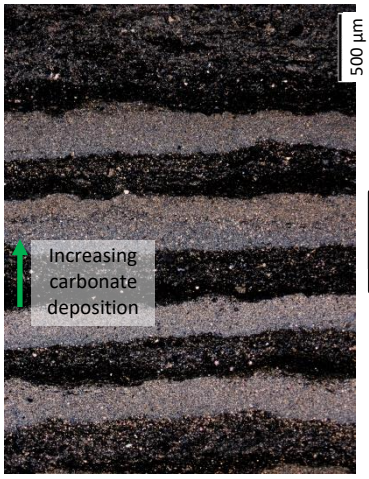
Supplementary material B *– Additional images of aragonite, calcite and detrital/peloidal carbonates from* ***Yaal Chac****'s Unit 2 via thin section microscopy. The euhedral morphology of aragonite and calcite crystals enabled their mineralogy to be clearly differentiated within their homogenous sublayers. Plane- and cross-polarised images taken under 200x magnification using a petrographic microscope at the University of Nottingham.*

	Plane-polarised	Cross-polarised
Aragonite - Needle-shape characteristic of aragonite - Euhedral crystalline structure		
		
		

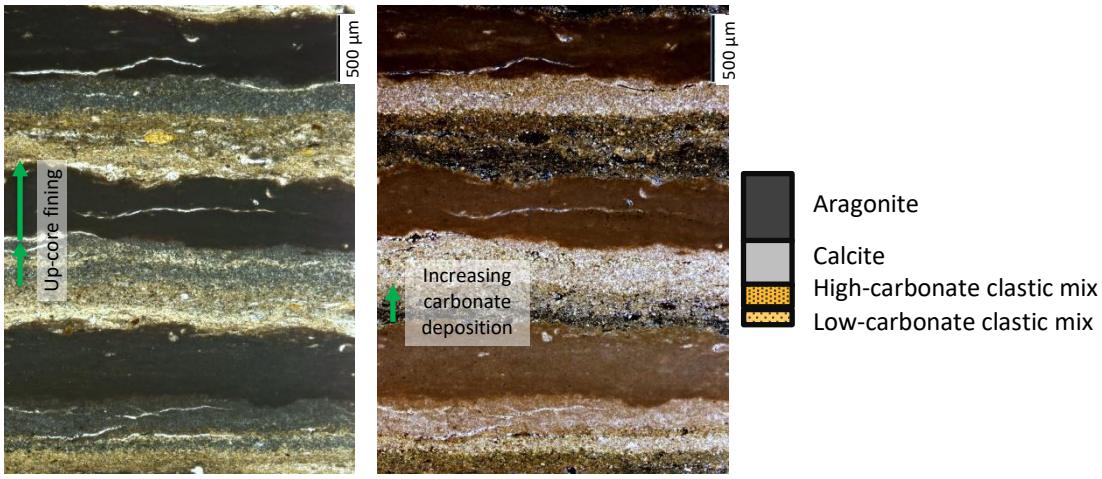
	Plane-polarised	Cross-polarised
Calcite - Rhombic-shape characteristic of calcite - Euhedral crystalline structure		
		
		

	Plane-polarised	Cross-polarised
Detrital/ peloidal carbonate - Irregular size and shape of carbonates - peloid grains may represent faecal pellets - linear grains may represent shell fragments		
		
		

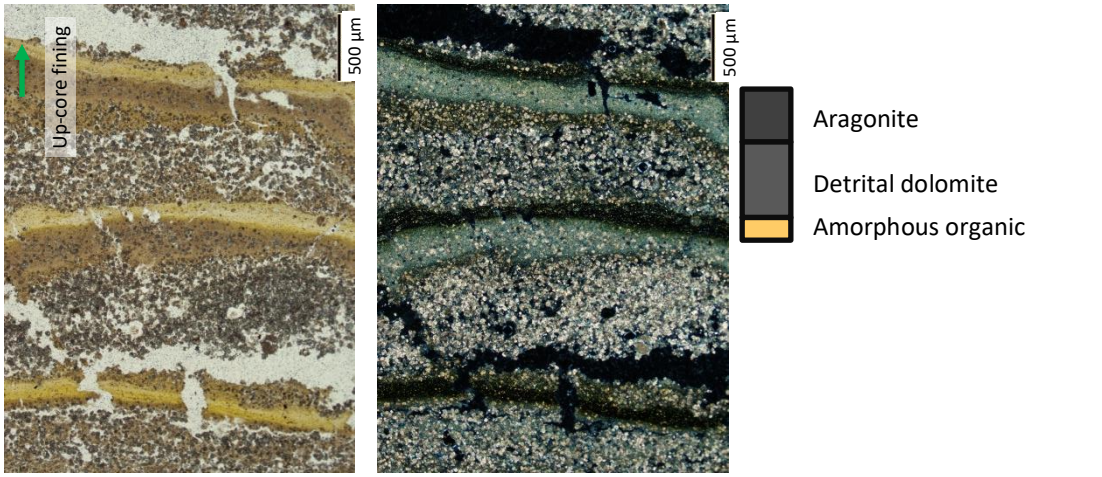
Supplementary material C *– Additional magnified (x4) images of typical varves from each of* ***Nar Gölü's*** *microfacies subclasses, as seen in plane-polarised (left) and cross-polarised (right) light. Coloured boxes display the extent of one varve, its distinct sublayers and the approximate boundaries measured; the colour and label of these boxes correspond with the conceptual diagram of microfacies (Table 3.7). All images are positioned such that the carbonate sublayers are deposited after the organic sublayers.*

	Plane polarised	*Cross polarised*	*Composition*
M1a			 Calcite Low-carbonate clastic mix Amorphous organic/diatoms
M1b			 Calcite Low-carbonate clastic mix
M2a			 Aragonite High-carbonate clastic mix Low-carbonate clastic mix

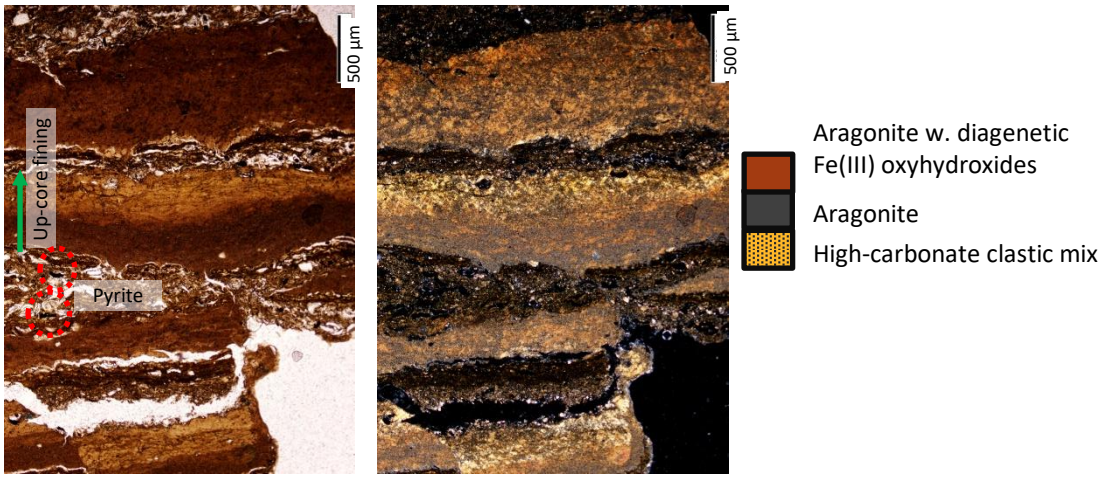
M2b


500 µm
Up-core fining
500 µm
Increasing carbonate deposition
Aragonite
Calcite
High-carbonate clastic mix
Low-carbonate clastic mix

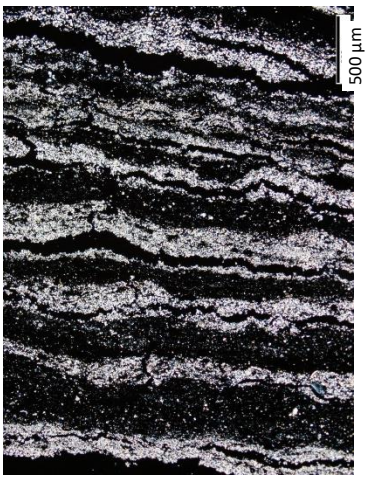
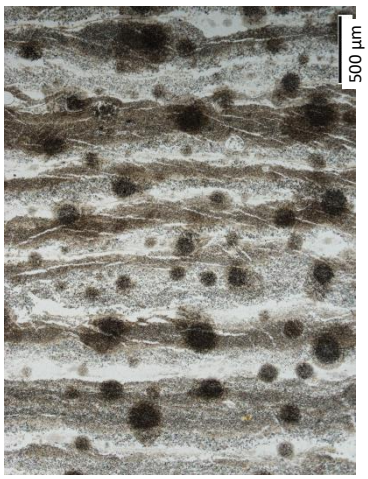
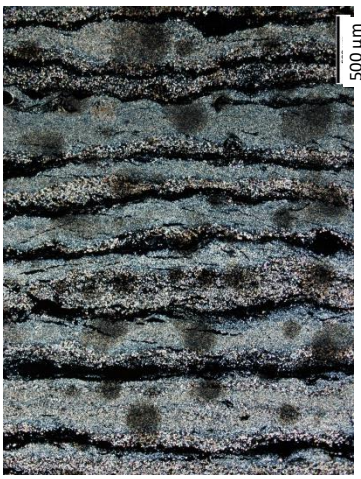
M2c


500 µm
Up-core fining
500 µm
Aragonite
Detrital dolomite
Amorphous organic

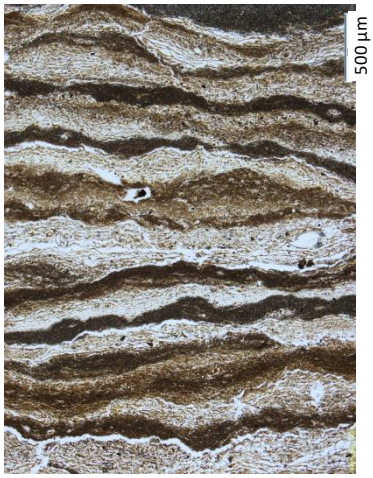
M3

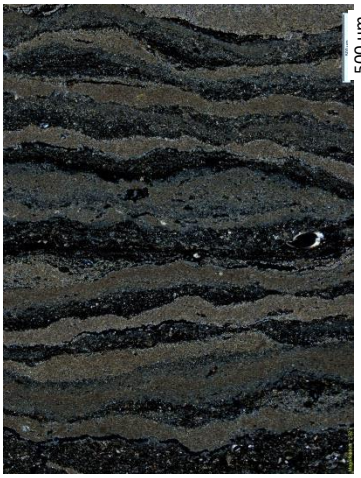

500 µm
Up-core fining
Pyrite
500 µm
Aragonite w. diagenetic Fe(III) oxyhydroxides
Aragonite
High-carbonate clastic mix

Supplementary material D *– Additional magnified (x4) images of typical varves from each of* ***Yaal Chac's*** *microfacies subclasses, as seen in plane-polarised (left) and cross-polarised light (right). Coloured boxes display the extent of one varve, its distinct sublayers and the approximate boundaries measured; the colour and label of these boxes correspond with the conceptual diagram of microfacies (Table 4.6). All images are positioned such that the carbonate sublayers are deposited after the organic sublayers.*

	Plane polarised	***Cross polarised***	***Composition***
M1a			 Calcite Bacterial mat
L1 *Non-varved*			 Aragonite Calcite Bacterial mat
M1b			 Aragonite Calcite Bacterial mat *Dark blotches represent air bubbles within the resin blocks, formed during the preparation of this thin section

M2a

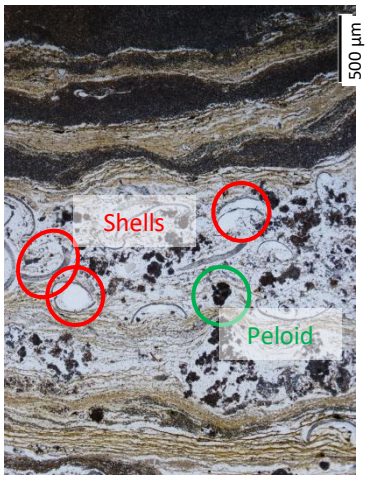


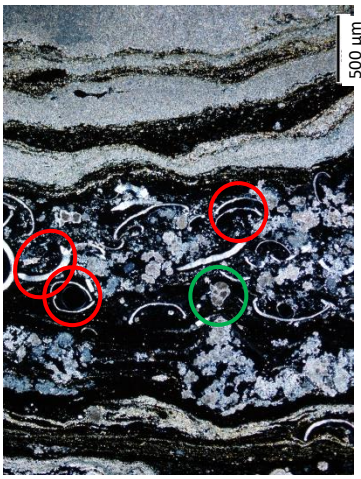


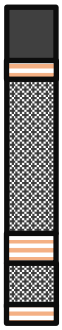


Aragonite
Bacterial mat

M2b





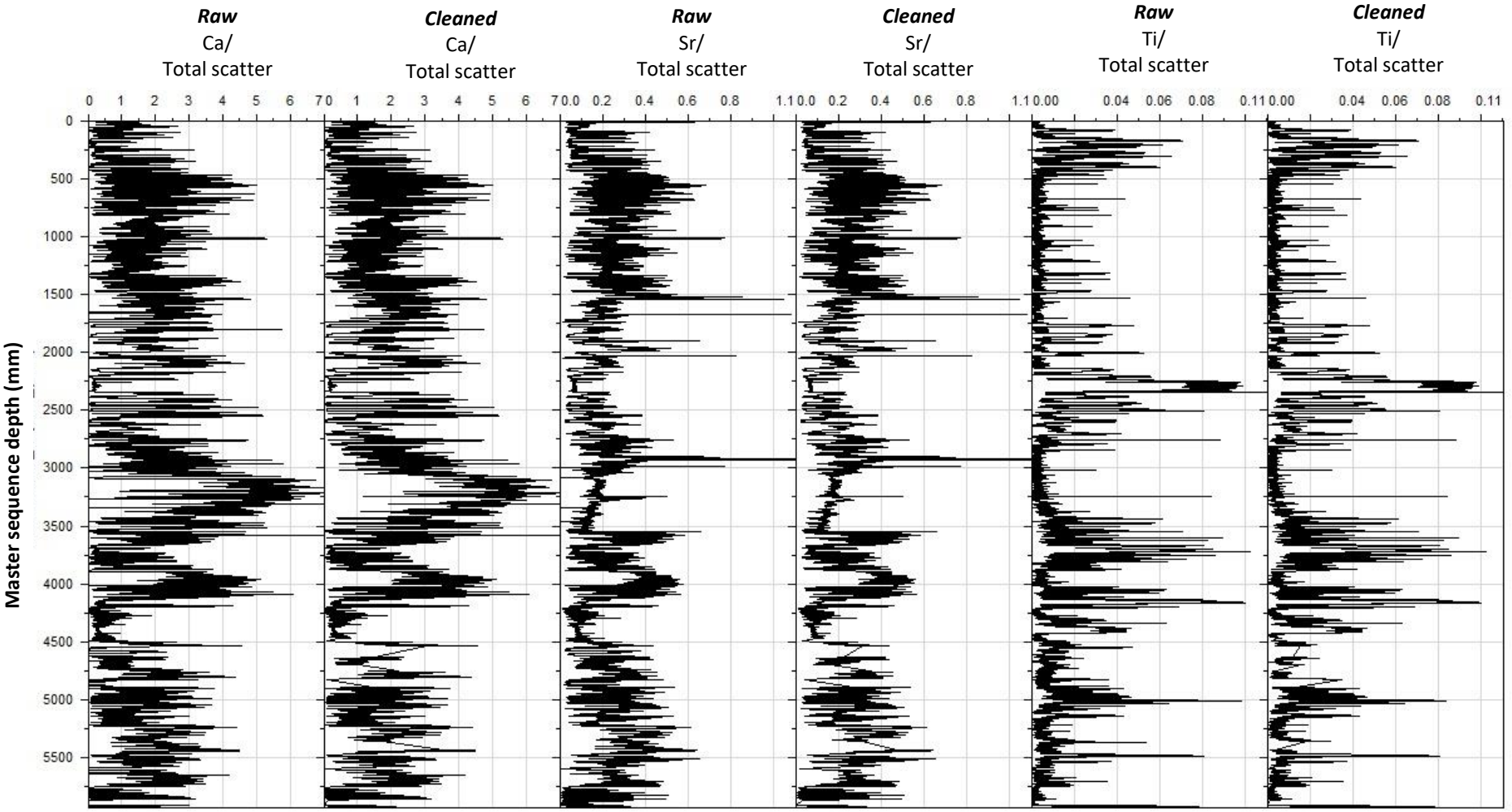


Aragonite
Bacterial mat

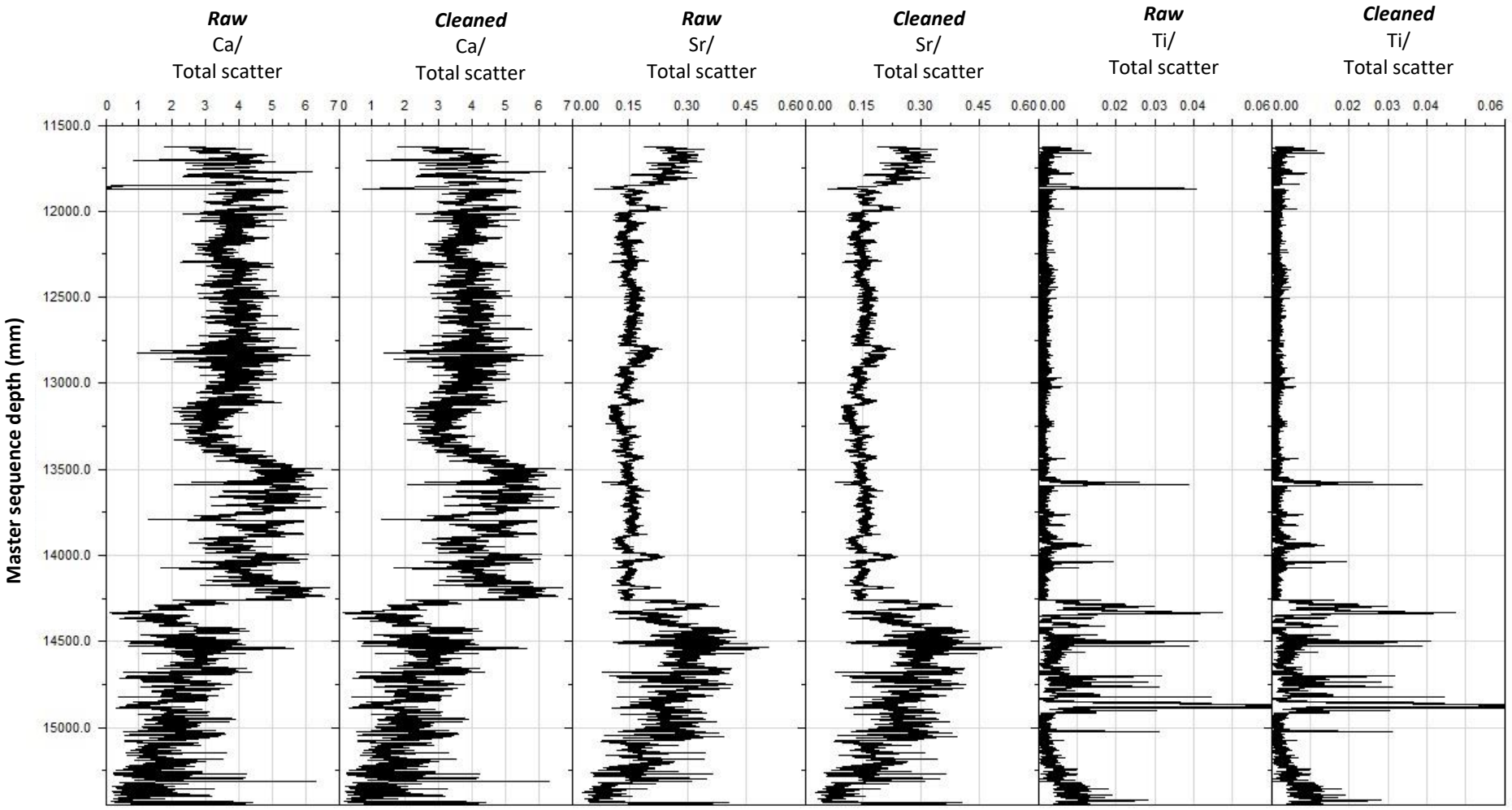
Peloids & detrital carbonates (inc. shell fragments)

Bacterial mat

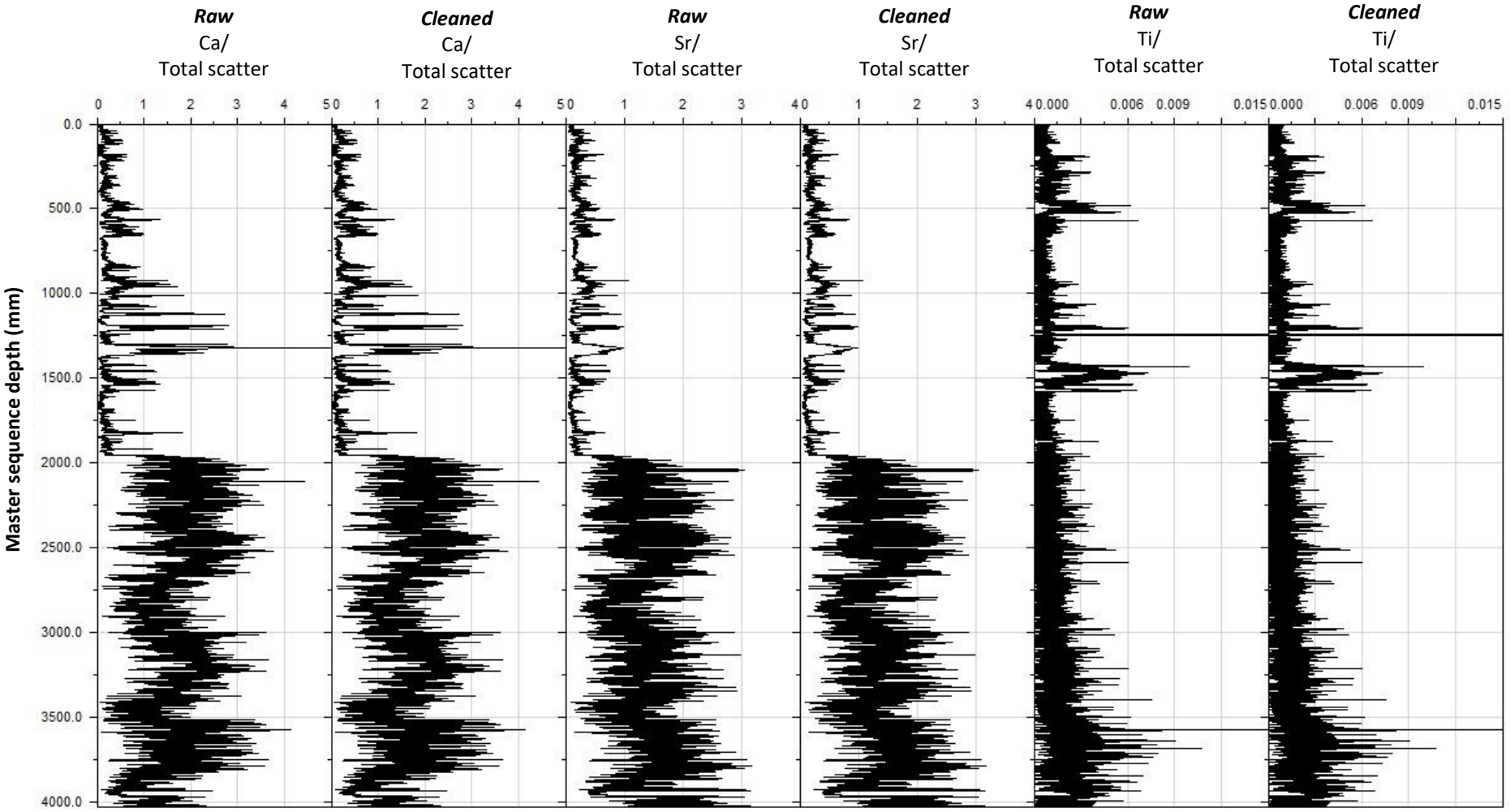
Bacterial mat



Supplementary material E *– Comparison between the raw and cleaned geochemical profiles of Ca, Sr, and Ti detection variability through Nar Gölü's Unit 1; all data presented has been normalised using total scatter, and the cleaned records pertain to the omission of invalid data (validity = 0). Comparison highlights that minimal data was lost when cleaning data.*



Supplementary material F *– Comparison between the raw and cleaned geochemical profiles of Ca, Sr, and Ti detection variability through Nar Gölü's Unit 4; all data presented has been normalised using total scatter, and the cleaned records pertain to the omission of invalid data (validity = 0). Comparison highlights that minimal data was lost when cleaning data.*



Supplementary material G *– Comparison between the raw and cleaned geochemical profiles of Ca, Sr, and Ti detection variability through Yaal Chac's full YC14 sequence; all data presented has been normalised using total scatter, and the cleaned records pertain to the omission of invalid data (validity = 0). Comparison highlights that minimal data was lost when cleaning data.*